UNIVERSITÉ DE STRASBOURG

École Doctorale de Physique et Chimie-Physique (ED182)

Institut de Physique et Chimie des matériaux de Strasbourg

(UMR 7504 CNRS-Unistra)

N° Ordre : 5878

THÈSE

présentée par :

Frédéric PAYET

Soutenue le : **03 février 2022**

pour obtenir le grade de :

Docteur de l'université de Strasbourg

Discipline/ Spécialité : Chimie-Physique des Matériaux

Exfoliation d'oxydes lamellaires fonctionnalisés : approches de synthèse et caractérisations avancées. Vers un réassemblage non-électrostatique

THÈSE dirigée par :

M. ROGEZ Guillaume	Dr., IPCMS (UMR7504 CNRS-Université de Strasbourg)

RAPPORTEURS :

M. FERRAGE Eric	Dr., IC2MP-Hydrassa (UMR7285 CNRS-Université de Poitiers)
M. FLEURY Benoit	Dr., IPCM (UMR8232 CNRS-Sorbonne Université)

AUTRES MEMBRES DU JURY :

Mme. DEMANGE Valérie	Dr., ISCR (UMR6226 CNRS-Université de Rennes)
Mme. PREVOT Vanessa	Dr., ICCF (UMR6296 CNRS-Université de Clermont-Ferrand)
Mme. BEGIN-COLIN Sylvie	Pr., IPCMS (UMR7504 CNRS-Université de Strasbourg)

MEMBRES INVITES :

M. SCHOSSELER François	Dr., ICS (UPR22 CNRS)
M. RABU Pierre	Dr., IPCMS (UMR7504 CNRS-Université de Strasbourg)

A mon frère Thomas

Remerciements

Au-delà du simple emploi, ces trois années de doctorat furent un moment d'apprentissage et de d'émerveillement scientifique. Remplie de journées à la paillasse, parsemée de discussions riches et prenantes, et complétée par de la lecture d'articles scientifiques, cette thèse fut des plus enrichissantes. J'ai découvert le fascinant monde des matériaux bidimensionnels, mêlant à la fois chimie expérimentale, celle analytique et la physique.

Au-delà du caractère scientifique, ce fut une expérience humaine. J'ai eu la chance de d'interagir avec bon nombres de personnes qui m'ont transmis leurs connaissances, aidé dans mon projet, partagé leur vision de la Science. Toutes ces rencontres ont contribué à la réussite de ce projet mais aussi à mon développement personnel. Ainsi, plus que de simples collègues, ce furent un mentor, des personnes inspirantes et des amis qui m'ont accompagné durant ce périple.

Pour tout cela, je tiens à vous remercier.

Un immense merci à Guillaume Rogez, mon directeur de thèse. Tout au long de ces trois années, j'ai adoré travaillé avec toi : entre les discussions de cinq minutes qui se transformèrent en réunion d'une heure, entre les différents congrès et les moments autour d'un verre ! Merci pour ta jovialité, ton honnêteté et ton empathie. Je me rends compte que j'eus la chance d'avoir un encadrant tant à l'écoute et passionné. Tu m'as tellement appris sur la façon de faire de la science. Tu m'as encouragé à tester mes idées et à m'amuser à la paillasse du labo. Tu as fait preuve de pédagogie et de bienveillance envers moi mais aussi envers tous les autres doctorants. Merci pour ces trois ans et pour cette rencontre formidable.

Je remercie François Schosseler pour sa précieuse contribution pour la diffusion de lumière, ce domaine complexe et passionnant que j'ai découvert avec lui. Je te remercie pour ton temps accordé et tes explications qui m'ont permis d'étoffer mon travail et mes connaissances.

Je remercie Pierre Rabu à la fois pour son accueil à l'IPCMS, en tant que directeur de l'institut, et aussi pour ses conseils et son aide sur mon sujet de thèse.

Un grand merci à Sylvie Bégin, qui fut tout à tour ma directrice d'école d'ingénieur, ma maître de stage ma collègue et ma présidente de jury. Je te remercie pour l'énergie que tu as mis au service ma formation à l'ECPM, pour l'aide apportée pour préparer le concours de l'école doctorale, pour les conseils apportés et aussi pour les moments de partage.

Je remercie les membres du jury Éric Ferrage, Benoit Fleury, Valérie Demange et Vanessa Prévot d'avoir jugé mon travail et de m'avoir octroyé le titre de docteur.

Je remercie Christine Tavio-Guého pour les mesures de PDF, Fabrice Leroux pour la RMN, Doru Constantin et Jérôme Combet pour les mesures de SAXS, Corinne Bouillet pour les images de TEM, Cédric Leuvrey pour les images de MEB, Mircea Rastei pour l'AFM, Anne Boos et Pascale Ronot pour l'analyse ICP-AES. Ce fut un plaisir de collaborer avec vous tous et sans votre participation, ce projet n'aurait pu être une telle réussite.

Je remercie Nathalie Viart pour l'accueil au sein du DCMI. Je te remercie pour ton écoute, tes conseils et ton enseignement en cristallographie. Merci d'avoir animé le DCMI et d'y avoir fait un département vivant.

Aux membres du DCMI, je vous remercie tous pour les discussions et l'aide apportée. Ce fut un plaisir de travailler à vos côtés et d'avoir partagé des moments d'échange à la paillasse, au détour d'un couloir, autour d'un café ou d'un repas. Je remercie Céline et Marie-Noëlle pour toute l'aide au fonctionnement du labo. Je remercie Cédric Leuvrey pour m'avoir formé au MEB et pour son aide en général. Merci aux anciens doctorants pour leurs conseils et les moments partagés (Geoffrey, Francis, Paula, Kévin, Florian, Kubra). Merci aux doctorants qui prennent la relève (Joanna, Yuhui, Joëlle, Wissal, Laurianne et bien d'autres).

Jtiens particulièrement à remercier mes amis (qui n'apprécient pas le terme « collègue » !) : Alex, Pier, Barbara et Guillaume. Ils ont coloré de joie et de rire ces trois années. Sans eux ce doctorat aurait été plus routinier et avec moins d'éclat. Merci pour toutes les discussions, des plus sérieuses au plus farfelues. Merci pour les moments au labo, au bar, en randonnée… j'espère que notre amitié continuera au-delà de cette parenthèse enchanté.

Je tiens à remercier ma famille qui m'a toujours soutenu et encouragé. Maman, Papa, Colas, Pipic, Manda, Anaïs, Fabien, Cynthia, Etienne, Emeline, Franck, Lana, j'aurai mille choses (et plus !) pour lesquelles vous remercier !

Enfin, merci à mon frère Thomas, qui a toujours été là et qui le sera toujours.

Table of Contents

Chapter I

General Introduction

Chapter I. General Introduction

I.1. The field of 2D materials

In the materials science landscape, nanoscale objects have taken a stunning and growing place.[1–4] The nanomaterials are distinguishable from their bulk homologous by new properties, arising from their size, their shape or their cooperative interactions *via* assembly. Apart from their composition and structure, the nanomaterials are classified according to their dimensionality. 0D materials such as nanoparticles or quantum dots, displays three nanoscale dimensions while 1D materials, such as nanotubes, are characterized by two nanoscale dimensions. Finally, 2D materials are plate-like particles which display one nanoscale dimension, assimilated to their thickness, and two larger ones, also called lateral sizes. An ideal 2D monolayer can be seen as the thinnest crystallite according to the c-axis, leading to a very large surface/thickness ratio, also named aspect ratio.[5] From the strong anisotropic shape of 2D materials arises their major interest: some of their physical properties also present anisotropic characteristic (*e.g.* electron transport in graphene) whereas their large surface make them chemically reactive and efficient in chemical reaction occurring at interfaces.

Optoelectronics constitutes one of the main fields of applications of 2D materials when they are integrated into nanodevices such as Field Effect Transistor.[6,7] The electron confinement and the modification of energy band structure (compared to the bulk) lead to changes in their electronic and absorption/emission properties. For instance, Transition Metal Dichalcogenides (TMD) nanosheets display a larger excitonic effect from which derives their optical response. Similarly, P. Ganter and B. Lotsch recently reviewed the optical tunability of nanosheets thin films:[8] the refractive index is related to the nature of the materials while the thickness of the film can be modulated by temperature, magnetic field or pH (***Figure 1***). A. Boileau *et al*, design a transparent and conductive thin film using 2D nanosheets as seed.[9] By the same way, these authors and other teams illustrate the processability of nanosheets: large millimeter scale substrate can be entirely and homogeneously coated by 2D materials [8–10]

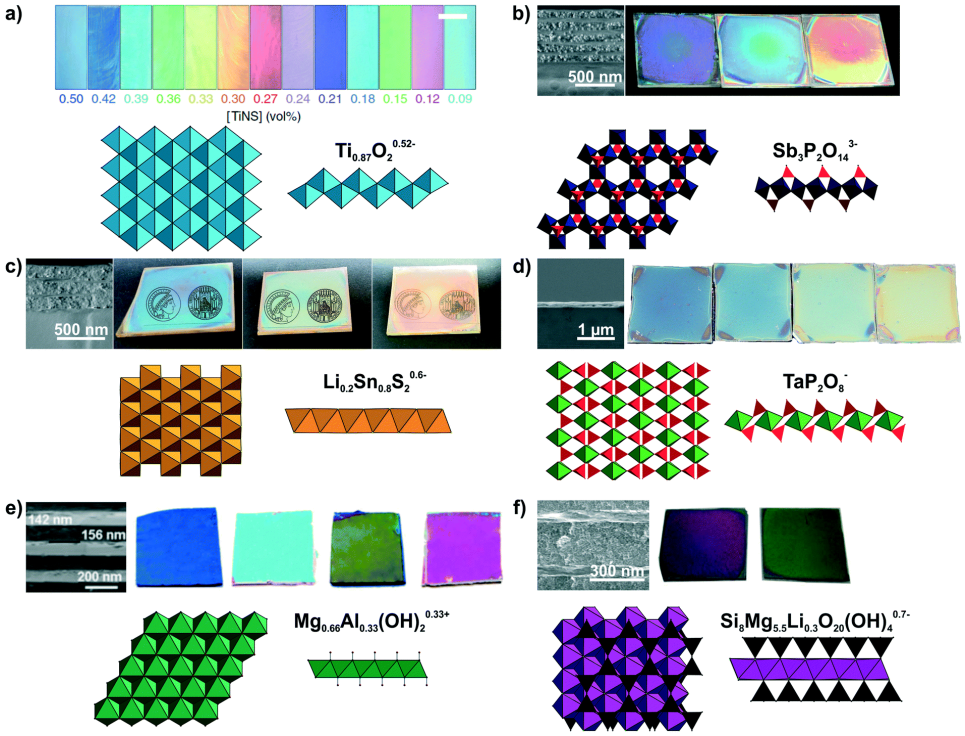

***Figure 1: Charged layered nanosheets, processed into thin films. The tuning of the color is made by film thickness modulation.*[8]**

In addition, plenty of other applications emerge, benefiting from the high surface area and/or the chemical reactivity of 2D materials. The photocatalysis, requiring crystalline and stable large-area materials, find in 2D materials suitable candidates especially as their band structure can be modulated.[11–13] Similarly, the challenges of energy storage might be overcome by integrating 2D materials to batteries, capacitors or solar cell.[14–16] For instance, C. Heard *et al* detailed the peculiar scope of transition metal oxides nanomaterial for energy application as they allow a significant stabilization of defects or non-stoichiometries due to flexibility of the 2D materials.[15] In addition, oxide nanosheets can combine redox, acid-base and catalytic properties. Finally, J. ten Elshof *et al* stressed on the sensing ability of 2D nanosheets when assembled or staked into porous systems.[17]

Nevertheless, the blooming of applications of 2D materials is only achievable by an intensive research on their synthesis. Up to now, many approaches haves been developed or are still in development to synthesize crystalline nanosheets, with peculiar efforts devoted to produce nanomaterials as large and thin as possible. Two families of synthesis are distinguishable from their starting point and the characteristic of the resulting nanosheets: the bottom-up and the top-down approaches. In the following, we will briefly describe the former while having a deeper look on top-down methods, also called exfoliation.

I.2. Synthesis of inorganic nanosheets

I.2.1 Bottom-up approach

As enounced above, the properties of the 2D materials are strongly correlated to their structure and composition at the nanoscale. Hence, the crystallinity and presence of defects have to be carefully controlled. The ideal approach to synthesize high-quality nanomaterials is the bottom-up one. Typically, the 2D materials are built from molecular or atomic precursors which react to form nuclei, subsequently grown until forming a monolayer. The nucleation and growth steps are determinant in the final morphology as a 3D growth mechanism can compete with the 2D one, leading to thick and/or non-homogeneous materials.

Some bottom-up physical techniques consist in the deposition of the nanomaterials onto a substrate with a controlled intake of precursor and the environment. One can quote the Pulsed-Laser Deposition (PLD)[18,19] or the Atomic Layer Deposition (ALD)[20] which allows to get submicrometer-large monolayer of a defined material. These two techniques are very popular in research field to deposit quasi defect-free oxide in epitaxial relation with the substrate. Nevertheless, this latter point constitutes the major limitations of these techniques, especially due to the reduced number of relevant substrate for applications, despite some recent works intend to circumvent such limitations.[21,22] The cost and non-scaling possibility are additional drawbacks of ALD or PLD.

As a counterpart, nanosheets can be synthesized in solution *via* chemical methods. A precise choice of the molecular precursor and of the synthesis conditions allows now to obtain a several 2D materials in colloidal state.[23] For instance, S. Carenco *et al.* investigated thoroughly the growth mechanism of the oxysulphur Gd_2O_2S nanoplatelets.[24] In addition, the wet bottom-up methods are more convenient for further use and integration of nanosheets into devices. However, some challenges still have to be overcome notably increasing the lateral size and extending the approach to a larger panel of materials.

Despite the high crystallinity of the 2D materials obtained, bottom-up approach cannot provide large and processable nanosheets in solution. Therefore, more suitable synthetic paths rely on the top-down approaches, mainly characterized by their diversity and versatility in terms of methods and nature of the nanosheets that can be obtained. In this work, we will not discuss on bottom-up approaches anymore even though the challenges in this field are appealing.

I.2.2 Top down-approach

I.2.2.1 The starting point: the layered materials

At the opposite to bottom-up approaches, the top-down approaches relies on producing 2D materials from their layered bulk equivalent, by delamination or exfoliation of the stacked layers. The nature and consequently the energy of the forces that held the layers together allow to define classes of

layered materials. In the following, we will describe the two main categories of layered materials as depicted in ***Figure 2*** but we mention that the panel of such materials is far more extended and rich. First, we will consider the layered materials for which the interlayer forces are short-range Van der Waals forces and then we will describe the ones where electrostatic forces dominate.

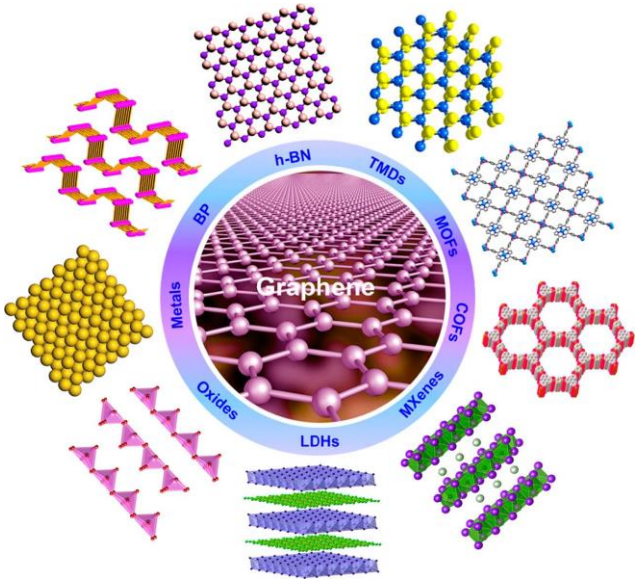

Figure 2: Schematic representation of different classes of 2D materials or their corresponding layered bulk which have been studied.[25]

I.2.2.2 Weakly-bonded layered materials

The iconic "Van der Waals" materials firstly obtained was graphene, from the exfoliation of graphite in 2004.[26] This homoatomic material, based on sp^2 carbon atom in a honeycomb structure, displays interesting properties such as a large electron mobility (15000 $cm^2.V^{-1}$ at 300 K).[26] Both its applications and its production have been extensively studied, which has boosted the field of quantum science in parallel.[27,28] Although graphene maintains its hegemony in the field of 2D materials, the synthesis of other 2D follows with also appealing properties.

Similarly to graphite, the Transition Metal Dichalcogenides (TMDs) are layered materials held by Van der Waals forces. With general formula MX_2, with M a transition metal (*e.g.* Mo, W to quote the most common) and X is a chalcogen element (*e.g.* S, Se or Te), TMDs constitute a large class of materials, ranging from metallic (NbS_2, VSe_2) to insulator (HfS_2) through semi-conducting (MoS_2, WS_2) behavior.[29] In addition, TMDs can crystallize in different structures. For instance, MoS_2 which is found in four forms (2H, 1T, 1T' and 3R) according to the arrangement of Mo and S layers.[1] Finally, unlike the inert graphene, TMDs are chemically reactive and some works report their surface modifications by molecules.[30,31]

Another homoatomic layered structure is black phosphorous, composed by phosphorous atoms arranged, in an a puckered honeycomb structure (orthorhombic crystal) where all the atoms are linked with three other phosphorous (three atoms in the same plane while the fourth one lies in a parallel one).[32]Considered as a graphene analogue and also called phosphorene, it displays a relatively high hole mobility (1000 $cm^2.V^{-1}s^{-1}$) and great mechanical properties.[33]

MAX phases have a general formula $M_{n+1}AX_n$ (n=1, 2 or 3) with M a transition metal, A an element from the IIIA or IVA group (e.g. Al, Si, Sn) and X either carbon or nitrogen. The corresponding 2D materials, called MXenes, are obtained by etching the A element from the structure, leaving metal carbide or nitride layers. These materials rise interest due to their electrical properties as they display a metallic behavior.[34,35]

Metal phosphorous trichalcogenides, also called transition metal hexathiohypodiphosphates with a general formula MPX_3 with M a transition metal and X either Sulphur or Selenium, are notably known to display ferroelectric and magnetic properties as for instance $NiPS_3$ but can also be applied in catalysis.[36–38]

These Van der Waals layered materials we presented above illustrate the structural and compositional diversity of 2D materials. Nonetheless, their main applications are usually restricted to the field of electronics and/or quantum devices. In the following of this work we will instead consider charged layered materials which possess a different and somehow extended field of applications.

I.2.2.3 Strongly-bonded layered materials

Contrary to Van der Waals materials, a large family of layered materials possess charged slabs, compensated by ions or slabs of opposite charge. These layered materials thus display charged species in between their layers which can be exchanged by incoming entities (ions, molecules, complexes, etc). The efficiency of such exchange is defined by the cation exchange capacity (CEC) *i.e.* the amount of species that can be replaced per mass of materials during an ion-exchange reaction. This property is related to the layer charge density, hence to the structure and composition of the materials. In addition to electrostatic, the driving force behind this exchange is a gradient of concentration between the interlamellar space and the surrounding media, considered as distinct. A usual analogy consists in imaging a semi-permeable membrane between the two spaces. Hence, charged species can migrate into the interlayer space as well as solvent molecules. In this latter situations, also called swelling, the distance between the inorganic layer can be hugely increased, even leading to the exfoliation. This mechanism will be discussed in more detail below. From this reactive interlayer species derives most of the uses of charged layered materials, also making their specificity compared to Van der Waals materials.

Clays are silicate layered materials in which one inorganic layer can be decomposed into sub-layers. In the case of 1:1 clays such as Serpentine or Kaolonite, one sub layer is constituted by SiO_4tetrahedra, sharing their corner and the other sub-layer is based on $Al(O_{6-n}OH_n)$ octahedra (or Mg equivalent), sharing their edges. The two distinct sub-units are joined by common oxygen. In the case of 2:1-type clays such as Montmorillonite or Hectorite, the alumina-based sub-layer is sandwiched between two silica sub-units. (***Figure 3 (a)***).[5] An isomorphous substitution of the Si^{4+} by Al^{3+} or Fe^{3+}, or Al^{3+} by Mg^{2+}, Fe^{2+} for instance can occur. This compositional modification leads to partial compensation of the negative charges, carried by the O atoms. Hence, the layers are negatively charged and the charge is compensated by exchangeable cations in the interlayer space. It is worth mentioning that if no substitution is done, there is no interlayer cation.

In addition to their natural abundance, clays minerals were thoroughly studied for their large swelling behavior. Therefore, before considering their 2D states, many works took advantages of clays' reactive interlayer spaces to insert cations, or a panel of molecules. At present day, 2D clay nanosheets are found in the field of catalysis, energy or composite materials.

Contrary to clay minerals, Layered Simple Hydroxides (LSHs) or Layered Double Hydroxides (LDHs) are positively charged layered. LSHs have the general formula $M_2(OH)_3X$ with M a divalent metallic cation (*e.g.* Co, Cu, Ni or Zn) and X an anionic species (e.g. NO_3^- Cl^-, $CH_3CO_2^-$).[39] LDHs have the general formula $[M^{2+}_{1-x}M^{3+}_x(OH)_2]^{x+}$ $(A^{n-})_{x/n}$, yH_2O with M^{2+} a divalent metallic cation (*e.g*. Mg, Zn, Ni, Fe or Cu), M^{3+} a trivalent metallic cation (*e.g.* Al, Fe or Mn) and A is the intercalated anion (***Figure 3 (b)***).[40] The layered hydroxides are obtained at relatively low temperature in liquid media. As clays minerals, LSHs and LDHs are intercalating compounds which have been modified from decades with organic molecules or negatively charged species. Nevertheless, LSH and LDH are known to be sensitive materials (*e.g*. to pH, temperature) and often poorly crystalline.

Nowadays, the use of layered hydroxides covers a wide range of applications from analytical,[41] to biomedical[42] or magnetic ones.[43,44]

Considering the extent of structural and compositional diversity of negatively charged layered oxides (to our knowledges, only one positively charged layered oxide is reported in literature),[45] it is impossible to draw a general formula and to exhaustively describe them.[3,46,47] Therefore, we restrict our topic to the nonetheless interesting layered oxides displaying an ABO_3 perovskite-like structure (A is a large cation from s, d or f block, B is a small transition metal). Mainly based on tantalum, niobium or titanium, the interlayer cation and charge density varies, defining three main families: the Dion-Jacobson $A'[A_{n-1}B_nO_{3n+1}]$, the Ruddlesden-Popper phase $A_2'[A_{n-1}B_nO_{3n+1}]$ displaying twice the number of interlayer cations compared to Dion-Jacobson and the Aurivillius phase $Bi_2O_2[A_{n-1}B_nO_{3n+1}]$ in which the interlayer space is filled with bismuth oxide.[46] The Aurivillius phases are usually converted into protonated Ruddlesden-Popper analogue by leaching the interlayer oxide by acid treatment, making their interlamellar space available for exchange reaction.

The synthesis of most of the perovskite-like layered oxide is performed *via* a solid state reaction. Despite this method does not belong to the trends of "green chemistry", their synthesis are quite well mastered, leading to a controlled crystallinity. Doping is even possible to tuned the properties or and functionalities to the layered oxides. As previous papers,[48,49] Y. Matsumoto *et al*. co-doped the layered oxide $K_2La_2Ti_3O_{10}$ with Er or Yb to confer two distinct emission bands in the visible to the native oxide.[50]

In addition to their thermal stability or their high dielectric constant, some of them display a ferroelectric behavior, which as many of their properties, arises from the distortion of the constitutive AO_6 octahedra.[51,52] However, according to M. Osada and T. Sasaki, maintaining these properties at the nanoscale are still challenging as polarization are considerably quenched when considering the monolayer.[4,53] However, they constitute ideal candidates for the future of dielectrics In addition the distortion of the structure into also results in acid-base properties which was judiciously used in catalytic applications in many work, especially the nanosheet forms of these oxides.[54–58]

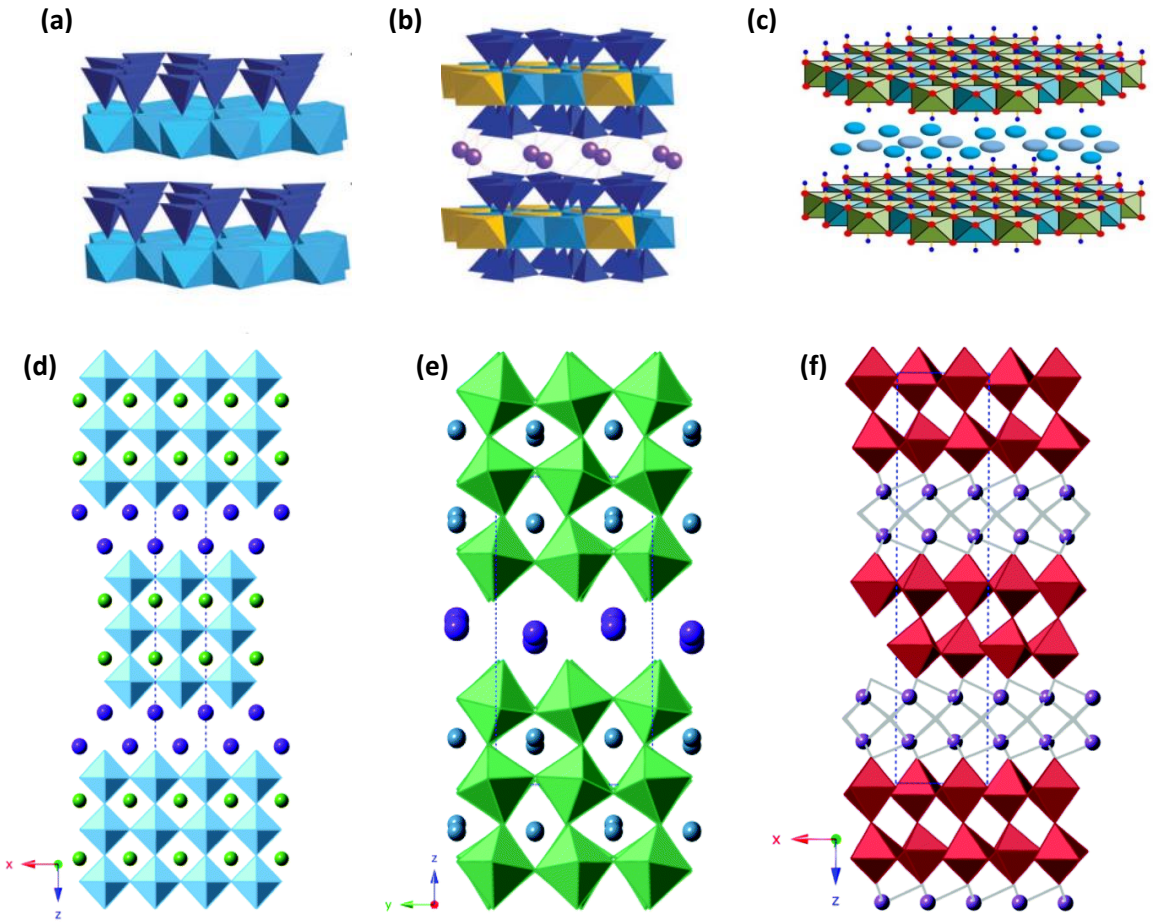

Figure 3: (a) Typical 1:1clays and (b) 2:1 clay[59] (c) Example of LDH[60] (d) to (f) Layered oxides with a perovskite-like structure with (c) a Dion-Jacobson phase A'[$A_{n-1}B_nO_{3n+1}$], (d) the Ruddlesden-Popper phase $A_2'[A_{n-1}B_nO_{3n+1}]$ and (e) an Aurivillius phase $Bi_2O_2[A_{n-1}B_nO_{3n+1}]$.[46]

Among all the layered materials we described, our team bet on the potentially of perovskite-like layered oxides. Contrary to Van der Waals materials, the post-synthesis chemistry resulting from these charged layered materials is very broad, especially their interlayer space while displaying a structural stability against temperature, pH change, reductive atmosphere unlike LDHs. Therefore, the scope of this work is limited to perovskite-like oxides, even if we will sporadically consider other layered materials (*e.g.* graphene).

I.2.2.4 Exfoliation methods

In order to obtain single nanosheets, the corresponding layered materials must be exfoliated *i.e.* the cohesive forces between adjacent slabs must be broken. Many teams have devoted their work to optimize the exfoliation process and experimental conditions to preserve the crystallinity of the bulk layered materials and their lateral size. Each exfoliation method among the existing panel is often dedicated to a restricted family of layered materials and no universal exfoliation process can be found. Hence, for some category of layered materials the choice is quite limited as depicted below. In the following, we will present the main exfoliation processes which are up to now used to produced 2D

materials but a more complete benchmark is resumed in ***Recently,*** J. ten.Elshof *et al.* reported the immediacy of the exfoliation in contrast with others works[99]

Table 1.

For Van der Waals, the micromechanical cleavage (commonly named Scotch-tape method) has allowed historically to obtain graphene and to deposit it on a substrate. Typically, a macroscopic crystal of a bulk layered materials is peeled with an adhesive Scotch-Tape, a perpendicular mechanical force is applied on the layers, leaving the intralayer bonds untouched. The process is repeated several times to reach the thinnest slab as possible. Then, the graphene is transferred to a substrate, using a second less adhesive Scotch tape.[26,27,61] After its applications to graphene, micromechanical cleavage was extended to TMDs and other materials followed.[62,63] This method is mainly dedicated to academic research on Van der Waals materials as it cannot be scaled-up to industrial production of nanosheets.

Exfoliation method	Materials	Advantages	Drawback	Ref
Micromechanical cleavage	Van der Waals (e.g. graphite, TMD)	Large area flakes Fast	Poor control of the flakes thickness and size Non-homogeneous deposition Non-scalable	26,61–63
Ball-milling	Graphite, Boron-nitride, Black phosphorous	Scalable	No size control Induction of defects	64–67
Sonication-assisted liquid exfoliation	Van der Waals materials (*e.g*. graphite, TMDs)	Liquid media High exfoliation yield Scalable	Induction of defects Poor shape and size control	68–72
Shear force assisted liquid exfoliation	Van der Waals materials (*e.g.* graphite, TMDs)	Liquid media High exfoliation yield Scalable	Poor shape and size control	70,73–79
Selective etching	MAX	Mostly monolayer Large area nanosheets High exfoliation yield	Use of corrosive chemical (HF, LiF, NaF) Need an additional ultrasound ion-exchange step	34,35,80
Intercalation / Electrochemical exfoliation	Van der Waals (*e.g*. graphite, TMD)	High yield Mostly single nanosheets	Small surface area Sensitive intercalant and dangerous process	81–86
Ion exchange	Charged layered oxide (*e.g*. layered titanates, layered perovskite) MAX	Large area nanosheets No damage of the structure High exfoliation yield	Long reaction time* Exfoliating agent can be inconvenient for further use	10,87–96
Microfluidization	Graphite	Mild conditions, low defect High exfoliation yield	Only applied for graphene production	97,98

*Recently, J. ten.Elshof *et al.* reported the immediacy of the exfoliation in contrast with others works[99]

Table 1: Exfoliation methods for the production of 2D materials

Contrary to dry methods such as micromechanical cleavage or sometimes ball-milling, exfoliation in liquid media allows a scalable production of large quantity 2D materials. Hence, the resulting nanosheets can be handled more easily for applications, from deposition on a substrate to as-synthesized

inks. Among the wet-processes, sonication-assisted exfoliation was extensively developed, especially for the production of graphene and 2D transition metal dichalcogenides.[27,68,69,71,85,100] Typically, the layered material is poured in a solvent, with or without surfactants, which is then sonicated by a sonication tip or bath. The cavitation forces which arise *i.e.* the collapsing of microbubble in the vicinity of the layered materials, lead to opposite mechanical forces on two adjacent layers. Even though many parameters such as solvent, sonication mode and power, and exfoliation time have to be carefully adjusted,[101] a large quantity of few-layer nanosheets can be obtained in a few hours, in a colloidal state. Nevertheless, inherent damages and defects accompany the nanosheets, as the process is violent, and fragmentation may occur, leading to smaller nanosheets compared to the initial crystal size. Moreover, the exfoliation process is always followed by centrifugation steps, either to only remove non-exfoliated materials or to make a size selection.[102]

Another mechanically-assisted liquid exfoliation was developed by J. Coleman *et al.* to circumvent the defect induction and fragmentation of sonication.[73] Shear-force-assisted liquid exfoliation consists in applying shear force on the layered material whose slabs glide one from the other. The same authors also investigated the scalable production of graphene with a peculiar care on defects at the final stage. They proved the efficiency of shear-force compared to sonication despite the need of an important optimization of the experimental parameters: indeed exfoliation time, concentration of the initial materials, shear rate, solvent, working volume can be tuned to reach the highest degree of exfoliation.[70] Besides, this work shows that the size and thickness of the resulting nanomaterials also derive from the precise control of these parameters. Subsequent works modeled the shear-force exfoliation of Van der Waals materials to confirm some experimental hypotheses such as the existence of a minimum shear rate.[103–105] Shear-force exfoliation is now extended to a plethora of Van der Waals materials.[75,76,106,107]

Even though the technique is comparable to sonication in terms of yield for graphene, its performance are less impressive with TMDs.[101] In addition, shear-force assistance also inherits the same drawbacks as sonication *i.e.* fragmentation of the sheets and need to remove unexfoliated materials.

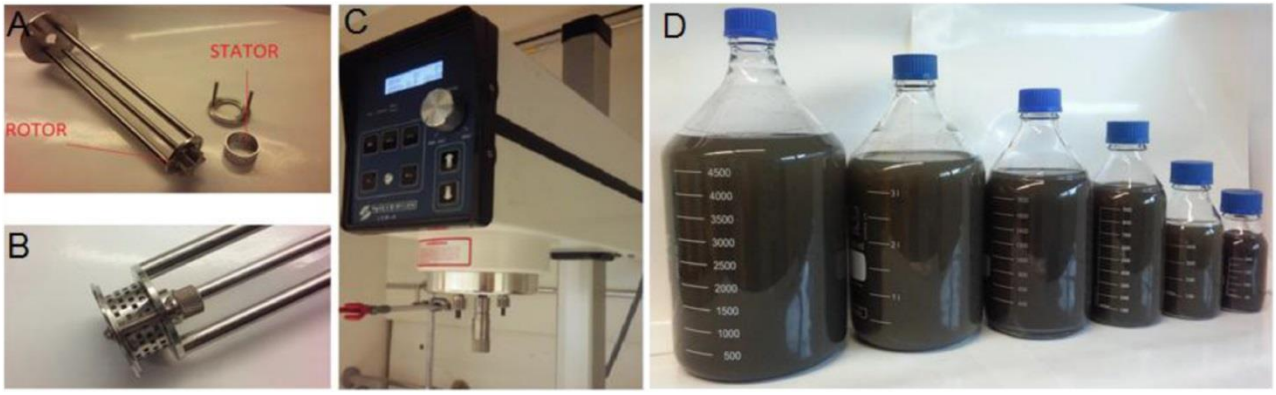

Figure 4: (A) Rotor and Stator (B) Assembly of the rotor and stator (C) The apparatus used for the exfoliation and (D) Large quantities of WS_2 nanosheets. [73]

The three exfoliation techniques described above only concern layered materials with weak interlayer interactions, even if sporadic sonication or shear-force exfoliation of layered oxides have been reported.[78,95,108] Concerning charged oxides, only the ion-exchange method is available for their

exfoliation. Initially applied by T. Sasaki *et al* for the exfoliation of layered titanates,[87,88,93,94] the method is now generalized to mostly all charged layered oxides,[89–91,109–111] hydroxydes[14,72,112,113] and even MXene.[95] In ion-exchange the exfoliation does not rely on mechanical force but on the swelling capacity of charged layered oxide. In a first step, the initial interlayer protons are replaced by bulky organo-ammonium ions, typically tetrabutylammonium ions. The maximum amount of inserted ammonium is function of the cation exchange capacity and above all of the size of the cations. This initial insertion is accompanied by an increase of the interlayer space. The intercalated guests subsequently drive the swelling of the layered structure as a concentration equilibrium must be reached with the external media. Besides, T. Sasaki *et al*. demonstrated that the key parameter is the ratio $\frac{TBA^+}{H^+}$, H^+ referring to the protons in the initial phase.[88] The authors indeed found a maximum value of this ratio beyond which the exfoliation does not occur. For these high ratios, an osmotic swelling occurs but the coherence between the slabs remains.[10,114] In addition to its concentration, the size and nature of the organic cation influence the mean thickness and lateral size of the nanosheets.[93,94]

Ion-exchange assisted exfoliation allows to generate colloidal nanosheets, with a high aspect ratio. Apart from a gentle stirring, the process is non-violent, leaving the initial structure untouched and does not produce fragmentation. The exfoliation yield is relatively high compared to mechanical-force driven exfoliation.

The main limitation is the reaction time which is extended over days to weeks. However, the recent work of J. ten Elshof *et al*. suggest that exfoliation occur in a few seconds after the insertion of the ammonium ions, meaning that the exfoliation time can be considerably reduced.[92,99] In addition, the organo-ammonium can be an obstacle to the further use of the nanosheets.

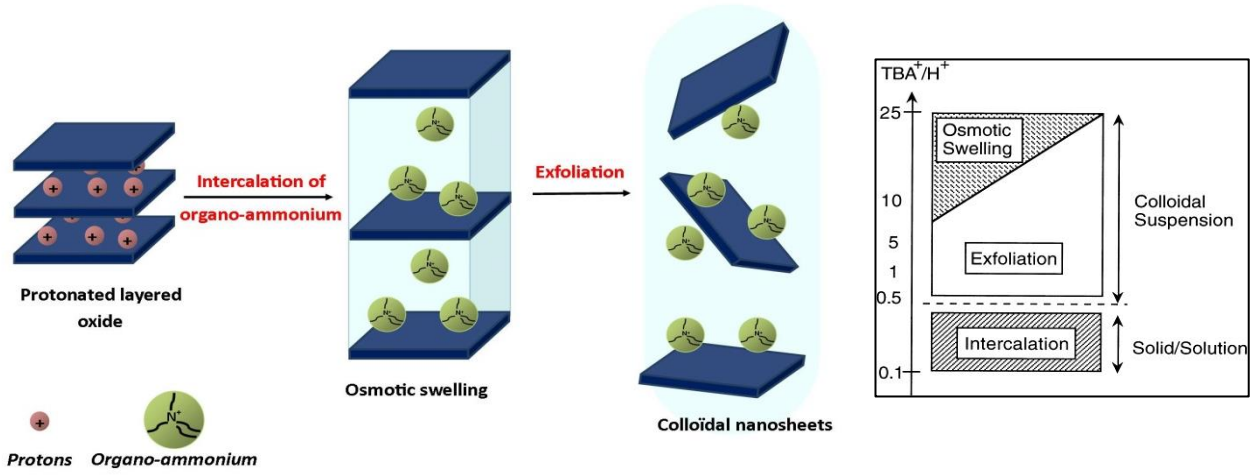

Figure 5: Schematic view of the ion-exchange mechanism and the corresponding final state of the charged layered oxide according to the ratio $\frac{TBA^+}{H^+}$***.***[88]

In ****Recently,*** J. ten.Elshof *et al*. reported the immediacy of the exfoliation in contrast with others works[99]

Table 1 we present some exfoliation methods and as stated in literature, we use the terms "exfoliation yield" to characterize the process. Here we would like draw the attention of the readers on the definition of such quantity and on the quality criteria chosen to characterized exfoliation.

First, it is worth mentioning that many papers do not give a clear definition of the "yield" as it appears evident that it takes the general definition of the ratio between the mass of the nanosheets in suspension over the initial mass of layered materials.[78,115,116]. In addition, for all liquid-phase exfoliation, the final nanosheets suspension is commonly obtained after a centrifugation step. This selective process contribute to the misestimating of the yield as the mass of nanomaterials in the supernatant does not only correspond to exfoliated nanosheets but also to more buoyant nanomaterials which can be thick and small.

The definition of the exfoliation yield does not consider the mean thickness and lateral size of the nanosheets as well as their respective distribution. H. Ploehn *et al.* showed that only coupling set of techniques such as Atomic Force Microscopy, Transmission Electron Microscopy and Dynamic Light scattering and making statistical analysis allow a quantitative and reliable estimation of the nanosheets concentration and aspect ratio.[117]

Finally, neither the aspect ratio nor the exfoliation yield reflects the presence of defects on the nanomaterials. Except for graphene where the Raman spectroscopy can probe the G and D bands, significant of the structure of graphene,[27,67] no specific technique up to now allows to directly quantify potential damages induced by exfoliation.

In the following, considering the misleading sense of exfoliation yield, we will not use it as a relevant parameter to characterize exfoliation. In addition, we will particularly take care of the potential damages caused by exfoliation by using microscopy techniques.

Since the scope of this work is restricted to charged oxides, the unique exfoliation method is at this stage ion-exchange. The resulting oxides nanosheets can be used as-synthesized. However, innovative works began to assemble oxides nanosheets to provide addition of their properties or even synergetic effects. Besides, adding functionality to nanosheets can also be reached by coupling them with organic molecules

I.3. Towards nanosheets-based multifunctional materials

I.3.1 3D architectures using 2D materials

A new area is emerging based on the assembly of 2D materials, referred as nanoarchitectonics. Due to their anisotropic shape, assemblies using only 2D materials are restricted to layered or stacked structures to maximize the surface of interaction between the nanomaterials. However, such architecture can be nowadays easily obtained by either layer-by-layer[118,119] or by Langmuir-Blodgett,[120] which constitutes the most popular techniques to build alternate architectures.

Concerning the Van der Waals-type nanosheets, their assembly into heterostructures is well established and many devices are up to now based on the coupling of two or more 2 D nanomaterials.[6,7,121] For instance, K. Novoselov *et al*. built a 13-layers heterostructure based on three different Van der Waals materials, graphene, boron nitride and MoS_2, to design new light-emitting diodes with a quantum efficiency closed to 10%.[122] In this example, each layer is directly deposited on top of the previous one without any addition of intermediate. Ease of assembly rises from the absence of epitaxial relation or repulsive interactions

This situation is entirely different for charged layered nanosheets for which it is clear that two like-charge nanosheets cannot be directly associated. Nevertheless, charged oxide nanosheets can be coupled with other materials or with opposite-charge nanosheets as reviewed recently by T. Sasaki *et al.*[16,123,124] or by other teams.[99,125,126] For instance, M. Osada *et al*. coupled a charged perovskite-like 2D nanosheets, $[Ca_2Nb_3O_{10}]^-$ with the neutral-charge MoS_2 by Langmuir-Blodgett[127] or as depicted in ***Figure 6***, T. Sasaki *et al.* associated two charged oxide nanosheets using Langmuir-Blodgett with tetrabutylammonium in between the layers. In this last example, the heterostructure displays a ferroelectric behavior while the nanosheets alone do not, proving the potentiality of assemblies using perovskite-like 2D materials. Otherwise, the use of polymers as intermediate layer is an alternative allowing to couple graphene and charged titanates nanosheets for instance.[128]

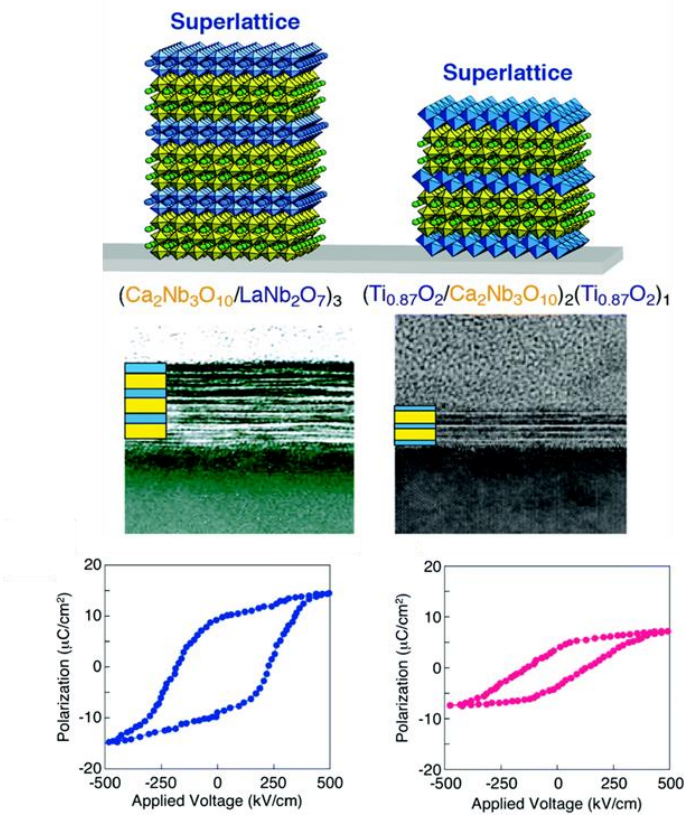

Figure 6: Two alternate structures composed of distinct charged oxide nanosheets. The two architectures display artificial ferroelectric behavior.[123]

However, nanoarchitectonics of charged layered oxides relies on electrostatic and a non-functional counter-charge species are usually used (organo-ammonium ion or charged polymer). Regarding supramolecular chemistry, many driving force for assemblies can be envisioned if dealing with molecules (*e.g.* hydrogen bond, π-π interaction, formation of covalent bond, hydrophobic interaction).[129–131] Therefore, combining organic species and inorganic nanosheets is promising path towards novels architectures.

I.3.2 Towards organic-inorganic hybrid 2D materials

As stated above, some layered materials such as Transition Metal Dichalcogenides or charged oxides and hydroxides show a chemical reactivity which allows their surface modification by organic molecules. This additional moiety modifies the properties of the nanomaterials such as their hydrophilicity, their colloidal stability or their optical response.[132,133] Two synthetic pathways can be envisioned: the post-modification of the nanosheets after their exfoliation or, the prior functionalization of the layered oxide *via* its interlayer space followed by the exfoliation of the obtained layered hybrid

The post-exfoliation functionalization requires the prior dispersion of the nanosheets in solution. The incoming molecule usually replaces the native surfactant (*e.g.* tetrabutylammonium ion in the case of charged oxide nanosheets).[30,31,90] For instance, J. Wiley *et al*. modify niobate oxide nanosheets with a large panel of molecules (aliphatic or aromatic amines or alcohols) and characterized their association by spectroscopies (FTIR and Raman). Besides, Y. Sugahara *et al.* performed the grafting of phosphonate surfactant onto water-dispersible TBA^+-oxide nanosheets. The exchange occurs at the cyclohexane-water interface and the reaction leads to phase transfer of the inorganic nanosheets, whose surface becomes then hydrophobic.[134] The same authors improved the process by using microchannel, hence reducing the phase transfer time from 7 hours initially to 4.6 s.[135] However, in this method, the homogeneity of the grafting is not insured and the organic coverage cannot be easily estimated.

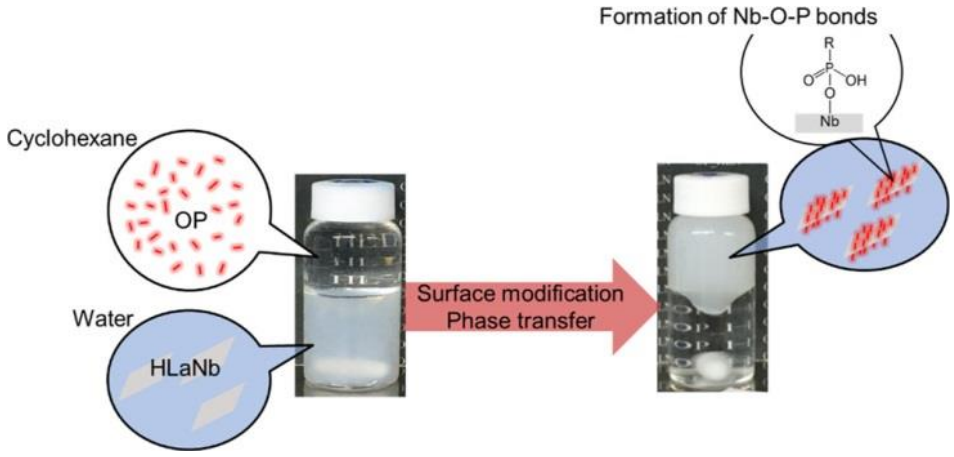

Figure 7: Surface modification of exfoliated oxide nanosheets leading to their phase transfer, from water (bottom) to cyclohexane (top).[134]

In another approach, functionalized nanosheets can be obtained by exfoliating a hybrid layer material. The first step of this strategy is the insertion or grafting of the molecular species into the interlayer space. The chemistry of intercalation of layered compounds is extremely wide and well documented.[41,136–138] The reaction consists in exchanging species by another one with a large amount of the desired molecules to favour the exchange. The insertion is often accompanied by a modification of the interlayer distance. The mechanism usually suffers from long reaction times (from hours to days). To circumvent this main drawback, our team and others took advantage of microwave reaction to fasten the intercalation process and synthesize a hybrid layered oxides, with inserted amine and alcohol derivatives in a few hours.[139–143]

Tuning the design of the layered hybrid possibly allows to reach many properties. For instance, conjugated aromatic molecules have been inserted into clays, layered hydroxides or oxides, conferring luminescence properties to the native inorganic materials.[144,145] However, in the case of luminescent molecules, the layered hybrid either cannot be exfoliated as the molecules insertion leads to pillaring *i.e.* the bridging of two adjacent layers by the molecules (case of the porphyrins[146]) or the exfoliation was not the goal and hence was not performed. Nevertheless, hybrid nanosheets with luminescence would be a relevant system in the scope of probing nanosheets exfoliation and re-assembly or adding functionality to a heterostructure.

In addition to multifunctionality, hybridization modifies the interlayer space in the way that the insertion of a molecule usually increases the interlayer distance, inevitably leading to the decrease of the electrostatic interaction between the slabs. According to Y. Oaki, the hybridization allows "a rigid-to-soft" modification of the layered materials. Hence, Y. Oaki *et al*. took advantage of this "softness" to exfoliate a hybrid charged layered titanate by a swelling process in organic solvent, without using a delaminating agent such as TBA^+.[116,147–149] The resulting 2D materials have a quite large lateral size and the functionalization remains intact after the exfoliation process.

Similarly, J.-H. Choy *et al.* consider the functionalization of layered oxides $HCa_2Nb_3O_{10}$ with a bifunctional alkyl amino acid (the two functional groups constitute the endpoints of the molecules).[150] The amine group interacts with the inorganic layer while the acid one is facing the interlayer and thus, other acid groups. By increasing the pH and deprotonating acid, the corresponding negatively-charged carboxylates repel each other which leads to the exfoliation of the layered hybrid. The resulting nanosheets are electrostatically stabilized in water. This example constitutes another strategy to exfoliate charged layered oxides without ion-exchange.

In the same trend, only few papers report the exfoliation of hybrid charged layered oxides by liquid phase exfoliation method such as sonication or shear-force, until now dedicated to van der Waals materials.[74,77,151] As electrostatic interaction are decreased these methods can provide enough mechanical force to overcome the interaction between the layers. For instance, Y. Sugahara *et al*. modify a hexaniobate phase by phenylphosphonic acid and the resulting hybrid is sonicated in acetonitrile for 1 hour as depicted in ***Figure 8***. The exfoliation time is far more reduced compared to the other processes

concerning the charged layered oxides. In addition, the grafting by a phosphonic acid insures the preservation of the functionalization during the violent process. The sonication or shear-force seems to be as relevant as they are in the case of van der Waals materials.

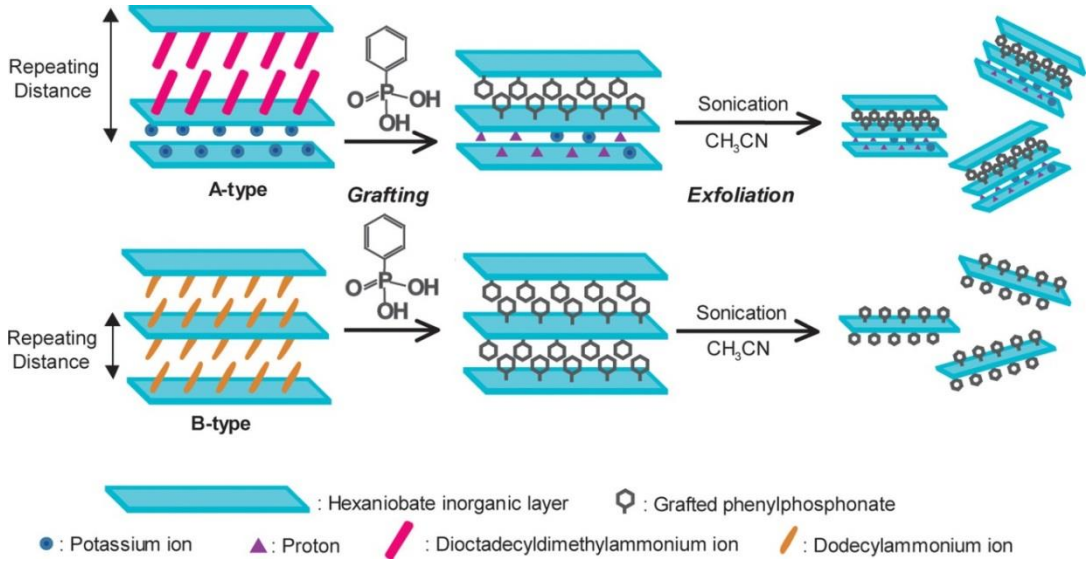

Figure 8: Representative view of the functionalization of the layered hexaniobate $KNb_6O_{17}.3H_2O$ by phenylphosphonic acid and the exfoliation of the layered hybrid. [151]

I.4. Objectives and structure of the thesis

In regards the potentiality of heterostructures based on 2D materials, our main goal consists in synthesizing novel architectures with innovative properties from the assemblies of nanosheets. Among all the 2D materials, the layered oxides displaying a perovskite-like structure are attractive for their properties which make them suitable for many applications. Therefore, we focus our scope on this family of material, especially on the Aurivillius phase $Bi_2SrTa_2O_9$. However, building assemblies requires an interaction between two entities. We aim at building assemblies no longer based on electrostatic interactions but using molecular interactions. Hence, it is necessary to design building blocks *i.e.* functionalized perovskite-like oxide nanosheets. Thus, three objectives can be defined:

First, we will focus on the **design of hybrid layered oxides**, by grafting functional molecules into the interlayer space. The organic entities should allow a non-electrostatic re-assembly of the corresponding functionalized nanosheets and/or adding properties**.**

This objective is addressed in **Chapter II**. After a brief review of our experience on microwave-assisted exfoliation of oxides, we will describe the grafting of specific molecules chosen for their functional groups or their properties.

Secondly, **the exfoliation of the hybrid layered oxides** has to be investigated and optimized to produce large, thin, functionalized and colloidal nanosheets in solution.

Considering the hybrid oxides many exfoliation methods can be used. In **Chapter III**, we will consider the ion-exchange method to exfoliated hybrid layered oxides by using either organo-ammonium or polymers. Subsequently, we will investigate the shear exfoliation of hybrid materials in **Chapter IV** with a focus on the optimization of the process. The resulting nanosheets will be characterized with a peculiar interest on the lateral size, the thickness and the functionalization in **Chapter V**. For this purpose, local imaging techniques and scattering techniques will allow to fully describe the nanosheets.

Finally, after synthesizing the hybrid oxide nanosheets and according the nature of the organic moieties, we will consider adapted strategies to couple the nanosheets with another 2D materials into heterostrutures in **Chapter VI**. The preliminary results will be exposed to highlight the feasibility and relevancy of our approach.

I.5. Bibliography

(1) Tan, C.; Cao, X.; Wu, X.-J.; He, Q.; Yang, J.; Zhang, X.; Chen, J.; Zhao, W.; Han, S.; Nam, G.-H.; Sindoro, M.; Zhang, H. Recent Advances in Ultrathin Two-Dimensional Nanomaterials. *Chem. Rev.* **2017**, *117* (9), 6225–6331.

(2) Gupta, A.; Sakthivel, T.; Seal, S. Recent Development in 2D Materials beyond Graphene. *Progress in Materials Science* **2015**, *73*, 44–126.

(3) Hinterding, R.; Feldhoff, A. Two-Dimensional Oxides: Recent Progress in Nanosheets. *Zeitschrift für Physikalische Chemie* **2018**, *233* (1), 117–165.

(4) Osada, M.; Sasaki, T. The Rise of 2D Dielectrics/Ferroelectrics. *APL Materials* **2019**, *7* (12), 120902.

(5) Nakato, T.; Kawamata, J.; Takagi, S. *Inorganic Nanosheets and Nanosheets-Based Materials*; Springer.

(6) Mas-Ballesté, R.; Gómez-Navarro, C.; Gómez-Herrero, J.; Zamora, F. 2D Materials: To Graphene and Beyond. *Nanoscale* **2011**, *3* (1), 20–30.

(7) Witomska, S.; Leydecker, T.; Ciesielski, A.; Samorì, P. Production and Patterning of Liquid Phase–Exfoliated 2D Sheets for Applications in Optoelectronics. *Advanced Functional Materials* **2019**, *29* (22), 1901126.

(8) Ganter, P.; Lotsch, B. V. Photonic Nanoarchitectonics with Stimuli-Responsive 2D Materials. *Mol. Syst. Des. Eng.* **2019**, *4* (3), 566–579.

(9) Boileau, A.; Hurand, S.; Baudouin, F.; Lüders, U.; Dallocchio, M.; Bérini, B.; Cheikh, A.; David, A.; Paumier, F.; Girardeau, T.; Marie, P.; Labbé, C.; Cardin, J.; Aureau, D.; Frégnaux, M.; Guilloux-Viry, M.; Prellier, W.; Dumont, Y.; Demange, V.; Fouchet, A. Highly Transparent and Conductive Indium-Free Vanadates Crystallized at Reduced Temperature on Glass Using a 2D Transparent Nanosheet Seed Layer. *Advanced Functional Materials n/a* (n/a), 2108047.

(10) Sano, K.; Kim, Y. S.; Ishida, Y.; Ebina, Y.; Sasaki, T.; Hikima, T.; Aida, T. Photonic Water Dynamically Responsive to External Stimuli. *Nat Commun* **2016**, *7* (1), 1–9.

(11) Luo, B.; Liu, G.; Wang, L. Recent Advances in 2D Materials for Photocatalysis. *Nanoscale* **2016**, *8* (13), 6904–6920.

(12) Osterloh, F. E. Inorganic Nanostructures for Photoelectrochemical and Photocatalytic Water Splitting. *Chem. Soc. Rev.* **2013**, *42* (6), 2294–2320.

(13) Zhang, G.; Liu, G.; Wang, L.; Irvine, J. T. S. Inorganic Perovskite Photocatalysts for Solar Energy Utilization. *Chem. Soc. Rev.* **2016**, *45* (21), 5951–5984.

(14) ten Elshof, J. E.; Yuan, H.; Gonzalez Rodriguez, P. Two-Dimensional Metal Oxide and Metal Hydroxide Nanosheets: Synthesis, Controlled Assembly and Applications in Energy Conversion and Storage. *Advanced Energy Materials* **2016**, *6* (23), 1600355.

(15) Heard, C. J.; Čejka, J.; Opanasenko, M.; Nachtigall, P.; Centi, G.; Perathoner, S. 2D Oxide Nanomaterials to Address the Energy Transition and Catalysis. *Advanced Materials* **2019**, *31* (3), 1801712.

(16) Xiong, P.; Ma, R.; Wang, G.; Sasaki, T. Progress and Perspective on Two-Dimensional Unilamellar Metal Oxide Nanosheets and Tailored Nanostructures from Them for Electrochemical Energy Storage. *Energy Storage Materials* **2019**, *19*, 281–298.

(17) Dral, A. P.; ten Elshof, J. E. 2D Metal Oxide Nanoflakes for Sensing Applications: Review and Perspective. *Sensors and Actuators B: Chemical* **2018**, *272*, 369–392.

(18) Boyd, I. W. Thin Film Growth by Pulsed Laser Deposition. *Ceramics International* **1996**, *22* (5), 429–434.

(19) Huang, Y.-L.; Liu, H.-J.; Ma, C.-H.; Yu, P.; Chu, Y.-H.; Yang, J.-C. Pulsed Laser Deposition of Complex Oxide Heteroepitaxy. *Chinese Journal of Physics* **2019**, *60*, 481–501.

(20) Schlom, D. G.; Chen, L.-Q.; Pan, X.; Schmehl, A.; Zurbuchen, M. A. A Thin Film Approach to Engineering Functionality into Oxides. *Journal of the American Ceramic Society* **2008**, *91* (8), 2429–2454.

(21) Boileau, A.; Dallocchio, M.; Baudouin, F.; David, A.; Lüders, U.; Mercey, B.; Pautrat, A.; Demange, V.; Guilloux-Viry, M.; Prellier, W.; Fouchet, A. Textured Manganite Films Anywhere. *ACS Appl. Mater. Interfaces* **2019**, *11* (40), 37302–37312.

(22) Baudouin, F.; Demange, V.; Ollivier, S.; Rault, L.; Brito, A. S.; Maia, A. S.; Gouttefangeas, F.; Bouquet, V.; Députier, S.; Bérini, B.; Fouchet, A.; Guilloux-Viry, M. Orientation Control of KNbO3 Film Grown on Glass Substrates by $Ca_2Nb_3O_{10}^-$ Nanosheets Seed Layer. *Thin Solid Films* **2020**, *693*, 137682.

(23) Sanchez, C.; Rozes, L.; Ribot, F.; Laberty-Robert, C.; Grosso, D.; Sassoye, C.; Boissiere, C.; Nicole, L. "Chimie Douce": A Land of Opportunities for the Designed Construction of Functional Inorganic and Hybrid Organic-Inorganic Nanomaterials. *Comptes Rendus Chimie* **2010**, *13* (1), 3–39.
(24) Larquet, C.; Carriere, D.; Nguyen, A.-M.; Le, T. K.-C.; Frogneux-Plé, X.; Génois, I.; Le Griel, P.; Gauzzi, A.; Sanchez, C.; Carenco, S. Unraveling the Role of Alkali Cations in the Growth Mechanism of Gd2O2S Nanoparticles. *Chem. Mater.* **2020**, *32* (3), 1131–1139.
(25) Zhang, H. Ultrathin Two-Dimensional Nanomaterials. *ACS Nano* **2015**, *9* (10), 9451–9469.
(26) Novoselov, K. S.; Geim, A. K.; Morozov, S. V.; Jiang, D.; Zhang, Y.; Dubonos, S. V.; Grigorieva, I. V.; Firsov, A. A. Electric Field Effect in Atomically Thin Carbon Films. *Science* **2004**, *306* (5696), 666–669.
(27) Backes, C.; Abdelkader, A. M.; Alonso, C.; Andrieux-Ledier, A.; Arenal, R.; Azpeitia, J.; Balakrishnan, N.; Banszerus, L.; Barjon, J.; Bartali, R.; Bellani, S.; Berger, C.; Berger, R.;*et al*., M. Production and Processing of Graphene and Related Materials. *2D Mater.* **2020**, *7* (2), 022001.
(28) Geim, A. K.; Novoselov, K. S. The Rise of Graphene. *Nature Mater* **2007**, *6* (3), 183–191.
(29) Chhowalla, M.; Shin, H. S.; Eda, G.; Li, L.-J.; Loh, K. P.; Zhang, H. The Chemistry of Two-Dimensional Layered Transition Metal Dichalcogenide Nanosheets. *Nature Chem* **2013**, *5* (4), 263–275.
(30) Daukiya, L.; Seibel, J.; De Feyter, S. Chemical Modification of 2D Materials Using Molecules and Assemblies of Molecules. *Advances in Physics: X* **2019**, *4* (1), 1625723.
(31) Zhou, L.; He, B.; Yang, Y.; He, Y. Facile Approach to Surface Functionalized MoS_2 Nanosheets. *RSC Adv.* **2014**, *4* (61), 32570–32578.
(32) Brown, A.; Rundqvist, S. Refinement of the Crystal Structure of Black Phosphorus. *Acta Crystallographica* **1965**, *19* (4), 684–685.
(33) Chen, P.; Li, N.; Chen, X.; Ong, W.-J.; Zhao, X. The Rising Star of 2D Black Phosphorus beyond Graphene: Synthesis, Properties and Electronic Applications. *2D Mater.* **2017**, *5* (1), 014002.
(34) Naguib, M.; Mochalin, V. N.; Barsoum, M. W.; Gogotsi, Y. 25th Anniversary Article: MXenes: A New Family of Two-Dimensional Materials. *Advanced Materials* **2014**, *26* (7), 992–1005.
(35) Xiao, X.; Wang, H.; Urbankowski, P.; Gogotsi, Y. Topochemical Synthesis of 2D Materials. *Chemical Society Reviews* **2018**, *47* (23), 8744–8765.
(36) Brec, R. Review on Structural and Chemical Properties of Transition Metal Phosphorous Trisulfides MPS_3. *Solid State Ionics* **1986**, *22* (1), 3–30.
(37) Samal, R.; Sanyal, G.; Chakraborty, B.; Rout, C. S. Two-Dimensional Transition Metal Phosphorous Trichalcogenides (MPX_3): A Review on Emerging Trends, Current State and Future Perspectives. *J. Mater. Chem. A* **2021**, *9* (5), 2560–2591.
(38) Liu, J.; Li, X.-B.; Wang, D.; Lau, W.-M.; Peng, P.; Liu, L.-M. Diverse and Tunable Electronic Structures of Single-Layer Metal Phosphorus Trichalcogenides for Photocatalytic Water Splitting. *J. Chem. Phys.* **2014**, *140* (5), 054707.
(39) Rabu, P.; Delahaye, E.; Rogez, G. Hybrid Interfaces in Layered Hydroxides: Magnetic and Multifunctional Superstructures by Design. *Nanotechnology Reviews* **2015**, *4* (6), 557–580..
(40) Meyn, M.; Beneke, K.; Lagaly, G. Anion-Exchange Reactions of Layered Double Hydroxides. *Inorg. Chem.* **1990**, *29* (26), 5201–5207.
(41) Mousty, C.; Prévot, V. Hybrid and Biohybrid Layered Double Hydroxides for Electrochemical Analysis. *Anal Bioanal Chem* **2013**, *405* (11), 3513–3523.
(42) Park, D.-H.; Choi, G.; Choy, J.-H. Bio-Layered Double Hydroxides Nanohybrids for Theranostics Applications. In *Photofunctional Layered Materials*; Yan, D., Wei, M., Eds.; Springer International Publishing: Cham, 2015; Vol. 166, pp 137–175.
(43) Rogez, G.; Viart, N.; Drillon, M. Multiferroic Materials: The Attractive Approach of Metal–Organic Frameworks (MOFs). *Angewandte Chemie International Edition* **2010**, *49* (11), 1921–1923.
(44) Wang, Q.; O'Hare, D. Recent Advances in the Synthesis and Application of Layered Double Hydroxide (LDH) Nanosheets. *Chem. Rev.* **2012**, *112* (7), 4124–4155.
(45) Blazquez-Alcover, I.; Huvé, M.; Mocuta, C.; Thiaudière, D.; Roussel, P.; Pautrat, A.; Mentré, O.; Daviero-Minaud, S. Original Positively Charged Nanoflakes by Liquid Exfoliation of Layered Oxybromide Cobaltites. *CrystEngComm* **2017**, *19* (2), 304–312.
(46) Uppuluri, R.; Gupta, A. S.; Rosas, A. S.; Mallouk, T. E. Soft Chemistry of Ion-Exchangeable Layered Metal Oxides. *Chem. Soc. Rev.* **2018**, *47* (7), 2401–2430..
(47) Wang, L.; Sasaki, T. Titanium Oxide Nanosheets: Graphene Analogues with Versatile Functionalities. *Chemical Reviews* **2014**, *114* (19), 9455–9486.

(48) Kudo, A. Luminescent Properties of Rare-Earth-Metal Ion-Doped $KLaNb_2O_7$ with Layered Perovskite Structures. *Chem. Mater.* **1997**, *9* (3), 664–669.
(49) Kudo, A.; Kaneko, E. Photoluminescent Properties of Ion-Exchangeable Layered Oxides. *Microporous and Mesoporous Materials* **1998**, *21* (4–6), 615–620.
(50) Taniguchi, T.; Murakami, T.; Funatsu, A.; Hatakeyama, K.; Koinuma, M.; Matsumoto, Y. Reversibly Tunable Upconversion Luminescence by Host–Guest Chemistry. *Inorg. Chem.* **2014**, *53* (17), 9151–9155.
(51) Benedek, N. A. Origin of Ferroelectricity in a Family of Polar Oxides: The Dion—Jacobson Phases. *Inorg. Chem.* **2014**, *53* (7), 3769–3777.
(52) Dobal, P. S.; Katiyar, R. S. Studies on Ferroelectric Perovskites and Bi-Layered Compounds Using Micro-Raman Spectroscopy. *Journal of Raman Spectroscopy* **2002**, *33* (6), 405–423.
(53) Peña, M. A.; Fierro, J. L. G. Chemical Structures and Performance of Perovskite Oxides. *Chem. Rev.* **2001**, *101* (7), 1981–2018.
(54) Dias, A. S.; Lima, S.; Carriazo, D.; Rives, V.; Pillinger, M.; Valente, A. A. Exfoliated Titanate, Niobate and Titanoniobate Nanosheets as Solid Acid Catalysts for the Liquid-Phase Dehydration of d-Xylose into Furfural. *Journal of Catalysis* **2006**, *244* (2), 230–237.
(55) Geselbracht, M. J.; White, H. K.; Blaine, J. M.; Diaz, M. J.; Hubbs, J. L.; Adelstein, N.; Kurzman, J. A. New Solid Acids in the Triple-Layer Dion–Jacobson Layered Perovskite Family. *Materials Research Bulletin* **2011**, *46* (3), 398–406.
(56) Tagusagawa, C.; Takagaki, A.; Takanabe, K.; Ebitani, K.; Hayashi, S.; Domen, K. Layered and Nanosheet Tantalum Molybdate as Strong Solid Acid Catalysts. *Journal of Catalysis* **2010**, *270* (1), 206–212.
(57) Takagaki, A.; Sugisawa, M.; Lu, D.; Kondo, J. N.; Hara, M.; Domen, K.; Hayashi, S. Exfoliated Nanosheets as a New Strong Solid Acid Catalyst. *J. Am. Chem. Soc.* **2003**, *125* (18), 5479–5485.
(58) Kiba, S.; Haga, J.-I.; Hashimoto, S.; Nakato, T. Adsorptive and Photocatalytic Removal of Phenol by Layered Niobates Organically Modified Through Intercalation and Silylation. *J. Nanosci. Nanotech.* **2010**, *10* (12), 8341–8348.
(59) Wimpenny, J. Clay Minerals. In *Encyclopedia of Engineering Geology*; Bobrowsky, P., Marker, B., Eds.; Springer International Publishing: Cham, 2016; pp 1–11.
(60) Stamate; Pavel; Zavoianu; Marcu. Highlights on the Catalytic Properties of Polyoxometalate-Intercalated Layered Double Hydroxides: A Review. *Catalysts* **2020**, *10* (1), 57.
(61) Novoselov, K. S.; Jiang, D.; Schedin, F.; Booth, T. J.; Khotkevich, V. V.; Morozov, S. V.; Geim, A. K. Two-Dimensional Atomic Crystals. *PNAS* **2005**, *102* (30), 10451–10453.
(62) Li, H.; Yin, Z.; He, Q.; Li, H.; Huang, X.; Lu, G.; Fam, D. W. H.; Tok, A. I. Y.; Zhang, Q.; Zhang, H. Fabrication of Single- and Multilayer MoS_2 Film-Based Field-Effect Transistors for Sensing NO at Room Temperature. *Small* **2012**, *8* (1), 63–67.
(63) Late, D. J.; Shirodkar, S. N.; Waghmare, U. V.; Dravid, V. P.; Rao, C. N. R. Thermal Expansion, Anharmonicity and Temperature-Dependent Raman Spectra of Single- and Few-Layer $MoSe_2$ and WSe_2. *ChemPhysChem* **2014**, *15* (8), 1592–1598.
(64) Lee, D.; Lee, B.; Park, K. H.; Ryu, H. J.; Jeon, S.; Hong, S. H. Scalable Exfoliation Process for Highly Soluble Boron Nitride Nanoplatelets by Hydroxide-Assisted Ball Milling. *Nano Lett.* **2015**, *15* (2), 1238–
(65) Sun, P.; Kuga, S.; Wu, M.; Huang, Y. Exfoliation of Graphite by Dry Ball Milling with Cellulose. *Cellulose* **2014**, *21* (4), 2469–2478.
(66) Liu, W.; Zhu, Y.; Xu, X.; Wang, S.; Zhang, X. Preparation of Few-Layer Black Phosphorus by Wet Ball Milling Exfoliation. *J Mater Sci: Mater Electron* **2020**, *31* (12), 9543–9549.
(67) Knieke, C.; Berger, A.; Voigt, M.; Taylor, R. N. K.; Röhrl, J.; Peukert, W. Scalable Production of Graphene Sheets by Mechanical Delamination. *Carbon* **2010**, *48* (11), 3196–3204.
(68) Coleman, J. N.; Lotya, M.; O'Neill, A.; Bergin, S. D.; King, P. J.; Khan, U.; Young, K.; Gaucher, A.; De, S.; Smith, R. J.; Shvets, I. V.; Arora, S. K.; Stanton, G.; Kim, H.-Y.; Lee, K.; Kim, G. T.; Duesberg, G. S.; Hallam, T.; Boland, J. J.; Wang, J. J.; Donegan, J. F.; Grunlan, J. C.; Moriarty, G.; Shmeliov, A.; Nicholls, R. J.; Perkins, J. M.; Grieveson, E. M.; Theuwissen, K.; McComb, D. W.; Nellist, P. D.; Nicolosi, V. Two-Dimensional Nanosheets Produced by Liquid Exfoliation of Layered Materials. *Science* **2011**, *331* (6017), 568–571.
(69) Cunningham, G.; Lotya, M.; Cucinotta, C. S.; Sanvito, S.; Bergin, S. D.; Menzel, R.; Shaffer, M. S. P.; Coleman, J. N. Solvent Exfoliation of Transition Metal Dichalcogenides: Dispersibility of Exfoliated Nanosheets Varies Only Weakly between Compounds. *ACS Nano* **2012**, *6* (4), 3468–3480.
(70) Paton, K. R.; Varrla, E.; Backes, C.; Smith, R. J.; Khan, U.; O'Neill, A.; Boland, C.; Lotya, M.; Istrate, O. M.; King, P.; Higgins, T.; Barwich, S.; May, P.; Puczkarski, P.; Ahmed, I.; Moebius, M.; Pettersson, H.;

Long, E.; Coelho, J.; O'Brien, S. E.; McGuire, E. K.; Sanchez, B. M.; Duesberg, G. S.; McEvoy, N.; Pennycook, T. J.; Downing, C.; Crossley, A.; Nicolosi, V.; Coleman, J. N. Scalable Production of Large Quantities of Defect-Free Few-Layer Graphene by Shear Exfoliation in Liquids. *Nature Materials* **2014**, *13* (6), 624–630.

(71) Ciesielski, A.; Samorì, P. Graphene via Sonication Assisted Liquid-Phase Exfoliation. *Chem. Soc. Rev.* **2013**, *43* (1), 381–398.

(72) Wu, Q.; Sjåstad, A. O.; Vistad, Ø. B.; Knudsen, K. D.; Roots, J.; Pedersen, J. S.; Norby, P. Characterization of Exfoliated Layered Double Hydroxide (LDH, Mg/Al=3) Nanosheets at High Concentrations in Formamide. *J. Mater. Chem.* **2007**, *17* (10), 965–971.

(73) Biccai, S.; Barwich, S.; Boland, D.; Harvey, A.; Hanlon, D.; McEvoy, N.; Coleman, J. N. Exfoliation of 2D Materials by High Shear Mixing. *2D Mater.* **2019**, *6* (1), 015008.

(74) Kopecká, K.; Melánová, K.; Beneš, L.; Knotek, P.; Mazur, M.; Zima, V. Exfoliation of Layered Mixed Zirconium 4-Sulfophenylphosphonate Phenylphosphonates. *Dalton Trans.* **2020**, *49* (12), 3816–3823.

(75) Harvey, A.; Boland, J. B.; Godwin, I.; Kelly, A. G.; Szydłowska, B. M.; Murtaza, G.; Andrew Thomas; Lewis, D. J.; O'Brien, P.; Coleman, J. N. Exploring the Versatility of Liquid Phase Exfoliation: Producing 2D Nanosheets from Talcum Powder, Cat Litter and Beach Sand. *2D Mater.* **2017**, *4* (2), 025054.

(76) Huang, X.; Li, Y.; Yin, X.; Tian, J.; Wu, W. Liquid-Phase Exfoliation of Kaolinite by High-Shear Mixer with Graphite Oxide as an Amphiphilic Dispersant. *Langmuir* **2019**, *35* (43), 13833–13843.

(77) Yan, M.; Collins, S. M.; Midgley, P. A.; Feldblyum, J. I. Factors Governing the Chemical Stability of Shear-Exfoliated ZnSe(Alkylamine) II–VI Layered Hybrids. *Chem. Mater.* **2020**, *32* (6), 2379–2388.

(78) Lee, J. M.; Kang, B.; Jo, Y. K.; Hwang, S.-J. Organic Intercalant-Free Liquid Exfoliation Route to Layered Metal-Oxide Nanosheets via the Control of Electrostatic Interlayer Interaction. *ACS Appl. Mater. Interfaces* **2019**, *11* (12), 12121–12132.

(79) Machida, S.; Guégan, R.; Sugahara, Y. A Novel Approach to Characterization of a Relatively Unstable Intercalation Compound under Ambient Conditions: Revisiting a Kaolinite-Acetone Intercalation Compound. *Dalton Trans.* **2021**, *50* (18), 6290–6296.

(80) Naguib, M.; Kurtoglu, M.; Presser, V.; Lu, J.; Niu, J.; Heon, M.; Hultman, L.; Gogotsi, Y.; Barsoum, M. W. Two-Dimensional Nanocrystals Produced by Exfoliation of Ti3AlC2. *Advanced Materials* **2011**, *23* (37), 4248–4253.

(81) Liu, H.; Xu, L.; Liu, W.; Zhou, B.; Zhu, Y.; Zhu, L.; Jiang, X. Production of Mono- to Few-Layer MoS_2 Nanosheets in Isopropanol by a Salt-Assisted Direct Liquid-Phase Exfoliation Method. *Journal of Colloid and Interface Science* **2018**, *515*, 27–31.

(82) Dines, M. B. Lithium Intercalation via N-Butyllithium of the Layered Transition Metal Dichalcogenides. *Materials Research Bulletin* **1975**, *10* (4), 287–291.

(83) Joensen, P.; Frindt, R. F.; Morrison, S. R. Single-Layer MoS_2. *Materials Research Bulletin* **1986**, *21* (4), 457–461.

(84) Niu, L.; Li, M.; Tao, X.; Xie, Z.; Zhou, X.; Raju, A. P. A.; Young, R. J.; Zheng, Z. Salt-Assisted Direct Exfoliation of Graphite into High-Quality, Large-Size, Few-Layer Graphene Sheets. *Nanoscale* **2013**, *5* (16), 7202–7208.

(85) Yuwen, L.; Yu, H.; Yang, X.; Zhou, J.; Zhang, Q.; Zhang, Y.; Luo, Z.; Su, S.; Wang, L. Rapid Preparation of Single-Layer Transition Metal Dichalcogenide Nanosheets via Ultrasonication Enhanced Lithium Intercalation. *Chem. Commun.* **2015**, *52* (3), 529–532.

(86) Zeng, Z.; Sun, T.; Zhu, J.; Huang, X.; Yin, Z.; Lu, G.; Fan, Z.; Yan, Q.; Hng, H. H.; Zhang, H. An Effective Method for the Fabrication of Few-Layer-Thick Inorganic Nanosheets. *Angewandte Chemie International Edition* **2012**, *51* (36), 9052–9056.

(87) Sasaki, T.; Watanabe, M.; Hashizume, H.; Yamada, H.; Nakazawa, H. Macromolecule-like Aspects for a Colloidal Suspension of an Exfoliated Titanate. Pairwise Association of Nanosheets and Dynamic Reassembling Process Initiated from It. *J. Am. Chem. Soc.* **1996**, *118* (35), 8329–8335.

(88) Sasaki, T.; Watanabe, M. Osmotic Swelling to Exfoliation. Exceptionally High Degrees of Hydration of a Layered Titanate. *J. Am. Chem. Soc.* **1998**, *120* (19), 4682–4689.

(89) Ebina, Y.; Sasaki, T.; Watanabe, M. Study on Exfoliation of Layered Perovskite-Type Niobates. *Solid State Ionics* **2002**, *151* (1), 177–182.

(90) Akbarian-Tefaghi, S.; Rostamzadeh, T.; Brown, T. T.; Davis-Wheeler, C.; Wiley, J. B. Rapid Exfoliation and Surface Tailoring of Perovskite Nanosheets via Microwave-Assisted Reactions. *ChemNanoMat* **2017**, *3* (8), 538–550.

(91) Yuan, H.; Besselink, R.; Liao, Z.; ten Elshof, J. E. The Swelling Transition of Lepidocrocite-Type Protonated Layered Titanates into Anatase under Hydrothermal Treatment. *Scientific Reports* **2014**, *4* (1), 1–6.

(92) Besselink, R.; Stawski, T. M.; Castricum, H. L.; Blank, D. H. A.; ten Elshof, J. E. Exfoliation and Restacking of Lepidocrocite-Type Layered Titanates Studied by Small-Angle X-Ray Scattering. *J. Phys. Chem. C* **2010**, *114* (49), 21281–21286.

(93) Geng, F.; Ma, R.; Yamauchi, Y.; Sasaki, T. Tetrabutylphosphonium Ions as a New Swelling/Delamination Agent for Layered Compounds. *Chem. Commun.* **2014**, *50* (69), 9977–9980.

(94) Maluangnont, T.; Matsuba, K.; Geng, F.; Ma, R.; Yamauchi, Y.; Sasaki, T. Osmotic Swelling of Layered Compounds as a Route to Producing High-Quality Two-Dimensional Materials. A Comparative Study of Tetramethylammonium versus Tetrabutylammonium Cation in a Lepidocrocite-Type Titanate. *Chem. Mater.* **2013**, *25* (15), 3137–3146.

(95) Xuan, J.; Wang, Z.; Chen, Y.; Liang, D.; Cheng, L.; Yang, X.; Liu, Z.; Ma, R.; Sasaki, T.; Geng, F. Organic-Base-Driven Intercalation and Delamination for the Production of Functionalized Titanium Carbide Nanosheets with Superior Photothermal Therapeutic Performance. *Angewandte Chemie International Edition* **2016**, *55* (47), 14569–14574.

(96) Shori, S.; Pellechia, P. J.; zur Loye, H.-C.; Ploehn, H. J. Covalent Grafting of Phenylphosphonate on Calcium Niobate Platelets. *Journal of Colloid and Interface Science* **2015**, *437*, 97–110.

(97) Karagiannidis, P. G.; Hodge, S. A.; Lombardi, L.; Tomarchio, F.; Decorde, N.; Milana, S.; Goykhman, I.; Su, Y.; Mesite, S. V.; Johnstone, D. N.; Leary, R. K.; Midgley, P. A.; Pugno, N. M.; Torrisi, F.; Ferrari, A. C. Microfluidization of Graphite and Formulation of Graphene-Based Conductive Inks. *ACS Nano* **2017**, *11* (3), 2742–2755.

(98) Xu, Y.; Cao, H.; Xue, Y.; Li, B.; Cai, W. Liquid-Phase Exfoliation of Graphene: An Overview on Exfoliation Media, Techniques, and Challenges. *Nanomaterials* **2018**, *8* (11), 942.

(99) Yuan, H.; Dubbink, D.; Besselink, R.; ten Elshof, J. E. The Rapid Exfoliation and Subsequent Restacking of Layered Titanates Driven by an Acid-Base Reaction. *Angewandte Chemie International Edition* **2015**, *54* (32), 9239–9243.

(100) Xia, Z. Y.; Pezzini, S.; Treossi, E.; Giambastiani, G.; Corticelli, F.; Morandi, V.; Zanelli, A.; Bellani, V.; Palermo, V. The Exfoliation of Graphene in Liquids by Electrochemical, Chemical, and Sonication-Assisted Techniques: A Nanoscale Study. *Advanced Functional Materials* **2013**, *23* (37), 4684–4693.

(101) Backes, C.; Higgins, T. M.; Kelly, A.; Boland, C.; Harvey, A.; Hanlon, D.; Coleman, J. N. Guidelines for Exfoliation, Characterization and Processing of Layered Materials Produced by Liquid Exfoliation. *Chem. Mater.* **2017**, *29* (1), 243–255.

(102) Ogilvie, S. P.; Large, M. J.; O'Mara, M. A.; Lynch, P. J.; Lee, C. L.; King, A. A. K.; Backes, C.; Dalton, A. B. Size Selection of Liquid-Exfoliated 2D Nanosheets. *2D Mater.* **2019**, *6* (3), 031002.

(103) Gravelle, S.; Kamal, C.; Botto, L. Liquid Exfoliation of Multilayer Graphene in Sheared Solvents: A Molecular Dynamics Investigation. *J. Chem. Phys.* **2020**, *152* (10), 104701.

(104) Nishad, W.; Subbiah, S.; Swaminathan, N. A Qualitative Understanding of High Intensity Mechanical Shearing and Exfoliation of Graphite Nanoplatelets in a Three-Body Contact Using Molecular Dynamic Simulations. *Journal of Manufacturing Processes* **2021**, *71*, 645–652.

(105) Seo, D.; Kim, W.-S.; Kim, D. H. Numerical Simulation of Taylor-Couette Fluidic Device for the Exfoliation of Two-Dimensional Materials. *Chemical Engineering Journal* **2020**, *399*, 125726.

(106) Daab, M.; Rosenfeldt, S.; Kalo, H.; Stöter, M.; Bojer, B.; Siegel, R.; Förster, S.; Senker, J.; Breu, J. Two-Step Delamination of Highly Charged, Vermiculite-like Layered Silicates via Ordered Heterostructures. *Langmuir* **2017**, *33* (19), 4816–4822.

(107) John, S. K.; Anappara, A. A. Aqueous Dispersions of Highly Luminescent Boron-Rich Nanosheets by the Exfoliation of Polycrystalline Titanium Diboride. *New J. Chem.* **2019**, *43* (25), 9953–9960.

(108) Keeney, L.; Smith, R. J.; Palizdar, M.; Schmidt, M.; Bell, A. J.; Coleman, J. N.; Whatmore, R. W. Ferroelectric Behavior in Exfoliated 2D Aurivillius Oxide Flakes of Sub-Unit Cell Thickness. *Advanced Electronic Materials* **2020**, *6* (3), 1901264.

(109) Nakato, T.; Sugawara, J. Colloidal State of Exfoliated Oxide Nanosheets of Layered Niobate Characterized with a Molecular-Level Spectroscopic Technique and Macroscopic Observations. *BCSJ* **2007**, *80* (12), 2451–2456.

(110) Nakato, T.; Miyamoto, N. Sol–Gel Transition of Nanosheet Colloids of Layered Niobate $K_4Nb_6O_{17}$. *J. Mater. Chem.* **2002**, *12* (5), 1245–1246.

(111) Nakato, T.; Miyamoto, N.; Harada, A. Stable Liquid Crystalline Phases of Colloidally Dispersed Exfoliated Layered Niobates. *Chem. Commun.* **2004**, *0* (1), 78–79.
(112) Liu, Z.; Ma, R.; Osada, M.; Iyi, N.; Ebina, Y.; Takada, K.; Sasaki, T. Synthesis, Anion Exchange, and Delamination of Co−Al Layered Double Hydroxide: Assembly of the Exfoliated Nanosheet/Polyanion Composite Films and Magneto-Optical Studies. *J. Am. Chem. Soc.* **2006**, *128* (14), 4872–4880.
(113) Ma, R.; Sasaki, T. Two-Dimensional Oxide and Hydroxide Nanosheets: Controllable High-Quality Exfoliation, Molecular Assembly, and Exploration of Functionality. *Acc. Chem. Res.* **2015**, *48* (1), 136–143.
(114) Song, Y.; Iyi, N.; Hoshide, T.; Ozawa, T. C.; Ebina, Y.; Ma, R.; Miyamoto, N.; Sasaki, T. Accordion-like Swelling of Layered Perovskite Crystals via Massive Permeation of Aqueous Solutions into 2D Oxide Galleries. *Chem. Commun.* **2015**, *51* (96), 17068–17071.
(115) Nakada, G.; Igarashi, Y.; Imai, H.; Oaki, Y. Materials-Informatics-Assisted High-Yield Synthesis of 2D Nanomaterials through Exfoliation. *Advanced Theory and Simulations* **2019**, *2* (4), 1800180.
(116) Noda, K.; Igarashi, Y.; Imai, H.; Oaki, Y. Efficient Syntheses of 2D Materials from Soft Layered Composites Guided by Yield Prediction Model: Potential of Experiment-Oriented Materials Informatics. *Advanced Theory and Simulations* **2020**, *3* (7), 2000084.
(117) Gao, H.; Shori, S.; Chen, X.; zur Loye, H.-C.; Ploehn, H. J. Quantitative Analysis of Exfoliation and Aspect Ratio of Calcium Niobate Platelets. *Journal of Colloid and Interface Science* **2013**, *392*, 226–236.
(118) Ariga, K.; Yamauchi, Y.; Rydzek, G.; Ji, Q.; Yonamine, Y.; Wu, K. C.-W.; Hill, J. P. Layer-by-Layer Nanoarchitectonics: Invention, Innovation, and Evolution. *Chem. Lett.* **2014**, *43* (1), 36–68.
(119) Sasaki, T.; Ebina, Y.; Tanaka, T.; Harada, M.; Watanabe, M.; Decher, G. Layer-by-Layer Assembly of Titania Nanosheet/Polycation Composite Films. *Chem. Mater.* **2001**, *13* (12), 4661–4667.
(120) Yuan, H.; Lubbers, R.; Besselink, R.; Nijland, M.; ten Elshof, J. E. Improved Langmuir–Blodgett Titanate Films via in Situ Exfoliation Study and Optimization of Deposition Parameters. *ACS Appl. Mater. Interfaces* **2014**, *6* (11), 8567–8574.
(121) Xiong, P.; Ma, R.; Sakai, N.; Nurdiwijayanto, L.; Sasaki, T. Unilamellar Metallic MoS_2/Graphene Superlattice for Efficient Sodium Storage and Hydrogen Evolution. *ACS Energy Lett.* **2018**, *3* (4), 997–
(122) Withers, F.; Del Pozo-Zamudio, O.; Mishchenko, A.; Rooney, A. P.; Gholinia, A.; Watanabe, K.; Taniguchi, T.; Haigh, S. J.; Geim, A. K.; Tartakovskii, A. I.; Novoselov, K. S. Light-Emitting Diodes by Band-Structure Engineering in van Der Waals Heterostructures. *Nature Materials* **2015**, *14* (3), 301–306.
(123) Osada, M.; Sasaki, T. Nanoarchitectonics in Dielectric/Ferroelectric Layered Perovskites: From Bulk 3D Systems to 2D Nanosheets. *Dalton Transactions* **2018**, *47* (9), 2841–2851.
(124) Ma, W.; Ma, R.; Wang, C.; Liang, J.; Liu, X.; Zhou, K.; Sasaki, T. A Superlattice of Alternately Stacked Ni–Fe Hydroxide Nanosheets and Graphene for Efficient Splitting of Water. *ACS Nano* **2015**, *9* (2), 1977–
(125) Jia, L.; Wan, H.; Liu, X.; Chen, G.; Zhang, N.; Li, J.; Zhou, W.; Cao, Y.; Ma, R.; Qiu, G. Alternate Restacking of 2 D CoNi Hydroxide and Graphene Oxide Nanosheets for Energetic Oxygen Evolution. *ChemSusChem* **2019**, *12* (24), 5274–5281.
(126) Ziegler, C.; Werner, S.; Bugnet, M.; Wörsching, M.; Duppel, V.; Botton, G. A.; Scheu, C.; Lotsch, B. V. Artificial Solids by Design: Assembly and Electron Microscopy Study of Nanosheet-Derived Heterostructures. *Chem. Mater.* **2013**, *25* (24), 4892–4900.
(127) Taniguchi, T.; Li, S.; Nurdiwijayanto, L.; Kobayashi, Y.; Saito, T.; Miyata, Y.; Obata, S.; Saiki, K.; Yokoi, H.; Watanabe, K.; Taniguchi, T.; Tsukagoshi, K.; Ebina, Y.; Sasaki, T.; Osada, M. Tunable Chemical Coupling in Two-Dimensional van Der Waals Electrostatic Heterostructures. *ACS Nano* **2019**, *13* (10), 11214–11223..
(128) Cai, X.; Ma, R.; Ozawa, T. C.; Sakai, N.; Funatsu, A.; Sasaki, T. Superlattice Assembly of Graphene Oxide (GO) and Titania Nanosheets: Fabrication, in Situ Photocatalytic Reduction of GO and Highly Improved Carrier Transport. *Nanoscale* **2014**, *6* (23), 14419–14427.
(129) Lehn, J.-M. Constitutional Dynamic Chemistry: Bridge from Supramolecular Chemistry to Adaptive Chemistry. In *Constitutional Dynamic Chemistry*; Barboiu, M., Ed.; Topics in Current Chemistry; Springer: Berlin, Heidelberg, 2012; pp 1–32.
(130) Lehn, J.-M. Supramolecular Chemistry. *Science* **1993**, *260* (5115), 1762–1763.
(131) Ariga, K.; Komatsu, H.; Hill, J. P. Nanophotonics and Supramolecular Chemistry. *Nanophotonics* **2013**, *2* (4), 265–277.
(132) Sangian, D.; Ide, Y.; Bando, Y.; Rowan, A. E.; Yamauchi, Y. Materials Nanoarchitectonics Using 2D Layered Materials: Recent Developments in the Intercalation Process. *Small* **2018**, *14* (33), 1800551.

(133) Gu, T.-H.; Kwon, N. H.; Lee, K.-G.; Jin, X.; Hwang, S.-J. 2D Inorganic Nanosheets as Versatile Building Blocks for Hybrid Electrode Materials for Supercapacitor. *Coordination Chemistry Reviews* **2020**, *421*, 213439.
(134) Sugaya, T.; Ozaki, M.; Guégan, R.; Idota, N.; Sugahara, Y. Surface Modification of Layered Perovskite Nanosheets with a Phosphorus Coupling Reagent in a Biphasic System. *Langmuir* **2019**, *35* (20), 6594–6601.
(135) Sugaya, T.; Guégan, R.; Idota, N.; Tsukahara, T.; Sugahara, Y. Highly Efficient Surface Modification of Layered Perovskite Nanosheets with a Phosphorus Coupling Reagent Making Use of Microchannels. *Langmuir* **2020**, *36* (26), 7252–7258.
(136) Airoldi, C.; Nunes, L. M.; de Farias, R. F. The Intercalation of N-Alkyldiamines into Crystalline Layered Titanate. *Materials Research Bulletin* **2000**, *35* (13), 2081–2090.
(137) Ogawa, M. Solid-State Intercalation of Naphthalene and Anthracene into Alkylammonium-Montmorillonites. *Clays and Clay Minerals* **1992**, *40* (5), 485–490.
(138) Sangian, D.; Naficy, S.; Dehghani, F.; Yamauchi, Y. A Review on Layered Mineral Nanosheets Intercalated with Hydrophobic/Hydrophilic Polymers and Their Applications. *Macromolecular Chemistry and Physics* **2018**, *219* (13), 1800142.
(139) Wang, Y.; Delahaye, E.; Leuvrey, C.; Leroux, F.; Rabu, P.; Rogez, G. Efficient Microwave-Assisted Functionalization of the Aurivillius-Phase $Bi_2SrTa_2O_9$. *Inorg. Chem.* **2016**, *55* (8), 4039–4046.
(140) Wang, Y.; Delahaye, E.; Leuvrey, C.; Leroux, F.; Rabu, P.; Rogez, G. Post-Synthesis Modification of the Aurivillius Phase $Bi_2SrTa_2O_9$ via In Situ Microwave-Assisted "Click Reaction." *Inorg. Chem.* **2016**, *55* (19), 9790–9797.
(141) Wang, Y.; Leuvrey, C.; Delahaye, E.; Leroux, F.; Rabu, P.; Taviot-Guého, C.; Rogez, G. Tuning the Organization of the Interlayer Organic Moiety in a Hybrid Layered Perovskite. *Journal of Solid State Chemistry* **2019**, *269*, 532–539.
(142) Akbarian-Tefaghi, S.; Teixeira Veiga, E.; Amand, G.; Wiley, J. B. Rapid Topochemical Modification of Layered Perovskites via Microwave Reactions. *Inorg. Chem.* **2016**, *55* (4), 1604–1612.
(143) Boykin, J. R.; Smith, L. J. Rapid Microwave-Assisted Grafting of Layered Perovskites with n-Alcohols. *Inorg. Chem.* **2015**, *54* (9), 4177–4179.
(144) Ogawa, M.; Kuroda, K. Photofunctions of Intercalation Compounds. *Chem. Rev.* **1995**, *95* (2), 399–438.
(145) Okada, T.; Sohmiya, M.; Ogawa, M. Photochromic Intercalation Compounds. In *Photofunctional Layered Materials*; Yan, D., Wei, M., Eds.; Structure and Bonding; Springer International Publishing: Cham, 2015; pp 177–211.
(146) Taviot-Guého, C.; Halma, M.; Charradi, K.; Forano, C.; Mousty, C. Structural and Electrochemical Characterization of Metallo-Porphyrins Intercalated into ZnCr-Layered Double Hydroxides: Some Evidence of Dimer Formation. *New J. Chem.* **2011**, *35* (9), 1898–1905.
(147) Nakada, G.; Imai, H.; Oaki, Y. Few-Layered Titanate Nanosheets with Large Lateral Size and Surface Functionalization: Potential for the Controlled Exfoliation of Inorganic–Organic Layered Composites. *Chem. Commun.* **2018**, *54* (3), 244–247.
(148) Oaki, Y. Exfoliation Chemistry of Soft Layered Materials toward Tailored 2D Materials. *Chem. Lett.* **2021**, *50* (2), 305–315.
(149) Honda, M.; Oaki, Y.; Imai, H. Hydrophobic Inorganic–Organic Composite Nanosheets Based on Monolayers of Transition Metal Oxides. *Chem. Mater.* **2014**, *26* (11), 3579–3585.
(150) Han, Y.-S.; Park, I.; Choy, J.-H. Exfoliation of Layered Perovskite, $KCa_2Nb_3O_{10}$,into Colloidal Nanosheets by a Novel Chemical Process. *J. Mater. Chem.* **2001**, *11* (4), 1277–1282.
(151) Kimura, N.; Kato, Y.; Suzuki, R.; Shimada, A.; Tahara, S.; Nakato, T.; Matsukawa, K.; Mutin, P. H.; Sugahara, Y. Single- and Double-Layered Organically Modified Nanosheets by Selective Interlayer Grafting and Exfoliation of Layered Potassium Hexaniobate. *Langmuir* **2014**, *30* (4), 1169–1175.

Chapter II

Functionalization and reactivity of layered oxides

Chapter II. Functionalization and reactivity of layered oxides

II.1. Introduction

II.1.1 State of the art

Layered oxides are highly designable materials as they can be modified by topochemical reactions such as ion-exchange.[1–3] This process was extensively reviewed by T. Mallouk in 2002[4] and updated by the same group in 2018.[5] It consists in exchanging the native cation of the interlayer space by a positively charged species: cations, molecules, nanoparticles, etc…, leaving the inorganic slabs unchanged or only slightly modified. The interlayer distance of the resulting hybrid materials is then modified. Many papers report the insertion of amine into a lamellar oxide structure:[6–8]the amine is protonated in the form of ammonium following an acid-base reaction and hence is able to electrostatically interact with the negatively charged slabs. Similarly, covalent grafting of organic molecules has been described. This grafting takes advantage of the chemical reactivity of oxides:[9–11]at their surface, the apical oxygens are active sites (nucleophilic species) for condensation reaction (etherification in the case of alcohol grafting) which lead to a direct bond between the inorganic slab and the organic molecule. In this case, the molecule cannot be exchanged anymore unless the breaking of the covalent grafting bond happens.

In addition to the electrostatic interaction, the driving force of ion-exchange mechanism is the concentration gradient of the species between the interlayer space and the surrounding media (usually the solvent in which the inserted species are dispersed and soluble): the larger this gradient is, the faster and efficient the reaction is. An analogy can be made with a porous membrane and an osmotic mechanism.

Limitations on this process come from the cation exchange capacity (CEC) of the layered structure and the steric hindrance between molecules, which prevent the total exchange or grafting. Moreover, most ion-exchange reactions suffer from a slow kinetic. This is all the more true as the inserted molecules are large (*i.e.* they have a small diffusion coefficient). Reaction time can go from hours to days and even weeks.[1,2] Heating can fasten the exchange (increasing of the diffusion coefficient according to the Stokes-Einstein law) but it remains limited. Overcoming the low kinetic of ion-exchange is echoing to organic chemistry: besides catalyst, the use of microwave allows reactions to be considerably fastened.[12] The microwave assistance was extended to coordination and materials chemistry as for instance to synthesize nanoparticles or to make solid state reaction of oxides.[13] The extensive use of this approach relies on its applicability to a large panel of materials whose most of them can interact with microwave. Indeed, materials are categorized in three classes according their interaction:[13]

- Reflectors which completely reflects the microwaves and are usually used as waveguides.
- Transmitters which are transparent to microwaves. Most of microwave reactors are transmitters such as Teflon or glasses.
- Absorbers which are heated up after the absorption of microwave. It is the case of most of the materials and they constitute the reactant in synthesis but also the product.

Concerning layered oxide, they display a high k-dielectric constant, a required parameter in microwave heating. Indeed, a dielectric constant means electric dipoles which can respond to the electric field of microwave.[14] Thus few teams report the use of microwave in the intercalation of molecules and/or particles into layered oxide.[15,16] However, it is worth noting that the exact behavior of oxide when exposed to microwave during a reaction remains unclear. For instance, the inorganic material is usually dispersed in a polar solvent, which also absorbs microwaves and contributes to the global heating. Despite lack of precise knowledge on the mechanism, the use of microwave was pragmatically successful and lead to intercalated layered compounds.[17,18] Notably, our team took advantages of microwave to insert amines and graft alcohols and diols quickly and efficiently into perovskite-like structure.[8,9,19,20] The reaction time was incredibly lowered (from days to few hours), keeping the crystallinity of the inorganic layer unchanged. Besides, the insertion or grafting rate was similar to the one obtained by conventional experimental conditions despite some structural differences ascribe to the degree of interdigitation of organic entities.[19]

II.1.2 Objectives

In this chapter, we will briefly review the insertion and grafting reactions into some layered oxides. We will essentially focus our study on the Aurivillius phase $Bi_2SrTa_2O_9$ (BST), but we will also investigate the functionalization of a niobiate-perovskite layered material (the Dion-Jacobson phase $KLaNb_2O_7$). We will rapidly recall their microwave assisted-functionalization by amines and the corresponding characterization. Then, we will describe the modification of their interlayer space by alcohols derivatives. Finally, we will consider a titanate phase $K_{0.8}Ti_{1.73}Li_{0.27}O_4$ with a lepidocrocite structure and we will study its interlayer modification and discuss its reactivity.

Furthermore, this study aims at elaborating strategies to overcome some inherent issues of functionalization: lack of reactivity of some chemical functions, preferential grafting of amine versus alcohol, or hydrolysis of the grafted molecule. Hence, we show below that knowing the inorganic phase and its reactivity, knowing the molecule and its properties (solubility, pKa,…) and using some modifications in the experimental settings with respect to the ones generally used, it could be possible to design new hybrid layered phase which fulfill requirements for exfoliation and further reassembly.

Hence, we will finally investigate the functionalization of amine- or alcohol-based hybrid by specific molecules. We will first describe the grafting of alkylphosphonic acid which allows a strong coupling with the inorganic layer material. Then, we will show that it is possible to synthesize layered hybrid with a free functional group (amine or thiol) in the interlamellar spacing *via* the use of a silane as anchoring function. Finally, functional molecules such as pyrenes, for their luminescence properties, or nucleosides, for their ability to be specifically coupled, are also grafted onto the interlayer space of a layered oxide.

II.2. Functionalization by *n*-alkylamines and *n*-alcohols

II.2.1 Functionalization the layered Aurivillius oxide, $Bi_2SrTa_2O_9$

Herein, we consider the Aurivillius phase $Bi_2SrTa_2O_9$ (BST) which was extensively studied for its potential ferroelectric behavior.[21,22] Previous studies in our group were also based on this oxide.[8,9,19] BST is obtained through a two-step stoichiometric solid-state reaction between Bi_2O_3, $SrCO_3$ and Ta_2O_5. The corresponding protonated phase $H_2Bi_{0.1}Sr_{0.85}Ta_2O_7.2H_2O$ (HST) is obtained *via* the leaching of the (Bi_2O_2) layer (see **Chapter I**) by acidic treatment with microwave assistance (70°C for 3 hours) (see **Experimental Section**).[20]

X-Ray-Diffraction (XRD) patterns of both BST and HST are shown in ***Figure 1.*** BST can be indexed in an orthorhombic cell and HST can be indexed in a tetragonal cell with lattice parameter a = 0.552 nm, b = 0.552 nm, c = 2.51 nm as reported in literature.[23] The protonated phase HST displays (*100*), (*110*) and (*200*) reflections at 22.7°, 32.3° and 46.4° respectively. These reflections are meaningful of the structure of the inorganic $Bi_{0.1}Sr_{0.85}Ta_2O_7^{2-}$ layer. The low angle peak at 8.7° corresponds to the (*001*) reflection which attests for the layered structure. The related distance d_{001} = 0.99 nm is the sum of the inorganic layer thickness and the interlayer spacing ($d_{001}= d_{layer}+ d_{interlayer}$). Nevertheless this d_{001} is usually called "interlayer distance" or "interlamellar distance". In the following, we denoted d_{001} as the interlayer distance too for simplification, but one has to keep in mind that it includes the inorganic layer thickness.

The interlayer modification with alkylamine is performed with microwave assistance. The precursor HST reacts with ethylamine (C_2NH_2), 1-butylamine (C_4NH_2) or 1-dodecylamine ($C_{12}NH_2$) in a large excess. The reaction is carried out in THF, in presence of water (about 10% in volume) at 110°C for 1 hour. The importance of water in such reaction has been underlined in the literature and in our group. Y. Wang showed that in fact this reaction does not proceed in dried solvents.[8,24] The powder is isolated by centrifugation and then washed three times with water to remove un-inserted molecules and dried in air overnight.

The resulting hybrid powders are denoted C_2N-HST, C_4N-HST and C_{12}N-HST. Their XRD patterns are shown in ***Figure 1***. The three hybrids display (*100*), (*110*) and (*200*) reflections at 26.4°, 32.3° and 46.2°. However, three new peaks are now distinguishable close to the three in-plane reflections. They correspond to the splitting of the (*100*), (*110*) and (*200*) peaks of HST. This duplication results from the distortion of the structural (TaO_6) octahedra when interacting with the ammonium moiety. Despite this distortion, the inorganic structure remains essentially unchanged. The XRD patterns also display low angles peaks corresponding to the (*00l*) reflections and characteristic of a layered structure. The interlayer distances of the hybrids are 1.55 nm, 2.06 nm and 3.47 nm for C_2N-HST, C_4N-HST and C_{12}N-HST respectively. The interlayer space is thus extended compared to HST, in line with the insertion of the molecules, and it increases as the carbon chain length increases.

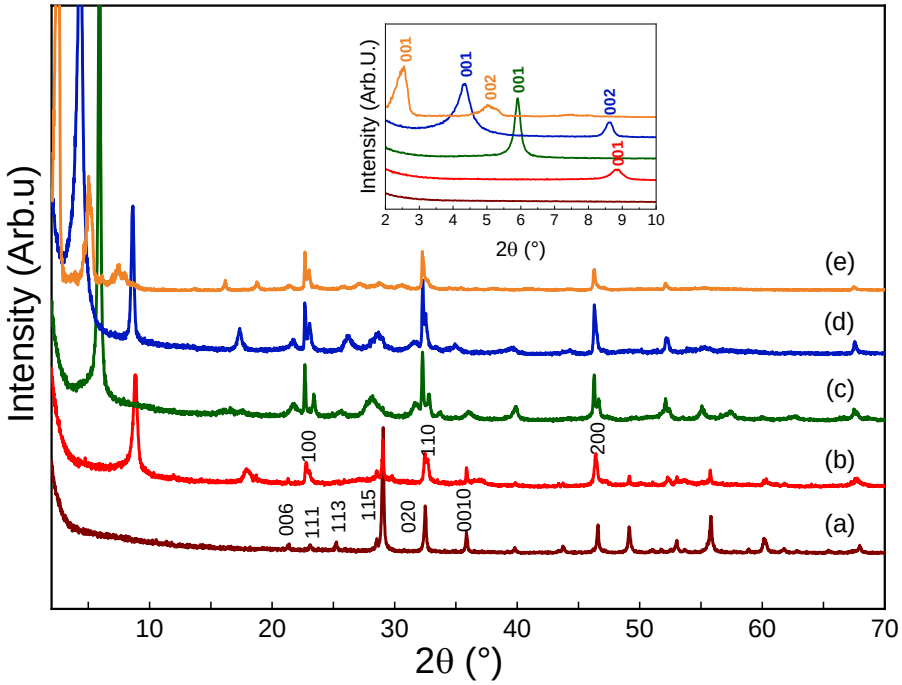

Figure 1: XRD patterns of (a) BST, (b) HST, (c) C_2N-HST, (d) C_4N-HST and (e) C_{12}N-HST. The insert is a magnification of the low angles region.

Fourier-Transform-Infrared (FTIR) spectroscopy also emphasizes the presence of the alkylamine into the layers. The spectra of HST, C_2N-HST, C_4N-HST and C_{12}N-HST are shown in ***Figure.2***. The NH_3 degenerate deformation band at 1584 cm^{-1}, 1583 cm^{-1} and 1567 cm^{-1} for C_2N-HST, C_4N-HST and C_{12}N-HST respectively is characteristic of primary ammonium. In addition, for C_4N-HST and C_{12}N-HST, the intensity of C-H vibration bands around 2900 cm^{-1} are consistent with the carbon chain length (it is far more intense in the case of C_{12}N-HST). As 1-ethylamine contains only one (CH_2) and one (CH_3) groups, these bands are barely visible in the spectrum of C_2N-HST. In all FTIR spectra, an intense band below 700 cm^{-1} is ascribed to the M-O bond deformation and attests the presence of the inorganic slabs. The position of this band varies according the molecule which interacts with the layer. However, no clear tendency has been observed by our group or in literature and we do not draw any other conclusions from this band.

The protonated layered oxide HST can also be functionalized by alcohols derivatives. Y. Wang in our group[19] as well as other groups[24,25,17] have shown that the alcohol group reacts with the inorganic slab, resulting in a covalent bond between the two entities. Thus, the organic molecules are less likely to be exchanged by other ones, unlike amines. In this work, we functionalized HST with microwave assistance according the method developed in our group.[20]

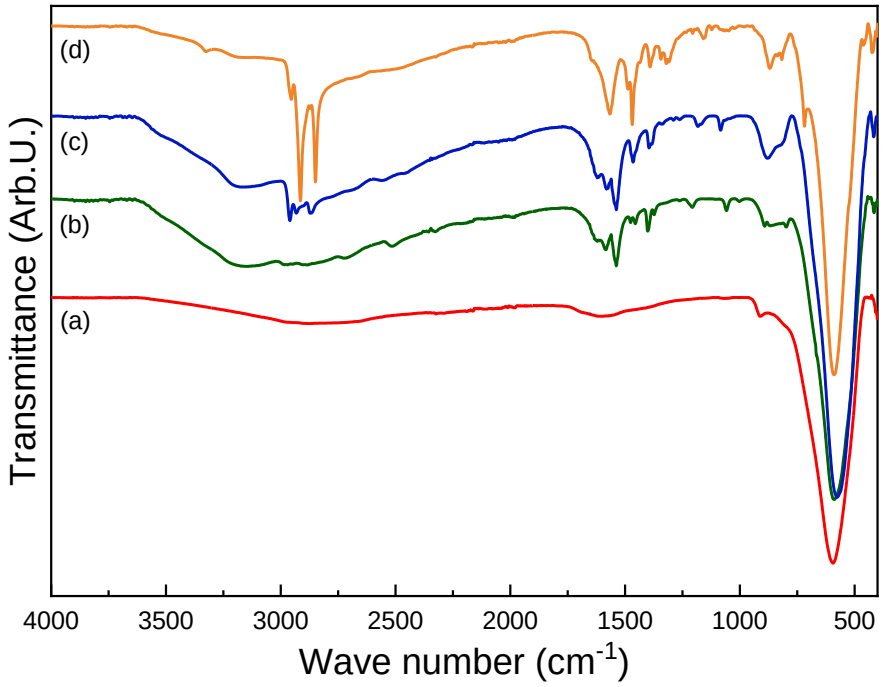

Figure.2: FTIR spectra of (a) HST, (b) C_2N-HST, (c) C_4N-HST and (d) C_{12}N-HST.

The precursor C_4N-HST is poured into the pure alcohol in liquid form: we considered ethanol, 1-dodecanol as model molecules (for the latter, heating at 70 °C is necessary to obtain the liquid state), benzylalcohol (1-phenylmethanol) as an instance of aromatic molecule and finally 2-(benzylthio)ethanol, an intermediate case with a specific thiol function which might be useful for further elemental detection. The reaction was heated at 130°C for 130 min with microwave and with a small amount of water (about 1 mol %). The as-obtained white powder is isolated by centrifugation, washed one time with water and two times with acetone and dried in air overnight (Note: washings were made with water for grafting of 2-(benzylthio)ethanol)

The resulting hybrids materials are denoted C_2O-HST, C_{12}O-HST, BenzO-HST and BenzSC_2O-HST respectively. We first characterized them with XRD and the patterns are shown in ***Figure 3.*** All diagrams display the (*100*), (*110*) and (*200*) reflections at 22.6°, 32.2° and 46.2° respectively. Thus, the functionalization by alcohol did not modify the inorganic layer structure. In addition, all the XRD patterns in ***Figure 3*** show low angle (*00l*) reflections, meaningful of a layered structure. The corresponding interlayer distance is 1.54 nm, 2.03 nm, 2.08 nm and 4.02 nm for C_2O-HST, BenzO-HST, BenzSC_2O-HST, and C_{12}O-HST respectively. The evolution of this interlayer distance compared to the one of C_4N-HST (*i.e.* the precursor, 2.06 nm) was expected for C_2O-HST and C_{12}O-HST: by increasing the carbon chain length, the interlayer is increasing and reversely. However, we notice that for aromatic compounds, this trend is not followed. BenzO-HST and BenzSC_2O-HST have an interlayer distance similar to the one of C_4N-HST: we ascribe this particularity to the aromatic ring which modifies the interaction between molecules and/or between the inorganic layer and the molecules.

In parallel, we investigate the grafting of longer molecules such as 1-octadecanol ($C_{18}OH$) into the inorganic layers of HST. The first experiments, using C_4N-HST as precursor and the same experimental conditions as previously, did not allow to synthesize the hybrid $C_{18}O$-HST. The resulting powder was poorly crystalline with an interlayer distance close to HST: the 1-butylamine was removed from the structure without any insertion and grafting of the alcohol. Therefore, we carried out the grafting reaction of $C_{18}OH$ using $C_{12}O$-HST as precursor. The interlayer distance of $C_{12}O$-HST, 4.02 nm, is much larger than the one of C_4N-HST which might help to graft longer molecule. The experimental settings are close to the grafting of alcohol *i.e.* in presence of a small amount of water (about 1 mol %) and microwave heating at 130 °C for 130 min. The only difference is that the precursor and alcohol are both at solid state at the beginning (the alcohol melt during the temperature ramp to reach 130 °C). The resulting powder, denoted $C_{18}O$-HST, is first characterized by XRD. The corresponding pattern is shown in ***Figure 3***. It displays a series of reflections at low angles corresponding of the second to fifth harmonic of the (*001*) reflection (which is not seen on the XRD patterns because it appears at a too low angle *i.e.* below 2°). The interlayer distance is d_{001} = 6.67 nm. In addition, the XRD pattern displays (*100*), (*110*) and (*200*) reflections which are characteristic of the layered structure. This diagram, typical of layered system, shows that despite the huge extension of the slabs along the c-axis, there is still coherence between the inorganic layers. Yet it is worth noticing that the crystallinity is poorer than for the other compounds.

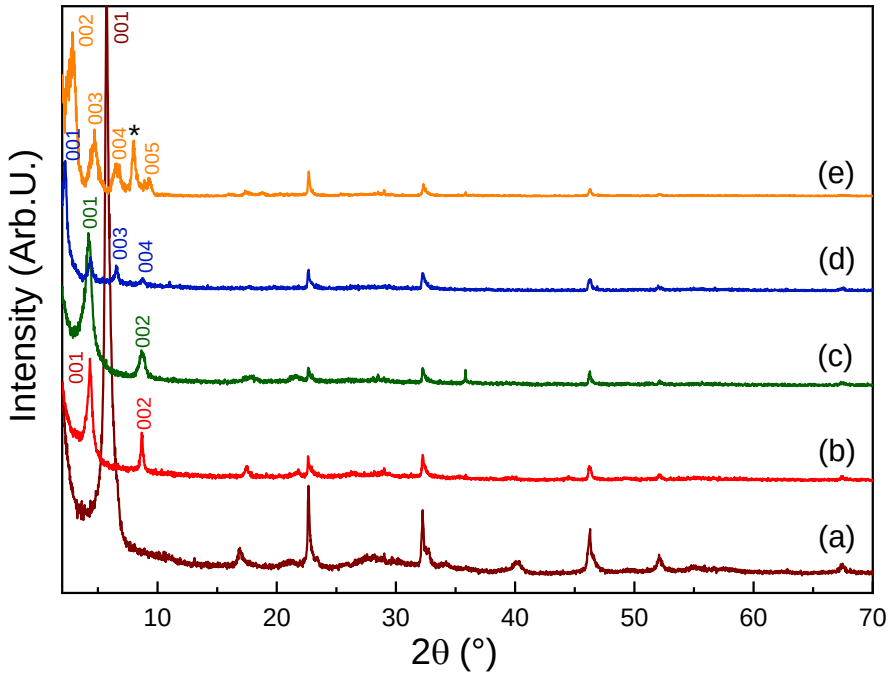

Figure 3: XRD patterns of (a) C_2O-HST, (b) BenzO-HST, (c) BenzSC_2O-HST, (d) $C_{12}O$-HST and (e) $C_{18}O$-HST. The peak with a star corresponds to an impurity of HST.

We carried out FTIR spectroscopy to further study the grafting of the alcohols derivatives. The FTIR spectra of the alcohol-based hybrids are shown in ***Figure 4.*** First, we notice the disappearance of the NH_3 degenerate deformation band around 1587 cm^{-1}, characteristic of the ammonium moiety in C_4N-HST. The covalent grafting of the alcohol is evidenced by the C-O vibration band shift: it appears at around

1050 cm^{-1} for the free molecules and moves to 1145 cm^{-1} for C_2O-HST, $C_{12}O$-HST and $C_{18}O$-HST, to 1133 cm^{-1} for BenzO-HST and 1123 cm^{-1} for $BenzSC_2O$-HST. The three former hybrids also display (CH_3) bending bands at 1470cm^{-1} (asymmetric) and 1380 cm^{-1} (symmetric). The C-H stretching bands between 2850 cm^{-1} and 2950 cm^{-1} also confirms the presence of long alkyl chain in the case of $C_{12}O$-HST and $C_{18}O$-HST. For BenzO-HST and $BenzSC_2O$-HST, a clear band at is observed at 1450 cm^{-1} and it is characteristic of the C=C stretching band, showing the integrity of the molecules.

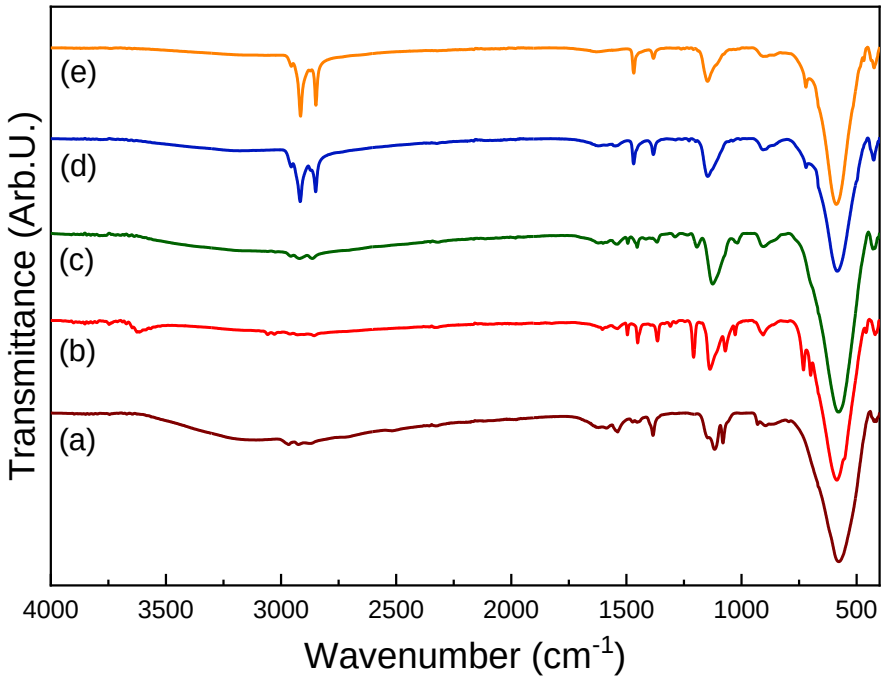

Figure 4: FTIR spectra of (a) C_2O-HST, (b) BenzO-HST, (c) $BenzSC_2O$-HST, (d) $C_{12}O$-HST and (e) $C_{18}O$-HST.

We showed above that microwave assistance is efficient to graft alcohol derivatives into HST using intermediate hybrid compound C_4N-HST. It is worth underlining that not only aliphatic molecules can be hosted but aromatic compounds can also be grafted. In addition, we demonstrated that long molecules like $C_{18}OH$ can be grafted into HST by using $C_{12}O$-HST as intermediate. This general strategy presented here will be use in the following to grafted more complex molecules as thymidine or adenosine into HST

II.2.2 Functionalization of the layered Dion-Jacobson oxide, $KLaNb_2O_7$

As stated in the General Introduction, in the frame of the building assembly strategy towards new heterostructures and new properties, we have to consider the functionalization of a second inorganic layer material. It must be different from BST (or its corresponding protonated HST) in terms of composition, to enable unambiguous characterization of the heterostructure that may be formed ultimately. In this work, we are for the moment interested in a proof of concept, so the properties of the inorganic layer are not a major stake for now. We considered the niobate Dion-Jacobson phase, $KLaNb_2O_7.xH_2O$ whose catalytic properties have been investigated during the past decades above all its role in the water splitting.[26,27] Here,

the inorganic layers have also a perovskite-like structure, like BST/HST. Although a slight difference in terms of reactivity are expected,[28,29] the two structurally-close compounds behave similarly towards amines and alcohols in a functionalization reaction, as already observed in literature.[18]

$KLaNb_2O_7.xH_2O$ (KLN) is synthesized by a solid-state reaction between stoichiometric quantities of K_2CO_3, La_2O_3 and Nb_2O_5.[30] Its XRD pattern is shown in ***Figure 5*.** The structure corresponds to what is described in literature.[3] However, the XRD pattern also emphasizes the presence of an impurity of $La_{1.67}Nb_5O_{15}$. We carried out additional trial by adding 10% of K_2CO_3 as it is volatile and might be deficient in the first experiment. We also increased the temperature. Yet, we were not able to remove this side product in any experiments.

The protonated phase $HLaNb_2O_7.xH_2O$ (HLN) is obtained by acidic treatment of KLN at room temperature for 1 day. As this reaction involves concentrated nitric acid (6.5 M) and considering the relative short reaction time, the use of microwave-assistance was not relevant at this stage. The XRD pattern is shown in ***Figure 5*.** The (*100*) and (*110*) reflections at 22.7° and 32.8° respectively are similar to the one of HST and characteristic of the in-plane structure. The (*001*) reflection at 8.2° corresponds to an interlayer distance of d_{001} = 1.11 nm. The impurity of $La_{1.67}Nb_2O_{15}$ is still observed and acidic treatment did not allow to remove it. Meanwhile, the by-product is not a layered compound and we experimentally noticed that it did not react with amines or alcohols. Thus, we proceeded functionalization (and subsequent exfoliation, see **Chapter V**) on HLN.

In a first step, we inserted alkylamines into HLN with microwave assistance according to published procedure.[18] HLN reacts with the chosen amines, 1-butylamine (C_4NH_2) or 1-dodecylamine ($C_{12}NH_2$), used in a large excess. The reaction is carried out in THF with a small amount of water (10% volume), at 110°C for 1 hour. Then the powder is collected by centrifugation (14000 rpm, 10 min), washed three times with water and dried in air overnight.

The resulting hybrids are denoted as C_4N-HLN and C_{12}N-HLN. The XRD patterns of both hybrids display the (*110*) and (*110*) reflections at 22.7° and 32.8°, meaning that the inorganic layer structure remains essentially unchanged. In addition, the interlayer distance of 2.08 nm and 3.30 nm for C_4N-HLN and C_{12}N-HLN are larger than the one of HLN. It attests the extension along the c-axis of the interlayer space in line with the insertion of the molecules.

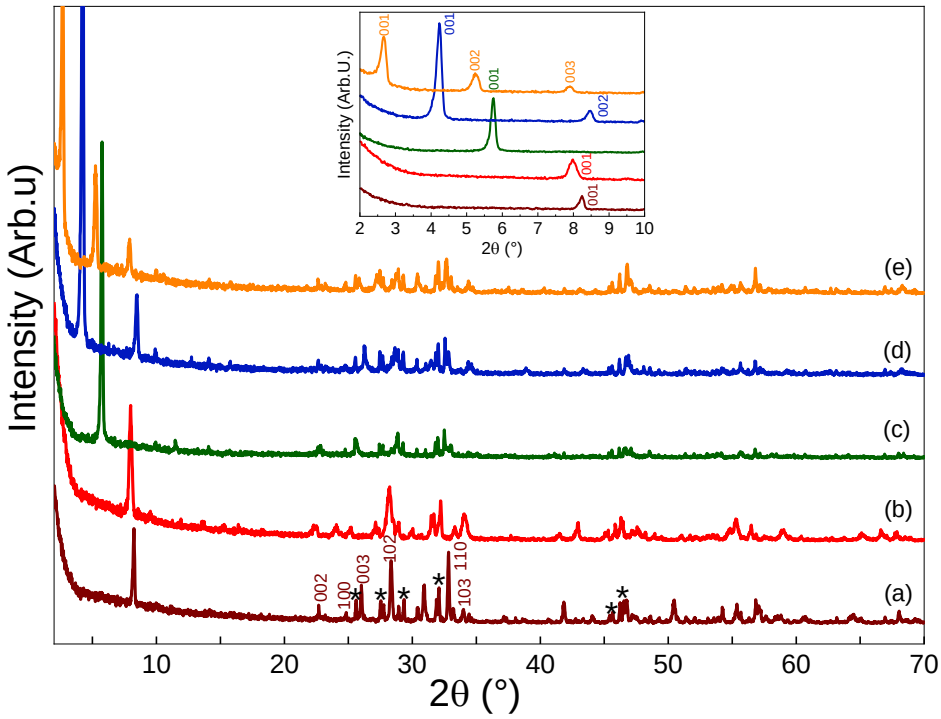

Figure 5: XRD patterns of (a) KLN, (b) HLN, (c) C_3O-HST, (d) C_4N-HLN and $C_{12}N$-HLN. The peaks with the star on the XRD pattern of KLN correspond to an impurity of $La_{1.67}Nb_5O_{15}$. These peaks are also found in all the XRD patterns.

The FTIR spectra of C_4N-HLN and $C_{12}N$-HLN (***Figure 6***) also confirm the insertion of organic entities. The NH_3 degenerate deformation band at 1585 cm^{-1} as well as the NH_3 rocking vibration band at 890 cm^{-1} emphasize the presence of the ammonium moiety. The C-H vibration bands at 2850 cm^{-1} and 2915 cm^{-1} are characteristic of the alkyl chain.

The insertion of amines works indeed as described in the literature using classical process[2,3] and using microwave activation.[18] As we succeed the functionalization by amines, we investigated the modification of HLN by alcohols. We consider C_4N-HLN as precursor (by analogy with the pre-intercalation method used with HST). However, the resulting hybrids do not show an increase of their interlayer space and the FTIR spectra do not display the C-O vibration band around 1120cm^{-1} which is characteristic of the alcohol moiety. On the contrary, the spectra are closed to the one of C_4N-HLN. Thus, we investigate the direct grafting of small alcohol into HLN without any intermediate. HLN was poured into the alcohol, the 1-propanol, with a small amount of water (about 1 mol %). The mixture was heated with microwave at 130°C for 130 min. The resulting compound is denoted C_3O-HLN and its XRD pattern is shown in ***Figure 5***. The characteristic (*100*), (*110*) reflections of the $LaNb_2O_7^-$ layer are still observed at 24.7° and 33.0° respectively. The interlayer distance of 1.54 nm confirms the extension of the interlayer along the c-axis due to the organic content. FTIR spectrum of C_3O-HLN is shown in ***Figure 6.*** It displays a C-O vibration band at 1115 cm^{-1} corresponding to the stretching of the C-O-Nb bond. The band is shifted compared to the C-O vibration band at 1080 cm^{-1} of free 1-propanol which is also observed on the

spectrum, probably due to incomplete washing. In addition, the weak C-H stretching bands around 2900 cm^{-1} are characteristic of the alkyl chain.

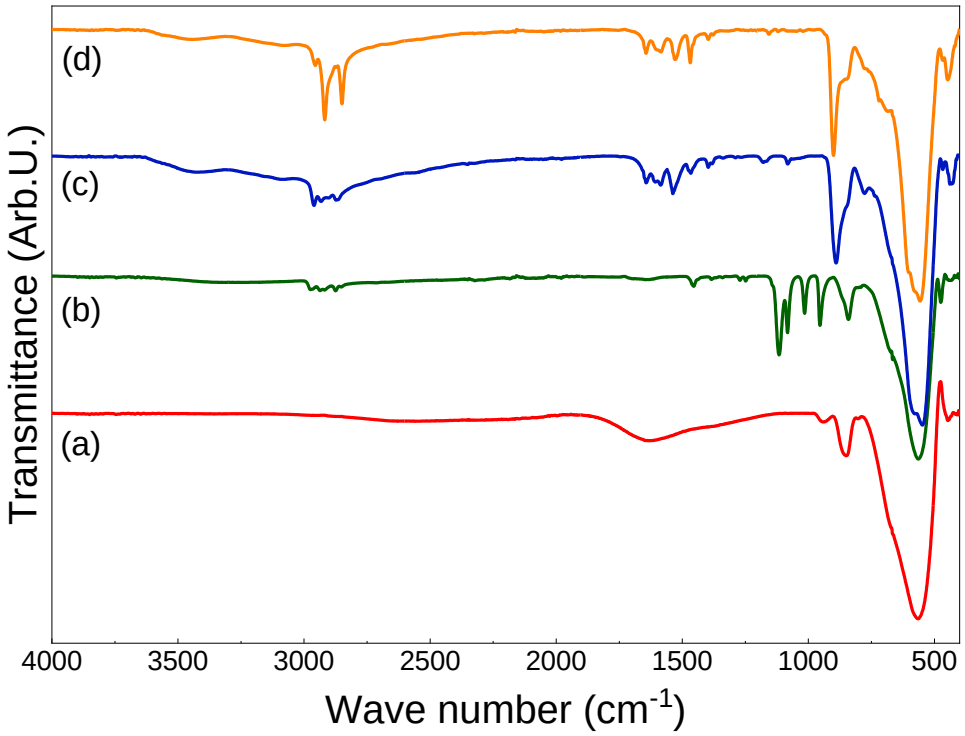

Figure 6: FTIR spectra of (a) HLN, (b) C_3O-HLN, (c) C_4N-HLN and (d) $C_{12}N$-HLN.

In conclusion, we showed that HLN can be modified by alkylamine by using microwave assistance. However, the grafting of alcohols using C_4N-HLN as precursor does not work. Thus, we synthesized C_3O-HLN directly from HLN. The impossibility to replace amines by alcohols in RN-HLN had already been described by J. Wiley *et al.* C_3O-HLN will be used as precursor for subsequent grafting of longer and more complex alcohols derivatives into HLN.

II.2.3 Functionalization of the layered lepidocrocite titanate, $K_{0.8}Ti_{1.73}Li_{0.27}O_4$

Once again, in the trend of further re-assembling oxide nanosheets with distinct properties, we wanted to investigate the organic modification of a third layered oxide. Titanate layered materials have drawn attention since decades notably due to their photocatalytic properties.[31,32] Among them, the lepidocrocite-like titanate, $K_{0.8}Ti_{1.73}Li_{0.27}O_4.xH_2O$ (KTO) was extensively studied by T. Sasaki *et al.* whose works on exfoliation, characterization and use of this phase are pioneering and constitute a basement for later works on nanosheets.[6,33–35] Hence many papers report its modification by organic entities such as alkylamine[7,36], organosilane[37,38]. Only one paper reports the intercalation of *n*-alcohol into layered titanates: the replacement of the prior amine into the structure is performed under high pressure (about 1 to 10 GPa).[39] Otherwise, so far there is no mention of *n*-alcohol grafting into titanates in

literature. Therefore, in the following we aim at exploring the covalent attachment of alcohol into KTO as we explored it for BST and KLN.

KTO is obtained through a stoichiometric solid state reaction between $LiCO_3$, K_2CO_3 and TiO_2 according published procedure.[40] The XRD pattern is shown in ***Figure 7***. The structure is in accordance with what is reported in literature.[40,41] The protonated form $H_{1.07}Ti_{1.73}O_4.xH_2O$ (HTO) is obtained by the acidic treatment of KTO at room temperature according to a procedure published by T. Sasaki *et al.*[40] Their group also evidenced the removal of the Li^+ cation from the structure and its replacement by protons H^+. The XRD pattern of HTO is shown in ***Figure 7.*** The diagram can be indexed in a C-based orthorhombic cell with cell parameters a = 0.3782 nm, b= 0.2993 nm and c= 0.9251 nm, in accordance with literature.[40]

We then investigate the microwave functionalization of HTO by alkylamine. Indeed as stated above, the microwave-assisted functionalization of HTO have never been reported. In addition to the synthesis of the hybrid materials, it appears interesting to study the applicability of microwave activation reaction to lepidocrocite-like layered materials, besides the perovskite-like layered ones.

The protonated HTO was poured in a mixture of THF and the alkylamine, 1-butylamine or 1-dodecylamine, heated at 110°C for 1 hour in presence of a small amount of water (about 10% volume). However, the resulting materials did not display any expansion along the c-axis. The observed interlayer distance remains close to the one of HTO. In addition, the (*h00*), (*h0l*) and (*0kl*) reflections were no longer visible. Similarly, the FTIR spectra do not show the presence of the alkylammonium. Unlike tetratitanates or perovskite-like titanates which have been successfully modified by microwave irradiation,[15,42] HTO seems to not follow the same trend. We hypothesize that the structure is more fragile and might be modified during the process as depicted by H. Yuan *et al.*[43]

Therefore, we performed the functionalization of HTO by amines at room temperature and atmospheric pressure, following protocols adapted from literature.[44] Typically, 120 mg of HTO was poured in an aqueous solution (50 ml) containing 3 ml of 1-buytlamine (40% in water). The solution was stirred at room temperature for 3 hours. The powder was isolated by centrifugation (14000 rpm, 10 min), washed three times with water and dried in air overnight.

The resulting hybrids are denoted as C_4N-HTO and C_{12}N-HTO and their XRD patterns are shown in ***Figure 7.*** The shift of the (*001*) peaks toward the low angle region attests the expansion of the interlayer distance. The corresponding interlayer distances are 1.60 nm and 2.74 nm for C_4N-HTO and C_{12}N-HTO respectively.

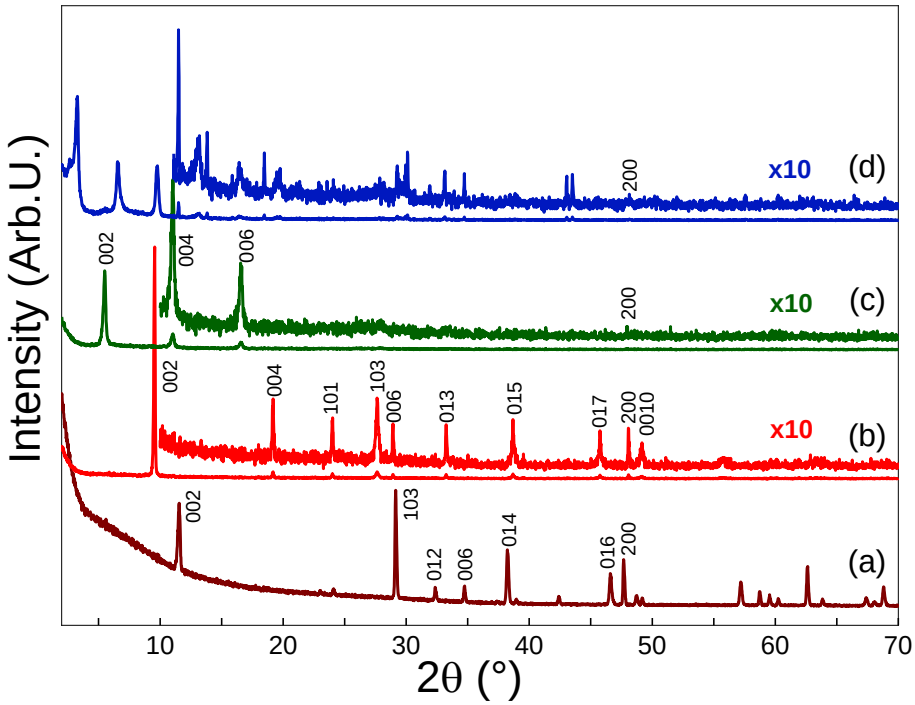

Figure 7: XRD patterns of (a) KTO, (b) HTO, (c) C_4N-HTO and (d) C_{12}N-HTO.

In a second step, we investigated the modification of the layered HTO by alcohols which, to our knowledge, has never been reported. However, whatever the precursor (C_4N-HTO or HTO alone) or the heating source (microwave, hot plate or room temperature), we were not able to graft alcohol onto the lepidocrocite-like titanate.

We ascribe this observation to the acidity of the HTO phase which related to the structure and composition of the layered phase.[28] This parameter might explain the difference towards insertion and grafting of the three inorganic layered phases HST, HLN and HTO. Acidity of an oxide can be related to its isoelectric point (IEP), estimated by plotting the zeta potential ξ of the inorganic phase as a function of pH. The IEP corresponds to the value of pH where as many positive and negative charges are present at the oxide surface *i.e.* ξ =0. In ***Figure 8***, the zeta potential profiles as a function of pH for HST, HLN and HTO are represented. The IEP of the three compounds are 4.6, 3.8 and 3.1 respectively. HTO is indeed the more acidic phase: the amines are then strongly bonded to the inorganic layer and cannot be exchanged by alcohol. At the opposite, HST is the less acidic one and the amines can be replaced by alcohols. HLN is in between HST and HTO: we were thus able to graft alcohol directly from HLN but not from C_4N-HLN.

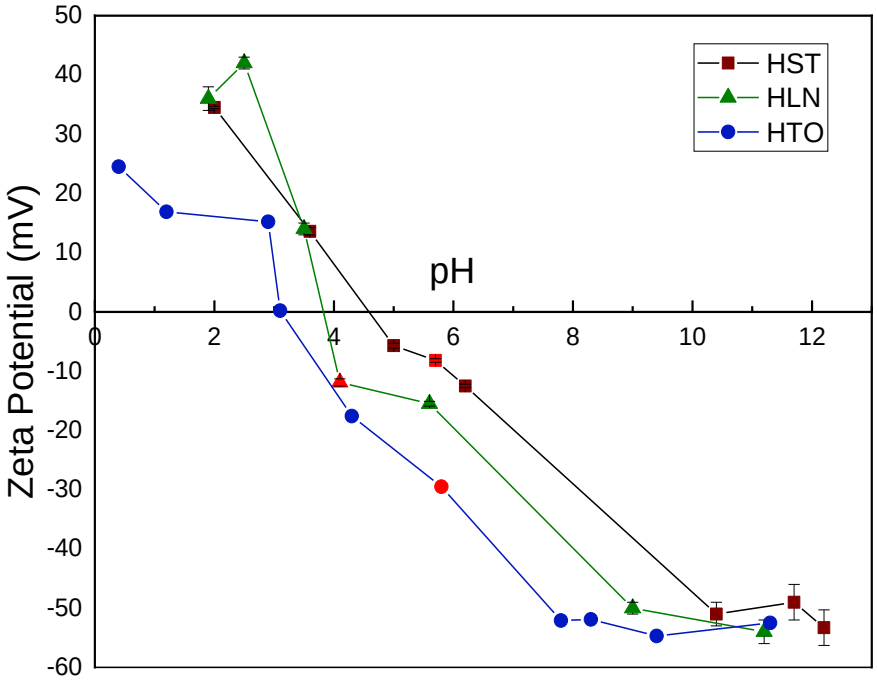

Figure 8: Isoelectric profiles of three protonated layered materials. The bare lines are help for the eyes and do not possess any physical meaning. The red point on each curve represent the zeta potentials of the bare dispersed solution of HST, HLN and HTO without addition of $HCl_{(aq)}$ or $NaOH_{(aq)}$.

II.2.4 Conclusion

In this part, we investigated the functionalization of three layered oxides, $Bi_2SrTa_2O_9$, $KLaNb_2O_7$ and $K_{0.8}Ti_{1.73}Li_{0.27}O_4$. We show that the protonated form of BST, $H_2Bi_{0.1}Sr_{0.85}Ta_2O_7$, is very reactive and can host amines (in form of ammoniums) and can be modified by the grafting of an alcohol. This hybridization was carried out with microwave assistance and leads to crystalline layered hybrid oxides. Similarly, $HLaNb_2O_7$ was functionalized by alkylamines under microwave irradiation. The grafting of alcohol is also allowed even if the precursor of such reaction cannot be the amine-based hybrid but has to be an alcohol-based hybrid. Finally, the titanate $H_{1.07}Ti_{1.73}O_4$ cannot be modified by alcohol grafting while amines are easily inserted by classical ion-exchange at room temperature.

In the following and the subsequent functionalization experiments, we focus on HST as it is the most versatile inorganic phase in terms of grafting. In some peculiar situations, we will consider the HLN phase (for instance when grafting phosphonic acid derivatives). However, we will not discuss further on HTO.

II.3. Functionalization by molecules of interest

II.3.1 Grafting by alkylphosphonic acid derivatives: a model system

II.3.1.1 Introduction

Surface modification of nanosheets allows a modulation of their properties and should play a major role in their stability. As seen above in **II.2**, grafting of alcohols is more suitable for further exfoliation than insertion of amines because of the covalent nature of the bond between the organic molecule and the inorganic moiety. Nevertheless, we observed the hydrolysis of this alcohol grafting when the hybrid compound was subjected to heating into water under microwave irradiation (without any pH modification). Moreover, the mechanical liquid-phase exfoliation method, either ultrasound or shear, usually leads to an increase of the temperature of the solvent (up to several degrees, depending on the experimental conditions and solvent viscosity). Therefore, we fear that C-O-M bond might be damaged during the exfoliation process.

In order to overcome this issue, we investigated the grafting of another kind of molecules, namely phosphonic acid derivatives. The latter molecules have already been coupled with a large panel of oxides to modify their surface.[45–47] Nevertheless, only few paper reports the interlayer modification of layered oxide with organophosphonic acid.[48] The team of Y. Sugahara *et al.* functionalized the hybrid *n*-decoxy-HLN (C_{10}O-HLN) with a series of *n*-alkylphosphonic acid and phenylphosphonic acid.[49] They highlight the important role of water in the grafting mechanism: the initial C-O-Nb bond must be hydrolyzed to allow the grafting of the phosphonic acid. This latter step corresponds to an esterification mechanism with water departure. Similarly, the group of H. Ploehn *et al.* grafted phenylphosphonic acid onto perovskite nanosheets.[48] They first carried out the exfoliation of a calcium niobate oxide through a conventional ion-exchange exfoliation using tetrabutylammonium hydroxide. Then, they performed a ligand exchange to functionalize the nanosheets. Thus, they proved that alkylamine-modified perovskite-like oxide can also be a precursor for phosphonic acid condensation. Furthermore, H. Mutin *et al*. demonstrated the advantages of surface modification by phosphonic acid group.[46] The P-O-M bond is less suitable to hydrolysis compared to alcohol or silane coupling reagent.[49] Moreover, the grafting of phosphonic acid has a clear spectroscopic signature and the phosphorous element is easier to detect and to be dosed in elemental analysis compared to carbon. This point would make the post-exfoliation characterization easier. Herein, we described the grafting of alkylphosphonic acids into the HST from an alkylamine-based precursor, C_4N-HST. We investigate the grafting mode of phosphonic acid thanks to advanced structural analysis (*i.e.* Pair Distribution Function (PDF)) and spectroscopic techniques.

II.3.1.2 Synthesis and characterization

The synthesis derives from the works on alcohols and amines insertion into HST. We were able to graft the 1-propylphosphonic acid $C_3H_7PO(OH)_2$, the 1-hexylphosphonic acid $C_6H_{13}PO(OH)_2$ and the 1-decylphosphonic acid $C_{10}H_{21}PO(OH)_2$ into HST *via* a pre-intercalation strategy, using C_4N-HST as precursor. Typically, C_4N-HST was poured into a 30-mL-microwave reactor in presence of the organophosphonic acid and 10 mL of non-anhydrous THF. This latter point crucial as the presence of

water is mandatory to the reaction occurs. The mixture was heated at 110°C under microwave irradiation for 130 minutes. After reaction, the obtained white powder was collected by centrifugation, washed three times with acetone and dried in air overnight.

The resulting compounds are denoted as C_3PO_3-HST, C_6PO_3-HST and $C_{10}PO_3$-HST respectively. It is worth mentioning that these notations were chosen for the sake of simplicity. Nevertheless a better designation would be $C_xPO(OH)$-HST which reflects the grafting of the phosphonic acid followed by the removal of water, as discussed above. ***Figure 9*** shows the XRD patterns of the series of hybrid compounds. The in-plane reflections assigned to (*100*), (*110*) and (*200*) planes (at 22.68°, 32.59° and 46.32° respectively) are also found in the XRD pattern of HST. It shows that the inorganic perovskite-like structure of the slabs remains unchanged after microwave-assisted functionalization. The layered structure of the compounds is evidenced by the intense low angle series of peaks corresponding to (*00l*) reflections. As expected, the interlayer distance increases with the size of the inserted molecule: 1.02 nm for HST, 1.97 nm for C_3PO_3-HST, 2.51 nm for C_6PO_3-HST and 3.26 nm for $C_{10}PO_3$-HST. These values are in accordance with a linear dependency of the interlayer distance in respect the carbon chain length. This relationship is expressed as $d_{001} = 0.184 * n_c + 1.41$ where d_{001} is the interlayer distance in nm and n_c is the number of carbon of the alkyl chain. The slope of 0.184 nm per C is larger than the C-C distance of 0.127 nm between two adjacent carbons. This statement testifies the titled bilayer arrangement of the organic molecules, rather than an interdigitation between the alkyl chains.

The tilt angle made by a molecule with respect to the normal of the layer plane is 44°, which is similar to the tilt angle of 42° for the amine hybrid.[8] In contrast, *n*-alkoxy derivatives display a tilt angle of 19°.[9] In addition, this tilt angle from XRD measurements is rather close to the one determined by PDF which is 30° (***Figure 16*****)** or the one determined experimentally by Y. Sugahara *et al.* on the Nb analogues.[49]

The intercept, *i.e.* the interlayer distance of a hybrid where only the phosphonate moiety is inserted, is worth 1.4 nm. It is consistent with the thickness of the inorganic layer (1 nm) plus the phosphate moiety (0.3 nm), determined from the PDF (***Figure 16***). The intercept for organophosphonic acid is larger than the intercept of 1.24 nm for amine-based hybrid[8] and the intercept of 1.04 nm for alcohol-based hybrid.[9] This statement is in accordance with the size of the respective functional group of the molecules.

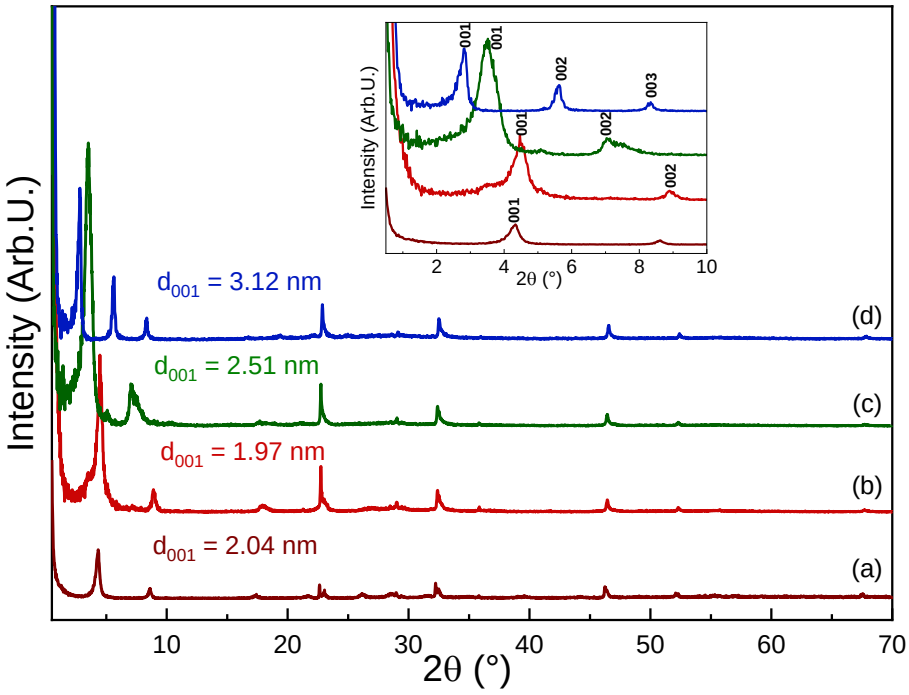

Figure 9: XRD patterns of (a) C_4N-HST, (b) C_3PO_3-HST, (c) C_6PO_3-HST and (d) $C_{10}PO_3$-HST. The insert is a magnification of the low-angle region where the (00l) reflections are present.

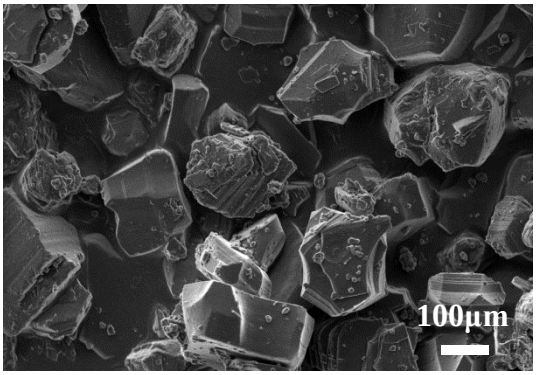

Figure 10: SEM image of $C_{10}PO_3$-HST.

A SEM image of the $C_{10}PO_3$-HST compound is shown in ***Figure 10***. We clearly see a platelet morphology which is in accordance with the layered structure we determine from XRD pattern. The crystal size is in the range of the micrometer scale. The morphology of the C_6PO_3-HST and C_3PO_3-HST crystals is similar and the sizes are in the same range.

The infrared spectra of C_3PO_3-HST, C_6PO_3-HST $C_{10}PO_3$-HST are shown in ***Figure 11*** and confirm the functionalization of the layered materials. The intensity of the bands between 2800 and 3000 cm^{-1}, corresponding to C-H stretching vibrations, increases as the carbon chain length increases. Their spectra show the characteristic P-C stretching vibration band at 1465 cm^{-1} which is also present in the spectrum of the corresponding free molecule (1-propylphosphonic acid, 1-hexylphosphonic acid and 1-

decylphosphonic acid). It evidences the integrity of each molecule is maintained after microwave reaction. Meanwhile the bands in the 1350-400 cm^{-1} range, corresponding to the phosphonic acid part, are different in the layered hybrids with respect to the molecule alone. The P-O stretching band (1013 cm^{-1}) is broadened whereas the intensity of the P-OH stretching band (920 cm^{-1}) is lowered in the hybrid compounds. In addition, the P=O stretching band (around 1200 cm^{-1}) is only hardly distinguishable in the hybrid compound. These observations are in line with what has been described for the grafting of alkylphosphonic acids onto titanium oxide particles or into Dion-Jacobson phase niobium oxide and confirm a covalent grafting of the alkylphosphonic acids onto the inorganic layers.[50,51]

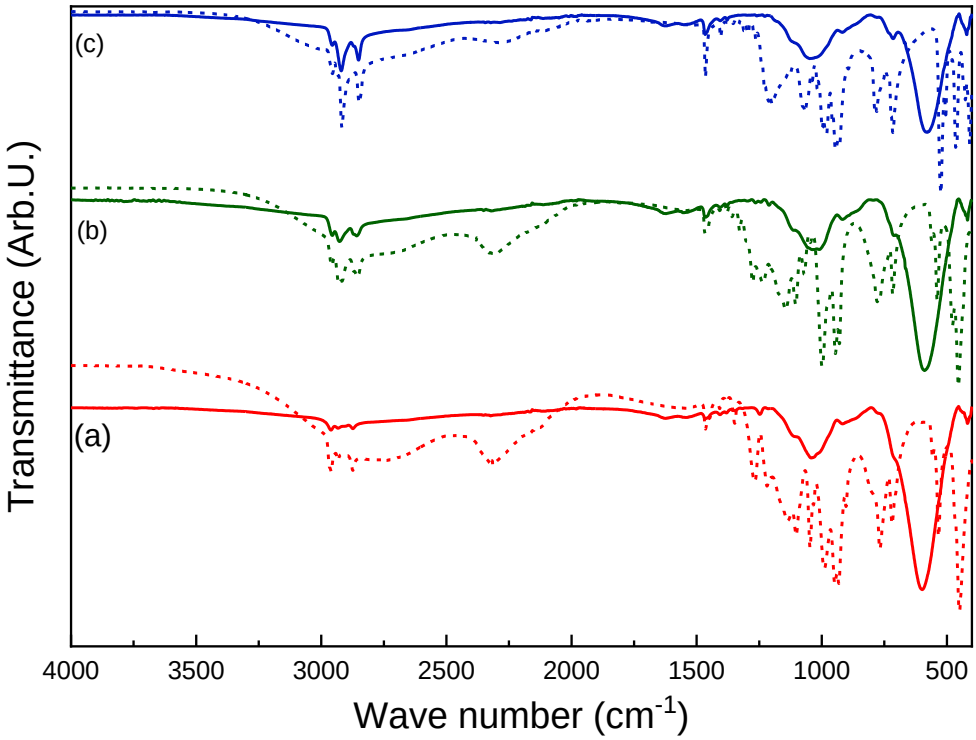

Figure 11 : FTIR spectra of (a) C_3PO_3-HST, (b) C_6PO_3-HST and (c) $C_{10}PO_3$-HST in solid line and their corresponding molecule 1-propylphosphonic acid, 1-hexylphosphonic acid and 1-decylphosphonic acid in dot line respectively.

Thermogravimetric analyses of the three hybrids materials were carried out under air with a heating rate of 5°.min^{-1}. The results are shown in ***Figure 12***. From 25° C to 150°C, the mass loss can be ascribed to the removal of adsorbed water on the compound surface or free water from the interlayer space. Then the TGA curves display a second mass loss from 150°C to 280°C. It may correspond to the departure of water molecules closer to the inorganic layer, located near the phosphonic acid moieties (***Figure 16*** **a**). The more significant mass loss occurs between 280 °C and 400 °C (about 2.3 %, 5.3 % and 11.1 % for C_3PO_3-HST, C_6PO_3-HST and $C_{10}PO_3$-HST respectively). As it is associated to an exothermic event, it can be ascribed to the decomposition of the organic contents. We notice that the organic content increases when increasing the carbon chain length which is in line with a similar grafting mode, as shown with XRD data. Following this loss, the TGA curves of the three hybrids show a slight gain of mass,

which is not observed for HST. We might ascribe this event to the gain of oxygen and the formation of an oxophophorous compound, derived from the initial $(SrTa_2O_7)^{2-}$ layer. Thus, the forth mass loss (up to 800°C) might result from the departure of the protons (in forms of water) and the departure of the phosphorous (in form of phosphate or phosphonate). This event may correspond to a topochemical reaction which leads to the formation of tungsten bronze phase, associated to α-$Bi_{0.1}Sr_{0.85}Ta_2O_6$ phase according to previous works.[19,52] In addition, a partial Bi removal may also happen.

In addition to thermogravimetric analyses, elemental analyses (C, H, N, Ta and P) were carried out (see **Experimental Section**). The results are summed up in ***Table 1*** as well as the calculated formula of the three hybrids compounds. As expected, the content on carbon atoms increases when increasing the carbon chain length. The $\frac{Ta}{P}$ ratios are similar for C_3PO_3-HST and $C_{10}PO_3$-HST whereas the ratio $\frac{Ta}{P}$ for C_6PO_3-HTS is larger. It means that a smaller amount of 1-hexylphosphonic acid was grafted. As the length of the alkyl chain should not have any peculiar difference in reactivity between the phosphonate derivatives, we suspected that the commercially molecule is not pure and it might contains some phosphonic ethers which are less reactive than their corresponding phosphonic acids. Unfortunately, during the course of this PhD work, we could neither check this hypothesis nor attempt insertion using a purer 1-hexylphosphonic acid. Finally, for each hybrid compound, the content of N is around 0.4%: it is attributed to remaining trace of 1-butylamine into the layers. Meanwhile, the XRD pattern does not show any impurity of C_4N-HST (***Figure 9***) for C_3PO_3-HST, C_6PO_3-HST and $C_{10}PO_3$-HST. Therefore, we assume these are traces of the incomplete exchange of C_4N-HST by C_xPO_3-HST during the microwave functionalization.

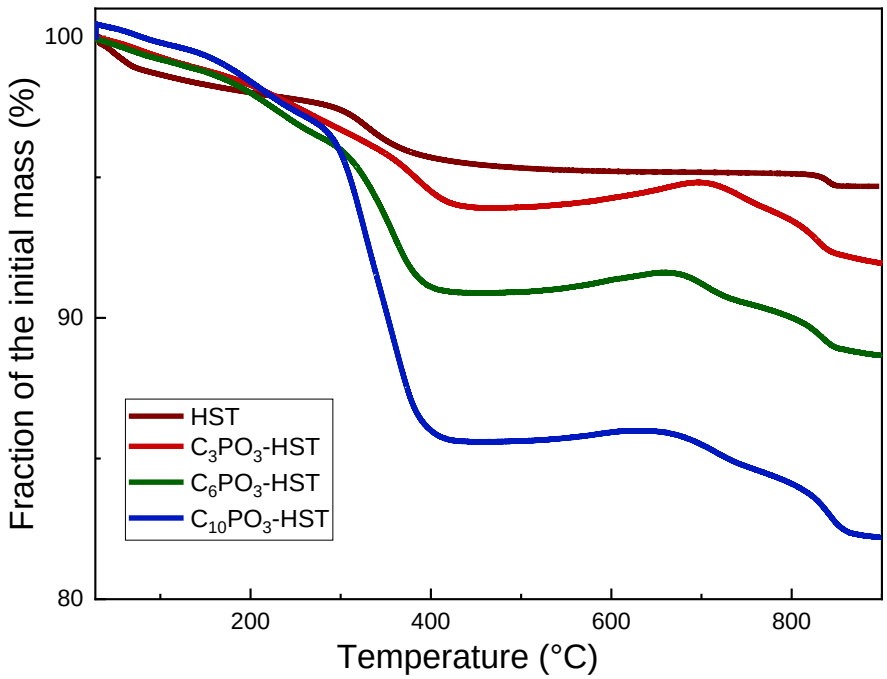

Figure 12: TGA/TDA curves of HST (brown), C_3PO_3-HST (red), C_6PO_3-HST (green) and $C_{10}PO_3$-HST (blue).

Product	Layered material	Carbon content found (calc) (%)	Nitrogen content found (calc) (%)	Hydrogen content found (calc) (%)	Tantalum content found (calc) (%)	Phosphorous content found (calc) (%)
C_3PO_3-HST	$(C_3H_7PO(OH))_{0.6}(C_4H_9NH_3)_{0.25}H_{1.05}Bi_{0.1}Sr_{0.85}Ta_2O_7.$ $1.3H_2O$	4.99 (5.86)	0.39 (0.39)	1.26 (2.04)	74.06 (75.68)	4.15 (3.89)
C_6PO_3-HST	$(C_6H_{13}PO(OH))_{0.45}(C_4H_9NH_3)_{0.25}H_{1.3}Bi_{0.1}Sr_{0.85}Ta_2O_7.$ $2H_2O$	6.55 (6.73)	0.50 (0.60)	1.79 (2.06)	52.86 (52.01)	1.91 (2.00)
$C_{10}PO_3$-HST	$(C_{10}H_{21}PO(OH))_{0.9}(C_4H_9NH_3)_{0.3}H_{0.8}Bi_{0.1}Sr_{0.85}Ta_2O_7$ $.2H_2O$	13.79 (13.42)	0.41 (0.52)	2.74 (2.38)	46.00 (44.52)	3.30 (3.43)

Table 1: C, H, N, micro-analysis and proposed formula for C_3PO_3-HST, C_6PO_3-HST and $C_{10}PO_3$-HST.

Solid-state ^{13}C CP/MAS and ^{31}P MAS NMR study was performed on $C_{10}PO_3$-HST, in collaboration with F. Leroux (ICCF, Clermont-Ferrand). The assignment was performed using ChemNMR in the Chemdraw® suite.

^{13}C CP/MAS NMR confirms the successful insertion of 1-decylphosphonic acid (***Figure 13 (a)***). In addition, the NMR spectrum evidences the presence of an impurity at 20.4 ppm, attributed to traces of 1-butylamine (in keeping with elemental analysis showing 0.41% of N). It has not been possible to remove this impurity. The solid-state ^{31}P MAS NMR spectrum of $C_{10}PO_3$-HST (***Figure 13 (b)***) shows a broad signal at around 28 ppm, upfield-shifted by about 10 ppm with respect to the 1-decylphosphonic acid spectrum, which confirms the grafting of the organic moiety to the tantalum oxide sheets. Similar conclusion can be drawn from ^{13}C CP/MAS and ^{31}P MAS NMR spectra for C_3PO_3-HST and C_6PO_3-HST. (not shown).

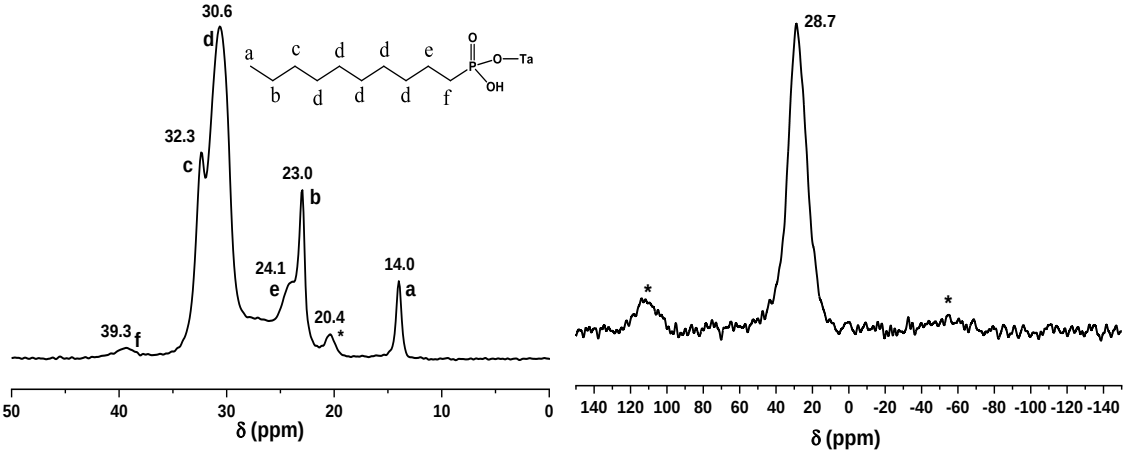

Figure 13: (a) ^{13}C CP/MAS NMR spectrum of $C_{10}PO_3$-HST (the asterisk is attributed to the presence of an impurity of 1-butylamine. (b) ^{31}P MAS NMR spectrum of $C_{10}PO_3$-HST (the signals marked with asterisks are attributed to spinning sidebands).

II.3.1.3 Advanced structural characterization

In order to precise further the structure of the bulk material, total X-ray scattering and PDF analysis were carried out (Coll. C. Taviot-Guého, ICCF, Clermont-Ferrand). This approach is especially powerful to get an accurate description of the short range structure of compounds exhibiting small crystalline domain size and high preferential orientation. The choice was made to focus on $C_{10}PO_3$-HST. From XRD, IR and NMR analysis, we can expect a similar grafting of the phosphonic acid in C_3PO_3-HST and C_6PO_3-HST. The following structural discussion on PDF results is a transcription of a part of an article we published,[53] focused on the characterization and exfoliation of $C_{10}PO_3$-HST.

Pair Distribution Function relies on the analysis of the scattered intensity as a function of the scattering vector q. Herein we neglect inelastic scattering for clarity reasons. It is worth mentioning that our samples are crystalline and isotropic materials. Thus, the scattered intensity can be expressed according the Debye scattering equation:

$$I(q) = \sum_j \sum_k b_j b_k \frac{\sin(qr_{jk})}{qr_{jk}}$$

Where b_j and b_k are the average diffusion length of the atoms j and k respectively, q is the diffusion vector, r_{jk} is the distance between the atoms j and k.

If j≠k, then the equation becomes

$$I(q) = \sum_j \sum_{k \neq j} b_j b_k \frac{\sin(qr_{jk})}{qr_{jk}} + \sum_j |b_j|^2$$

The second part of this equation corresponds to the incoherent scattering. The first part, called the structure factor of the total static scattering and denoted F(q), is meaningful of the interferences which arise from the scattering of ordered atoms. It is expressed as followed

$$F(q) = \frac{1}{N}\left(I(q) - \sum_j |b_j|^2 \right)$$

Where N is the total number of atoms on the sample. The structure factor of the total normalized scattering intensity is defined as:

$$S(q) = \frac{F(Q)}{\left(\sum_j b_j\right)^2} + 1$$

This structure factor of the total normalized scattering S(q) is defined in the reciprocal space. Its Fourrier-transform leads to the normalized pair distribution function G(r), defined in the real space. This latter is defined as:

$$G(r) - 1 = \frac{1}{(2\pi)^3 \rho_0} \int_0^{q_{max}} 4\pi q^2 (S(q) - 1) \frac{\sin(qr)}{qr} dq$$

Where ρ_0 is the atomic density (atoms per $Å^3$).

G(r) represents the probability to find in the structure a pair of atoms at a ***r*** distance from each other. A subsequent fitting of this PDF function allows to have the distance between atoms and get a better insight of the organization of the atoms that cannot be determined from XRD data.

The experimental PDF for $C_{10}PO_3$-HST sample is presented in ***Figure 14***. It shows a series of well-defined peaks at low *r* and a rapid decay in the amplitude that may be attributed to a limited structural coherence ~100 Å in the stacking direction of the layers. Weak oscillations are still visible up to 200 Å.

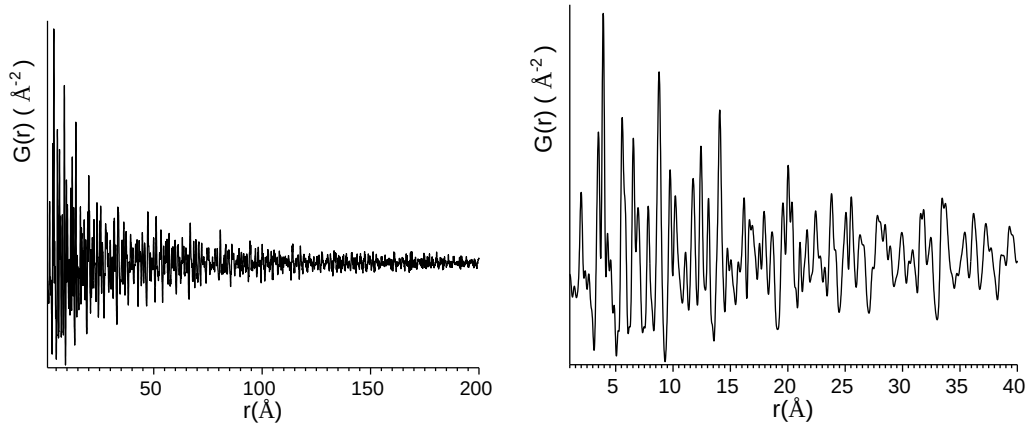

Figure 14: (a) Experimental PDF for $C_{10}PO_3$-HST sample obtained up to 200 Å and (b) details in the range from 1 to 40 Å

As a starting model, we considered the structural data reported by Whittle *et al.* for $Bi_2SrTa_2O_9$ and the calculated PDF is displayed in ***Figure 15 (a).***[54] In this simulation, only the $SrTa_2O_7^{2-}$ perovskite block was considered with a partial substitution of Sr by Bi in agreement with the experimental chemical composition of $C_{10}PO_3$-HST sample. To take into account the fact that the interlayer distance is 32.6 Å in $C_{10}PO_3$-HST sample, the *c* parameter of the orthorhombic cell was increased from 24.97 Å to 65.2 Å and the *z* coordinates of the atoms of the perovskite block were adjusted accordingly. The five main peaks labelled from P1 to P5 in the simulated PDF of the perovskite block are dominated by the contributions of M-O and M-M pairs (with M = Ta, Sr/Bi) corresponding to the successive coordination shells around M cations as illustrated in ***Figure 15 (c)***. As expected, the experimental PDF of $C_{10}PO_3$-HST shares many common structural features with this model. However, distinct differences are also visible in particular at low *r* due to the additional presence of the intercalated decylphosphonic $C_{10}PO_3$ chain.

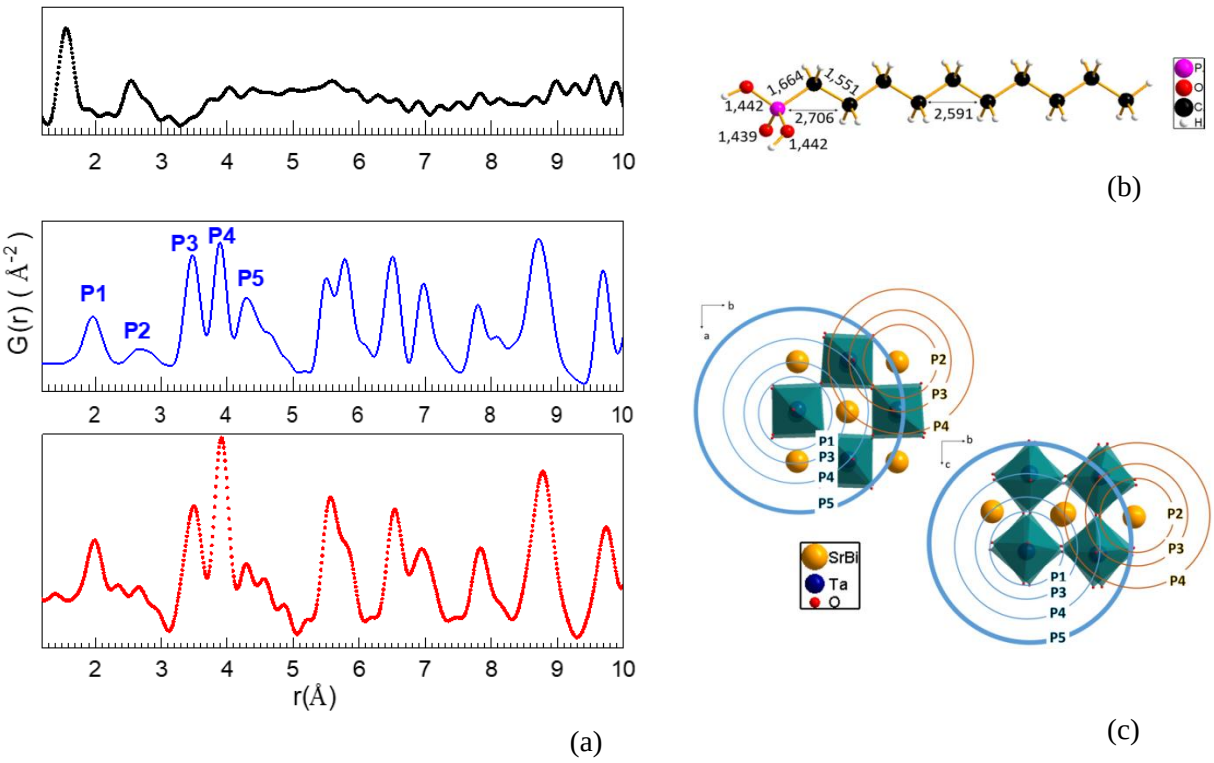

Figure 15: (a) Experimental PDF for $C_{10}PO_3$-HST (bottom) is compared to the model PDF for "$Sr_{0.85}Bi_{0.1}Ta_2O_7$" perovskite layers (middle) and the experimental PDF for 1-decylphosphonic acid (top). Distances between nearest atoms (b) along the decylphosphonic chain and (c) $Bi_{0.1}Sr_{0.85}Ta_2O_7$ perovskite layer model.

The experimental PDF of 1-decylphosphonic acid used for the synthesis is also given in ***Figure 15 (a)***. It shows two well defined peaks at ~1.57 Å including P-C/P-O/C-C bonds and at ~2.58 Å corresponding to C--C distance between second nearest neighbours as illustrated in ***Figure 15 (b)***. Since these molecules are held together by Van der Waals interactions, an overlap of sharp and broad peaks is observed for *r* above ~3 Å which is characteristic of the occurrence of both intramolecular and intermolecular distances. We can readily draw parallels with hybrid materials for which the variety of bonding interactions leads to very different widths of the PDF peaks and this is what makes the interpretation of PDF data of hybrid materials complicated as already reported elsewhere.[55,56] Handling the correlated motions to model the PDF data for molecular solids and hybrid materials over a wide range of *r* is a current challenge.

In the case of the $C_{10}PO_3$-HST sample, we limited our scope to PDF data in the low *r* region, where the distances refer only to near neighbour atoms, strongly bonded and dependent to each other, thus allowing the application of the common *r*-dependent peak broadening method.[57] As emphasized before, the first peaks in the PDF correspond to first atomic neighbour distances within the perovskite block and along intercalated decylphosphonic $C_{10}PO_3$, and also contain information about the nature of the bonding interaction between these two components. To extract quantitative information about the interaction between phosphonic group and the perovskite layer, we attempted a least squares profile refinement of the experimental PDF using the software PDFGui.[58] The starting model was constructed by inserting $C_{10}PO_3$

chains into the open space between $Sr_{0.85}Bi_{0.1}Ta_2O_7$ layers in a similar way as proposed for n-alkylphosphonate derivatives of $HLaNb_2O_7.xH_2O$.[49] In these materials, it was assumed a monodentate Nb-O-P linkage and a tilt angle of the *n*-alkyl chains of ~57°. Based on the chemical analysis of the $C_{10}PO_3$-HST sample, up to 45% of TaO_6 octahedra could be concerned by a Ta-O-P linkage. At the scale of the unit cell, one cannot use partial occupancy parameters to handle such a partial grafting onto TaO_6 octahedra, otherwise aberrant close $C_{10}PO_3$ interatomic distances appear. To circumvent this difficulty, we considered an ordering of the grafted chains on to perovskite layers as depicted in ***Figure 16(a).*** In this model, the shortest distance between the carbon atoms from the neighbouring alkyl chains is ~4.4 Å which is consistent with intermolecular distances reported in lipid-layer-like arrangements.[59] We also consider the presence of water molecules close to the tantalum oxide layers, in between phosphonic groups, and forming hydrogen bonds with them.

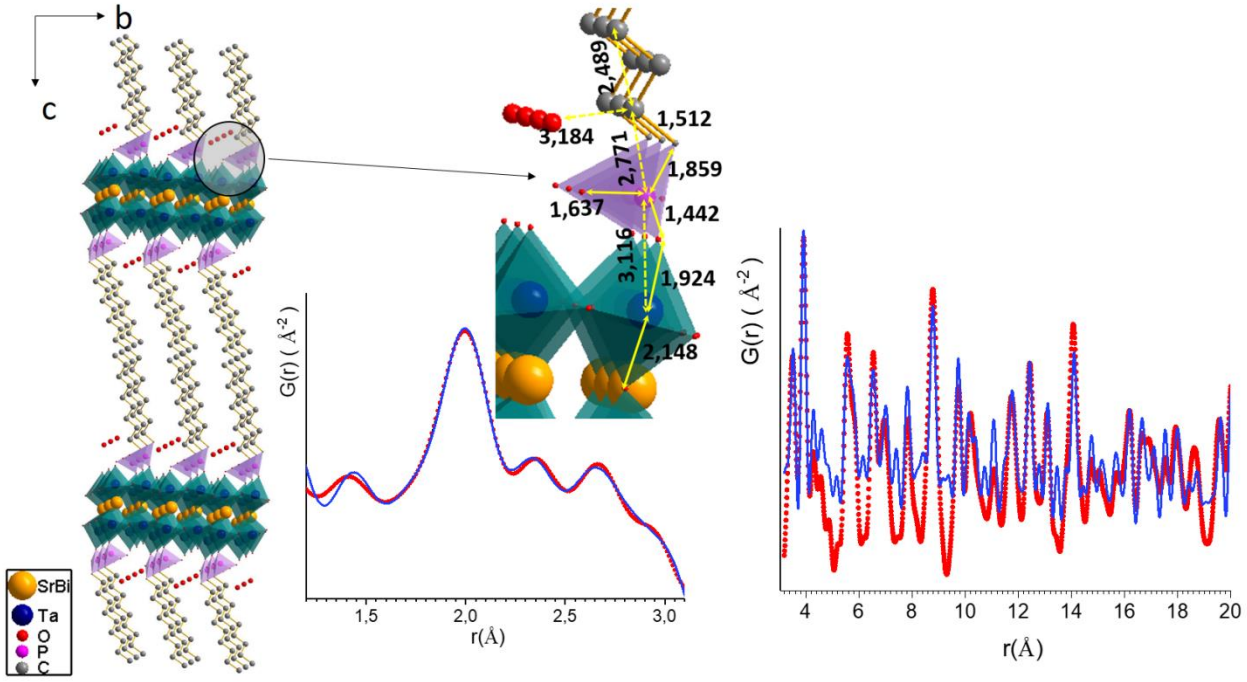

(a) (b) (c)

Figure 16: (a) Proposed structural arrangement of $C_{10}PO_3$ chains between $Sr_{0.85}Bi_{0.1}Ta_2O_7$ layers for $C_{10}PO_3$-HST sample. (b) Refinement of the structural model in the short range by fitting the experimental PDF of $C_{10}PO_3$-HST below 3.2 Å: the red points correspond to the experimental PDF and the blue curve represents the calculated PDF (R_w agreement factor = 8.6%). In inset are visualized the refined interatomic distances (in Å) consistent with a Ta-O-P linkage. (c) PDF refinement of the structural model in the range from 3 to 20 Å (R_w = 59.0%)

As can be seen in ***Figure 16(b)***, this model performs very well from a very short length scale *i.e.* within a unit cell for *r* values below 3.2 Å thus yielding structural information only on local bonding. In this refinement, the constraints of the space group were strictly observed. A stepwise adjustment of the structural parameters of the model was performed (*i.e.* atomic coordinates, isotropic displacement parameters and one *r*-dependent peak width parameter r_{cut}) ensuring that the structural integrity of either components was not destroyed. The refined structural parameters are available in **Appendix II**. The Ta-O

bond lengths in the fragment Ta-O-P and in $Bi_{0.1}Sr_{0.85}Ta_2O_7$ cannot be distinguished from each other, resulting in a single peak at ca. 2.0 Å on the PDF. However, the present structural model implying a grafting of the phosphonate moiety fits well with the PDF data and refined distances shown in ***Figure 16 (b)*** are consistent with a Ta-O-P linkage. This result therefore supports the findings from FTIR and ^{31}P NMR spectroscopy analyses. It is important to note that this structural model featuring $C_{10}PO_3$-HST as a periodic assembly of $C_{10}PO_3$ chains arranged as a bilayer between $Bi_{0.1}Sr_{0.85}Ta_2O_7$ perovskite blocks fails to reproduce to an acceptable level the atomic correlations above 3.2 Å (***Figure 16* (c)**).We attribute this failure mainly to the fact that we did not take into account the variety of bonding interactions in such materials which would require using separate isotropic displacement models to described PDF peak widths.[55] The "freezing" of $C_{10}PO_3$ units in the interlayer space can also be questioned given the flexibility of long n-alkyl chains. All the same, the PDF results confirm and clarify the grafting of PA group onto the $Sr_{0.85}Bi_{0.1}Ta_2O_7$ layers and corroborate the conclusions drawn from FTIR and NMR spectroscopy analysis.

II.3.1.4 Conclusion

We investigate the grafting of alkylphosphonic acid into $SrTa_2O_7^{2-}$ sheets through microwave-assisted reaction. The resulting materials C_xPO_3-HST (x = 3, 6, 10) are layered materials with an organic moiety covalently attached to the inorganic layers. This grafting was evidenced for $C_{10}PO_3$-HST by Pair Distribution Function, coupled with spectroscopic techniques (FTIR and NMR). The integrity of both inorganic layer and organic molecules is preserved all along the functionalization process.

II.3.2 Grafting of aromatic phosphonic acid derivatives

Besides linear alkylphosphonic acid, we investigated the grafting of aromatic phosphonic acid to prove that we can extend our strategy and protocol beyond simple aliphatic alkylphosphonic acid. Herein, we consider the following molecules denoted as $NCArPO_3H_2$ and $HOArPO_3H_2$ (***Figure 17***), synthesized by P.-A. Jaffrès (CEMCA, Brest). The grafting reaction of these two molecules was carried out in similar conditions as the grafting of the aliphatic phosphonic acid presented above (see also **Experimental Section**). The resulting hybrid compounds are denoted as $NCArPO_3$-HST and $HOArPO_3$-HST. Once again, these notations were chosen for simplicity while a more accurate denomination would be HOArPO(OH)-HST and NCArPO(OH)-HST.

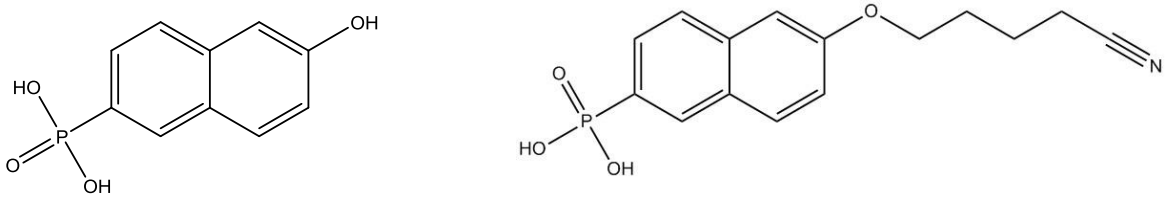

(6-hydroxynaphtalen-2-yl)phosphonic acid *(6-(4-cyanobutoxy)naphtalen-2-yl)phosphonic acid*

Figure 17: Two aromatic phosphonic acids denoted as $HOArPO_3H_2$ and $NCArPO_3H_2$.

II.3.2.1 Characterization

XRD patterns of both hybrid materials are shown in ***Figure 18 left***. The (*100*), (*110*) and (*200*) reflections at 22.7°, 32.2° and 46.4° respectively testify the integrity of the layer structure during the grafting reaction. The out-of-plane reflections (*00l*) in both XRD patterns show that $HOArPO_3$-HST and $NCArPO_3$-HST have a layered structure.

For $NCArPO_3$-HST, the interlayer distance is d_{001} = 2.94 nm. This distance is in line with the length of the molecule (about 1.5 nm) and indicates the formation of a tilted bilayer, analogous to the one described for linear alkylphosphonic acid (described above). In the present case tough, as the tilt angle cannot be determined from the evolution of the interlayer distance upon a variation of the alkyl chain length, it is not possible to completely rule out a partial interdigitation of the inserted molecules. More advanced studies such as the PDF analysis, described above, would have to be carried out to precise the organization of the molecules within the interlayer space.

For $HOArPO_3$-HST, on the contrary, the interlayer distance is small, d_{001} = 1.65 nm, much smaller than the one of the starting material C_4N-HST (2.04 nm). Considering the thickness of the inorganic layer (about 1nm) and the length of the molecule (about 0.9 nm), this observed short lamellar distance indicates a pillaring arrangement of the molecule.

The FTIR spectra of $HOArPO_3$-HST and $NCArPO_3$-HST are rather similar, the one of $NCArPO_3$-HST being better defined than the one of $HOArPO_3$-HST. These spectra evidence the presence of the organic molecules. Both spectra display a characteristic stretching P-O band at 1006 cm^{-1} while the intensity of the P-OH stretching bands at 978 cm^{-1} and 940 cm^{-1} is lowered compared to the molecule alone. The P-C band at 1474 cm^{-1} and the C=C band at 1625 cm^{-1} confirms the integrity of the molecule. For $NCArPO_3$-HST, the low-intense band at 2240 cm^{-1} corresponds to the C≡N stretching, also observed on the spectrum of the $NCArPO_3H_2$. As stated above concerning the arrangement of the organic molecules in $HOArPO_3$-HST, the observed interlayer distance points to a pillaring arrangement, corresponding to a simultaneous grafting of the $-PO_3$ group on a layer and the -OH group on the facing layer. However, no clear spectroscopic signature of such double grafting could be evidenced, contrarily to what has been described for aliphatic alcohols for which a blue shift of about 100 cm^{-1} of the C-O stretching band can be observed upon grafting.[9]

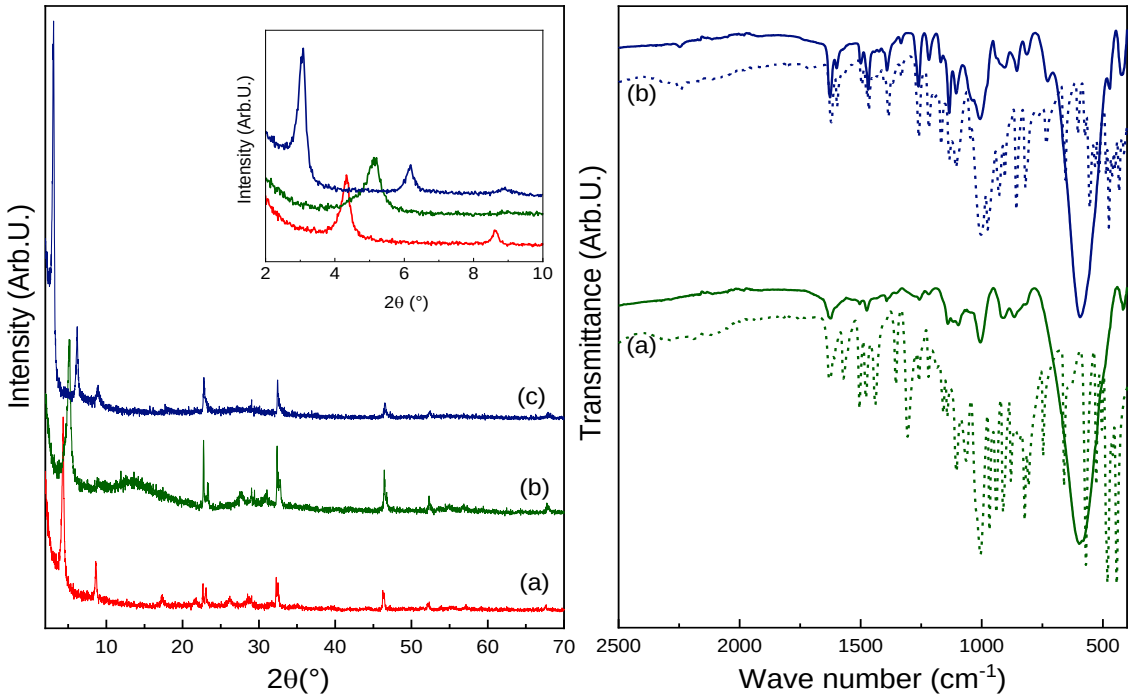

Figure 18: Right) XRD patterns of (a) C_4N-HST, (b) $HOArPO_3$-HST and (c) $NCArPO_3$-HST. Left) FTIR spectra of (a) $HOArPO_3$-HST and (b) $NCArPO_3$-HST in solid line as well as their corresponding molecules in dot line.

Figure 19 **(a)** shows the ^{13}C CP/MAS NMR spectrum of $NCArPO_3$-HST which confirms the successful grafting of the molecules and the preservation of its integrity during the microwave-assisted functionalization. Similarly to $C_{10}PO_3$-HST, an impurity of 1-butylamine remains after the reaction and the washing. ***Figure 19 (b)*** shows the ^{31}P MAS NMR spectrum of $NCArPO_3$-HST, displaying a broad band at 14 ppm. This peak is upfield-shifted compared to the spectrum of the free molecule, meaningful of the successful grafting of the phosphonic acid moiety onto the oxide layer. The NMR spectra of $HOArPO_3$-HST (not shown) also confirm its grafting onto the inorganic HST layer.

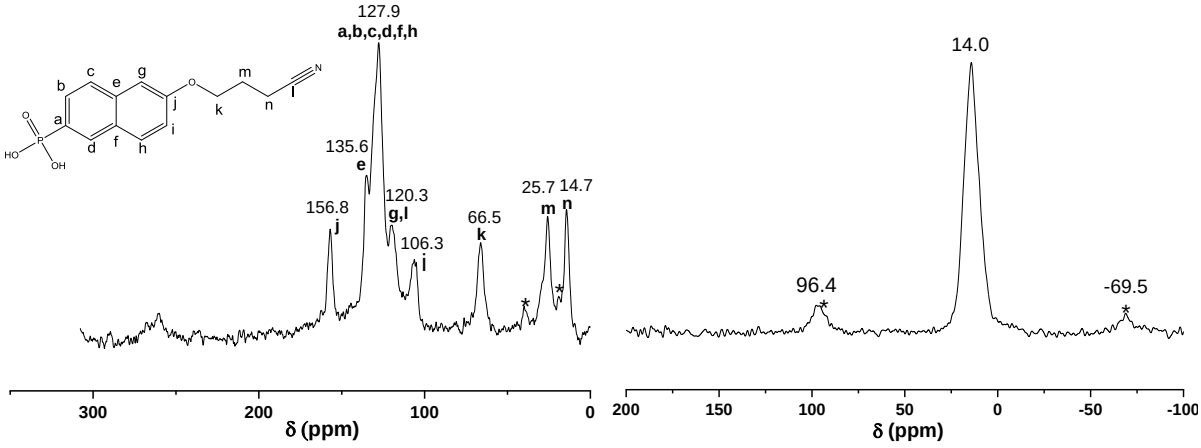

Figure 19: (a) ^{13}C CP/MAS NMR spectrum and (b) ^{31}P MAS NMR spectrum of $NCArPO_3$-HST (the signals with asterisks are attributed to spinning sidebands.

II.3.2.2 Conclusion

Here we have shown that aromatic phosphonic acids can be inserted and grafted onto HST layers. Phosphonic acid derivatives are reactive towards the $SrTa_2O_7^{2-}$ sheet: the direct chemical environment of a phosphonic acid seems to have minor influence on its reactivity (unlike amine where the pKa, and hence the reactivity is easily influenced by neighboring group). In addition, the P-C bond does not suffer from breaking, insuring the molecule integrity. This point is all the more crucial as, on the contrary alkylphosphates are degraded during the insertion-grafting process as we will see below in **II.3.5**.

II.3.3 Grafting of organosilane derivatives

II.3.3.1 Introduction

Previously, we have shown that microwave-assisted reaction is an efficient pathway to decorate the interlamellar space of a layered oxide, HST, with a panel of organic molecules. A grafting group is the mandatory condition as it allows interaction with the inorganic layer. Alkylamines interact through electrostatic interactions with the charged slabs while alcohols derivatives and phosphonic acid are covalently attached *via* an etherification (for alcohols) and estherification (for phosphonic acid) reaction. Nevertheless, hybridization with bi-functional or multifunctional molecules allows for much more subsequent use of the hybrid materials: their interlayer space may then display available reactive functions which might interact and/or react with a molecule or inorganic materials.[20,60] For instance, many works have focused on the modification of an inorganic material to get a surface covered by amines.[61–64] Such reactive surface is hydrophilic, can be positively charged by pH control, and can react with molecules through EDC/NHS coupling.[65]

However, getting available free amines into the interlamellar space remains a challenge : Y. Wang *et al.* have proved that a diamine interacts with two adjacent layers through the two amine's moieties[8]. Similarly, they showed that a hydroxyalkylamine interacts preferentially with the inorganic charged layer through the amine moiety, leaving the alcohol free.[9] Up to now it has not been possible to favour the reverse situation where the alcohol is grafted leaving the amine free. Thus, these studies underline the difficulty to have free amines at the surface of the layers (*i.e.* amine which points at the center of the interlayer space) due to the preferential electrostatic interaction of amines with the charged slabs.

We propose to overcome this issue by using an organosilane as coupling reagent, typically the 1-aminopropyl(trimethoxysilane). Building on previous work of Ruiz-Hitzky and Rojo, A. Clearfield *et al* were the first to graft aminopropyl(triethoxysilane) into a layered tetratitanate.[66] The authors used a pre-intercalation strategy by inserting 1-propylamine into the protonated titanate before the grafting of the organosilane. In addition, the grafting of organosilane is suspected to be catalyzed by the alkylamine, already present into the layered structure as proposed by K. Isoda *et al*.[67] Besides, according to M. Ogawa *et al,* the control of the precursor structure *i.e*. the arrangement of the alkylamine into the interlayer play a major role on the organosilane arrangement in the interlamellar space (pillaring versus monolayer).[68] Subsequently, many organosilane derivatives have been chosen to modify layered oxides or hydroxides.[37,69–71]

In the following part, we will describe the functionalization of HST by three organosilanes: the 1-amino(propyl(trimethoxy)silane (APTS), the 1-mercaptopropyl(triethoxy)silane (MPTS) and the

octyl(triethoxy)silane (C8TS) which will serve as a model compound with different surface functional group. Spectroscopic techniques are used to precise the grafting mode of the organosilane on the slabs. We also investigate how microwave assistance modifies the grafting of APTS compared to classical process and how the precursor, C_4N-HST, plays a role on such functionalization.

II.3.3.2 Synthesis and characterization

The grafting of organosilanes on HST layer was carried out following a procedure adapted from the reported one for the functionalization of layered titanates .[38] Typically, the precursor C_4N-HST is poured into 25 mL of toluene in a round-bottom flask, under argon, heated at reflux (110°C) for 3 days. Then, the white powder is centrifuged and washed two times with ethanol and one time with acetone. It is worth mentioning that the reaction takes place in a non-polar anhydrous media (*i.e.* toluene) as well as under inert atmosphere, to prevent from rapid and unwanted hydrolysis of the organosilane precursors. Traces of water might lead to the appearance of non-grafted silica materials which cannot be easily separated from the layered hybrids. The resulting compounds are denoted as APTS-HST, MPTS-HST and C8TS-HST.

The as-synthesized hybrid materials are characterized by XRD (***Figure 20***). The low angle peaks, corresponding to the *(00l)* reflections, attest the layered structure of all the hybrid materials. An increase of the interlayer distance d_{001} is observed for APTS-HST (2.35 nm) and C8TS-HST (2.57 nm) compared to C_4N-HST (2.05 nm). It is consistent with the grafting of the organosilanes. However, we did not observe any significant modification of the d_{001} in the XRD pattern of MPTS-HST compared to C_4N-HST (1.96 nm and 2.05 nm respectively) and we cannot draw any conclusion from it. The *(100)*, *(110)* and *(200)* reflections at 22.7°, 32.3° and 46.4° are present on the XRD patterns of APTS-HST, MPTS-HST and C8TS-HST, similarly to the one of C_4N-HST. It confirms that the integrity of the inorganic layer structure is retained without any modification due to the organosilane grafting.

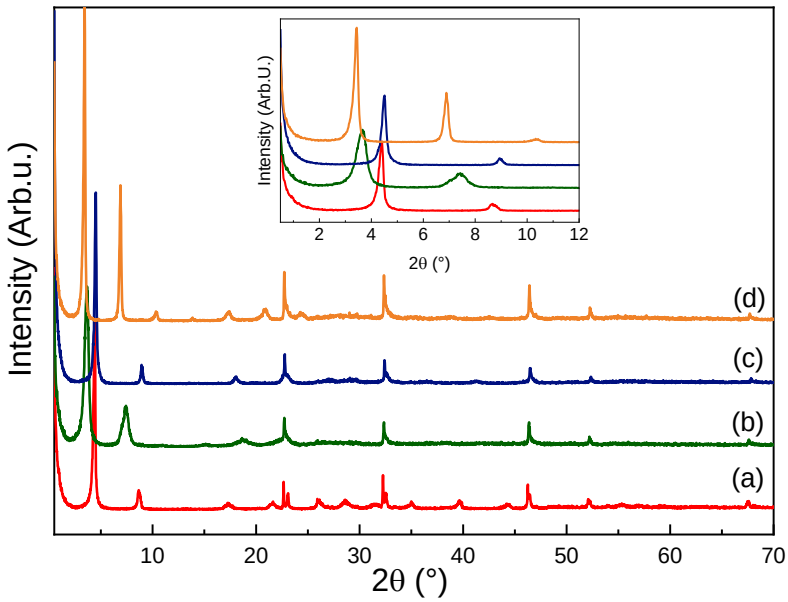

Figure 20: XRD patterns of (a) C_4N-HST, (b) APTS-HST, (c) MPTS-HST and (d) C8TS-HST. The insert is a magnification of the low-angle region.

SEM images of the three compounds (***Figure 21***) show platelet morphology, characteristic of the layered structure. The stacking is especially seen in the SEM image of C8TS-HST where the interlayer space is larger. The SEM images do not show any side particles with a distinct contrast and shape. Thus, the grafting reaction occurred homogeneously on the inorganic layers and did not lead the formation of amorphous silica particles, the presence of which could not have been highlighted by XRD (if in small amount).

Similarly, TEM images of bulk APTS-HST show without ambiguity its platelet morphology and confirm its layered structure. An intensity profile has been performed on the image ***Figure 22 (c)***. It allows to determine the d_{001} distance between two adjacent layers: an average distance d_{001} = 1.97 nm was found (average done over 7 adjacent slabs). This value from microscopy imaging appears smaller than the one determined from XRD. We ascribe this difference to a shrinkage of the layered structure due to insertion of the compound into the microscope chamber, which is under vacuum (the remaining adsorbed solvent and water molecules are expelled from the interlayer space leading to a decrease of d_{001}). In addition, in TEM, the observed gap between slabs depends on the viewing angle which induces a larger uncertainty: the sample must lie perpendicularly to the Cu grid in order to get an accurate estimation of the interlayer distance.

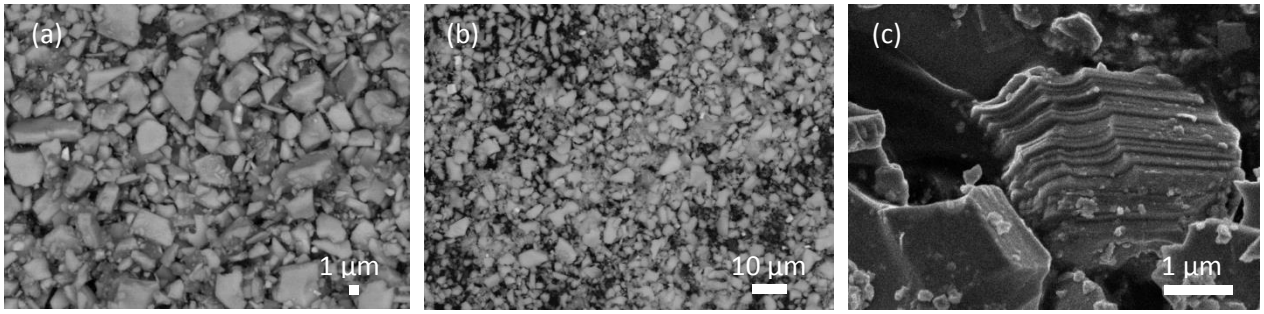

Figure 21: SEM images of (a) APTS-HST, (b) MPTS- HST and (c) C8TS-HST.

The clichés also emphasize the softness of all the layers, acquired with the functionalization. We clearly see that a pack of slab can be bent without breaking in the structure (***Figure 22***). The layered material is no longer rigid as HST can be. So, APTS-HST constitutes a stunning example of what functionalization can bring to pure inorganic materials and the usefulness to the rigid-to-soft approach in materials chemistry as described by Y.Oaki.[72] High resolution TEM has been performed on APTS-HST in order to highlight a potential silica monolayer formed by the organosilane grafting. However, we could not draw any conclusion due to the small contrast of this hypothetic layer and due to the sputtering of the oxide (even working at low energy, 100 kV). In the same way, EDX analysis could not evidence the presence of the organosilane. Inherent difficulties of the TEM imaging of oxides are discussed in more details in **Chapter IV.**

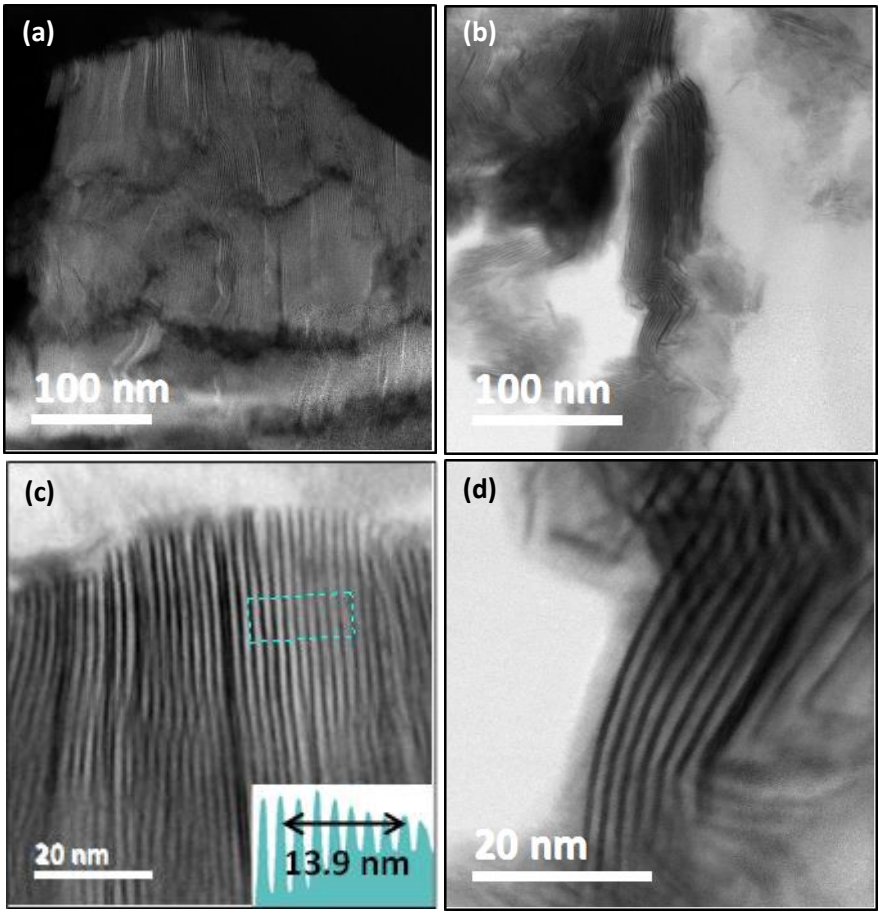

Figure 22: (a) to (d) TEM images of bulk APTS-HST. The images (c), (d) show a magnification of the layered structure.

Here spectroscopic techniques are far more relevant to precise the grafting of silane moieties. The FTIR spectra of APTS-HST, MPTS-HST and C8TS-HST are shown in ***Figure 23.***

In the case of APTS-HST, the intensity of C-H vibration bands is lowered compared to C_4N-HST. The large band between 1070 and 1110 cm^{-1} is characteristic of the asymmetric vibration of the Si-O-Si bond. [73,74]Thus it is meaningful of the condensation of silica onto the inorganic layer or between two organosilanes. However, several bands such as the (C-O) bending band and the symmetric stretching of (C-O) at 1010 cm^{-1} and 960 cm^{-1} respectively, lead us to consider the non-hydrolysis of all the Si-O-R bonds during the reaction. Thus, at this point we hypothesize the grafting on the HST layer was successful and that there is no bonding between two adjacent organosilanes in APTS-HST.

Concerning MPTS-HST, its spectrum displays an intense stretching C-O and Si-O band at 970 cm^{-1} and 800 cm^{-1} respectively, relevant of the 1-mercaptopropyl(triethoxysilane). However, the band, corresponding to the Si-O-M vibration, is only barely visible at 1077cm^{-1}: we cannot clearly attest the grafting of the 1-mercaptopropyl(triethoxysilane) onto the inorganic slabs.

Finally, the C8TS-HST spectrum displays intense C-H vibration bands around 2900 cm^{-1} as well as a Si-O-Si vibration band at 1078 cm^{-1} (shifted compared to APTS-HST). It emphasizes the grafting of C8TS into the layered host. Like APTS-HST and MPTS-HST, the symmetric C-O stretching band remains intense, indicating the absence of hydrolysis of the Si-OEt bonds or at least its incompleteness. This is in

line with what is reported in literature. Some authors indeed report the partial hydrolysis of the methoxy or ethoxy group attached to the pristine organosilane.[38,67,75] In addition, J. Carrasco *et al.* demonstrate that the condensation of organosilane into the interlayer space of layered double hydroxide leads to a majority of both monodentate and bidentate bridgings of the organosilane.[75]A negligible proportion of tridentate was also evidenced. In our situation *i.e*. using layered oxides, a single organosilane molecule cannot be directly grafted with two Si-O-Ta bonds to the layer due to geometrical considerations. However, we cannot exclude that two adjacent organosilanes may react together and thus lead to the formation of a network.

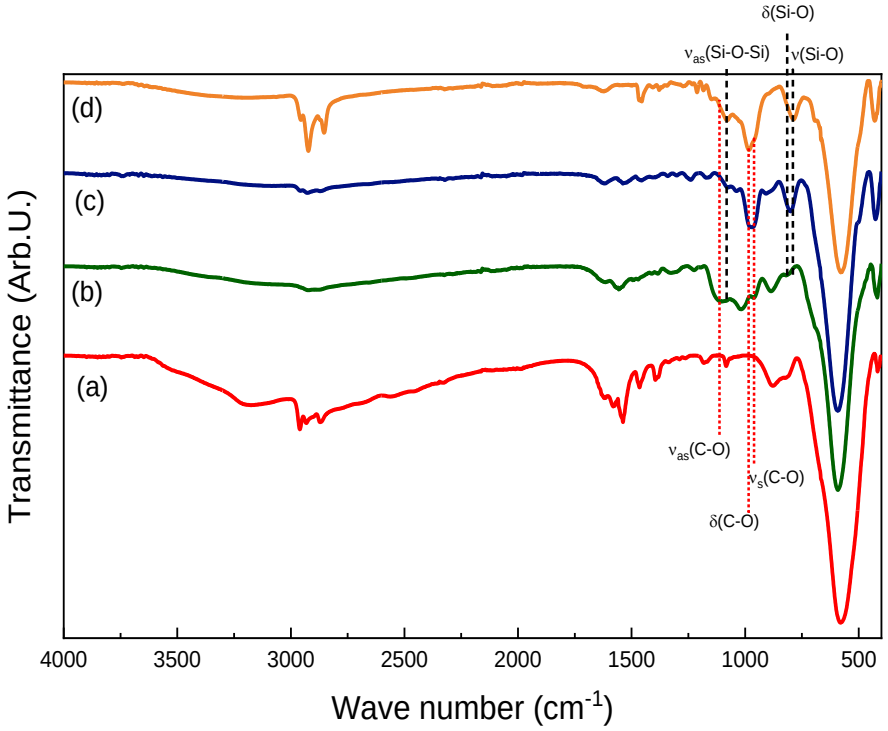

Figure 23: FTIR spectra of (a) C_4N-HST, (b) APTS-HST, (c) MPTS-HST and (d) C8TS-HST.

C, H, N analysis was carried out on the APTS-HST, MPTS-HST and C8TS-HST. The results are summed up in ***Table 2.*** The nitrogen content in MPTS-HST and C8TS-HST is ascribed to 1-butylamine impurities. In the case of APTS-HST, this impurity cannot be deduced from C, H, N analysis as the pristine APTS contains also nitrogen. Yet in regards with MPTS-HST and C8TS-HST and some compounds made from C_4N-HST, we suspected that an impurity of 1-butylamine also remains in APTS-HST. We are unable to quantify it without further characterization (such as ^{29}Si NMR). Thus, the proposed formula of APTS-HST has an over-estimated organic content. Despite the non-consideration of 1-butylamine, the ratio $\frac{n(C)\,(mol)}{n(N)(mol)}$ in APTS-HST is 3.8. This value means that a (-OMe) group remains attached to the silicium after the reaction *i.e.* two or one Si-OMe bonds were hydrolyzed during the reacting. This finding is in accordance with the FTIR spectra of APTS-HST. Concerning MPTS-HST and C8TS-HST, we are unable draw a similar conclusion as we cannot defined a relevant ratio $\frac{n(C)\,(mol)}{n(N)(mol)}$. We make the assumption that the reactivity of MPTS and C8TS towards hydrolysis might be similar to APTS.

Therefore, we also consider that one (-OEt) bond remains after the reaction for the determination of the formula of MPTS-HST and C8TS-HST.

Product	Layered material	Carbon content found (calc) (%)	Nitrogen Content found (calc) (%)	Hydrogen content found (calc) (%)
APTS-HST	$(C_3H_9NSiO(OMe)(OH))_{1..2}H_{0.8}\ Bi_{0.1}Sr_{0.85}Ta_2O_7.xH_2O$	7.34 (7.50)	2.25 (2.18)	1.79 (2.25)
MPTS-HST	$(C_3H_7SSi(OEt)(OH))_{0.45}(C_4NH_{12})_{0.3}\ H_{1.25}\ Bi_{0.1}Sr_{0.85}Ta_2O_7.H_2O$	6.04 (6.04)	0.67 (0.61)	1.37 (1.87)
C8TS-HST	$(C_8H_{17}Si(OEt)(OH))_{0.65}(C_4NH_{12})_{0.1}H_{1.25}\ Bi_{0.1}Sr_{0.85}Ta_2O_7.0.3H_2O$	11.58 (12.58)	0.17 (0.19)	2.06 (2.54)

Table 2: C, H, N micro-analysis and proposed formula for ATPS-HST, MPTS-HST and C8TS-HST.

II.3.3.3 Influence of the synthesis conditions: microwave *vs* classical heating

As we developed the functionalization assisted by microwave, we also tried to apply this approach to the grafting of organosilanes onto inorganic layered oxide. Trials were carried out to synthesize APTS-HST using microwave assistance. Typically, the precursor C_4N-HST is poured into 10 mL of toluene in a glass reactor, under inert atmosphere, for 130 minutes. We first used the same temperature as the reference procedure *i.e.* 110°C. In a second experiment, we increase the temperature up to 130°C. The resulting powder is collected by centrifugation, washed two times with ethanol, one time with acetone and dried in air overnight.

The XRD patterns of the as-synthesized APTS-HST, following three different procedures, are shown in ***Figure 24***. The three products display (*100*), (*110*) and (*200*) reflections at 22.7°, 32.5° and 46.3° respectively. The inorganic structure of the slab remains unchanged whatever the procedure. Similarly, all products display (*001*) reflections at low angles, showing the lamellar structure. However, depending on the synthetic process, a change in the d_{001} is observed. For a temperature of synthesis of 110°C, d_{001} increases slightly by using the microwave (2 hours) instead of classical heating (72 hours), from 2.35nm to 2.49 nm. The crystallinity of ATPS-HST is yet similar when using microwave as heating source (crystallite size along the c-axis is 160 nm in both situations). This spatial expansion is more pronounced when heating at higher temperature (130°C) with microwave, even during shorter times, from 2.35 to 2.85 nm. Yet, in the XRD patterns of APTS-HST synthesized at 130°C, we can distinguish a splitting of the (*001*) reflections, which is all the more visible for the (*002*) reflection. We hypothesize that the APTS grafting is no longer in form of a monolayer whereas it begins to form a second layer.

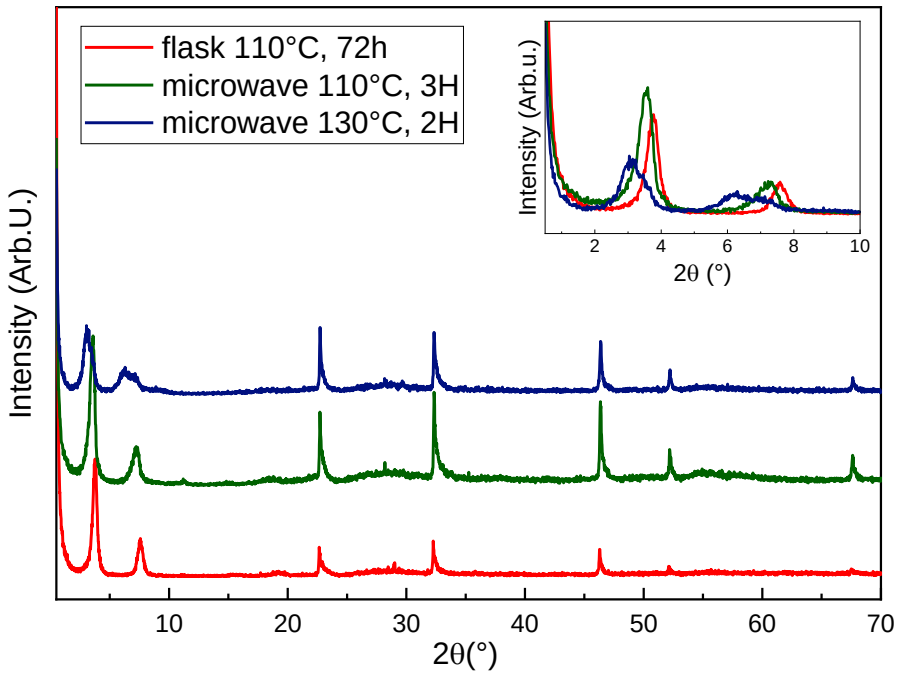

Figure 24: XRD patterns of APTS-HST, synthesized following three different procedures.

The FTIR spectra of the three compounds in ***Figure 25*** are similar: the same bands are present without any additional ones. The single difference relies on the relative intensity of the band at 1017 cm^{-1} and 1110 cm^{-1} corresponding to the Si-O-Si vibration and the C-O stretching band respectively. In the spectrum of APTS-HST synthesized at 130°C, with microwave assistance, the intensity gap between these two bands appears to be larger than in APTS-HST, synthesized at 110°C. Besides, the Si-O-Si vibration band is more intense. These observations support the hypothesis of multiple layers of silica or pillaring. Nevertheless, additional characterizations (NMR and PDF notably) must be performed to elucidate the structure formed by the organosilane in that case.

We demonstrate once again the powerfulness of microwave synthesis: it allows to graft organosilanes onto HST, resulting in a crystalline layered materials similar to the one synthesized by conventional heating. The gain of time (from 3 days to 2 hours) is yet less impressive than the case of alcohol grafting (from a week to 2 hours). The use of higher temperatures, under solvothermal conditions, allows to obtain a hybrid compound with a larger interlayer distance, but with a lower crystallinity which will have to be optimized in further studies.

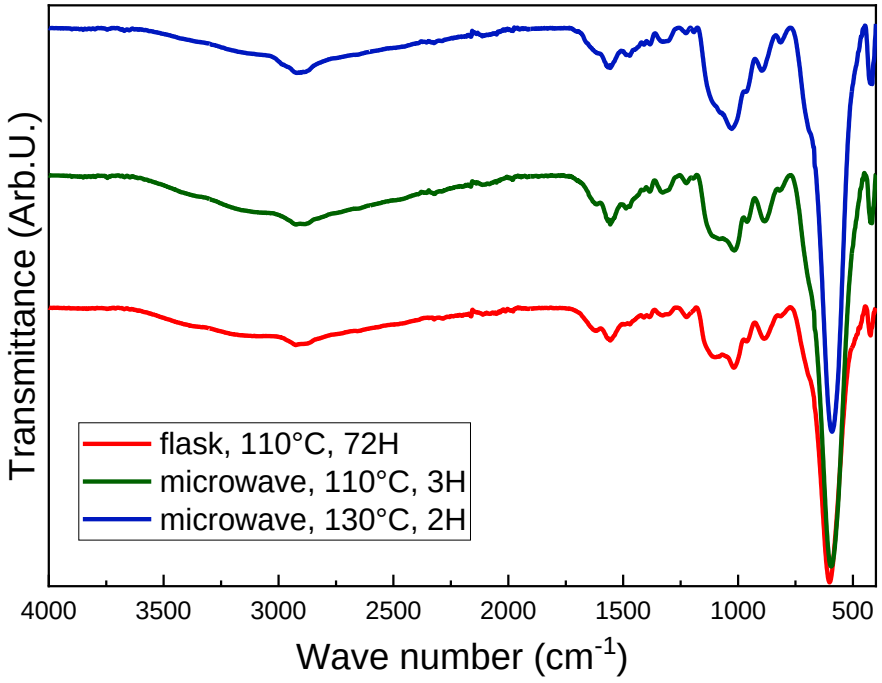

***Figure 25: FTIR spectra of APTS-HST synthesized according three different procedures*.**

Finally, we aim at assessing the importance of using an amine-based precursor in the APTS-HST synthesis. Thus, we carried out APTS grafting using $C_{12}O$-HST as precursor: the 1-dodecanol should not interact with the APTS in anyways and thus should not get involved in its grafting. The experimental conditions are similar to the grafting of APTS using C_4N-HST.

XRD patterns and FTIR spectra of $C_{12}O$-HST and of the resulting compounds do not display any change. As the XRD patterns of the precursor and of the resulting compound are similar, this indicates the absence of hydrolysis of the C-O-Ta bond, where the grafting of organosilane takes place. Indeed, the reaction conditions (dry non-polar solvent) and the nature of the precursor (hydrophobic) prevent the efficient hydrolysis of the alcohol moiety.

In an amine-based hybrid, the water may come from the precursor itself as it is more hydrated than an alcohol based hybrid.[8,9] Therefore, even if the total removal of the amine group is difficult, as stated above, it appears that amine-based precursor is preferable to an alcohol-based one to graft organosilane. It would then be interesting to compare for precursors of the same alkyl chain length, $C_{12}N$-HST *vs* $C_{12}O$-HST or C_4N-HST *vs* C_4O-HST, since as discussed above the mechanism of organosilane grafting into inorganic layer involves the alkylamine as catalyst.[67]

II.3.3.4 Conclusion and Perspectives

Taking advantages of the reactivity of the inorganic layer of $SrTa_2O_7^{2-}$ and using organosilane as coupling reagent, we were able to obtain new hybrid materials, APTS-HST, MPTS-HST and C8TS-HST. The layers were covalently modified through a hydrolysis/condensation of the organosilane and functional groups were added at the inner surface of the layered materials. We confirm the crucial role of the amine precursor in the reaction and show that microwave assistance can be used to graft organosilane. However,

in-depth experiments and characterization must be done to fully describe the grafting, to quantify it and to highlight the organization of organosilane within the interlay space.

Here we performed surface design of layered materials. APTS-HST compound displays free amines in its interlamellar space, making it a promising candidate to exfoliation with pH modification as already done by J.H.Choy *et al.* with a carboxylate-based hybrid materials[76] or J. ten Elshof *et al.*[60]. MPTS-HST can further be exfoliated into nanosheets which could be deposited into gold surface and might lead to a good coverage *via* RS-Au bond formation. C8T-HST represents a good candidate to undergo through exfoliation in organic media, due to its organophilic behavior.

II.3.4 Grafting of functional molecule: the use of luminescent pyrene derivatives

II.3.4.1 Introduction

Luminescence can be an intrinsic property of a material. In the case of layered oxide, S. Ida *et. al.* showed that BST emits in the blue region when excited at 305 nm.[77] Meanwhile, the signal has a low intensity, even if the quantum yield is not reported. The authors investigated the luminescence of the protonated phase HST and of a phase derived from HST *via* functionalization by 1-ethylamine. They observed a blue shift of the emission in the two cases compared to BST (from 515 nm for BST to 475 nm for both HST and the hybrid powder). Similarly, they performed exfoliation of the functionalized phase but they do not notice any significant difference on the emission spectra of the nanosheets compared to the parent bulk. So, luminescence of BST cannot be applied directly to finely characterize either the functionalization or the exfoliation of HST.

Otherwise, luminescence properties can come from the addition of a molecule or a chemical such as lanthanide ions (*i.e.* doping of the materials). A. Kudo and T. Sakata have modified the KLN phase with rare-earth-metal ions to add specific luminescent signature to the inorganic layered material.[78] They also studied the luminescent mechanism which is dependent on the doping ion. Besides A. Kudo and K. Eichi showed that in the case of rare-earth ion, doping was more efficient than exchanging the interlayer cation by rare-earth ions, as in most cases only the luminescence of the guest cations is detected.[79]

Finally, layered materials have been hybridized with luminescent organic molecule such as porphyrins,[80,81] phthalocyanines,[82] pyrenes,[83] aromatic olefin or organometallic complexes such as Ruthenium poly(pyridine) complexes.[84] The scope of applications is very broad, from photocatalysis to non-linear optic.[85] Among all this luminescent hosts, pyrenes display a peculiar behavior: its luminescence is dependent on its aggregation state. At low concentration, pyrene molecules display a monomer-type excitation. When increasing the concentration, pyrenes molecules are strongly correlated due to π-π interactions and form an excimer. This later displays an emission spectrum in the form of a quenched and shifted-broad-intensity band which contrasts with the monomer signature.[86] This aggregation-induced luminescence has been use to characterize the loading of pyrene into LDHs: at high loading, the excimer luminescence is observed while when “diluted” with alkyl chain, the hybrid materials show the monomer luminescence.[87] Until now, many works have been conducted on aggregation-induced-emission molecules.[88–90]

Herein, we propose a new use of pyrene derivatives: a probe for the exfoliation degree of a hybrid material. The idea is to follow the evolution of the luminescence of pyrene-based hybrid along the exfoliation process and to determine if the pyrene luminescence can act as a probe for the exfoliation degree, qualitatively, or even quantitatively.

Thus, we consider three pyrene derivatives, possessing an alcohol as anchoring group to ensure the grafting of the pyrene along the exfoliation process: the 1-hydroxypyrene (PyrOH), the 1-pyrenemethanol ($PyrC_1OH$) and the 1-pyrenebutanol ($PyrC_4OH$). We synthesized and characterized hybrid materials from these molecules and we studied their photoluminescence properties in the **Chapter VI.**

II.3.4.2 Synthesis and characterization

The grafting of the pyrene derivatives was carried out using microwave assistance. The precursor $C_{12}O$-HST and the pyrene derivatives are poured into 10 mL of non-dried THF in a microwave reactor without additional water. The reaction mixture is heated at 110°C for 3 hours. The resulting powder is collected by centrifugation, washed three times with acetone and dried in air overnight. The as-synthesized hybrids are denoted as PyrO-HST, $PyrC_1O$-HST and $PyrC_4O$-HST. Trials were made with C_4N-HST as precursor but the resulting powder were poorly crystalline and the grafting was not successful in the case of 1-pyrenebutanol. Alcohol-based hybrids are more suitable precursors for the grafting of other alcohols or of phosphonic acid as discussed above.

The hybrid powders have a brownish color as shown in ***Figure 26*** **.** Their shade contrasts with the usual white color of most of the synthesized compounds like $C_{12}O$-HST, C_xPO_3-HST and the organosilane-HST hybrids. Herein we do not focus on the photophysical properties of PyrO-HST, $PyrC_1O$-HST and $PyrC_4O$-HST. They will be discussed in a subsequent part in **Chapter VI.**

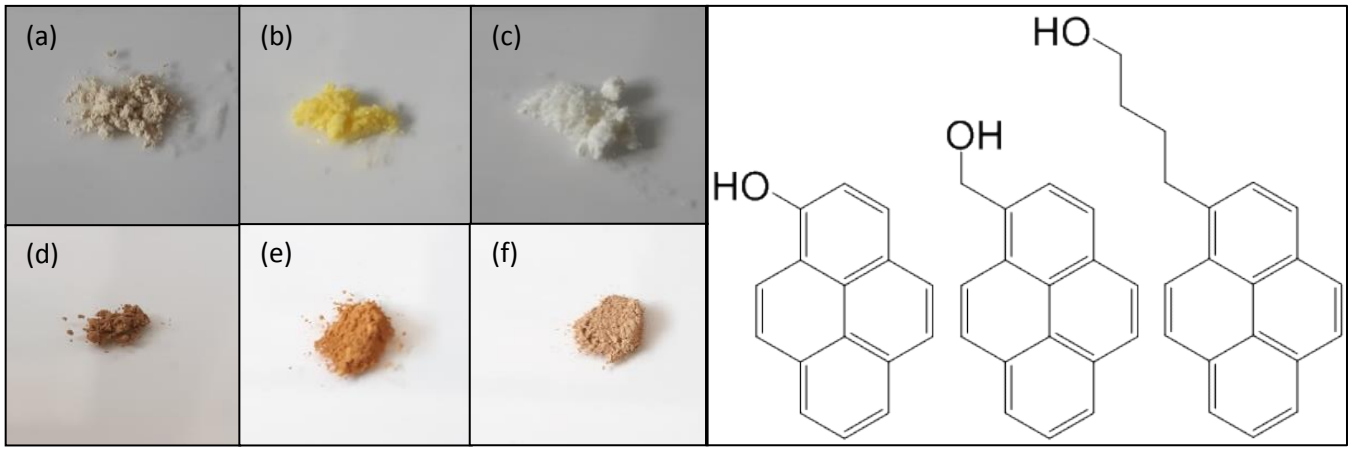

Figure 26: Left) Photograph of the pyrenes derivatives (a) 1-hydroxypyrene, (b) 1-pyrenemethanol, (c) 1-pyrenebutanol and the corresponding hybrid materials (d) PyrO-HST, (e) $PyrC_1O$-HST and (f) $PyrC_4O$-HST. Right) The molecular structure of 1-hydroxypyrene, 1-pyremethanol and 1-pyrenebutanol.

XRD patterns of PyrO-HST, $PyrC_1O$-HST and $PyrC_4O$-HST are shown in ***Figure 27.*** The (*100*), (*110*) and (*200*) reflections at 22.7°, 32.5° and 46.3° respectively prove the integrity of the inorganic layer. The (*00l*) reflections at low angles show that the hybrids possess a layered crystalline structure. As

expected, the interlayer distance d_{001} increases while increasing the molecule length: 2.25 nm, 2.66 nm and 3.24 nm for PyrO-HST, PyrC_1O-HST and PyrC_4O-HST respectively. The evolution of the interlayer distance as a function of the number of carbon atoms of the side alkyl chain is not linear, even if we only have three points. This indicates that the tilt angle between the molecules and the inorganic layer is not the same for the three molecules and/or their degree of interdigitation is different. Given the thickness of the inorganic layer (about 1 nm) and the size of the molecules (about 0.8 nm, 1.0 nm and 1.3 nm for PyrOH, PyrC_1OH and PyrC_4OH respectively), the observed interlamellar distances are compatible with a bilayer arrangement. The degree of interdigitation, if any, cannot be determined, as the tilt angle is not known, but there is no complete interdigitation. In the case of PyrO-HST, where no carbon atom separates the aromatic molecules from the inorganic layer, we can relate the indecisive situation with the work of S. Gago *et al.*[91] The authors investigated the grafting of pyrenyl derivatives such as 1-pyrenecarboxylic acid or sodium1-pyrenesylfonate into of layer Zn-Al double hydroxide. They also faced the impossibility of stating on the arrangement of pyrene derivatives into the interlayer space. Besides, they studied the photoluminescent properties of the hybrid compound and showed that many molecular arrangements cohabit into a same sample.

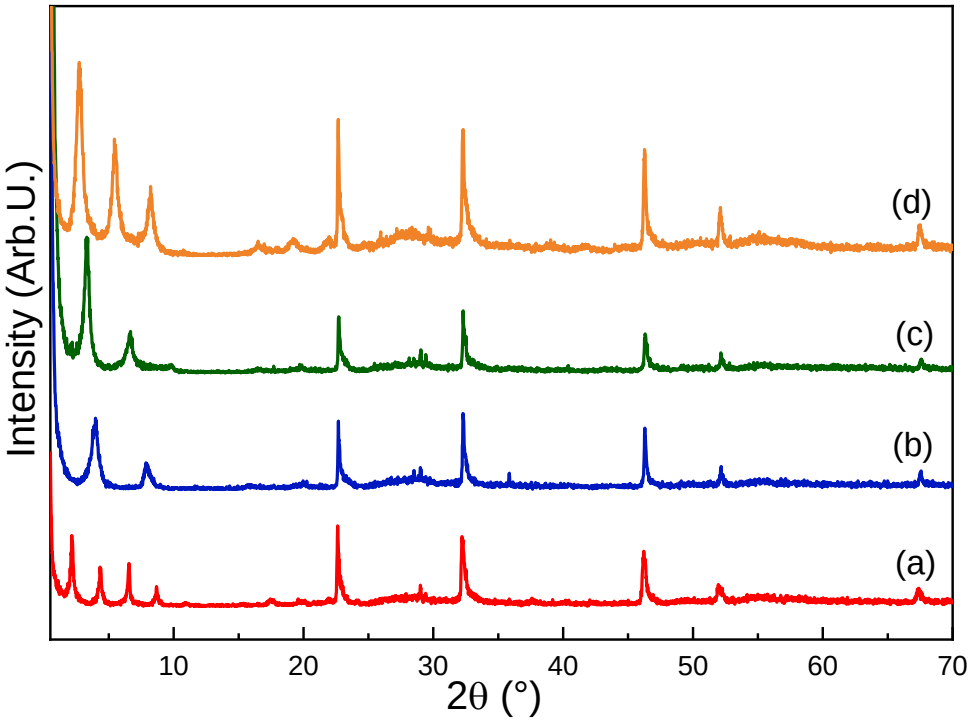

Figure 27: XRD patterns of (a) C_{12}O-HST, (b) PyrO-HST, (c) PyrC_1O-HST and (d) PyrC_4O-HST.

In ***Figure 28***, the FTIR spectra emphasize the deintercalation of C_{12}O-HST from the structure (disappearance of the intense C-H vibration bands around 2900 cm^{-1}) and the grafting of the pyrene derivatives. Indeed, the C-O-Ta vibration band is clearly observed at 1136 cm^{-1} for PyrC_1O-HST and PyrC_4O-HST and at 1281 cm^{-1} for PyrO-HST. The shift for the later hybrid (compared to PyrC_xO-HST) is ascribed to the direct bond between the oxygen and the conjugated aromatic ring. Similarly, the =C-H

vibration band at 840 cm^{-1} is characteristic of aromatic compounds, showing the integrity of the pyrene molecules.

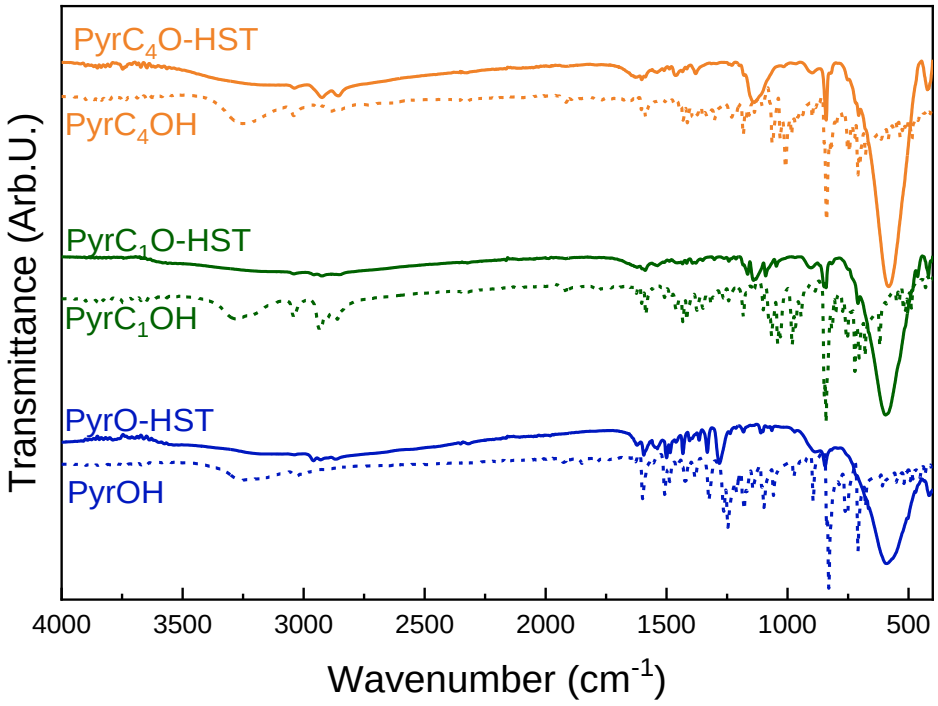

Figure 28: FTIR spectra of PyrO-HST, PyrC$_1$O-HST and PyrC$_4$O-HST (solid line) and their corresponding molecule (dot line).

TGA/TDA analyses were carried out on the three pyrene-functionalized materials (***Figure 29***). Between 25°C to 200°C, the mass loss is ascribed to adsorbed water removal. The decomposition of the pyrene derivative begins around 260°C with a slight mass loss corresponding to an exothermic event (more visible on PyrC$_1$O-HST curves). It is follows by a more consistent mass loss of 9 %, 12% and 15% for PyrO-HST, PyrC$_1$O-HST and PyrC$_4$O-HST respectively. The increasing organic mass loses are in accordance with the respective molecular weight of the pyrene derivatives, considering the same grafting rate. The C, H, N, microanalysis (***Table 3***) allows to propose a formula for the three pyrene-based hybrid and also shows that some impurities of 1-butylamine might remain even if using C$_{12}$O-HST as precursor.

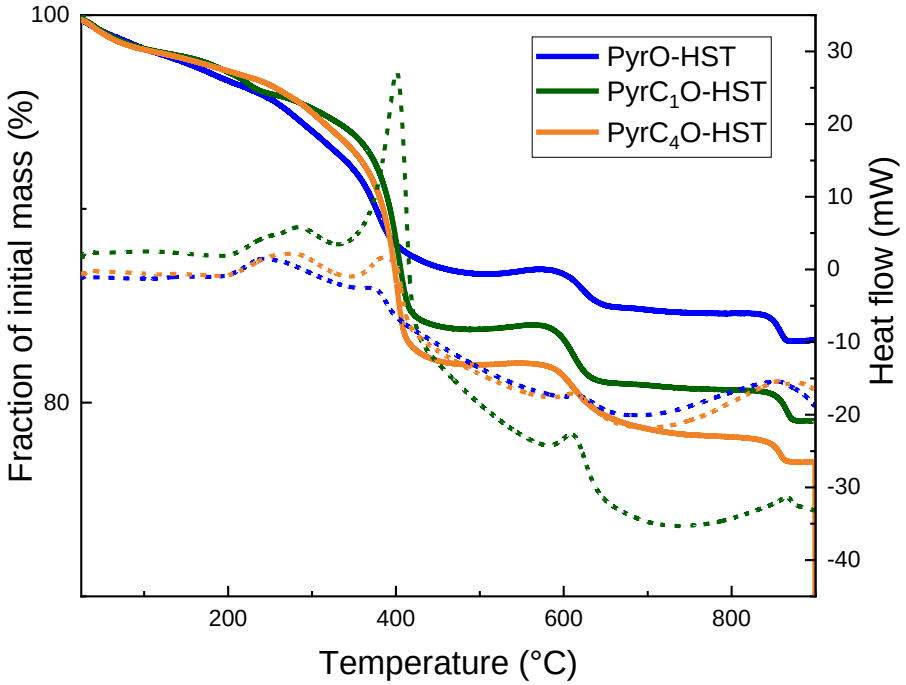

Figure 29: TGA curves of PyrO-HST, PyrC$_1$O-HST and PyrC$_4$O-HST in solid line and their corresponding TDA curves in dot line

Products	Layered materials	Carbon content found (calc) (%)	Nitrogen Content found (calc) (%)	Hydrogen content found (calc) (%)
PyrO-HST	$(C_{16}H_9O)_{0.3}(C_4H_9NH_3)_{0.6}H_{1.1}$ $Bi_{0.1}Sr_{0.85}Ta_2O_6.2H_2O$	10.46 (12.1)	1.12 (1.18)	1.53 (2.13)
PyrC$_1$O-HST	$(C_{17}H_{11}O)_{0.23}H_{1..77}$ $Bi_{0.1}Sr_{0.85}Ta_2O_6.0.1H_2O$	7.68 (7.54)	0 0	0.64 (0.73)
PyrC$_4$O-HST	$(C_{20}H_{17}O)_{0.45}(C_4H_9NH_3)_{0.15}$ $Bi_{0.1}H_{1..4}Sr_{0.85}Ta_2O_6.0.1H_2O$	16.85 (16.14)	0.3 (0.29)	1.79 (1.81)

Table 3: C, H, N micro-analysis and proposed formula for PyrO-HST, PyrC$_1$O-HST and PyrC$_4$O-HST

II.3.4.3 Conclusion

The grafting of 1-hydroxypyrene, 1-pyrenemethanol and 1-pyrenebutanol was achieved by using microwave assistance and C_{12}O-HST as precursor. The resulting hybrid materials are crystalline colored compounds. The presence of the organic molecules was also evidence by FTIR spectroscopy and elemental analyses. Thus, not only linear chain but also aromatic molecule can be grafted onto HST and thus can hopefully be exfoliated later on.

II.3.5 Grafting of nucleobase derivatives: towards an assembly building block

II.3.5.1 Introduction

Supramolecular assemblies are complex structures based on the specific recognition of at least two distinct but complementary building blocks. The most stunning instance of such assembly is found in the field of biology: the DNA macromolecule consists in double helix strands whose the building blocks are complementary nucleobases derivatives.[92] There are four of them composed of a phosphate group, a ribose or desoxyribose and a nucleobase. They are Adenosine-5'-monophosphate (AMP), Guanosine-5'-monophosphate (GMP), Cytosine-5'-monophosphate (CMP) and Thymidine-5'-monophosphate (TMP) (***Figure 30***). They interact in a two-by-two complementary way: AMP associates specifically with TMP through hydrogen bonds whereas CMP and GMP are pairing together (***Figure 31***). Besides, their crucial role in DNA, these nucleotides and their derivatives are involved in biological mechanisms. We can quote the production of energy in a cell through the hydrolysis of Adenosine-5'-triphosphate (ADP) into Adenosine-5'-diphosphate (ADP). Therefore, several works have been conducted to integrate these molecules with nano-objects to reach biological properties.[93–96] For instance, J.H. Choy *et al* have inserted AMP into LDH as a proof of concept to a novel nano-carrier.[97] Single-wall carbon nanotubes have been functionalized with AMP through a chemical coupling reaction, opening the application field of such materials.[61] Meanwhile, the main advantage of nucleotide remains their ability to interact specifically. The diversity of the assembling possibilities with these peculiar molecules and the systems developed using the specific interaction of nucleobases have been reported in various reviews.[98–100]

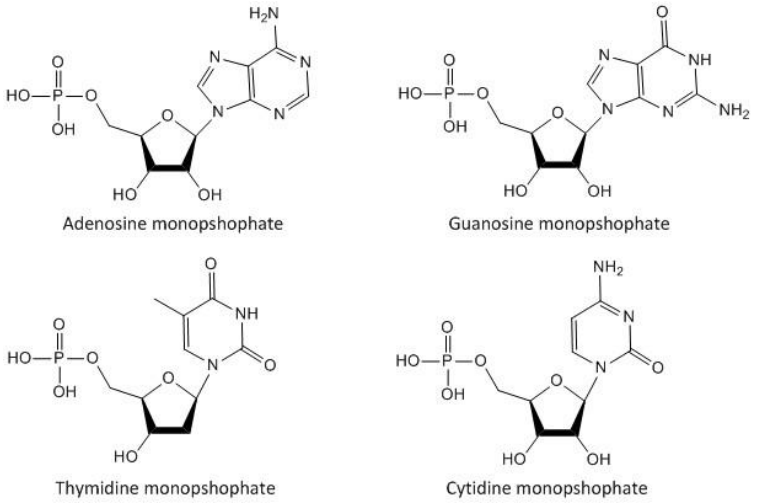

Figure 30: The four nucleotides monophosphate, composed of a phosphonic group, a ribose or desoxyribose part and the nucleobase.

In this study, we consider the potentiality of nucleotides or nucleoside (nucleotides without the phosphate moiety) to build non-electrostatic reassembly of inorganic nanosheets. Thus, in a first step, we aim at functionalizing layered oxides (HST in a first step) with such molecules to open a new path in the

nanosheets assembling process. We focus firstly on the nucleoside pair Adenosine/Thymidine as well as their phosphate derivatives, AMP and TMP afterwards.

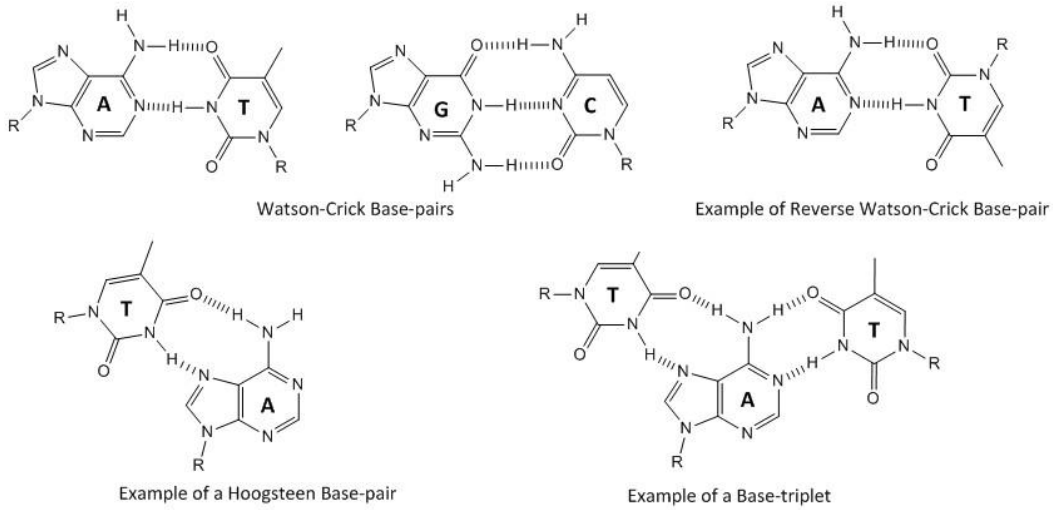

Figure 31: Assembling possibilities with nucleosides.[98]

II.3.5.2 Synthesis and characterization of nucleoside-grafted materials

The grafting of nucleosides into layered HST was carried out with microwave-assistance, using C_{12}O-HST as precursor. It is poured in 10 mL of THF with a large molar excess of nucleoside (about 10 times) with 1.5 ml of water. The mixture is heated at 110°C for 3 hours and the resulting powder is collected by centrifugation, washed three times with water and dried in air overnight. The resulting compounds are white powders, denoted as Adenosine-HST and Thymidine-HST.

The XRD patterns of both hybrids are shown in ***Figure 32.*** The in-plane reflection peaks (*100*), (*110*) and (*200*) testify the structural integrity of inorganic layer of $SrTa_2O_7^{2-}$. The out-of-plane reflection (*00l*) peaks at low angle show that Adenosine-HST and Thymidine-HST have a layered structure. The interlayer distance of Adenosine-HST and Thymidine-HST are 2.51 nm and 2.47 nm respectively. These values are significantly smaller than the interlayer distance d_{001} = 4.01 nm of C_{12}O-HST which corroborates the removal of the 1-dodecanol moiety. Besides, the interlayer distances of both Adenosine-HST and Thymidine-HST are similar which is consistent with their similar molecular structure.

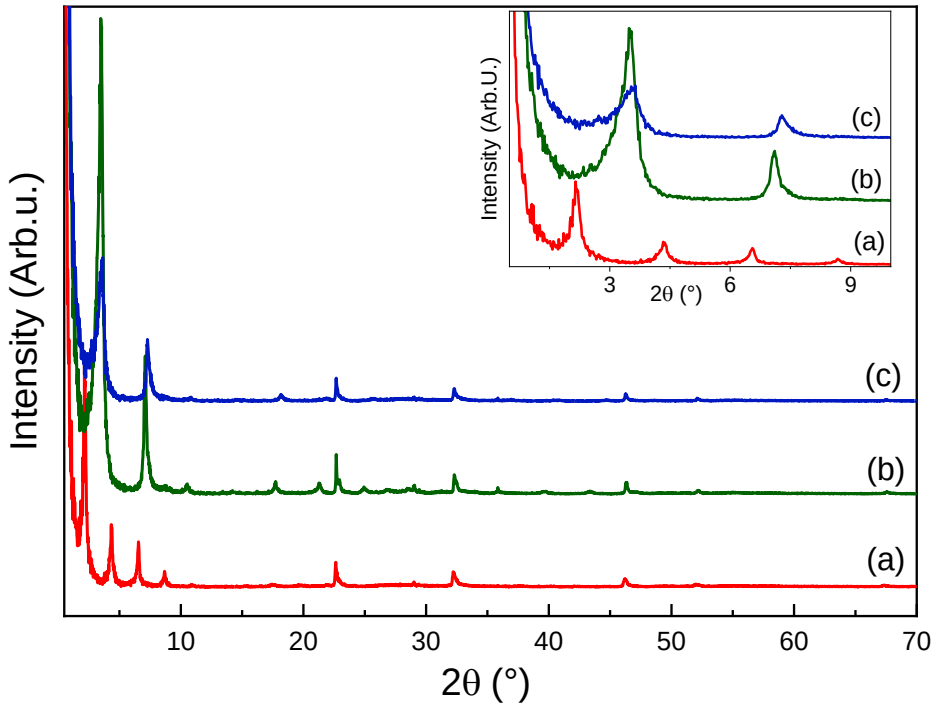

Figure 32: XRD patterns of (a) C_{12}O-HST, (b) Adenosine-HST and (c) Thymidine-HST. The insert is a magnification of the low angle region.

The presence of the nucleosides into inorganic layers is emphasized by the FTIR spectra of the hybrids (***Figure 33***). First, the intense (C-H) vibration bands around 2900 cm^{-1}, characteristic of $C_{12}OH$, have disappeared. Moreover, most of the FTIR bands of the nucleoside alone are found in spectrum of the corresponding hybrid. For instance, the C=N stretching band and the N-H stretching band of primary amine at 1664 cm^{-1} and 1603 cm^{-1} respectively are still present in the spectrum of Adenosine-HST. In the same way, the C=O stretching band at 1695 cm^{-1} is similarly found in Thymidine-HST and the nucleoside spectra. However, some bands are shifted in the spectra of the hybrid materials with respect to the spectra of the pristine molecules: we ascribed this phenomenon to the grafting of the molecule and/or interactions with neighbouring molecules.

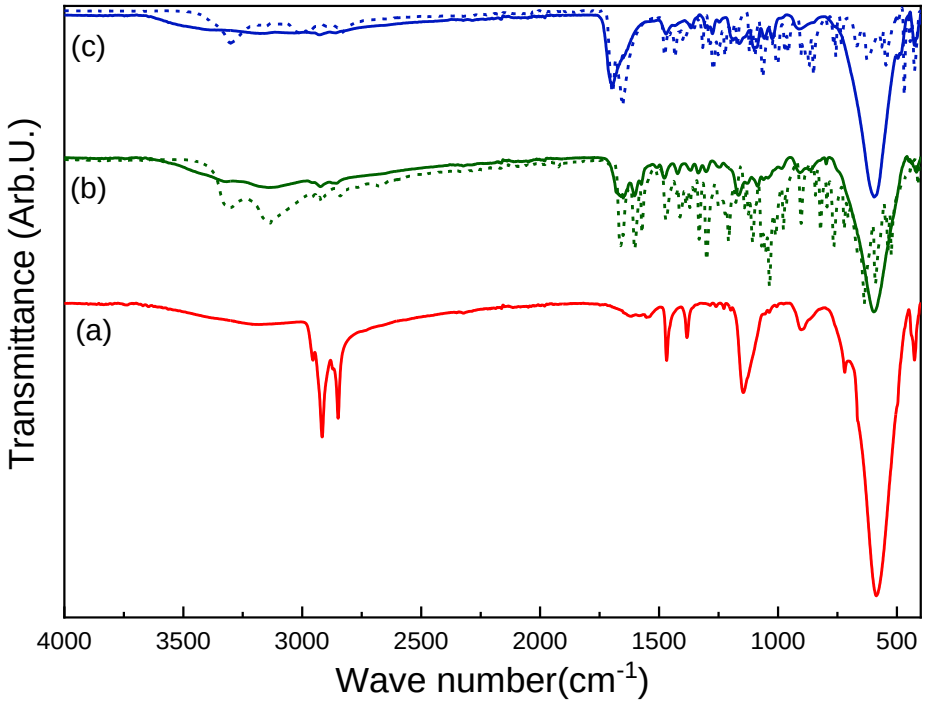

Figure 33: FTIR spectra of (a) C_{12}O-HST (b) Adenosine-HST and (c) Thymidine-HST in solid line and their corresponding molecule in dot line.

To clarify the molecular integrity of the nucleosides, solid state ^{13}C CP/MAS NMR was carried out on the hybrids. The resulting spectra are shown in ***Figure 34*** and ***Figure 36*** for Adenosine-HST and Thymidine-HST respectively. First of all, the four peaks at low chemical shift correspond to 1-butylamine impurities which could not be removed along the whole process *i.e*. the synthesis of C_{12}O-HST from C_4N-HST, followed by the subsequent synthesis of Adenosine-HST from C_{12}O-HST.

In the solid state ^{13}C CP/MAS NMR spectrum of Adenosine-HST (***Figure 34*),** the peaks above 110 ppm correspond to the carbon of the nucleobase (*i.e.* the adenine) without any ambiguity, supported by the simulated ^{13}C CP/MAS NMR spectrum in ***Figure 35***. The peaks between 110 ppm and 55 ppm correspond to the ribose part of the molecule. The carbons b and d are easily attributed.

However, an ambiguity remains concerning the precise attribution of carbons a, c and c'. Indeed the grafting of an hydroxyl group leads to a downfield shift of about 10 ppm of the chemical shift of the α-carbon.[9,24,25] Here it is not possible to determine which hydroxyl group is involved in the etherification reaction with the inorganic layer. It is even more likely that multiple grafting modes exist in the compound. Nevertheless, the important point here is that the integrity of adenosine and its grafting into HST *via* an etherification reaction can be attested.

Finally, we can exclude the interaction of adenosine with the HST through the amine. Given the pKa of 3.8 corresponding to this amine, we know from literature and our own experience that the protonation of the amine group does not happen in the reaction conditions.[6] The acidity of the interlayer protons is not strong enough to protonate the amine and form the corresponding positively-charged ammonium.

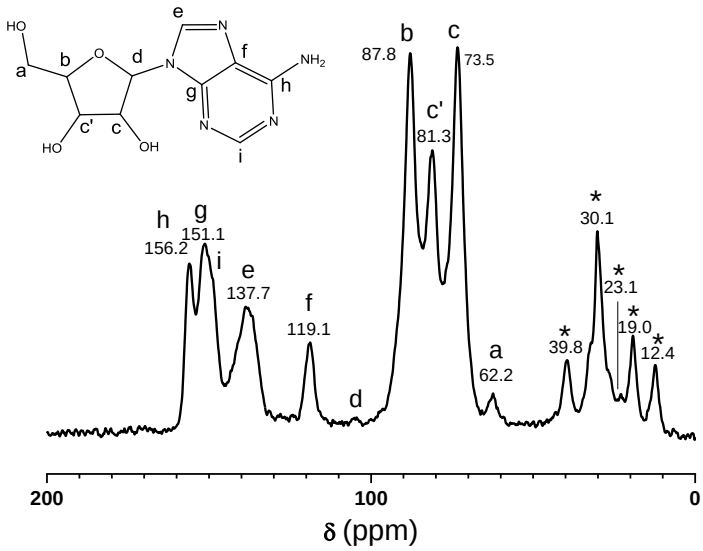

Figure 34: Solid state ^{13}C CP/MAS NMR spectrum of Adenosine-HST.

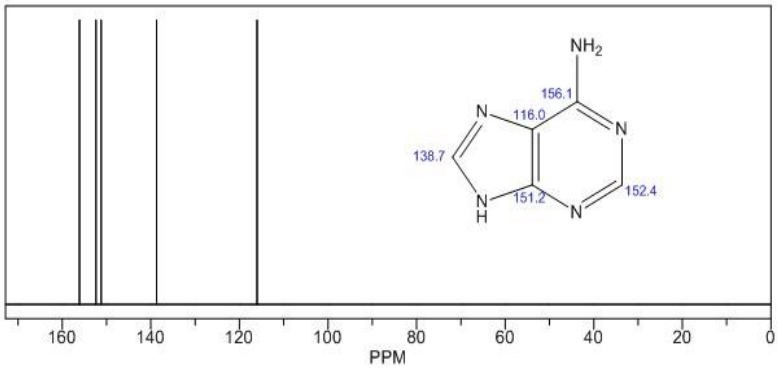

Figure 35: Simulated ^{13}C NMR spectrum of Adenine.

The solid state ^{13}C CP/MAS NMR spectrum of Thymidine-HST is presented in ***Figure 36***. The peaks above 100 ppm are ascribed to the thymine part (supported by the simulated spectrum of thymine in ***Figure 37***) whereas the peaks below 100 ppm correspond to the 2-desoxyribose part of thymidine. Here again, an ambiguity concerning the precise attribution of the carbons c and a remains. One of the two hydroxyl group is grafted, but it is not possible to precise which one. There again, the important is that ^{13}C NMR proves the molecular integrity and the grafting of thymidine into HST.

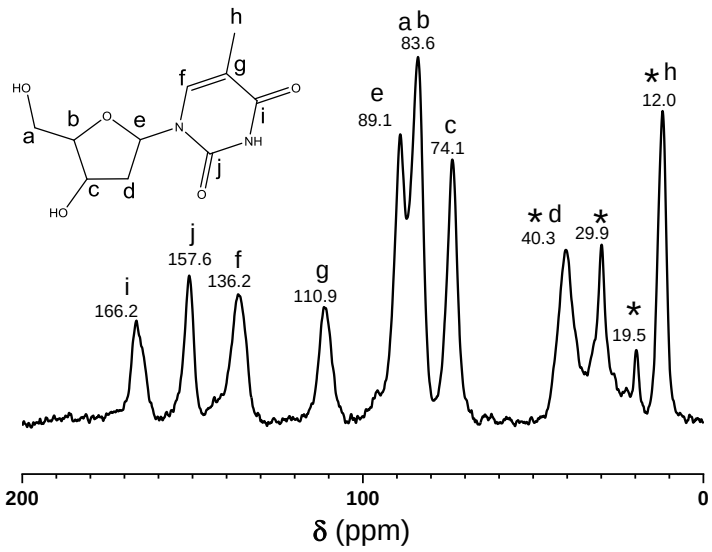

Figure 36: Solid state ^{13}C CP/MAS NMR spectrum of Thymidine-HST.

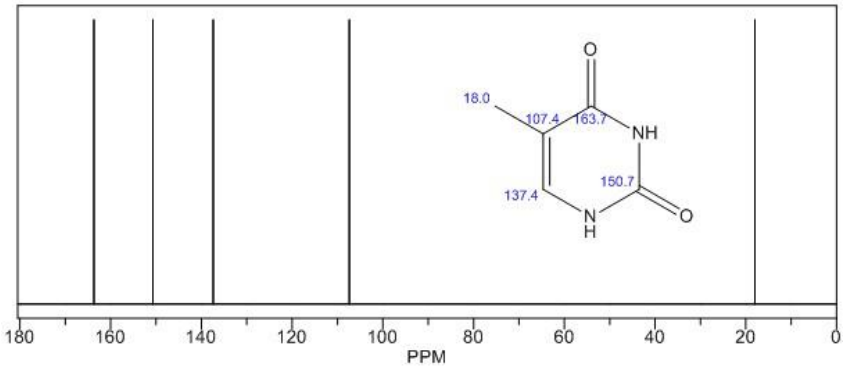

Figure 37: Simulated ^{13}C NMR of Thymine.

Thermogravimetric TGA/TDA analyses were performed on Adenosine-HST and Thymidine-HST. The TGA/TDA profiles of both hybrid materials are shown in ***Figure 38***. The two profiles are similar, displaying the same mass losses. The first one (between 25°C and 200°C) is ascribed to the removal of adsorbed water. The second mass loss corresponds to the decomposition of the nucleoside. As suggested by the TDA profiles, this decomposition is a complex mechanism with at least four exothermic events. This is consistent with the complexity of the organic molecules inside the inorganic layers. Besides, the organic contents are 14.9 % and 12.7 % for Adenosine-HST and Thymidine-HST respectively. Considering their close molecular mass, the grafting yield of Adenosine and Thymidine into HST is similar. C, H, N analysis supports this statement (***Table 4***). A ratio $\frac{C\,(mol)}{N(mol)}$ was estimated to 2.2 and 5.4 for Adenosine-HST and Thymidine-HST respectively, which is consistent with the structure of the nucleosides. The chemical formula for both compounds was determined from elemental analysis: they are $(C_{10}H_{12}N_5O_3)_{0.45}H_{1.55}Sr_{0.85}Bi_{0.1}Ta_2O_7.4H_2O$ and $(C_{10}H_{13}N_2O_5)_{0.45}H_{1.55}Sr_{0.85}Bi_{0.1}Ta_2O_7.4.5H_2O$ for Adenosine-HST and Thymidine-HST respectively.

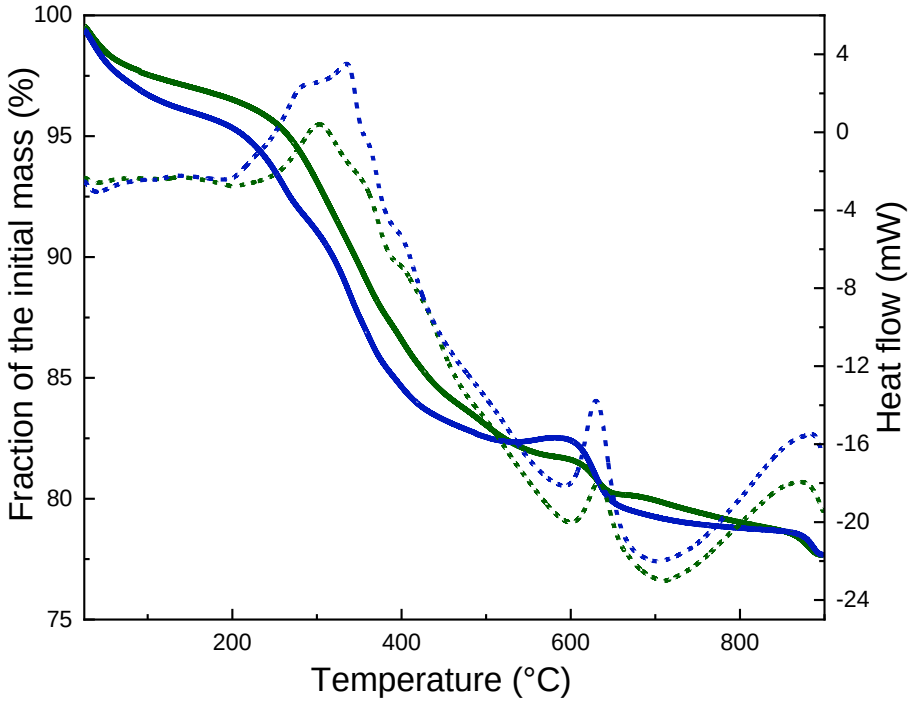

Figure 38: TGA profiles of Adenosine-HST (green) and Thymidine-HST (blue) in solid line and their corresponding TDA curves in dot line.

Products	Layered materials	Mass losses water + organic phase found (calc) (%)	Mass losses organic phase found (calc) (%)	Mass losses water found (calc) (%)	Carbon content found (calc) (%)	Nitrogen Content found (calc) (%)	Hydrogen content found (calc) (%)
Adenosine-HST	$(C_{10}H_{12}N_5O_3)_{0.45}H_{1.55}$ $Bi_{0.1}Sr_{0.85}Ta_2O_7.3H_2O$	19.9 (18.57)	15.49 (15.25)	4.41 (7.32)	7.09 (7.32)	3.84 (4.27)	1.23 (1.76)
Thymidine-HST	$(C_{10}H_{13}N_2O_4)_{0.45}H_{1.55}$ $Bi_{0.1}Sr_{0.85}Ta_2O_7.3.5H_2O$	17.01 (22.35)	12.71 (13.78)	4.91 (8.57)	7.17 (7.34)	1.54 (1.71)	1.30 (1.96)

Table 4: Corresponding mass losses of water and organic content; C, H, N micro-analysis. Proposed formula for Adenosine-HST and Thymidine-HST

II.3.5.3 Characterization of nucleotide-grafted materials

The nucleosides adenosine and thymidine presented in the previous paragraph were grafted *via* their alcohol moiety. As already discussed, the Ta-O-C is likely to be broken when heated or hydrolyzed upon exposure to water during long times. Hence the grafting by an alcohol group may be damaged during the exfoliation process. At the opposite the Ta-O-P bond are known to be more stable and as presented above, aliphatic or aromatic phosphonic acid have been successfully grafted onto HST layer. Thus, we chose to investigate the functionalization of the HST layers by a nucleotide: it is composed of the

nucleoside plus a phosphate moiety (***Figure 30***). Unfortunately, the phosphonate analogue is not available. Therefore, we focus on adenosine-5'-(dihydrogen phosphate) denoted as AMP.

The functionalization experiments were carried out with microwave assistance. Typically, the precursor C_4N-HST was poured into 10 mL of THF with an excess of AMP (about 8 times) and 1.5 ml of water. The reaction was heated at 110°C for 3 hours. The resulting powder was collected by centrifugation, washed three times with water and dried in air overnight. The resulting compound is denoted AMP-HST.

XRD pattern and IR spectrum show without ambiguity the non-insertion of the AMP into HST. We modify the experimental conditions: shorter times, at room temperature, without addition of water, with C_{12}O-HST as precursor and with conventional heating. Unfortunately, none of these derived experiments leads to the synthesis of AMP-HST. The XRD patterns and IR spectrum only revealed the presence of phosphate moiety into the layer. Thus, we conclude that the phosphate group of the AMP (R-OPO_3 bond) is too sensitive to hydrolysis which for the insertion-grafting conditions.

II.3.5.4 Conclusion

We successfully grafted the nucleosides, adenosine and thymidine, into HST through microwave-assistance. The resulting hybrid materials were characterized with XRD, FTIR, ^{13}C CP/MAS NMR and thermogravimetry which emphasize the grafting of the nucleoside *via* the ribose/desoxyribose moiety. However, multiple grafting modes (through different alcohols) are likely to happen. The nucleobase part (adenine and thymine) of the nucleosides points towards the center of the interlayer space. They should thus remain accessible for later recognition through hydrogen bonding. Besides, these hybrids demonstrate that the microwave-assistance allows the grafting of complex molecules without any damage. On the contrary, a series of trials to graft Adenosine-5'-monophosphate into HST was unsuccessful. It appears the insertion attempts, whether under microwave conditions or at room temperature, lead to the hydrolysis of the phosphate moiety of AMP. The free phosphate seems then to be grafted (or at least inserted into the structure). Thus our functionalization strategy cannot be extended to phosphate derivatives.

II.4. Conclusion of Chapter II

In this chapter, we first briefly reviewed the insertion of amine and grafting of alcohols into layered oxides (HST, HLN and HTO) with microwave assistance. This work has been initiated and developed by Y. Wang *et a.l*[8,9,19,20] Here, we updated them to introduce the synthesis with microwave assistance of hybrid materials, which are later used as precursor for subsequent functionalization (for instance C_4N-HST and C_{12}O-HST) . We showed that amine and alcohols are easily inserted/grafted into HST whereas alcohol grafting in HLN and HTO is more complex or even impossible. We ascribed this difference of reactivity to the acidity of the inorganic layer. Additional works must be carried out to fully understand the influence of structure and composition of the inorganic layer on its reactivity.

In a second part, we described the microwave-assisted functionalization of HST by organic moiety with a different anchoring group or functional carbon skeleton. First, we investigated the grafting of alkylphosphonic acid into HST to take advantage of phosphonic acid moiety as the P-O-Ta is known to

be resistant against hydrolysis.[49,53] We were able to graft three alkylphosphonic acids with a chain length of 3, 6, or 10 carbons. The resulting compounds display the same grafting mode for the phosphonic acid group on the inorganic layer. A fine structural characterization by PDF analysis on $C_{10}PO_3$-HST highlighted the precise arrangement of the molecules in the interlayer space and assessed the grafting of the molecules. In the same way, we have shown that aromatic phosphonic acids can be grafted into HST layers, following the same procedure.

Secondly, we took advantage of the reactivity of organosilane derivatives to modify the surface of $SrTa_2O_7^{2-}$ sheets. This approach allowed us to get free amine in the interlayer space of HST, which is impossible in a classic ion-exchange mechanism. We obtained a hybrid, APTS-HST, whose the amine can be further used for reaction and coupling with other surfaces or molecules. Similarly, two additional organosilanes, C8TS and MPTS, were used to design the surface properties of oxide sheets such as their hydrophobicity. However, some points have still to be clarified as the organization of the silane into the interlamellar space as well as their degree of hydrolysis/condensation. ^{29}Si NMR and PDF should allow to elucidate these points.

We also showed that pyrene derivatives, molecules with a fluorescence property, can be coupled with a layered material to result in a hybrid material. We expected the hybrid to display the aggregate-state fluorescence of the pyrene molecules. A study of the photophysical properties is described in **Chapter VI**.

Finally, we consider nucleobases derivatives *i.e.* nucleosides and nucleotides as promising pairs to non-electrostatically guide assemblies. Thus, we successfully grafted the complementary paired molecules, adenosine and thymidine, into HST *via* microwave-assistance. We demonstrated the integrity of such complex molecules thanks to spectroscopy (IR, NMR). We also highlighted that, despite the presence of amine on adenosine, the grafting occurred through alcohol groups due to a low pKa of the amine. However, we found that the nucleotides (*i.e.* nucleosides plus phosphate moiety) are too fragile to bear microwave functionalization and cannot be inserted into HST.

Hence, we build a library of hybrid layered materials whose organic moiety is smartly grafted into the inorganic layers. These organic-inorganic layered oxides form the starting point on the production of functionalized oxide nanosheets. They now can undergo exfoliation. We will develop this specific step in the next chapters.

II.5. Bibliography

(1) Rebbah, H.; Borel, M. M.; Raveau, B. Intercalation of Alkylammonium Ions and Oxide Layers |TiNbOt|⁻. *Materials Research Bulletin* **1980**, *15* (3), 317–321.

(2) Nedjar, R.; Borel, M. M.; Raveau, B. Intercalation of Primary Monoamines in the Lamellar Protonic Oxide $HNb_3O_8 \cdot H_2O$. *Zeitschrift für anorganische und allgemeine Chemie* **1986**, *540* (9–10), 198–204.

(3) Gopalakrishnan, J.; Bhat, V.; Raveau, B. $AILaNb_2O_7$: A New Series of Layered Perovskites Exhibiting Ion Exchange and Intercalation Behaviour. *Materials Research Bulletin* **1987**, *22* (3), 413–417.

(4) Schaak, R. E.; Mallouk, T. E. Perovskites by Design: A Toolbox of Solid-State Reactions. *Chem. Mater.* **2002**, *14* (4), 1455–1471. https://doi.org/10.1021/cm010689m.

(5) Uppuluri, R.; Gupta, A. S.; Rosas, A. S.; Mallouk, T. E. Soft Chemistry of Ion-Exchangeable Layered Metal Oxides. *Chem. Soc. Rev.* **2018**, *47* (7), 2401–2430.

(6) Sasaki, T.; Izumi, F.; Watanabe, M. Intercalation of Pyridine in Layered Titanates. *Chem. Mater.* **1996**, *8* (3), 777–782.

(7) Airoldi, C.; Nunes, L. M.; de Farias, R. F. The Intercalation of N-Alkyldiamines into Crystalline Layered Titanate. *Materials Research Bulletin* **2000**, *35* (13), 2081–2090.

(8) Wang, Y.; Delahaye, E.; Leuvrey, C.; Leroux, F.; Rabu, P.; Rogez, G. Efficient Microwave-Assisted Functionalization of the Aurivillius-Phase $Bi_2SrTa_2O_9$. *Inorg. Chem.* **2016**, *55* (8), 4039–4046.

(9) Wang, Y.; Nikolopoulou, M.; Delahaye, E.; Leuvrey, C.; Leroux, F.; Rabu, P.; Rogez, G. Microwave-Assisted Functionalization of the Aurivillius Phase $Bi_2SrTa_2O_9$: Diol Grafting and Amine Insertion vs. Alcohol Grafting. *Chem. Sci.* **2018**, *9* (35), 7104–7114.

(10) Wang, C.; Tang, K.; Wang, D.; Liu, Z.; Wang, L.; Zhu, Y.; Qian, Y. A New Carbon Intercalated Compound of Dion–Jacobson Phase $HLaNb_2O_7$. *J. Mater. Chem.* **2012**, *22* (22), 11086–11092.

(11) Tahara, S.; Sugahara, Y. Interlayer Surface Modification of the Protonated Triple-Layered Perovskite $HCa_2Nb_3O_{10} \cdot xH_2O$ with *n*-Alcohols. *Langmuir* **2003**, *19* (22), 9473–9478. https://doi.org/10.1021/la0343876.

(12) Kappe, C. O. Microwave Dielectric Heating in Synthetic Organic Chemistry. *Chem. Soc. Rev.* **2008**, *37* (6), 1127–1139.

(13) Rao, K. J.; Vaidhyanathan, B.; Ganguli, M.; Ramakrishnan, P. A. Synthesis of Inorganic Solids Using Microwaves. *Chem. Mater.* **1999**, *11* (4), 882–895.

(14) Gabriel, C.; Gabriel, S.; H. Grant, E.; H. Grant, E.; S. J. Halstead, B.; Michael P. Mingos, D. Dielectric Parameters Relevant to Microwave Dielectric Heating. *Chem. Soc. Rev.* **1998**, *27* (3), 213.

(15) Tang, Y.; Nian, J.; Yu, B.; Yang, W. Intercalation of N-C12H25NH2 into Layered Titanate with the Aid of Microwave Radiation. *Materials Letters* **2009**, *63* (23), 1992–1994.

(16) Cui, W.; Wang, H.; Liang, Y.; Han, B.; Liu, L.; Hu, J. Microwave-Assisted Synthesis of Ag@AgBr-Intercalated K4Nb6O17 Composite and Enhanced Photocatalytic Degradation of Rhodamine B under Visible Light. *Chemical Engineering Journal* **2013**, *230*, 10–18.

(17) Boykin, J. R.; Smith, L. J. Rapid Microwave-Assisted Grafting of Layered Perovskites with *n*-Alcohols. *Inorg. Chem.* **2015**, *54* (9), 4177–4179.

(18) Akbarian-Tefaghi, S.; Teixeira Veiga, E.; Amand, G.; Wiley, J. B. Rapid Topochemical Modification of Layered Perovskites via Microwave Reactions. *Inorg. Chem.* **2016**, *55* (4), 1604–1612.

(19) Wang, Y.; Leuvrey, C.; Delahaye, E.; Leroux, F.; Rabu, P.; Taviot-Guého, C.; Rogez, G. Tuning the Organization of the Interlayer Organic Moiety in a Hybrid Layered Perovskite. *Journal of Solid State Chemistry* **2019**, *269*, 532–539.

(20) Wang, Y.; Delahaye, E.; Leuvrey, C.; Leroux, F.; Rabu, P.; Rogez, G. Post-Synthesis Modification of the Aurivillius Phase Bi2SrTa2O9 via In Situ Microwave-Assisted "Click Reaction." *Inorg. Chem.* **2016**, *55* (19), 9790–9797.

(21) Dobal, P. S.; Katiyar, R. S. Studies on Ferroelectric Perovskites and Bi-Layered Compounds Using Micro-Raman Spectroscopy. *Journal of Raman Spectroscopy* **2002**, *33* (6), 405–423.

(22) Keeney, L.; Smith, R. J.; Palizdar, M.; Schmidt, M.; Bell, A. J.; Coleman, J. N.; Whatmore, R. W. Ferroelectric Behavior in Exfoliated 2D Aurivillius Oxide Flakes of Sub-Unit Cell Thickness. *Advanced Electronic Materials n/a* (n/a), 1901264.

(23) Rae, A. D.; Thompson, J. G.; Withers, R. L. Structure Refinement of Commensurately Modulated Bismuth Strontium Tantalate, $Bi_2SrTa_2O_9$. *Acta Crystallogr B Struct Sci* **1992**, *48* (4), 418–428.

(24) Suzuki, H.; Notsu, K.; Takeda, Y.; Sugimoto, W.; Sugahara, Y. Reactions of Alkoxyl Derivatives of a Layered Perovskite with Alcohols: Substitution Reactions on the Interlayer Surface of a Layered Perovskite. *Chem. Mater.* **2003**, *15* (3), 636–641.

(25) Tahara, S.; Ichikawa, T.; Kajiwara, G.; Sugahara, Y. Reactivity of the Ruddlesden−Popper Phase $H_2La_2Ti_3O_{10}$ with Organic Compounds: Intercalation and Grafting Reactions. *Chem. Mater.* **2007**, *19* (9), 2352–2358.

(26) Dias, A. S.; Lima, S.; Carriazo, D.; Rives, V.; Pillinger, M.; Valente, A. A. Exfoliated Titanate, Niobate and Titanoniobate Nanosheets as Solid Acid Catalysts for the Liquid-Phase Dehydration of d-Xylose into Furfural. *Journal of Catalysis* **2006**, *244* (2), 230–237.

(27) Wu, Q.; Yan, Y.; Zhang, Q.; Lu, J.; Yang, Z.; Zhang, Y.; Tang, Y. Catalytic Dehydration of Carbohydrates on In Situ Exfoliatable Layered Niobic Acid in an Aqueous System under Microwave Irradiation. *ChemSusChem* **2013**, *6* (5), 820–825.

(28) Bhuvanesh, N. S. P.; Gopalakrishnan, J. Solid-State Chemistry of Early Transition-Metal Oxides Containing D0 and D1 Cations. *Journal of Materials Chemistry* **1997**, *7* (12), 2297–2306. https://doi.org/10.1039/a703996d.

(29) Parks, G. A. The Isoelectric Points of Solid Oxides, Solid Hydroxides, and Aqueous Hydroxo Complex Systems. *Chem. Rev.* **1965**, *65* (2), 177–198.

(30) Takahashi, S.; Nakato, T.; Hayashi, S.; Sugahara, Y.; Kuroda, K. Formation of Methoxy-Modified Interlayer Surface via the Reaction between Methanol and Layered Perovskite HLaNb2O7.Cntdot.XH2O. *Inorg. Chem.* **1995**, *34* (20), 5065–5069.

(31) Allen, M. R.; Thibert, A.; Sabio, E. M.; Browning, N. D.; Larsen, D. S.; Osterloh, F. E. Evolution of Physical and Photocatalytic Properties in the Layered Titanates $A_2Ti_4O_9$ (A = K, H) and in Nanosheets Derived by Chemical Exfoliation. *Chem. Mater.* **2010**, *22* (3), 1220–1228.

(32) Fuse, Y.; Ide, Y.; Ogawa, M. Hybridization of Epoxy Resin with a Layered Titanate and UV Light Durability and Controlled Refractive Index of the Resulting Nanocomposite. *Polym. Chem.* **2010**, *1* (6), 849–853.

(33) Sasaki, T.; Watanabe, M.; Hashizume, H.; Yamada, H.; Nakazawa, H. Macromolecule-like Aspects for a Colloidal Suspension of an Exfoliated Titanate. Pairwise Association of Nanosheets and Dynamic Reassembling Process Initiated from It. *J. Am. Chem. Soc.* **1996**, *118* (35), 8329–8335.

(34) Sasaki, T.; Watanabe, M. Osmotic Swelling to Exfoliation. Exceptionally High Degrees of Hydration of a Layered Titanate. *J. Am. Chem. Soc.* **1998**, *120* (19), 4682–4689.

(35) Sano, K.; Kim, Y. S.; Ishida, Y.; Ebina, Y.; Sasaki, T.; Hikima, T.; Aida, T. Photonic Water Dynamically Responsive to External Stimuli. *Nat Commun* **2016**, *7* (1), 1–9.

(36) Matsui, H.; Oaki, Y.; Imai, H. Surface-Functionalized Hydrophilic Monolayer of Titanate and Its Application for Dopamine Detection. *Chem. Commun.* **2016**, *52* (60), 9466–9469.

(37) Ide, Y.; Ogawa, M. Preparation and Some Properties of Organically Modified Layered Alkali Titanates with Alkylmethoxysilanes. *Journal of Colloid and Interface Science* **2006**, *296* (1), 141–149.

(38) Ide, Y.; Ogawa, M. Interlayer Modification of a Layered Titanate with Two Kinds of Organic Functional Units for Molecule-Specific Adsorption. *Angewandte Chemie International Edition* **2007**, *46* (44), 8449–8451.

(39) Nakano, S.; Sasaki, T.; Takemura, K.; Watanabe, M. Pressure-Induced Intercalation of Alcohol Molecules into a Layered Titanate. *Chem. Mater.* **1998**, *10* (8), 2044–2046.

(40) Sasaki, T.; Kooli, F.; Iida, M.; Michiue, Y.; Takenouchi, S.; Yajima, Y.; Izumi, F.; Chakoumakos, B. C.; Watanabe, M. A Mixed Alkali Metal Titanate with the Lepidocrocite-like Layered Structure. Preparation, Crystal Structure, Protonic Form, and Acid−Base Intercalation Properties. *Chem. Mater.* **1998**, *10* (12), 4123–4128.

(41) Tanaka, T.; Ebina, Y.; Takada, K.; Kurashima, K.; Sasaki, T. Oversized Titania Nanosheet Crystallites Derived from Flux-Grown Layered Titanate Single Crystals. *Chem. Mater.* **2003**, *15* (18), 3564–3568.

(42) Kurnosenko, S. A.; Silyukov, O. I.; Mazur, A. S.; Zvereva, I. A. Synthesis and Thermal Stability of New Inorganic-Organic Perovskite-like Hybrids Based on Layered Titanates $HLnTiO_4$ (Ln = La, Nd). *Ceramics International* **2020**, *46* (4), 5058–5068.

(43) Yuan, H.; Besselink, R.; Liao, Z.; ten Elshof, J. E. The Swelling Transition of Lepidocrocite-Type Protonated Layered Titanates into Anatase under Hydrothermal Treatment. *Scientific Reports* **2014**, *4* (1), 1–6.

(44) Fuse, Y.; Ide, Y.; Ogawa, M. Composition-Dependent Ion-Exchange Reactivity of Potassium Lithium Titanates. *BCSJ* **2008**, *81* (6), 767–772.

(45) Queffélec, C.; Petit, M.; Janvier, P.; Knight, D. A.; Bujoli, B. Surface Modification Using Phosphonic Acids and Esters. *Chem. Rev.* **2012**, *112* (7), 3777–3807.
(46) Guerrero, G.; Alauzun, J. G.; Granier, M.; Laurencin, D.; Mutin, P. H. Phosphonate Coupling Molecules for the Control of Surface/Interface Properties and the Synthesis of Nanomaterials. *Dalton Trans.* **2013**, *42* (35), 12569–12585.
(47) Weinberger, C.; Heckel, T.; Schnippering, P.; Schmitz, M.; Guo, A.; Keil, W.; Marsmann, H. C.; Schmidt, C.; Tiemann, M.; Wilhelm, R. Straightforward Immobilization of Phosphonic Acids and Phosphoric Acid Esters on Mesoporous Silica and Their Application in an Asymmetric Aldol Reaction. *Nanomaterials* **2019**, *9* (2), 249.
(48) Shori, S.; Pellechia, P. J.; zur Loye, H.-C.; Ploehn, H. J. Covalent Grafting of Phenylphosphonate on Calcium Niobate Platelets. *Journal of Colloid and Interface Science* **2015**, *437*, 97–110. https://doi.org/10.1016/j.jcis.2014.09.024.
(49) Shimada, A.; Yoneyama, Y.; Tahara, S.; Mutin, P. H.; Sugahara, Y. Interlayer Surface Modification of the Protonated Ion-Exchangeable Layered Perovskite $HLaNb_2O_7{\bullet}xH_2O$ with Organophosphonic Acids. *Chem. Mater.* **2009**, *21* (18), 4155–4162.
(50) Shimada, A.; Yoneyama, Y.; Tahara, S.; Mutin, P. H.; Sugahara, Y. Interlayer Surface Modification of the Protonated Ion-Exchangeable Layered Perovskite $HLaNb_2O_7{\bullet}xH_2O$ with Organophosphonic Acids. *Chem. Mater.* **2009**, *21* (18), 4155–4162.
(51) Acton, O.; Dubey, M.; Weidner, T.; O'Malley, K. M.; Kim, T.-W.; Ting, G. G.; Hutchins, D.; Baio, J. E.; Lovejoy, T. C.; Gage, A. H.; Castner, D. G.; Ma, H.; Jen, A. K.-Y. Simultaneous Modification of Bottom-Contact Electrode and Dielectric Surfaces for Organic Thin-Film Transistors Through Single-Component Spin-Cast Monolayers. *Advanced Functional Materials* **2011**, *21* (8), 1476–1488.
(52) Ollivier, P. J.; Mallouk, T. E. A "Chimie Douce" Sythesis of Perovskite-Type $SrTa_2O_6$ and $SrTa_{2-X}Nb_xO_6$. *Chem. Mater.* **1998**, *10* (10), 2585–2587.
(53) Payet, F.; Bouillet, C.; Leroux, F.; Leuvrey, C.; Rabu, P.; Schosseler, F.; Taviot-Guého, C.; Rogez, G. Fast and Efficient Shear-Force Assisted Production of Covalently Functionalized Oxide Nanosheets. *Journal of Colloid and Interface Science* **2022**, *607*, 621–632.
(54) Whittle, K. R.; Hyatt, N. C.; Reaney, I. M. Phase Transitions in Lanthanum-Doped Strontium Bismuth Tantalate. *Chem. Mater.* **2008**, *20* (20), 6427–6433.
(55) Prill, D.; Juhás, P.; Schmidt, M. U.; Billinge, S. J. L. Modelling Pair Distribution Functions (PDFs) of Organic Compounds: Describing Both Intra- and Intermolecular Correlation Functions in Calculated PDFs. *J Appl Cryst* **2015**, *48* (1), 171–178.
(56) Petkov, V.; Parvanov, V.; Trikalitis, P.; Malliakas, C.; Vogt, T.; Kanatzidis, M. G. Three-Dimensional Structure of Nanocomposites from Atomic Pair Distribution Function Analysis: Study of Polyaniline and $(Polyaniline)_{0.5}V_2O_5{\cdot}1.0H_2O$. *J. Am. Chem. Soc.* **2005**, *127* (24), 8805–8812.
(57) Proffen, T.; Billinge, S. J. L. PDFFIT, a Program for Full Profile Structural Refinement of the Atomic Pair Distribution Function. *J Appl Cryst* **1999**, *32* (3), 572–575.
(58) Farrow, C. L.; Juhas, P.; Liu, J. W.; Bryndin, D.; Božin, E. S.; Bloch, J.; Proffen, T.; Billinge, S. J. L. PDFfit2 and PDFgui: Computer Programs for Studying Nanostructure in Crystals. *J. Phys.: Condens. Matter* **2007**, *19* (33), 335219.
(59) Boczula, D.; Cały, A.; Dobrzyńska, D.; Janczak, J.; Zoń, J. Structural and Vibrational Characteristics of Amphiphilic Phosphonate Salts. *Journal of Molecular Structure* **2012**, *1007*, 220–226.
(60) Yuan, H.; Dubbink, D.; Besselink, R.; ten Elshof, J. E. The Rapid Exfoliation and Subsequent Restacking of Layered Titanates Driven by an Acid-Base Reaction. *Angewandte Chemie International Edition* **2015**, *54* (32), 9239–9243.
(61) Blondeau, P.; Xavier Rius-Ruiz, F.; Düzgün, A.; Riu, J.; Xavier Rius, F. Covalent Functionalization of Single-Walled Carbon Nanotubes with Adenosine Monophosphate: Towards the Synthesis of SWCNT–Aptamer Hybrids. *Materials Science and Engineering: C* **2011**, *31* (7), 1363–1368. https://doi.org/10.1016/j.msec.2011.05.001.
(62) Grasset, F.; Saito, N.; Li, D.; Park, D.; Sakaguchi, I.; Ohashi, N.; Haneda, H.; Roisnel, T.; Mornet, S.; Duguet, E. Surface Modification of Zinc Oxide Nanoparticles by Aminopropyltriethoxysilane. *Journal of Alloys and Compounds* **2003**, *360* (1), 298–311.
(63) Zheng, J.; Zhu, Z.; Chen, H.; Liu, Z. Nanopatterned Assembling of Colloidal Gold Nanoparticles on Silicon. *Langmuir* **2000**, *16* (10), 4409–4412.

(64) Wei, Z. Q.; Wang, C.; Zhu, C. F.; Zhou, C. Q.; Xu, B.; Bai, C. L. Study on Single-Bond Interaction between Amino-Terminated Organosilane Self-Assembled Monolayers by Atomic Force Microscopy. *Surface Science* **2000**, *459* (3), 401–412.

(65) Noblet, T.; Boujday, S.; Méthivier, C.; Erard, M.; Hottechamps, J.; Busson, B.; Humbert, C. Two-Dimensional Layers of Colloidal CdTe Quantum Dots: Assembly, Optical Properties, and Vibroelectronic Coupling. *J. Phys. Chem. C* **2020**, *124* (47), 25873–25883.

(66) Sylvester, P.; Cahill, R.; Clearfield, A. Pillaring of Layered Tetravalent Metal Phosphates and Oxides Using (3-Aminopropyl)Trimethoxysilane. *Chem. Mater.* **1994**, *6* (10), 1890–1898.

(67) Isoda, K.; Kuroda, K.; Ogawa, M. Interlamellar Grafting of γ-Methacryloxypropylsilyl Groups on Magadiite and Copolymerization with Methyl Methacrylate. *Chem. Mater.* **2000**, *12* (6), 1702–1707. https://doi.org/10.1021/cm0000494. Ogawa, M.; Saito, K.; Sohmiya, M. A Controlled Spatial Distribution of Functional Units in the Two Dimensional Nanospace of Layered Silicates and Titanates. *Dalton Trans.* **2014**, *43* (27), 10340–10354.

(69) Tao, Q.; He, H.; Li, T.; Frost, R. L.; Zhang, D.; He, Z. Tailoring Surface Properties and Structure of Layered Double Hydroxides Using Silanes with Different Number of Functional Groups. *Journal of Solid State Chemistry* **2014**, *213*, 176–181.

(70) Guo, W.; Zhao, Y.; Zhou, F.; Yan, X.; Fan, B.; Li, R. Silylated Layered Double Hydroxide Nanosheets Prepared by a Large-Scale Synthesis Method as Hosts for Intercalation of Metal Complexes. *Applied Catalysis A: General* **2016**, *522*, 101–108.

(71) Kiba, S.; Haga, J.-I.; Hashimoto, S.; Nakato, T. Adsorptive and Photocatalytic Removal of Phenol by Layered Niobates Organically Modified Through Intercalation and Silylation. *J. Nanosci. Nanotech.* **2010**, *10* (12), 8341–8348.

(72) Oaki, Y. Exfoliation Chemistry of Soft Layered Materials toward Tailored 2D Materials. *Chem. Lett.* **2021**, *50* (2), 305–

(73) Innocenzi, P. Infrared Spectroscopy of Sol–Gel Derived Silica-Based Films: A Spectra-Microstructure Overview. *Journal of Non-Crystalline Solids* **2003**, *316* (2–3), 309–319.

(74) Singh, L. P.; Bhattacharyya, S. K.; Mishra, G.; Ahalawat, S. Functional Role of Cationic Surfactant to Control the Nano Size of Silica Powder. *Appl Nanosci* **2011**, *1* (3), 117–122.

(75) Carrasco, J. A.; Seijas-Da Silva, A.; Oestreicher, V.; Romero, J.; Márkus, B. G.; Simon, F.; Vieira, B. J. C.; Waerenborgh, J. C.; Abellán, G.; Coronado, E. Fundamental Insights into the Covalent Silane Functionalization of NiFe Layered Double Hydroxides. *Chem. Eur. J.* **2020**, *26* (29), 6504–6517.

(76) Han, Y.-S.; Park, I.; Choy, J.-H. Exfoliation of Layered Perovskite, $KCa_2Nb_3O_{10}$,into Colloidal Nanosheets by a Novel Chemical Process. *J. Mater. Chem.* **2001**, *11* (4), 1277–1282.

(77) Ida, S.; Ogata, C.; Unal, U.; Izawa, K.; Inoue, T.; Altuntasoglu, O.; Matsumoto, Y. Preparation of a Blue Luminescent Nanosheet Derived from Layered Perovskite $Bi_2SrTa_2O_9$. *J. Am. Chem. Soc.* **2007**, *129* (29), 8956–8957.

(78) Kudo, A.; Sakata, T. Luminescent Properties of Nondoped and Rare Earth Metal Ion-Doped K2La2Ti3O10 with Layered Perovskite Structures: Importance of the Hole Trap Process. *J. Phys. Chem.* **1995**, *99* (43), 15963–15967.

(79) Kudo, A.; Kaneko, E. Photoluminescent Properties of Ion-Exchangeable Layered Oxides. *Microporous and Mesoporous Materials* **1998**, *21* (4–6), 615–620. https://doi.org/10.1016/S1387-1811(98)00037-7.

(80) Wypych, F.; Bubniak, G. A.; Halma, M.; Nakagaki, S. Exfoliation and Immobilization of Anionic Iron Porphyrin in Layered Double Hydroxides. *Journal of Colloid and Interface Science* **2003**, *264* (1), 203–207.

(81) Yui, T.; Kameyama, T.; Sasaki, T.; Torimoto, T.; Takagi, K. Pyrene-to-Porphyrin Excited Singlet Energy Transfer in LBL-Deposited LDH Nanosheets. *J. Porphyrins Phthalocyanines* **2007**, *11* (06), 428–433.

(82) Carrado, K. A.; Thiyagarajan, P.; Winans, R. E.; Botto, R. E. Hydrothermal Crystallization of Porphyrin-Containing Layer Silicates. *Inorg. Chem.* **1991**, *30* (4), 794–799.

(83) DellaGuardia, R. A.; Thomas, J. K. Photoprocesses on Colloidal Clay Systems. Quenching Studies and the Effect of Surfactants on the Luminescent Properties of Pyrene and Pyrene Derivatives Adsorbed on Clay Colloids. *J. Phys. Chem.* **1983**, *87* (18), 3550–3557.

(84) Ghosh, P. K.; Bard, A. J. Photochemistry of Tris(2,2'-Bipyridyl)(Ruthenium(II) in Colloidal Clay Suspensions. *J. Phys. Chem.* **1984**, *88* (23), 5519–5526.

(85) Ogawa, M.; Kuroda, K. Photofunctions of Intercalation Compounds. *Chemical Reviews* **1995**, *95* (2), 399–438.

(86) Minquan, W.; Guodong, Q.; Mang, W.; Xianping, F.; Zhanglian, H. The Influence of the Matrix on the Fluorescence Properties of Pyrene. *Materials Science and Engineering: B* **1996**, *40* (1), 67–71.
(87) Costa, A. L.; Gomes, A. C.; Pillinger, M.; Gonçalves, I. S.; Seixas de Melo, J. S. Controlling the Fluorescence Behavior of 1-Pyrenesulfonate by Cointercalation with a Surfactant in a Layered Double Hydroxide. *Langmuir* **2015**, *31* (16), 4769–4778.
(88) Hong, Y.; Lam, J. W. Y.; Tang, B. Z. Aggregation-Induced Emission: Phenomenon, Mechanism and Applications. *Chem. Commun.* **2009**, No. 29, 4332–4353.
(89) Hong, Y.; Lam, J. W. Y.; Tang, B. Z. Aggregation-Induced Emission. *Chem. Soc. Rev.* **2011**, *40* (11), 5361–5388.
(90) Zhao, Y.; Gao, W.; Yang, Y.; Zhang, H.; Redshaw, C.; Feng, X.; Li, J.; Lam, J. W. Y.; Tang, B. Z. Aggregation-Induced Emission Luminogens for Direct Exfoliation of 2D Layered Materials in Ethanol. *Advanced Materials Interfaces* **2020**, *7* (21), 2000795.
(91) Gago, S.; Costa, T.; Melo, J. S. de; Gonçalves, I. S.; Pillinger, M. Preparation and Photophysical Characterisation of Zn–Al Layered Double Hydroxides Intercalated by Anionic Pyrene Derivatives. *J. Mater. Chem.* **2008**, *18* (8), 894–904.
(92) Watson, J. D.; Crick, F. H. C. A Structure for Desoxyribose Nucleic Acid. *Nature* **1953**, *171*, 737–738.
(93) Kundu, J.; Neumann, O.; Janesko, B. G.; Zhang, D.; Lal, S.; Barhoumi, A.; Scuseria, G. E.; Halas, N. J. Adenine− and Adenosine Monophosphate (AMP)−Gold Binding Interactions Studied by Surface-Enhanced Raman and Infrared Spectroscopies. *J. Phys. Chem. C* **2009**, *113* (32), 14390–14397.
(94) Mohapatra, B.; Pratibha, P.; Verma, S. Directed Adenine Functionalization for Creating Complex Architectures for Material and Biological Applications. *Chem. Commun.* **2017**, *53* (35), 4748–4758.
(95) Dutta, R. K.; Shaida, M. A.; Singla, K.; Das, D. Highly Efficient Adsorptive Removal of Uranyl Ions by a Novel Graphene Oxide Reduced by Adenosine 5′-Monophosphate (RGO-AMP). *J. Mater. Chem. A* **2019**, *7* (2), 664–678.
(96) Wu, G.; Lu, H. Progress in Biomedical Applications of Functionalized Nucleic Acid Nanodevices (NANDs). *ChemNanoMat* **2016**, *2* (5), 354–363. https://doi.org/https://doi.org/10.1002/cnma.201600036.
(97) Choy, J.-H.; Kwak, S.-Y.; Park, J.-S.; Jeong, Y.-J.; Portier, J. Intercalative Nanohybrids of Nucleoside Monophosphates and DNA in Layered Metal Hydroxide. *J. Am. Chem. Soc.* **1999**, *121* (6), 1399–1400.
(98) Sivakova, S.; Rowan, S. J. Nucleobases as Supramolecular Motifs. *Chem. Soc. Rev.* **2005**, *34* (1), 9–21.
(99) Pu, F.; Ren, J.; Qu, X. Nucleobases, Nucleosides, and Nucleotides: Versatile Biomolecules for Generating Functional Nanomaterials. *Chem. Soc. Rev.* **2018**, *47* (4), 1285–1306. https://doi.org/10.1039/C7CS00673J.
(100) del Prado, A.; González-Rodríguez, D.; Wu, Y.-L. Functional Systems Derived from Nucleobase Self-Assembly. *ChemistryOpen* **2020**, *9* (4), 409–430.

Chapter III

Ion-exchange-assisted liquid exfoliation of hybrid layered oxides

Chapter III. Ion exchange-assisted liquid exfoliation of hybrids layered oxides

III.1. Introduction

III.1.1 State of the art

In the **General Introduction**, we reviewed the top-down exfoliation processes which are up to now applied to produce 2D-nanosheets from layered materials. Concerning the charged layered oxides, ion-exchange with bulky organo-ammonium ion (or positively charged organo-ion) remains the hegemonic path to get large-scaled nanosheets.[1–4] Mainly developed by T. Sasaki *et al.* in the nineties,[5–8] its allows to obtained nanosheets whose the lateral sizes can reach the micrometer scale. Nevertheless, this approach to get nanosheets in suspension presents two main drawbacks. Firstly, the ion-exchange mechanism is time-consuming: the exfoliation process can last from days to weeks. Despite the work of ten Elshof *et al*. who proposed that exfoliation occurs much faster that believed,[9] most of the synthesis protocols still involve long-exfoliation time. Secondly, in literature, no mention is made on ion-exchange exfoliation on *hybrid* layered materials. This method is only dedicated to bare protonated layered oxide such as HST, HLN or HTO as they present high layer charge density, which helps for the insertion of the organo-ammonium ion. Thus, any functionalization of the nanosheets has to be performed after exfoliation.[10] It might be slowed down or even impossible due to competition with the organo-ammonium and colloidal stability issues. J. Wiley *et al.* reported the post-functionalization of exfoliated HLN nanosheets (obtained using TBAOH and microwave assistance).[11] They functionalized these TBA^+- HLN nanosheets by *n*-alkoxy and *n*-alkylamine derivatives but they only analyzed the dried nanomaterials which are stacked in a disordered pile. Therefore, it is difficult to assess the stability of the hybrid nanosheets as well as the homogeneous functionalization of the oxide layers. These drawbacks might be circumvented. In **Chapter II**, we demonstrated that low-kinetic exchange mechanism can be fastened with the use of microwave assistance and that a large panel of hybrid layered materials can be easily obtained,[12–14] as also reported in literature.[15,16] In parallel , J. Wiley *et al.* also proved that microwave radiation can be applied to quickly exfoliate "nude" layered oxides.[11] Thus, we take advantage of hybrid layered materials (synthesized with microwave assistance) and we investigate their ability to be exfoliated by ion-exchange exfoliation using microwave assistance in order to obtain functionalized oxide nanosheets. A particular attention has to be paid to the preservation of the functionalization during the exfoliation process.

In parallel to ion-exchange using organo-ammonium ion, polymeric chains can be inserted into lamellar material and, depending on the conditions, it might lead to exfoliation (see **Chapter I**).[17] This approach was developed in the field of nanocomposite where interesting properties derive from the dispersion of inorganic entities such as nanosheets into a polymer matrix. The nanocomposite usually displays better mechanical properties (*e.g.* larger Young modulus), flame retardant properties, etc…[18] It is

worth mentioning that this polymer-assisted exfoliation method was mainly carried out with clays minerals or hybrid clay minerals.[19,20] To our knowledge, only few papers report the combination of perovskite-like layered oxides and polymer.[21–23] For instance, S. Idota *et al.* modified HLN by grafting a polymerization initiator by using phosphonates moieties as anchoring group. The new hybrid allows the polymerization of poly(N-isopropylacrylamide) and insure the covalent attachment of the polymer to the oxide layer.[23] This *in-situ* polymerization leads to the exfoliation of their layered oxides. Besides, unlike Y. Sugahara *et al*., most of the authors do not intend to exfoliate *via* the polymer assistance as they only look for mixing the two entities. Therefore, the exfoliating power/potential of polymers may be extended to layered oxide other than clays and especially to hybrid layered oxides (*i.e.* functionalized ones).

III.1.2 Objectives

In this chapter, we will investigate the ion-exchange-assisted liquid exfoliation of some hybrid layered oxides synthesized in **Chapter II**. We split up this study into two main parts.

Firstly, we will discuss on the exfoliation using simultaneously microwave assistance and organo-ammonium ion. Thus, we assume the exfoliation will work according an ion-exchange mechanism: the TBA^+ is expected to replace the remaining protons and might lead to a swelling phenomenon and the subsequent delamination of the functionalized slabs. In the following, we will refer to the use of organo-ammonium to exfoliate hybrid as ion-exchange. The considered starting materials will be successively alkylamine-based hybrids and alcohol-based hybrids.

Secondly, we will study the exfoliation using a polymer as exfoliating agent. We focus our study on the exfoliation of $C_{10}PO_3$-HST. The choice of the polymer is motivated by subsequent use of such nanosheets into assembling process to build alternated stacked architectures. Therefore, the chosen polymer must be able to interact *via* hydrogen bonding with distinct polymer-coated nanosheets. Hence, we will investigate the exfoliation of $C_{10}PO_3$-HST by poly(ethylene)glycol (PEG), poly(acrylic)acid (PAA), and poly(ethylene)imine (PEI) as the former is a hydrogen-acceptor while the latter two are both hydrogen donors and acceptors.

Before any discussion on exfoliation through ion-exchange mechanism, we quickly introduce the routine techniques which allowed us to characterize the degree of exfoliation of the layered hybrids. Our estimation of this parameter relies on using liquid-cascade centrifugation (LCC), Scanning Electron Microscopy (SEM) and Dynamic Light Scattering (DLS) with a commercial apparatus (Malvern Zetasizer). Thus we get an overview of the nanomaterials behavior in solution while also getting a local accurate snapshot of their morphology. An in-depth study of nanosheets in solution and after deposition on a substrate is described in **Chapter V**. Herein, we only aim at discriminating quickly exfoliated from non-exfoliated materials. We introduce here these routine characterization techniques but they are also used and for some of them, only used in next chapters.

III.2. Fast and routine characterization of nanomaterials in solution

III.2.1 Liquid-cascade centrifugations to perform size selection on nanomaterials

We carried out ion-exchange exfoliation as described in **Experimental section**. The size and shape of the nanomaterials obtained as dispersion in a solvent are strongly dependent on the morphology and structure of the native hybrid. Concerning the lateral dimension, the maximum size of the functionalized nanosheets is deduced from the crystals size of the corresponding bulk layered materials. From SEM images of some layered hybrids such as $C_{10}PO_3$-HST or C8TS-HST (see **Chapter II**), the larger crystals are about few micrometers. Hence, in the best circumstances, the maximum lateral size of the nanosheets will be in the same range. Moreover, we also notice the dispersity in size of the crystals, which may be reflected in the nanomaterials solutions.

Concerning the exfoliation degree, many teams report the non-total exfoliation of the starting materials ("bare layered oxides): unmodified layered materials might remain after the exfoliation process.[24]

Thus, the post-exfoliation suspension contains a continuum of lateral sizes and thicknesses (number of stacked layered which still hold together). It is of upmost importance to select the nanosheets according their size and exfoliation degree. Most common methods rely on the sedimentation-based separation (SBS) *i.e.* applying a centrifugal force on the system to discriminate the particle according their mass and their frictional coefficient (which is shape-dependent).[25] Large and thick particles can be easily separated from thin and small ones in one step. That requires equilibrium of the system which is usually reached after hours. Overcoming this time-consuming process was done by Coleman *et al.* who carried out liquid-cascade centrifugation process to achieve a separation of exfoliated graphene sheets from remaining graphite.[26] They performed consecutive centrifugations with an increasing centrifugal force and managed to obtained suspensions with mostly narrow size distribution from a polydisperse solution of graphene. In addition, the authors stressed on the universality of this selective process as it can be translated to any solvent and any 2D-nanomaterials.

Therefore, we applied this liquid-cascade centrifugation method to the nanomaterials suspensions that we obtained as described in ***Figure 1.*** The stock solution of nanomaterials is first centrifuged at 450 rpm for five minutes. The resulting supernatant is separated from the bottom containing the more massive particles. Then the supernatant also goes through centrifugation at a higher rotation speed. This step is repeated **N** times with an increasing centrifugation speed at each step. At the end, **N** bottoms (denoted as Bottom X with X= 1 to **N**) and a supernatant (denoted as supernatant **N**) are characterized in DLS and SEM. For instance, in the case of $C_{10}PO_3$-HST, four centrifugations of 5 minutes each with an increasing speed between 400 and 1600 rpm were necessary to result in a high-quality dispersion of hybrid nanosheets (ascertained by the quality of the DLS intensity autocorrelation functions measured on the resulting four bottoms and one supernatant). An additional centrifugation step on the last supernatant at 14000 rpm (18400g) allows to collect the nanosheets and to remove very small flakes or possible non-

grafted molecules. The nanosheets were further redispersed in the appropriate solvent, allowing to control the concentration of the dispersion.

It is worth mentioning that, unlike Coleman *et al*. who performed a dedicated long and low-speed centrifugation step to remove un-exfoliated materials,[27] we only performed liquid cascade centrifugation process. Thus, the unexfoliated nanomaterials are mostly removed in the two first steps. Therefore, no narrow size distribution can be obtained on the first two bottom dispersions.

We also underline that a unique but longer exfoliation step could not provide an equivalent solution as liquid cascade centrifugation: the separation of the bottom and supernatant is indeed done manually and re-dispersion of the bottom might occur during the process. Thus, performing this procedure several times allows to mitigate the effect of manual separation.

Finally, from our experience and based on DLS correlogram and SEM images, we assessed that 4 centrifugation steps are enough to reach a dispersion with a good quality (*i.e.* exponential-shaped intensity auto-correlation function in the range of 1 to 0 at high and low delay times respectively and few-hundred nanometer-scale flakes). Additional centrifugation steps might lead to too low-concentrated solution which might be difficult to characterize by microscopy.

However, it is not the unique alternative to discriminate particles according to their size. One can quote density gradient ultracentrifugation,[28] size exclusion chromatography or field flow fractionation, which can provide better results.[25] However, they are not routinely available at IPCMS and were not used in this work. As a perspective to this work, further studies on the exfoliation of functionalized layered oxides should focus on the use of these more accurate separation techniques.

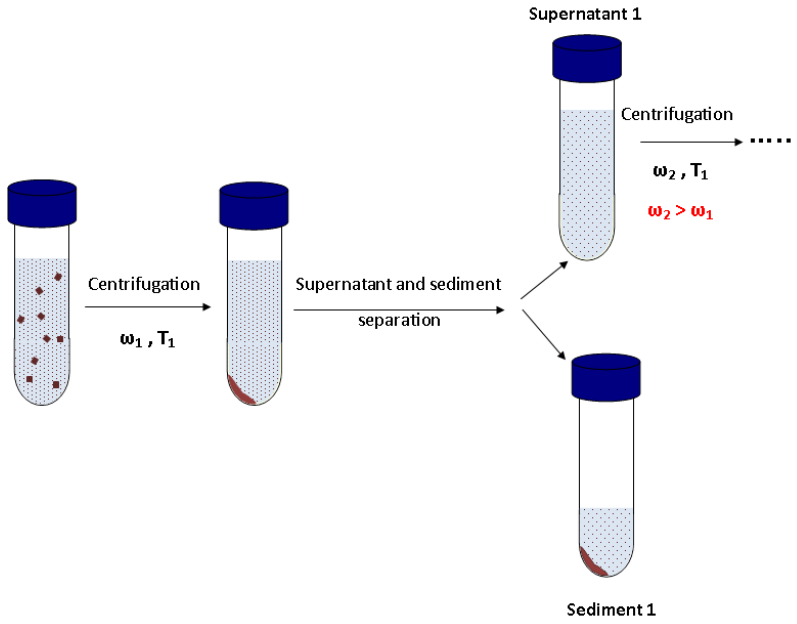

Figure 1: Schematic view of the liquid-cascade centrifugations process. The centrifugation speed ω is progressively increased step-by-step.

III.2.2 Dynamic Light Scattering (DLS) with commercial instrument

Here we aim at highlighting the use of DLS to characterize quickly the bottoms and supernatant from the selective centrifugation process.

A commercially available instrument (such as the Malvern Zetasizer that IPCMS is equipped with) is very convenient for small spherical object such as nanoparticles. In the case of spherical nanoparticles, the determination of hydrodynamic diameter relies on the hard-sphere model in the Rayleigh scattering regime and matches usually quite well with the size determined from TEM images. The problem is that this tool is far less adapted for non-spherical, polydisperse and/or large particle such as nanosheets. Hence the Zetasizer cannot lead to a straightforward approximation of the lateral size of the nanosheets.

J. Coleman *et al.* used commercial DLS on a series of nanosheets with different composition (mainly Van der Waals materials) and size distribution. They were able to determine a semi-empirical relation between the hydrodynamic size from DLS and size determined from TEM.[26] Unfortunately this study cannot be transposed to our functionalized oxide nanosheets. First of all, the remaining charged density, inherent to our oxide nanosheets, can have an effect on the scattering of the objects (attractive forces as electrostatic ones tend to decrease the apparent diffusion coefficient).[29] In addition, the few-layer nanosheets we synthesized are functionalized which also modifies their dynamic behavior.

However, the intensity auto-correlation functions $G^{(2)}(t,k)$, on which the calculations of the size distribution are based, can be trust as they are not model dependent . Thus we consider these intensity auto-correlation functions to characterize the quality of the solution *i.e.* the nanomaterials size distribution and concentration:

- the $G^{(2)}(t,k)-1$ must be comprised between 1 and 0, with a decreasing exponential shape for a quite monodisperse solution with a concentration that does lead to multiple scattering events.[29]
- An intensity correlation function out of these boundaries is significant of a too concentrated and/or polydisperse solution with big particles.
- If $\lim_{t\to 0}(G^{(2)}(t,k)-1) \ll 1$, the solution is not concentrated enough and number fluctuation inside the scattering volume might happen.[29]

Figure 2 shows three auto-correlation functions, each corresponding to the three situations described above. Thanks to DLS with Zetasizer, we can have quickly an indication of the quality of the solution.

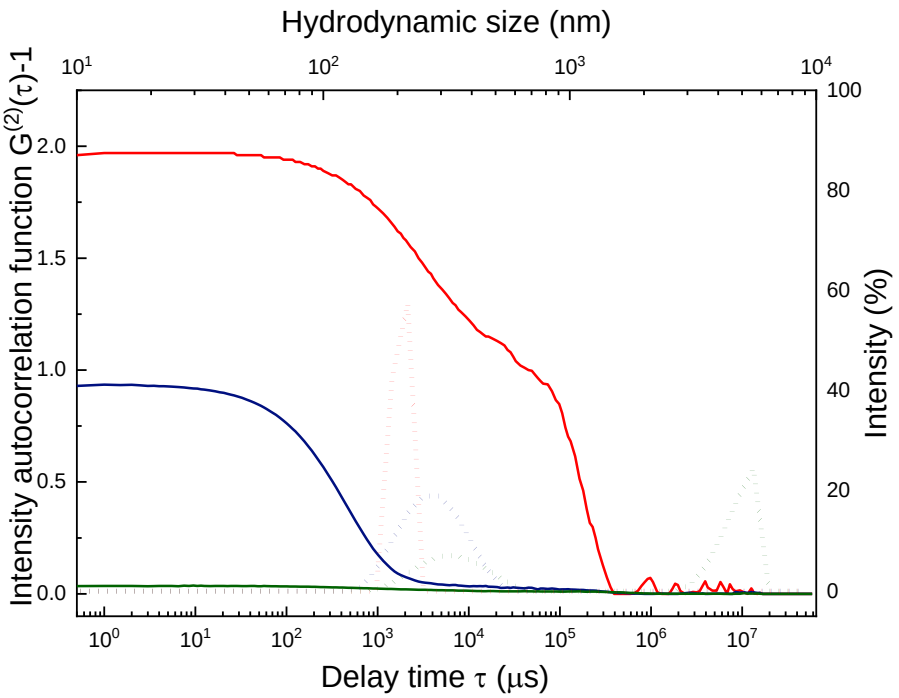

Figure 2: Examples of intensity auto-correlation functions of a too-high concentrated (red), too low-concentrated (green) and high-quality nanosheets dispersion (blue) in solid line and their corresponding size distribution profiles in dot line.

In conclusion, performing DLS with a commercial Zetasizer does not allow to determine the size distribution and the polydispersity of a nanosheets suspension, but provides rapidly very useful indication of the quality of the suspensions. In order to further characterize the nanomaterials obtained, we always carried out SEM in STEM mode as complementary techniques.

III.2.3 Scanning Electron Microscopy in Scanning Tunneling mode

Scanning Electron Microscopy (SEM) allows to image the nanomaterials after their deposition on a Cu grid with a carbon lacey. The deposition consists in a drop-casting where each drop is dried with a heating plate. Five to ten drops usually provide enough materials to perform the imaging.

We took advantages of the SEM techniques. First, its low-accelerating voltage (*i.e.* low-energy electrons) does not lead to the destruction of the nanomaterials (this is the case in TEM, see **Chapter V**). Secondly, its Scanning Tunneling Electron Microscopy (STEM) mode allows to discriminate the nanomaterials thickness through the contrast (which is proportional to the atomic number). The stacking or the number of layers is thus highlighted. In addition, the spatial resolution is improved compared to the classic SEM imaging due to a smaller interaction volume, linked to the thickness of the observed materials. This interaction volume differs from the characteristic teardrop-shaped one in SEM.

III.3. Coupling of ion-exchange and microwave assistance: soft exfoliation of hybrid layered oxides

III.3.1 Introduction

Previously, we demonstrate that despite the functionalization, the hybrid layered oxides present a remaining charge density. Thus, there are still protons in the vicinity of the slabs which can be involved in an exchange mechanism. Therefore, we believe ion-exchange assisted exfoliation can be carried out on the hybrid we synthesized and might lead to functionalized oxide nanosheets in solution.

In addition, we demonstrated previously as well as J. Wiley *et al.*, that kinetic of ion-exchange mechanism can be fasten by the assistance of microwave.[11–13,15] Hence, we investigate the coupling of ion exchange and the use of microwave in a synthetic process to provide functionalized oxide nanosheets.

First, we study the application of this method on bare protonated layered oxide HST as performed by J. Wiley *et al.*[11] The relative ratio $\frac{TBA^+}{H^+}$, which governs ion-exchange exfoliation, is modified to determine the best experimental parameters.

In a second step, we investigate the combination of ion-exchange and microwave assistance for the exfoliation of hybrid layered oxides. We will study both *n*-alkylamine and *n*-alkoxy derivatives to highlight a potential effect of the nature of the molecular layer. Similarly, we vary the ratio $\frac{TBA^+}{H^+}$ to find the ideal exfoliation conditions.

The characterization procedure of the nanosheets was inspired by the work of J. Wiley *et al.*[11] In their paper, the authors considered that the reaction was fully complete (*i.e*. an exfoliation yield of 100%). Thus they performed a post-exfoliation centrifugation step to collect all the nanomaterials without size selection. The sediments, considered as being only exfoliated nanosheets, are characterized by XRD and spectroscopies (FTIR, Raman, etc...).[11]

Similarly, we carried out here a single centrifugation step and we analyzed the bottoms (in form of powder) with XRD and FTIR spectroscopy. However, it is worth mentioning that the centrifugal speed was set up to let nanomaterials in the supernatant, allowing an additional STEM analysis without redispersion step.

III.3.2 Exfoliation of bare layered oxide

Firstly, we quickly study the "classical" ion-exchange exfoliation on HST to allow comparison with the results obtained by using other protocols. HST was exfoliated using the swelling method as described by T. Sasaki *et al.* in presence of tetrabutylammonium hydroxide (TBAOH) in water for 10 days at room temperature. The ratio $\frac{TBA^+}{H^+}$ was set at 10, a value which allows the swelling of the layered structure. A centrifugation at 1600 rpm for 10 min was carried out. The supernatant and the bottom are collected separately. The SEM images of the supernatant in ***Figure 3*** show that exfoliation occurred as

expected from the literature. Hence, we will be able to compare our results in the following part with the data from this "classical" exfoliation.

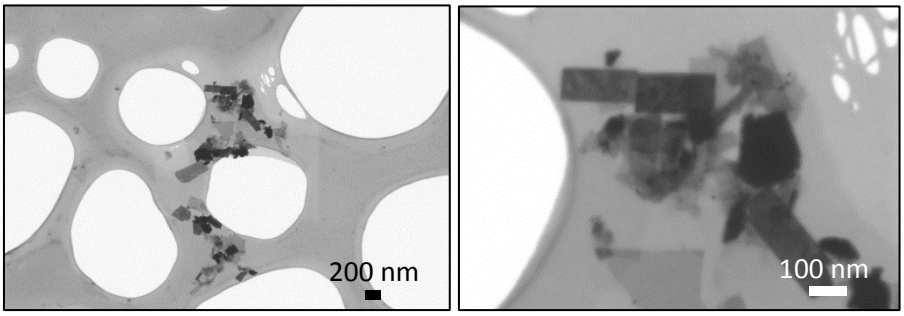

Figure 3: SEM image of TBA^+-HST nanosheets, synthesized by the classical swelling method.

In a second step we carried out ion-exchange exfoliation using microwave assistance. HST was set to react with TBAOH at 80°C for 1 hour with microwave assistance, varying the ratio $\frac{TBA^+}{H^+}$ (set at 0, 1, 3, 5, and 10). This short reaction time and temperature are similar to what is reported in the unique paper dealing with this approach[11] and these two parameters are the main difference with classical route. The resulting solution was centrifuged at 1600 rpm for 10 min. The bottom and supernatant were collected separately.

Figure 4 shows the XRD patterns of the bottom for different ratios $\frac{TBA^+}{H^+}$. We notice than the XRD patterns of the bottoms are similar to the XRD pattern of HST: the (*100*), (*110*) and (*200*) reflections are still observed and the (*00l*) reflections have not been modified (the corresponding interlayer distance is equal to 0.99 nm for all ratios $\frac{TBA^+}{H^+}$). Similarly, the FTIR spectra of all the bottoms are identical to the one of HST (not shown). No signature of TBA^+ can be observed. We conclude that insertion of the bulky TBA^+ did not occur whatever the amount of TBAOH. Thus, microwave assistance cannot fasten the swelling process of HST and a pre-intercalation method seems mandatory to insert such bulky entity with the microwave procedure. These observations contrast with the published results of J. Wiley *et al*. We ascribe such difference to the reactivity of the oxides used (HLN for J.Wiley *et al*. and HST in the present case).

For comparison, we also show in ***Figure 4 (b)*** the XRD patterns of exfoliated few-layer nanosheets of HST, obtained by the classical ion-exchange route. The pattern does not display any (*001*) reflections while the (*100*), (*110*) and (*200*) reflections are barely distinguishable. Thus, for fully exfoliated materials, the corresponding XRD pattern should not display any peak.

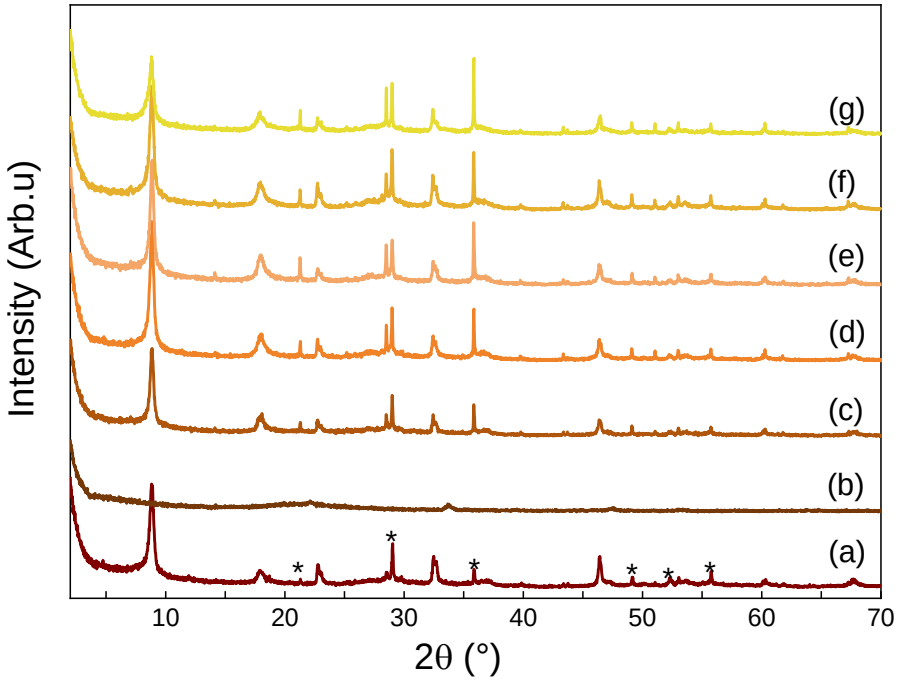

Figure 4:XRD patterns of (a) HST, (b) exfoliated HST from classical ion-exchange mechanism and (c) to (g) bottoms of exfoliated HST solution with a ratio TBA^+/H^+ = 0, 1, 3, 5, 10 respectively. Peaks with an asterisk correspond to an impurity of BST, present in the batch of HST for this peculiar set of experiments.

III.3.3 Exfoliation of alkylamine-based hybrid layered oxides

We then investigated the ion-exchange exfoliation of 1-ethylamine-inserted hybrid layered material denoted as C_2N-HST. To our knowledge, this set of experiments is the first attempt of exfoliation with ion exchange on a hybrid phase. Typically, C_2N-HST was brought in contact with TBAOH at ratio $\frac{TBA^+}{H^+}$ = 0, 0.5, 1, 3, 5, 7 and 10, in water, at 80°C with microwave assistance for 1 hour. It is worth mentioning that, as the functionalization decreases the layer charge density, the number of protons at its surface also decreases (from 2 protons per unit cell for HST to 1.2 protons per unit cell for C_2N-HST).[12] Thus, the amount of TBAOH to produce such ratios is slower compared to the exfoliation experiments on HST.

The as-exfoliated solutions were centrifuged at 1600 rpm for 20 min. The bottoms were collected, dried at room temperature and the subsequent powders were analyzed. Therefore, it means that we analyze here the non-exfoliated, partially exfoliated and restacked materials as J. Wiley *et al*. did.[11] In our case, dealing with functionalized materials and possibly functionalized nanosheets, we reasonably assume that any change in the functionalization observed in the material present in the bottom will indicate a change in functionalization of the possibly formed nanosheets, present in the supernatant. Since at this stage, we are essentially interested in finding a fast and efficient protocol to exfoliated functionalized material while keeping the functionalization intact, this first study allows to discriminate rapidly the promising strategies from others.

Figure 5 shows the XRD patterns of the "exfoliated" C_2N-HST bottoms for different ratios $\frac{TBA^+}{H^+}$. For ratios $\frac{TBA^+}{H^+} > 0$, the interlayer distances d_{001} are larger than the one of the native C_2N-HST (1.58 nm) and are around 2.0 nm for all ratios. For ratios 0.5 and 1, two slightly different interlamellar distances are observed, indicating the presence of two layered phases. Since the (*100*), (*110*) and (*200*) reflections are seen at 22.6°, 23.3° and 46.3° respectively, and coupled with the presence of the (*00l)* reflections, it means that the in-plane structure is preserved during the process and coherence between the slabs is maintained. Thus, the bottoms contain non-exfoliated materials which are functionalized with TBA^+ ions or for the smallest ratios, 0.5 and 1, a mixture of the staring C_2N-HST and TBA-HST.

For $\frac{TBA^+}{H^+} = 0$, the interlayer distance d_{001}= 1.45 nm is slightly smaller than that of C_2N-HST while the peaks corresponding to the inorganic in-plane structure are preserved. Hence, heating at 80°C did not modify the initial hybrid. The reduction of the interlayer distance might be ascribed to a better drying of the powder or to a rearrangement of the organic molecules during the process, as already observed during the insertion of phenyl-butylamine into HST.[30]

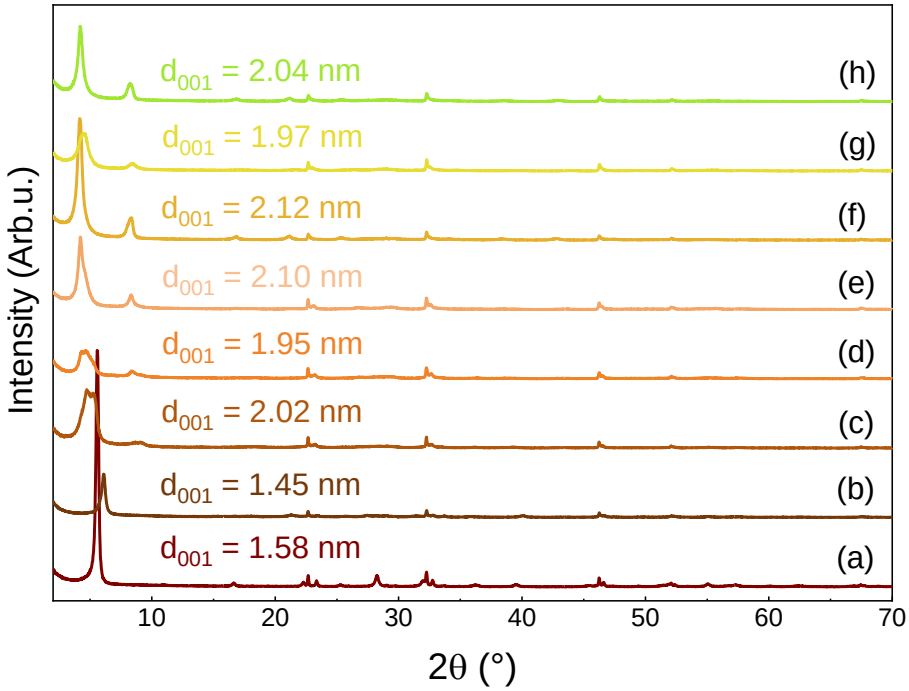

Figure 5: XRD patterns of (a) C_2N-HST and (b) to (h) bottoms from exfoliated C_2N-HST solution with a ratio TBA^+/H^+ = 0, 0.5, 1, 3, 5, 7, 10 respectively .

FTIR spectra shown in ***Figure 6*** emphasize these statements. For the ratios $\frac{TBA^+}{H^+} > 0.5$, the presence of TBA^+ ion is confirmed by the C-H stretching bands around 2900 cm^{-1} as well as the (CH_3) bending bands at 1484 cm^{-1} (asymmetric) and 1397 cm^{-1} (symmetric) which are more intense compared to C_2N-HST spectrum. We also notice that the spectra evidence the presence of water, highlighted by the large and intense bands at 3200 cm^{-1} and the band at 1640 cm^{-1}. The overnight drying at room temperature (the same as the one performed for C_2N-HST) did not enable the complete removal of water. This is an

indication of more bounded water into the layer due to the insertion of the TBA^+ cation. TGA analysis should be performed to confirm this statement.

Finally, from the study of the bottoms, it appears that C_2NH_2 molecules, initially present in the interlayer space, are removed from the structure and replaced by TBA^+ cation. As stated above, this observation is made for the bottoms, but a reasonable hypothesis is to consider that it is thus very unlikely that C_2NH_2 molecules remain attached to nanosheets if they are formed.

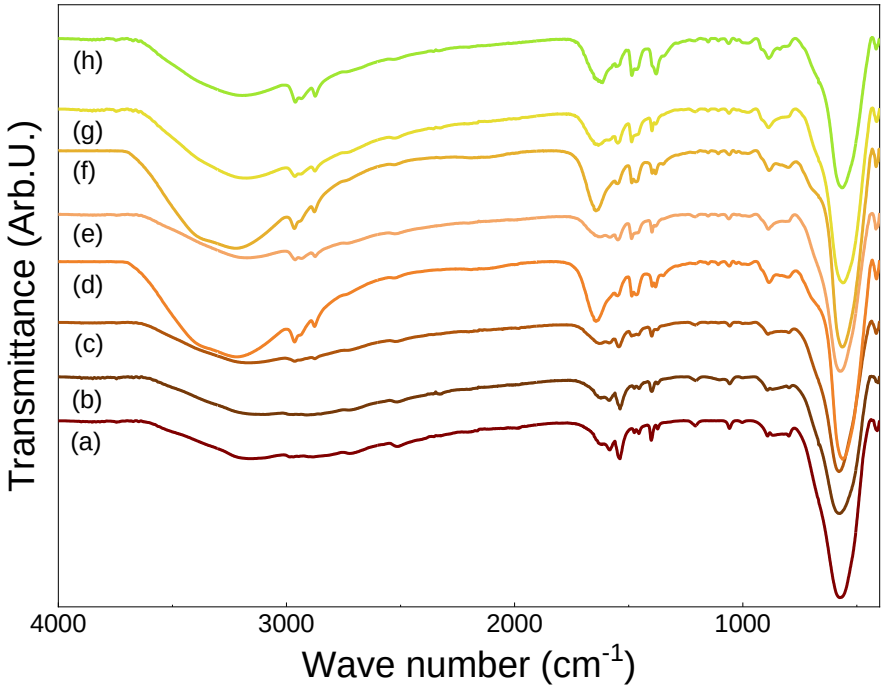

Figure 6: FTIR spectra of (a) C_2N-HST and (b) to (h) bottoms from exfoliated C_2N-HST solution with a ratio TBA^+/H^+ = 0, 0.5, 1, 3, 5, 7, 10 respectively .

The supernatant of the centrifugation step was also analyzed in XRD by drop casting the supernatant solution onto a glass substrate. For ratios $\frac{TBA^+}{H^+} > 0$, the XRD patterns do not display high angle peaks corresponding to the in-plane (*100*), (*110*) and (*200*) reflections (or they are only barely visible) (***Figure 7***). This disappearance can match with two explanations.

The first one corresponds to the exfoliation of the layered C_2N-HST *i.e.* loss of coherence between the slabs. The second explanation is linked to the sample preparation: either there was not enough matter on the glass substrate or the nanomaterials, exfoliated, non-exfoliated and restacked, laid flatly on the substrate (in that case, the in-plane reflections cannot be seen with XRD in a Bragg-Brentano geometry). Even if the two explanations do not exclude each other, the latter seems more reasonable. Indeed, for the ratio $\frac{TBA^+}{H^+} = 0$ (*i.e.* no delaminating agent was added; the hybrid was just heated at 80 °C) the in-plane reflections are also lost which cannot correspond to exfoliation. This does not mean that exfoliation did not happen for ratios $\frac{TBA^+}{H^+} > 0$ but XRD cannot ascertain its occurrence.

In addition, the XRD patterns show low angle peaks that are not harmonic one of the other. The peaks at around 7.6° correspond to an interlayer distance close to 1.2 nm. This interlayer distance is to be assimilated with the interlayer of nude HST (d_{001} = 1.06 nm). The slight difference is ascribed to higher water content. Thus, the exfoliation process leads to non-functionalized nanomaterials. The second low-angle peak is seen at 2.71°, 4.68°, 4.90°, 3.24° and 4.14°, corresponding to an interlayer distance of 3.51 nm, 1.89 nm, 1.80 nm, 2.74 nm and 2.20 nm, for the ratios $\frac{TBA^+}{H^+} = 0.5, 1, 3, 5$ and 10 respectively. It is worth mentioning that this peak is barely visible for the ratios $\frac{TBA^+}{H^+} = 0.5$ and 1. These observations are consistent with the results of T. Sasaki *et al.* who show that the swelling phenomenon (*i.e.* the interlayer water content) decreases when increasing the amount of TBA^+ behind a defined value. Indeed in the case of low ratios $\frac{TBA^+}{H^+}$, the reaction leads to a swollen phase where a great amount of water is in between the slabs, and upon a gentle stirring, to exfoliation. For high ratios, the insertion of the TBA^+ is not accompanied by additional water and no exfoliation occurs. In the present case, with microwave-assisted ion-exchange from C_2N-HST, we can infer from the XRD patterns that a simple TBA^+ insertion occurs in the case of high ratios $\frac{TBA^+}{H^+}$, and on the contrary, that exfoliation occurs in the case of low ratio $\frac{TBA^+}{H^+}$ as the restacking observed in the recovered supernatants occurs in a form of a swollen layered phase.

FTIR spectra of the supernatants (not shown) are identical to the spectrum of TBAOH without displaying the Ta-O band: the nanomaterials are not concentrated enough to be detected by this spectroscopy.

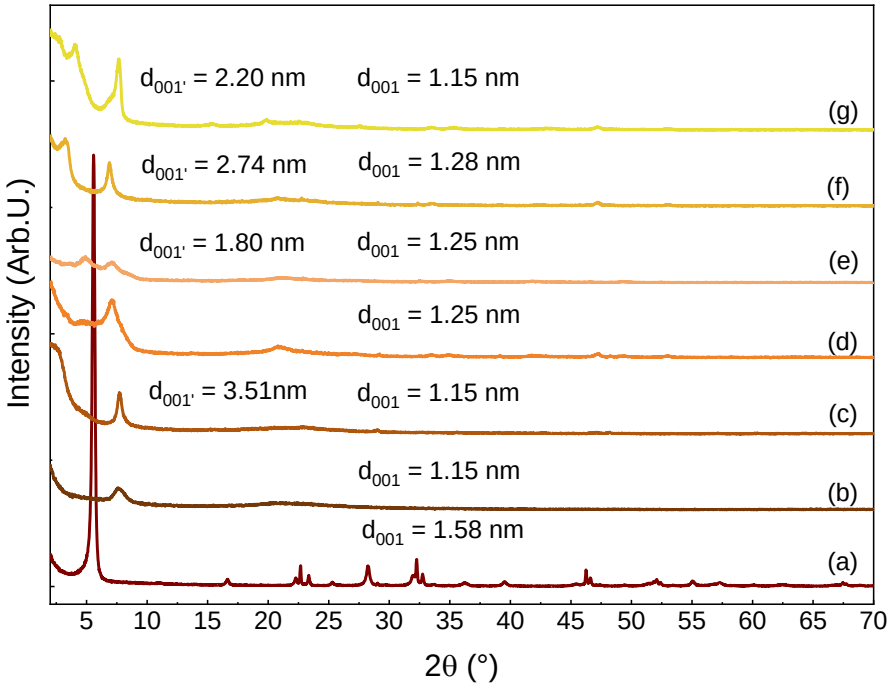

Figure 7: XRD patterns of (a) C_2N-HST and (b) to (g) supernatants from exfoliated C_2N-HST solution with a ratio TBA^+/H^+ = 0, 0.5, 1, 3, 5, 10 respectively.

Ion-exchange of the remaining protons in C_2N-HST by TBA^+ and microwave assistance enable to exfoliate alkylamine-based hybrids, for low ratios $\frac{TBA^+}{H^+}$. Nevertheless, as expected for exchangeable amine, the initial amines are replaced by the bulky swelling agent during the process. Thus, the alkylamine-based hybrid precursor is not suitable for this exfoliation strategy. Hybrid layered oxide with a covalent attachment of the organic entity may be more relevant. Therefore, we investigate in the following part the ion-exchange exfoliation of alcohol-based hybrid.

III.3.4 Exfoliation of alcohol-based hybrid layered oxides

We consider here $C_{12}O$-HST as precursor. The exfoliation process took place in water in presence of TBAOH at different ratios $\frac{TBA^+}{H^+}$. The suspension is heated at 80°C with microwave for 1 hour. A subsequent centrifugation at 1600 rpm for 20 min is performed to roughly separate exfoliated materials from unexfoliated ones. The resulting supernatant and bottom are collected and analyzed.

XRD patterns of the different bottoms are shown in ***Figure 8***. The in-plane (*100*), (*110*) and (*200*) reflections are observed which is consistent with the presence of particles that do not lie flatly on the substrate, which is more likely to happen for non-exfoliated materials (with a small aspect ratio). In parallel, an evolution of the (*00l*) reflections with the ratio $\frac{TBA^+}{H^+}$ is observed. The initial peaks of $C_{12}O$-HST corresponding to (*002*), (*003*) and (*004*) reflections are progressively modified (we note that the (*001*) reflection is masked by the background). When increasing the ratio $\frac{TBA^+}{H^+}$, the intensity of the peak at 6.58° (*i.e*. the (*003*) reflection) decreased until its total disappearance for the ratio $\frac{TBA^+}{H^+}$ = 20. In parallel, the intensity of the peak at 8.75°, corresponding to the (*004*) reflection, increases. The intensity of the peaks at 4.3 ° remains unchanged. In addition, the (*002*) and (*004*) peak positions correspond to the expected ones for the (*001*) and (*002*) reflections of intercalated TBA^+ into HST. Thus, we hypothesize the replacement of the initial $C_{12}OH$ by TBA^+ cation for high ratios $\frac{TBA^+}{H^+}$.

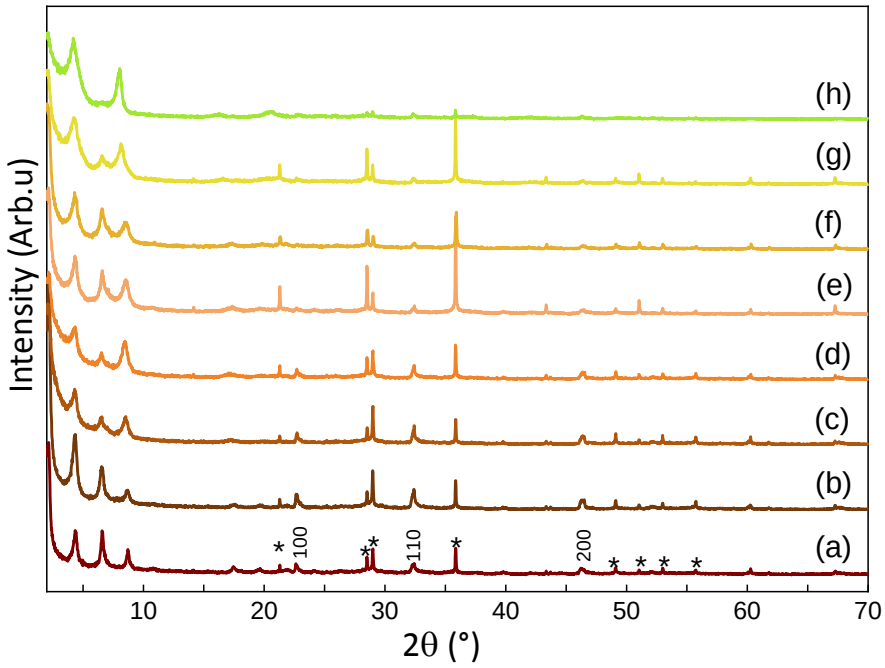

Figure 8: XRD patterns of (a) C_{12}O-HST and(b) to(h) bottom of exfoliated C_{12}O-HST with TBA^+ at different ratio TBA^+/H^+ = 0, 0.5, 1, 3, 5, 10 and 20. The peaks with a star correspond to an impurity of BST present in the batch of C_{12}O-HST for this peculiar set of experiments.

The replacement of the 1-dodecanol by TBA^+ is further confirmed by FTIR spectroscopy. The FTIR spectra of the bottoms of C_{12}O-HST nanomaterial solution are shown in ***Figure 9***. When increasing the ratio $\frac{TBA^+}{H^+}$, the intensity of the C-O-Ta vibration band at 1140 cm^{-1} decreases in favor of the C-OH vibration band at 1060 cm^{-1} which progressively appears. It is far more pronounced for the high ratios $\frac{TBA^+}{H^+} = 10, 20$. In parallel the ($CH_3$) asymmetric bending bands at 1485 cm^{-1} becomes more intense, meaningful of the presence of the TBA^+. The band at 1640 cm^{-1} corresponding to water follows the same trend. Thus, TBA^+ is replacing the $C_{12}OH$ and it is inserted into the structure. Yet the free 1-dodecanol remains adsorbed onto the hybrid compounds. It means that hydrolysis of the C-O-Ta bond is likely to happen when heating and/or in presence of a large quantity of ammonium derivatives.

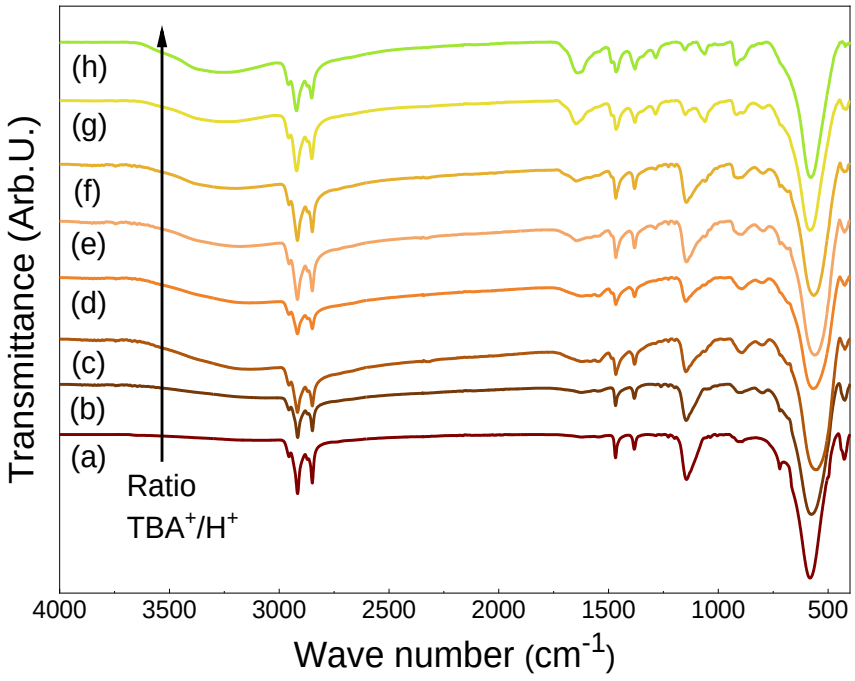

Figure 9: FTIR spectra of (a) C_{12}O-HST and (b) to (h) supernatant of exfoliated C_{12}O-HST at different ratios TBA^+/H^+ = 0, 0.5, 1, 3, 5, 10, 20 respectively.

III.3.5 Conclusion

We carried out ion-exchange liquid exfoliation using TBAOH as delaminating agent and microwave-assistance. The experiments were conducted on nude layered HST, C_2N-HST and C_{12}O-HST. For the former material, the TBA^+ ion was even not inserted into the structure; the microwave exfoliation process keeps HST unchanged. In the case of C_2N-HST, we evidenced the replacement of the 1-methylamine by TBA^+. The same phenomenon occurs when exfoliating C_{12}O-HST by ion-exchange: the C-O-Ta bond is hydrolyzed and the alcohol is replaced by the organo-ammonium. Thus, ion-exchange with microwave assistance might indeed be able to produce nanosheets. However, the prior functionalization is partially or completely replaced by the exfoliating agent TBA^+. Therefore, this approach is not adapted to produce functionalized oxide nanosheets from the corresponding hybrid layered materials. Nevertheless, it would be interesting to evaluate this process with other, more robust molecular graftings. For instance, phosphonate-based materials would be suitable for such process. Unfortunately, this study could not be performed during the course of this PhD work.

III.4. Polymer-assisted exfoliation of hybrids layered oxides

III.4.1 Introduction

In this part, we aim at studying the polymer-assisted exfoliation of hybrid layered oxides such as C_4N-HST, C_{12}O-HST , benzSC_2O-HST and $C_{10}PO_3$-HST as this exfoliation method is barely described in literature for functionalized layered oxides.[21,22] Considering the exfoliation process we chose *i.e.* the exfoliation using the polymer in solution,[20] many parameters have to be tuned in order to favour exfoliation instead of intercalation or phase separation of both polymer and layered materials.

For instance, J. Lemmon et *al.* investigated the exfoliation of clays and Van der Waals materials by polyethylene oxide.[31] The authors showed that the ratio polymer/clay of 0.15 and 0.30 g/g lead to an homogeneous nanocomposites but where coherence between the slabs is maintained. Beyond these ratios, a two-phases system is observed, composed of intercalated-polymer into the layered materials and crystalized polymer alone.

Similarly, X. Han *et al.* demonstrated that the topology of the polyethylene (*i.e.* its molecular weight and its structure (branched or linear)) influences its ability to exfoliate graphite into few-layer graphene.[32] They found that the more branched polymer allowed to obtained high concentrated suspension of graphene.

H.G. Jeon *et al.* studied the behavior of dodecylamine-modified Na-montmorillonite toward two different polymers, a nitrile-based copolymer and a high density polyethylene (HDPE).[33] The authors showed that in similar experimental conditions, the nitrile-based copolymer was able to exfoliate the hybrid clay whereas the HDPE was only intercalated. Thus, for defined layered materials, the chemical nature of the polymer and its interaction with the layers is determinant in the exfoliation process.

In addition, the chosen solvent for reaction must allow both easy dispersion of the layered materials and solubility of the polymers. Besides, this latter issue usually leads the authors to modify the surface of the layered materials, such as clays which are mainly hydrophilic, to dispersed them in a suitable organic solvent for composite synthesis.[33,34]

Therefore, in the following, we decided to investigate the exfoliation of hybrid layered materials by three kinds of polymer: the poly(ethyleneglycol) denoted as PEG, the poly(ethylenimine) denoted as PEI and the poly(acrylic acid) denoted as PAA (***Figure 10***). Concerning the former one, we will also investigate how its molecular weight and its terminal functions impact its interactions with the considered layered hybrid.

For polymer-assisted exfoliation using PEG, the solvent we chose is tetrahydrofuran (THF) as it can solubilize the PEG and all the hybrids are dispersed on it. In the case of PEI and PAA, the solvent must be polar and able to break the inter-hydrogen bonds to fully solubilize the polymer. Water and isopropanol were chosen as potential candidates.

The influence of the molar ratio between the two entities was not investigated in this PhD work. The amount of polymer was set in order to get a high ratio polymer/hybrid material. Hence, the diffusion

of the polymer into the layers will be favoured. The excess of polymer *i.e.* the chains that does not interact with the hybrid materials, is removed by washing all the suspensions: a centrifugation step at 14000 rpm for 10 min is carried out, followed by the re-dispersion of the materials by low-power sonication in an appropriate solvent.

Here, we do not consider the temperature as a relevant parameter to tune. We know that temperature might increase the diffusion of species into the layered structure as well as the solubility of the polymer. Nevertheless, it also favours the damaging of the initial functionalization. Thus, we will work at room temperature for long reaction time, as it is performed for classical ion-exchange exfoliation.[3,8]

Furthermore, the choice of these three polymers was also motivated by the further assembly we might build with the polymer-coated hybrid nanosheets. As we focus on non-electrostatic reassembly, we need one hydrogen-acceptor polymer, role played by the PEG, and one hydrogen-donor polymer, which can be both PEI and PAA. These two latter are also hydrogen-acceptor which offers three possibility of assembly: {PAA-nanosheet+PEI-nanosheet}, {PEG-nanosheet+PEI-nanosheets} and {PEG-nanosheet+PAA-nanosheets}. It is worth mentioning that PEI can be a charged polymer when protonated and a control of pH must be done when using the resulting nanosheets for assemblies.

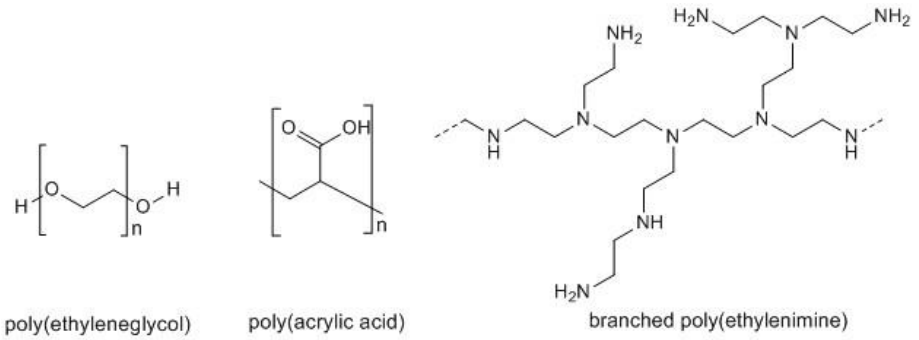

Figure 10: The three considered polymers for polymer-assisted exfoliation process.

III.4.2 PEG-assisted exfoliation of hybrid layered oxides

III.4.2.1 PEG-assisted exfoliation of the bare layered oxide HST

Using the same reasoning we made for TBA^+-exchange exfoliation, we start by studying the polymer-assisted exfoliation of HST. The following set of experiment can be considered as a "classical" exfoliation route with polymer assistance. HST is dispersed in 10 mL of THF in presence of the polymer (with a equimolar molar ratio with respect to the layered hybrid), the poly(ethylene glycol), denoted as PEG, with a molar mass of 600, 2000 or 6000 $g.mol^{-1}$ or the methoxypoly(ethylene glycol) amine, denoted as PEGN5000, with a molar mass of 5000 $g.mol^{-1}$. The reaction takes place at room temperature for 24 hours. The solution is centrifuged at 1600 rpm for 20 minutes. The resulting supernatant and bottom are washed as described above and finally re-dispersed in water.

Figure 11 left shows the XRD patterns of the bottoms after washing, for PEG of different molecular masses. All patterns display (*100*), (*110*) and (*200*) reflections which mean the inorganic

structure of the $SrTa_2O_7^{2-}$ remains unchanged. These reflections are more likely to be seen for non-exfoliated materials, especially if the corresponding peaks are well-defined. The series of (*00l*) reflections is consistent with a layered structure and correspond to an interlayer distance of 1.01 nm for the four experiments. This distance is close to that of HST which indicates the various polymers were not inserted into HST.

The FTIR spectra in ***Figure 11 right*** complete the analysis of this set of experiments. The spectrum in ***Figure 11 right (b)*** corresponding to the exfoliation trial with PEG2000 shows a band at 1104 cm^{-1} and a weak band at 2870 cm^{-1}. These bands correspond well to the C-O and CH_2 stretching bands of PEG2000 respectively. Therefore, PEG2000 is present in the bottom after exfoliation process despite the washing. As the interlayer distances, determined from XRD patterns, are similar to the one of HST, the polymer is likely adsorbed on the external surface of the non-exfoliated material which is collected in the bottom. Similarly, a low-intense C-O band is visible on the spectrum when using PEG600. In contrast, the spectra ***Figure 11 right (c)*** and ***(d)*** of the bottoms from exfoliation with PEG6000 and PEGN5000 do not display any band corresponding to the polymers (the large band at 1630 cm^{-1} is characteristic of water). Thus, in the case of PEG6000 and PEGN5000, there is no trace of the polymer after washing. This observation is in line with the non-exfoliation of HST using PEG6000 and PEGN5000.

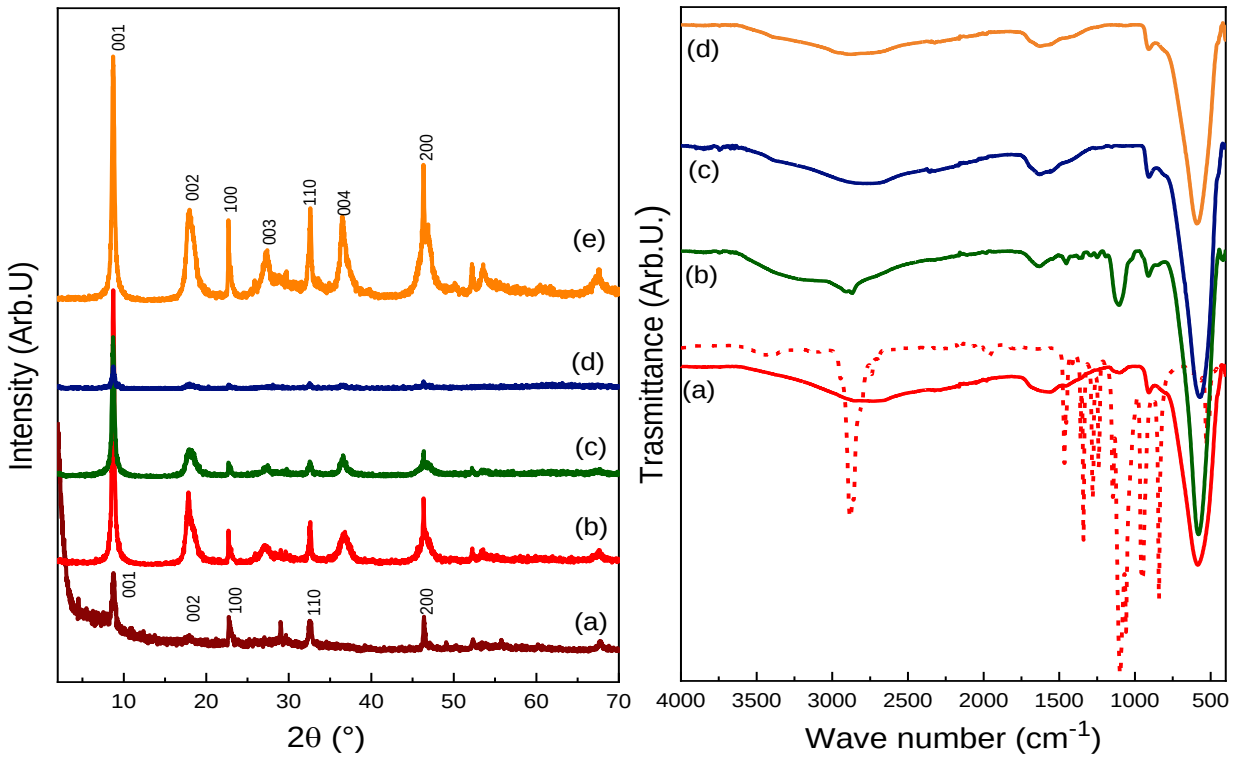

Figure 11: (Left) XRD patterns of (a), HST and bottom from HST exfoliation with (b) PEG 600, (c) PEG2000, (d) PEG6000 and (e) PEGN5000. (Right) FTIR spectra of bottom from HST exfoliation with (a) PEG600, (b) PEG2000, (c) PEG6000 and (d) PEGN5000. The spectrum in dot line corresponds to the polymer PEG spectral signature.

As for the supernatants, the SEM images are shown in ***Figure 12***. In the case of reaction with PEG6000 and PEGN5000, the SEM images only show non-exfoliated and stacked materials and this observation is in line with the previous characterization. On contrary, with PEG600 and PEG2000, we are able to observe few-layer nanomaterials from the supernatant solution. It is worth noticing than PEG600 allows to produce large few-layer nanomaterials in large quantity but the thickness is larger than when using PEG2000. This observation confirms what we assumed from XRD pattern and FTIR spectrum of the bottoms: there is indeed an interaction between PEG600 or PEG2000 and HST. Yet the exfoliation is uncomplete and an important quantity of non-exfoliated materials remains when using these polymers in these experimental conditions.

On the contrary there is no interaction between the heavier polymers, PEG6000 and PEGN5000, and HST and no exfoliation occurs when using them.

From the previous finding we might assume that smaller polymeric chains are easily intercalated into bare layered structure such as HST, leading to more exfoliated nanomaterials.

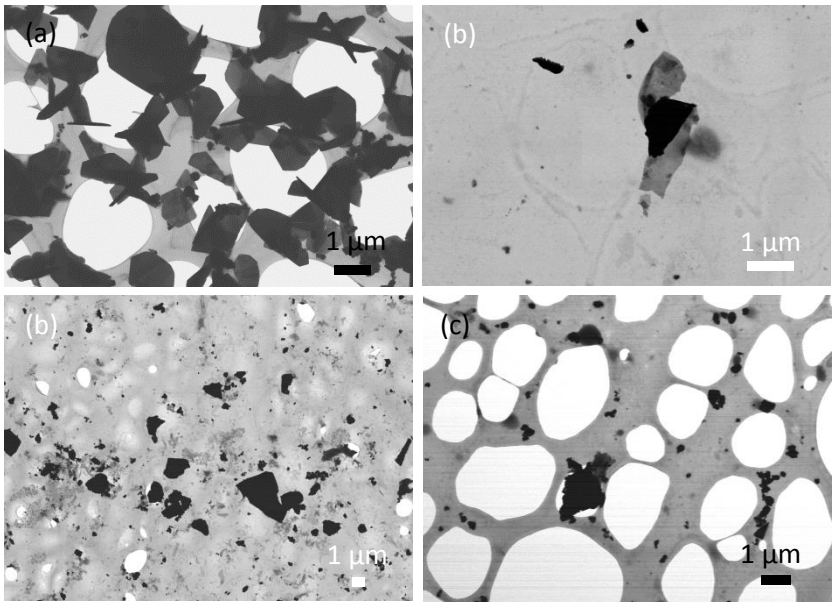

Figure 12: SEM images of supernatant from HST exfoliation with (a) PEG600 (b) PEG2000, (c) PEG6000 and (d) PEGN5000.

III.4.2.2 PEG600-assisted exfoliation of hybrid layered oxides

In the following, we now investigate the exfoliation of hybrid layered oxides: C_4N-HST, C_{12}O-HST, benzSC_2O-HST and $C_{10}PO_3$-HST. We consider the poly(ethylenegycol) with a molar mass of 600 g.mol^{-1}, denoted as PEG600, as exfoliating agent. The reaction took place in THF solution with a presence of a small amount of water at room temperature for four days. The resulting solution was centrifuged at 1600 rpm for 20 minutes; the supernatant and the bottom were washed and re-dispersed in water. First, we characterize the bottom to highlight a potential effect of the expected polymer insertion on the initial functionalization.

XRD patterns of the bottoms of C_4N-HST, C_{12}O-HST, BenzSC_2O-HST and $C_{10}PO_3$-HST after the exfoliation process are shown in ***Figure 13***. All patterns display the in-plane reflections (*100*), (*110*) and

(*200*) at 22.7°, 32.4° and 46.4° respectively. Thus the inorganic structure of the $SrTa_2O_7^{2-}$ layer is maintained during exfoliation and that some materials might not have been exfoliated. The presence of (*00l*) reflections at low angle also supports this statement.

In the case of exfoliation attempt from C_4N-HST and C_{12}O-HST, the (*001*) reflection appears at 8.5 ° and 8.9 ° respectively in the form of one single peak without harmonic. The corresponding interlayer distance is about 1 nm which is similar to the one of HST. So, the polymer exfoliation has led to the removal of the initial functionalization even in the case of C_{12}O-HST, despite the covalent nature of the grafting.

Now we consider the exfoliation from BenzSC_2O-HST and $C_{10}PO_3$-HST. The (*001*) reflections at low angles observed in the bottoms correspond to an interlayer distance of 1.86 nm and 2.89 nm respectively. These values are smaller than these of the corresponding precursor (2.04 nm for BenzSC_2O-HST and 3.36 nm for $C_{10}PO_3$-HST). We ascribe this small shrinkage of the interlayer space to a greater interdigitation of the organic molecules inside or to a modification of the angle between the molecules and the inorganic layers. Polymer-assisted exfoliation from BenzSC_2O-HST and $C_{10}PO_3$-HST does not seem to be damaging for the initial functionalization. Yet we do not observe an increase of the interlayer distance as would be expected if insertion of PEG600 between the decorated layers had occurred.

Secondly, for the same grafting group (*i.e.* the alcohol), the hydrolysis is more or less likely to happen depending on the nature of the carbon backbone of the molecule (BenzSC_2OH has a terminal aromatic ring plus a linear chain). As expected, amines are easily removed from the layered structure.

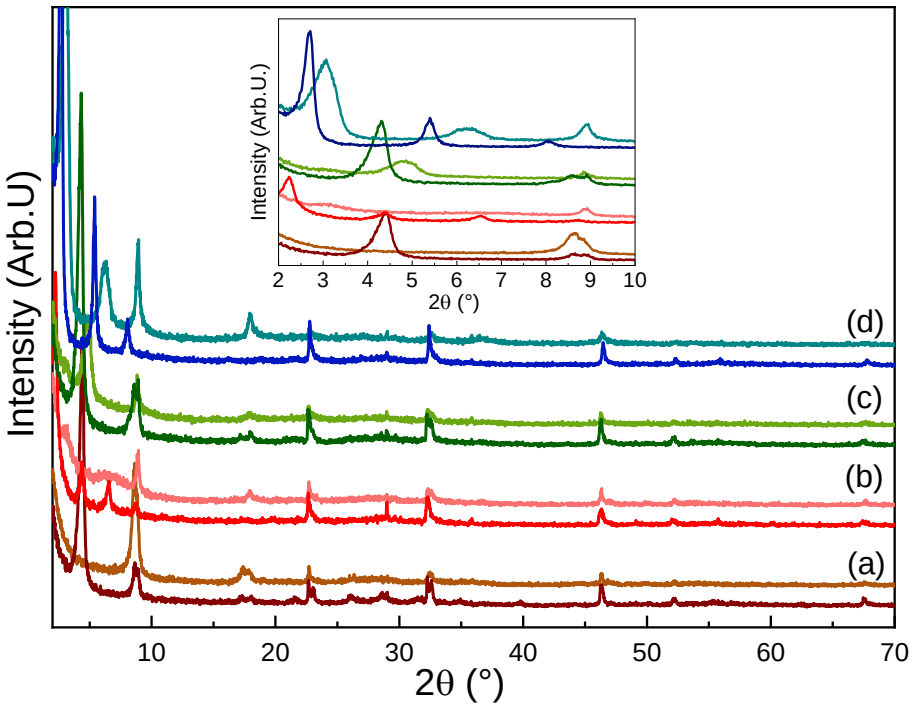

Figure 13: XRD patterns of (a) C_4N-HST, (b) C_{12}O-HST, (c) BenzSC_2O-HST and (d) $C_{10}PO_3$-HST before exfoliation (in dark color) and bottoms after exfoliation attempt with PEG600 (in light colors).

FTIR spectra of the bottoms are presented in ***Figure 14***. In the case of exfoliation from C_4N-HST, the spectrum does not display any band corresponding either to the 1-butylamine or to the polymer. The spectrum is similar to the one of HST.

For exfoliation from $C_{12}O$-HST, the C-H stretching bands at 2855 cm^{-1} and 2918 cm^{-1} are less intense compared to the same bands in the spectrum of $C_{12}O$-HST. Thus, the content in 1-dodecanol is reduced on the "exfoliated" phase (at least in the bottom part). Similarly, the C-OTa stretching band is still visible at 1147 cm^{-1} whereas its intensity is lowered. In parallel, a C-O stretching band at 1104 cm^{-1} is observed which we assign to PEG600. Thus, we can ascertain the presence of PEG600 on the bottom but a partial removal of the initial 1-dodecanol might occur during the exfoliation process.

Finally, the resulting bottoms materials from exfoliation of $BenzSC_2O$-HST and $C_{10}PO_3$-HST display the same spectrum than their corresponding precursor except they show an additional band at 1104 cm^{-1}. We ascribe this intense signal to the C-O stretching band of PEG600. Thus, PEG600 is at least adsorbed at the surface of the materials in the bottoms resulting from the exfoliation from $BenzSC_2O$-HST and $C_{10}PO_3$-HST.

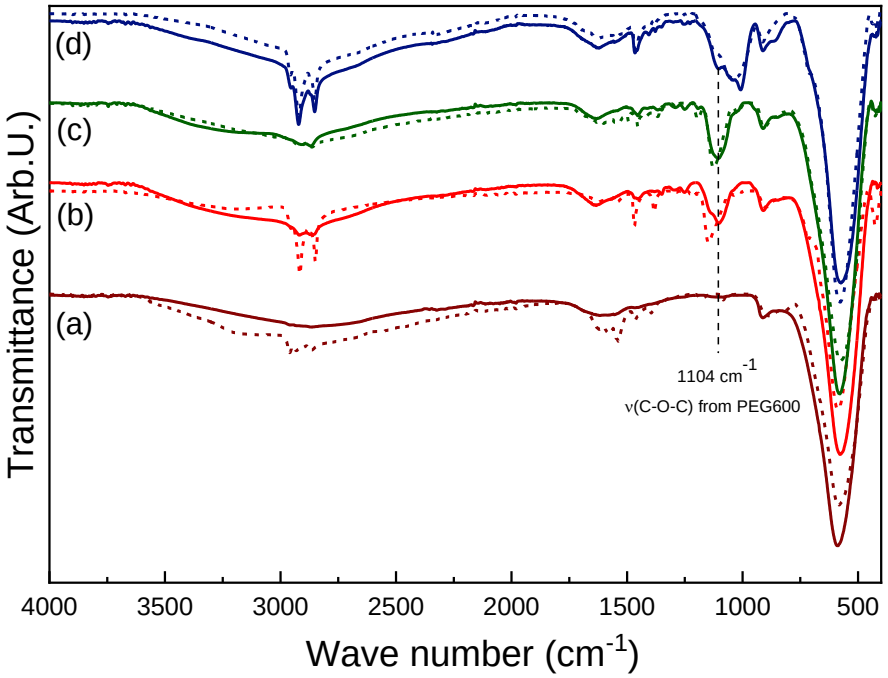

Figure 14: FTIR spectra of (a) C_4N-HST, (b) $C_{12}O$-HST, (c) $BenzSC_2O$-HST and (d) $C_{10}PO_3$-HST before exfoliation (dot line) and bottoms after exfoliation with PEG600 (solid line).

Analysis from the bottoms allowed us to discriminate the good candidates for further study *i.e.* the materials for which the initial functionalization is preserved during the PEG600-assisted exfoliation process.

Therefore, we image only the supernatants of the solutions resulting from the exfoliation of $BenzSC_2O$-HST and $C_{10}PO_3$-HST. The SEM images of the two supernatants are shown in ***Figure 15***. Considering the nanomaterials shown in these images, we clearly distinguish delaminated materials which are packed but without any coherence between the slabs. Few non-exfoliated materials remain but most of

them are few-layer materials. We cannot consider here that exfoliation lead to totally delaminated monolayer nanosheets as depicted by the images ***Figure 15 (c)*** and ***(f)***. The size of the resulting nanomaterials is in the range of the micrometer which is of the same order of magnitude that obtained by T. Sasaki et *al via* ion-exchange.[5,6,1] Yet in both cases, we notice the polydispersity in size of the sample (no liquid cascade centrifugation has been performed here) and polydispersity in shape. Despite the gentle stirring during the synthesis, fragmentation of the crystals occurred and leads to many populations in size and thickness which is added to the initial size distribution of the crystal. It will therefore not be surprising to get such or even higher dispersity when using mechanical-force assisted exfoliation instead of polymer-assisted exfoliation (see **Chapter IV** and **Chapter V**).

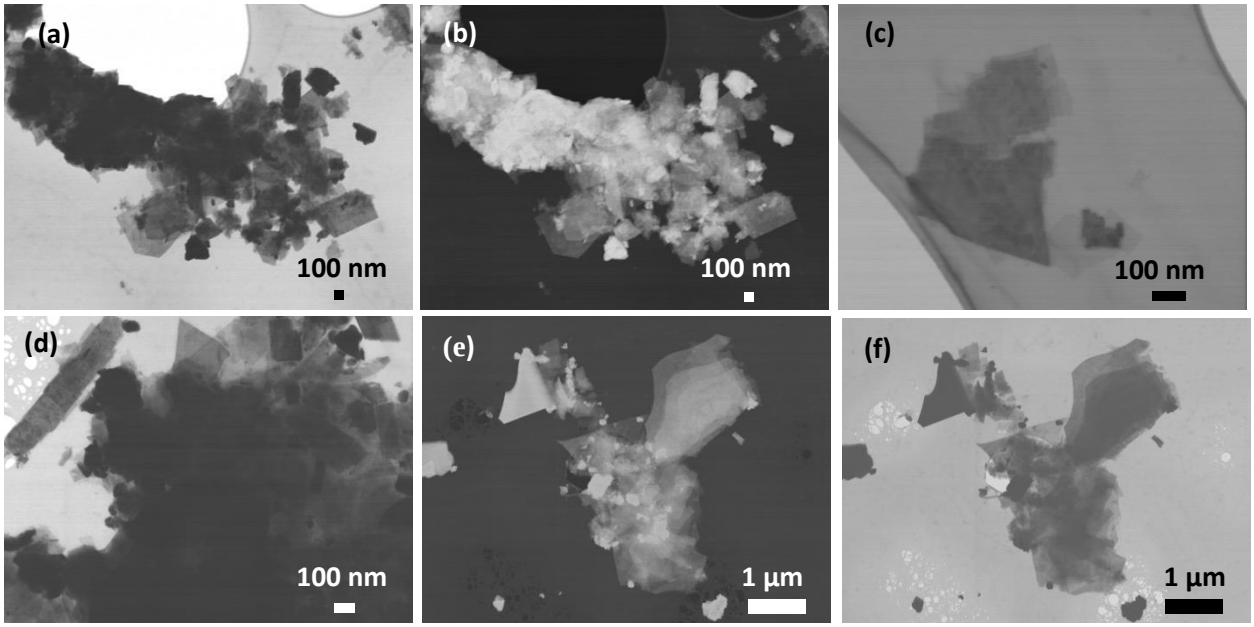

Figure 15: SEM images of (a) to (c) BenzSC$_2$O-HST (d) to (f) C$_{10}$PO$_3$-HST nanomaterials resulting from the exfoliation with the PEG600.

III.4.2.3 PEGN5000-assisted exfoliation of hybrid layered oxides

In the following, we explore the polymer-assisted exfoliation of the same precursors, C_4H-HST, C_{12}O-HST, BenzSC$_2$O-HST and $C_{10}PO_3$-HST by using the methoxypoly(ethylene glycol) amine with a molar mass of 5000 g.mol^{-1} (PEGN5000). Here we aim at studying the potential effects which arise from additional group to the poly(ethylene glycol) *i.e* its interaction with the prior functionalization (in analogy with the replacement of alcohol by TBA$^+$) or its effect on the exfoliation degree. The exfoliation experiments are carried out in THF in presence of the hybrid layered precursor, the PEGN5000 and a small amount of water. The reaction took place at room temperature for four days. The resulting solution was centrifuged at 1600 rpm for 20 minutes; the bottom and the supernatant were washed and re-dispersed in water.

First, we characterized the bottoms to investigate the effect of PEGN5000 on the functionalization of the layered hybrids. The XRD patterns of the bottoms are shown in ***Figure 16.*** All the patterns display in-plane (*100*), (*110*) and (*200*) reflections which are characteristic of the layer $SrTa_2O_7^{2-}$ structure. The

bottoms, resulting from the exfoliation of C_4N-HST, $C_{12}O$-HST and $BenSC_2O$-HST, display the same (*001*) reflection at 8.9°. It corresponds to an interlayer distance of 0.99 nm. This value is similar to the interlayer distance of HST. We notice that in the case of $BenzSC_2O$-HST, the peak associated to the (*001*) reflection is low in intensity compared to the same peaks for the two bottoms from C_4N-HST and $C_{12}O$-HST. From these observations from XRD pattern of the bottoms, it appears that exfoliation of $BenzSC_2O$-HST with PEGN5000 leads to the removal of the initial molecule while it was not the case when exfoliating with PEG600.

In contrast, the bottom resulting from the exfoliation of $C_{10}PO_3$-HST displays a series of (*00l*) reflections corresponding to an interlayer distance of 2.92 nm. It is shorter than the one of the precursor $C_{10}PO_3$-HST as also observed when exfoliating using PEG600. As stated from the XRD of the bottom when exfoliating with PEG600, the alkylphosphonic acid seems to remains grafted onto the inorganic layer upon the exfoliation process.

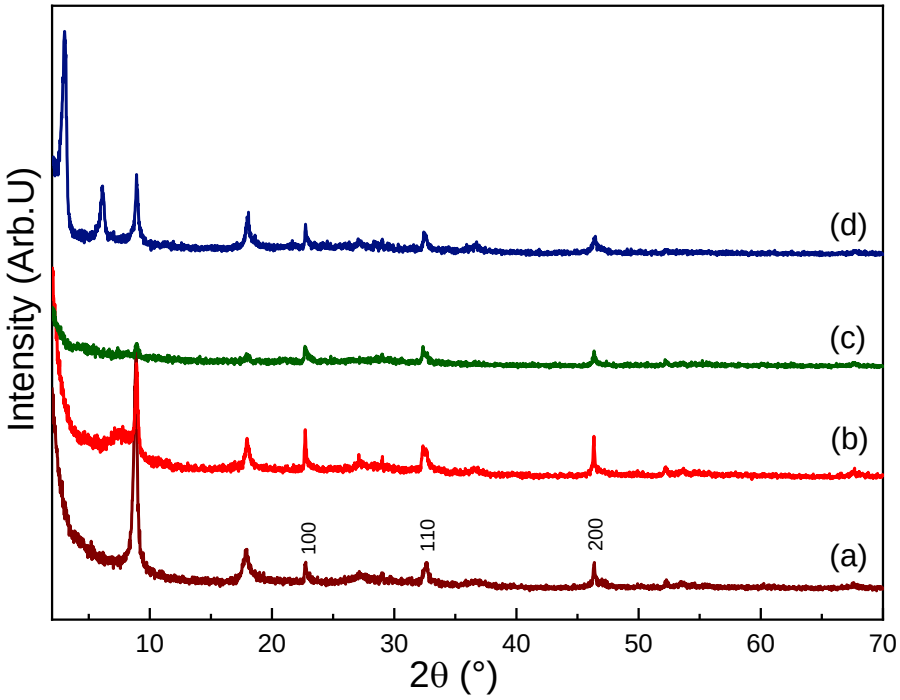

Figure 16: XRD patterns of bottoms of (a) C_4N-HST, (b) $C_{12}O$-HST, (c) $BenzSC_2O$-HST and (d) $C_{10}PO_3$-HST after exfoliation with PEGN5000.

The FTIR spectra allow to clarify the potential presence of the polymer onto the nanomaterials in the resulting bottoms. Concerning the exfoliation from C_4N-HST, no clear signature of any organic molecules is emphasized. The exfoliation experiment leads to a "nude" phase, assimilated to HST, onto which the PEGN5000 is not even adsorbed.

The experiments from $C_{12}O$-HST and $BenzSC_2O$-HST lead to similar spectra, displaying a broad CH_2 stretching band around 2870 cm^{-1} and an intense C-O stretching band at 1104 cm^{-1}. This latter band displays a shoulder at 1148 cm^{-1}, barely distinguishable, corresponding to the initial C-OTa stretching band of the grafted molecules $C_{12}OH$ and $BenzSC_2OH$. We notice the clear disappearance of the strong CH stretching bands of $C_{12}OH$. These features can be interpreted as evidencing the presence of

PEGN5000 and demonstrate that a part of the initial C-O-Ta was broken during the process, *i.e.* the initial functionalization with an alcohol anchoring function was partially removed.

In the case of the exfoliation from $C_{10}PO_3$-HST, the spectrum is similar to the precursor plus an additional band at 1104 cm^{-1} which testifies the presence of the PEGN5000.

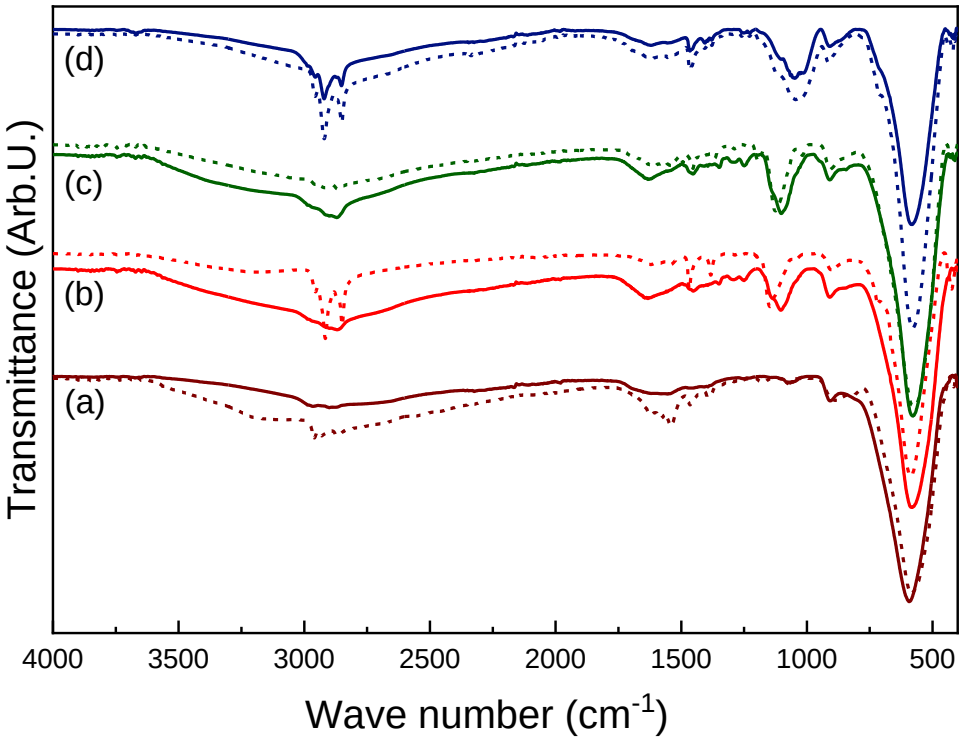

Figure 17: FTIR spectra of (a) C_4N-HST, (b) $C_{12}O$-HST, (c) $BenzSC_2O$-HST and (d) $C_{10}PO_3$-HST before (dot line) and after (solid line) their exfoliation with PEGN5000.

Considering the results from the bottoms, we only carried out SEM analysis on the supernatant of the exfoliation experiments with $BenzSC_2O$-HST and $C_{10}PO_3$-HST as we did for exfoliation with PEG600. The SEM images of both supernatants are shown in ***Figure 18***. Concerning the supernatant from $BenzSC_2O$-HST, images from ***Figure 18 (a)*** to ***(c)*** show large delaminated nanomaterials which can be considered as few-layer nanosheets. Some non-exfoliated (dark contrasted objects) are observed to a smaller extent. Concerning the supernatant from $C_{10}PO_3$-HST, the corresponding ***Figure 18 (d)*** to ***(f)*** show large exfoliated nanomaterials: we clearly see that exfoliation occurred even the oxide nanosheets appear restacked, as seen in ***Figure 18 (e).*** Compared to exfoliation $BenzSC_2O$-HST, some un-exfoliated layered oxides are also observed in a larger extent compared to exfoliated materials. This difference might arise from the centrifugation step which was more efficient in the case of $BenzSC_2O$-HST.

With PEGN5000, the resulting nanomaterials are in the same size range as for exfoliation with PEG600 (*i.e.* around 1 µm) and size/shape polydispersity is similar. The main difference lies on the partial damaging of the alcohol grafting for both $C_{12}O$-HST and $BenzSC_2O$-HST with PEGN5000, while $BenzSC_2O$-HST seems to conserve its integrity when exfoliating with PEG600. We hypothesize that effect

is due to the amine moiety on the PEGN5000 which might favour the breaking of the C-O-Ta bond. This finding is line with reported competition between alcohol and amine grafting into layered oxides.[13]

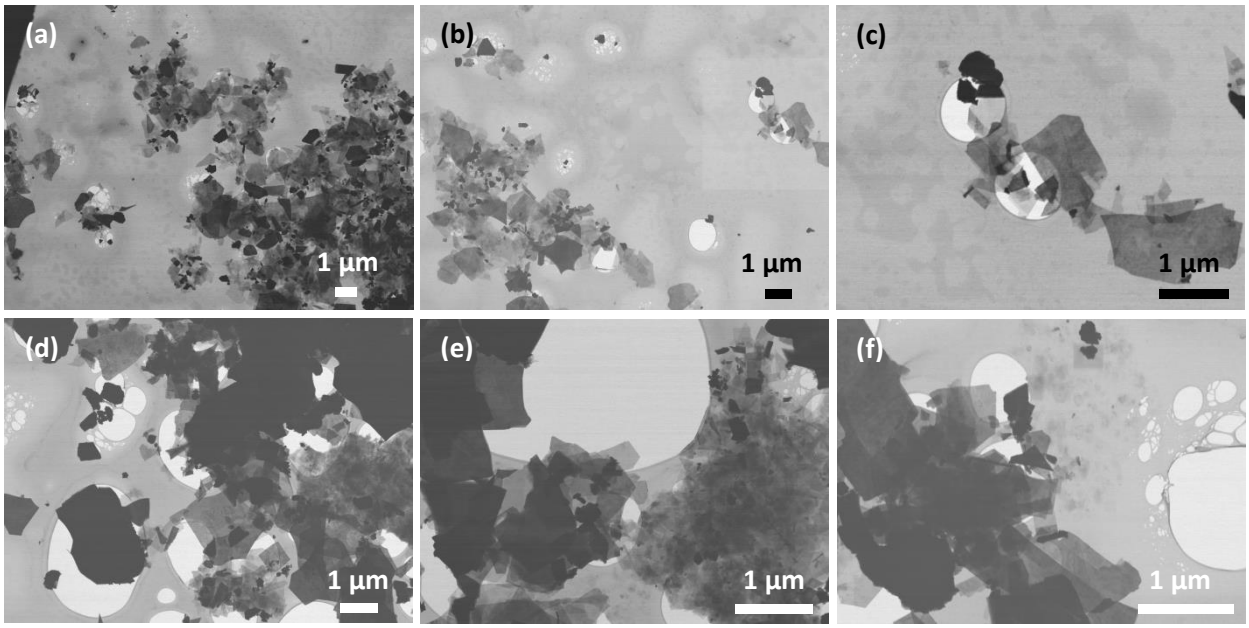

Figure 18: SEM images of (a) to (c) BenzSC$_2$O-HST and (d) to (e) C$_{10}$PO$_3$-HST nanomaterials from supernatant after exfoliation using PEGN5000 as exfoliating agent.

III.4.2.1 Conclusion

Polymer-assisted exfoliation can be performed on hybrid materials while keeping their functionalization. The initially grafted molecules are maintained in the case of alkylphosphonic acid, but are de-inserted and un-grafted in the case of amine and partially in the case of alcohol.

We also mention the difference in reactivity of polymer towards the initial functionalization: the amine terminated PEGN5000 tends to favour the damaging of the alcohol-based hybrid during the exfoliation process.

In addition, the exfoliation trials of the bare layered oxide HST using the same polymer as for the hybrid were almost inefficient, leading only to a very partial and limited exfoliation. Thus, the functionalization helps for the diffusion of the polymer into the layers, notably due to a larger interlayer distance compared to HST.

In addition, we showed that two linear PEGs with relatively distinct molar masses can exfoliate hybrid layered oxides even if short polymer chain seems to be more efficient. However, we have not yet considered the structure (branched or linear) of the polymer.

Finally, *in-situ* study should be performed to elucidate the mechanism of exfoliation: does the exfoliation occur after the polymer insertion into the layers or does it occur just with the gentle stirring and the swelling of the structure, as described by Y. Oaki,[35,36] followed by polymer absorption?

III.4.3 PAA-assisted exfoliation of hybrid layered oxides

We consider the poly(acrylic acid) (PAA) as a potential exfoliating agent. This polymer is a hydrogen-bond donor and acceptor. As a result, many intra-hydrogen bonds must be broken to solubilize the polymer *i.e.* the solvent used must be protic and polar. Thus we excluded THF and carried out two sets of experiments in water and 2-propanol (IPA). Here, we consider two hybrid precursors, C_4N-HST and $C_{10}PO_3$-HST. It is worth mentioning that pouring a hydrophobic compound such as $C_{10}PO_3$-HST into water should not result in a well dispersed powder in water. However, the solution becomes turbid as the reaction goes, meaning that some particles are indeed dispersed. We ascribe this evolution to presence of the absorption of water-soluble polymer.

Unfortunately, the exfoliation trials using PAA as exfoliating agent were not successful. The experiments involving C_4N-HST leads to the complete removal of the 1-butylamine and the interlayer distance is similar to the one of HST. Concerning the exfoliation using $C_{10}PO_3$-HST, the dispersion of the compound was not optimal and the resulting nanomaterials correspond to stacked layers without any modification of the interlayer space. The $C_{10}PO_3$-HST, dispersed in water, indicates that it might be possible to find better conditions to reach exfoliation with PAA.

Nevertheless, the solvent is crucial in this method and as we saw, might be the limiting factor. Therefore, other methods of exfoliation might be promising alternatives if we want to use PAA as exfoliating agent, especially the one using the melt polymer as both solvent and exfoliating agent.[20]

III.4.4 PEI-assisted exfoliation of hybrid layered oxides

Similarly to PAA, we investigated the exfoliation of $C_{10}PO_3$-HST by poly(ethylene imine) (PEI). This polymer is mostly used as a positively charged polymer since its amine groups can be easily protonated at low pH.[37,38] Nevertheless, here we take more advantage of its ability to form hydrogen bond than its ability to be protonated. Two experiments were carried out: the first one in water and the second in IPA where pH (*i.e.* protonation) issues are no longer relevant. The hybrid precursor was poured into 25 mL of water (pH around 9) or IPA with a small amount of water and the PEI. The reaction was stirred at room temperature for 2 days. As discussed previously, the $C_{10}PO_3$-HST is barely dispersible in water. Therefore, the reaction started using THF were the $C_{10}PO_3$-HST is dispersible. The addition of the polymer led to a white precipitate which was collected by centrifugation (14000 rpm, 15 minutes) and then re-dispersed in water and stirred at room temperature for 2 days. After 2 days of stirring, the solution was centrifuged at 1600 rpm for 20 minutes.

The XRD patterns and the FTIR spectra of the bottoms are presented in ***Figure 19***. The XRD patterns show that exfoliation occurring in water modify the interlayer space of the initial $C_{10}PO_3$-HST. We observe a shift of the (*001*) reflection towards the high angle and the broadening of the corresponding low-angle peak. The experiment in IPA does not modify the (*001*) reflections. In both cases, the (*100*), (*110*) and (*200*) reflections are observed even if the corresponding peaks are of low-intensity.

The FTIR spectrum of the bottoms synthesized in water displays characteristic bands of the PEI as the N-H stretching band at 1550 cm^{-1} and the water characteristic band at 1640 cm^{-1}. In addition, the band of the $C_{10}PO_3$ moiety is still observed: the P-C stretching band at 1464 cm^{-1} as well as the large band

corresponding to the PO_3 vibration mode between 970 cm^{-1} and 1200 cm^{-1}. The spectrum of the bottom synthesized in IPA is similar to the spectrum of $C_{10}PO_3$-HST plus the band of water at 1640 cm^{-1} which in more intense.

From the study of the bottoms, it appears that the phosphonic acid functionalization is preserved upon treatment with PEI, both in water and in IPA. Therefore, it is worth studying the supernatant to investigate the potential exfoliation

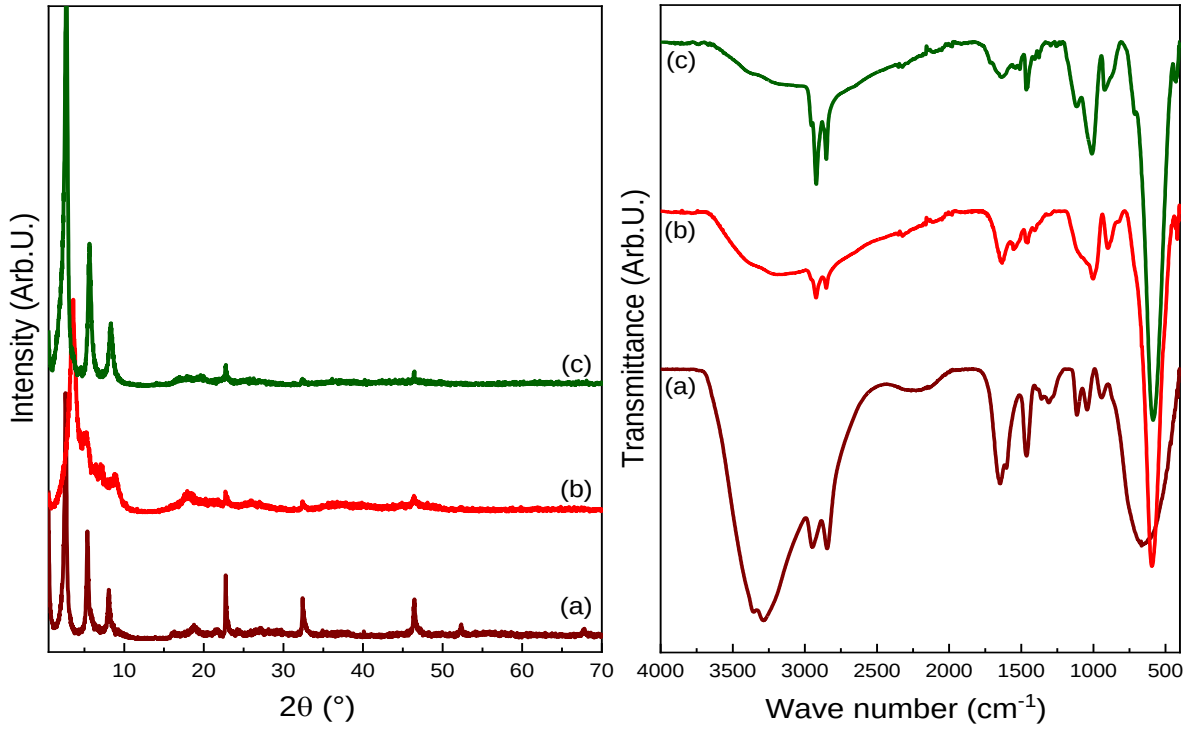

Figure 19: Left) XRD patterns of (a) $C_{10}PO_3$-HST and the bottoms from the exfoliation of $C_{10}PO_3$-HST with PEI in (b) water and (c) IPA. Right) FTIR spectra of (a) PEI and the bottoms from exfoliation of $C_{10}PO_3$-HST with PEI in (b) water and (c) IPA.

The SEM images of supernatants of the exfoliation with PEI presented in ***Figure 20*** show delaminated nanomaterials. Once again, the objects are in the range of the micrometer, polydispersed in size and shape. Thus, the resulting nanomaterials look like the ones from exfoliation with PEG600 and PEGN5000. However, these images show a smaller amount of few-layer nanosheets than what has been observed with both poly(ethylene glycol) polymers. This observation is confirmed by the aspect of the solutions which are less trouble in the case of PEI- assisted exfoliation. We ascribe this difference to the difficulty to get a suitable solvent for both the hybrid oxide and the polymer.

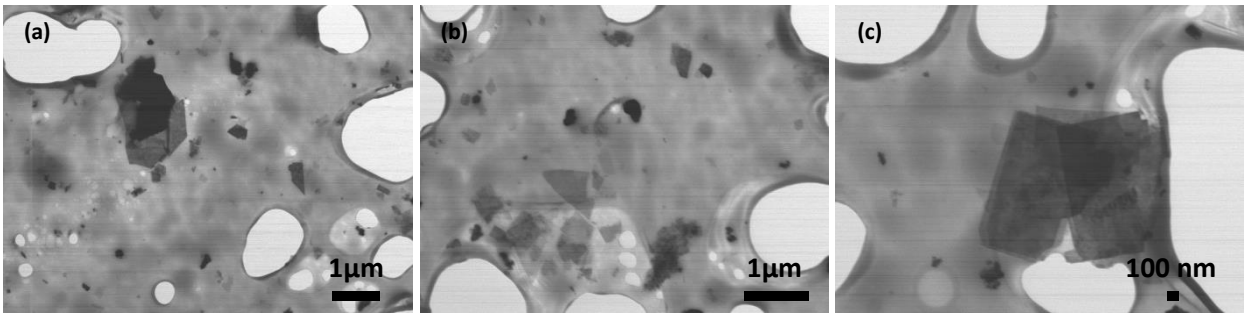

Figure 20: SEM images of the supernatant from the exfoliation of $C_{10}PO_3$-HST with PEI in water.

III.4.5 Conclusion

In this part, we investigated the exfoliation of hybrid layered oxide by the assistance of polymer as exfoliating agent. We used three kinds of polymers. First, the poly(ethylene glycol) derivatives, as PEG600 and PEGN5000, allow exfoliation of hybrid oxides. Yet the functionalization is damaged during the process except in the case of $C_{10}PO_3$-HST where the grafting is more resistant (as expected by the design of such hybrid). The resulting nanomaterials have lateral sizes equivalent to nanosheets obtained through conventional ion-exchange exfoliation of "nude" layered oxides. In addition, the SEM images indicate an important exfoliation rate, even though the quantitative assessment of such exfoliation rate is somehow difficult to establish (see Chapter 5).

In contrast, our trials of exfoliation using poly(acrylic acid) were not successful. Either the prior functionalization is removed from the structure or the polymer is only adsorbed at the surface of the layered materials in the case of $C_{10}PO_3$-HST.

Finally, exfoliation using poly(ethylene imine) leads to nanomaterials in solution. However, the functionalization is partially damaged and the exfoliating rate seems to be lower than exfoliation with PEG. Limitations might arise from solubility issues and alternative should be considered if we want to exfoliate with PEI.

Further studies should be conducted to investigate the mechanism behind such exfoliation as well as the structure and composition of the hybrid nanosheets (*e.g.* the amount of polymer chain per unit cell of nanosheets, the interaction between the initial molecules and the polymer, the amount of remaining initial molecules).

III.5. Conclusion of Chapter III

In this chapter, we investigated the exfoliation of hybrid layered oxides using either organoammonium ion or polymer as exfoliating agent. In the former case, we combine ion-exchange and microwave heating to exfoliate hybrid layered oxides. Unfortunately, the functionalization of the hybrid is removed in case of amine and alcohol grafting in favor of the tetrabutylammonium cation. The resulting material is equivalent to a "nude" layered oxide which has been in contact with TBA^+ in a conventional ion-exchange process.

In the case of polymer-assisted exfoliation, nanomaterials (*i.e.* few-layer nanosheets) can be obtained when using PEG600, PEGN5000 and PEI to delaminate BenzSC_2O-HST or $C_{10}PO_3$-HST. The exfoliation rate and the lateral size of the nanomaterials are similar to these obtained from a conventional ion-exchange mechanism. However, in-depth characterizations have to be carried out to confirm the presence of the organic decoration on the nanomaterials and the amount of adsorbed polymer.

Both polymer-assisted exfoliation and ion-exchange exfoliation are efficient on layered oxide. However, when delaminating a hybrid material, the exfoliating agent competes with the grafted/inserted molecules and tends to replace them. In addition, in the case of ion-exchange, the TBA^+ ion does not display any interesting property or subsequent use. Thus, we conclude that ion-exchange is not suitable to produce functionalized oxide nanosheets according to this procedure. Polymer-assisted exfoliation has to be explored (for instance *in-situ* polymerization)[20] and remains a promising exfoliating method as the functionalization can be preserved depending on its nature and the nature of the polymer used.

Therefore, we focus on mechanical force-assisted exfoliation in the following as no additional exfoliating agent is needed and the hybridization should remain untouched.

III.6. Bibliography

(1) Ebina, Y.; Sasaki, T.; Watanabe, M. Study on Exfoliation of Layered Perovskite-Type Niobates. *Solid State Ionics* **2002**, *151* (1), 177–182.

(2) Lee, W.-J.; Yeo, H. J.; Kim, D.-Y.; Paek, S.-M.; Kim, Y.-I. Exfoliation of Dion-Jacobson Layered Perovskite into Macromolecular Nanoplatelet. *Bulletin of the Korean Chemical Society* **2013**, *34* (7), 2041–2043.

(3) Geng, F.; Ma, R.; Yamauchi, Y.; Sasaki, T. Tetrabutylphosphonium Ions as a New Swelling/Delamination Agent for Layered Compounds. *Chem. Commun.* **2014**, *50* (69), 9977–9980.

(4) Le, P. T. P.; ten Elshof, J. E.; Koster, G. Shape Control of $Ca_2Nb_3O_{10}$ Nanosheets: Paving the Way for Monolithic Integration of Functional Oxides with CMOS. *ACS Appl. Nano Mater.* **2020**, *3* (9), 9487–9493.

(5) Sasaki, T.; Watanabe, M.; Hashizume, H.; Yamada, H.; Nakazawa, H. Macromolecule-like Aspects for a Colloidal Suspension of an Exfoliated Titanate. Pairwise Association of Nanosheets and Dynamic Reassembling Process Initiated from It. *J. Am. Chem. Soc.* **1996**, *118* (35), 8329–8335.

(6) Sasaki, T.; Watanabe, M. Osmotic Swelling to Exfoliation. Exceptionally High Degrees of Hydration of a Layered Titanate. *J. Am. Chem. Soc.* **1998**, *120* (19), 4682–4689.

(7) Sasaki, T.; Watanabe, M. X-Ray Diffraction Study on Crystalline and Osmotic Swelling of a Layered Titanate. *Molecular Crystals and Liquid Crystals Science and Technology. Section A. Molecular Crystals and Liquid Crystals* **1998**, *311* (1), 417–422.

(8) Maluangnont, T.; Matsuba, K.; Geng, F.; Ma, R.; Yamauchi, Y.; Sasaki, T. Osmotic Swelling of Layered Compounds as a Route to Producing High-Quality Two-Dimensional Materials. A Comparative Study of Tetramethylammonium versus Tetrabutylammonium Cation in a Lepidocrocite-Type Titanate. *Chem. Mater.* **2013**, *25* (15), 3137–3146.

(9) Besselink, R.; Stawski, T. M.; Castricum, H. L.; Blank, D. H. A.; ten Elshof, J. E. Exfoliation and Restacking of Lepidocrocite-Type Layered Titanates Studied by Small-Angle X-Ray Scattering. *J. Phys. Chem. C* **2010**, *114* (49), 21281–21286.

(10) Miyamoto, N.; Kuroda, K.; Ogawa, M. Exfoliation and Film Preparation of a Layered Titanate, $Na_2Ti_3O_7$, and Intercalation of Pseudoisocyanine Dye. *J. Mater. Chem.* **2004**, *14* (2), 165–170.

(11) Akbarian-Tefaghi, S.; Rostamzadeh, T.; Brown, T. T.; Davis-Wheeler, C.; Wiley, J. B. Rapid Exfoliation and Surface Tailoring of Perovskite Nanosheets via Microwave-Assisted Reactions. *ChemNanoMat* **2017**, *3* (8), 538–550.

(12) Wang, Y.; Delahaye, E.; Leuvrey, C.; Leroux, F.; Rabu, P.; Rogez, G. Efficient Microwave-Assisted Functionalization of the Aurivillius-Phase $Bi_2SrTa_2O_9$. *Inorg. Chem.* **2016**, *55* (8), 4039–4046.

(13) Wang, Y.; Nikolopoulou, M.; Delahaye, E.; Leuvrey, C.; Leroux, F.; Rabu, P.; Rogez, G. Microwave-Assisted Functionalization of the Aurivillius Phase $Bi_2SrTa_2O_9$: Diol Grafting and Amine Insertion vs. Alcohol Grafting. *Chem. Sci.* **2018**, *9* (35), 7104–7114.

(14) Payet, F.; Bouillet, C.; Leroux, F.; Leuvrey, C.; Rabu, P.; Schosseler, F.; Taviot-Guého, C.; Rogez, G. Fast and Efficient Shear-Force Assisted Production of Covalently Functionalized Oxide Nanosheets. *Journal of Colloid and Interface Science* **2022**, *607*, 621–632.

(15) Akbarian-Tefaghi, S.; Teixeira Veiga, E.; Amand, G.; Wiley, J. B. Rapid Topochemical Modification of Layered Perovskites via Microwave Reactions. *Inorg. Chem.* **2016**, *55* (4), 1604–1612.

(16) Boykin, J. R.; Smith, L. J. Rapid Microwave-Assisted Grafting of Layered Perovskites with n-Alcohols. *Inorg. Chem.* **2015**, *54* (9), 4177–4179.

(17) Gopakumar, T. G.; Lee, J. A.; Kontopoulou, M.; Parent, J. S. Influence of Clay Exfoliation on the Physical Properties of Montmorillonite/Polyethylene Composites. *Polymer* **2002**, *43* (20), 5483–5491.

(18) Chen, B.; Evans, J. R. G.; Greenwell, H. C.; Boulet, P.; Coveney, P. V.; Bowden, A. A.; Whiting, A. A Critical Appraisal of Polymer–Clay Nanocomposites. *Chem. Soc. Rev.* **2008**, *37* (3), 568–594.

(19) Akelah, A.; Moet, A. Polymer-Clay Nanocomposites: Free-Radical Grafting of Polystyrene on to Organophilic Montmorillonite Interlayers. *JOURNAL OF MATERIALS SCIENCE* **1996**, *31* (13), 3589–3596.

(20) Alexandre, M.; Dubois, P. Polymer-Layered Silicate Nanocomposites: Preparation, Properties and Uses of a New Class of Materials. *Materials Science and Engineering: R: Reports* **2000**, *28* (1), 1–63.

(21) Fuse, Y.; Ide, Y.; Ogawa, M. Hybridization of Epoxy Resin with a Layered Titanate and UV Light Durability and Controlled Refractive Index of the Resulting Nanocomposite. *Polym. Chem.* **2010**, *1* (6), 849–853.

(22) Asai, Y.; Ariake, Y.; Saito, H.; Idota, N.; Matsukawa, K.; Nishino, T.; Sugahara, Y. Layered Perovskite Nanosheets Bearing Fluoroalkoxy Groups: Their Preparation and Application in Epoxy-Based Hybrids. *RSC Adv.* **2014**, *4* (51), 26932–26939.

(23) Idota, N.; Fukuda, S.; Tsukahara, T.; Sugahara, Y. Preparation of Thermoresponsive Nanosheets Exhibiting Phase Transitions in Water via Surface Modification of Layered Perovskite Nanosheets with Poly(N-Isopropylacrylamide) (PNIPAAm). *Chemistry Letters* **2014**.
(24) Bonaccorso, F.; Bartolotta, A.; Coleman, J. N.; Backes, C. 2D-Crystal-Based Functional Inks. *Advanced Materials* **2016**, *28* (29), 6136–6166.
(25) Backes, C.; Abdelkader, A. M.; Alonso, C.; Andrieux-Ledier, A.; Arenal, R.; Azpeitia, J.; Balakrishnan, N.; Banszerus, L.; Barjon, J.; Bartali, R.; Bellani, S.; Berger, C.; Berger, R.; Ortega, M. M. B.; Bernard, C.; Beton, P. H.; Beyer, A.; Bianco, A.; Bøggild, P.; Bonaccorso, F.; Barin, G. B.; Botas, C.; Bueno, R. A.; Carriazo, D.; Castellanos-Gomez, A.; Christian, M.; Ciesielski, A.; Ciuk, T.; Cole, M. T.; Coleman, J.;*et al.*. Production and Processing of Graphene and Related Materials. *2D Mater.* **2020**, *7* (2), 022001.
(26) Lotya, M.; Rakovich, A.; Donegan, J. F.; Coleman, J. N. Measuring the Lateral Size of Liquid-Exfoliated Nanosheets with Dynamic Light Scattering. *Nanotechnology* **2013**, *24* (26), 265703.
(27) Paton, K. R.; Varrla, E.; Backes, C.; Smith, R. J.; Khan, U.; O'Neill, A.; Boland, C.; Lotya, M.; Istrate, O. M.; King, P.; Higgins, T.; Barwich, S.; May, P.; Puczkarski, P.; Ahmed, I.; Moebius, M.; Pettersson, H.; Long, E.; Coelho, J.; O'Brien, S. E.; McGuire, E. K.; Sanchez, B. M.; Duesberg, G. S.; McEvoy, N.; Pennycook, T. J.; Downing, C.; Crossley, A.; Nicolosi, V.; Coleman, J. N. Scalable Production of Large Quantities of Defect-Free Few-Layer Graphene by Shear Exfoliation in Liquids. *Nature Materials* **2014**, *13* (6), 624–630.
(28) Svedberg, T.; Pedersen, K. O. *The Ultracentrifuge*; Oxford: The Clarendon Press, 1940.
(29) Finsy, R. Particle Sizing by Quasi-Elastic Light Scattering. *Advances in Colloid and Interface Science* **1994**, *52*, 79–143.
(30) Wang, Y.; Leuvrey, C.; Delahaye, E.; Leroux, F.; Rabu, P.; Taviot-Guého, C.; Rogez, G. Tuning the Organization of the Interlayer Organic Moiety in a Hybrid Layered Perovskite. *Journal of Solid State Chemistry* **2019**, *269*, 532–539.
(31) Lemmon, J. P.; Wu, J.; Oriakhi, C.; Lerner, M. M. Preparation of Nanocomposites Containing Poly(Ethylene Oxide) and Layered Solids. *Electrochimica Acta* **1995**, *40* (13–14), 2245–2249.
(32) Han, X.; Gao, J.; Hu, G.; Tang, X.; Chen, T. Effect of Hydrocarbon Polymer, Feed Ratio, and Interfacial Interaction on the Liquid Exfoliation of Graphite. *J Nanopart Res* **2020**, *22* (11), 341.
(33) Jeon, H. G.; Jung, H.-T.; Lee, S. W.; Hudson, S. D. Morphology of Polymer/Silicate Nanocomposites. *Polymer Bulletin* **1998**, *41* (1), 107–113.
(34) Ogata, N.; Jimenez, G.; Kawai, H.; Ogihara, T. Structure and Thermal/Mechanical Properties of Poly(l-Lactide)-Clay Blend. *Journal of Polymer Science Part B: Polymer Physics* **1997**, *35* (2), 389–396.
(35) Oaki, Y. Exfoliation Chemistry of Soft Layered Materials toward Tailored 2D Materials. *Chem. Lett.* **2021**, *50* (2), 305–
(36) Yamamoto, Y.; Oaki, Y.; Imai, H. Coupled Exfoliation and Surface Functionalization of Titanate Monolayer for Bandgap Engineering. *Advanced Materials Interfaces* **2017**, *4* (7), 1601014.
(37) Sasaki, T.; Ebina, Y.; Tanaka, T.; Harada, M.; Watanabe, M.; Decher, G. Layer-by-Layer Assembly of Titania Nanosheet/Polycation Composite Films. *Chem. Mater.* **2001**, *13* (12), 4661–4667.
(38) Cai, X.; Ozawa, T. C.; Funatsu, A.; Ma, R.; Ebina, Y.; Sasaki, T. Tuning the Surface Charge of 2D Oxide Nanosheets and the Bulk-Scale Production of Superlatticelike Composites. *J. Am. Chem. Soc.* **2015**, *137* (8), 2844–2847.

Chapter IV

Mechanical force-assisted liquid exfoliation of hybrid layered oxides

Chapter IV. Mechanical force-assisted liquid exfoliation of hybrid layered oxides

IV.1. Introduction

IV.1.1 State of the art

In the previous chapter, we have explored the exfoliation of hybrid layered oxides *via* ion-exchange mechanism or polymer assistance. Both processes involve the use of a delaminating agent (organoammonium or a polymer chain) which compete with the pristine functionalization (*i.e.* they tends to replace the molecules already grafted or inserted).

In parallel, in the **Chapter I**, we reviewed alternatives to ion-exchange exfoliation such as mechanical force-assisted exfoliation.[1–4] The applied force is either orthogonal to the layers plane in case of sonication or collinear to the layer plane in case of shear-forces. Both techniques occur in a liquid medium, allowing large scale production of nanomaterials and making them easier to be handled.[5] In addition, there is no need of exfoliating agent as the driving force of delamination is brought by a high speed disperser or a sonication tip. Unfortunately, this mechanical force-assisted liquid exfoliation is up to now mainly dedicated to weakly-bonded layered materials such as graphite or transition metal dichalcogenides (TMD).[1,6–8] This limitation arises from the cohesion force between the layers: it should be weak enough to be broken by mechanical forces.

Therefore, only few papers report the use of sonication or shear-force to synthesize few-layers nanomaterials from charged layered oxides.[9,10] The electrostatic interactions in presence insure a strong coherence between the slabs, which cannot be overcome by external mechanical forces. It is of upmost importance to reduce these electrostatic interactions if one wants to exfoliate with mechanical force. A straightforward solution is to move the layers away from each other *i.e.* to increase the interlayer distance, as the Coulomb forces decreases with distance. We can reach this goal by functionalizing a charged layered oxide, HST (see **Chapter II**): the insertion of molecules leads to the increase of the d_{001} compared to HST interlayer distance, whatever the molecules. Thus, hybrid materials should be more suitable to be exfoliated by mechanical forces. The group of Y. Oaki reported the use of sonication or just of stirring (*i.e.* weak shear forces) to exfoliate hybrid layered titanates, resulting in large delaminated flakes (around the micrometer scale) and thin enough to be considered as nanosheets.[11–14] Their results contrast with the previous mentioned works on sonication-assisted exfoliation of "nude" layered oxides.[15] In these latter cases, the nanomaterials are thick and small compared to the nanosheets from Y. Oaki's works. This difference perfectly highlights the contribution of the functionalization.

However, a number of questions are raised from the introduction of molecules such as how strong the potential intermolecular interactions (*e.g.* hydrophobic interaction) are, compared to electrostatic ones or what the minimal distance to weaken enough the Coulomb forces is. Nevertheless, it is worth mentioning that a clear description of the electrostatic interaction between the slabs of charged layered

clays[16] or soft matter system[17,18] is reported in literature. Beyond the pioneer Poisson-Boltzmann theory which only predicts repulsion between two equally charged walls,[19] these papers considers ion-ion interactions and/ or finite size of the counterions which lead to a theory, called the strong coupling regime which predicts a regime where electrostatic contribution is attractive. This theory will help answer inherent questions to exfoliation of charged layered oxides.

In addition, mechanical force-assisted liquid exfoliation requires to pay attention to many parameters to be efficient. The group of J. Coleman *et al*. has extensively contributed to the study of these parameters which impose their size and shape to nanomaterials in liquid phase exfoliation.[20,21] For instance, they underlined that the nature of the solvent and its interaction with the inorganic slabs should be carefully investigated through enthalpic considerations (*e.g*. minimizing the enthalpy of mixing) in order to reach high delamination yield and colloidal stability.[22] Thus, this choice of exfoliation method involves optimization of many experimental settings with respect to the considered layered material.

IV.1.2 Objectives

In this Chapter, we first aim at giving some elements of answer concerning the mechanical exfoliation of layered oxides. First, we will focus on determining the electrostatic interaction between slabs in a nude layered oxide. The goal is to study the impossibility to sonicate or to use shear-force to separate two adjacent charged layers. We inspire ourselves of the work of J. Coleman *et al*. on TMD to calculate the required energy to delaminate two slabs.[20,22]

In a second step, we will investigate the shear-force assisted exfoliation of hybrid materials we synthesized previously. Considering the work of J. Coleman *et al.* and its advices to liquid phase exfoliation,[23] we study the influence of relevant parameters to determine the best exfoliation conditions. We will pay attention to solvent and how we choose it for exfoliation. Then, we will have a look on the shear rate (which is linked to the high-shear disperser speed) and the exfoliation time. In addition, we will also address the influence of the grafted molecule on the hybrid exfoliation especially its impacts on dispersibility.

In the following, exfoliation trials are essentially performed on C_{12}O-HST: the attachment of the molecule to the inorganic layer is covalent, preventing from easy removal during the process. In addition, despite local heating in the vicinity of the rotor/stator, temperature increase remains limited enough to prevent the hydrolysis of the Ta-O-C bond. Finally, we chose a long alkyl chain to confer organophilicity which allows the use organic solvent for exfoliation.

Since we reviewed in the **Chapter I** the alternative to shear force exfoliation force *i.e.* the sonication-assisted liquid exfoliation and its main drawbacks compared to shear exfoliation, we will not perform here a complete study of sonication-assisted exfoliation and the optimization of the parameters. We assume that the same conclusions can be applied for both techniques and we will just briefly compare the resulting nanomaterials produced in each case.

IV.2. Relevance of the mechanical force for the exfoliation of hybrid layered oxides

IV.2.1 Introduction

In the **Chapter I**, we reviewed the top-down exfoliation methods which are up to now used to obtained nanosheets. Each method is dedicated to a defined layered material. In this work, we aim at transposing the shear-exfoliation method to charge layered oxide.

First, we study why such method was not envisioned initially for the exfoliation of perovskite-like layered oxides. For this purpose, we will calculate the energy of interaction between two adjacent charged oxide layers by computing electrostatic interactions which are involved in such materials. Thus, we will be able to find the corresponding shear force that it is required in order to overcome the layers' interactions and to exfoliate them.

In a second step, we will adopt the same reasoning on hybrid layered materials and highlight how the functionalization of the charged oxide impacts the cohesion between the inorganic layers and if shear exfoliation is more likely to operate efficiently on these hybrid systems.

IV.2.2 Case of the bare layered oxide

Shear force-assisted exfoliation consists in applying a mechanical force which is collinear to the layers. This external force, brought by shear-mixing, must overcome the interaction between two adjacent slabs. Coleman *et al*. have theorized and calculated the minimal force which must be applied to exfoliated TMD materials.[5] In the following, we consider a model closely related to the one of J. Coleman *et al.* in order to determine the minimal energy for exfoliation and the corresponding shear force.

First, we have to focus on energetic issues. We consider two plates, assumed to be square-shaped with a lateral length **L**. These plates have a thickness **d** as seen below (***Figure 1***). We now consider three different states for those plates corresponding to three distinct states during exfoliation process:

- The initial state corresponds to a close-packed system where the slabs are facing each other.
- In the intermediate state, the layers are shifted one to the other by a distance **L-X** according to the in-plane a-axis.
- The final state corresponds to the total delamination of the two layers *i.e.* the plates are not facing each other anymore and no plate-to-plate interaction is present.

By assuming that the layers are identical, we denoted as E_{PP} the interfacial binding of the plates. Similarly, we consider the interfacial binding of the liquid solvent, E_{LL}, and the interfacial binding at the solid-liquid interface between plate and solvent, E_{LP}. The total energy of the system at the three stages is respectively:

$$E_{initial} = -L^2(E_{PP} + E_{LL} + 2E_{LP}) \qquad \textbf{\textit{Equation 1}}$$

$$E_{inter} = -L(xE_{LL} + 2(2L - x)E_{LP} + xE_{PP}) \qquad \textbf{\textit{Equation 2}}$$

$$E_{final} = -L^2(4E_{LP}) \qquad \textbf{\textit{Equation 3}}$$

Thus, the energy change on the exfoliation process can be estimated as

$$\Delta E = E_{final} - E_{initial} = -L^2(2E_{LP} - E_{LL} - E_{PP}) \qquad \textbf{\textit{Equation 4}}$$

In the case where only dispersive force are involved as London force, one can use the geometrical mean approximation, developed by F. Fowkes[24] and defined as $E_{LP} = \sqrt{E_{LL}E_{PP}}$. In the present situation, electrostatic interactions also participate in the total binding between two plates. However, we will consider that the geometric approximation can be applied. Thus, the difference of energy between initial and final step can be simplified as follows,

$$\Delta E = L^2 \left(\sqrt{E_{LL}} - \sqrt{E_{PP}}\right)^2 \qquad \textbf{\textit{Equation 5}}$$

In the case of Van der Waals materials, a good agreement between this model and experimental data was found, for instance, shear force-assisted exfoliation of graphite into graphene.[5] In the present case, the final result will be less quantitative due to the use of the geometrical mean approximation for charged layers, but will remain qualitatively correct.[25]

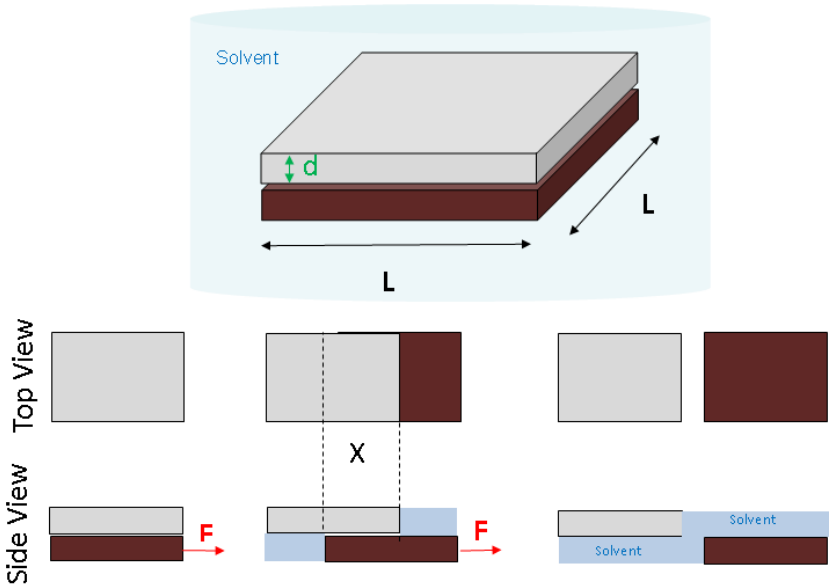

Figure 1: Schematic representation of two facing layers at three different steps of the shear force exfoliation process.

In addition, by integrating ***Equation 3***, one can find the minimum force which must be applied to separate the two plates:

$$F_{min} = -\frac{\partial E_{inter}}{\partial x} = L(E_{LL} - 2E_{LP} + E_{PP}) \qquad \textbf{\textit{Equation 6}}$$

Considering Newtonian fluid, the shear force is defined as $F = \eta\dot{\gamma}L^2$ with $\dot{\gamma}$ is the shear rate and η is the dynamic viscosity of the fluid. We relate it with the minimal force for exfoliation. Thus, we have:

$$\dot{\gamma_{min}} = \frac{(\sqrt{E_{PP}} - \sqrt{E_{LL}})^2}{\eta L} \qquad \textbf{\textit{Equation 7}}$$

Equation 7 involves the dynamic viscosity of the solvent, showing here an insight of how the solvent is important, in the liquid phase exfoliation. The lateral size of the layers also plays a role: the broader the solid-liquid interface is, the more facilitated the exfoliation is. However, this lateral size might evolve during the process as fragmentation of the initial crystal occurs. Finally, this minimum shear rate is related to interfacial binding energy E_{LL} and E_{LP}. In that case, we assimilated this binding energy to the surface energy of the solvent and the plates respectively. Despites this assumption, their determination remains the tricky point. These values are related to the surface tension of the liquid and the plate by: $\Gamma = E - TS$ where Γ is the surface tension, E is the surface energy, T is the temperature and S is the surface entropy.

For the liquid-liquid interface *i.e.* the solvent, the value S_{LL} is usually between 0.07 and 0.14 $mJ.m^2.K^{-1}$. J. Coleman *et al.* chose a mean value of $S_{LL} = 0.1 mJ.m^{-2}.K^{-1}$.[5] In addition, the surface tension Γ_{LL} is tabulated for common solvent. Thus, the surface energy E_{LL} can be easily determined. In our situation, we mainly focus on propan-2-ol (isopropanol or IPA) for shear-force exfoliation (see below for detailed explanations) with $\rho_{IPA} = 785\ kg.m^{-3}$, $\eta_{IPA} = 2.37\times10^{-3}$ Pa.s and $\Gamma_{IPA} = 2.17\times10^{-2}\ J.m^{-2}$. Thus we can estimate the surface energy of the isopropanol: $E_{LL} = E_{IPA} = 52\ mJ.m^{-2}$ at 298 K.

On contrary, the surface tension of the plate, *i.e.* the inorganic layer, is strongly related to the interaction between two plates. It is the determination of such quantities which differentiates Van der Waals materials and charged layered oxides. For the former, only attractive Van der Waals forces have to be taken into account and can be calculate using the Derjaguin-Landau-Vermey-Overbeek (DLVO) theory. For instance, the surface energy of graphene is estimated to be $71\ mJ.m^{-2}$.[5]

For charged layered oxide, an additional contribution of electrostatic force has to be considered. A straightforward assumption is imputing a repulsive character to coulombic forces between like-charged surfaces, as depicted in Poisson-Boltzmann model (also called mean-field theory).[17] Indeed, in colloidal science, the electrostatic forces tend to favour the stability and separation of particles in solution.[19] Nevertheless, literature reports examples of charged objects where the electrostatic contribution is attractive *i.e.* there is a negative osmotic pressure from the counterions.[16,26] Such counter-intuitive situation occurs for high-charge-density surfaces, like charged biological membranes or DNA, for multivalent counter-ion or for solvent with low dielectric constant. These peculiar situations are now well-described by the strong-coupling theory which accounts for highly charged surfaces where the counterions are organized in a 2D layer between the surfaces.[17,27] ***Figure 2 (a)*** and ***(b)*** show two kinds of counterions organization at the surface corresponding to the two models.

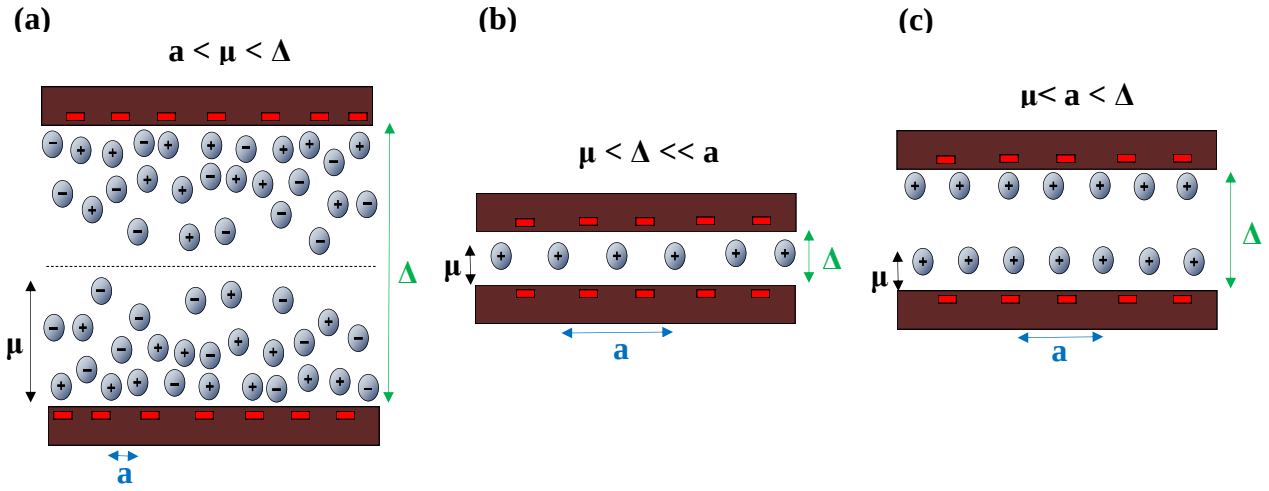

Figure 2: Schematic view of two like-charged plates in (a) the mean-field regime, (b) strong coupling regime and (c) intermediate regime. Δ, μ and a are the characteristic length of the system (see below).

The question whether our system *i.e.* bare charged layered oxide, belongs to mean-field theory or strong-coupling regime theory can be elucidated.

First, we calculate the following characteristic lengths for our system:

- The Bjerrum length $l_B = \frac{e^2}{4\pi\varepsilon\varepsilon_0 k_\beta T}$ ***Equation 8***
- The rescaled Bjerrum length $\tilde{l}_B = q^2\, l_B$ ***Equation 9***
- The Gouy-Chapman length $\mu = \frac{1}{2\pi q l_B \sigma_S}$ ***Equation 10***
- The electrostatic coupling parameter $\Xi = \frac{l_B}{\mu} = 2\pi q^3 l_B^2 \sigma_S$ ***Equation 11***
- The lateral separation between the counterion $a = \sqrt{\frac{q}{2\pi\sigma_S}} = \mu\sqrt{\Xi}$ ***Equation 12***

where **e**, is the elemental charge and is worth 1.6×10^{-19} eV; **q** is the counterion valence; ε is the dielectric constant of the interlayer space media. Here, considering the thickness of the interlayer and the nature of the counterions (*i.e.* protons), we assume that the interlayer space can be considered as water, thus, **ε** = 78.5; $\boldsymbol{\varepsilon_0}$ is the vacuum permittivity and is worth 8.85×10^{-12} F.m^{-1}; $\boldsymbol{\sigma_S}$ is the layer charge density and worth 0.0625 Å^{-2}.

In a second step, if the following criteria are fulfilled, the system can be considered to be in the strong coupling regime:

$$\Xi \gg 1 \qquad \textit{Equation 13}$$

$$\left(\frac{\Delta}{\mu}\right)^2 < \Xi \text{ or } \Delta < a \qquad \textit{Equation 14}$$

In practice, the larger Ξ is**,** the larger is the probability for the system to exhibit "attractive" electrostatic forces. Thus, this situation actually happens for Ξ > 12 in the case where no dielectric jump

$\delta_\varepsilon = \frac{\varepsilon_{liq}-\varepsilon_{layer}}{\varepsilon_{liq}+\varepsilon_{layer}}$ occurs.[17,27] Otherwise, one has to take into account such correction and the critical value of Ξ is modified (it shifts to lager value).

Equation 14 is known as the Rouzina-Bloomfield criterion. Δ represents the distance between two slabs which can be calculated for HST by using its interlayer distance d_{001} = 10 Å. Knowing the thickness of an inorganic layer (~ 9Å), we have Δ_{HST} = 1 Å.

For HST, the counterions are the protons with a valence q = +1. In addition, we approximate the relative dielectric constant of HST to the one of BST which is worth 100.[28] Thus, the dielectric jump is $\delta_\epsilon = -0.12$. This value is low enough to neglect the effect of the dielectric jump. The characteristic lengths and electrostatic coupling parameters can thus be determined:

$$l_B = \tilde{l}_B = 7.2\ \text{Å} \qquad \mu = 0.35\text{Å} \qquad a = 1.59\ \text{Å} \qquad \Xi = 21$$

We notice that the criteria from ***Equation 13*** and ***14*** are fulfilled ($\Xi_{HST} > 12$ and $\Delta_{HST} < a_{HST}$). Thus, the contribution of the electrostatic interactions should be attractive as HST can be described by the strong coupling regime. Besides, for two like-charged plates, the total energy of the system is the sum of the electrostatic energetic contribution and the repulsive entropic contribution of the counterions:

$$E_{electrostatic} = U_{Energetic} + U_{entropic} = \left|2\pi l_B \sigma_S^2 \left(-1 + \frac{2\mu}{\Delta}\right) k_\beta T\right| \qquad \textbf{Equation 15}$$

It results that $E_{electrostatic} = 348\ \text{mJ.m}^{-2}$ for HST. In the following, we will only consider this electrostatic contribution and we will neglect the Van der Waals interactions. Thus, we can determine the minimum shear rate to separate two oxide layers.

As we consider the square plate has a lateral dimension of 1 µm and we consider isopropanol for exfoliation, we calculate the minimum shear rate from ***Equation 7***. We find that $\dot{\gamma_{min}} = 5.6 \times 10^7\ s^{-1}$. This value is much larger than the minimum shear rate needed for exfoliation of graphite (~10^4 s^{-1}). Besides, this shear rate cannot be reached by our IKA Ultraturax disperser with respect to its geometry and power capacity. This minimum shear rate corresponds to a speed of 4.7×10^5 rpm while the maximum shear rate available is 6×10^4 s^{-1} (which corresponds to a maximum speed of 30000 rpm). Thus, we demonstrate here that electrostatic interaction cannot be overcome by shear-force and HST cannot be delaminated by mechanical force-assisted liquid exfoliation.

This finding apparently infirms the work of S-J. Hwang *et al.* who used mechanical force to exfoliate bare charged layered oxides such as HTO ($H_{1.07}Ti_{1.73}O_4$) or MnO_2.[15] One explanation might be that our calculations are only made for shear force while the authors combine both shear and cavitation forces. Moreover, the charge density of the inorganic sheets they consider is smaller than the ones in HST.

However, we can also allocate these opposite results to the limitations of our model. Indeed, according the work of R. Netz *et al.*,[27] and considering the value of Ξ_{HST} , we might consider that HST would rather belong to an intermediate regime between the strong coupling one and the mean-field one (see ***Figure 2 (c)***). In this in-between, the electrostatic contribution might be repulsive or/and attractive. In

addition, the strong coherence of the oxide layers would rather come from stronger Van der Waals interaction as the layer oxide displays a large polarization.[28] Monte-Carlo simulation or Molecular Dynamic should be performed in subsequent work to precisely determine the interactions between the slabs. Nevertheless, our calculations allows to illustrate that shear-force is less adapted for charged layered oxides. In any case, we will show experimentally that high-shear disperser is inefficient to exfoliate HST.

IV.2.3 Case of hybrid layered oxide

We demonstrate previously that bare layer oxide cannot be exfoliated by shear-force. We now review the case of hybrid layered oxide in which the layers are more distant one from each other due to the grafted molecules. To our knowledge, no description of such system in terms of energy of interactions has been reported in literature. We consider the case of $C_{12}O$-HST which will be used in the following exfoliation experiments. Its interlayer distance d_{001} is worth 40 Å corresponding to a slab-to-slab distance of $\Delta_{C12O\text{-}HST}$ = 31Å. In addition, the functionalization allows to reduce the charge density of one inorganic layer. From the elemental formula, we deduce that $\sigma_S = 3.44\times10^{-2}$ Å^{-2} (mostly half the charge density of HST). The interlayer medium is mostly composed of hydrocarbon chain with $\varepsilon_r = 2$. We calculate the characteristic values from ***Equation 9*** to ***Equation 12***:

$$l_B = \ell_B = 280\text{Å} \qquad \mu = 1.6\times10^{-2}\text{Å} \qquad \Xi = 1.75\times10^{4} \qquad a = 2.15\ \text{Å}$$

In that case, $\Xi \gg 1$ but the Rouzina-Bloomfield criterion is not fulfilled. Besides, as $\Xi > \frac{\Delta/\mu}{\ln(\Delta/\mu)}$, the system does not belong to the mean-field regime anymore. Here, $C_{12}O$-HST belongs to the intermediate regime and corresponds to the situation described in ***Figure 2 (c)*** where $\mu < a < \Delta$. As in the case of HST, we consider here a 2D-arrangement of the counterions (*i.e.* the protons) in the vicinity of the inorganic slab. The electrostatic contribution might be attractive but no clear description of such regime is reported. In addition, the short-range Van der Waals interactions are decreased in $C_{12}O$-HST and there is not interdigitation between the molecules. Thus we can exclude the addition of hydrophobic interactions between the two facing organic layers. Considering the coherence between the slabs and the absence of interdigitation of the molecules, we can hypothesize the attractive behavior of the electrostatic force from charged slabs, even at a larger distance, which allows to maintain the stacking.

Even if the hybrid system presents attractive electrostatic forces, the grafted molecules decrease the overall interactions between the two oxide layers. Thus, the system should be more adapted for exfoliation using shear-force assistance. Once again, more advanced studies should be carried out to elucidate the interactions between the slabs in hybrid layered materials

IV.3. Optimization of shear force-assisted liquid exfoliation

IV.3.1 Introduction

In ion-exchange assisted exfoliation, there are two core elements, the exfoliating agent and the layered materials, whose interactions are crucial in the exfoliation mechanism. One has to determine the optimal ratio between both components.[29] In addition, the exfoliation time is poorly studied; most of the experiments are conducted over days or weeks to insure the exfoliation even though some studies report that exfoliation occurs in fact almost immediately.[30] Besides, experiments are restricted to be carried out in water.

At the opposite, shear force-assisted liquid exfoliation does not involve any additional chemical. It should prevent the replacement of the initial functionalization during the exfoliation process. Thus, the exfoliation can occur in organic solvent which can be tuned to prevent nanosheets degradation as observed by M. Yan *et al.* in their study of chemical stability of Zn-Se upon exfoliation.[31] Nevertheless, the shear-assisted exfoliation requires optimization: many parameters must be tuned to reach a concentrated solution of nanosheets.

In the following, we will focus on the main exfoliation parameters which are the solvent, the exfoliation time and the shear rate. Thus, we study how their control is correlated to the size, thickness and shape of the obtained hybrid nanosheets, starting with C_{12}O-HST as precursor. Influence of the grafted molecules will also be discussed by studying shear-exfoliation of two hybrids, C_{12}O-HST and BenzO-HST presented in **Chapter II**, whose main difference is their carbon skeleton. Otherwise, the other relevant parameters such as volume and temperature are set constant all along the experiments. A complete description of their impact on shear exfoliation has been reported by Coleman *et al.*[5,23] We assume that their conclusions can be transposed to our system and exfoliation process.

As already discussed in **Chapter I**, we do not consider an exfoliation yield to quantitatively characterize the exfoliation and follow the influence of one parameter. The definition and estimation of such yield vary in many works of the literature and cannot be directly transposed to our system.[5,15,32] Therefore, in this part, we do not intend to calculate an exfoliation rate (*e.g.* by weighting the nanomaterials in suspension for instance). The quality of exfoliation will be evaluated from Scanning Electron Microscopy images and intensity auto-correlation function (also called correlogram) from Dynamic Light Scattering (Zetasizer).

IV.3.2 Role of the solvent

IV.3.2.1 Solubility parameters and choice of the solvent

In liquid-phase exfoliation, the importance of solvent is obvious. First, it transposes a mechanical movement (rotor) into the mechanical force which allows exfoliation. The shear rate is inversely proportional to the dynamic viscosity of the solvent. The viscosity is also implied in the aggregation

mechanism of particles in solution. In addition, we easily guess its crucial role in the subsequent colloidal stability of the nanomaterials. Therefore, the choice of the solvent must be done rationally, based on theoretical background. Thus, we first review how solvents are involved in exfoliation from literature, before discussing the experimental data.

In their works, J. Coleman *et al.* have largely investigated the dispersion of nanomaterials in a solution.[22] The authors intended to generalize the Hildebrand solubility parameters which dictate the solubility of a solute (usually a molecule or a polymer) into a liquid media. The classical Hildebrand solubility parameters account for the possible interactions a molecule might have with another one (such as hydrogen bond, Van der Waals interactions). Thus the mixing of two components in liquid phase is dictated by:

$$\Delta G_{mix} = \Delta H_{mix} - T\Delta S_{mix} \qquad \textbf{\textit{Equation 16}}$$

Mixing is favourable when $\Delta G_{mix} < 0$ which implies that, as ΔS_{mix} is small for large and rigid objects, ΔH_{mix} must be minimized. This minimization is carried out by choosing the right solvent *i.e.* the solvent which allow the ΔH_{mix} to be as small as possible. The latter is expressed as

$$\frac{\Delta H_{mix}}{V_{mix}} = \Phi\,(1-\Phi)\left(\delta_{T,S} - \delta_{T,N}\right)^2 \qquad \textbf{\textit{Equation 17}}$$

Where Φ is the solute volume fraction, $\delta_{T,S}$ and $\delta_{T,N}$ are the Hildebrand solubility parameters of the solvent and the solute respectively. The Hildebrand parameter results from the addition of three distinct contributions, δ_D, δ_P, δ_H such as $\delta^2_{Hildebrand} = \delta^2_D + \delta^2_P + \delta^2_H$ where δ_D account for the non-polar interaction, δ_P accounts for polar interactions and δ_H accounts for all the other interactions including hydrogen bond. We notice that mixing will be favoured when $\delta_{T,S}$ and $\delta_{T,N}$ are similar.

Coleman *et al.* derived a similar expression with a factor $\frac{1}{3}$ as ***Equation 17*** when the solute is 2D plate. Thus, they underline the necessity of matching solubility parameters of solvent and nanomaterials in order to thermodynamically ensure the exfoliation and the dispersibility of the nanomaterials. The enthalpy of mixing can be assimilated to the energy required for exfoliation and the solubility parameters $\delta_{T,S}$ and $\delta_{T,N}$ are linked to the surface energy of solvent and inorganic layers respectively. Besides, we have seen with ***Equation 7*** that the minimum shear rate is also minimized when there is a matching between both surface energy of solvent and layered materials.

In our case, dealing with hybrid layered oxides whose surface properties are modified by the grafting of an organic molecule, we hypothesize that it is more relevant to consider the solubility parameter of the grafted molecules than the solubility parameter of the inorganic layer itself. In addition, we must also consider the remaining charge density at the vicinity of the inorganic layer despite the long alkyl chain.

A spontaneous reasoning would lead to use the same solvent as the one used for functionalization, in which the molecules are at least soluble. Nevertheless, if THF was able to disperse and stabilize of functionalized nanosheets, we should not be able to get stacked and crystalline layered materials after

functionalization. Besides, M. Yan *et al.* demonstrate the disability of THF to produce nanosheets in liquid exfoliation of layered ZnSe hybrids (functionalized by alkylamine).[31] We must look at other polar solvents which are better known to be efficient in mechanical-assisted exfoliation.

Therefore, we first consider 2-propanol (IPA) as relevant candidate for shear force exfoliation. IPA is polar protic solvent which can usually solubilize alcohol derivatives. It was proved to be efficient in exfoliation of molybdenum trioxide,[33] boron-nitride (BN),[1] the Aurivillius phase $CoBi_2O_2F_4$,[10] and zirconium phosphate derivatives.[34] In addition, compared to usual efficient exfoliation solvent such as N-methylpyrrolidone (NMP) or dimethylformamide (DMF), 2-propanol is less toxic, easier to manipulate and allows a better use of nanosheets (*e.g.* deposition on a substrate).

Y. Sugahara *et al.* delaminated a perovskite-like layered oxide, $HLaNb_2O_7$, decorated with fluoroalkoxy chain, *via* sonication-assisted exfoliation. Despites the strong hydrophobicity of the organic chain, acetonitrile, an aprotic and highly polar solvent was used as exfoliation solvent and allowed the exfoliation. Therefore, as our hybrid materials can be related to some extend to the one of Y. Sugahara *et al.*, we hypothesize that nanosheets might be easily obtained using acetonitrile.

In parallel, Y. Oaki *et al.* reported the exfoliation of a hybrid layered titanate by stirring the materials in toluene at relative low temperature (80°C). Thus, we also investigated the shear-exfoliation of hybrid layer oxide using toluene: the energy brought by the disperser should compensate the energy brought by temperature in Y. Oaki's experiment.

Finally, it is interesting to study the opposite situation *i.e.* using a protic and highly polar solvent such as water. In that case, we expect charge stabilization of the inorganic layer but mismatching with the long alkyl chain.

In ***Table 1***, we list the solubility parameters of the considered solvents as well as 3 hydrocarbons which mimic grafted alkoxy derivatives (we suppose the grafted function *i.e.* the alcohol does not play any role in solubility of the attached molecules).

We notice that the non-polar contribution of isopropanol and acetonitrile is close to the one of *n*-dodecane whereas the non-polar parameters of water and toluene are a bit higher and lower respectively. However, the main difference between the solvent relies on their polar and H-bonding parameter.

Toluene is barely polar and displays a weak δ_H parameter. These criteria match with the *n*-dodecane parameters, which do not show any polar or H-bonding contribution. Thus, regarding the solubility parameters, toluene should be the best solvent to exfoliate layered hybrid with an alkyl chain.

In opposition, isopropanol and acetonitrile display higher δ_H and δ_P parameter than toluene and should be less suitable for exfoliation of C_{12}O-HST.

Finally, water displays both the highest δ_P and δ_H among the considered solvents which should make it, not surprisingly, the worse solvent for C_{12}O-HST exfoliation.

In the following, we will determine experimentally the best solvent for shear exfoliation of C_{12}O-HST and compared the results with the predictions we draw from Hildebrand solubility parameters.

Solvent	Non-Polar δ_D $(M.Pa)^{-1/2}$	Polar δ_P $(M.Pa)^{-1/2}$	H-Bonding δ_H $(M.Pa)^{-1/2}$	Hildebrand parameter $(\delta^2 = \delta_D^2 + \delta_P^2 + \delta_H^2)$ $(MPa)^{-1/2}$	Surface tension $(\times 10^{-3}\ N.m^{-1})$	ε_r
n-pentane	14.5	0	0	14.5	15.8 at 20°C	1.841
n-decane	15.8	0	0	15.8	/	1.989
n-dodecane	16.1	0	0	16.1	/	2.002
Toluene	18.0	1.4	2.0	18.1	28.5 at 25°C	2.430
Tetrahydrofuran	16.8	5.7	8	19.4	/	7.47
2-propanol	15.8	6.1	16.4	23.6	21.7 at 20°C	18.23
Acetonitrile	15.3	18.0	6.1	24.3	29.3 at 25°C	35.94
Water	15.5	16	42.3	47.8	72.0 at 25°C	78.5

Table 1: Detail of the Hildebrand solubility parameters, surface tension and dielectric constant of solvents used for exfoliation.

IV.3.2.2 Exfoliation and characterization

The exfoliation experiments were carried out using C_{12}O-HST or BenzO-HST as hybrid layered materials. Typically, 20 mg of the compound was dispersed in 40 mL of the chosen solvent at room temperature. The disperser tip was immersed until it laid at around 1 cm from the bottom of the beaker (diameter of 3.5 cm). The rotor speed was set at 11500 rpm (*i.e.* a nominal shear rate of 2.3×10^4 s^{-1}) and the exfoliation time was 5 minutes. Following the exfoliation, the resulting solution went through a selective centrifugation process as described in **Chapter III**. The resulting nanosheets solution is characterized by DLS (Zetasizer) and SEM in STEM mode (see **Chapter III**).

First, we visually observed the bare exfoliated C_{12}O-HST solution. The exfoliation experiments, carried out with acetonitrile or isopropanol, lead to a stable white and blurry solutions right after the exfoliation. This observation attests the presence of dispersed layered oxides.

In addition, it is worth mentioning that dispersing the hydrophobic C_{12}O-HST in water was not trivial as the powder tends to stay at the air-water interface or was stuck on the beaker wall. However, by moving up and down the disperser at the beginning, a part of the powder was dispersed. At the end, a white and blurry solution is obtained even if sediment quickly appears at the bottom of the beaker.

The experiments using toluene as solvent does not lead to solution with the same aspect: the solution appears as clear, without any dispersion. Besides, during the exfoliation, the C_{12}O-HST powder tends to be stuck to the beaker wall. These observations are in contradiction with what is expected by the comparison of solubility parameters. However, we cannot be conclusive here, only with the aspect of the solutions.

After the selective centrifugation process, the supernatants from shear-exfoliation of C_{12}O-HST in different solvents are characterized by DLS. ***Figure 3*** shows the intensity auto-correlation functions of the supernatant 4 in various solvents and their corresponding size distribution. Considering the model used by the Zetasizer software to calculate a distribution function *i.e.* the model of homogeneous and monodisperse hard sphere, the size distributions cannot be fully trusted (see **Chapter V**). However, the

number of "peaks" is related to the number of relaxation times which is still valid for "in range" correlogram, independently of the model.

The C_{12}O-HST nanomaterials in acetonitrile and isopropanol lead to a correlogram in the good range, which displays at least two characteristic decay times as illustrated by the size distribution. Thus, nanomaterials with a large aspect ratio are expected to be present in a large proportion on these two solutions.

Surprisingly, the exfoliation of the hydrophobic layered hybrid C_{12}O-HST in water leads to a good auto-correlation function which testifies the presence of scatterers in the supernatant. Thus, we were able to disperse and even exfoliate C_{12}O-HST in water. We ascribe such finding to the remaining charge density of the inorganic layer. As proposed by S.J Hwang *et al.*, the protons might interact with water through hydrogen bond which might allow the use of this strongly polar solvent for exfoliation.[15]

In contrast, when using toluene as solvent, the intensity autocorrelation function of the supernatant corresponds to a solution with few or no scatterers. The correlogram is mostly similar to the one of the solvent. This result is in accordance with the clear aspect of the bare solution of exfoliated C_{12}O-HST and the behavior of the powder during the exfoliation process. Thus, we can conclude that toluene, an almost apolar solvent, is not suitable for shear-exfoliation at room temperature. Once again, we ascribe this observation to the remaining charge density *i.e.* the presence of protons next to the oxide layer. Thus, a polar solvent appears to be a *sine qua non* condition for exfoliation of hybridized HST derivatives.

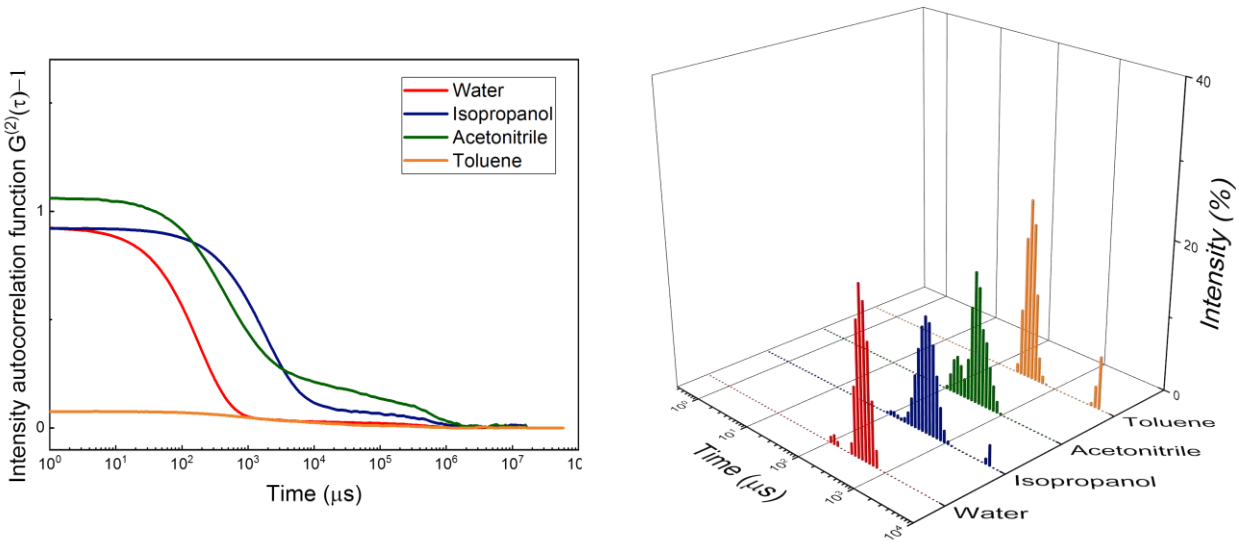

Figure 3: Intensity auto-correlation functions of exfoliated C_{12}O-HST in different solvents and their corresponding size distribution.

Our finding contrasts with the results of Y. Oaki *et al.* who were able to exfoliated a layered titanate in toluene with gentle stirring and heating.[35] Regarding the nature of toluene, we can exclude the hydrolysis of the C_{12}O- moiety. Therefore the difference between the two works may arise from the

difference in oxide charge density and the "screening" of the charge by the organic layer which might be more effective in the hybrid system of Y. Oaki *et al.*

The SEM clichés, like in ***Figure 4,*** allow to better discriminate the different solvents and their effect on exfoliation. The clichés presented in ***Figure 4 (a)*** and ***(b)*** correspond to nanosheets of C_{12}O-HST when using water as solvent. We can clearly observe few-layer nanomaterials with lateral size about 300 nm. Besides, these images highlight the regular shape and angle of the nanomaterials as well as their soft character (exemplified by the folded few-layer nanomaterials in ***Figure 4 (b)***). In parallel, a pile of stacked and thicker layered oxides is seen, showing that exfoliation is incomplete and that selective centrifugation process cannot completely separate materials according to their exfoliation degree. Despites the polydispersity in thickness, we notice that no materials similar to the bulk one (in terms of thickness and lateral size) were imaged: the shear force-assisted exfoliation breaks the hybrid layered oxide into smaller materials.

The exfoliation of C_{12}O-HST in isopropanol leads to better exfoliated materials as depicted by the images ***Figure 4 (c)*** and ***(d).*** Globally, the nanomaterials are larger and thinner than the ones obtained in water. The nanomaterials display the same straight edges with the same angles. Besides, the cliché ***Figure 4 (d)*** confirms that most of the objects are few-layer nanosheets. A monolayer of hybrid oxide has a barely visible contrast in bright field, either in SEM or in TEM (see **Chapter V**).

Finally, exfoliation in acetonitrile allows to produce nanosheets as seen in ***Figure 4 (e)*** and ***(f)***. Piles of few-layer nanosheets can be easily observed as well as non-exfoliated materials (or at least thicker layered oxides). These two images also demonstrate the polydispersity in size and shape in the supernatant.

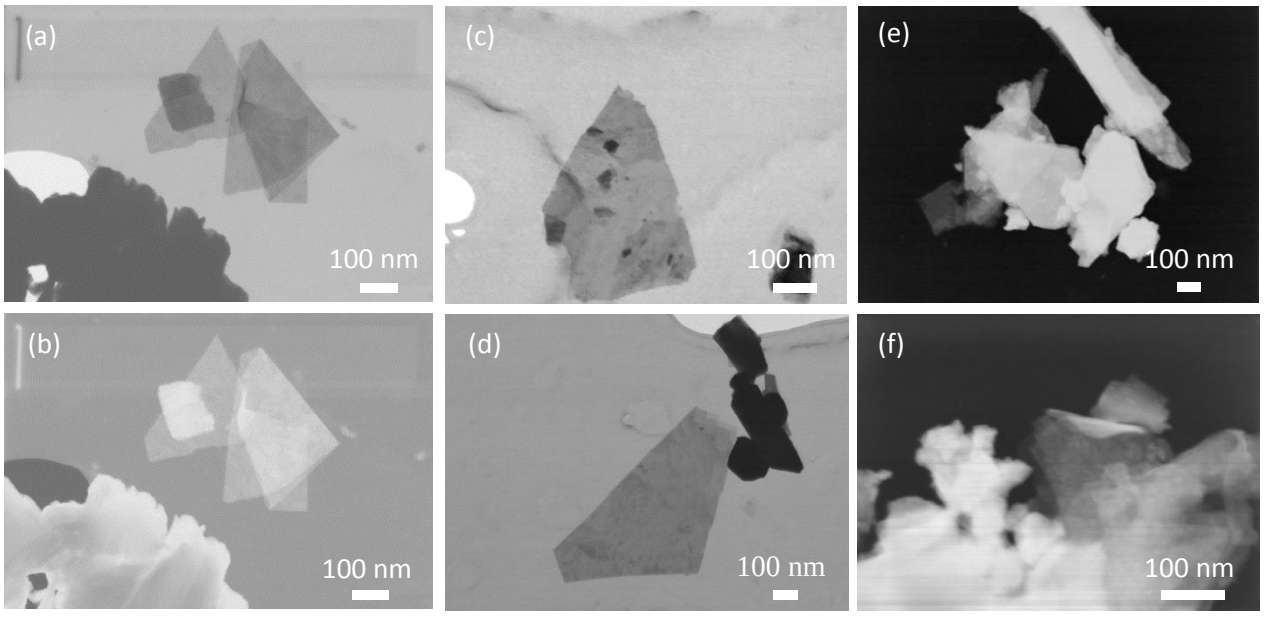

Figure 4: STEM images of C_{12}O-HST nanosheets from exfoliation in (a), (b) water, (c) (d) in isopropanol and (e) (f) acetonitrile.

From the SEM clichés, we can conclude that both isopropanol and acetonitrile are suitable for the exfoliation of C_{12}O-HST as they lead to few-layer materials in solution. Water is less efficient because the proportion of few layer nanomaterials compared to thick one is smaller. Finally, as no image of nanosheets (or even non-exfoliated materials) was obtained, we can assess the non-efficiency of toluene in shear-exfoliation of C_{12}O-HST.

IV.3.2.3 Conclusion

Unlike Van der Waals materials where the matching of solubility parameter is crucial, we demonstrate above that hybrid layered oxides as C_{12}O-HST work differently. Toluene which displays the closest Hildebrand solubility parameter to the one of long alkyl chain (18.1 and 16.1 $(MPa)^{-1/2}$ respectively) is the less suitable solvent among the ones we used. Acetonitrile and isopropanol having higher solubility parameters (24.3 and 23.6 $MPa^{-1/2}$ respectively) are the most efficient to exfoliate C_{12}O-HST. Water with a solubility parameter of 47.8 $MPa^{-1/2}$, is more efficient than toluene but remains less suitable than isopropanol or acetonitrile. Therefore, we hypothesize that for hybrid layered oxides, the polarity of the solvent has to be considered in priority before considering the two other solubility parameters. This hypothesis will be supported by exfoliation of BenzO-HST in different solvents (see below).

IV.3.3 Influence of the shear rate

In a second step, we investigate the influence of the shear rate which is set up by the rotor speed. J. Coleman *et al.* demonstrated the power dependency of the concentration in nanomaterials with respect to the shear rate. In addition, the authors showed that increasing the rotor speed can lead to similar or larger nanosheets when exfoliating graphene, which is somehow counter-intuitive.[5,4] Therefore, a peculiar look will be put on the size an thickness of the resulting nanomaterials. We choose here acetonitrile as exfoliation solvent as we proved its efficiency in previous paragraph. Isopropanol could also have been chosen. Once again, the layered hybrid oxide is C_{12}O-HST.

IV.3.3.1 Synthesis and characterization

The hybrid oxide, C_{12}O-HST (25 mg), was poured into 40 mL of acetonitrile. The powder was dispersed and exfoliated *via* the use of a disperser at different speeds, corresponding to different shear rates. Six different speeds were chosen, from 8000 rpm to 30000 rpm (***Table 2***). The exfoliation time is set to 5 minutes. After the exfoliation, the resulting solution went through the selective centrifugation process. The supernatant of the last centrifugation step is characterized by DLS and SEM.

Rotor speed (rpm)	8000	9500	11500	14500	20500	30000
Shear rate (s^{-1})	15900	18900	22900	28900	40800	59700

Table 2: Table of equivalence between rotor speed and shear rate, calculated using the following equation $\dot{\gamma} = \frac{\pi DV}{\Delta R}$ ***where*** $\dot{\gamma}$ ***is the shear rate, D is the rotor diameter (5 mm),V is the rotor speed,*** ΔR ***is the gap between rotor and stator (0.1 mm).***[5]

The ***Figure 5*** shows the intensity auto-correlation functions of the supernatant from exfoliation experiments at different shear rates. At the minimum rotor speed, the correlogram is out of range, meaningful of large and polydisperse C_{12}O-HST particles in solution. When increasing the speed, from 9500 rpm and above, the corresponding auto-correlation function for supernatant is in-range (limits at 0 and at infinite are 1 and 0 respectively).

The solutions corresponding to exfoliation at 9500 rpm, 11500 rpm and 14500 rpm display correlograms with at least two decay times. It might be relevant of two size populations of nanomaterials. However, when increasing the speed (20500 rpm and 30000 rpm), the resulting auto-correlation function is similar to the one of monodisperse and relatively small nanomaterials.

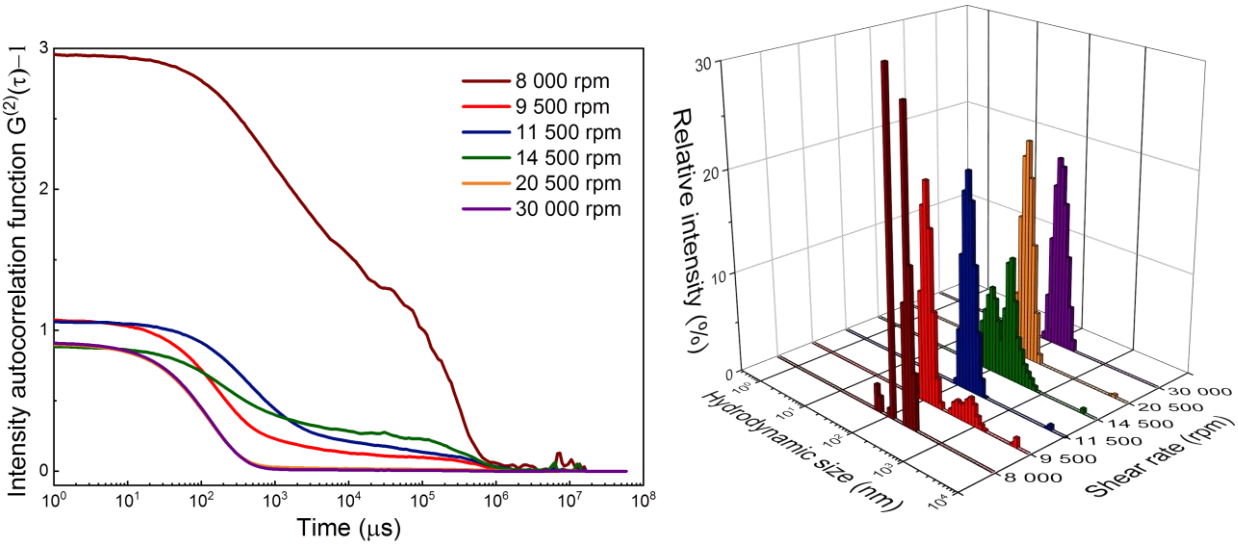

Figure 5: (Left) Intensity auto-correlation functions from suspension of exfoliated C_{12}O-HST in acetonitrile, obtained after exfoliation at different shear rates and (right) their corresponding size distribution determined using the Zetasizer.

The SEM clichés in ***Figure 6*** illustrate the evolution of the nanomaterials mean size depending on the nominal shear rate. Exfoliating at low shear rate, leads to the fragmentation of a part of the initial layered oxide but thick and large micrometer-scaled materials remain. This snapshot is in accordance with the autocorrelation function presented in ***Figure 5.*** Increasing the shear rate allows to get more exfoliated nanomaterials but also smaller as depicted by ***Figure 6 (b)*** and ***(c).*** Besides, for high shear rate, we notice the appearance of small particles (around 50 nm) which become numerous at the maximum rotor speed of 30000 rpm. However, all the experiments display polydispersity in size, thickness and shape which is all the more noticeable for the suspension obtained using low shear rate.

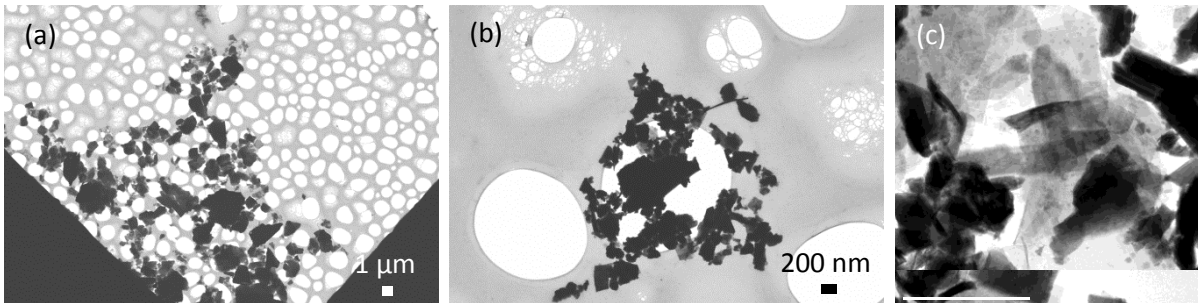

Figure 6: (a),(b)SEM images and (c)TEM image of exfoliated C_{12}O-HST from exfoliation experiments carried out using a rotor speed of (a) 8000 rpm, (b) 14500 rpm and (c) 30 000 rpm.

IV.3.3.2 Conclusion

We show that shear rate strongly impacts the nanomaterials size and thickness. At low shear rate, large and un-exfoliated layered oxides are predominant in the last supernatant while at high shear rate, the objects are smaller (less than 200 nm) with a better size distribution. Therefore, in the following, we choose an intermediate shear rate of 22900 s^{-1} (*i.e.* a speed of 11500 rpm) for exfoliation in order to get large enough flakes even though thicker and larger particles will also remain.

IV.3.4 Influence of the exfoliation time

One of the main advantages of shear force-assisted liquid exfoliation is the short exfoliation time compared to the ion-exchange assisted exfoliation or to the exfoliation of hybrid oxides by swelling in organic solvent.[13,14] Many exfoliation times can be found in literature dealing with shear force-assisted liquid exfoliation of layered materials. For hybrid zirconium phosphate, V. Zima *et al.* considered a short exfoliation time of only 3 min,[34] while for kaolinite X. Huang *et al.* chose the same exfoliation time of 20 min as Coleman *et al*. did for graphene.[5,20,36] Longer exfoliation times are also usually reported for a large panel of materials,[8,15,31,37,38] but they do not exceed 6 hours. Besides, according J. Coleman *et al.*[5] increasing the exfoliation time at a fixed shear rate does not affect the lateral size.

Similarly to the previous paragraph, we will quickly study here the influence of the exfoliation time on the nanosheets size and thickness.

IV.3.4.1 Exfoliation and characterization

We carried out shear-force exfoliation of C_{12}O-HST in acetonitrile at a rotor speed of 11500 rpm. We consider three exfoliation times: 5 minutes, 15 minutes and 60 minutes. The resulting few-layer nanosheets solutions went through a selective centrifugation process. Therefore, only the supernatants of the last centrifugation step are analyzed.

Figure 7 shows SEM pictures of C_{12}O-HST nanosheets from exfoliation during 5 and 60 minutes. Both experiments lead to the exfoliation of the native layered oxides with similar lateral size between 100 and 500 nm. We observe also thick nanomaterials in all three experiments as well as polydispersity in size

and shape. In our case, we were unable to characterize the quantity of nanomaterials in solution which would be the best indicator of the influence of exfoliation times.

Therefore, we performed weighting of the nanomaterials all along the centrifugation process to determine the mass of the remaining hybrid materials after each step. Unfortunately, the accuracy of the balance was not sufficient to determine the nanomaterials mass in the last supernatant. We thus were not able to draw any conclusion on the influence of the exfoliation time from a potential "yield".

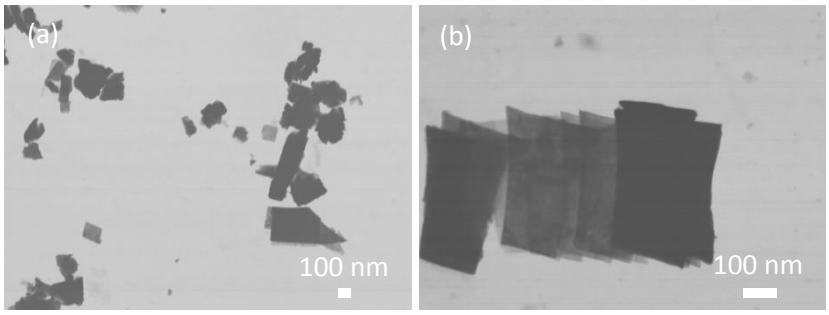

Figure 7: SEM images of C_{12}O-HST few-layer nanosheets from exfoliation in acetonitrile for (a) 5 min and (b) 60 min.

IV.3.4.2 Conclusion

Modifying the exfoliation time, from 5 minutes to 1 hour, does not modify the lateral size of the resulting few-layer nanosheets as observed by Coleman *et al.* for the shear exfoliation of graphene.[5] However, we cannot conclude precisely on its influence on the exfoliation yield which is tricky to quantify. Nevertheless, in the following we will consider longer exfoliation time as it should insure a better exfoliation yield.

IV.3.5 Influence of the grafted molecule on the hybrid exfoliation

Up to now we have modified three parameters on shear force exfoliation: the nature of the solvent, the shear rate and the exfoliation time. The two latter vary as expected from the literature. However, concerning the solvent influence, the conclusion differs from the work of J. Coleman *et al.* Indeed, we demonstrated that the layered hybrid oxide C_{12}O-HST is well exfoliated in acetonitrile or isopropanol despite the mismatch of solubility parameter. Indeed, one has to take into account the remaining charge density *i.e.* remaining protons at the layer vicinity which imposes the use of a polar solvent.

On this part, we aim at highlighting the role of the molecular grafting on the exfoliation of the hybrid oxide. Therefore, we study the shear force exfoliation of BenzO-HST, which presents an aromatic ring. Similarly to C_{12}O-HST, we will determine the best solvent for exfoliation. We do not investigate the influence of shear rate and exfoliation time as they appear to be less determinant on the nanomaterials dimensions than solvents.

IV.3.5.1 Exfoliation and characterization

We carried out shear exfoliation of BenzO-HST using a shear mixer at a nominal speed of 11500 rpm for 15 minutes. Typically, 20 mg of BenzO-HST were dispersed and exfoliated using three different solvents, water, toluene and acetonitrile. The resulting solution went through a selective centrifugation process. In the following, we base our discussion on the last supernatant which is characterized by DLS and SEM.

After exfoliation, we obtained white and blurry solutions when using acetonitrile or water as solvent. It indicates that nanomaterials are dispersed despite the polar solvent and the grafting, which confers hydrophobicity to the hybrid oxide. In contrast, the resulting solution when using toluene is clear and transparent which is meaningful of few or no nanomaterials in solution. Besides, the hybrid powder tends to stuck to the beaker wall during exfoliation as it goes for C_{12}O-HST.

Figure 8 shows the intensity auto-correlation functions of three solutions of BenzO-HST nanomaterials and three solutions of C_{12}O-HST nanomaterials for comparison. It is worth mentioning that concerning exfoliation of C_{12}O-HST, the correlograms are similar to the ones in ***Figure 3*** where the exfoliation time was 5 min. The autocorrelation function from experiments with toluene is a bit better but still does not tend to 1 at low delay times.

Considering the exfoliation using water as solvent, the autocorrelation function is out of range, meaningful of large and polydisperse materials. The correlogram of BenzO-HST in water differs from the correlogram of C_{12}O-HST in the same solvent. It might be due to either bigger non-exfoliated BenzO-HST materials or to very large exfoliated nanosheets with a huge size polydispersity.

The autocorrelation function of the nanomaterials dispersed in acetonitrile is similar for both BenzO-HST and C_{12}O-HST, and shows that acetonitrile is also able to disperse and exfoliate BenzO-HST. Nevertheless, there again, this autocorrelation function displays two decays times, which indicates the presence of two size populations in the suspension.

Concerning the exfoliation using toluene as solvent, the corresponding autocorrelation function is similar to the one of pure toluene. It means that there are not nanomaterials in solution or at a very low concentration. In comparison, the correlogram of C_{12}O-HST nanosheets in toluene is a bit better which means there is a little more particles in solution. Thus, the BenzO-HST has even less affinity with toluene. We ascribe this behavior to the remaining charge density and the related protons that tend to disfavour non-polar solvent for exfoliation. The better results with C_{12}O-HST compared to BenzO-HST can be explained by a better charge screening by the molecular layer. Such screening might be more efficient in the case of long alkyl chain compared to short aromatic ring. This assumption is supported by the work of Y. Oaki *et al*. who used toluene as solvent for exfoliation of octadecylamine-based titanates[13] whereas the authors rather used acetonitrile (polar solvent) for exfoliation benzylamine derivatives-based titanates oxides.[39]

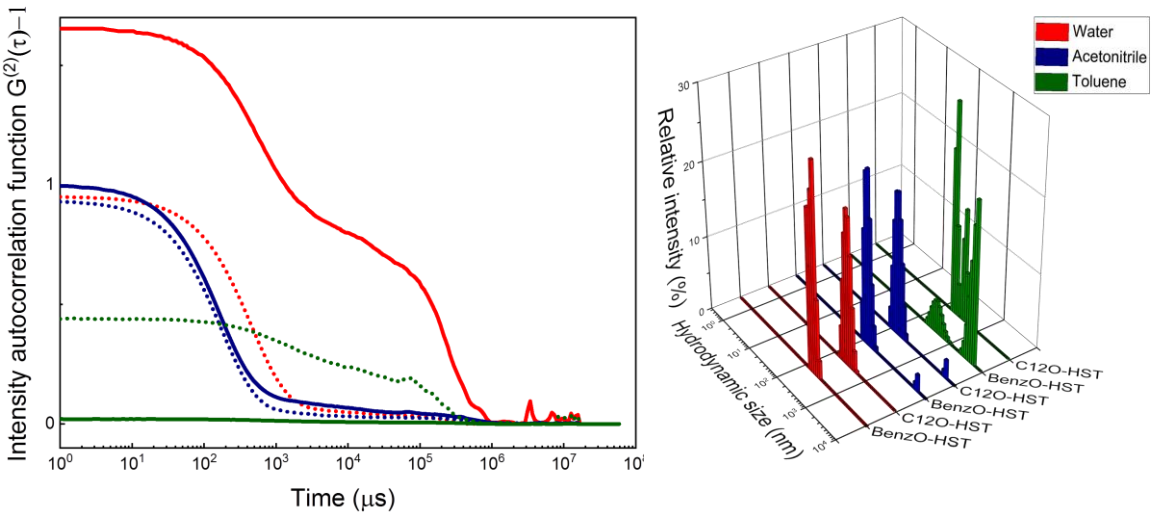

Figure 8: (Left) Intensity auto-correlation functions of exfoliated BenzO-HST (solid line) and C_{12}O-HST (dot line) after exfoliation in water (red), acetonitrile (blue) and toluene (green). (Right) The corresponding size distributions for the six experiments.

Figure 9 (a) to ***(c)*** show SEM images of BenzO-HST nanomaterials from an exfoliation of the corresponding hybrid oxide in acetonitrile. Large few-layer nanosheets (around 1μm of lateral size) can be observed as well as smaller nanosheets on top of them. These two distinct size populations are consistent with the DLS autocorrelation functions

Figure 9 (d) to ***(f)*** show SEM images of BenzO-HST nanomaterials from an exfoliation of the corresponding hybrid oxide in water. In that case, we were also able to record images of large few-layer nanosheets with non-exfoliated materials. These observations may appear contradictory with DLS results. However, local probing by near-field techniques such as SEM, TEM or AFM often gives the illusion of well exfoliated nanomaterials. Therefore, only in-solution characterization of nanomaterials can provide a general aspect of the nanomaterials. Thus, microscopic clichés should away be accompanied with scattering techniques to be fully consistent.

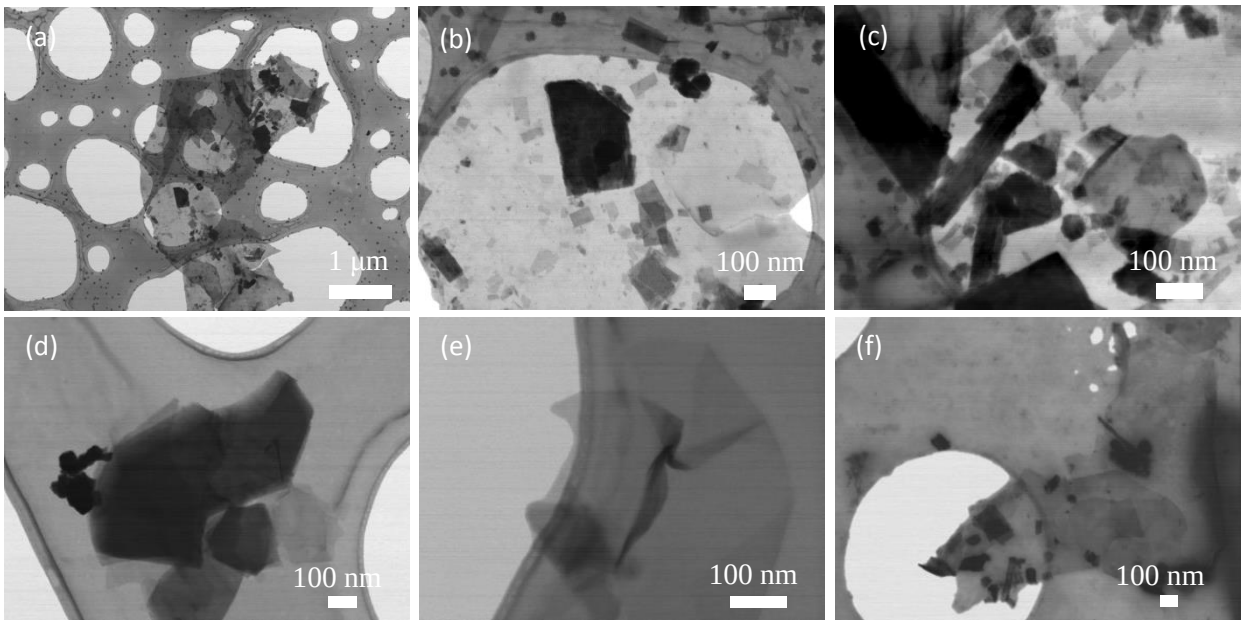

Figure 9: SEM images of BenzO-HST few-layer nanosheets after exfoliation in (a) to (c) acetonitrile and (d) to (f) in water. The small dots in images (a) to (c) correspond to an external contamination with nanoparticles during the deposition of the suspension on the grid.

IV.3.5.2 Conclusion

We investigated the influence of the solvent on the exfoliation of BenzO-HST. We have shown that acetonitrile is able to exfoliate BenzO-HST despite an important solubility parameter mismatch. Thus, we can extend the conclusion drawn for C_{12}O-HST to all hybrid layered oxides *i.e.* it is crucial to have a polar solvent to exfoliate such hybrid. In addition, we demonstrate a different behavior of the BenzO-HST compared to C_{12}O-HST according to the solvent: it proves that the grafting might have an effect notably on the screening of the charge density. Therefore, in the following we will adapt the exfoliation solvent to the hybrid layered material in presence.

IV.4. Comparison with sonication assisted exfoliation

As reviewed in the **Chapter I**, sonication is also a mechanical force-assisted liquid exfoliation where cavitation forces allow to delaminate the layered materials. However, its use in the exfoliation of Van der Waals materials suffers from some drawbacks. First, the method induces a fast and non-negligible heating of the solvent which might be detrimental for the exfoliation yield.[5,23] In addition, it was proved that the resulting nanosheets display defects, generated during the exfoliation as the cavitation process is brutal and exothermic. This latter point is of upmost importance when considering the properties of the nanosheets which are strongly dependent on their crystallinity.

In the case of charged layered oxides, some authors report the use of sonication-assisted exfoliation to synthesis oxide nanosheets.[10,33,40,41] However, they do not investigate the generation of defects during the process. In addition, none of them consider the comparison of the flake lateral size and size distribution produced by sonication and shear force. Therefore, in the following, we will investigate

the use of sonication to exfoliate a hybrid layered oxide, C_{12}O-HST. We will compare the as-synthesized nanosheets from their lateral size and/or size distribution to the nanosheet obtained by shear exfoliation. We assume than the same conclusions on solvent choice or exfoliation time, drawn for shear-exfoliation, can be applied to sonication-assisted exfoliation.

IV.4.1 Exfoliation and characterization

The hybrid layered oxide, C_{12}O-HST (20 mg), was dispersed in 40 mL acetonitrile (as we proved this solvent is efficient to exfoliate the considered hybrid). The power was set at 40%. To prevent from the rapid heating of the solution, the beaker was poured in an ice bath and we introduced an alternative pulse for the sonication (see **Experimental Section**). We performed two experiments under these conditions: the first one for 10 minutes while the second for 1 hour. The resulting solution went through a selective centrifugation process as described in **Chapter III**. We only analyze the last supernatant from this process by SEM.

Figure 10 shows SEM clichés of the supernatants. First, we notice the presence of nanomaterials which correspond to few layer-nanosheets as well as thicker nanomaterials. Thus, sonication-assisted exfoliation also allows to produce nanosheets from C_{12}O-HST. In addition, as for shear exfoliation, the solvent, acetonitrile, allows the delamination and stability of the nanomaterials. In the case of 10 minutes of sonication, the resulting nanomaterials in the supernatant are thicker than the ones after 60 minutes of sonication. It attests than a longer exfoliation time favours the delamination. Besides, when exfoliating for 60 minutes, the concentration of nanosheets is higher as attested by the large pile of nanosheets in ***Figure 10 (d)***.

These observations support the assumption we made on the application of the conclusions from IV.3.2 and IV.3.4 to sonication.

Concerning the lateral size, the nanomaterials produced by sonication-assisted exfoliation are smaller than the ones from the shear force-exfoliation. As depicted by ***Figure 10,*** the lateral sizes are around 100 nm either when exfoliating for 10 minutes or for 60 minutes. Thus, sonication leads to the rapid fragmentation of the initial layered oxide crystal. J. Carrasco *et al.* also reported the fragmentation of a layered double hydroxide when exfoliating by sonication assistance.[42] For a similar exfoliation time, shear-force seems to produce larger nanomaterials. However, we cannot state on the mean thickness or compare it with the one from shear-exfoliation.

In this study, we did not investigate the power of the sonication tip which should play an important role in exfoliation *(i.e.* it is the equivalent of shear rate in shear-exfoliation). The power was set at 40 % which is the maximum input power available with the apparatus. Thus, by decreasing this parameter, the resulting nanosheets might be larger whereas the mean thickness might increase.

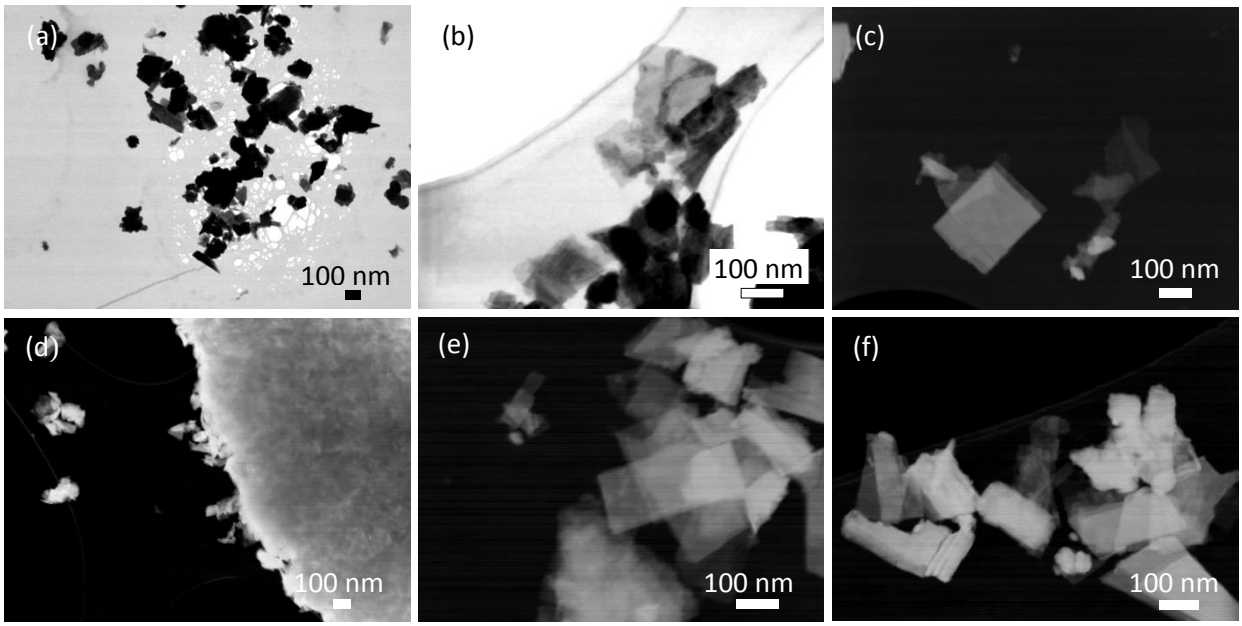

Figure 10: SEM images of C_{12}O-HST nanosheets from sonication-assisted exfoliation in acetonitrile for (a) to (c) 10 minutes and (d) to (f) 60 minutes.

IV.4.2 Conclusion

As sonication-assisted liquid exfoliation is also based on mechanical forces, the same conclusions on exfoliation parameters we drew for shear force can be applied to sonication. However, even if this process seems to produce more concentrated nanosheets suspension, the resulting nanomaterials are smaller compared to the ones from shear-force exfoliation. Therefore, in the following we will mainly focus on shear force exfoliation.

IV.5. Conclusion of Chapter IV

In this chapter, we first demonstrated the feasibility of producing functionalized oxide nanosheets from the corresponding layered hybrid using shear force assistance. First, we showed that a nude charged layered oxide cannot be exfoliated by this method due to strong electrostatic interactions. Indeed, using strong coupling regime theory, we demonstrated that these latter interactions participate in the attraction of two adjacent slabs and that they are too strong to be overcome by the use of shear forces.

Similarly, by using the same approach, we showed that this attractive behavior is reduced when functionalizing the layered oxides. The layer charged density is decreased by the functionalization. Furthermore, the interlamellar space of the oxide in the bulk material is larger, which leads to a weakening of the electrostatic interactions.

This theoretical study is in accordance with the experimental works of Y. Oaki and Y. Sugahara[14,35,37] but not with a recent experimental work of S. J. Hwang *et al*. [15] on a different layered oxide (*i.e.* mechanical force liquid exfoliation of bare charged layered oxides without hybridization "assistance"). However, the experimental exfoliation trials confirm the necessity of functionalization.

In the second part, we determined the best exfoliation conditions by varying several parameters. First, we investigated the influence of the solvent. It has to be polar to exfoliate and stabilize the hybrid layered oxide. This specificity, compared to Van der Waals materials, arises from the remaining charge density. This result opposes a report by Y. Oaki *et al* who. performed exfoliation of an alkylamine functionalized layered titanate using swelling in toluene.[35] This difference might come from the temperature, the nature of the oxide (*i.e.* the charge density) and the screening of the charges.

The shear rate was also modified and we concluded that a medium shear rate allows to get few-layer nanosheets, without leading to a large quantity of material with a much smaller lateral size. Besides, whatever the shear rate, size and shape polydispersity is observed even if it is less pronounced for high shear rate.

We studied the influence of the exfoliation time and conclude that it has a limited impact on the nanosheets lateral size. However, we suspected it might lead to more concentrate solution when it is longer. In the following chapter, long exfoliation time will be carried out in exfoliation procedure.

In addition, we showed that depending on the molecular grafting at the oxide layer surface, the exfoliating solvent has to be adapted. Nevertheless, we showed that the solvent must be polar for shear exfoliation of functionalized HST, whether the grafted molecule bears an aromatic group or a linear chain. Thus, the solvent should be adapted according to the hybrid.

Finally, we compared shear-force and sonication as they are both mechanical force-assisted liquid exfoliation processes. The latter produces smaller nanomaterials even on a short exfoliation time. Thus, in the next chapters, we will mainly consider shear-force as exfoliation method.

IV.6. Bibliography

(1) Coleman, J. N.; Lotya, M.; O'Neill, A.; Bergin, S. D.; King, P. J.; Khan, U.; Young, K.; Gaucher, A.; De, S.; Smith, R. J.; Shvets, *et a*l. i, V. Two-Dimensional Nanosheets Produced by Liquid Exfoliation of Layered Materials. *Science* **2011**, *331* (6017), 568–571.

(2) Bhimanapati, G. R.; Lin, Z.; Meunier, V.; Jung, Y.; Cha, J.; Das, S.; Xiao, D.; Son, Y.; Strano, M. S.; Cooper, V. R.; Liang, L.; Louie, S. G.; Ringe, E.; Zhou, W.; Kim, S. S.; Naik, R. R.; Sumpter, B. G.; Terrones, H.; Xia, F.; Wang, Y.; Zhu, J.; Akinwande, D.; Alem, N.; Schuller, J. A.; Schaak, R. E.; Terrones, M.; Robinson, J. A. Recent Advances in Two-Dimensional Materials beyond Graphene. *ACS Nano* **2015**, *9* (12), 11509–11539.

(3) Gupta, A.; Sakthivel, T.; Seal, S. Recent Development in 2D Materials beyond Graphene. *Progress in Materials Science* **2015**, *73*, 44–126.

(4) Biccai, S.; Barwich, S.; Boland, D.; Harvey, A.; Hanlon, D.; McEvoy, N.; Coleman, J. N. Exfoliation of 2D Materials by High Shear Mixing. *2D Mater.* **2019**, *6* (1), 015008.

(5) Paton, K. R.; Varrla, E.; Backes, C.; Smith, R. J.; Khan, U.; O'Neill, A.; Boland, C.; Lotya, M.; Istrate, O. M.; King, P.; Higgins, T.; Barwich, S.; May, P.; Puczkarski, P.; Ahmed, I.; Moebius, M.; Pettersson, H.; Long, E.; Coelho, J.; O'Brien, S. E.; McGuire, E. K.; Sanchez, B. M.; Duesberg, G. S.; McEvoy, N.; Pennycook, T. J.; Downing, C.; Crossley, A.; Nicolosi, V.; Coleman, J. N. Scalable Production of Large Quantities of Defect-Free Few-Layer Graphene by Shear Exfoliation in Liquids. *Nature Materials* **2014**, *13* (6), 624–630.

(6) Ciesielski, A.; Samorì, P. Graphene via Sonication Assisted Liquid-Phase Exfoliation. *Chem. Soc. Rev.* **2013**, *43* (1), 381–398.

(7) Harvey, A.; Boland, J. B.; Godwin, I.; Kelly, A. G.; Szydłowska, B. M.; Murtaza, G.; Andrew Thomas; Lewis, D. J.; O'Brien, P.; Coleman, J. N. Exploring the Versatility of Liquid Phase Exfoliation: Producing 2D Nanosheets from Talcum Powder, Cat Litter and Beach Sand. *2D Mater.* **2017**, *4* (2), 025054.

(8) Griffin, A.; Harvey, A.; Cunningham, B.; Scullion, D.; Tian, T.; Shih, C.-J.; Gruening, M.; Donegan, J. F.; Santos, E. J. G.; Backes, C.; Coleman, J. N. Spectroscopic Size and Thickness Metrics for Liquid-Exfoliated h-BN. *Chem. Mater.* **2018**, *30* (6), 1998–2005.

(9) Keeney, L.; Smith, R. J.; Palizdar, M.; Schmidt, M.; Bell, A. J.; Coleman, J. N.; Whatmore, R. W. Ferroelectric Behavior in Exfoliated 2D Aurivillius Oxide Flakes of Sub-Unit Cell Thickness. *Advanced Electronic Materials* **2020**, *6* (3), 1901264.

(10) Yu, X.; Mitoudi-Vagourdi, E.; Johnsson, M. The Aurivillius Compound $CoBi_2O_2F_4$– an Efficient Catalyst for Electrolytic Water Oxidation after Liquid Exfoliation. *ChemCatChem* **2019**, *11* (24), 6105–6110.

(11) Honda, M.; Oaki, Y.; Imai, H. Hydrophobic Inorganic–Organic Composite Nanosheets Based on Monolayers of Transition Metal Oxides. *Chem. Mater.* **2014**, *26* (11), 3579–3585.

(12) Matsui, H.; Oaki, Y.; Imai, H. Surface-Functionalized Hydrophilic Monolayer of Titanate and Its Application for Dopamine Detection. *Chem. Commun.* **2016**, *52* (60), 9466–9469.

(13) Yamamoto, Y.; Oaki, Y.; Imai, H. Coupled Exfoliation and Surface Functionalization of Titanate Monolayer for Bandgap Engineering. *Advanced Materials Interfaces* **2017**, *4* (7), 1601014.

(14) Oaki, Y. Exfoliation Chemistry of Soft Layered Materials toward Tailored 2D Materials. *Chem. Lett.* **2021**, *50* (2), 305–315.

(15) Lee, J. M.; Kang, B.; Jo, Y. K.; Hwang, S.-J. Organic Intercalant-Free Liquid Exfoliation Route to Layered Metal-Oxide Nanosheets via the Control of Electrostatic Interlayer Interaction. *ACS Appl. Mater. Interfaces* **2019**, *11* (12), 12121–12132.

(16) Jellander, R.; Marčelja, S.; Quirk, J. . Attractive Double-Layer Interactions between Calcium Clay Particles. *Journal of Colloid and Interface Science* **1988**, *126* (1), 194–211.

(17) Moreira, A. G.; Netz, R. R. Simulations of Counterions at Charged Plates. *Eur. Phys. J. E* **2002**, *8* (1), 33–58.

(18) Šamaj, L.; Trulsson, M.; Trizac, E. Strong-Coupling Theory of Counterions with Hard Cores between Symmetrically Charged Walls. *Phys. Rev. E* **2020**, *102* (4), 042604.

(19) Israelachvili, J. N. Intermolecular and Surface Forces. 706.

(20) Cunningham, G.; Lotya, M.; Cucinotta, C. S.; Sanvito, S.; Bergin, S. D.; Menzel, R.; Shaffer, M. S. P.; Coleman, J. N. Solvent Exfoliation of Transition Metal Dichalcogenides: Dispersibility of Exfoliated Nanosheets Varies Only Weakly between Compounds. *ACS Nano* **2012**, *6* (4), 3468–3480.

(21) Griffin, A.; Nisi, K.; Pepper, J.; Harvey, A.; Szydłowska, B. M.; Coleman, J. N.; Backes, C. Effect of Surfactant Choice and Concentration on the Dimensions and Yield of Liquid-Phase-Exfoliated Nanosheets. *Chem. Mater.* **2020**, *32* (7), 2852–2862.
(22) Hughes, J. M.; Aherne, D.; Coleman, J. N. Generalizing Solubility Parameter Theory to Apply to One- and Two-Dimensional Solutes and to Incorporate Dipolar Interactions. *Journal of Applied Polymer Science* **2013**, *127* (6), 4483–4491.
(23) Backes, C.; Higgins, T. M.; Kelly, A.; Boland, C.; Harvey, A.; Hanlon, D.; Coleman, J. N. Guidelines for Exfoliation, Characterization and Processing of Layered Materials Produced by Liquid Exfoliation. *Chem. Mater.* **2017**, *29* (1), 243–255.
(24) Fowkes, F. M. ATTRACTIVE FORCES AT INTERFACES. *Ind. Eng. Chem.* **1964**, *56* (12), 40–52.
(25) Coleman, J. Private Communication. November 2021.
(26) Linse, P.; Lobaskin, V. Electrostatic Attraction and Phase Separation in Solutions of Like-Charged Colloidal Particles. 12.
(27) Naji, A.; Jungblut, S.; Moreira, A. G.; Netz, R. R. Electrostatic Interactions in Strongly Coupled Soft Matter. *Physica A: Statistical Mechanics and its Applications* **2005**, *352* (1), 131–170.
(28) Shimakawa, Y.; Kubo, Y.; Tauchi, Y.; Kamiyama, T.; Asano, H.; Izumi, F. Structural Distortion and Ferroelectric Properties of SrBi2(Ta1−xNbx)2O9. *Appl. Phys. Lett.* **2000**, *77* (17), 2749–2751.
(29) Sasaki, T.; Watanabe, M. Osmotic Swelling to Exfoliation. Exceptionally High Degrees of Hydration of a Layered Titanate. *J. Am. Chem. Soc.* **1998**, *120* (19), 4682–4689.
(30) Yuan, H.; Dubbink, D.; Besselink, R.; ten Elshof, J. E. The Rapid Exfoliation and Subsequent Restacking of Layered Titanates Driven by an Acid-Base Reaction. *Angewandte Chemie International Edition* **2015**, *54* (32), 9239–9243.
(31) Yan, M.; Collins, S. M.; Midgley, P. A.; Feldblyum, J. I. Factors Governing the Chemical Stability of Shear-Exfoliated ZnSe(Alkylamine) II–VI Layered Hybrids. *Chem. Mater.* **2020**, *32* (6), 2379–2388.
(32) Akbarian-Tefaghi, S.; Rostamzadeh, T.; Brown, T. T.; Davis-Wheeler, C.; Wiley, J. B. Rapid Exfoliation and Surface Tailoring of Perovskite Nanosheets via Microwave-Assisted Reactions. *ChemNanoMat* **2017**, *3* (8), 538–550.
(33) Hanlon, D.; Backes, C.; Higgins, T. M.; Hughes, M.; O'Neill, A.; King, P.; McEvoy, N.; Duesberg, G. S.; Mendoza Sanchez, B.; Pettersson, H.; Nicolosi, V.; Coleman, J. N. Production of Molybdenum Trioxide Nanosheets by Liquid Exfoliation and Their Application in High-Performance Supercapacitors. *Chem. Mater.* **2014**, *26* (4), 1751–1763.
(34) Kopecká, K.; Melánová, K.; Beneš, L.; Knotek, P.; Mazur, M.; Zima, V. Exfoliation of Layered Mixed Zirconium 4-Sulfophenylphosphonate Phenylphosphonates. *Dalton Trans.* **2020**, *49* (12), 3816–3823.
(35) Mizuguchi, R.; Imai, H.; Oaki, Y. Formation Processes, Size Changes, and Properties of Nanosheets Derived from Exfoliation of Soft Layered Inorganic–Organic Composites. *Nanoscale Adv.* **2020**, *2* (3), 1168–1176.
(36) Huang, X.; Li, Y.; Yin, X.; Tian, J.; Wu, W. Liquid-Phase Exfoliation of Kaolinite by High-Shear Mixer with Graphite Oxide as an Amphiphilic Dispersant. *Langmuir* **2019**, *35* (43), 13833–13843.
(37) Asai, Y.; Ariake, Y.; Saito, H.; Idota, N.; Matsukawa, K.; Nishino, T.; Sugahara, Y. Layered Perovskite Nanosheets Bearing Fluoroalkoxy Groups: Their Preparation and Application in Epoxy-Based Hybrids. *RSC Adv.* **2014**, *4* (51), 26932–26939.
(38) Dutta, S.; Pal, S.; De, S. Mixed Solvent Exfoliated Transition Metal Oxides Nanosheets Based Flexible Solid State Supercapacitor Devices Endowed with High Energy Density. *New J. Chem.* **2019**, *43* (31), 12385–12395.
(39) Nakada, G.; Imai, H.; Oaki, Y. Few-Layered Titanate Nanosheets with Large Lateral Size and Surface Functionalization: Potential for the Controlled Exfoliation of Inorganic–Organic Layered Composites. *Chem. Commun.* **2018**, *54* (3), 244–247.
(40) Keeney, L.; Smith, R. J.; Palizdar, M.; Schmidt, M.; Bell, A. J.; Coleman, J. N.; Whatmore, R. W. Ferroelectric Behavior in Exfoliated 2D Aurivillius Oxide Flakes of Sub-Unit Cell Thickness. *Advanced Electronic Materials n/a* (n/a), 1901264.
(41) Kimura, N.; Kato, Y.; Suzuki, R.; Shimada, A.; Tahara, S.; Nakato, T.; Matsukawa, K.; Mutin, P. H.; Sugahara, Y. Single- and Double-Layered Organically Modified Nanosheets by Selective Interlayer Grafting and Exfoliation of Layered Potassium Hexaniobate. *Langmuir* **2014**, *30* (4), 1169–1175.
(42) Carrasco, J. A.; Harvey, A.; Hanlon, D.; Lloret, V.; McAteer, D.; Sanchis-Gual, R.; Hirsch, A.; Hauke, F.; Abellán, G.; Coleman, J. N.; Coronado, E. Liquid Phase Exfoliation of Carbonate-Intercalated Layered Double Hydroxides. *Chem. Commun.* **2019**, *55* (23), 3315–3318.

Chapter V

Shear-force exfoliation and advanced characterization of hybrid nanosheets

Chapter V. Shear-force exfoliation and advanced characterization of hybrid nanosheets

V.1. Introduction

V.1.1 State of the art

In **Chapter II**, we synthesized hybrid layered oxide where the organic moiety is an alkylphosphonic acid. Such hybrid is known to be more resistant against hydrolysis than alcohol-based or amine-based hybrid, due to the strong covalent P-O-M bond between organic and inorganic part.[1–3] Besides, this statement was confirmed by the exfoliation experiments using ion-exchange assistance or polymer assistance described in **Chapter III**. Therefore, the phosphonic acid-based hybrid is the best candidate to be exfoliated by shear-force assistance while keeping the functionalization intact.

Concerning the exfoliation using shear force assistance, we reviewed the parameters which control the size, shape and concentration of the nanosheets (see **Chapter IV**). The study was carried out on C_{12}O-HST but the conclusion can be adapted to another hybrid.

In the previous chapter, the nanosheets were mainly characterized by Scanning Electron microscopy (SEM) and Dynamic Light Scattering using a commercial apparatus. However, additional characterizations must be conducted to fully precise the geometric characteristics of the obtained nanomaterials and notably the integrity of its functionalization which is a crucial point in our approach

However, this latter issue requires the use of a combination of techniques to be fully conclusive. Literature reports are indeed often questionable regarding the characterization of the organic moiety onto hybrid nanosheets, whether this organic functionalization is added onto preformed nanosheets[4] or the molecules are already inserted/grafted in the bulk hybrid materials.[2,3,5,6]

In addition, the integrity of the inorganic structure should also be questioned. In the case of shear-exfoliation of Van der Waals materials, this process was proved to essentially preserve the initial structure.[7,8] Yet, in some peculiar situations, degradation of the nanomaterials can occur due to the oxidation to air or heating.[9]

Finally, the size and thickness of the nanosheets are one of the most important characteristics when dealing with 2D-materials with the credo “the larger and thinner is the better”. Most of the papers rely on microscopic images (Transmission Electron Microscopy (TEM) or Atomic Force Microscopy (AFM)) to get a statistical mean lateral size and/or thickness after deposition of the nanosheets suspension on a substrate. Nevertheless, the samples are not necessary representative of the whole suspension; the size distribution may be strongly different. In addition, the deposition process might be non-trivial when dealing with functionalized and/or charged nanosheets. Therefore, few papers report the use of light

scattering techniques to estimate the mean dimensions of the nanomaterials in solution. The mean hydrodynamic diameters are usually calculated using a spherical-particle model which neglects the anisotropy of the 2D materials and their peculiar dynamic behavior. To the best of our knowledge, extensive Static Light Scattering (SLS) or Dynamic Light Scattering (DLS) study of nanomaterials from liquid phase exfoliation has very seldom been reported.[10–12]

Several studies also report the use of Small Angle-X ray Scattering (SAXS) or Wide Angle X-ray scattering (WAXS) to provide information of the geometry of nanomaterials in suspension. These two techniques, applied to large nanosheets, are much sensitive to the spacing between the nanomaterials and the thickness of both organic and inorganic layer. For instance, K. Norrish was among the first to study the swelling behavior of montmorillonite thanks to SAXS.[13] Many papers followed, including the work of C. Shang and J. Rice who used SAXS to estimate the mean thickness of the particle and to determine the radius of gyration of montmorillonite particles in suspension (diluted solution), which give them access to the mean lateral size.[14] Similarly, J. ten Elshof *et al.* used SAXS to study the stacking of lepidocrocite-like titanate nanosheets depending of the ratio $\frac{TBA^+}{H^+}$ or of the pH.[15] However, these specific characterizations are not available in a laboratory (or sporadically found with a more limited q-range and a weaker X-ray flux, which increases the acquisition times) and cannot be conducted for a daily routine.

V.1.2 Objectives

In the following, we study the exfoliation by shear-force assistance of alkylphosphonic acid layered oxide and we present the characterization of the resulting nanosheets. This chapter is divided into three parts.

Firstly, we will describe the shear-force exfoliation of three alkylphosphonic acid based hybrid, synthesized previously (see **Chapter II**): C_3PO_3-HST, C_6PO_3-HST and $C_{10}PO_3$-HST. A comparison must be held with the work of H. Imai on the exfoliation of hybrid titanates in an organic solvent by heating and stirring.[5,16,17] Then, we will proceed as in **Chapter IV** and we will study by XRD the bottoms and supernatant after selective centrifugation process. Finally, we will present the elemental analysis, done by Inductive Coupled Plasma-Atomic Emission Spectroscopy (ICP-AES) of the nanomaterials suspension which will allow to estimate a concentration of nanosheets.

In a second part, we will focus on the local study of the hybrid nanomaterials after their deposition on a Cu grid or a substrate. We will describe the SEM analysis of the nanomaterials, including elemental analysis to be compared with data from ICP-AES. We will then study the structure of the hybrid nanosheets by high resolution TEM. This technique will also allow to highlight the mechanisms involved in the fragmentation of the crystal during the exfoliation process. Finally, we will describe the possibilities we have at our disposal for the deposition of nanomaterials from the suspension to the substrate. The as-deposited nanomaterials will be characterized by AFM which gives access to the thickness of one monolayer and of few-layer nanosheets.

In the final part, we will investigate the characterization of the hybrid nanomaterials in solution. For this purpose, we consider light scattering techniques (SLS and DLS) and X-ray scattering technique

(SAXS and WAXS). We will briefly describe the model we use and the inherent assumptions we make. Then, we will analyze the SLS and DLS experimental data in order to get a reliable measurement of the mean lateral size of the nanomaterials in solution. This as-estimated value will be combined with SAXS data to determine the mean thickness of the nanomaterials.

V.2. Shear-force exfoliation of layered phosphonic acid-based hybrid

V.2.1 Synthesis of the nanosheets

As described in **Chapter IV**, we must consider a polar solvent, which can solubilize the long alkyl chain (similar δ_d) and displaying a higher δ_H parameter than acetonitrile since a free P-OH group is present close to the inorganic layer. The 2-propanol (or isopropanol, IPA) seems to be a relevant candidate as it displays a higher δ_H than acetonitrile (16.4 $MPa^{-1/2}$ and 6.1 $MPa^{-1/2}$ respectively) and can interact with the P-OH group *via* hydrogen bond with its C-OH moiety. IPA has a δ_D close enough to the one of the alkyl chain (15.8 $MPa^{-1/2}$ and 16.1 $MPa^{-1/2}$ respectively). In addition, its low boiling point makes it an ideal choice for the deposition of nanosheets onto substrate.

Concerning the shear rate, we choose an intermediate shear rate of $\dot{\gamma}$ = 22900 s^{-1} corresponding to a rotor speed of 11500 rpm, fast enough to delaminate the sheets.

In addition, the exfoliation experiments are performed during 1 hour to favour delamination, which is still reasonable time for rapid mechanical force-assisted liquid exfoliation process.

Typically, the hybrid powder C_xPO_3-HST (20 mg) was dispersed in 40 mL of IPA. The high-speed disperser's tip was immerged in the solution until the tip laid at 1 cm from the bottom of the beaker. Besides, the tip was not centered to avoid vortex formation. The exfoliation was performed by alternating 10 minutes of shearing and 20 minutes of rest, due to a tool limitation, until cumulating 1 hour of shear (*i.e.* a total experiment time of 3 hours).

The resulting nanomaterials suspension went through a selective centrifugation process as described in **Chapter III**. The supernatant and the bottoms were washed by a centrifugation step at 14 000 rpm for 20 minutes and re-dispersed in IPA. In the following, most of the analyses are performed on the last supernatant.

Due to the low concentration of the suspension obtained after selective centrifugation process and the resulting difficulty to image the nanomaterials, samples for TEM or SEM characterizations were obtained after a single centrifugation step at 1600 rpm for 20 minutes to remove unexfoliated materials.

In addition to this experiment and in order to compare with the results described by Y. Oaki *et al.*[5,18] another process was also studied. 10 mg of the hybrid $C_{10}PO_3$-HST were poured into 50 ml of toluene. The solution was stirred for 5 days at 60 °C. The resulting solution was centrifuged at 1600 rpm for 20 minutes to remove unexfoliated materials. The supernatant is analyzed with SEM and the results are

compared to the shear-exfoliation of $C_{10}PO_3$-HST in IPA and of $C_{12}O$-HST in toluene we performed in **Chapter IV.**

V.2.2 Characterization of the re-stacked nanomaterials.

The XRD patterns of the different bottoms and the last supernatant from the selective centrifugation process are shown in ***Figure 1***. The (*100*), (*110*) and (*200*) reflections at 22.8°, 32.5° and 46.5° respectively are present and well defined for the bottom1 but tend to disappear in the following centrifugation steps until their total disappearance for the supernatant4. As already discussed in **Chapter III**, this progressive disappearance of the structure peak can be ascribed either to loss in coherence between the slab or to preferential orientation of the nanomaterials on the substrate. However, the evolution of the XRD patterns with respect to the centrifugation step points to a progressive loss of coherence between the slabs.

The (*00l*) reflections at 2.9°, 5.64° and 8.4° are identical on the XRD patterns of the bottoms and on the pattern of $C_{10}PO_3$-HST, indicating the presence of non-exfoliated or re-stacked materials. The associated peaks are also decreasing with respect to the centrifugation steps.

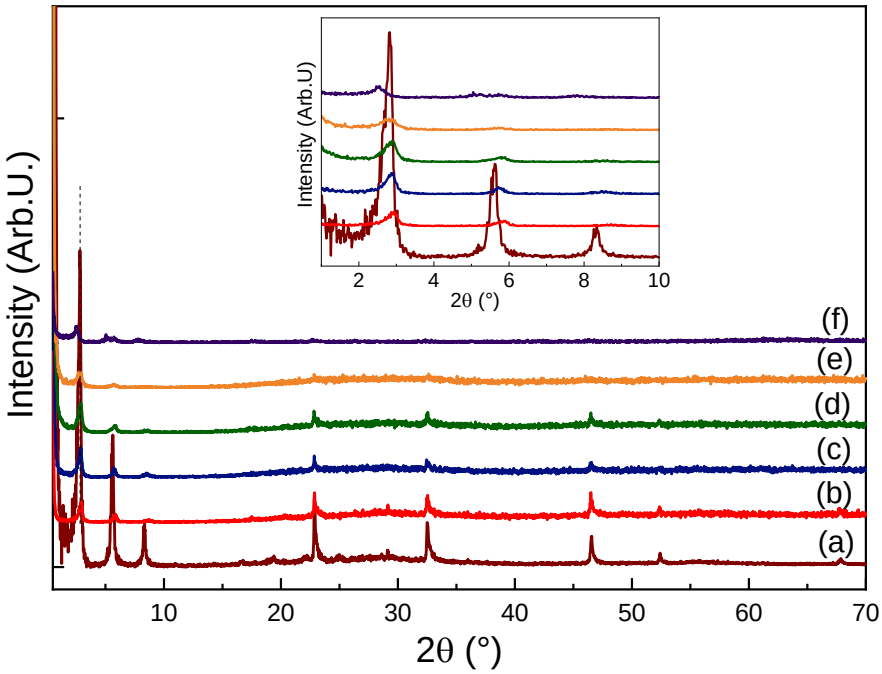

Figure 1: XRD patterns of (a) $C_{10}PO_3$-HST and (b) to (f) of $C_{10}PO_3$-HST nanomaterials from the bottoms 1 to 4 and the supernatant 4 after exfoliation and liquid cascade centrifugation processes.

Elemental analysis was carried out to determine the ratio $\frac{Ta}{P}$ in the supernatant for the three hybrids. The results are summed up in ***Table 1***. First we can notice that the contents in Ta and P are similar in the three solutions of nanomaterials of C_xPO_3-HST (x= 3, 6, 10). In addition, the ratio $\frac{Ta}{P}$ remains the same for the nanomaterials suspension compared to the bulk layered materials in the case of

C_3PO_3-HST and $C_{10}PO_3$-HST. This observation is consistent with the preservation of the initial functionalization of the oxide layer: we can exclude the possibility of remaining free molecules in the solution as the supernatant was washed with a centrifugation step. In the case of C_6PO_3-HST nanomaterials in suspension, the ratio $\frac{Ta}{P}$ differs from the one of the corresponding bulk. Besides, the evolution of the ratio from the bulk to the suspension is non-coherent: in the case of a leaching of the organic molecule, we expect the ratio $\frac{Ta}{P}$ to be larger (*i.e.* a decrease of the phosphorous content) but the reverse situation occurred. We could not find a reasonable explanation for such an evolution. Therefore, we ascribe this difference to an error in the estimation of the ratio $\frac{Ta}{P}$ of the bulk C_6PO_3-HST. This assumption is supported by the similar value of the ratio $\frac{Ta}{P}$ for all the nanomaterials suspensions. Besides, the mass content of materials is similar in all the three suspensions after the selective centrifugation process. At this stage we cannot assess the concentration as the mean dimensions of the nanomaterials is required for the calculation. However, we can calculate an exfoliation yield defined as the ratio $\frac{m_{nanosheets}}{m_{bulk}}$ which allows to compare our exfoliation method to the literature. We found an exfoliation yield of 6% which is line with what is reported by Y. Oaki *et al*. for the swelling of hybrid layered titanates in organic solvent (yield about 10%).[18] We mention that this comparison is somehow difficult with other papers as the exfoliation yield is expressed differently and this data does not necessarily expressed the exfoliation degree.

Sample	Tantalum content (weight%)	Phosphorous content (weight%)	Atomic Ratio $\frac{Ta}{P}$
Bulk C_3PO_3-HST	74 ± 5	4.2 ± 0.4	3.1 ± 0.5
Suspension of C_3PO_3-HST nanomaterials	20.8 ± 0.6	1.1 ± 0.2	3.1 ± 0.5
Bulk C_6PO_3-HST	53 ± 2	1.9 ± 0.1	4.7 ± 0.5
Suspension of C_6PO_3-HST nanomaterials	22.6 ± 0.3	1.44 ± 0.03	2.70 ± 0.07
Bulk $C_{10}PO_3$-HST	46 ± 4	3.3 ± 0.1	2.4 ± 0.2
Suspension of $C_{10}PO_3$-HST nanomaterials	23 ± 1	1.4 ± 0.2	2.7 ± 0.4

Table 1: Results from ICP-AES analysis of C_3PO_3-HST, C_6PO_3-HST and $C_{10}PO_3$-HST in bulk and after shear force-assisted exfoliation.

V.2.3 Conclusion

According to the XRD analysis, we can conclude that the non-exfoliated and re-stacked materials have kept their integrity (*i.e.* the inorganic structure plus the functionalization), and hence we make the hypothesis that the exfoliated materials in the supernatant have also remained intact. The ICP-AES analysis is in line with this assumption as the ratio $\frac{Ta}{P}$ did not change in the nanomaterials suspension compared to the layered bulk.

V.3. Characterization of functionalized nanosheets by microscopy.

V.3.1 Introduction

Despite the XRD analysis of the different bottoms from selective centrifugation process, we could not ascertain the integrity of the crystalline structure of the inorganic oxide layers as nanosheets in suspension. In addition, even though we know the elemental proportion of the Ta and P elements, the dimensions of the nanomaterial are required to assess the concentration in particles.

Therefore, a local imaging by SEM, TEM or AFM is crucial: these techniques will allow to estimate a lateral size and thickness of the nanomaterials. Furthermore, Energy Dispersive X-Ray analysis (EDX) and Electron Energy Loss Spectroscopy (EELS) will allow to study their composition. Thus, in this part, we will describe the imaging of hybrid nanosheets after their deposition. We mainly focus on $C_{10}PO_3$-HST as the conclusion can be extended to the two other alkylphosphonic acid derivatives. In addition, specifically for TEM in STEM mode, we also consider an analogous hybrid layered oxide, $C_{10}PO_3$-HLN, which was synthesized following the same procedure as $C_{10}PO_3$-HST. Besides, the SEM images are carried out from a solution which only underwent one single centrifugation. A part of the following results was recently published.[19]

V.3.2 Scanning Electron Microscopy in STEM mode

After the deposition of the $C_{10}PO_3$-HST nanomaterials solution onto a Cu grid (5-10 drops), the grid is analyzed in SEM using STEM mode which provides a better resolution and allows to have access to the bright field mode. The accelerating voltage was set at 25 kV.

Figure 2 shows several images of nanomaterials from a suspension after exfoliation. As already observed in **Chapter IV** and exemplified once again by ***Figure 2 (a)*** to ***(f)***, the shear-force-assisted liquid exfoliation allows to produce quite large few-layer nanosheets (lateral size around ~1 μm). These exfoliated nanomaterials coexist with smaller but unexfoliated materials, characterized by their darker contrast in bright field. However, the experimental conditions we set for the exfoliation of $C_{10}PO_3$-HST (*i.e*. in IPA at 11 500 rpm for 1hour) are effective.

Figure 2 (b) and ***(c)*** show a well-shaped few-layer nanomaterial whose delamination is incomplete. This observation points out the usefulness of another step for exfoliation consisting in a lower speed shear-force on the last supernatant as J. Coleman *et al.* did.[7,20] During this work, such a process has not been tried.

Figure 2 (g) to ***(f)*** illustrate the polydispersity of the few-layer materials in terms of size, shape and thickness. Besides, considering these three images and the observation of many small and thin objects, we can draw a tendency on the nanomaterials, which tend to be smaller as they are thinner (well-exfoliated). In addition, an evolution of the shape of the nanomaterials is evidenced: the smaller objects tend to have more edges and a non-regular shape which differs from the quasi parallelepipedic-shaped

large flakes. We hypothesize that the fragmentation of the layers or set of layers does not occur according to preferential in-plane directions. This point is further discussed in more details below.

During SEM imaging, we did not notice any modification of the nanomaterials due to their damaging under the electron beam, even at relatively high magnification.

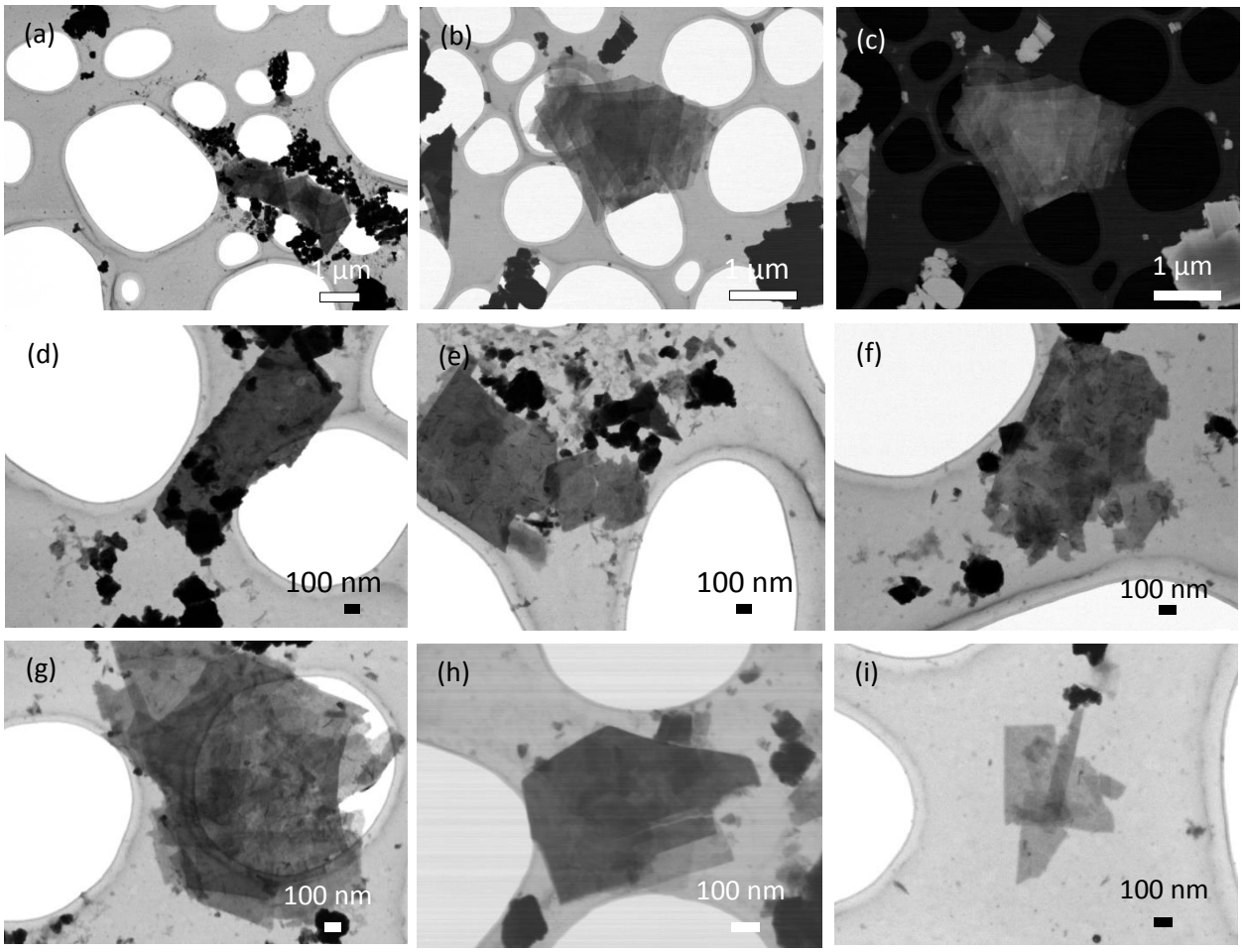

Figure 2: SEM images in STEM mode of $C_{10}PO_3$-HST nanomaterials.

Finally, we performed EDX analysis on a stack of $C_{10}PO_3$-HST nanomaterials as the analysis could not be carried out using a single nanosheet due to a too low resulting signal (not enough secondary electrons). We clearly observe on ***Figure 3*** that the oxygen and the tantalum are the most abundant elements on the nanomaterials whereas strontium and phosphorous are present in a smaller proportion. The high proportion of carbon, oxygen, nitrogen, copper and aluminium observed is ascribed to the carbon membrane, supported by the copper grid and the holder in aluminum. The elements O, Ta, Sr and P are homogeneously distributed onto the nanomaterials while they are absent on the membrane of the copper grid (except for oxygen). All the elements of the $C_{10}PO_3$-HST hybrid are present (even the bismuth despite its low content in the inorganic structure). Thus, the 1-decylphosphonic acid appears to be still grafted onto the $SrTa_2O_7^{2-}$ layer, thus confirming the stability of the functionalization during the exfoliation

process. We notice that the analysis was performed on a stack of $C_{10}PO_3$-HST, which is not a monolayer nanosheet, but it is definitely smaller and thinner than a crystallite from the non-exfoliated material.

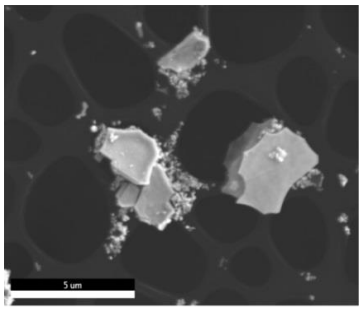

Element (band)	Weight (%)	Atomic (%)
C (K)	12.5	28.7
N (K)	0.3	0.6
O (L)	13.8	23.8
Cu (L)	5.2	2.3
Al (K)	38.5	39.2
Ta (M)	23.2	3.5
Sr (L)	4.7	1.5
P (K)	0.2	0.2
Bi (M)	1.6	0.2

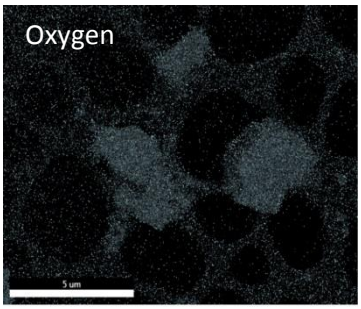

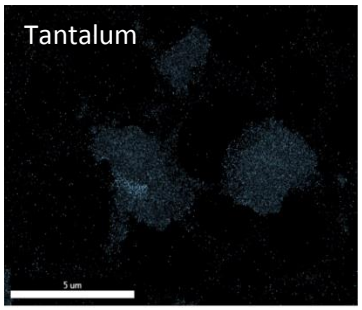

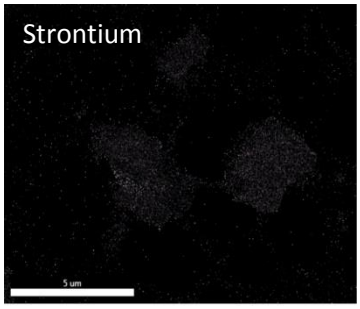

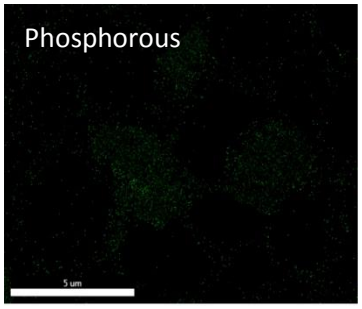

Figure 3: SEM image of a stack of $C_{10}PO_3$-HST materials and the elemental composition in oxygen, tantalum, strontium and phosphorous. Scale bar is 5 µm.

The shear force-assisted liquid exfoliation allows to produce few-layer nanosheets in solution as illustrated by the SEM images. However, it is interesting to compare our method for the exfoliation of hybrid layered oxides to an alternative one, described by Y. Oaki *et al.*[16,18] The process is based on heating and gentle stirring the hybrid powder in toluene, leading to a swelling phenomenon and subsequent delamination. SEM images of $C_{10}PO_3$-HST using this method are shown in ***Figure 4***. First, we note the presence of organic content which is the result of an inefficient washing step but it does not disturb the analysis of the hybrid nanomaterials. Besides, few-layer nanosheets can be obtained, with a majority displaying a lateral size close to 1 µm. However, the relatively dark contrast tends to indicate few-layer or thicker nanomaterials. We also notice that smaller but thinner nanosheets can be observed as depicted in ***Figure 4 (c)*** which testifies the polydispersity of the sample. Nevertheless, the nanomaterials generally display a more geometric shape and straight edges than the one from shear-exfoliation.

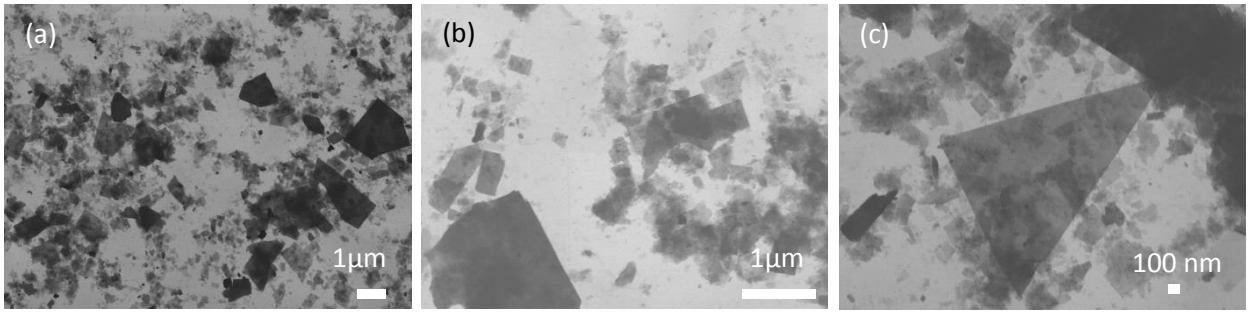

***Figure 4: SEM image of $C_{10}PO_3$-HST nanomaterials by exfoliation of the corresponding bulk according the procedure described by Oaki et al.*[16,18]**

Thus, it is worth mentioning that compared to shear force-exfoliation in toluene, carried out in **Chapter IV** where no nanosheet was obtained, the Oaki's process allows to produce hybrid few-layer nanosheets. This difference in behavior might arise from the temperature: in the latter case, heating might increase the "solubility"/dispersibility of the nanomaterials and might favour the swelling process. However, the resulting nanomaterials are also polydisperse and the exfoliation is incomplete. A positive point is that the nanosheets appear to be less damaged. As a perspective, it would be relevant to perform this exfoliation method using different solvent such as IPA to improve the exfoliation yield while maintaining the large size of the flakes.

V.3.3 Transmission Electron Microscopy in STEM mode

In order to study more precisely the structure and thickness of the nanosheets, we performed TEM in STEM mode in collaboration with Corinne Bouillet at IPCMS. The accelerating voltage was set at 100 kV. The images obtained at relatively low magnification on TEM could be recorded without too important contamination (*i.e.* formation of carbon coating).

V.3.3.1 Geometric dimensions of the nanosheets

Similarly to SEM, large few-layer nanosheets are seen in TEM with a lateral size around several hundred nanometers as depicted by ***Figure 5.*** The large few-layer nanosheets have a regular shape but display a polydispersity in size. In addition to exfoliated materials, non-exfoliated ones are also observed as expected since we did not perform selective centrifugation for the suspension used for TEM to guarantee a sufficient concentration of materials.

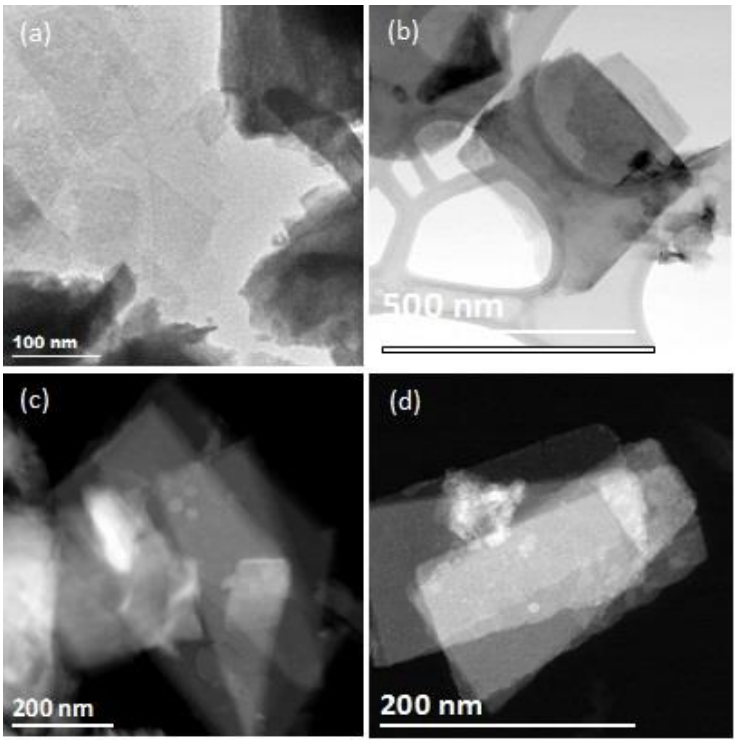

Figure 5: TEM images in STEM mode of $C_{10}PO_3$-HST nanomaterials showing large few-layer nanosheets.

Apart from this classical orientation of the nanomaterials, lying flatly on the membrane, we also observed series of images where the inorganic layers are oriented perpendicularly to the membrane. This unconventional orientation for high aspect ratio nanomaterials was not observed for the other hybrids such as C_{12}O-HST or BenzO-HST. Nevertheless, it has already been observed in literature for other materials.[21,22]

The images ***Figure 6 (a)*** and ***(b)*** show two unexfoliated materials which lie vertically on the membrane. The layers are clearly distinguishable as well as the distance between them. It is worth noticing the regularity of the oxide layer stacking which is characteristic of coherent slabs of an unexfoliated material. Unfortunately it was not possible to determine precisely the interlayer distance with this image due to the tilt angle made by the nanomaterials with respect to the normal of the membrane.

The order between the slabs in ***Figure 6 (a)*** and ***(b)*** contrasts with the piling of the nanosheets depicted in ***Figure 6 (d)*** and ***(e)***. In this latter case, the layers are less parallel one to each other and the spacing between them is not uniform. We ascribe this alteration of order between adjacent slabs to the exfoliation process which either disturbs the slabs without total exfoliation or produces nanosheets which are restacked with time or with the deposition process. The former case can match with the pile with an offset between the slabs we mentioned previously (***Figure 2 (b)***). The second situation might correspond to the image ***Figure 2 (g)*.**

Whereas the situation described in ***Figure 6 (a), (b), (d)*** and ***(e)*** corresponds to non-exfoliated materials (or at least made of more than 10 sheets), ***Figure 6 (c)***and ***(f)*** show exfoliated materials made of only three nanosheets, the atomic structure of which is evidenced in ***Figure 6 (f)*.**

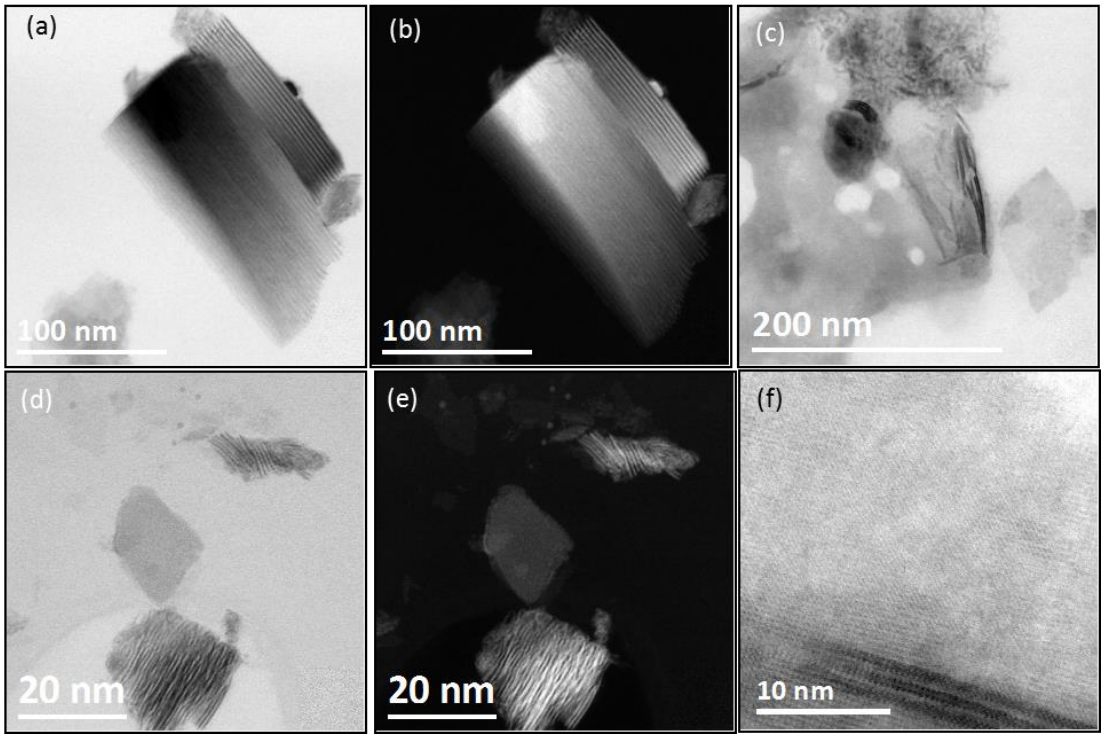

Figure 6: TEM images in STEM mode of vertically lying (a) (b) non-exfoliated $C_{10}PO_3$-HST, (c) few-layer $C_{10}PO_3$-HST nanosheets (d) (e) restacked and disordered $C_{10}PO_3$-HST nanosheets and (f) exactly three-layer $C_{10}PO_3$-HST nanosheets.

Using TEM in HAADF-STEM mode offers the possibility to have dark field image, in which the contrast is related to the atomic number (*i.e.* the area of heaviest atoms produces a larger quantity of backscattered electrons). Thus, a defined structure is associated with a defined intensity. We take advantage of this property to determine more exactly the number of layers in a pile of materials. ***Figure 7*** shows a dark field STEM image where nanosheets are in a staircase position, allowing to differentiate several steps *i.e.* different thicknesses. The second image in ***Figure 7*** exhibits a single hybrid nanosheet.

On these two clichés, an intensity profile was carried out along the arrow and the results are shown on the graph ***Figure 7***. In the case of the monolayer, a gap of 1300 counts separates the monolayer from the membrane on which the nanomaterials lie. For stacked nanosheets, the first gap, corresponding to the difference between the nanomaterials and the membrane, is worth 3200 counts whereas the gap between consecutive steps is worth 1100, 1100 and 1200 counts successively. These three values are assimilated to a monolayer intensity. The slight difference compared to the step observed for one single nanosheet on the grid is ascribed to either a denser arrangement of the organic layer of the hybrid when interacting with the carbon membrane or to the contamination from imaging. The same phenomenon was reported by K. Virdi *et al.* on their intensity profile analysis of TBA^+-exfoliated oxide nanomaterials.[23] The authors explained this observation by re-arrangement of the organic layer in contact with the grid.

According to the intensity value we found for one single monolayer, the first step of the stack intensity profile matches with three hybrid layers. This latter situation perfectly illustrates the spurious and spontaneous trend to ascribe the term "monolayer" to nano-objects, by judging their transparency. Only an

intensity profile analysis allows the accurate estimation of the number of layers in presence on a nanomaterial.

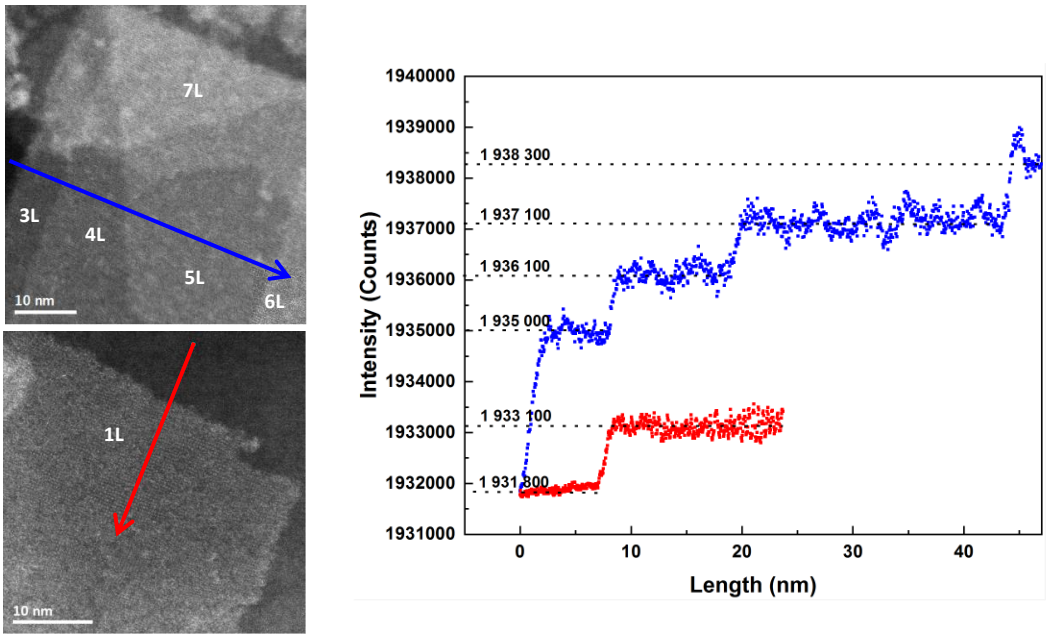

Figure 7: TEM images in STEM mode of a stacked of seven hybrid nanosheets and one monolayer of $C_{10}PO_3$-HST as well as the corresponding intensity profile.

V.3.3.2 Structure of the inorganic moiety

In addition, a crucial issue is the preservation of the inorganic structure all along the exfoliation process. The functionalization step does not modify the oxide layer and a straightforward XRD analysis supports this statement (see **Chapter II**). The same cannot be easily said for the exfoliation process. T. Sasaki *et al.* use XRD on a suspension of few-layer nanosheets, obtained by the ion-exchange mechanism.[24] Such, XRD characterization on colloidal nanomaterials requiring concentrated suspensions and synchrotron radiation, could not be performed during this work.

Here, like in most of the works on nanomaterials, we used TEM to determine the inorganic structure of a monolayer or few-layer nanosheets. ***Figure 8 (a)*** and ***(b***) show the dark and bright field clichés of a $C_{10}PO_3$-HST monolayer respectively. Especially in the dark field image, the inorganic network is emphasized by the observed regular pattern. A Fast-Fourier-Transform (FFT) was carried out on the nanosheets and is presented in ***Figure 8 (c***). From the FFT, the in-plane reflections distances are estimated to be d_{100} = 0.3987 nm and d_{110} = 0.2832 nm. Considering a cubic structure, these lattice parameters are closely the same as the ones determined from XRD pattern of the bulk $C_{10}PO_3$-HST (0.3904 nm and 0.2759 nm respectively). Thus, the shear-exfoliation process does not modify the inorganic structure of the perovskite-like oxide. This statement is supported by the analysis of hybrid nanosheets from a different oxide layer. Indeed, we also used our approach to synthesized $C_{10}PO_3$-HLN nanosheets (*i.e.* functionalization by the 1-decylphosphonic acid of a HLN-based precursor, followed by the shear-exfoliation in the same condition than $C_{10}PO_3$-HST). SEM clichés show a similar size, size

distribution, shape and thickness of the nanomaterials than $C_{10}PO_3$-HST. Concerning the structure of the $LaNb_2O_7^{2-}$ layer, ***Figure 8 (d)*** to ***(e)*** show HRTEM images and a FFT of $C_{10}PO_3$-HLN nanosheets. The determined in-plane reflection distances are worth d_{100} = 0.3124 nm and d_{110} = 0.2214 nm, which matches with the corresponding distance from the XRD pattern of the bulk (0.3151 nm and 0.2729 nm respectively).

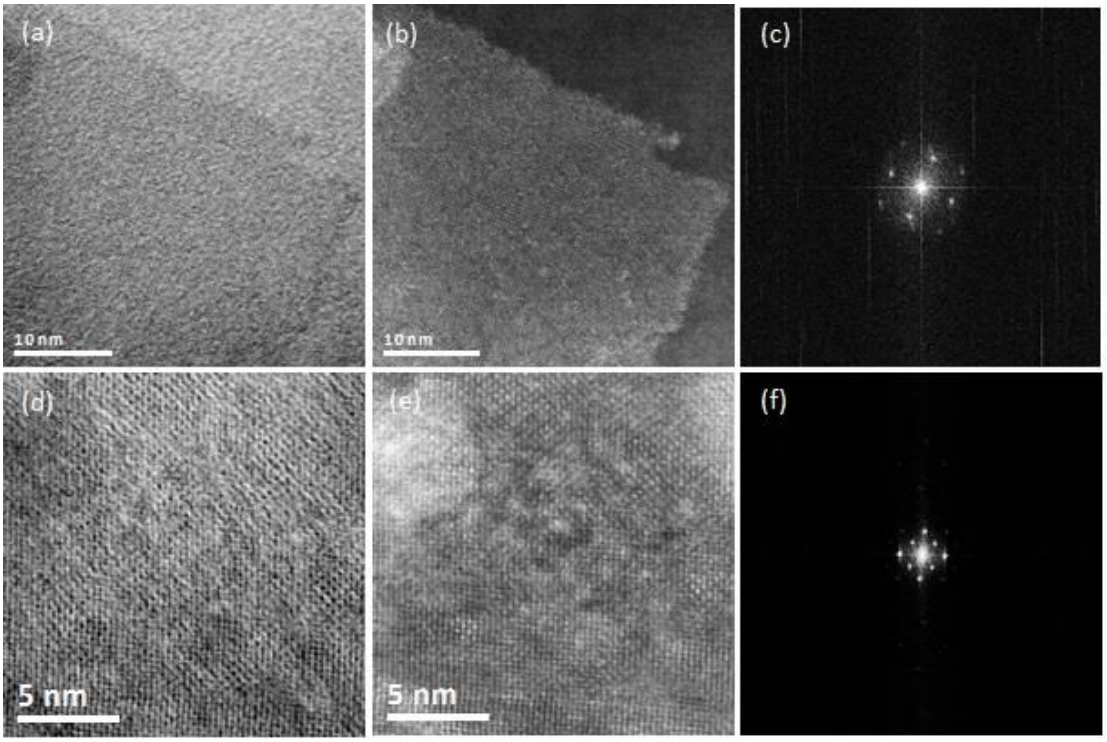

Figure 8: High resolution TEM images of a monolayer nanosheet of (a) (b) $C_{10}PO_3$-HST or (d) (e) $C_{10}PO_3$-HLN and (c) (f) the corresponding FFT.

V.3.3.3 Evidence of the phosphonic acid grafting

Electron energy Loss Spectroscopy (EELS) was finally used to provide the elemental composition of the nanosheets. As we aim at emphasizing the presence of the grafting onto the inorganic oxide layer, a clear spectroscopic signal of phosphorous is mandatory. Due to overlap between the M_4, and M_5 edges of strontium and the $L_{2,3}$ edge of phosphorous, the hybrid $C_{10}PO_3$-HST cannot be chosen for this part of the study. Therefore, we pursue the elemental analysis by EELS using the analogous compound $C_{10}PO_3$-HLN. We demonstrated above that $C_{10}PO_3$-HLN nanosheets are crystalline, with the same inorganic structure as the parent bulk. The behavior of the organic part of $C_{10}PO_3$-HLN should behave as $C_{10}PO_3$-HST regarding the effect of the shear-force exfoliation.

The EELS spectrum of $C_{10}PO_3$-HLN few-layer nanosheet is shown in ***Figure 9***. The two sharp edges at 849 eV and 831 eV testify to the presence of La and correspond to the M_4 and M_5 edges respectively. The edge at 527 eV is characteristic of the K edge of oxygen. One would have expected to see an edge corresponding to an energy loss of niobium. Nevertheless, the EELS spectrum of a related

Nb_2O_5 does not display any relevant and well-defined edge in the region between 50 to 900 eV. A spectrum performed at higher energy should be recorded to clearly see edges from niobium atoms.

The edge at 120 eV is ascribed to the edge $L_{2,3}$ of the phosphorous. This latter edge emphasizes the presence of the 1-decylphosphonic acid at the surface of the oxide layer of HLN. In addition, an edge at 294 eV can be ascribed to the $L_{2,3}$ edge of K. This suggests that the initial K^+ into the interlayer space of the prior KLN might not be completely removed from the structure, even after the protonation step and the two subsequent functionalization steps by 1-butylamine and 1-decylphosphonic acid.

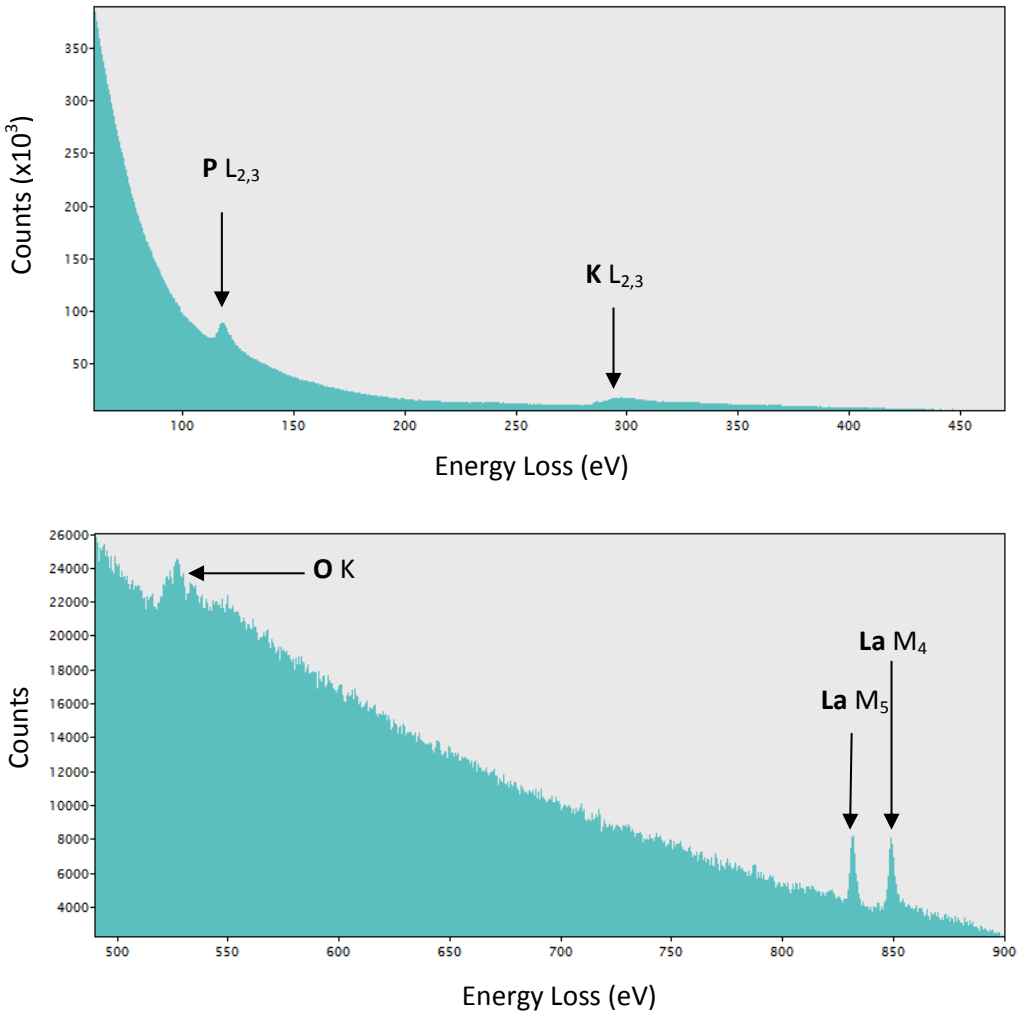

Figure 9: EELS spectrum of $C_{10}PO_3$-HLN nanosheets, obtained at 200 kV.

V.3.3.4 Fragmentations and defects

As mentioned previously, the exfoliation provides large nanomaterials, with sharp edges and parallelepipedic shape along with smaller and less regular objects. This observation indicates that fragmentation and crack occur which deserve a closer look.

Figure 10 (a) to ***(c)*** show the breaking of a stack of layers according to a defined direction, leading to rectangular-shaped nanomaterials. We notice that the fragments have a lateral size around 100

nm. In contrast the images ***Figure 10 (c)*** to ***(d)*** show a crack on a few-layer nanosheet which does not lead to a well-shaped material. The resulting fragments can display many edges and even appear to be curved. These fragments have a lateral size of 50 nm or less.

These two situations have also been observed in literature. A. Liscio *et al.* studied the evolution of the shape and size of graphene oxide nanosheets. They demonstrated that two populations of nanomaterials can coexist. The first one corresponds to random fragmentation of the pristine bulk, whose fragments display the same shape. The nanomaterial remains quite large. The second mechanism, which tends to be predominant as the exfoliation goes, is the edge erosion. The crack begins at the edges of the sheets, from a seed defect and propagates. The resulting fragments have a different shape but their area remains constant as well as their form factor.

These two mechanisms match well with the TEM images and explain the presence of small nanosheets after exfoliation.

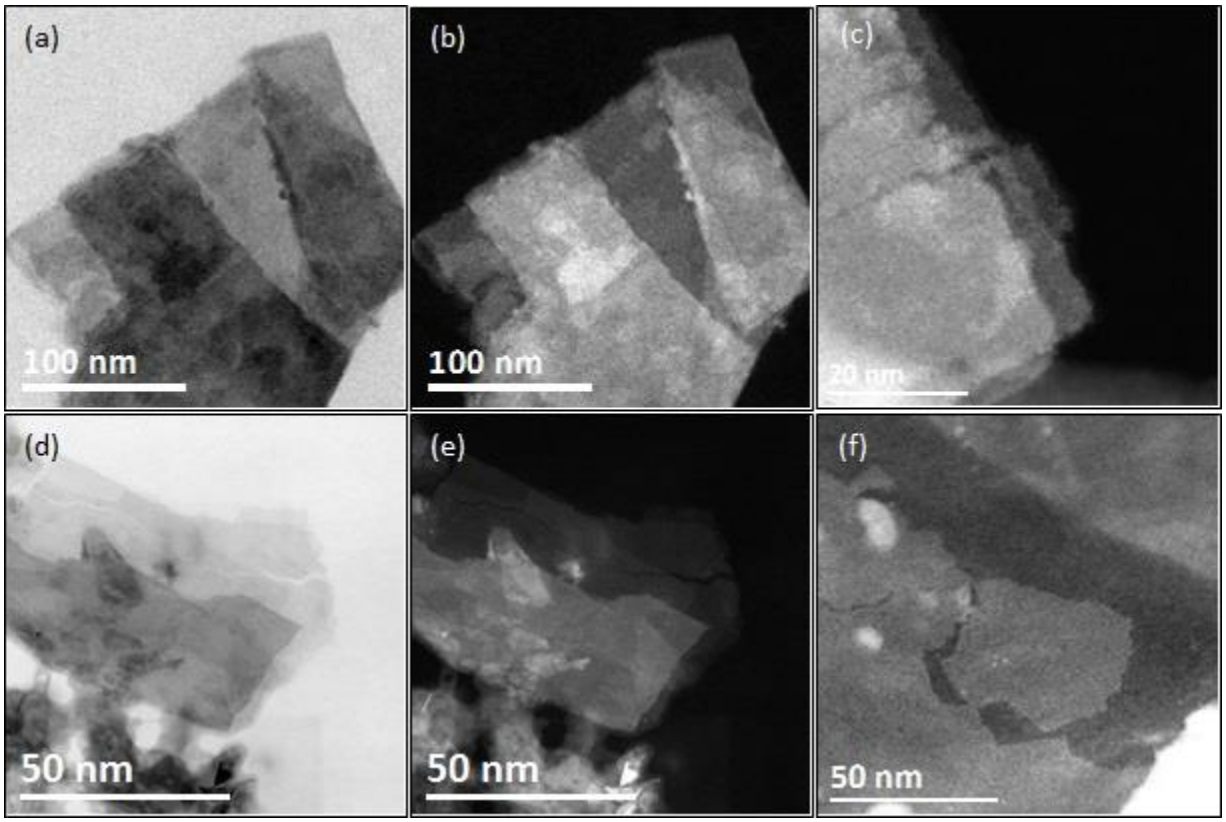

Figure 10: TEM images in STEM mode of $C_{10}PO_3$-HST nanomaterials showing breaking and fragmentation of one or several monolayers.

In addition to the fragmentation, TEM allows us to precisely image the surface of a few-layer nanosheet. Surprisingly, we observed a third type of fragmentation which produces small particles (around 20 nm). These fragments were only observed on top of nanosheets as depicted by ***Figure 11 (b)***. In parallel, we observed holes in few-layer nanosheets with a similar size (***Figure 11 (a)***). This phenomenon might be the consequence of the non-homogeneous grafting of the molecules during the functionalization step. In some areas, the electrostatic interaction can thus be stronger as well as the overall interaction

between the two adjacent slabs. Therefore, during the exfoliation, when the largest part of one hybrid layer tends to be delaminated, a minor part resists and remains stacked, leading to hole formation on one side and small fragmentations on the other side.

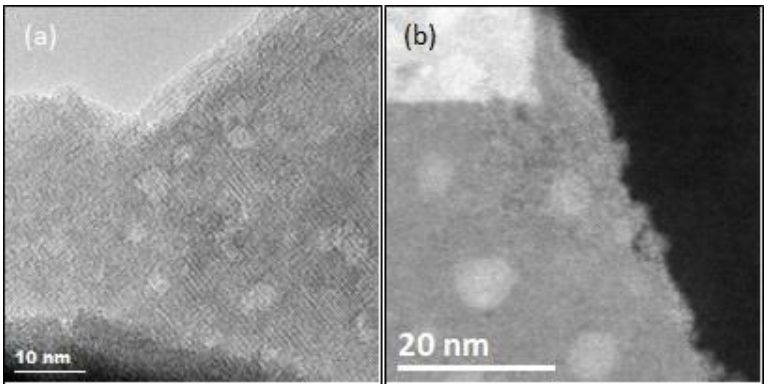

Figure 11: TEM images in STEM mode showing singularities observed on few-layer nanosheets.

V.3.3.5 Difficulty of imaging

Finally, we highlight the difficulty of imaging thin nanomaterials such as 2D nanosheets. The imaging conditions must be carefully chosen to correctly observe a nanomaterial. First, dealing with hybrid materials implies a potential contamination due to solvent or the grafted molecules. Therefore, putting the copper grid under vacuum is helpful to remove adsorbed organic molecules, which limits the contamination during imaging. This point is crucial for the record of High Resolution images of thin nanomaterials.

Then, the main issue arises from the interaction of the nanomaterials with the high energetic electron beam. Indeed, compared to SEM where the accelerating tension is 25 kV, in TEM, the accelerating voltage is much higher to allow the electron to go through the sample. However, this energy impacts the imaging. For instance, in ***Figure 12 (a)*** and ***(b)***, a few-layer nanosheet was imaged at 200 kV. The two images were recorded successively and a clear difference is observed; less matter seems to be present in the image ***Figure 12 (b)*** due to the damaging of the nanomaterial during the record. We also reported the formation of hole when keeping the beam focused on the same spot. This phenomenon is known as *knock-out* mechanism where the energetic electrons sputter the oxide materials.[25]

A second set of imaging was out carried with a less energetic electron beam (the acceleration voltage was 100 kV). The incident particles should be less prompt to break the bond between atoms but have more "time" to interact with matter. The images ***Figure 12 (c)*** and ***(d)*** show a few-layer nanosheet with a very straight edge, imaged at 100 kV. After recording the corner (surrounded by a black circle) at high resolution, an image at a medium magnification was recorded. Shrinkage of the nanosheets is emphasized by the nanosheet aspect and the curvature of the corner. It seems that a densification of the material occurred. This phenomenon is reported in literature as radiolysis [25] and it is reflected by the amorphization of the oxide layers. T. Sasaki *et al*. draw the same conclusion from an *in-situ* TEM study of $HCaNb_3O_{10}$ exfoliation.[26] Therefore, the record at this accelerating voltage needs optimization. Especially,

one must ensure to provide a current density as low as possible. For instance the HRTEM images in ***Figure 8*** were recorded at 100 kV with a nominal current density of 2.2 $pA.m^{-2}$.

To circumvent radiolysis or knock-out phenomena, two possibilities can be considered. First, working at a lower accelerating voltage, as J. Coleman *et al.* did for imaging graphene nanosheets.[7] It should allow the preservation of the chemical bonds. The authors worked at 60 kV in STEM mode to record HRTEM clichés. Secondly, the opposite situation *i.e.* increasing the accelerating voltage, is also viable. For instance, B. Lotsch *et al.* used STEM mode at 300 kV to image both perovskite and LDH nanosheets.[27] At this nominal tension, the electrons display a high kinetic energy which results in a minimal interaction with matter. These two perspectives of study as well as Cryo TEM are interesting to finely study the fragile hybrid nanosheets without damage.

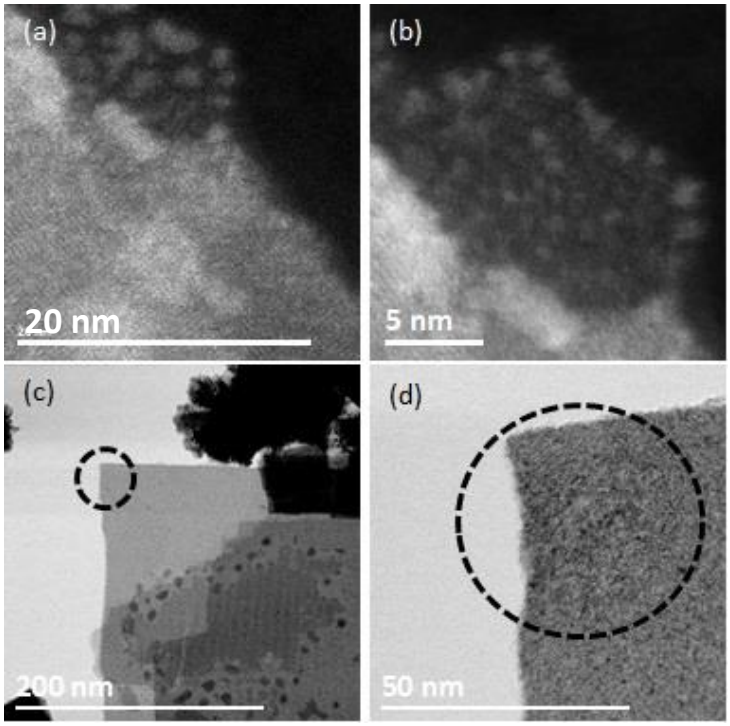

Figure 12: TEM images in STEM mode of $C_{10}PO_3$-HST illustrating (a), (b) the knock-out and (c), (d) the radiolysis process during the imaging.

V.3.4 Atomic Force Microscopy

Atomic Force Microscopy (AFM) provides a topographical image of the surface of the substrate and the deposited objects and is a useful technique, complementary to far-field microscopies. The precision along the z-axis is better than 1 nm which is mandatory for thin 2D materials. The scanned area is of 5 µm×5 µm which makes easier a statistical analysis on the lateral size and thickness on the nanomaterials. In an optimized situation, the nanosheets lie as flatly as possible without forming aggregates. The covering of the substrate is strongly related to the deposition method, the nature of the nanosheets and the surface modification of the substrate.

In this part, we aim at exposing the different deposition methods, we used during this PhD work and the resulting AFM image we recorded from the substrates. This study benefitted from many discussions with Mircea Rastei at IPCMS.

V.3.4.1 Sample preparation

Many works on nanosheet synthesis and characterization do not insist on the sample preparation for AFM imaging. Nevertheless, one must take care of the deposition process to avoid aggregation of the nanomaterials or to reach a good coverage of the substrate.

J. Coleman *et al.* used AFM to get statistical estimation of the graphene nanosheets lateral size.[7,28] The authors carried out the drop casting of a dilute suspension of graphene (10 µL) onto an Si/SiO_2 wafer. The solvent is chosen to display a low boiling point. Thus, they can heat the substrate during the process to quickly evaporate the solvent and to avoid the aggregation of the nanomaterials. A final rinsing step is performed to eliminate the weakly adsorbed nanosheets or the potential aggregates.

For bare charged layered oxide, T. Sasaki *et al.* also used a drop-casting of a diluted titanate nanosheets suspension. However, the team modified the bare Si/SiO_2 wafer with a poly(ethylenimine) (PEI) at low pH. Hence, the substrate surface is positively charged which favours the adhesion of negatively charged oxide layers.[29] The same team reported improvements in the drop-casting method to circumvent inherent drawbacks (*e.g.* coffee ring effect) by slowly pipetting the solvent under heating to favour uniform deposition.[30] Similarly, the same group uses also spray deposition to build film of nanosheets onto PEI-coated substrate.[31] In contrast, Y. Matsumoto *et al*. considered a dip-coating approach to deposit TBA^+- nanosheets on a graphitic substrate.[32]

Concerning hybrid nanosheets, both J. Wiley *et al.* and V. Zima *et al.* use a mica substrate.[4,33] The former chooses a drop-casting approach with a subsequent drying step at ambient temperature for few hours. The nanomaterials are dispersed in ethanol at a low concentration. The latter considered the spin-coating method, followed by a drying at 60 °C for 24 hours. In comparison, Y. Oaki *et al.* drop-casted a diluted suspension of functionalized nanosheets on a Si/SiO_2 substrate.[18]

It appears there are as many deposition techniques of colloidal nanomaterials as there are nanosheets design and exfoliation processes. Therefore, we investigated many deposition methods to optimize the nanomaterials imaging by AFM. Our choice is based on literature and takes into account the nature of our nanosheets *i.e.* hybrid charged oxide nanosheets with a hydrophobic organic coating. Therefore, in a first hand, we investigate the three deposition techniques: the dip-coating, the drop-casting and the spray as depicted in ***Figure 13.*** Unfortunately**,** we could not implement the new deposition technique derived by drop casting, developed by T. Sasaki *et al*. which seems efficient for high substrate coverage.[30]

The dip-coating consisted in immersing the substrate into the suspension of nanomaterials with a slight stirring for 1 hour. The drop-casting relied on dropping the nanomaterials suspension onto a substrate, heated at 120°C or not. Hence the solvent is either quickly or slowly evaporated. The spray deposition was carried out on a large volume of a very diluted suspension (10 mL of the nanomaterials suspension into 20 mL of solvent). Then, the solution was sprayed on the substrate, heated at 120°C, for 30s.

Following the work of T. Sasaki *et al.* who used electrostatic interactions to favour the deposition of the nanomaterials,[29] we chose to work with a PEI-modified Si/SiO_2 substrate even though functionalized nanosheets are less charged than bare ones. Typically, a Si/SiO_2 substrate of 1 cm ×1 cm was cleaned-up with immersion into a HCl:MeOH (1:1 vol) mixture for 20 minutes, followed by immersion into a H_2SO_4 concentrated solution and washing with water. Then the clean substrate was immersed into a PEI solution (2.5 $mg.mL^{-1}$) for 1 hour at pH = 9. Finally, the substrate was abundantly rinsed with water and IPA.

We worked with diluted suspensions of nanomaterials (suspension of $C_{10}PO_3$-HST few-layer nanosheets resulting from a selective centrifugation process) in a low boiling point solvent (IPA). After each deposition process, we carried out a heating of the sample on a hot plate at 120°C for 5 minutes to fully remove traces of solvent.

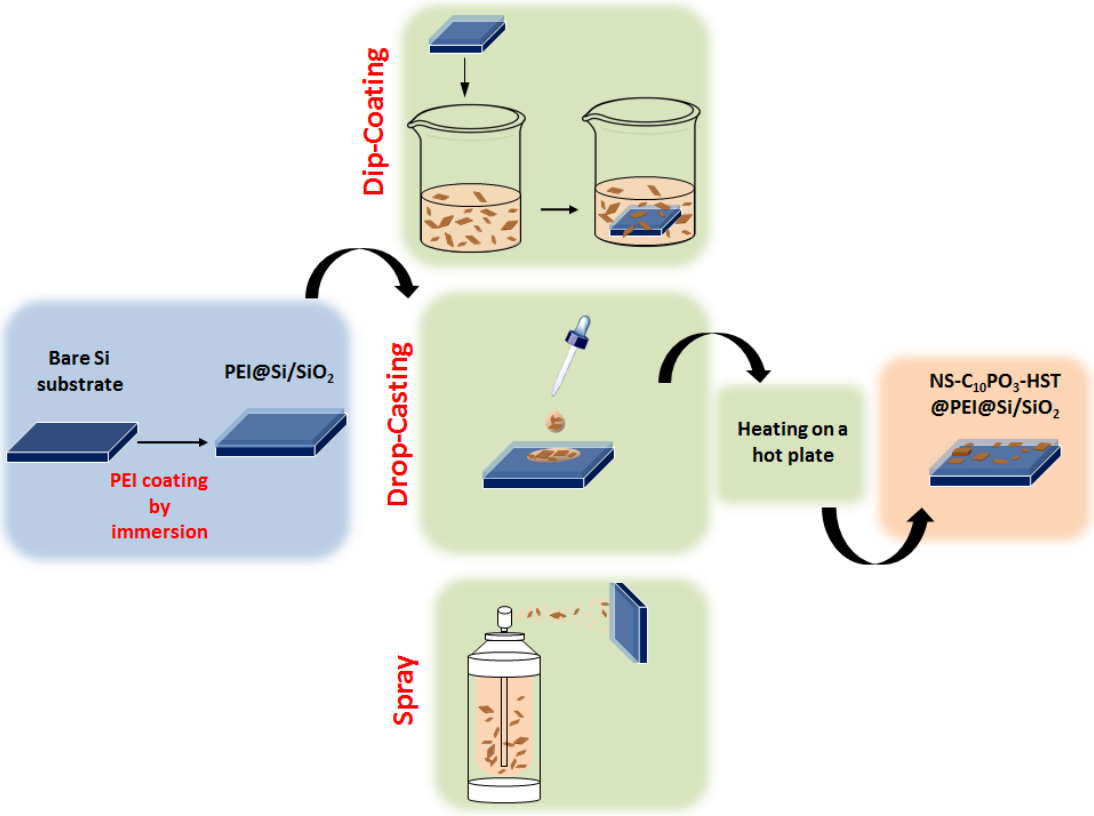

Figure 13: Schematic view of the deposition process of $C_{10}PO_3$-HST nanosheets onto a Si/SiO_2 substrate for AFM imaging.

V.3.4.2 Imaging of substrates coated with hybrid nanosheets

The efficiency of the three deposition techniques is assessed by AFM. ***Figure 14*** shows relevant AFM pictures of a substrate surface, prepared by dip-coating, drop-casting and spray.

The dip-coating approach leads to a high coverage of the substrate by small particles as shown in ***Figure 14 (a).*** We cannot easily find an area with large isolated nanosheets as the large flakes were usually found either along with thick materials or with many small particles on top of them. These smaller

nanomaterials (~50 nm) arise from the second fragmentation process (edge erosion) we discussed above (see ***V.3.3.4***). They tend to preferentially and/or quickly cover the substrate as they display a larger diffusion coefficient and are more likely to get in contact with the substrate.

The drop casting method can lead to either good deposits or non-analyzable ones depending on the temperature. We noticed that during the process, when heating the substrate at 120 °C, a "coffee-ring" pattern was observed during the drying of the drop.[34] This phenomenon results from a fast withdrawal of the drop volume from the edges to the center, leading to a fast increase of the concentration of the nanomaterials at the edges of the drop, resulting in aggregate formation within this "coffee ring". These piles of nanomaterials contain most of the few-layer nanosheets which are stacked with other nanomaterials. In that case, no interesting image can be recorded. At the opposite, when the drop dries over few hours at room temperature, the "coffee ring" pattern is avoided, a more homogeneous coverage of the substrate is obtained and nanosheets can be detected with AFM as shown in ***Figure 14 (b).***

The spray deposition requires a sufficient amount of solution for an effective surface coverage by nanomaterials. The final deposit is similar to the ones obtained from drop-casting at room temperature (***Figure 14 (c)***). Optimization of the spray process, especially the concentration of the nanomaterial suspension and the nature of the substrate may lead to a better coverage of the surface.

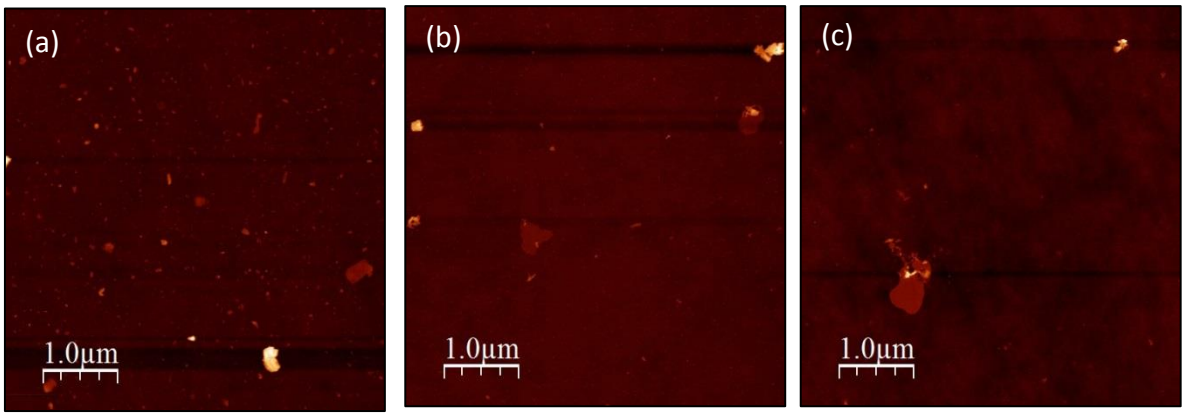

Figure 14: AFM images of $C_{10}PO_3$-HST nanosheets deposited on a Si/SiO_2 substrate by (a) dip-coating, (b) drop casting at room temperature and (c) spray.

The experimental determination of the monolayer thickness is carried out using a substrate prepared by drop-casting at room temperature. Many images of nanosheets were recorded in order to accurately determine the thickness of a monolayer. In ***Figure 15***, four nanosheets are seen on AFM images with a topographical profile. The mean thickness of the nanosheets (one inorganic layer plus two organic layers) is estimated at 4.1 ± 0.5 nm which is in good agreement with the value obtained from XRD (3.4 nm). The slight difference arises from a different arrangement (tilt angle) of the organic layer due to its two distinct interfaces (one with the substrate and one with the air), compared to what is measured in the layered bulk materials from XRD. It is worth mentioning that no thinner nanosheets were imaged on this substrate.

The lateral size of $C_{10}PO_3$-HST monolayers is around ~500 nm even if anisotropic shapes are seen, in accordance with the TEM and SEM analysis. For instance, the monolayer ***Figure 15 (a)*** displays a maximum lateral distance of 744 nm while its minimum one is 390 nm. These dimensions are representative of all the imaged nanosheets. In addition, we emphasize the peculiar curvature of some nanosheets edges which agrees with the nanomaterials of similar size we observed in TEM and SEM. These curved shapes were also observed by Y. Oaki *et al.* even though the authors did not use mechanical-force assistance for exfoliation (just heating plus a slight stirring).[18,35] Similarly, V. Zima *et al.* also imaged curved-shape hybrid zirconium phosphate nanosheets after exfoliation with shear forces.[33]

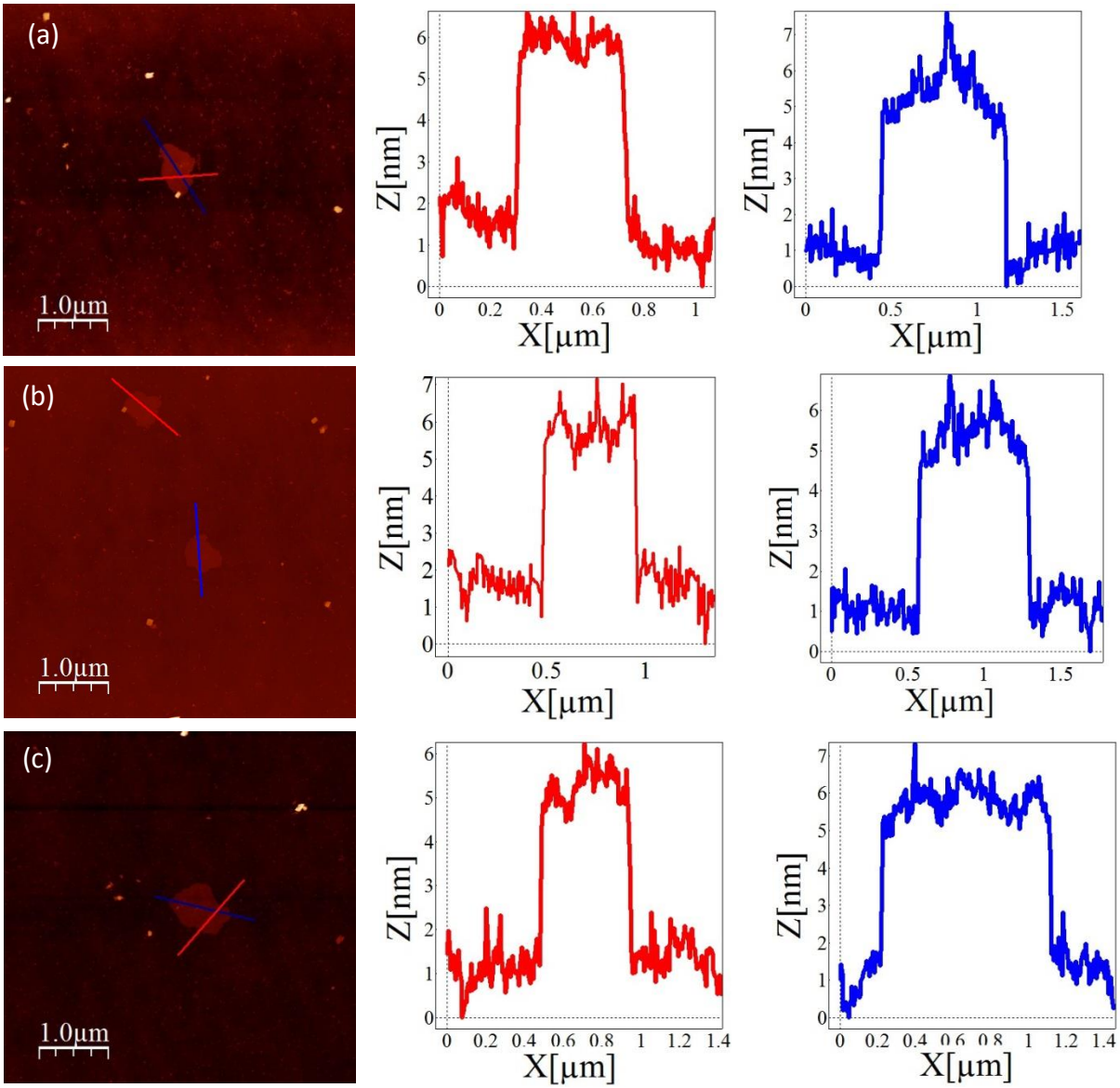

Figure 15: (a) to (c) AFM images of $C_{10}PO_3$-HST nanosheets and Z-profiles of monolayer.

V.3.5 Conclusion

Using microscopic techniques, we closely studied the nanomaterials after their deposition on a surface. Through SEM and TEM, we were able to observed few-layer nanosheets which can be stacked. Their lateral sizes are between 500 nm and 1 μm despites the presence of small nanomaterials. This polydispersity in thickness, size and shape is explained by the two breaking mechanisms. The number of layers in a stacked pile can be determined by using intensity profile on dark-field images. In addition, TEM evidences some defects on the nanosheets (like holes) which might arise from non-homogeneous functionalization of the interlayer space.

AFM images confirm the previous observations concerning the lateral size and the shape of the nanosheets. This technique allowed determine the mean thickness of a hybrid monolayer of $C_{10}PO_3$-HST around 4 nm, in accordance with the 3.4 nm, determined by XRD of the bulk layered hybrid, which supports the preservation of the functionalization after exfoliation as highlighted previously with IPC-AES results.

V.4. Characterization of nanosheets suspensions by scattering techniques

V.4.1 Static and Dynamic Light Scattering (SLS and DLS)

V.4.1.1 State of the art

Although the microscopic techniques as TEM or AFM provide essential pieces of information on the structure and composition of functionalized oxide nanosheets, they cannot assess the mean geometric characteristics of a nanosheets population in solution. Therefore, scattering techniques have a great potential to overcome the shortcomings of microscopy. Light scattering is a characterization technique, available at the lab scale and largely used in the field of nanoparticles. Nevertheless, light scattering remains absent from the set of usual characterizations for 2D materials.

Either a commercial tool is used without any assumption on the results[36] or semi empirical relation are drawn as performed by J. Coleman *et al.*[10] The authors investigated the light scattering characterization of few-layered nanosheets also using a commercial apparatus and they found a semi-empirical relation, supported by TEM images. The nanosheets dimension corresponds to a sphere whose diameter is closely equivalent to the lateral size of the nanosheets. However, the authors did not assess any size distribution and a prior knowledge of the sample is required to get a reliable measurement. Unfortunately, a straightforward transposition of their work to our nanomaterials cannot be made: our system displays an organic coating, which might modify the dynamic behavior of the nanomaterials in solution.

F. Van der Kooij *et al.* performed a light scattering study (both Static Light Scattering (SLS) and Dynamic Light Scattering (DLS)) on well-defined nanosheets in terms of shape, size and size distribution

as they considered gibbsite $Al(OH)_3$ platelets, known to display a regular hexagonal shape with a lateral size close to 100 nm.[11] Thus, the polydispersities of both size and shape are smaller compared to suspension of nanosheets, obtained by liquid phase exfoliation of layered materials like graphene or charged layered oxides. The authors assimilated the gibbsite 2D platelets to thin disks and were able to analyze suspension by both SLS and DLS. Finally, they were able to provide a mean hydrodynamic size which matches with lateral size determined by TEM as well as sedimentation coefficients. In this case, the range of concentration was low enough to neglect interaction between the particles (*e.g.* electrostatic interactions)

P. Holmqvist *et al.* studied the effect of hydrodynamic and electrostatic interactions on the dynamic of nanosheets, using light scattering on the same gibbsite platelets.[12,37] The concentration range was broader than in the work of van der Kooij *et al*., from dilute suspension up to liquid-crystal transition. The authors found a good agreement between their experimental results and the theory which computes electrostatic interaction between platelets.

Besides the influence of charge on the dynamic behavior of nanoparticles , D. Shah *et al.* considered hybrid nanomaterials:[38] the authors studied the static and dynamic behavior of layered silicate, coated and stabilized by poly(methyl methacrylate) in chloroform. They were able to derive the hydrodynamic diameter of the particles using the form factor of an oblate ellipsoid. Another noticeable point in their work is that there is no control of the particles shape. Thus, their system is in fact closer to the hybrid nanosheets we synthesized.

Except D. Shah *et al.*, all the works on light scattering of nanosheets we reviewed deal with ideal nanosheets in terms of shape. All of them consider small lateral size (around 100 nm) with a narrow size distribution.[11,12,38–40] Thus, the nanosheets scattering can be easily described in the Guinier regime, in which the determination of both geometric dimension and diffusion coefficient are well defined and can be more or less easily assessed. Yet a characterization by light scattering of hybrid nanosheets obtained by liquid-assisted exfoliation, meaning intrinsic shape and size polydispersity, is not described in literature.

In the following part, we described the characterization of a suspension of $C_{10}PO_3$-HST nanosheets, using light scattering. The determination of the geometric dimensions of the scattering nanomaterials will be assessed by both static and dynamic light scattering. In the former case, this evaluation of the lateral size goes through the study of the radius of gyration whereas in DLS it will be determine through the diffusion coefficient.

Therefore, before giving the results of the light experiment, we will describe the choice of the model and give a brief theoretical background on which our analysis relies, especially the adaptation and use of CONTIN software which optimizes the data treatment of a long light scattering experiments.

All the following light scattering experiments and analysis were carried out in collaboration with François Schosseler (Institut Charles Sadron, Strasbourg) who developed a computational method based on the CONTIN procedure to analyze routinely light scattering data.[41]

V.4.1.2 Description of the models

In this work, we assimilate the hybrid nanosheets to thin uniform thin disk with a diameter **d** and a thickness **l** (***Figure 16***) as van der Kooij *et al.* did in their work on gibbsite platelets.[11] It is worth mentioning we do not consider here a multiple-layer system *(i.e.* one inorganic oxide layer surrounded by two organic layers). Indeed, light scattering is sensitive to variation/fluctuation of refractive index, thus we consider that our hybrid $C_{10}PO_3$-HST display a global refractive index n_{ns}. Besides, the scattering power of the denser inorganic layer is much larger than the one of the low-density organic layer which supports the model. In addition, in the following, we will not take into account any effects of the remaining charges at the oxide layer surface, notably on their dynamic behavior. We assume that electrostatic interactions between two nanosheets can be neglected due to organic solvent in which the nanosheets are dispersed and to the steric hindrance of the organic layers.

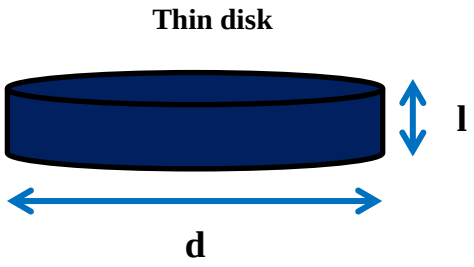

$$P(q) = \int_0^{\pi/2} \frac{sin^2(\frac{ql}{2}\cos(\theta)}{(\frac{ql}{2}co(\theta)^2} \frac{4J_1^2(\frac{qd}{2}\sin(\theta))}{(\frac{qd}{2}\sin(\theta))^2} \sin(\theta)\, d\theta$$

Form factor of a thin disk

Figure 16: Model of thin disk for a hybrid nanosheet and the corresponding form factor.[42]

V.4.1.3 Sample preparation

A suspension of colloid must fulfill some requirements to be correctly analyzed in light scattering techniques. First, one must eliminate residual dust or sediment from the solution by filtration of the suspension. As the scattered intensity is related to the volume of the scatterers, large particles like dust scatter much light that smaller ones (*i.e.* the nanomaterials of interest). Thus, presence of dust or large sediment leads to wrong size determination (overestimated). In the present work, we did not directly filter the $C_{10}PO_3$-HST nanosheets suspension as we suspect the nanomaterials to preferentially stick to the filter. Therefore, we avoid dust and sediment by using pre-filtrated solvent (*i.e.* filtrated IPA using a 0.22µm-pore filter) for the redispersion of the suspension after the final washing step of the selective centrifugation process.

In addition, the nanosheets suspension must not be too concentrated in order to minimize the inter-particles interaction and the phenomenon of multiple scattering.[43] Although some papers reports the light scattering analysis of concentrated suspension,[12] this situation is not in the scope of this work as it will add complexity to a yet non-trivial characterization. In this following study, the concentration in nanoparticles was estimated 45 $mg.L^{-1}$ determined by ICP-AES results. With respect to a formula unit, considered to be the same as the one of the bulk $(C_{10}H_{21}PO_2(OH))_{0.9}H_{1.1}Bi_{0.1}Sr_{0.85}Ta_2O_{6.1}$, this corresponds to a concentration of 0.06 $mmol.L^{-1}$. And if we consider monolayer squared nanosheets of lateral size about 800 nm this corresponds to a concentration in nanosheets of about 2×10^{-8} $mmol.L^{-1}$.

V.4.1.4 Experimental settings

Light scattering experiments were performed using a compact ALV/CGS-8 goniometer equipped with a He-Ne laser (14 mW, λ = 632.8 nm, vertically polarized) and an ALV-7002/USB-25 correlator. The temperature of the matching index fluid (toluene) was kept at 25 ± 0.1°C using a circulating water bath. The scattered light is repeatedly recorded for 1 min at different detector positions *i.e.* at different scattering vectors *q* defined as:

$$q = \frac{4\pi n}{\lambda} sin\frac{\theta}{2}$$

where n is the solvent refractive index, λ the laser wavelength and θ the angle between the detector position and the direction of the incident beam. Recording at several scattering vectors allow to probe both size and shape dependencies.

As the scattering intensity was found to evolve in time, measurements were cycled for several hours to characterize the kinetics of this evolution (See **Experimental Section**). All the scattering intensities are normalized by the intensity scattered by a toluene standard measured at an angle of 90° and at 25°C.

The autocorrelation functions of the scattered electromagnetic field were analyzed with the CONTIN software[44,45] using a set of scripts described elsewhere.[41,46] These scripts allow a batch analysis of the large number of measurements generated by the experimental procedure. Besides, the procedure contains a selection step based on some criteria to discriminate and remove the wrong measurements:

- $\frac{\Delta I}{< I >} < 0.5$ where < I > is the mean intensity, ΔI is the difference of intensity between two recording points. It can be rephrased as: the measure is discarded if $I_{max} >> < I >$; Typically, this is mostly observed when the sample contains very large particles like dust (***Figure 17 (c)***)
- $G^{(2)}(q,0)-1 < 1$, where $G^{(2)}(q,t)$ is the intensity correlation function. Otherwise, the data fitting cannot be performed mathematically (***Figure 17 (d)***).

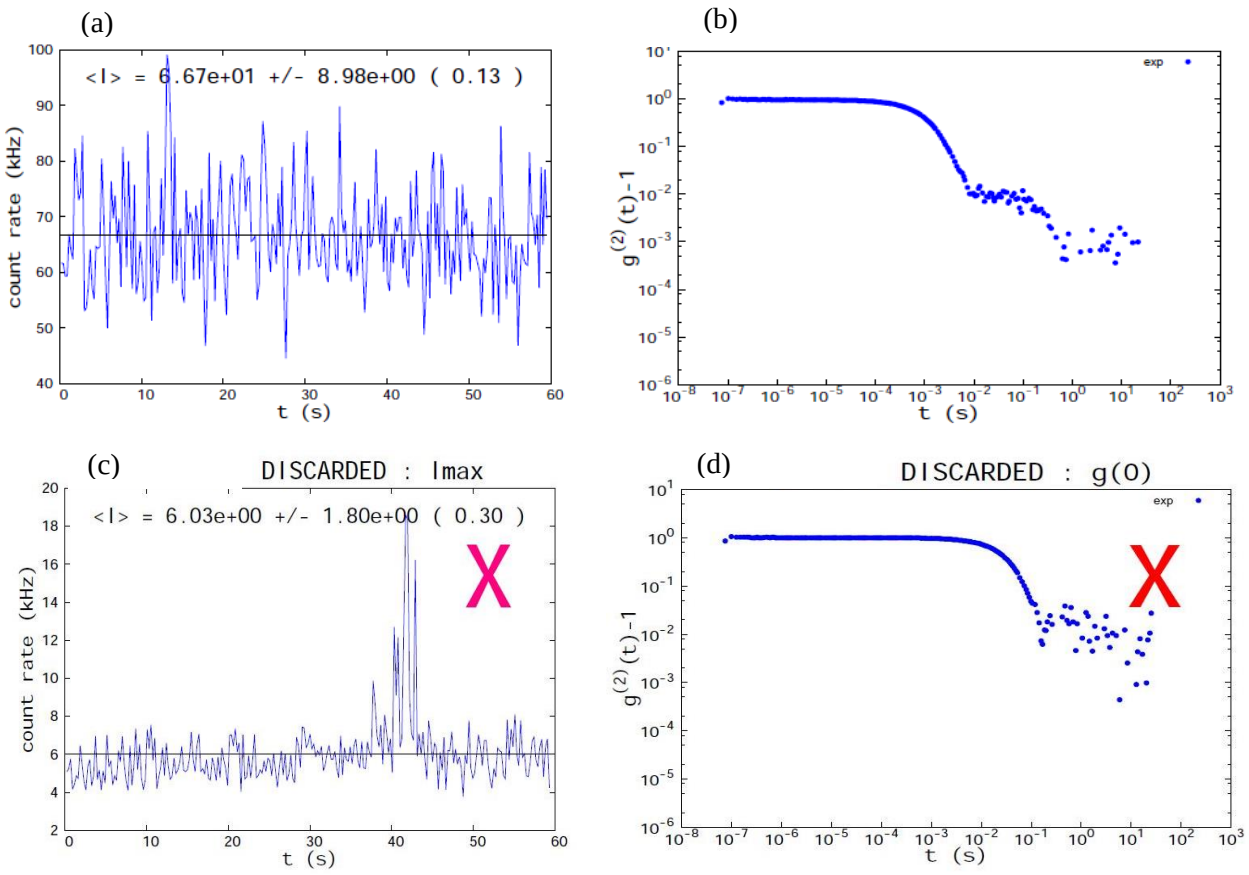

Figure 17: (a) Scattered intensity signal for a measurement of 1 min and (b) its corresponding intensity autocorrelation function. Both (a) and (b) fulfill the quality criteria. (c) Scattered intensity profile whereby I_{max} >> < I >, illustrated by the intensity spike at 40s. (d) Intensity autocorrelation function where $G^{(2)}(0)-1 > 1$ (the logarithm scale cannot allow to clearly see the out-out range value at short times).

V.4.1.5 Static light scattering: theoretical background

F. van der Kooij *et al.* carried out static light scattering analysis of platelets by considering the following equation:[11]

$$I(q) \propto V^2 P(q) S(q) \qquad \textbf{Equation 1}$$

where V is the volume of the particles, *P(q)* is the form factor and *S(q)* is the static structure factor. This expression is valid for spherical object and can be applied for platelet in the case of low concentrated solution *(i.e.* no interaction between the particles), thus *S(q)* = 1. The form factor *P(q)* is defined as shown in ***Figure 16***.

However, as seen in SEM and AFM images (***Figure 2*** and ***Figure 14***), the $C_{10}PO_3$-HST nanosheets exhibit both size and shape dispersities, which prevent from using the form factor of thin disks to analyze the static scattering intensity. Therefore, we consider a more general expression of the scattered intensity, applicable to any system:

$$I(q) \propto \int n(V)V^2\left(1 - \frac{q^2 R_g^2(V)}{3} + O(q^4)\right)dV \qquad \textbf{Equation 2}$$

where q is the scattering vector, *n(V)* is the number of colloid with volume *V* radius of gyration $R_g(V)$. $O(q^4)$ is the forth order term, detailed by F. Schosseler and L. Leibler elsewhere.[47] The radius of gyration of an obejct characterizes the distribution of mass of a system with respect to its mass center and can usually be expressed analytically in terms of its characteristic dimensions. Thus, the radius of gyration for the considered thin disks is given by:

$$R_g^2 = \frac{d^2}{8} + \frac{l^2}{12} \qquad \textbf{Equation 3}$$

The determination of radius of gyration in SLS is carried out using the Zimm representation $I^{-1}(q)$ as a function of q^2. Usually, the use of ***Equation 2*** to estimate R_g is valid in the Guinier regime ($qR_g << 1$), which allows the series expansion.

Considering the range of the scattering vectors allowed by the experimental set up (between 2.5×10^{-2} nm^{-1} and 4.5×10^{-3} nm^{-1}), the diameter of the nanomaterials must be inferior to 150 nm to determine the radius of gyration from ***Equation 2***. However, with AFM and SEM images, we observed much larger nanomaterials. Thus, we may not be in the Guinier regime for light scattering experiments.

Nevertheless, as there is a partial compensation of the different contributions to the q^4 terms, we will be able to estimate the quantity R_g outside the Guinier regime. Therefore, in the Zimm representation, the fitting of the data will be performed using a parabolic function instead of the conventional linear fit.[47] The radius of gyration R_g is deduced from the coefficients of the parabolic fits. The extrapolated value of I(q=0), obtained by the parabolic fit, and its time evolution will be considered to ascertain the reliability of the method. The time evolution of I(q=0) has to be indeed consistent with the time evolution of I(q) and should not display too large error bars

V.4.1.6 Static Light Scattering: results.

Before assessing the radius of gyration of the hybrid nanosheets, we consider the time evolution of the sample over the whole experiments (144 cycles or 36 hours). As depicted by ***Figure 18***, the scattered intensity remains mostly constant over the time scale of the experiments, proving the colloidal stability of the $C_{10}PO_3$-HST nanosheets in IPA. Nevertheless, a slow decrease of the scattered intensity is observed for all angle scattering angles even if this tendency is much pronounced for low angles where the contribution of large particles is more important. Thus, some larger particles in suspension are close to the limits of colloidal stability. On the other hand, this slight decrease indicates that the exfoliated nanosheets do not reaggregate, otherwise a fast decrease of scattered intensity would be observed.

This progressive sedimentation can complicate the extrapolations of the scattered intensity to q=0 in the Zimm representation. Therefore, we first build interpolating functions through the experimental points at a given angle to compute interpolated values at a given same time, for all scattering angles. These interpolated values allow a more accurate extrapolation in the Zimm representation.

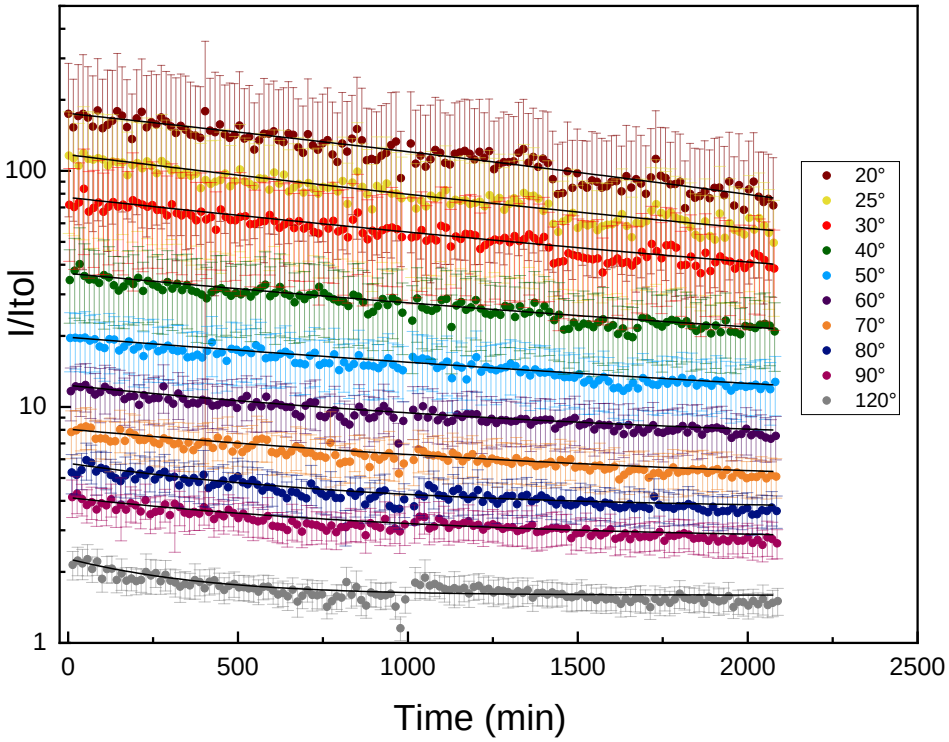

Figure 18: Time evolution of the scattered intensity for different scattering angles. The dark lines correspond to interpolation using an exponential fit.

Figure 19 (a) shows a typical Zimm representation, built from the interpolated data presented in ***Figure 18,*** for a given time. As the system is out of the Guinier regime, an extrapolating parabolic fit is carried out to obtained the fit parameters including the extrapolated intensity at zero scattering vector I(q=0). This Zimm representation and fit are performed for all cycles, allowing to obtain the time evolution of I(q=0) as depicted in ***Figure 19 (b)***. In this graph, the blue line corresponds to the data obtained by using exponential interpolating fit on the curves I(q)=f(t) and the use of such smoothing interpolating function reduces greatly the dispersion of the values of I(q=0). In addition, its temporal evolution is in accordance with the decreasing trend observed for the scattering intensity for all q vectors.

It is worth mentioning that the choice of the interpolation method affects a lot the dispersion of the values of I(q=0) as well as the errors bars. For comparison, we show in ***Figure 19 (b)*** (red squared symbols) values of I(q=0) obtained from interpolated values using sliding parabolic fits. The dispersion and the errors bars are much larger than when using exponential fits.

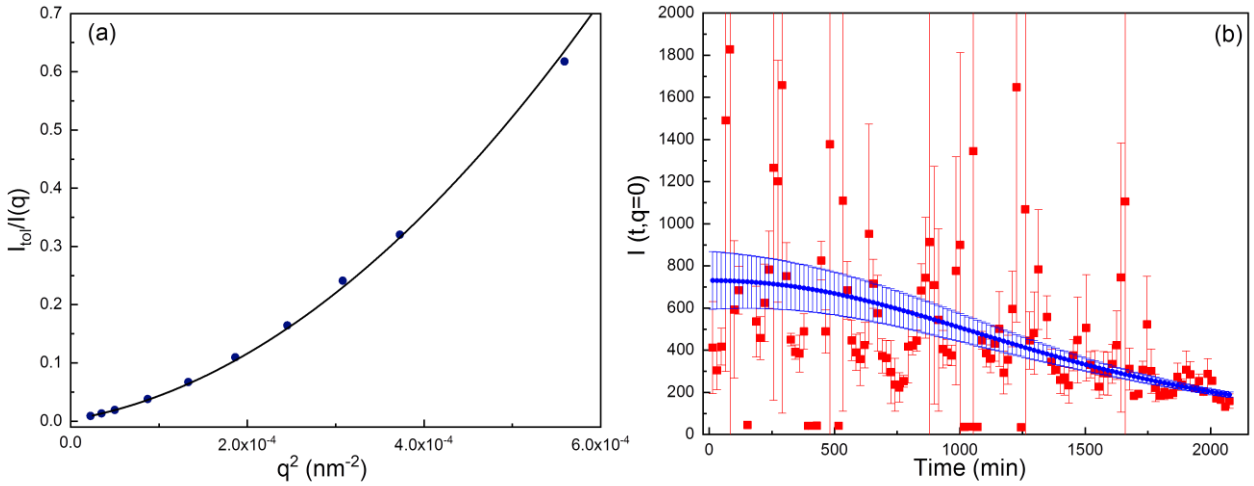

Figure 19: (a) Typical Zimm representation of interpolated scattering intensity values at a given time. The continuous line is a parabolic fit over the five smallest q values. Interpolated values were obtained from the exponential interpolating fit of I(t)=f(t) for all scattering vectors. (b) Time evolution of I(q=0); the blue line corresponds to the data obtained from the exponential interpolating fit while the red squared symbols are the values obtained when using a sliding parabolic interpolating fit.

The z-average radius of gyration is determined from the Zimm representation, notably from the first order coefficient of the parabolic fit. The temporal evolution of R_g is shown in ***Figure 20***. Similarly to the extrapolated scattered intensity I(q=0), the exponential interpolating fit leads to narrow dispersion of the values, in contrast with a parabolic interpolation. The as-determined values of the radius of gyration are above 400 nm all along the experiments. Besides, at the beginning the qR_g values are in the range between 2.8 and 7 and between 1.9 and 4.6 after 35 hours. Thus, it confirms our approach, which considers the system out of the Guinier regime. It is worth mentioning that the non-monotonous behavior of the effective gyration radius might be ascribed to artefacts from the smoothing procedure, considering the error bars associated with the values of R_g.

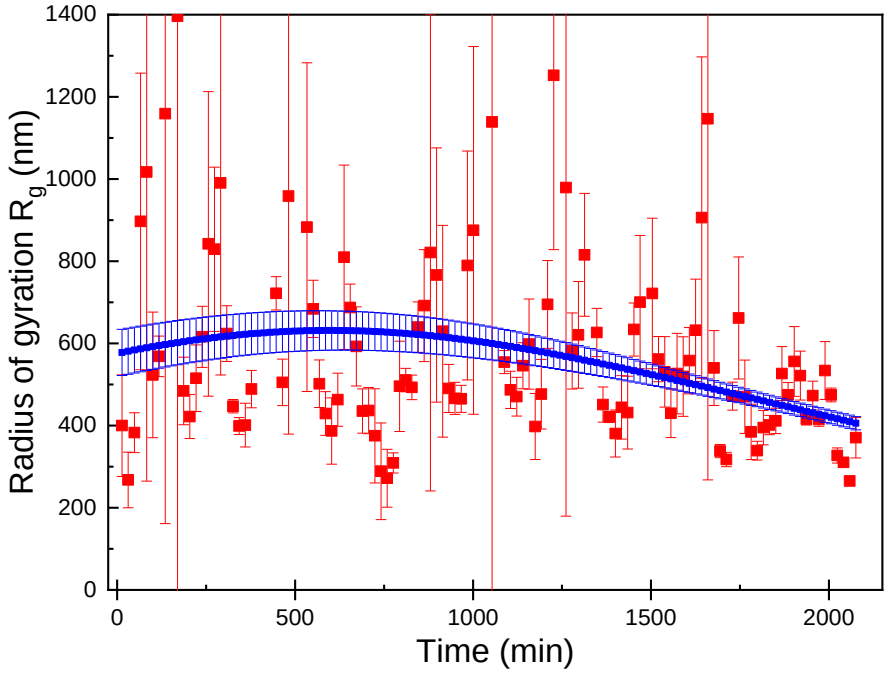

Figure 20: Time evolution of the apparent z-average radius of gyration. The continuous line corresponds to values obtained from exponential interpolating fits while the red squared symbols correspond to values obtained from parabolic interpolating fits.

Using ***Equation 3*** and assuming all the scatterers being monolayer of thickness 3.3 nm, we can estimate an apparent diameter for the $C_{10}PO_3$-HST nanosheets about 1700 nm at the beginning of the experiment and about 1100 nm after 35 hours.

V.4.1.7 Dynamic Light Scattering: theoretical background

In addition to SLS, the determination of the geometric dimension of nanomaterials can also be performed using DLS, based on the identification of the electric field autocorrelation function:

$$G^{(1)}(q,t) = \int n(V)V^2\left(1 - \frac{q^2R_g^2(V)}{3} + O(q^4)\right)e^{-q^2D(V)t}dV \qquad \textbf{Equation 4}$$

$$G^{(1)}(q,t) = \int P(V,q)e^{-q^2D(V)t}dV \qquad \textbf{Equation 5}$$

where *D(V)* is the diffusion coefficient of the colloids with a volume *V*, *P(V,q)* is the size distribution.
For hard sphere, *D(V)* is simply related to their hydrodynamic radius R according the Stokes-Einstein relation:[43]

$$D(V) = D = \frac{k_\beta T}{6\pi\eta R} \qquad \textbf{Equation 6}$$

The same equation can be applied for non-spherical colloidal nanomaterials by considering an equivalent sphere of radius R_h. The equivalent radius R_h can be more or less related to the dimension of the colloid. In the case of thin disk with a small aspect ratio, we can be expressed it as:

$$d = \pi R_h \qquad \textbf{\textit{Equation 7}}^{11}$$

In addition to the mean equivalent radius, ***Equation 5*** defines an apparent size distribution P(V,q) which can only be recovered by sophisticated method. A direct inverse Laplace transform of ***Equation 4*** is indeed very sensitive to experimental noise. Moreover, a least squares fit of a discretized version of ***Equation 4*** is not possible since it corresponds to an-ill conditioned problem. Therefore, we use the CONTIN software, a least squares fit approach with a Tikhonov regularization taking into account *a priori* conditions on the physical acceptable solution (*i.e.* prior knowledge on the system is required to perform least squares approach such as the baseline, the model of errors or the particle size range) [43–45]

The first step of the CONTIN method consists in analyzing the normalized intensity auto correlation function $G^{(2)}(q,t)$ which is defined as :

$$G^{(2)}(q,t) = \frac{<I(q,0)I(q,t)>}{<I(q,t)>} \qquad \textbf{\textit{Equation 8}}$$

Where *t* is the delay time which is in the range of 10^{-7}s to 10^{2} s. This function is automatically calculated from the scattered signal by the correlator without any assumption. The CONTIN software first fits the experimental intensity autocorrelation function in the form of the following expression:

$$G^{(2)}(t) = \int P'(\tau) e^{-\frac{t}{\tau}} d\tau + G_\infty \qquad \textbf{\textit{Equation 9}}$$

P'(τ) and τ are positive fitting parameters (noting that the former has no physical meaning), G_∞ defines the asymptotical value of $G^{(2)}(t)$. This intensity correlation function is related to the electric field autocorrelation function by the Siegert relation, valid for non-interacting particles:

$$G^{(2)}(t) = 1 + \beta (G^{(1)}(t))^2 \qquad \textbf{\textit{Equation 10}}$$

Thus, after fitting $G^{(2)}(t)$, the CONTIN software will calculate the value of $\beta G^{(1)}(t)$ using the previous Siegert relation, then it will fit these values by setting the fitting parameter P(V) and τ, the relaxation time which is defined as $\tau = q^2 D(V)$. It is worth mentioning that the second fitting step is only applied to the measurements which follow the requirements defined above. Another important think to notice is that several relaxation times might be observed for non-spherical particles as they display two components in their apparent diffusion coefficient: one component corresponds to translational motion of a particle while the second translates its rotation. Thus, for high aspect ratio nanosheets, a coupling between both rotational and translational diffusion coefficients might complicate the analysis of the autocorrelation

function by CONTIN. Some papers report the use of depolarized light source to performed DLS in order to discriminate the two contributions of the apparent diffusion coefficient.[12,39,40]

In addition, for polydisperse system as it is for the $C_{10}PO_3$-HST suspension, where the conditions of the Guinier regime are not met at each scattering angle, ***Equation 4*** can introduce an effective dependence of the measured diffusion coefficient on the scattering vector. This dependency contrasts with the case of monodisperse spherical nano-objects where the diffusion coefficient is constant. Thus, for polydisperse suspension, an estimation of the true diffusion coefficient can be obtained by extrapolating D(q) as a function of q^2 to q=0.

V.4.1.8 Dynamic Light Scattering: Results.

A typical intensity autocorrelation is shown in ***Figure 21 (Left)***, illustrating the CONTIN procedure which takes into account the intensity autocorrelation function, then performs a fit of the electric autocorrelation function to get the relaxation time distribution for one measurement. A single-peak Gaussian distribution is observed in that case. By extension, the relaxation time distributions, for a defined scattering vector over the whole experiment time (***Figure 21 (Right)***), shows consistently only one broad mode of relaxation The mean relaxation times and its distribution are extended over one decade of relaxation times with respect to the q value. In fact, the relaxation times obtained by CONTIN analysis were in very good agreement with those deduced from the slope at the origin of the field correlation function and we found no perturbation by the coupling between the rotational and translational diffusion modes. Therefore, in the following, we will simply analyze the data like for a suspension of Brownian hard spheres and we will deduce characteristic sizes of our platelets by assimilating them to non-interacting thin disks. Thus, we may use ***Equation 6*** and ***Equation 7*** to estimate the equivalent radius R_h for all scattering vectors.

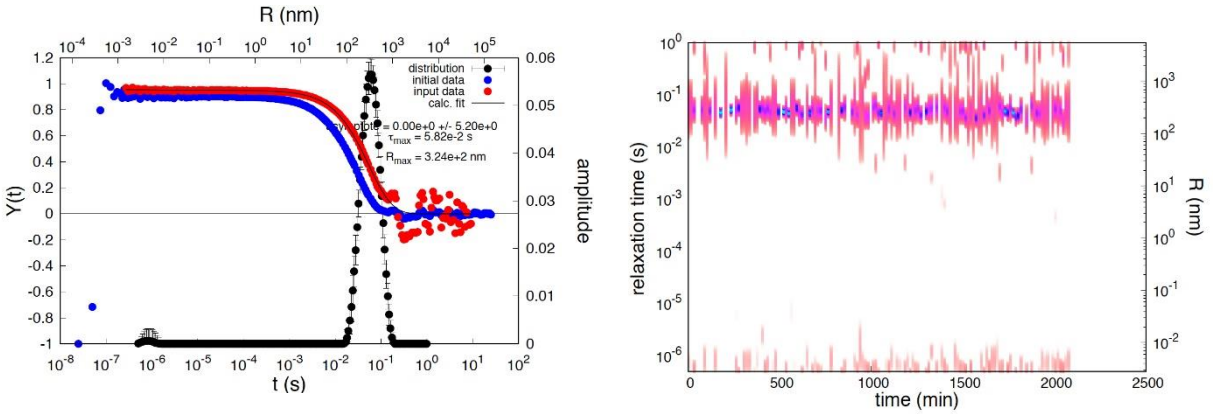

Figure 21: (Left) Typical correlation functions together with the distribution of relaxation times obtained through CONTIN analysis: (blue) intensity autocorrelation function minus 1; (red) electric field autocorrelation function; (black) distribution of relaxation times; (continuous line) result of the CONTIN fit. Right) Set of distribution of relaxation times measured at scattering angle 30° as a function of time. The color codes the amplitude of the distribution of relaxation times, increasing from pale pink to cyan. The top x-axis (left) and the right y-axis (right) give the equivalent Stokes-Einstein sphere radius corresponding to the relaxation time scale. CONTIN analysis gives

consistently one single mode of relaxation with some spurious small peaks corresponding to unphysical hydrodynamic sizes.

In order to determine the effective equivalent radius, we follow the same procedure we carried out in SLS analysis *i.e*. we begin by interpolating the experimental data to perform a subsequent extrapolation of these interpolated values at zero scattering vector. ***Figure 22*** shows the time evolution of equivalent sphere radius, calculated using Stokes-Einstein relation, for two scattering angles (30° and 90°). We notice a slight decrease of the values over the experiment which is more pronounced at low angles. This observation is consistent with the temporal evolution of the scattered intensity although the interpolation is made using linear fit in DLS.

Then, in ***Figure 23***, we plot $1/R_h$ as a function of q^2. The experimental data points were fitted in order to determine the diffusion coefficient or the equivalent radius, extrapolated at q=0. Due to the dispersion of the data points, we choose to use parabolic fit on the whole q range instead of the five smallest scattering angles as we did for the scattered intensity in the Zimm representation (***Figure 19 (a)***). In fact, whatever the choice of fitting method of these data, it reflects the steady upward shift of the diffusion coefficient with time, which translates in a steady decrease of the extrapolated hydrodynamic radius as depicted by the $R_h(q=0)$ curves in ***Figure 23 insert.***

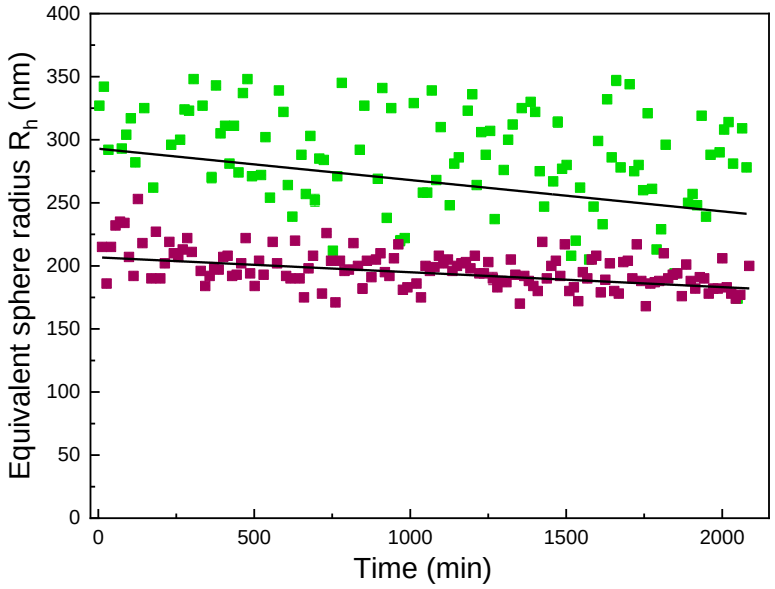

Figure 22: Decrease with time of the equivalent Stokes-Einstein sphere radius for scattering angle 30° (green circles) and 90° (purple squares). The straight lines correspond to the interpolation of the data through a weighted least squares linear fit.

From DLS results and using ***Equation 7,*** we estimate the $C_{10}PO_3$-HST nanosheets apparent diameter about 1000 nm at the beginning of the experiments and about 800 nm after 35 hours. We notice that compared to SLS results, the lateral size determined by DLS is closer to the value we obtained from TEM or AFM images.

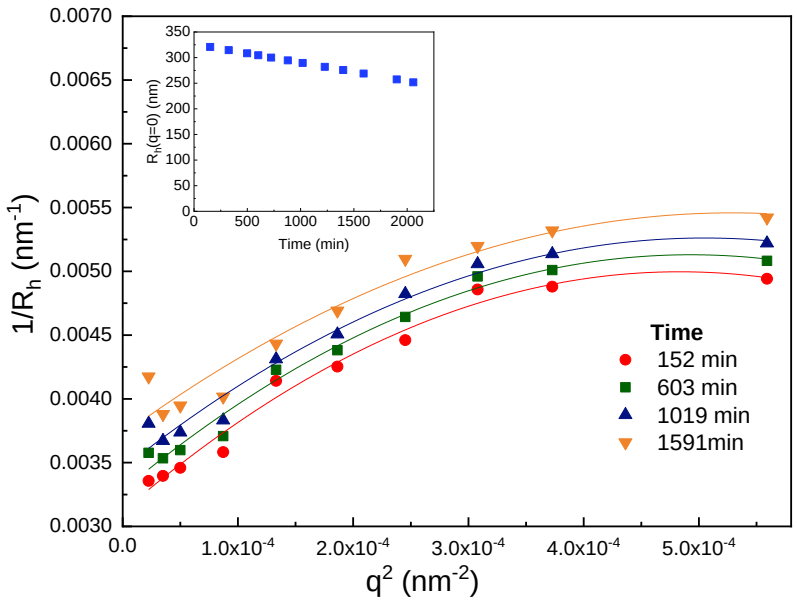

Figure 23: Typical plots of $1/R_h$ as a function of q^2. The inset shows the temporal evolution of $R_h(q=0)$ extrapolated using a parabolic fit of the data.

V.4.1.9 Conclusion

We carried out light scattering experiment on a suspension of $C_{10}PO_3$-HST nanosheets, suitable for the technique *i.e.* dust- and sediment-free solution in a good range of concentration (assessed by the Zetasizer and determined by ICP-AES). The CONTIN software allowed a standardized analysis of scattered signal which mainly displays one relaxation time.

As depicted by TEM images, the large lateral size of the nanosheets combined with the scattering vector range did not allow to use conventional equation in the Guinier regime. Thus, interpolation of the data and Zimm representation were used to elucidate the radius of gyration in SLS and the equivalent sphere radius in DLS through the diffusion coefficient.

Although estimated out of the regular Guinier range and with caveats, the average lateral dimension about 1µm is in a good agreement with the values deduced from TEM and AFM images, taking into account that the scattering techniques provide z-average dimensions over the size distribution, which tend to be larger than the averages obtained through a limited number of measurement in the direct space.

However, despite these congruent results, the polydispersity as determined by van der Koij *et al.* could not be assessed due to impossibility to discriminate the dispersity in size from the one in shape one as well as their large distribution. Their effect is evidenced by the fluctuations of the diffusion coefficient with respect to the scattering vector. In addition, the effect of charge is hidden in the polydispersities.

V.4.2 Small angle and Wide angle X-ray scattering

V.4.2.1 State of the art

The structural static description of hybrid nanosheets can be completed by the X-ray scattering at low and wide angle. Despite their limited accessibility, SAXS and in a less extend WAXS are very popular in the 2D materials field as it allows to screen both long-range distances (*i.e.* small scattering vectors) and smaller distance (large scattering vectors) respectively. Similarly to light scattering, models have been developed to extend the use of such powerful technique to anisotropic shaped nanomaterials and now a plethora of system can be studied by X-ray scattering.

Among all the system, the colloids clays suspension at different concentrations range were analyzed by X-ray scattering, especially to probe the inter-particles distance and a potential coupling between orientation and position like in liquid-crystalline phase.[48] C. Shang and J. Rice computed the radius of gyration of montmorillonite particles from a diluted suspension, using a multilayer model in the Guinier regime.[14] In addition to the inorganic layer, the authors distinguished the two adjacent counter ions layers from the solvent as they display a lower electron density. A good agreement between the model and the experimental data were found, using modified Guinier approximation.

L. Michot et *al.* characterized many phases of nontronite clay suspension by SAXS allowing to the elucidate the interlayer distance, ranging from 200 Å up to 900 Å, too large and broad to be probed by XRD.[49] They also could build phase diagram of nontronite for different size of particles.[50]

Concerning layered oxide, we can quote the work of R. Besselink *et al.* who highlighted the progressive delamination and loss of coherence of titanates layers as a function of the $\frac{TBA^+}{H^+}$.[15] The outcome of their work confirms the previous conclusions draw by T. Sasaki *et al.* on the influence of this ratio. However, they do not intend to extract mean thickness and/or lateral size of the nanosheets, as they formerly determined them by AFM.

In the following, the will present a preliminary X-ray scattering study of a suspension of $C_{10}PO_3$-HST nanosheets. Although P. Davidson *et al*. successfully considered a thin disk model for clays (using the form factor depicted in ***Figure 16***,[51] it seemed more appropriate to use the stacked disk model used by C. Shang and J. Rice in order to compute the presence of organic layer in the scattering phenomenon. However, similarly to light scattering, in a first approximation, we will not take into account the residual charge density of the hybrid nanosheets.

This X-ray scattering study was conducted in collaboration with Doru Constantin (Institut Charles Sadron, Strasbourg) while the experiment was carried out at the Synchrotron Soleil (Saclay), on the SWING beam line.

V.4.2.2 Description of the model

As X-ray scattering is more sensitive to electron density as light scattering, we can no longer consider the hybrid $C_{10}PO_3$-HST nanosheets as a homogenous entity. Therefore, we choose the model of stacked disks as it involves two domains with distinct electron density as depicted in ***Figure 24***.[14,42]

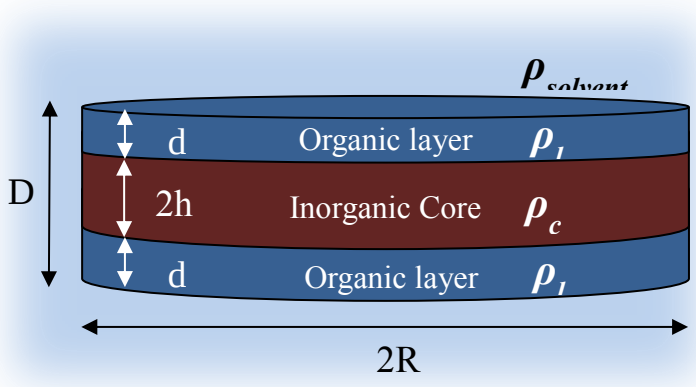

Figure 24: Representation of $C_{10}PO_3$-HST nanosheet as a thin disk with two distinct electron densities ρ_c and ρ_l for the core and the organic layer respectively.

The scattered intensity of such objects is mainly decomposed between the contribution of the discoid core and the one of the discoid organic layer as written in the following equation:

$$I(q) = \int_0^{\pi/2} [\Delta\rho_{total}(V_{total}F_{total}(q,\alpha) - V_{core}F_{core}(q,\alpha)) + \Delta\rho_{core}V_{core}F_{core}]^2 * S(q,\alpha)\sin(\alpha)\,d\alpha + background$$

Equation 11

Where the $\Delta\rho_i$ is the contrast defined as $\Delta\rho_{i} = \rho_i - \rho_{solvent}$, V_{total} and V_{core} are the total volume and the core volume respectively, $F_{total}(q,\alpha)$ and $F_{core}(q,\alpha)$ are defined as

$$F_{total}(q,\alpha) = \frac{sin^2(q(d+h)\cos(\alpha))}{q(d+h)cos(\theta)} \frac{2{J_1}^2(qR\sin(\alpha))}{qRsin(\theta)} \quad F_{core}(q,\alpha) = \frac{sin^2(qh\cos(\alpha))}{qhcos(\theta)} \frac{2{J_1}^2(qR\sin(\alpha))}{qRsin(\theta)}$$

Equation 12

Finally the structure factor $S(q,\alpha)$ is defined as:

$$S(q,\alpha) = 1 + \frac{1}{2}\sum_{k=1}^{n}(n-k)\cos(kDq\,cos\,(\alpha))e^{\frac{-kq^2(D\cos(\alpha)\sigma_d)^2}{2}}$$

Equation 13

Where n is the number of stacked disks, and σ_d is the Gaussian standard deviation of the organic layers thickness.

Equations 11 to ***13*** allow us to introduce the fitting parameters of the scattering profile obtained by SAXS and WAXS experiments. First, there are the geometric dimensions of the disk as the thickness of the organic d and the thickness of the core 2h. This latter represents the inorganic oxide layer of constant thickness of 9 Å. Thus, only the thickness of the organic layer will be considered as a fitting parameter as well as its standard deviation. The radius of the disk, has been fixed at the mean value of 500 nm (which corresponds to the mean radius we determined by SLS and DLS) as small fluctuations of this value will hardly affect the SAXS and WAXS profiles. The electron density of both core and organic layer are calculated by using SASview facilities. A scale term is also set up.

V.4.2.3 Experimental settings

In order to analyze the whole material obtained from shear-force assisted liquid exfoliation, the sample for SAXS-WAXS study were obtained by simply decanting the bare exfoliated nanomaterials suspension at room temperature in a test tube. After a week, we obtained shade gradient as depicted in ***Figure 25***. The suspension is then separated into 4 parts, denoted as Supernatant X (X=1, 2 , 3, 4) which will be analyzed in X-ray scattering without additional washing steps. Thus, the supernatant 1 might contain the more buoyant particles while in the supernatant 4 large and thick particles are more likely to be found. This "sedimentation" process provides quite concentrated suspensions, necessary to obtain enough scattered signals.

As a reference, we also analyzed bulk layered $C_{10}PO_3$-HST, just poured in an IPA with slight stirring (without exfoliation).

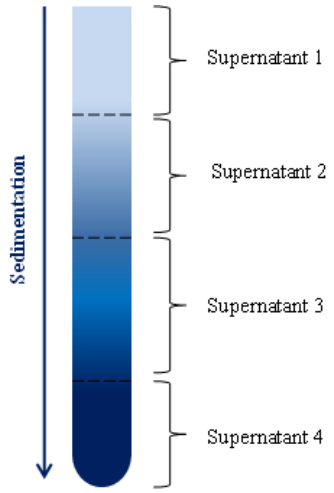

Figure 25: Schematic view of a test tube containing exfoliated hybrid nanomaterials after 1 week of decantation at room temperature. The color gradient mimics the concentration in particles and it is relevant of sedimentation.

The experiments were carried out at the SWING beamline, Synchrotron Soleil. The incident X-ray beam has an energy of 16 KeV (*i.e.* a wavelength of 0.776 nm). Two detector-sample distances were used, 0.5 m and 6 m corresponding to WAXS and SAXS geometry respectively. The raw data were normalized and the solvent contribution in the X-ray scattering profile was manually removed for all profiles. Unfortunately, this contribution could not be fully removed, leading to remaining broad peak at high scattering vectors. The SAXS and WAXS data are fitted using the open-access software SASview by using the stacked disk model described above.

V.4.2.4 SAXS results

Before assessing the geometric dimensions of exfoliated nanomaterials, we analyze the scattering profile of the reference sample, shown in ***Figure 26***. The low-scattering vector part of the curve, *i.e.* the SAXS part, does not display any pattern or oscillation except a Bragg peak, corresponding to the interlayer distance of $C_{10}PO_3$-HST. The WAXS profile also presents three Bragg peaks, corresponding to d_{001} and its two subsequent harmonics and some hollows can be distinguished.

As no characteristic pattern is shown in the SAXS profile, only the WAXS part was fitted using the stacked disk model as shown in ***Figure 26*** (red curve). The fitted parameters are shown in ***Table 2.*** We

first notice that the thickness of the core is 8 Å while the theoretical value is 9 Å (thickness of the inorganic layer determined from PDF). This difference might be explained by electronic density of the inorganic layer $SrTa_2O_7^{2-}$ which is more located at the vicinity of the heaviest atoms (Sr and Ta) than the lighter external oxygen atoms. The thickness of the organic layer and its standard deviation σ_d were fitted to get corresponding Bragg peaks with equivalent position and shape as the experimental profile. The n-stacking was determined to be 15 layers which correspond to 50-nm-thick objects. This result is consistent with the SEM images of bulk $C_{10}PO_3$-HST (see **Chapter II**).

The Bragg reflection corresponds to an interlayer distance of 33 Å (8 Å+ 2×12.5Å), the same as the bulk $C_{10}PO_3$-HST. Thus, no swelling phenomenon results from the immersion of $C_{10}PO_3$-HST into IPA solution. The oscillations of the fitted curves are not seen on the experimental curves due to polydispersity in thickness of the suspension.

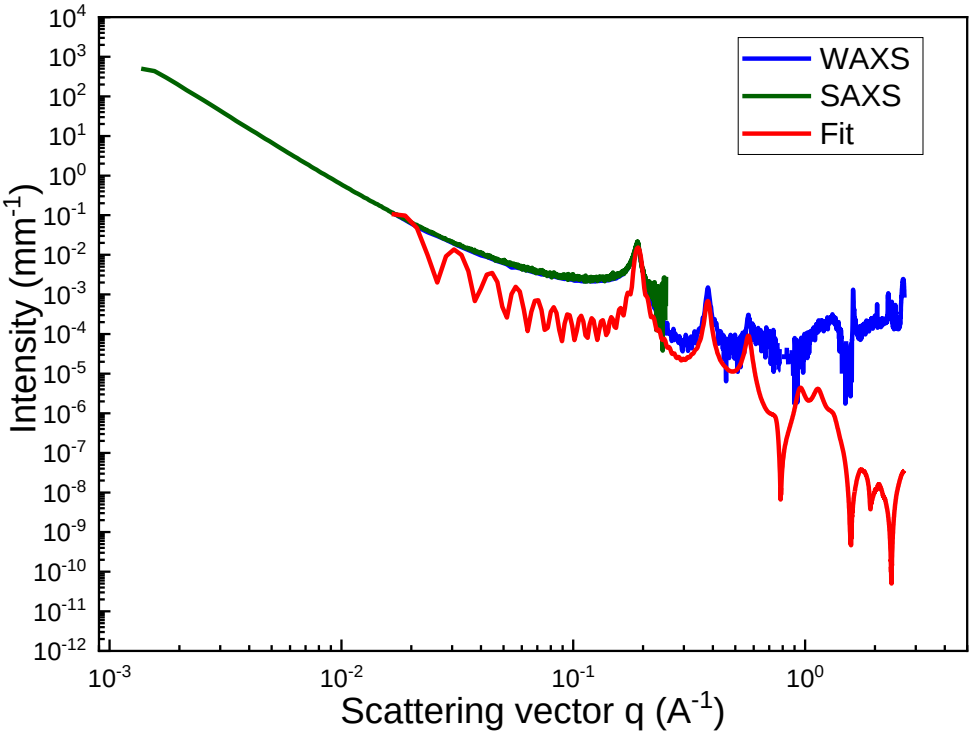

Figure 26: SAXS and WAXS profile of $C_{10}PO_3$-HST layered bulk after immersion in IPA for 1 week. The fitting (red line) was only performed on WAXS data.

The X-ray scattering profiles of supernatants 1 to 4 are shown in ***Figure 27***. First we notice that only in the case of supernatant 1, the SAXS profile displays oscillations which are related to the number of stacks. Otherwise, the supernatants 2 to 4 display similar SAXS profile as the reference *i.e.* no relevant analysis and fitting can be made. Therefore for these suspensions, only the WAXS profiles are shown and fitted.

Concerning the supernatant 1, Bragg peaks are seen in the WAXS part, corresponding to the interlayer distance d_{001} and its harmonics. The determined value of 33 Å agrees with the interlayer distance bulk $C_{10}PO_3$-HST. The presence of these peaks indicates that stacked materials remain in the

upper supernatant. Besides, the oscillations on the SAXS profiles correspond to a stacking number of 15 which matches with very thick objects with a thickness of 50 nm. In addition, the good fitting of the data was only achieved by setting the radius to 30 nm. Thus, in the supernatant 1, the nanomaterials have a 50 nm×60 nm dimensions. This result is surprising as we expected to find smaller and thinner nanomaterials in the upper fraction of the suspension.

	Reference	Supernatant 1	Supernatant 2	Supernatant 3	Supernatant 4
Thickness-core (Å)	8	8	8	8	8
Thickness-layer (Å)	12.5	12.5	12.4	12.5	12.6
Radius (Å)	5000	300	5000	5000	5000
n-stacking	15	15	9	11	15
σ_d	0.05	0.06	0.16	0.11	0.05

Table 2: X-ray scattering fitted parameters using the stacked-disk model.

The fit of the WAXS profiles of supernatants 2 to 4 are shown in ***Figure 27 (b)*** to ***(d)*** and the fitting parameters are summed up in ***Table 2.*** All profiles display Bragg peaks corresponding to the interlayer distance d_{001} of 33 nm. However, the peaks are broad and of small intensity in supernatant 2 while they become more defined and thinner for the lower supernatant 4. For supernatant 2, the fit provides a stacking number of 9, σ_d about 0.16 and a radius of 500 nm. Thus, in the supernatant 2, the nanomaterials are larger and thinner than the ones from supernatant 1 with a less regular interlayer distance. Considering polydispersity in the suspension (which is ascertained by the monotonous SAXS profile), the supernatant 2 might contain a panel of exfoliated few-layer nanomaterials with different thickness but also lateral size.

The WAXS profile of the supernatant 4 is similar to the one of the reference. The fitting also provides a stacking number of 15 with a radius of 500 nm. Thus, as expected the supernatant 4 contains unexfoliated materials which have sedimented during the process.

It is worth mentioning that the solvent contribution is still pronounced for supernatant 2 to 4 and masks relevant peaks/oscillations which would help to fully fit the WAXS profile. Thus, uncertainty remains on the staking number and the standard deviation on the layer thickness.

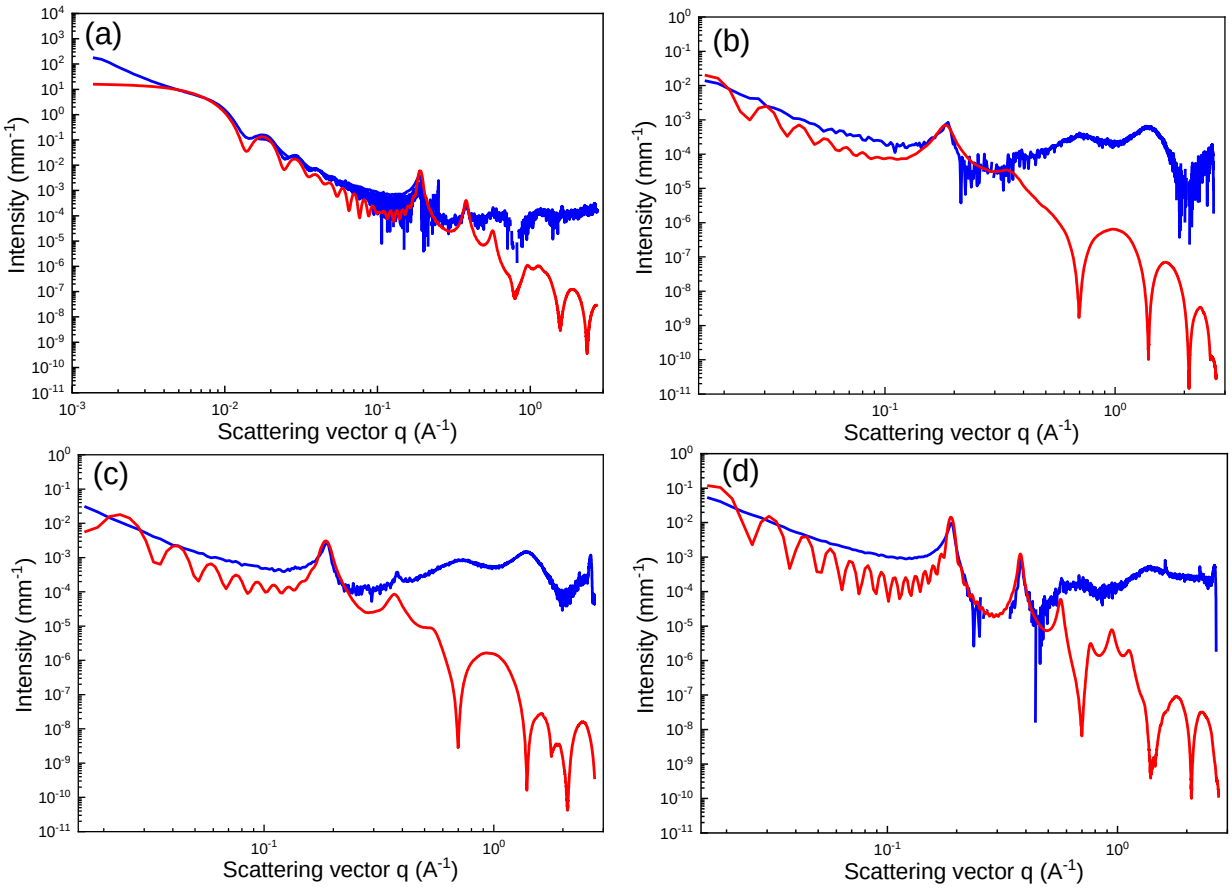

Figure 27: Experimental scattering profiles of (a) to (d) supernatant 1 to 4 respectively (in blue line) and the corresponding fitted curve using the stacked-disk model (red line). Only in the case of the supernatant 1, the SAXS and WAXS profile are shown together.

V.4.2.5 Conclusion

This preliminary study of X-ray scattering was carried out on a suspension of exfoliated $C_{10}PO_3$-HST nanomaterials that was slowly decanted. Surprisingly, the upper part of the suspension contains small non-exfoliated nanomaterials which are stable due to their organic coating. The supernatant 2 contains more few-layer nanosheets. The mean number of stacking was set to 9, which corresponds to 30-nm-thick materials. However, this value lacks precision as the fit was only carried out on WAXS profile which in addition still displays the solvent contribution. A further study should focus on the analysis of the solution after the selective centrifugation process in SAXS and WAXS

V.5. Conclusion of Chapter V

This Chapter was dedicated to the complete characterization of hybrid C_xPO_3-HST (X=3, 6, 10) nanosheets after their synthesis using the optimized exfoliation parameters, determined in **Chapter IV**. The exfoliation procedure and the selective centrifugation process allow to produce a suspension of nanomaterials. An elemental analysis of these suspensions by ICP-AES provides a ratio $\frac{Ta}{P}$ similar to the one determined from the bulk analysis. This result is very important as it confirms the preservation of the covalent grafting at the surface of the oxide layer.

Spectroscopies such as micro-Raman or X-ray Photoemission spectroscopy (XPS) would also be interesting to perform in further works.

In a second part, we focus on the far and near-field characterization of the $C_{10}PO_3$-HST nanosheets suspension deposits. A prior analysis by SEM allows to assess the shear-exfoliation process. Large nano-objects of about 1 μm are observed. Unfortunately, polydispersity in size and shape, inherent to this process and material, is present. Energy Dispersive X-ray Spectroscopy allows to get the composition of the imaged few-layer nanosheets. The constitutive elements of the inorganic layer, Sr and Ta, were found as well as the phosphorous of the 1-decylphosphonic acid.

Then, TEM imaging also showed large few-layer nanosheets about 500 nm or more, as well as stack of materials. Through the correlation between contrast and atomic number, we were able to determine the number of layers in a pile of materials and to identify a single monolayer. The inorganic structure is preserved during the exfoliation process. However, damages resulting from shear force exfoliation cannot be avoided. Similarly, some damages from the inside of the monolayer may happen. Finally, EELS spectra confirm the presence of the molecule on the nanosheets.

We were able to image few-layer nanosheets by AFM. The lateral size of the deposited objects is also in the range of the micrometer scale, in accordance with TEM and SEM. The thickness of a hybrid monolayer was determined to be around 4 nm which is close to the theoretical value of 3.3 nm determined by XRD of bulk layered materials

A further optimization of the deposition process would allow a better coverage of the substrate by hybrid nanosheets and hence a better statistical analysis of the nanosheets thickness in AFM.

In a third part, we aimed at assessing the mean lateral size of the nanomaterials in solution. Therefore, we explored the use of light scattering to characterize polydisperse and large nanosheets. It is worth mentioning that this light scattering study is one of the first reports of SLS and DLS applied to nanomaterials from liquid-phase exfoliation with a non-defined shape. We assimilated the nanosheets to thin disk. However, we could not use form factor to determine the geometric dimension of the nanosheets as the system is out of the Guinier regime. Therefore, we consider a Zimm representation with interpolated data to determine a mean radius of gyration, hence a mean lateral size of 1100 nm after 35 hours, by considering all the scatterers as monolayer. In addition, considering the equivalent sphere of the disk (hard sphere model) and using the same extrapolation method, we determined the diffusion

coefficient of the nanomaterials, hence the equivalent radius. DLS also provides a mean lateral size of 800 nm. Nevertheless, we cannot assess the dispersities.

Finally, X-ray scattering was used to determine the mean thickness of the nanomaterials in the entire suspension, without selective centrifugation. The separation of the colloid was based on their buoyancy and the rest solution was divided into four solutions. Using SASview, we fitted the SAXS and WAXS profile of four solutions according the stacked disk model. The upper part contains small and thick nanomaterials while the lower one contained unexfoliated hybrid materials. The nanosheets are dominant in the second top solution. The mean thickness of the nanosheets in this fraction is about 30 nm, with a radius of 500 nm. This value lacks of precision due to absence of pattern on the SAXS profile, solvent contribution and fitting error. This preliminary SAXS-WAXS study will have to be extended to the suspensions obtained after selective centrifugation.

V.6. Bibliography

(1) Shimada, A.; Yoneyama, Y.; Tahara, S.; Mutin, P. H.; Sugahara, Y. Interlayer Surface Modification of the Protonated Ion-Exchangeable Layered Perovskite $HLaNb_2O_7 \cdot xH_2O$ with Organophosphonic Acids. *Chem. Mater.* **2009**, *21* (18), 4155–4162.

(2) Kimura, N.; Kato, Y.; Suzuki, R.; Shimada, A.; Tahara, S.; Nakato, T.; Matsukawa, K.; Mutin, P. H.; Sugahara, Y. Single- and Double-Layered Organically Modified Nanosheets by Selective Interlayer Grafting and Exfoliation of Layered Potassium Hexaniobate. *Langmuir* **2014**, *30* (4), 1169–1175.

(3) Sugaya, T.; Ozaki, M.; Guégan, R.; Idota, N.; Sugahara, Y. Surface Modification of Layered Perovskite Nanosheets with a Phosphorus Coupling Reagent in a Biphasic System. *Langmuir* **2019**, *35* (20), 6594–6601.

(4) Akbarian-Tefaghi, S.; Rostamzadeh, T.; Brown, T. T.; Davis-Wheeler, C.; Wiley, J. B. Rapid Exfoliation and Surface Tailoring of Perovskite Nanosheets via Microwave-Assisted Reactions. *ChemNanoMat* **2017**, *3* (8), 538–550.

(5) Mizuguchi, R.; Imai, H.; Oaki, Y. Formation Processes, Size Changes, and Properties of Nanosheets Derived from Exfoliation of Soft Layered Inorganic–Organic Composites. *Nanoscale Adv.* **2020**, *2* (3), 1168–1176.

(6) Sugaya, T.; Guégan, R.; Idota, N.; Tsukahara, T.; Sugahara, Y. Highly Efficient Surface Modification of Layered Perovskite Nanosheets with a Phosphorus Coupling Reagent Making Use of Microchannels. *Langmuir* **2020**, *36* (26), 7252–7258.

(7) Paton, K. R.; Varrla, E.; Backes, C.; Smith, R. J.; Khan, U.; O'Neill, A.; Boland, C.; Lotya, M.; Istrate, O. M.; King, P.; Higgins, T.; Barwich, S.; May, P.; Puczkarski, P.; Ahmed, I.; Moebius, M.; Pettersson, H.; Long, E.; Coelho, J.; O'Brien, S. E.; McGuire, E. K.; Sanchez, B. M.; Duesberg, G. S.; McEvoy, N.; Pennycook, T. J.; Downing, C.; Crossley, A.; Nicolosi, V.; Coleman, J. N. Scalable Production of Large Quantities of Defect-Free Few-Layer Graphene by Shear Exfoliation in Liquids. *Nature Materials* **2014**, *13* (6), 624–630.

(8) Synnatschke, K.; Shao, S.; van Dinter, J.; Hofstetter, Y. J.; Kelly, D. J.; Grieger, S.; Haigh, S. J.; Vaynzof, Y.; Bensch, W.; Backes, C. Liquid Exfoliation of $Ni_2P_2S_6$: Structural Characterization, Size-Dependent Properties, and Degradation. *Chem. Mater.* **2019**, *31* (21), 9127–9139.

(9) Yan, M.; Collins, S. M.; Midgley, P. A.; Feldblyum, J. I. Factors Governing the Chemical Stability of Shear-Exfoliated ZnSe(Alkylamine) II–VI Layered Hybrids. *Chem. Mater.* **2020**, *32* (6), 2379–2388.

(10) Lotya, M.; Rakovich, A.; Donegan, J. F.; Coleman, J. N. Measuring the Lateral Size of Liquid-Exfoliated Nanosheets with Dynamic Light Scattering. *Nanotechnology* **2013**, *24* (26), 265703.

(11) van der Kooij, F. M.; Philipse, A. P.; Dhont, J. K. G. Sedimentation and Diffusion in Suspensions of Sterically Stabilized Colloidal Platelets. *Langmuir* **2000**, *16* (12), 5317–5323.

(12) Kleshchanok, D.; Heinen, M.; Nägele, G.; Holmqvist, P. Dynamics of Charged Gibbsite Platelets in the Isotropic Phase. *Soft Matter* **2012**, *8* (5), 1584–1592.

(13) Norrish, K. The Swelling of Montmorillonite. *Discuss. Faraday Soc.* **1954**, *18*, 120.

(14) Shang, C.; Rice, J. A. Interpretation of Small-Angle x-Ray Scattering Data from Dilute Montmorillonite Suspensions Using a Modified Guinier Approximation. *Phys. Rev. E* **2001**, *64* (2), 021401.

(15) Besselink, R.; Stawski, T. M.; Castricum, H. L.; Blank, D. H. A.; ten Elshof, J. E. Exfoliation and Restacking of Lepidocrocite-Type Layered Titanates Studied by Small-Angle X-Ray Scattering. *J. Phys. Chem. C* **2010**, *114* (49), 21281–21286.

(16) Honda, M.; Oaki, Y.; Imai, H. Hydrophobic Inorganic–Organic Composite Nanosheets Based on Monolayers of Transition Metal Oxides. *Chem. Mater.* **2014**, *26* (11), 3579–3585.

(17) Yamamoto, Y.; Oaki, Y.; Imai, H. Coupled Exfoliation and Surface Functionalization of Titanate Monolayer for Bandgap Engineering. *Advanced Materials Interfaces* **2017**, *4* (7), 1601014.

(18) Nakada, G.; Imai, H.; Oaki, Y. Few-Layered Titanate Nanosheets with Large Lateral Size and Surface Functionalization: Potential for the Controlled Exfoliation of Inorganic–Organic Layered Composites. *Chem. Commun.* **2018**, *54* (3), 244–247.

(19) Payet, F.; Bouillet, C.; Leroux, F.; Leuvrey, C.; Rabu, P.; Schosseler, F.; Taviot-Guého, C.; Rogez, G. Fast and Efficient Shear-Force Assisted Production of Covalently Functionalized Oxide Nanosheets. *Journal of Colloid and Interface Science* **2022**, *607*, 621–632.

(20) Backes, C.; Higgins, T. M.; Kelly, A.; Boland, C.; Harvey, A.; Hanlon, D.; Coleman, J. N. Guidelines for Exfoliation, Characterization and Processing of Layered Materials Produced by Liquid Exfoliation. *Chem. Mater.* **2017**, *29* (1), 243–255.

(21) Larquet, C.; Carriere, D.; Nguyen, A.-M.; Le, T. K.-C.; Frogneux-Plé, X.; Génois, I.; Le Griel, P.; Gauzzi, A.; Sanchez, C.; Carenco, S. Unraveling the Role of Alkali Cations in the Growth Mechanism of Gd2O2S Nanoparticles. *Chem. Mater.* **2020**, *32* (3), 1131–1139.
(22) Liu, J.; Guillemeney, L.; Choux, A.; Maître, A.; Abécassis, B.; Coolen, L. Fourier-Imaging of Single Self-Assembled CdSe Nanoplatelet Chains and Clusters Reveals out-of-Plane Dipole Contribution. *ACS Photonics* **2020**, *7* (10), 2825–2833.
(23) Virdi, K. S.; Kauffmann, Y.; Ziegler, C.; Ganter, P.; Blaha, P.; Lotsch, B. V.; Kaplan, W. D.; Scheu, C. Band Gap Extraction from Individual Two-Dimensional Perovskite Nanosheets Using Valence Electron Energy Loss Spectroscopy. *J. Phys. Chem. C* **2016**, *120* (20), 11170–11179.
(24) Ebina, Y.; Akatsuka, K.; Fukuda, K.; Sasaki, T. Synthesis and In Situ X-Ray Diffraction Characterization of Two-Dimensional Perovskite-Type Oxide Colloids with a Controlled Molecular Thickness. *Chem. Mater.* **2012**, *24* (21), 4201–4208.
(25) Egerton, R. F. Mechanisms of Radiation Damage in Beam-Sensitive Specimens, for TEM Accelerating Voltages between 10 and 300 KV. *Microscopy Research and Technique* **2012**, *75* (11), 1550–1556.
(26) Xu, F.-F.; Ebina, Y.; Bando, Y.; Sasaki, T. In-Situ Transmission Electron Microscopic Study of Perovskite-Type Niobate Nanosheets under Electron-Irradiation and Heating. *J. Phys. Chem. B* **2003**, *107* (28), 6698–6703.
(27) Ziegler, C.; Werner, S.; Bugnet, M.; Wörsching, M.; Duppel, V.; Botton, G. A.; Scheu, C.; Lotsch, B. V. Artificial Solids by Design: Assembly and Electron Microscopy Study of Nanosheet-Derived Heterostructures. *Chem. Mater.* **2013**, *25* (24), 4892–4900.
(28) Backes, C.; Campi, D.; Szydlowska, B. M.; Synnatschke, K.; Ojala, E.; Rashvand, F.; Harvey, A.; Griffin, A.; Sofer, Z.; Marzari, N.; Coleman, J. N.; O'Regan, D. D. Equipartition of Energy Defines the Size–Thickness Relationship in Liquid-Exfoliated Nanosheets. *ACS Nano* **2019**, *13* (6), 7050–7061.
(29) Maluangnont, T.; Matsuba, K.; Geng, F.; Ma, R.; Yamauchi, Y.; Sasaki, T. Osmotic Swelling of Layered Compounds as a Route to Producing High-Quality Two-Dimensional Materials. A Comparative Study of Tetramethylammonium versus Tetrabutylammonium Cation in a Lepidocrocite-Type Titanate. *Chem. Mater.* **2013**, *25* (15), 3137–3146.
(30) Shi, Y.; Osada, M.; Ebina, Y.; Sasaki, T. Single Droplet Assembly for Two-Dimensional Nanosheet Tiling. *ACS Nano* **2020**, *14* (11), 15216–15226.
(31) Sasaki, T.; Ebina, Y.; Tanaka, T.; Harada, M.; Watanabe, M.; Decher, G. Layer-by-Layer Assembly of Titania Nanosheet/Polycation Composite Films. *Chem. Mater.* **2001**, *13* (12), 4661–4667.
(32) Yilmaz, N.; Ida, S.; Matsumoto, Y. Electrical Conductivities of Nanosheets Studied by Conductive Atomic Force Microscopy. *Materials Chemistry and Physics* **2009**, *116* (1), 62–66.
(33) Kopecká, K.; Melánová, K.; Beneš, L.; Knotek, P.; Mazur, M.; Zima, V. Exfoliation of Layered Mixed Zirconium 4-Sulfophenylphosphonate Phenylphosphonates. *Dalton Trans.* **2020**, *49* (12), 3816–3823.
(34) Deegan, R. D.; Bakajin, O.; Dupont, T. F.; Huber, G.; Nagel, S. R.; Witten, T. A. Capillary Flow as the Cause of Ring Stains from Dried Liquid Drops. *Nature* **1997**, *389* (6653), 827–829.
(35) Matsui, H.; Oaki, Y.; Imai, H. Surface-Functionalized Hydrophilic Monolayer of Titanate and Its Application for Dopamine Detection. *Chem. Commun.* **2016**, *52* (60), 9466–9469.
(36) Carrasco, J. A.; Harvey, A.; Hanlon, D.; Lloret, V.; McAteer, D.; Sanchis-Gual, R.; Hirsch, A.; Hauke, F.; Abellán, G.; Coleman, J. N.; Coronado, E. Liquid Phase Exfoliation of Carbonate-Intercalated Layered Double Hydroxides. *Chem. Commun.* **2019**, *55* (23), 3315–3318.
(37) Heinen, M.; Holmqvist, P.; Banchio, A. J.; Nägele, G. Short-Time Diffusion of Charge-Stabilized Colloidal Particles: Generic Features. *J Appl Cryst* **2010**, *43* (5), 970–980.
(38) Shah, D.; Fytas, G.; Vlassopoulos, D.; Di, J.; Sogah, D.; Giannelis, E. P. Structure and Dynamics of Polymer-Grafted Clay Suspensions. *Langmuir* **2005**, *21* (1), 19–25..
(39) Holmqvist, P.; Meester, V.; Westermeier, F.; Kleshchanok, D. Rotational Diffusion in Concentrated Platelet Systems Measured with X-Ray Photon Correlation Spectroscopy. *J. Chem. Phys.* **2013**, *139* (8), 084905.
(40) Badaire, S.; Poulin, P.; Maugey, M.; Zakri, C. In Situ Measurements of Nanotube Dimensions in Suspensions by Depolarized Dynamic Light Scattering. *Langmuir* **2004**, *20* (24), 10367–10370.
(41) Klucker, R.; Munch, J. P.; Schosseler, F. Combined Static and Dynamic Light Scattering Study of Associating Random Block Copolymers in Solution. *Macromolecules* **1997**, *30* (13), 3839–3848.
(42) Guinier, A.; Fournet, G. *Small Angle Scattering of X-Ray*; Jhon Wiley and Sons, 1955.
(43) Finsy, R. Particle Sizing by Quasi-Elastic Light Scattering. *Advances in Colloid and Interface Science* **1994**, *52*, 79–143.

(44) Provencher, S. W. CONTIN: A General Purpose Constrained Regularization Program for Inverting Noisy Linear Algebraic and Integral Equations. *Computer Physics Communications* **1982**, *27* (3), 229–242.
(45) Provencher, S. W. A Constrained Regularization Method for Inverting Data Represented by Linear Algebraic or Integral Equations. *Computer Physics Communications* **1982**, *27* (3), 213–227.
(46) Echavarri Franco, I.; Lorchat, P.; Lamps, J.-P.; Schmutz, M.; Schröder, A.; Catala, J.-M.; Combet, J.; Schosseler, F. From Chain Collapse to New Structures: Spectroscopic Properties of Poly(3-Thiophene Acetic Acid) upon Binding by Alkyl Trimethylammonium Bromide Surfactants. *Langmuir* **2012**, *28* (10), 4815–4828.
(47) Schosseler, F.; Leibler, L. An Experimental Study of Gelation of Chains. *J. Phyique Lett.* **1984**, *45* (10), 501–507.
(48) Bihannic, I.; Baravian, C.; Duval, J. F. L.; Paineau, E.; Meneau, F.; Levitz, P.; de Silva, J. P.; Davidson, P.; Michot, L. J. Orientational Order of Colloidal Disk-Shaped Particles under Shear-Flow Conditions: A Rheological−Small-Angle X-Ray Scattering Study. *J. Phys. Chem. B* **2010**, *114* (49), 16347–16355.
(49) Michot, L. J.; Bihannic, I.; Maddi, S.; Funari, S. S.; Baravian, C.; Levitz, P.; Davidson, P. Liquid–Crystalline Aqueous Clay Suspensions. *PNAS* **2006**, *103* (44), 16101–16104.
(50) Michot, L. J.; Baravian, C.; Bihannic, I.; Maddi, S.; Moyne, C.; Duval, J. F. L.; Levitz, P.; Davidson, P. Sol−Gel and Isotropic/Nematic Transitions in Aqueous Suspensions of Natural Nontronite Clay. Influence of Particle Anisotropy. 2. Gel Structure and Mechanical Properties. *Langmuir* **2009**, *25* (1), 127–139.
(51) Lemaire, B. J.; Panine, P.; Gabriel, J. C. P.; Davidson, P. The Measurement by SAXS of the Nematic Order Parameter of Laponite Gels. *EPL* **2002**, *59* (1), 55.

Chapter VI

Hybrid nanosheets as building blocks for nanoarchitectonics

Chapter VI. Hybrid nanosheets as building blocks for nanoarchitectonics

VI.1. Introduction

Among the objectives of this PhD work, building heterostructures from the assembly of two or more distinct nanomaterials is the most challenging one. In the previous chapters, we described the nonetheless ambitious and complex synthesis of the building blocks for assemblies *i.e.* the functionalized oxide nanosheets. Once we have deeply characterized the as-synthesized hybrid nanomaterials, they can be integrated into nano-architectures. As reviewed in the **Chapter I**, many examples of "bare" nanosheets have been described. In the case of functionalized nanosheets, other assembling processes are available depending on the interaction the organic moiety can provide.

The first one is the π-stacking resulting from the interaction between aromatic rings. In literature, few papers report the synthesis of heterostructures based on 2D materials and guided by π-stacking.[1–3] For instance, R. Kumar *et al*. functionalized graphene and boron nitride (h-BN) with viologen and naphthol respectively, in order to couple them *via* the interaction of the aromatic rings.[1] The choice of the molecules was made considering their preferential interaction between each other, rather than homo-interaction between identical molecules.

Among the layered hybrids we designed, the pyrene-based layered oxides constitute a perfect system to build nano-architectures based on π-π interactions. In addition, the molecules display luminescent properties which are sensitive to their aggregation state.[4,5] This luminescence might be useful to characterize the exfoliation and the re-stacking of the pyrene-based hybrid in assemblies.

Concerning the hydrogen bond, they represent the most popular interaction to build architectures, especially in the field of supramolecular chemistry.[6,7] However, to our knowledge, there is no report of nanosheets assembly guided by hydrogen bond despite the huge diversity of organic molecules available. Therefore, we will investigate this pathway to assemble hybrid oxide nanosheets. Our choice of substrate/receptor couple fell on the complementary nucleosides, adenosine and thymidine. These molecules are indeed known to be part of DNA and have so far been used to build nano-architectures.[6,8,9] Inorganic nanomaterials have also been assembled using complementary nucleobase derivatives. The pioneer work of C. Mirkin *et al*.,[10] about the modification of gold nanoparticles by DNA strands opens the way to the modification and the self-assembly of metallic and oxide nanoparticles as well as carbon-base nanomaterials, as reviewed by A. Samanta and I Medintz.[11]

In the **Chapter II**, we synthesized hybrid layered oxides, containing adenosine or thymidine in their interlayer space. Thus, following the procedure we developed, nanosheets of such hybrid can be obtained and further used for assemblies.

Similarly, polymer-assisted liquid exfoliation was proved efficient to obtain hybrid nanosheets. As we used both hydrogen-acceptor and hydrogen-donor polymer (PEG and PEI respectively), in order to couple them to build architectures based on the recognition and interaction between the adsorbed polymers at the nanosheets surface.

Finally, covalent bonds can also be considered here to guide an assembly of two entities. Among all the possibilities of reaction between functional groups, we present three main instances which are the click chemistry, the amide formation and the gold-sulphur reaction.

The former case is useful as it involves quantitative reactions. To our knowledge, only one team reported the use of click chemistry to couple layered oxide nanosheets.[12] The authors used sonication-assisted exfoliation to produce hybrid nanosheets of two distinct oxides with precursors of azide-alkyne cycloaddition. Then the two nanosheets reacts in solution, leading to an alternated stack of 2D materials. The same team reported the synthesis of alternated architecture based on the thiol-ene click reaction.[13]

Another possibility would be to take advantage of amide bond formation using EDC-NHS coupling, as done in the field of nanoparticles.[14] To our knowledge, this approach has never been reported for the assembly of 2D nanosheets.

In previous work in the team, the layered oxide $H_2Bi_{0.1}Sr_{0.85}Ta_2O_7$ has already been functionalized in the team by molecules displaying terminal azide or alkyne.[15] Additionally, we have synthesized amine-terminated hybrid nanosheets (*i.e.* APTS-HST described in **Chapter II**), potentially adapted for the assembly *via* amide bond formation. Nevertheless, for the strategy of assembly based on covalent bond, we will focus in the following part on the gold-sulphur bond formation. This latter covalent bond is especially exploited to attached nano-objects on gold surface (substrate or nanoparticles).[16–18] The reaction between a terminal thiol and the gold can be performed with a relatively slight heating in solution. In addition, contrary to amide bond or other covalent bond, the Au-S is known to be "easily broken, allowing the migration of the sulphur on a gold surface.[17] We have synthesized a hybrid layered oxides, MPTS-HST which presents a terminal thiol, described in **Chapter II**. Thus, the corresponding nanosheets might be assembled at a gold surface.

In this chapter, we explore the building of different nano-architectures whose building blocks are the hybrid nanosheets we synthesized by the two-step procedure (functionalization of a layered oxides and its subsequent exfoliation). The following results and discussions constitute a preliminary work which would inspire future investigations in that way.

We mention that the hybrid layered oxides synthesis is described in **Chapter II** while the exfoliation procedure is similar to the one developed on $C_{10}PO_3$-HST. Thus, we will not exhaustively develop the synthesis of these functionalized nanosheets.

VI.2. Guided assembly using π-π interactions

VI.2.1 Luminescence properties of hybrid oxide: bulk *vs* nanosheets

VI.2.1.1 Synthesis and characterization

PyrO-HST, PyrC_1O-HST and PyrC_4O-HST, synthesized in **Chapter II**, are colored powders (from dark yellow to brown). Their UV-Vis spectra and the ones of their corresponding free molecules are shown in Erreur ! Source du renvoi introuvable.. The spectra of the hybrids display the same absorption bands as the corresponding free pyrene derivatives, explaining their similar color. Yet the bands are broader due to the contribution of the inorganic layer, which also display an absorption band around 320 nm.

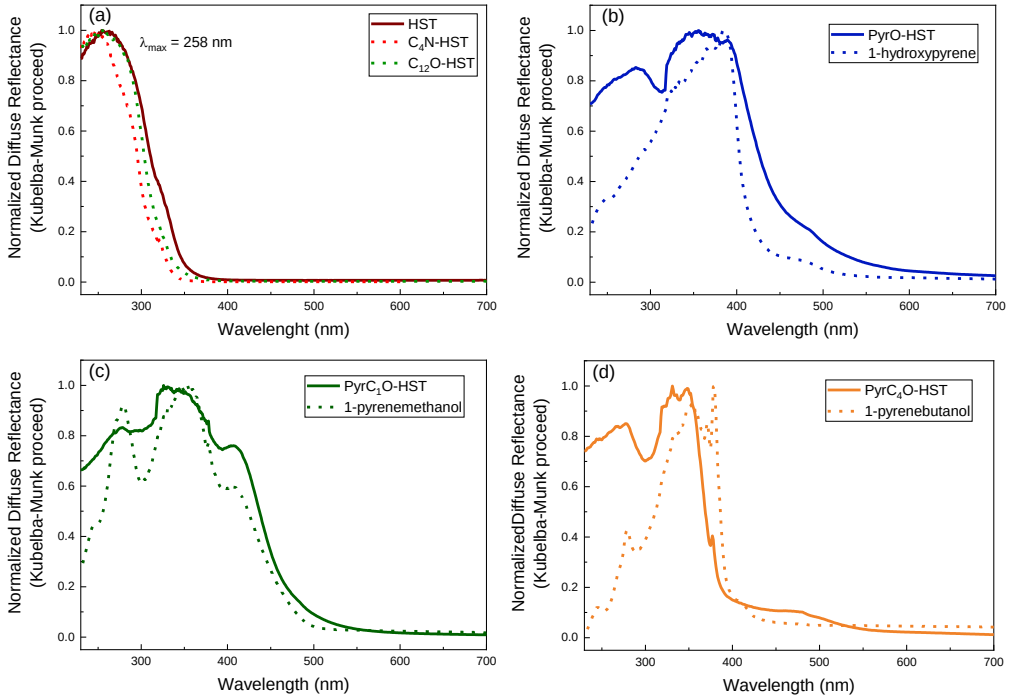

Figure 1: Solid state UV-Vis diffuse reflectance spectra of (a) HST, C_4N-HST, C_{12}O-HST,(b) PyrO-HST, (c) PyrC_1O-HST and (d) PyrC_4O-HSTand (b) to (d) their corresponding molecules in dot line.

The emission spectra of PyrO-HST, PyrC_1O-HST and PyrC_4O-HST were recorded as well as the one of the corresponding starting molecules using a common wavelength of 320 nm corresponding to the maximum of absorption (***Figure 2***). All the pyrene derivatives molecules (*i.e.* the crystallized pure powder) display the characteristic emission spectrum of an excimer, which was expected for densely packed pyrene derivatives. Similarly, the emission spectra of PyrC_1O-HST and PyrC_4O-HST display a unique broad band with a maximum at 545 nm and 472 nm respectively, characteristic of an excimer luminescence. The characteristic excimer band in the hybrid is red-shifted with respect to the one of the

molecule in the solid state by 33 nm for $PyrC_1O$-HST and 12 nm for $PyrC_4O$-HST. This shift may be ascribed to an effect of the inorganic layer. On the contrary, the emission spectrum of PyrO-HST is characteristic of a monomer-type luminescence with three vibronic bands. This signature is in accordance with the low grafting rate of PyrOH into HST and the presence of a relatively large amount of unremoved 1-butylamine. In the following we will only consider $PyrC_1O$-HST and $PyrC_4O$-HST

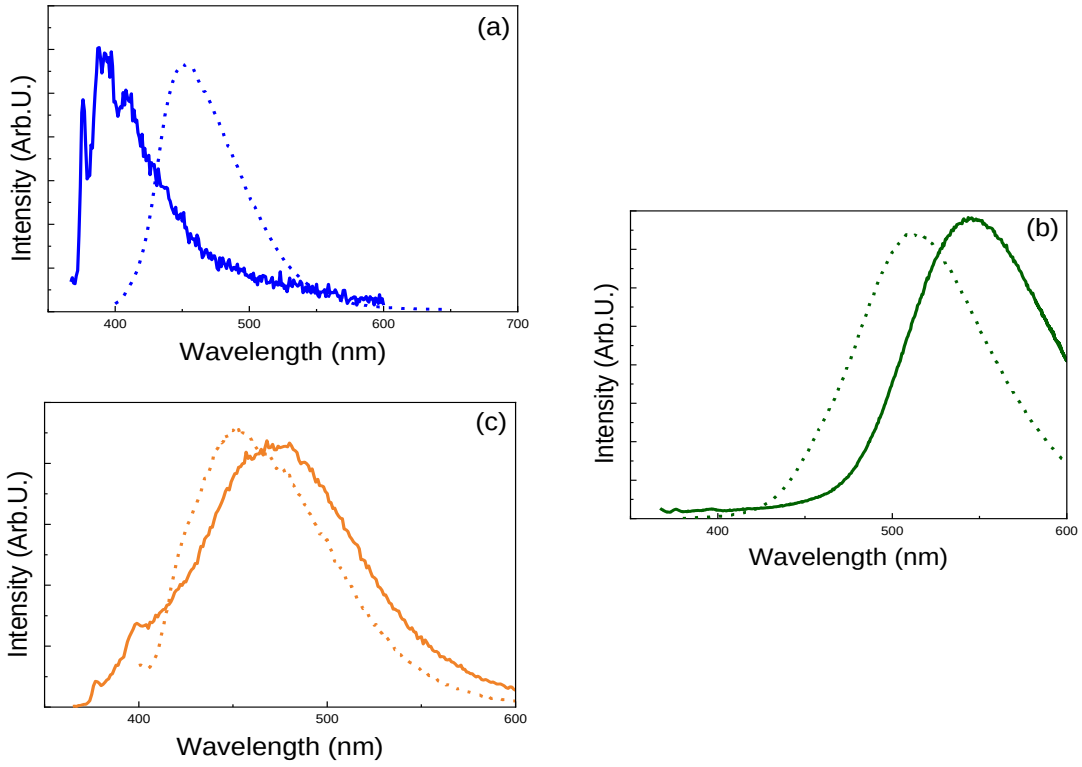

Figure 2: Emission spectra of (a) PyrO-HST, (b) $PyrC_1O$-HST and (c) $PyrC_4O$-HST (solid line) and their corresponding molecules (dot line)($\lambda_{excitation}$ = 320 nm).

We then investigated the evolution of the luminescence of $PyrC_4O$-HST by adding 1-heptanol (C_7OH) during its synthesis, at different molar ratios $\frac{n(PyrC_4O)}{n(C_7O)}$= 0, $\frac{3}{7}$, 1, $\frac{7}{3}$ and ∞. The resulting hybrids are layered materials with grafting of both molecules as stated from the XRD patterns and FTIR spectra (not shown). The characterizations notably confirm the progressive increase of the pyrene content when increasing the nominal ratio $\frac{n(PyrC_4O)}{n(C_7O)}$.

The excitation and emission spectra of the five hybrids are shown in ***Figure 3***. The same peaks are observed on the excitation spectra for all hybrids (λ_{em} =396 nm). A change in intensity is observed but only a careful determination of the quantum yields will allow to draw a precise conclusion about this evolution of the intensity. Unfortunately, such a determination of the quantum yield could not be performed during the course of this PhD. The main difference arises from their emission spectra (λ_{exc} = 345 nm). Increasing the ratio $\frac{n(PyrC_4O)}{n(C_7O)}$ from $\frac{3}{7}$, to ∞ allows to go from a monomer-type luminescence to the excimer luminescence of $PyrC_4O$-HST. This set of experiments shows that it would be possible to tune

the luminescence of a hybrid layered oxides with aggregation induced emission or quenching molecules by diluting the chromophore in the interlayer space with non-active entities. An analogous extended study was also reported by A. Costa *et al* on layer-double hydroxides.[5]

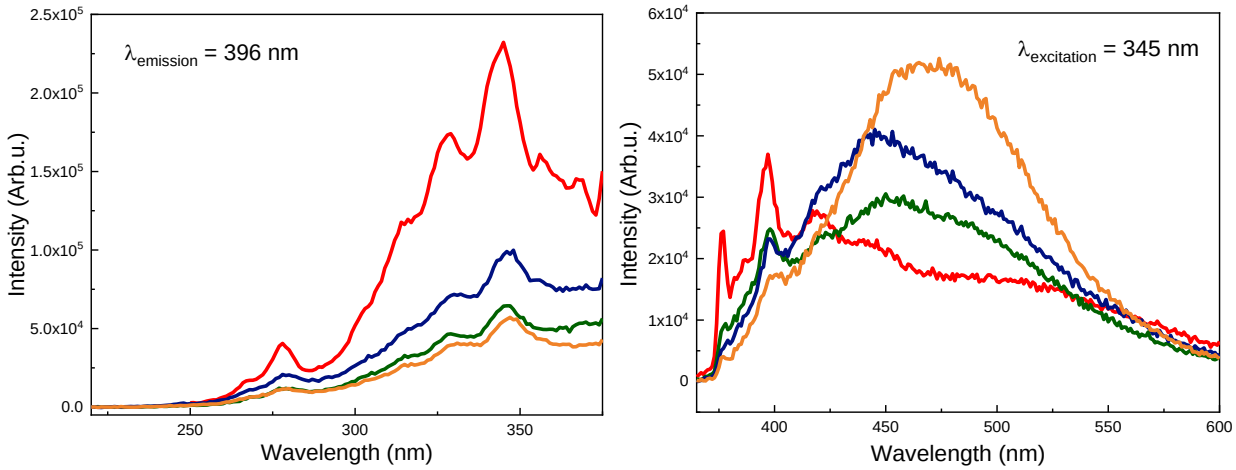

Figure 3: (a) Excitation spectra and (b) emission spectra of $(C_7O)_{0.7}(PyrC_4O)_{0.3}$-HST (red), $(C_7O)_{0.5}(PyrC_4O)_{0.5}$-HST (green), $(C_7O)_{0.3}(PyrC_4O)_{0.7}$-HST (blue) and $PyrC_4O$-HST (orange). C_7O-HST is not luminescent when excited at 320 nm.

The luminescent properties of a nanosheets suspension obtained from $PyrC_4O$-HST and $PyrC_1O$-HST was then investigated. The suspension was obtained by shear exfoliation. Typically, 20 mg of $PyrC_1O$-HST or $PyrC_4O$-HST were dispersed in IPA and shear at 11500 rpm for 1 hour. The suspension went through the selective centrifugation process. The resulting supernatant and bottoms were collected, washed and re-dispersed with IPA.

Figure 4 shows the emission spectra of a $PyrC_4O$-HST nanosheets suspension over the exfoliation process. The luminescent spectra correspond to a monomer-type luminescence from 10 minutes of exfoliation until 60 minutes without any shift or modification of the bands. No band corresponding to the excimer-type luminescence is seen on these spectra. However, we know from SEM images that stacked materials remain in the suspension over the whole experiments. Thus, we cannot quantify the exfoliation yield by comparing the relative intensity of the excimer and the monomer bands. The same conclusions are drawn for $PyrC_1O$-HST nanosheets.

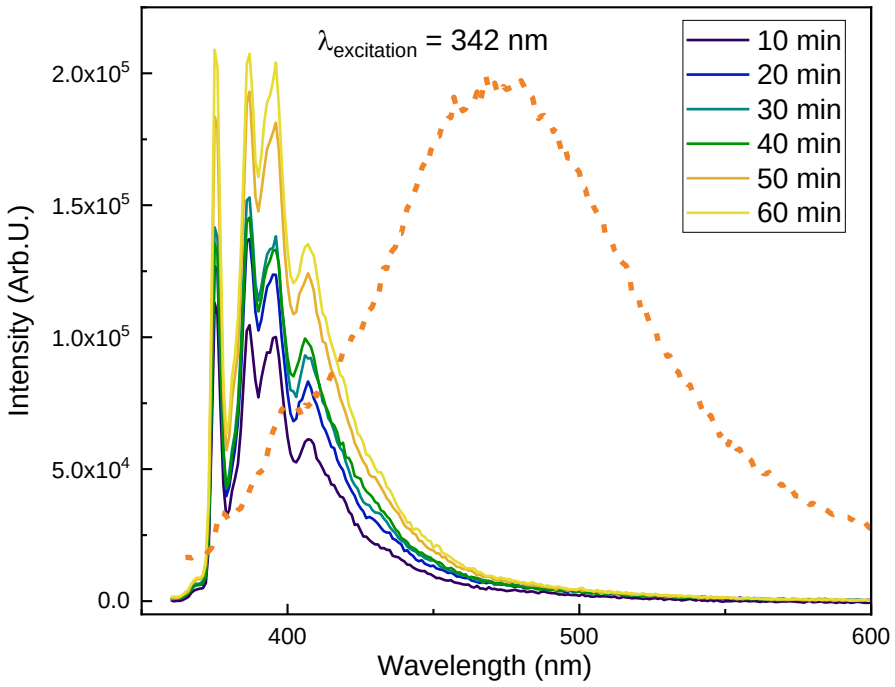

Figure 4: Emission spectra of bulk PyrC$_4$O-HST (orange dot line) and suspension of PyrC$_4$O-HST over the shear-exfoliation process from 10 minutes to 60 minutes.

VI.2.1.2 Conclusion

Luminescent nanosheets of pyrene-functionalized oxide have been synthesized. Unfortunately, this system does not enable to quantify the exfoliation. A more advanced study of the luminescence properties of the pyrene-based hybrid must be carried out by focusing on the quantum yield and the life time of the excited state.

In the following, we investigate the coupling of PyrC$_4$O-HST nanosheets with graphene.

VI.2.2 Assembly of graphene and pyrene-based nanosheets

VI.2.2.1 Synthesis and characterization

A nanosheets suspension of PyrC$_4$O-HST was obtained by following the procedure we described previously. Graphene was obtained by the sonication-assisted-exfoliation of expensed graphite (provided by D. Begin, ICPEES). Typically, 10 mg of graphite was dispersed in 40 mL of IPA and sonicated for 1 hour at 40% of the nominal power (80 W). The resulting dark suspension was centrifuged at 1600 rpm for 20 minutes. The supernatant and bottom were both collected and washed with IPA and re-dispersed in IPA. Few-layer graphene nanosheets are shown in ***Figure 5 (a)***, proving the sonication-assisted exfoliation of expensed graphite without tannic acid or other surfactant can be successful. However, we noticed the presence of sediment in the supernatant suspension one day after the process. Therefore, either the assembly experiments were performed right after graphene synthesis or an additional sonication step was carried out on the supernatant before using it.

The nanosheets of graphene and PyrC_4O-HST were assembled taking advantage of their molecular structure *i.e*. their cyclic carbon rings. Typically, 10 mL of the suspension of PyrC_4O-HST and 2 mL of the graphite solution was mixed together for 1 hour at room temperature. The as-made assembly suspension, denoted as PyrC_4O-HST@graphene, was analyzed without further centrifugation or washing. ***Figure 5 (b)*** shows a SEM image of PyrC_4O-HST@graphene. We observe a large few-layer graphene and, on top of it, smaller flakes which correspond to PyrC_4O-HST nanomaterials. However, some PyrC_4O-HST nanosheets are also observed on the membrane "alone". Thus, we cannot conclude on the specific interaction between the two entities. Moreover, no difference on the emission spectrum of the assembly and the one of hybrid nanosheets can be highlighted (not shown).

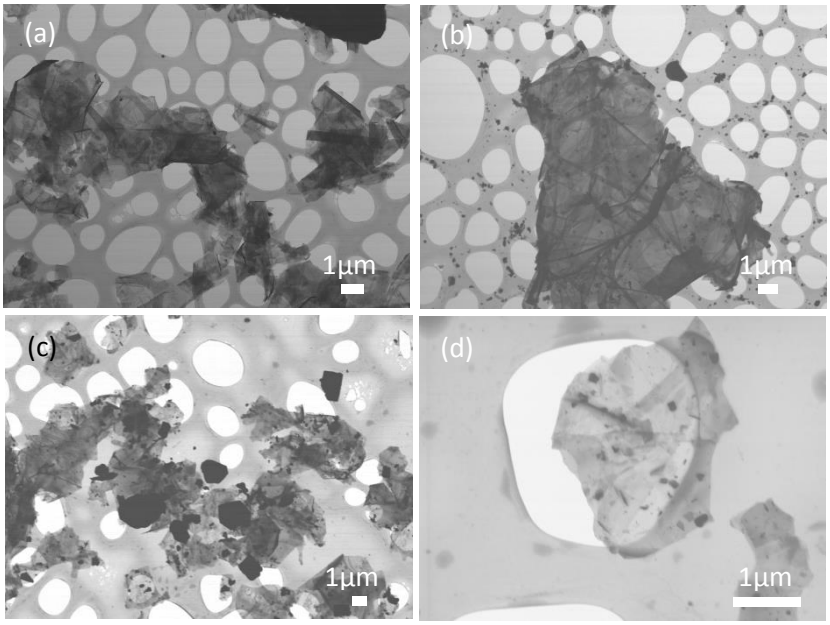

Figure 5: SEM images of (a) graphene, (b) PyrC_4O-HST@graphene obtained by mixing the corresponding nanosheets suspension, (c) and (d) PyrC_4O-HST@graphene obtained by the simultaneous exfoliation of expensed graphite and bulk PyrC_4O-HST.

As both 2D-building blocks can be obtain by mechanical force-assisted liquid exfoliation and as pyrene has proved to be efficient in the exfoliation of graphite,[19,20] we investigated the simultaneous exfoliation of graphite and PyrC_4O-HST.

Typically, 15 mg of PyrC_4O-HST and 3 mg of expensed graphite were dispersed in IPA and exfoliated using sonication-assistance. The solution was centrifuged at 1600 rpm for 20 minutes and the supernatant and bottom were collected.

Figure 5 (c) and ***(d)*** show SEM images of the supernatant nanomaterials. Large few-layer graphene sheets are observed as well as smaller and thicker ones with more geometrical shape, corresponding to the PyrC_4O-HST nanosheets. Thus, simultaneous exfoliation can also provide nanomaterials. It is worth noticing that this time, no PyrC_4O-HST flakes are found outside of the graphene flake area. This observation indicates that an interaction between the two 2D-materials occurred. However, the assembly displays the same luminescence spectrum than PyrC_4O-HST nanosheets suspension, with only small changes in band intensity. More advances studies taking into account the

respective concentration of graphene and PyrC_4O-HST nanosheets and the luminescence quantum yield would be needed in order to quantify the changes on the band intensities as observed by S. Vera-Lopez *et al.*[21] who demonstrate the potentiality of the pyrene as probe in graphene-based system.

VI.2.2.2 Conclusion and perspectives

The simultaneous exfoliation of graphite and the hybrid oxide appears to be more promising than the mixing of the two separated nanomaterials suspension for the elaboration of heterostructures.

The luminescence properties have to be investigated in more details and coupled with Raman spectroscopy (usual characterization technique for graphene-based materials and composites). Raman should allow the determination of graphene concentration and thus might help to quantify the interaction pyrene/graphene.

In further works, the deposition of luminescent nanosheets, with molecules displaying aromatic ring as pyrene, on a pre-coated substrate with graphene has to be explored. It would then be easier to assess the conductive properties of the system even if the luminescent behavior might be trickier to characterize.

VI.3. Guided assembly using hydrogen bond

VI.3.1 Complementary nucleoside-based hybrid

VI.3.1.1 Synthesis and Characterization

Nanosheets of Adenosine-HST and Thymidine-HST were obtained by shear-force-assisted liquid exfoliation. Typically, 20 mg of the hybrid materials was dispersed in 40 mL of isopropanol and exfoliated with the high-shear disperser at 11500 rpm for 1 hour. The suspension was then centrifuged at 1600 rpm for 20 minutes. The resulting supernatant and bottom were collected, washed with IPA by centrifugation and re-dispersed in 20 mL of IPA.

Figure 6 shows the SEM images of both Adenosine-HST and Thymine-HST nanomaterials from the supernatant. Despite some non-exfoliated materials, few layers nanosheets have been obtained in these experimental conditions. IPA is also a good solvent for nucleoside-based hybrids.

Before testing the assembly of two distinct oxide nanosheets, we aim at proving that the recognition by hydrogen bonds between adenosine and thymidine can happen in the experimental conditions we chose. Therefore, we firstly investigated the interaction between adenosine moieties, grafted onto HST, and free thymidine. Considering the nature of the nanomaterials (hybrid nanosheets at low-concentration), they cannot be analyzed easily by liquid-state NMR or mass spectroscopy which can probe the hydrogen bond formation and the resulting structure, as carried out by O. Shall and G. Gokel.[8,22] Thus to study the interaction between adenosine-HST and thymidine, we started using the bulk layered hybrid and the free molecules to potentially identify changes in XRD patterns, FTIR spectra and SEM images.

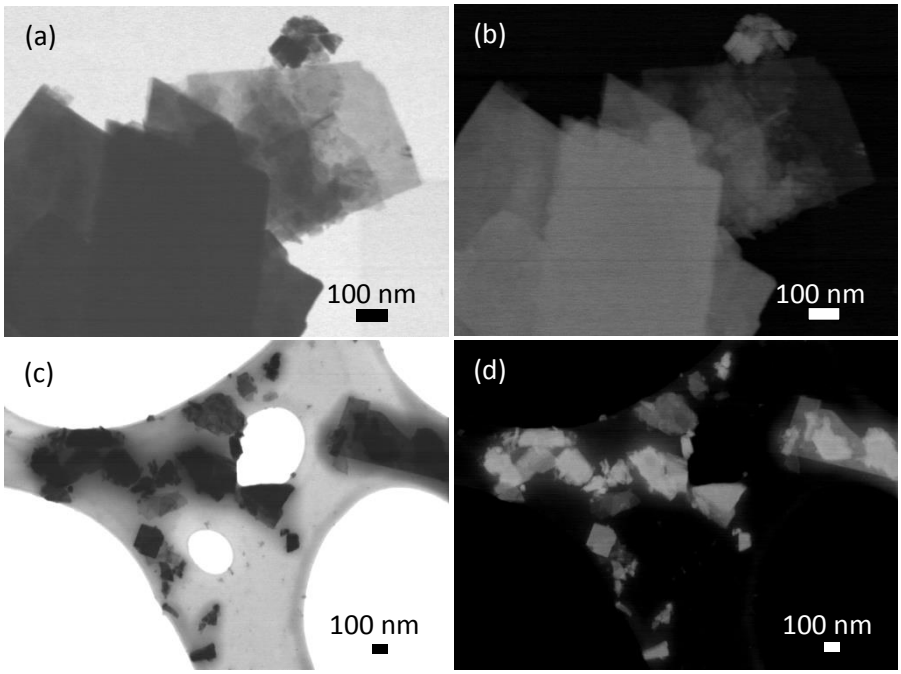

Figure 6: SEM images of (a) and (b) Thymidine-HST nanosheets and (c) and (d) of Adenosine-HST nanosheets in bright field and dark field. Note: an important organic content (solvent) remains on Adenosine-HST nanosheets

Typically, 20 mg of Adenosine-HST and 48 mg of thymidine were dispersed in 25 mL of IPA or water and stirred at room temperature for 2 days. The resulting suspension was centrifuged at 1600 rpm for 20 minutes. The supernatant and the bottom were collected, washed by centrifugation with the same solvent and re-dispersed in the same solvent.

Figure 7 shows the XRD patterns and the FTIR spectra of the experiments performed in water and IPA at room temperature. The in-plane reflections (*100*), (*110*) and (*200*), characteristic of the inorganic slab, are seen on all patterns. The interlayer distance is d_{001} = 2.41 nm for all materials. In addition, the FTIR spectra of the assemblies are identical to the one of Adenosine-HST, without any side band corresponding to thymidine. Thus, the analyzed materials corresponds to Adenosine-HST

The same experiments at a temperature of 40°C were carried out to probe the effect of temperature. However, the same conclusions as previously can be drawn from ***Figure 7*** *i.e.* there is no change in the layered hybrid Adenosine-HST.

Finally, the same set of experiments was performed using Thymidine-HST and free adenosine. Similarly, either in water or IPA, either at room temperature or at 40°C, the XRD patterns and FTIR spectra (not shown) correspond to the ones of Thymidine-HST which remains unchanged during the process.

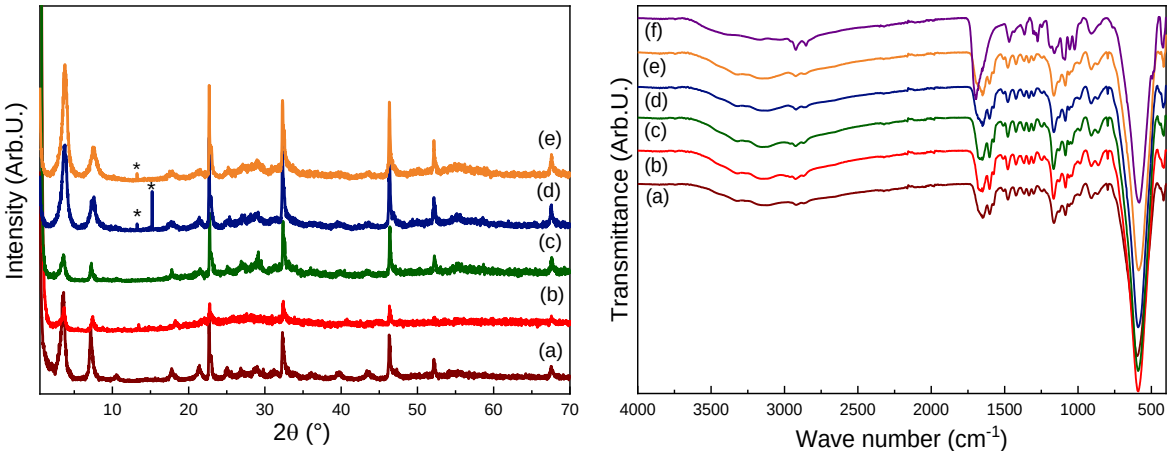

Figure 7: (Left) XRD patterns and (right) FTIR spectra of (a) Adenosine-HST, (b) to (e) the product of reaction between adenosine-HST and thymidine in (b) IPA at room temperature, (c) in IPA at 40 °C, (d) in water at room temperature and (e) in water at 40 °C and (f) Thymidine-HST. The stars on the XRD indicate the peaks corresponding to an impurity of thymidine due to an incomplete washing.

VI.3.1.2 Conclusions and Perspectives

Unfortunately, this preliminary investigation of the assembly of hybrid nanosheets using nucleobases did not enable to evidence the recognition and the interaction of Adenosine-HST or Thymidine HST with their complementary nucleoside. In addition, the characterization techniques we used cannot directly emphasize the formation of hydrogen bonds.

However, future work should still focus on this kind of assembly using complementary nucleobase. Especially, the simultaneous exfoliation and subsequent assembly of the two hybrid oxides might be promising as it goes for pyrene-based hybrid and graphene.

VI.3.2 Assembly using non-charged polymer-coated nanosheets

VI.3.2.1 Synthesis and characterization

We were able to synthesize $C_{10}PO_3$-HLN and to exfoliate it with PEG following the same procedure as for $C_{10}PO_3$-HST, described in **Chapter III**. Both PEI-coated $C_{10}PO_3$-HST and PEG-coated $C_{10}PO_3$-HLN are dispersed in water.

The assembly of the two distinct nanosheets into an alternated stacked structure was carried out by dip-coating of a PEI-coated substrate. First, the substrate was poured for 1 hour in a suspension of PEG-coated $C_{10}PO_3$-HLN nanosheets. Then, the substrate was poured in the suspension of PEI- coated $C_{10}PO_3$-HST nanosheets for 1 hour at pH =9.5 under gentle stirring. This procedure was repeated four times in order to reach an alternated stack of 8 layers.

Figure 8 (a) and ***(b)*** shows SEM images of two areas of a sample on which an alternated assembly was performed. Large and partially exfoliated nanomaterials can be seen on the image ***Figure 8 (a)***, where slabs of closely the same shape are partially delaminated. In ***Figure 8 (b)***, a disordered stack of thinner nanosheets are seen but with smaller lateral size. The first case corresponds to a unique material, only partially exfoliated, while the second is more likely to correspond to an alternated pile of the two native nanosheets.

EDS analysis was performed on four spots on the substrate and the resulting spectra are shown in ***Figure 8 (c)***. In three spectra, no trace of Ta and Sr elements was detected, only Nb and La were found as well as carbon and nitrogen. However, in the fourth spectrum (blue line), the Ta, Sr, Nb and La elements are detected plus a strong signal ascribed to nitrogen. On this spot, we thus emphasize the presence of the two nanosheets while, on the first three spectra, only the HLN-based nanosheets were detected. Besides, the PEI coating, natively present on HST-based nanosheets, is evidenced by the strong nitrogen signal which is only seen in the spectrum also displaying Ta signals.

The imaging and elemental analysis lead us to ascertain the major presence of the PEG-coated $C_{10}PO_3$-HLN nanomaterials. On the opposite, PEI-coated $C_{10}PO_3$-HST nanomaterials were less deposited. Such difference is either ascribed to the less-efficient exfoliation by PEI which leads inevitably to less nanomaterials in solution or to the potential repulsion between the PEI at the surface of the substrate and at the surface of the nanosheets (despite the pH control) or a combination of both hypotheses.

.

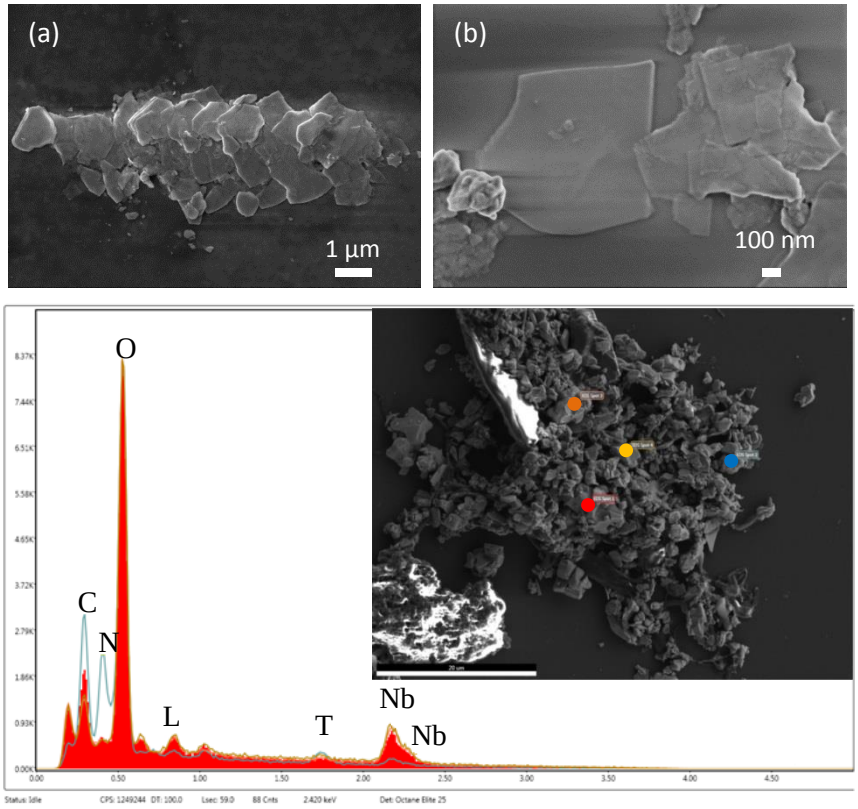

Figure 8: (a) and (b) SEM images of a PEI-coated substrate on which alternated depositions of PEG-coated $C_{10}PO_3$-HLN and PEI-coated $C_{10}PO_3$-HST nanosheets were carried out. (c) EDS spectrum of four spots of the substrate: the colored line corresponds to the spectrum of the spot while the filled red spectrum is their sum.

VI.3.2.2 Conclusion and Perspectives

This preliminary work is a proof of concept that hydrogen-guided assembly can be relevant to build alternated architectures using a layer-by-layer process. An important work on polymer-coated nanosheets deposition has to be carried out in future works.

The first substrate coverage by PEG-coated nanosheets should be as high as possible to allow the better attachment of the layers further deposited. Therefore, the polymer-assistance by PEI (and in a less extend PEG) has to be optimized to subsequently start the assembly process with high concentrated nanosheets suspension, containing mostly exfoliated few-layer materials. Secondly, the layer-by-layer process can also be optimized, notably by using the spray layer-by-layer.

VI.4. Assembly using covalent bond

VI.4.1 Synthesis and characterization

MPTS-HST hybrid layered oxide, displaying terminal thiol in its interlayer space has been synthesized in **Chapter II**. This thiol function is available thus at the surface of the corresponding nanosheets and can be coupled with a gold surface. The exfoliation of MPTS-HST was carried out using the procedure we developed for $C_{10}PO_3$-HST. Typically, 20 mg of MPTS-HST were dispersed in IPA and then sheared at 11500 rpm for 1 hour. The suspension went through a selective centrifugation process providing a suspension of nanosheets.

Figure 9 shows SEM images of MPTS-HST, obtained by shear force-exfoliation. The nanomaterials have a mean lateral size around 500 nm. However a non-negligible amount of smaller and thicker particles are seen.

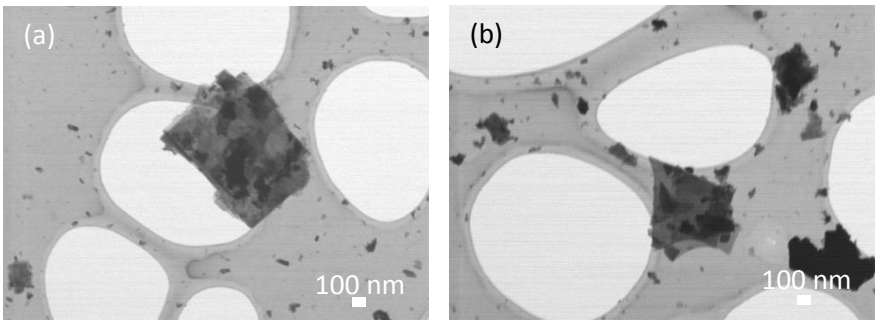

Figure 9: SEM images of MPTS-HST nanosheets

The MPTS-HST nanosheets suspension was deposited onto an Au substrate by drop casting at room temperature. The drop was dried in air and the substrate was then heated at 80°C for 30 minutes to remove traces of solvent and to allow the Au-S bond to be formed. We analyzed the as-obtained substrate by AFM. ***Figure 10*** is a representative AFM image of the MPTS-HST nanosheets on gold substrate. We observe small nanomaterials with a lateral size of 150 nm and a thickness of 20 nm. Unfortunately, we

could not record images of larger nanosheets. We ascribe this absence to the coffee ring effect which is observed despite the room temperature drying of the suspension drop.

In addition, as expected for gold substrate the roughness of the gold layer is far more important than the one of silicon-based substrate. A height profile of the substrate is indeed shown in ***Figure 10 (a)***, and evidences a roughness of 3 nm which is on the same range of a nanosheet monolayer thickness. This roughness might hinder the accurate evaluation of a monolayer thickness.

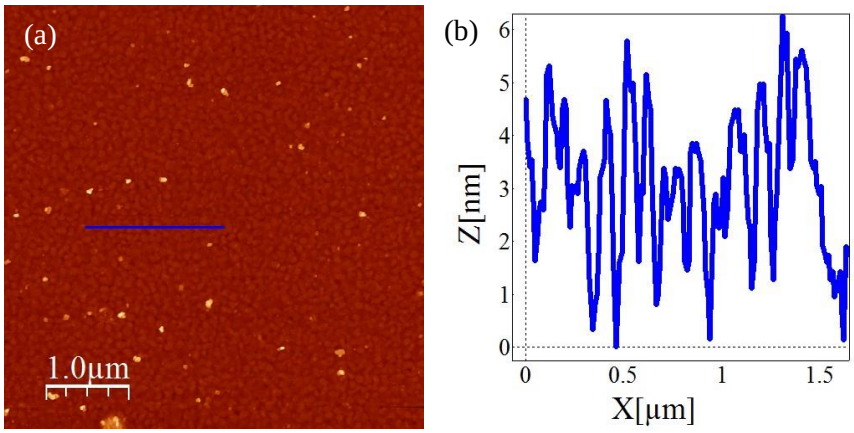

Figure 10: (a) AFM image of MPTS-HST nanosheets, deposited on a gold substrate. (b) Z-profile of the bare substrate, showing its roughness.

In the course of this PhD work, we could not optimize the deposition of MPTS-HST nanosheets on gold surface and probe the eventual formation of Au-S bond between nanomaterials and substrate by X-ray Photoemission spectroscopy for instance.

VI.4.2 Conclusion and Perspectives

We demonstrated that MPTS-HST nanosheets can be obtained by the process we developed previously. Preliminary works on their deposition onto a gold surface highlight a promising assembly. However, similarly to all deposition experiments described in this chapter, an optimization of the deposition has to be deepened to further characterize the covalent Au-S bond formation.

Herein we proposed the coupling of gold and nanosheets on a substrate. Nevertheless, in-solution coupling can be envisioned when considering gold nanoparticles which can be attached to the hybrid layer *via* the terminal thiol.

VI.5. Conclusion of Chapter VI

The scope of this chapter was to identify promising synthetic paths to build nanoarchitectures and to preliminary explore them.

First, we focused on pyrene-based oxide nanosheets which display luminescent properties. Therefore, we investigated the luminescence of the layered hybrid and the corresponding nanosheets. Unfortunately, the results obtained do not allow to probe the exfoliation degree. Then we coupled the pyrene-based nanosheets with graphene in solution and demonstrate that the simultaneous exfoliation of both entities is indeed promising.

In the second part we investigated the coupling of complementary nucleoside-based hybrids. We studied the recognition and interaction of the hybrid oxides and the free molecules. The assembly of Thymidine-HST and Adenosine-HLN is promising but we could not emphasize the formation of hydrogen bonds between the entities. Additional characterizations have to be carried out.

The polymer-coated nanosheets can also be integrated into assembly and we showed than stack of PEG- coated $C_{10}PO_3$-HLN and PEI-coated $C_{10}PO_3$-HST can be obtained on a substrate. Optimization of the process has to be performed, notably on the deposition process but this pathway gave the best result in terms of assembly.

Finally, we propose to take advantage of the terminal thiol of MPTS-HST and to make it react with a gold surface. The nanosheets were deposited onto a gold substrate. However, the bond formation could not be probed and there again the deposition needs optimization.

In addition, it would be relevant to perform the coupling in solution, hence the use of gold nanoparticles which might add functionality to the system (*i.e*. plasmonic effect).

VI.6. Bibliography

(1) Kumar, R.; Jalani, K.; George, S. J.; Rao, C. N. R. Non-Covalent Synthesis as a New Strategy for Generating Supramolecular Layered Heterostructures. *Chem. Mater.* **2017**, *29* (22), 9751–9757.

(2) Gerber, O.; Bégin-Colin, S.; Pichon, B. P.; Barraud, E.; Lemonnier, S.; Pham-Huu, C.; Daffos, B.; Simon, P.; Come, J.; Bégin, D. Design of $Fe_{3-X}O_4$ Raspberry Decorated Graphene Nanocomposites with High Performances in Lithium-Ion Battery. *Journal of Energy Chemistry* **2016**, *25* (2), 272–277.

(3) Ciesielski, A.; Samorì, P. Supramolecular Approaches to Graphene: From Self-Assembly to Molecule-Assisted Liquid-Phase Exfoliation. *Advanced Materials* **2016**, *28* (29), 6030–6051.

(4) Minquan, W.; Guodong, Q.; Mang, W.; Xianping, F.; Zhanglian, H. The Influence of the Matrix on the Fluorescence Properties of Pyrene. *Materials Science and Engineering: B* **1996**, *40* (1), 67–71.

(5) Costa, A. L.; Gomes, A. C.; Pillinger, M.; Gonçalves, I. S.; Seixas de Melo, J. S. Controlling the Fluorescence Behavior of 1-Pyrenesulfonate by Cointercalation with a Surfactant in a Layered Double Hydroxide. *Langmuir* **2015**, *31* (16), 4769–4778.

(6) Sivakova, S.; Rowan, S. J. Nucleobases as Supramolecular Motifs. *Chem. Soc. Rev.* **2005**, *34* (1), 9–21.

(7) Quinn, J. F.; Johnston, A. P. R.; Such, G. K.; Zelikin, A. N.; Caruso, F. Next Generation, Sequentially Assembled Ultrathin Films: Beyond Electrostatics. *Chem. Soc. Rev.* **2007**, *36* (5), 707–718.

(8) Schall, O. F.; Gokel, G. W. Molecular Boxes Derived from Crown Ethers and Nucleotide Bases: Probes for Hoogsteen vs Watson-Crick H-Bonding and Other Base-Base Interactions in Self-Assembly Processes. *J. Am. Chem. Soc.* **1994**, *116* (14), 6089–6100.

(9) del Prado, A.; González-Rodríguez, D.; Wu, Y.-L. Functional Systems Derived from Nucleobase Self-Assembly. *ChemistryOpen* **2020**, *9* (4), 409–430.
(10) Mirkin, C. A.; Letsinger, R. L.; Mucic, R. C.; Storhoff, J. J. A DNA-Based Method for Rationally Assembling Nanoparticles into Macroscopic Materials. *Nature* **1996**, *382* (6592), 607–609.
(11) Samanta, A.; Medintz, I. L. Nanoparticles and DNA – a Powerful and Growing Functional Combination in Bionanotechnology. *Nanoscale* **2016**, *8* (17), 9037–9095.
(12) Mochizuki, D.; Kumagai, K.; Maitani, M. M.; Wada, Y. Alternate Layered Nanostructures of Metal Oxides by a Click Reaction. *Angewandte Chemie International Edition* **2012**, *51* (22), 5452–5455.
(13) Kishimoto, F.; Mochizuki, D.; Maitani, M. M.; Suzuki, E.; Wada, Y. Construction of Highly Hierarchical Layered Structure Consisting of Titanate Nanosheets, Tungstate Nanosheets, $Ru(Bpy)_3^{2+}$, and Pt(Terpy) for Vectorial Photoinduced Z-Scheme Electron Transfer. *ACS Appl. Mater. Interfaces* **2018**, *10* (43), 37150
(14) Perton, F.; Tasso, M.; Muñoz Medina, G. A.; Ménard, M.; Blanco-Andujar, C.; Portiansky, E.; van Raap, M. B. F.; Bégin, D.; Meyer, F.; Begin-Colin, S.; Mertz, D. Fluorescent and Magnetic Stellate Mesoporous Silica for Bimodal Imaging and Magnetic Hyperthermia. *Applied Materials Today* **2019**, *16*, 301–314.
(15) Wang, Y.; Delahaye, E.; Leuvrey, C.; Leroux, F.; Rabu, P.; Rogez, G. Post-Synthesis Modification of the Aurivillius Phase $Bi_2SrTa_2O_9$ via In Situ Microwave-Assisted "Click Reaction." *Inorg. Chem.* **2016**, *55* (19), 9790–9797.
(16) Pensa, E.; Cortés, E.; Corthey, G.; Carro, P.; Vericat, C.; Fonticelli, M. H.; Benítez, G.; Rubert, A. A.; Salvarezza, R. C. The Chemistry of the Sulfur–Gold Interface: In Search of a Unified Model. *Acc. Chem. Res.* **2012**, *45* (8), 1183–1192.
(17) Bürgi, T. Properties of the Gold–Sulphur Interface: From Self-Assembled Monolayers to Clusters. *Nanoscale* **2015**, *7* (38), 15553–15567.
(18) Yonezawa, T.; Yasui, K.; Kimizuka, N. Controlled Formation of Smaller Gold Nanoparticles by the Use of Four-Chained Disulfide Stabilizer. *Langmuir* **2001**, *17* (2), 271–273.
(19) Duan, D.; Ye, H.; Meng, N.; Xu, C.; Han, B.; Chen, Y.; Zhong, M.; Xu, L. Efficient Exfoliation of Graphite in Chloroform with a Pyrene-Containing Hyperbranched Polyethylene as Stabilizer to Render Pyrene-Functionalized High-Quality Graphene. *Carbon* **2018**, *136*, 417–429.
(20) Schlierf, A.; Yang, H.; Gebremedhn, E.; Treossi, E.; Ortolani, L.; Chen, L.; Minoia, A.; Morandi, V.; Samorì, P.; Casiraghi, C.; Beljonne, D.; Palermo, V. Nanoscale Insight into the Exfoliation Mechanism of Graphene with Organic Dyes: Effect of Charge, Dipole and Molecular Structure. *Nanoscale* **2013**, *5* (10), 4205–4216.
(21) Vera-López, S.; Martínez, P.; San Andrés, M. P.; Díez-Pascual, A. M.; Valiente, M. Study of Graphene Dispersions in Sodium Dodecylsulfate by Steady-State Fluorescence of Pyrene. *Journal of Colloid and Interface Science* **2018**, *514*, 415–424. https://doi.org/10.1016/j.jcis.2017.12.052.
(22) Wang, K.; Schall, O. F.; Gokel, G. W. Detection of Hydrogen-Bonded Adenine-Thymine Base-Pair Complexes by Electrospray Mass Spectrometry. *Supramolecular Chemistry* **1996**, *7* (1), 85–90.

Conclusion and Perspectives

Conclusion and perspectives

Inheritance of an extensive scientific research on hybridization of layered materials, this work explores the next step after the interlayer modification of oxide by molecules *i.e.* the exfoliation of the layered hybrid into functionalized oxide nanosheets. Hence, the main contribution of this PhD works is the application of an exfoliation method, the shear force-assisted liquid exfoliation, to hybrid layered oxides to obtain corresponding nanosheets in solution. This pathway was successfully implemented and displays many advantages compared to classical routes.

Indeed, the shear force-assisted liquid exfoliation does not require additional surfactant, reduces the exfoliation time compared to ion-exchange and is less damaging for the inorganic structure compared to sonication. This seemingly simple process was optimized to reach a reasonable exfoliation efficiency *i.e.* a great proportion of large and thin nanosheets compared to un-exfoliated ones. We reviewed the essential parameters, such as solvent, shear rate and exfoliation time, to draw tendencies which allow us to smartly adapt these settings as a function of the nature of the organic moieties grafted onto the charged layered oxide.

In a second step, using optimal exfoliation conditions, we considered a phosphonic acid-based hybrid, $C_{10}PO_3$-HST to synthesize corresponding nanosheets. We were able to obtain a suspension of $C_{10}PO_3$-HST nanomaterials after 1 hour of exfoliation with a relatively long colloidal stability (about 1 week). The resulting suspension was thoroughly characterized either natively or after deposition on a substrate

We then showed that light scattering can provide an estimation of dimension of the nanomaterials. Despite the non-ideality of our system (polydispersity in shape, size and thickness) and despites the complexity of the model, we successfully used SLS and DLS to assess the mean lateral size of the functionalized nanosheets. Both static and dynamic approaches lead to congruent values which are similar to the dimensions obtained by near-field techniques (SEM, TEM or AFM). Besides, we also used these latter techniques to prove the preservation of the inorganic structure and of the functionalization. The phosphonic acid remains attached to the inorganic layer all along the process of exfoliation and size selection.

It is worth mentioning that the originality of the shear exfoliation method (up to now mainly dedicated to Van der Waals materials) relies on the organic coating at the surface of each oxide layer. The grafted molecules decrease the electrostatic interaction between the slabs, participate to the colloidal stability of the nanomaterials in solution and may convey some of their properties such as luminescence, hydrophobicity or reactivity. Therefore a fine a control of the functionalization step is crucial.

Considering the consistency of the method and its results, we extended its application to more functional hybrid layered oxides. Besides, we designed these hybrid oxides in the purpose of using their organic moieties to assemble them into complex nanoarchitectures. Hence, the second main objective of this work was to build assemblies from hybrid nanosheets, guided by non-electrostatic interactions. The

recognition and coupling of the hybrid nanosheets and the second distinct entity can rely on hydrogen bond, π-π interaction or covalent bond formation.

We considered some interesting strategies to combine 2D materials. For instance, the nucleoside-based layered hybrids display a great potential as their corresponding nanosheets possess a functional group at their surface than can form hydrogen bonds. By grafting complementary nucleoside on two different layered oxides it might be possible to couple them in alternated layers. After exfoliation of nucleoside-based oxide, we started to explore their assembly. Although the study is preliminary, it highlights the potentiality of such approach.

In this work, we also explored alternatives to shear-force exfoliation. Sonication-assisted exfoliation works similarly on the hybrid layered oxides even if the resulting nanosheets tend to be smaller in comparison. Ion-exchange on hybrid layered oxides was proved to be damaging for the native functionalization. On the contrary polymer-assisted exfoliation of hybrids gave stunning results in terms exfoliation yield. This method has to be further studied to end up to a nanosheet that benefits from both the polymer and the native functionalization

Nonetheless, regarding the hybrids synthesized in the course of this PhD, it might be interesting to develop new ones which combine more functionalities. Focusing on luminescent properties, we schematically represent in ***Figure 1*** the specifications of the molecules we will aim at grafting into the layered oxides. These entities must display an anchoring group (phosphonic acid is the best choice according our experience), luminescent properties (*i.e.* conjugated aromatic rings or coordination site for a rare-earth ion) and a terminal functional group (to favour the stability, to be used for exfoliation or for assembling possibilities) For instance considering **Molecule 1**, we might obtain an-aggregation-induced-luminescent hybrid, furthermore pH responsive which could be exfoliated *via* repulsion between the carboxylate.[1] Nanosheets combined with **Molecule 2** might be also a luminescent system with a terminal carboxylic aid. The carboxylate form would allow to stabilize the nanosheets. In addition, considering the thiol function, the system should be able to bind to gold nanoparticles. Besides, one can even envision the growth of gold nanoparticles in the vicinity of the nanosheets: the carboxylate might reduce gold cation (citrate method[2]) which will further be stabilized by the thiol function. The resulting system should display interesting photoluminescence properties, in a large range of wavelengths thank to the gold nanomaterials.

The inorganic oxide layer may also be tuned to modify the properties of the nanosheets. For instance, doping of the oxides has been already reported in literature.[3,4] Thus, it would be interesting to combine a luminescent oxide layer with a luminescent chromophore, with an overlapping of the absorption band of chromophore and the emission band of oxide.

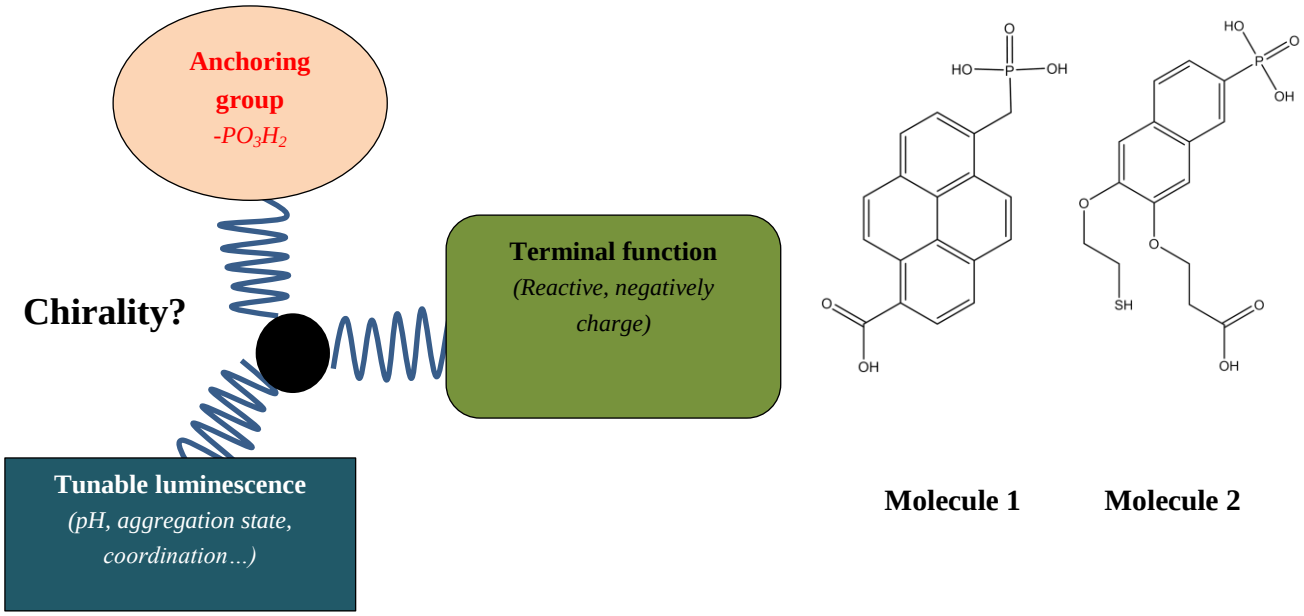

Figure 1: Schematic representation of the functionalities that a promising molecule should display to result in a new hybrid. The two molecules are instances which fulfill the specifications.

In addition to the design of new hybrids nanosheets, we also envision new applications to the hybrid nanomaterials we synthesized in this work, especially, the Adenosine-HST and the Thymidine-HST. For instance, it was proved that both adenosine and thymidine can bind metal ions such as Pt, Ag, Au or Cu.[5–7] Besides, the nucleoside based-complex can display some catalytic properties as demonstrated by S. Verma *et al*. and depicted in ***Figure 2***.[7]

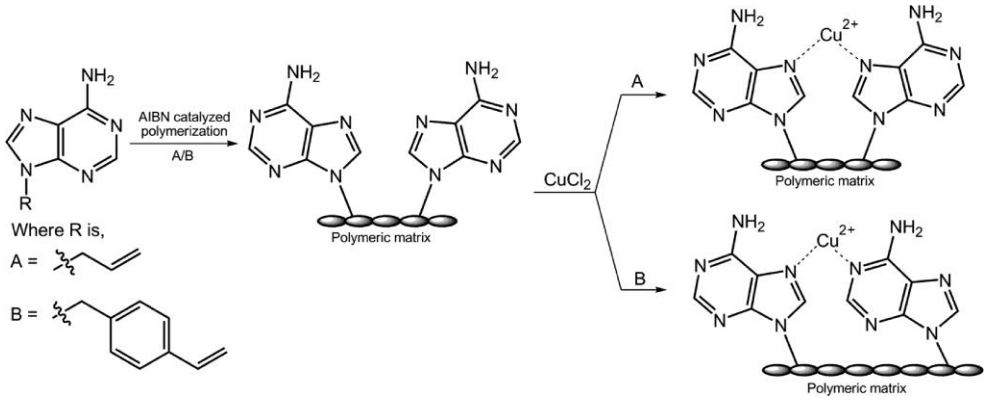

Figure 2: Schematic view of an adenine-based polymer showing two possibilities of Cu^{2+} binding [7]

The same authors also reported the interaction of adenine with graphene *via* π-π interactions. Hence, in future works, it could be relevant to use nucleoside-coated nanosheets to form complexes involving a metal ion and another coordinating ligand such.as oligopyridines.[8]

It could also be interesting to study how they can be coupled with DNA-modified gold nanoparticles as synthesized by C. Mirkin *et al*.[9] Many questions can rise from such system. How does a DNA strand interact with a homogeneous adenosine layer or thymidine layer? Can the assembly be 3D structured?

We thus think the hybrids we synthesized still offer unexplored applications, especially in the field of nanoarchitectonics.

Bibliography

(1) Han, Y.-S.; Park, I.; Choy, J.-H. Exfoliation of Layered Perovskite, $KCa_2Nb_3O_{10}$,into Colloidal Nanosheets by a Novel Chemical Process. *J. Mater. Chem.* **2001**, *11* (4), 1277–1282.

(2) Polte, J.; Ahner, T. T.; Delissen, F.; Sokolov, S.; Emmerling, F.; Thünemann, A. F.; Kraehnert, R. Mechanism of Gold Nanoparticle Formation in the Classical Citrate Synthesis Method Derived from Coupled In Situ XANES and SAXS Evaluation. *J. Am. Chem. Soc.* **2010**, *132* (4), 1296–1301.

(3) Kudo, A.; Kaneko, E. Photoluminescent Properties of Ion-Exchangeable Layered Oxides. *Microporous and Mesoporous Materials* **1998**, *21* (4–6), 615–620.

(4) Funatsu, A.; Ida, S.; Ogata, C.; Matsumoto, Y. Photoluminescence of Eu^{3+} and Tb^{3+} Ions Adsorbed on Oxide Nanosheets. *Bulletin of the Chemical Society of Japan* **2011**, *84* (8), 867–872.

(5) Lippert, B. Multiplicity of Metal Ion Binding Patterns to Nucleobases. *Coordination Chemistry Reviews* **2000**, *200–202*, 487–516.

(6) Navarro, J. A. R.; Lippert, B. Simple 1:1 and 1:2 Complexes of Metal Ions with Heterocycles as Building Blocks for Discrete Molecular as Well as Polymeric Assemblies. *Coordination Chemistry Reviews* **2001**, *222* (1), 219–250.

(7) Verma, S.; Mishra, A. K.; Kumar, J. The Many Facets of Adenine: Coordination, Crystal Patterns, and Catalysis. *Acc. Chem. Res.* **2010**, *43* (1), 79–91.

(8) Kramer, R.; Lehn, J. M.; Marquis-Rigault, A. Self-Recognition in Helicate Self-Assembly: Spontaneous Formation of Helical Metal Complexes from Mixtures of Ligands and Metal Ions. *PNAS* **1993**, *90* (12), 5394–5398.

(9) Mirkin, C. A.; Letsinger, R. L.; Mucic, R. C.; Storhoff, J. J. A DNA-Based Method for Rationally Assembling Nanoparticles into Macroscopic Materials. *Nature* **1996**, *382* (6592), 607–609.

Appendix

Appendix I. Experimental section

Appendix II. Complementary data to Pair Distribution Function Analysis

Appendix I. Experimental section

I. Apparatus

Microwave-assisted reaction

The functionalization of layered oxides or some exfoliation experiments using microwave assistance were performed using a microwave synthesis reactor Monowave 300, Anton Paar in a 30 mL glass reactor with an incident power of 70 W and a stirring at 800 rpm. The autogenous pressure does not exceed 6 bars. The protonation experiments (acidic conditions) for the synthesis of the protonated phase HST were carried out using the microwave synthesis reactor MultiwaveGO (Anton Paar) in a 50 mL-Teflon reactor.

High-shear disperser for shear-force exfoliation

The shear force-assisted liquid exfoliation experiments were performed using the T10 basic Ultra-Turrax high speed disperser (IKA) equipped with a 10 cm-long SN 10-5G 10 tip. This tip is composed of a rotor of diameter 5 mm and a stator of diameter 3.8 mm which accounts for a rotor/stator gap of 0.1 mm. The speed range is summed up in Erreur ! Source du renvoi introuvable. as well as their equivalent shear-force. During the exfoliation experiments the tip was placed 1cm from the bottom of the beaker (diameter 3.5 cm) and at least 2 cm of the tip must be immerged by the solvent (***Figure 1***) The maximum operating time is 10 minutes. Thus, longer experiments must be carried out by alternating dispersion step and rest step of minimum 10 minutes and 20 minutes respectively.

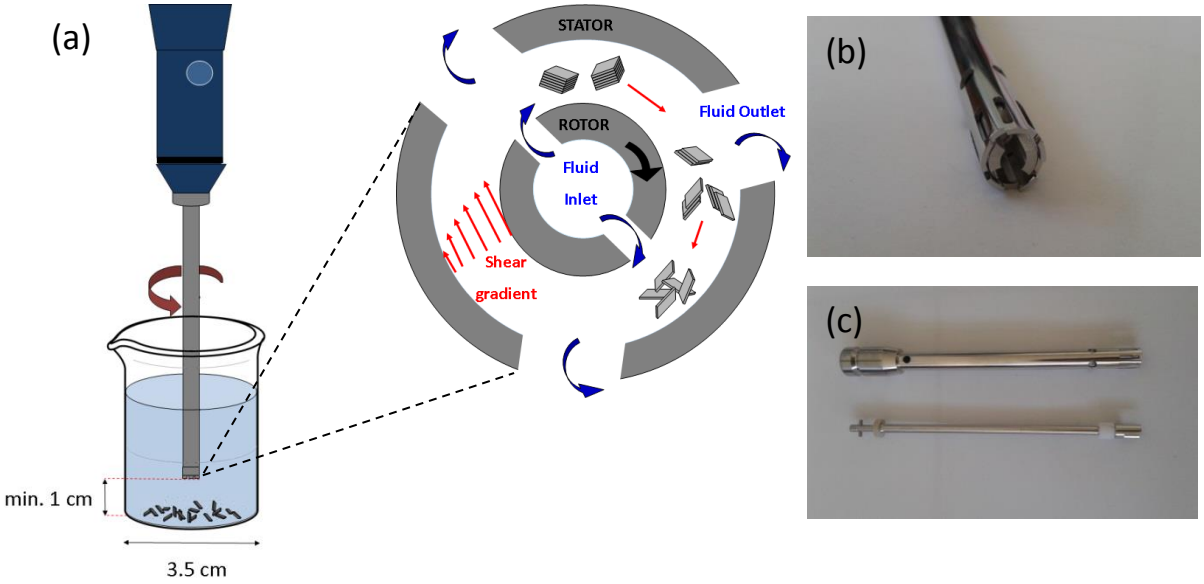

Figure 1: (a) Scheme of the exfoliation set up with a zoom in the rotor/stator zone (b) Side view of the tip where rotor and stator are assembled (c) Top view of the rotor and stator

Rotor speed (rpm)	8000	9500	11500	14500	20500	30000
Shear rate (s^{-1})	15900	18900	22900	28900	40800	59700

Table 1:Equivalence between rotor speed and shear rate, calculated using the following equation $\dot{\gamma} = \frac{\pi DV}{\Delta R}$ ***where*** $\dot{\gamma}$ ***is the shear rate, D is the rotor diameter (5 mm),V is the rotor speed, ΔR is the gap between rotor and stator (0.1 mm).***[1]

Sonication tip for sonication-assisted liquid exfoliation

The sonication experiments were performed using a VibraCell 75043 with a CV33 model tip (power 500W, 20 kHz). The tip was immersed until it laid at 1 cm from the bottom of the Teflon beaker (diameter of 3.5 cm). The beaker was poured in an ice bath during the exfoliation experiments to prevent the fast heating of the mixture and alternative steps of sonication (10 s) and rest (20 s) were performed to avoid heating. The power was set at 40 % of the maximal power.

Liquid-cascade centrifugation

The liquid cascade centrifugation is adapted from the procedure developed by J. Coleman *et al.*[1] The process described in **Chapter III** was carried out using a Sigma 3-30K and plastic tubes of 45 mL, with centrifugation speed from 3 to 30000g.

X-ray diffraction

The XRD patterns were collected in a Bragg-Brentano geometry (0.5° to 70°) using a D8Advance Bruker diffractometer (Cu Kα1=0.1540598 nm) equipped with a Lynx Eye detector discriminating in energy.

The Pair-Distribution Function (PDF)

The PDF records and analyses were performed by Christine Taviot-Guého from the Institute of Chemistry of Clermont-Ferrand. The atomic pair distribution functions were obtained from X-Ray Total Scattering data collected on a PANalytical Empyrean diffractometer equipped with a solid state GaliPIX3D detector, a focusing X-ray multilayer mirror and an Ag anticathode (Kα1= 0.5594214 Å, Kα2 = 0.5638120 Å). Powder samples were mounted in glass capillaries of 0.7 mm diameter. Data were recorded over the range of $1 < 2\theta < 145°$, which corresponds to an accessible maximum value for the scattering vector q max of 21.4 $Å^{-1}$. An optimized variable counting time strategy has been adopted to counteract the decrease of the scattered intensity at the highest angles because the X-ray form factor. An empty capillary of the same type was measured in the same way for background subtraction. The total time of measurement was 20 hours, the same for both the sample and the empty capillary. Data merging, background subtraction, $K\alpha_2$ stripping were done using HighScorePlus software provided by PANalytical Corporation. The program PDFgetX3 was used to generate corrected and normalized scattering structure functions S(q).[2] The PDF or G(r) were calculated from

the Fourier transform of the reduced structure functions truncated at 21 $Å^{-1}$. Finally, the program PDFgui was used to extract local structural information from the measured PDF.[3]

C, H, N analyses

The C, H, N analyses were carried out at the Service Commun d'Analyse of the University of Strasbourg. The Ta and P contents of C_xPO_3-HST and the corresponding nanosheets suspension were determined at the Plateforme d'Analyses of The School of Chemistry, Polymers and Materials of Strasbourg by Inductively Coupled Plasma-Atomic Emission Spectroscopy (ICP-AES), after dissolution in a mixture of hydrochloric, nitric and fluoric acids at 170°C in a closed autoclave.

Thermogravimetric and Thermodifferential analysis (TGA-TDA)

TGA-TDA analyses were carried out on powders using a TA instrument SDT Q600. The thermogravimetric profiles were performed under air stream with a heating rate of 5°C.min^{-1} until 900°C using a platinum crucible.

Infrared spectroscopy

Fourier-Transform Infrared Spectroscopy spectra were collected using a Spectrum II spectrometer (Perkin Elmer) in Attenuated-Total-Reflectance mode at room temperature from 400 cm^{-1} to 4000 cm^{-1}

UV-VIS spectroscopy

The UV-Vis spectra were collected using a Perkin-Elmer Lambda 950 spectrometer equipped with 150 mm integrating sphere with a mean resolution of 1 nm and a sampling rate of 270 nm.min^{-1}. For solid samples the spectra were recorded in a reflection mode while for materials in solution they were recorded in a transmission mode.

Spectrofluorimetry

The excitation spectra and emission spectra of nanosheets suspension or hybrid powder were recorded using a Horiba scientific Fluorolog The luminescence of the suspension was recorded using a 1cm×1cm quartz cell in a Right-Field geometry. The solid sample was hold between two thin quartz slides.

Solid State NMR

Solid state CP-MAS ^{13}C and ^{31}P NMR were performed by Fabrice Leroux (Institute of Chemistry of Clermont Ferrand, UMR 6296) with a 300 Bruker spectrometer at 75.47 or 121.49 MHz respectively, using a magic angle spinning (MAS) condition at 10 kHz and a 4 mm diameter size zirconia rotor. ^{13}C spectra obtained by protons enhanced cross-polarization method (CP) were referenced to the carbonyl of the glycine calibrated at 176.03 ppm. Recycling and Hartman-Hahn contact times were 5s and 1250 µs, respectively. Spinal ^{1}H phase decoupling was applied during ^{13}C

channel acquisition. ^{31}P spectra were calibrated to H_3PO_4 at 0.0 ppm, and recorded after $\frac{\pi}{2}$ simple impulsion.

Transmission Electron microscopy (TEM)

The TEM images of nanosheets were obtained in collaboration with Corinne Bouillet (IPCMS). The nanosheets suspension (5 to 10 drops) was deposited onto lacey carbon-coated copper grid, held at 1cm from a hot plate (100°C). To prevent from traces of residual solvent and contamination during the imaging, the Cu grid was stored in vacuum overnight before its insertion into the microscope. The images were obtained by using a JEOL 2100F, corrected from the spherical aberration on the condenser lens, allowing to reach 0.18 nm resolution at 100 kV in STEM mode. This voltage was mainly used to record images instead of 200 kV where knock-out damage occurred. The images were analyzed using the DigitalGatan Micrograph software.

Scanning Electron Microscopy (SEM)

SEM images of nanosheets suspension were recorded using a JEOL 6700 microscope operating at 25 kV in STEM mode (T-SEM). Sample preparation is identical to the one used for TEM

SEM images of bulk layered oxide or deposited nanosheet (on substrate) were recorded using a Zeiss GeminiSEM-500 operating at 25 kV.

Atomic force microscopy (AFM)

AFM images were recorded in collaboration with Mircea Rastei (IPCMS) using a Digital Instrument 3100 microscope. The imaging was performed in tapping mode, using the ScanAsyst optimization and the required Si/SiO_2 tip. The resolution was set at 1084 lines and the scan rate was in the range 0.1 to 0.9 Hz. The images were analyzed using the open-access WsXM software.

Dynamic Light Scattering

A commercial Zetasizer NanoZS (Malvern) was used to routinely characterize the nanosheets suspension. The measurements were carried out using a laser (wavelength of 632 nm) at 25 °C for 6 measures of 1 minute (1 cycle) in the backscattering geometry. Three cycles were recorded for each sample, each of them providing the intensity auto-correlation function as well as the particles size distribution, based on the cumulant method in the case of spherical nanoparticles.[4]

Zeta potential

The zeta potentials of dispersed nanomaterials were measured using the same Zetasizer NanoZS. Typically, 20 mg of HST, HLN or HTO were poured in 40 mL of water and dispersed using the Ultraturax high-shear disperser for 5 minutes, with a rotor speed of 11500 rpm. The pH of the solution was adjusted at the desired value by addition of volumes of HCl solution (0.1M or 0.01M or NaOH solution (0.1M or 0.01M). The slurry solution was quickly introduced in the transparent cell with two electrodes. The measurement was processed using the Smoluchowski model.

Multi-angles Light scattering experiments

Static Light Scattering and Dynamic Light Scattering were performed in collaboration with François Schosseler (Institut Charles Sadron) using a compact ALV/CGS-8 goniometer equipped with a He-Ne laser (14 mW, λ = 632.8 nm, vertically polarized) and an ALV-7002/USB-25 correlator. The temperature of the matching index fluid (toluene) was kept at 25 ± 0.1 °C using a circulating water bath. The scattered light was recorded for 1 minute at the position 20°, 25°, 30°, 40°, 50°, 60°, 70°, 80° 90° and 120° corresponding to 1 cycle. This cycle (around 14 minutes) was repeated over several hours to characterize the kinetic evolution of the scattered intensity over time. All scattered intensities were normalized by the intensity scattered by toluene standard, measured at 90° at 25°C.

The nanosheets suspension, analyzed in light scattering, corresponds to the last supernatant of the selective centrifugation process. This supernatant was washed by a centrifugation step at 14000 rpm for 15 minutes and the nanosheets were-dispersed using filtrated solvent (filter of 0.22 µm). Then the suspension is put in a transparent cylindrical tube of diameter 1cm.

The autocorrelation functions of the scattered electromagnetic field were analyzed with the CONTIN software[5,6] using a set of scripts described elsewhere.[7] These scripts allowed a batch analysis of the large number of measurements generated by the experimental procedure.

Small Angle X-Ray Scattering (SAXS) and Wide Angle X-ray Scattering (WAXS)

The SAXS experiments were carried out in collaboration with Doru Constantin (Institut Charles Sadron) and performed at the Soleil Synchrotron facilities on the Beamline SWING. The incident X-ray beam had an energy of 16 keV *(i.e*. a wavelength of 0.776 nm). The nanomaterials suspensions were contained in sealed glass capillary of 1.1 mm. Two detector-sample distances were used, 0.5 and 6m corresponding to WAXS and SAXS geometry respectively. The normalization and the removal of the solvent contribution in the X-ray scattering profiles were manually performed by an adjusting factor. The SAXS and WAXS profiles were fitted using an open-access software SASview, considering the stacked disk model.

II. Synthesis, exfoliation and assembly

Chapter II Functionalization and reactivity of charged layered oxides

II.2 Functionalization by *n*-alkylamine and *n*-alcohol

II. 2.1 Functionalization of the layered Aurivillius oxide, $Bi_2SrTa_2O_9$

$Bi_2SrTa_2O_9$ (BST) was synthesized by a two-step stoichiometric reaction. 883.0 mg (1.895 mmol) of Bi_2O_3, 279.8 mg of $SrCO_3$ and 837.4 mg of Ta_2O_5 were heated at 900°C for 660 min and 1200°C for 240 minutes (heating rate of 1.8°C.min^{-1}) with intermittent grinding according to published procedure.[8]

$H_2Bi_{0.1}Sr_{0.85}Ta_2O_7$ (HST) was synthesized by microwave-assisted reaction. Typically, 12 Teflon vials of 50 mL were filled with 200 mg (0.2 mmol) of BST and 20 mL of 4 M HCl solution and then heated at 70°C for 3 hours (maximum incident power 5 W) according to published procedure.[9] The resulting powder was collected and washed three times by centrifugation (14000 rpm, 10 minutes), re-dispersed in acetone and dried in air overnight.

C_xN-HST: 150 mg (0.26 mmol) of HST were dispersed in 10 mL of THF (non-anhydrous), 3 mL of 1-ethylamine (abbreviated as C_2NH_2), 1-butylamine (C_4NH_2) or 1-dodecylamine ($C_{12}NH_2$) (46, 30 and 13 mmol respectively) and 1.5 mL (83 mmol) of water using a 30 mL-glass vial. The mixture was heated with microwave irradiation at 110°C for 1 hour (the autogenous pressure did not exceed 5 bars). The powder was collected, washed three times with water by centrifugation (14000 rpm, 10 minutes), re-dispersed in acetone and dried in air overnight.

C_xO-HST or **BenzO-HST**: 100 mg (0.014 mmol) of C_4N-HST were dispersed in 8 mL of 1-methanol (abbreviated as C_2OH), benzylalcohol (BenzOH) or 1-dodecanol ($C_{12}OH$) (198,77 and 36 mmol respectively) (Note: for 1-dodecanol, a heating at 70°C for 1 hour was needed to melt the compound) and 100 µL (5.6 mmol) of water. The mixture was heated using microwave irradiation at 130°C for 130 minutes (the autogenous pressure was in between 0 and 6 bars). The powder was collected by centrifugation, washed 1 time with water and 2 times with acetone (14000 rpm, 10 minutes), re-dispersed in acetone and dried in air overnight.

C_{18}O-HST was obtained by the same procedure as C_2O-HST, C_{12}O-HST or BenzO-HST except that the precursor is C_{12}O-HST (100mg, 0.0014mmol).

BenzSC_2OH: 250 mg (0.035 mmol) of C_4N-HST was dispersed in 10 mL THF (non-anhydrous) with 103 µL (0.68 mmol) of 2-(benzylthio)ethanol (abbreviated as BenzSC_2OH) without any additional water. The mixture was heated with microwave irradiation at 110°C for 180 minutes. The powder was collected and washed three times with water by centrifugation (14000 rpm, 10 minutes). The powder was re-dispersed in acetone and dried in air overnight.

II. 2.2 Functionalization of the Dion-Jacobson oxide, $KLaNb_2O_7$

$KLaNb_2O_7$ (KLN) was obtained by the solid-state mixture of 685 mg (2.10 mmol) of La_2O_3, 1.117 g (4.20 mmol) of Nb_2O_5 and 290 mg (2.31 mmol) of K_2CO_3 (*i.e.* 10% excess of K_2CO_3) according to published procedure.[10] The mixture was grinded, pelletized and heated at 1100 °C for 72 hours (heating rate of 1.8 °C.min^{-1}). The resulting pellets were grinded in a fine white powder (around 1.83 g).

$HLaNb_2O_7$ (HLN): 1.8 g (3.78 mmol) of KLN was dispersed in a 6.5 M solution of HNO_3 and stirred at room temperature for 24 hours according to published procedure.[11] The powder was collected, washed three times with water by centrifugation (14000 rpm, 10 minutes), re-dispersed in acetone and dried in air overnight.

C_xN-HLN: 150 mg of HLN were dispersed in 10 mL of THF (non-anhydrous), 3 mL (30 mmol) of 1-butylamine (C_4NH_2) or 1-dodecylamine ($C_{12}NH_2$) (30 and 13 mmol respectively) and 1.5

mL of water using a 30 mL-glass vial. The mixture was heated with microwave irradiation at 110 °C for 1 hour (the autogenous pressure did not exceed 5 bars). The powder was collected, washed three times with water by centrifugation (14000 rpm, 10 minutes), re-dispersed in acetone and dried in air overnight.

C_3O-HLN: 100 mg (0.23 mmol) of HLN were dispersed in 8 mL (106 mmol) of 1-propanol (abbreviated as C_3OH) with 1 mL of water. The mixture was heated by microwave irradiation at 130°C for 130 minutes. The powder was collected and washed three times with water by centrifugation (14000 rpm, 10 minutes), re-dispersed in acetone and dried in air overnight.

II.2.3 Functionalization of the lepidocrocite titanate, $K_{0.8}Ti_{1.73}Li_{0.27}O_4$

$K_{0.8}Ti_{1.73}Li_{0.27}O_4$ (KTO) was synthesized by solid-state reaction between TiO_2 (4.08g, 51 mmol), K_2CO_3 (1.63 g, 11.8 mmol) and Li_2CO_3 (0.29 g, 4 mmol) leading to a ratio 10.4:2.4:0.8 according to published procedure.[12] The mixture was directly heated at 800°C for 30 minutes, followed by a subsequent heating at 900°C for 20 hours (heating rate of 1.5°C/min^{-1}) in a tubular oven. The resulting powder was grinded into a fine white powder.

$H_{1.17}Ti_{1.73}O_4$ (HTO) was synthesized by microwave-assisted reaction. Typically, 12 Teflon vials of 50 mL were filled with 200 mg (1.1 mmol) of KTO and 20 mL of 4M HCl solution and then heated at 70°C for 3 hours. The resulting powder was collected and washed three times by centrifugation (14000 rpm, 10 minutes), re-dispersed in acetone and dried in air overnight.

C_4N-HTO: 120 mg (0.8 mmol) of HTO were dispersed in 50 mL of water with 3 mL (30 mmol) of 1-butylamine (C_4NH_2). The mixture was stirred at room temperature for 3 hours. The powder was collected by centrifugation, washed three times with water by centrifugation (14000 rpm, 10 minutes), re-dispersed in acetone and dried in air overnight.

$C_{12}N$-HTO was synthesized using the same procedure as for C_4N-HTO.

$C_{12}O$-HTO: 50 mg (0.23 mmol) of C_4N-HTO or 50 mg (0.33 mmol) of HTO were dispersed in 8 mL (36 mmol) of 1-dodecanol with 100 µL (5.6 mmol) of water in a 30 mL-glass vial. The mixture was heated at 130°C for 130 minutes. The powder was collected, washed 1time with water and two times with acetone by centrifugation (14000 rpm, 10 minutes), re-dispersed in acetone and dried at air overnight.

II.3.1 Grafting by alkylphosphonic acid derivatives, a model system

C_xPO_3-HST: 100 mg (0.14 mmol) of C_4N-HST is dispersed in 10 mL of THF (non-anhydrous) with 1.3 mmol of alkylphosphonic acid (*i.e.* 168 mg for 1-propylphosphonic acid ($C_3PO_3H_2$), 224 mg for 1-hexylphosphonic acid ($C_6PO_3H_2$) or 280 mg for 1-decylphosphonic acid (abbreviated as $C_{10}PO_3H_2$)) without any additional water. The mixture was heated by microwave irradiation at 110°C for 180 minutes. The powder was collected and washed three times by acetone, re-dispersed in acetone and dried in air overnight.

II.3.2 Grafting of aromatic phosphonic acid derivatives

The considered molecules $NCArPO_3H_2$ and $HOArPO3H_2$ were synthesized by P.-A. Jaffrès (CEMCA, Brest) (see scheme in the text).

$NCArPO_3$-HST: 75 mg (0.11 mmol) of C_4N-HST and 120 mg (0.43 mmol) of $NCArPO_3H_2$ were dispersed in 9 mL of THF (non-anhydrous) with 100 µL (5.6 mmol) of water in a 30 mL-glass reactor. The mixture was heated by microwave irradiation at 130°C for 3 hours. The powder was collected, washed three times with water by centrifugation (14000 pm, 10 minutes), re-dispersed in acetone and dried in air overnight.

$HOArPO_3$-HST was obtained by the same procedure as $NCArPO_3$-HST.

II.3.3 Grafting of organosilane derivatives

APTS-HST (method 1): 50 mg (0.07 mmol) of C_4N-HST is dispersed in 25 mL of toluene with 3 mL (17 mmol) of (3-aminopropyl)triethoxysilane (abbreviated as APTS) in a 50 mL flask. The mixture was heated, at 110°C for 72 hours under inert atmosphere (argon). The powder was collected and washed two times with ethanol and one time with acetone, re-dispersed in acetone and dried in air overnight.

APTS-HST (method 2): 25 mg (0.04 mmol) of C_4N-HST is dispersed in 10 mL of toluene with 3 mL (17 mmol) of APTS under inert atmosphere. The reaction was heated by microwave irradiation at 110°C or 130°C for 3 hours. The powder was collected and washed 2 times with ethanol and 1 time with acetone, re-dispersed in acetone and dried in air overnight.

MPTS-HST and **C8TS-HST** were obtained by the same procedure as APTS-HST (method1).

II.3.4 Grafting of functional molecule: the luminescent pyrene derivatives.

$PyrC_xO$-HST: 25 mg (0.04 mmol) of $C_{12}O$-HST and 0.4 mmol (*i.e.* 88 mg of 1-hydropyrene (PyrOH), 93 mg of 1-pyrenemethanol ($PyrC_1OH$) or 100 mg of 1-pyrenebutanol ($PyrC_4OH$)) were dispersed in 10 mL of THF (non-anhydrous) without any additional water. The mixture was heated by microwave irradiation at 110°C for 3 hours. The powder was collected and washed three times with acetone by centrifugation (14000 rpm, 10 minutes), re-dispersed in acetone and dried in air overnight.

II.3.5 Grafting of nucleobases: towards an assembly building blocks

Adenosine-HST: 75 mg (0.1 mmol) of $C_{12}O$-HST and 310 mg (1.12 mmol) of adenosine are dispersed in 10 mL of THF (non-anhydrous) and 1.5 mL (83 mmol) of a water solution containing 50 mg (0.18 mmol) of adenosine in a 30 mL-glass vial. The mixture was heated by microwave irradiation at 110°C for 3 hours. The powder was collected, washed 3 times with water by centrifugation (14000 rpm, 10 minutes), re-dispersed in acetone and dried in air overnight.

Thymidine-HST was synthesized following the same procedure as Adenosine-HST.

Chapter III

III. 3 Coupling Ion-exchange and microwave-assistance: soft-exfoliation of hybrid layered oxides

III.3.2 Exfoliation of bare layered oxide

Exfoliation of HST (classic procedure): in a 25-mL flask, 25 mg (0.04 mmol) of HST was dispersed in 10 mL of water with 274 µL of TBAOH (40% mass in water), leading to a ratio $\frac{TBA^+}{H^+}$ =10. The mixture was gently stirred at room temperature for 10 days. The resulting nanomaterials suspension underwent through the selective centrifugation process described in **Chapter III**.

Exfoliation of HST (with microwave): 25 mg (0.04 mmol) of HST was dispersed in 10 mL of water with an amount of TBAOH (at 40 % mass in water) corresponding to the ratio $\frac{TBA^+}{H^+}$ = 0, 1, 3, 5 and 10 (from 0 to 274 µL) in a 30 mL-glass vial. The mixture was heated by microwaved irradiation at 80 °C for 1 hour. Then, the suspension was centrifuged at 1600 rpm for 20 minutes. The resulting supernatant and bottom were collected, washed with water by centrifugation at 14000 rpm for 10 minutes, re-dispersed in acetone and dried in air overnight.

III.3.3 Exfoliation of alkylamine-based layered oxide

Exfoliation of C_2N-HST: 25 mg (0.038 mmol) of C_2N-HST was dispersed in 10 mL of water with an amount of TBAOH (40 % mass in water) corresponding to the ratio $\frac{TBA^+}{H^+}$ = 0, 0.5, 1, 3, 5, 7 and 10 (from 0 to 165 µL) in a 30 mL-glass vial. The mixture was heated by microwaved irradiation at 80 °C for 1 hour. Then, the suspension was centrifuged at 1600 rpm for 20 minutes. The resulting supernatant and bottom were collected, washed with water by centrifugation at 14000 rpm for 10 minutes, re-dispersed in acetone and dried in air overnight.

III.3.4 Exfoliation of alcohol-based layered oxide

Exfoliation of C_{12}O-HST: 25 mg (0.035 mmol) of C_{12}O-HST was dispersed in a 10 mL of water with an amount of TBAOH (at 40 % mass in water) corresponding to the ratio $\frac{TBA^+}{H^+}$ = 0, 0.5, 1, 3, 5, 10 and 20 (from 0 to 302 µL) in a 30 mL-glass vial. The mixture was heated by microwaved irradiation at 80 °C for 1 hour. Then, the suspension was centrifuged at 1600 rpm for 20 minutes. The resulting supernatant and bottom were collected, washed with water by centrifugation at 14000 rpm for 10 minutes, re-dispersed in acetone and dried in air overnight.

III. 4 Polymer assisted exfoliation of hybrid layered oxides

VII.1.1.1 III.4.2. PEG-assisted exfoliation

III.4.2.1 PEG-assisted exfoliation of bare layered oxide

Exfoliation of HST with PEG: 20 mg (0.034 mmol) of HST were dispersed in 10 mL of THF (non-anhydrous) with an equivalent molar amount of poly(ethylene)glycol with a molar mass of 600 $g.mol^{-1}$, 2000 $g.mol^{-1}$ and 6000 $g.mol^{-1}$. The mixture was gently stirred at room temperature for 48 hours in a closed 50 mL-flask. The suspension was then centrifuged at 1600 rpm for 20 minutes. The resulting supernatant and bottom were collected, washed with water by centrifugation (14 000 rpm, 15 minutes) and re-dispersed in 20 mL of water.

Exfoliation of HST with amine-terminated PEG: 10 mg (0.017 mmol) of HST were dispersed in 10 mL THF with 72 mg (0.014 mmol) of amine-terminated PEG (PEGN5000). The mixture was gently stirred at room temperature for 48 hours in a closed 50 mL-flask. The suspension was then centrifuged at 1600 rpm for 20 minutes. The resulting supernatant and bottom were collected, washed with water by centrifugation (14000 rpm, 15 minutes) and re-dispersed in 20 mL of water.

III.4.2.2 PEG600-assisted exfoliation of hybrid layered oxides

Exfoliation of $C_{10}PO_3$-HST: 20 mg (0.021 mmol) of $C_{10}PO_3$-HST were dispersed in 10 mL of THF with an equivalent molar amount of polymer, PEG600, and 100 µL (5.6 mmol) of water. The mixture was gently stirred at room temperature for 48 hours. The suspension was then centrifuged at 1600 rpm for 20 minutes. The resulting supernatant and bottom were collected, washed with water by centrifugation (14000 rpm, 10 minutes) and re-dispersed in water.
The same procedure was applied for **BenzSC_2O-HST**, **$C_{12}O$-HST** and **C_4N-HST.**

III.4.2.3 PEGN5000-assisted exfoliation of hybrid layered oxides

Exfoliation of $C_{10}PO_3$-HST: 20 mg (0.021 mmol) of $C_{10}PO_3$-HST and 70 mg (0.014 mmol) of polymer, PEGN5000 were dispersed in 10 mL of THF with100 µL (5.6mmol) of water. The mixture was gently stirred at room temperature for 48 hours. The suspension was then centrifuged at 1600 rpm for 20 minutes. The resulting supernatant and bottom were collected, washed with water by centrifugation (14000 rpm, 10 minutes) and re-dispersed in water.

III.4.3 PAA-assisted liquid exfoliation of hybrid oxides

Exfoliation of $C_{10}PO_3$-HST with PAA: 20 mg (0.021 mmol) of $C_{10}PO_3$-HST and 250 mg (26 nmol) of poly(acrylic acid) (PAA) (M = 240000$g.mol^{-1}$, solution 25% weight in water) were dispersed in 25 mL of water or IPA. Note: $C_{10}PO_3$-HST and PAA were mixed together prior the addition of solvent in order to allow the dispersion of the hydrophobic $C_{10}PO_3$-HST in the solvent). The mixture was stirred gently at room temperature for 48 hours in a 50 mL-flask. The suspension was centrifuged at 1600 rpm for 20 minutes. The resulting supernatant and bottom were collected, washed with water by centrifugation (14000 rpm, 10 minutes) and re-dispersed in water or IPA.
The same procedure was applied with **C_4N-HST**.

III.4.4 PEI-assisted exfoliation of hybrid layered oxide

Exfoliation of $C_{10}PO_3$-HST with PEI: 20 mg (0.021 mmol) of $C_{10}PO_3$-HST and 216 mg (0.002 mmol) of poly(ethylenimine) (M = 60000g.mol^{-1}, solution 50% weight in water) were dispersed in water or IPA (Note: $C_{10}PO_3$-HST and PAA were mixed together prior the addition of solvent in order to allow the dispersion of the hydrophobic $C_{10}PO_3$-HST in the solvent). The mixture was stirred gently at room temperature for 48 hours in a 50 mL-flask. The suspension was centrifuged at 1600 rpm for 20 minutes. The resulting supernatant and bottom were collected, washed with water or IPA by centrifugation (14000 rpm, 10 minutes) and re-dispersed in water or IPA.

Chapter IV

IV.3 Optimization of shear force-assisted liquid exfoliation

IV.3.2 Role of the solvent

Exfoliation of $C_{12}O$-HST: 20 mg (0.03 mmol) of $C_{12}O$-HST were dispersed in 40 mL of different solvents: water, toluene, isopropanol or acetonitrile. The mixture was sheared using the high-shear disperser at a speed of 11500 rpm, for 5 minutes, in a Teflon beaker of diameter 3.5 cm. The suspension went through the selective centrifugation process. The last supernatant was collected, washed with the same solvent and re-dispersed in 20 mL of the same solvent.

IV.3.3 Influence of the shear rate.

Exfoliation of $C_{12}O$-HST: 20 mg (0.03 mmol) of $C_{12}O$-HST were dispersed in 40 mL of acetonitrile. The mixture was sheared using the high-shear disperser at different rotor speeds: 8000 rpm, 9500 rpm, 11500 rpm, 14500 rpm, 20500 rpm and 30000 rpm, for 5 minutes, in a Teflon beaker of diameter 3.5 cm. The suspension went through the selective centrifugation process. The last supernatant was collected, washed with acetonitrile by centrifugation (14000 rpm, 10 minutes) and re-dispersed in 20 mL of acetonitrile.

IV.3.4 Influence of the exfoliation time

Exfoliation of $C_{12}O$-HST: 20 mg (0.03 mmol) of $C_{12}O$-HST were dispersed in 40 mL of solvent of acetonitrile. The mixture was sheared using the high-shear disperser at 11500 rpm for 5 minutes, 15 minutes or 60 minutes, in a Teflon beaker of diameter 3.5 cm. The suspension went through the selective centrifugation process. The last supernatant was collected, washed with acetonitrile by centrifugation (14000 rpm, 10 minutes) and re-dispersed in 20 mL of acetonitrile.

IV.3.5 Influence of the grafted molecule on the exfoliation

Exfoliation of BenzO-HST: 20 mg (0.026mmol) of BenzO-HST were dispersed in 40 mL of different solvents: water, toluene and acetonitrile. The mixture was sheared using the high-shear disperser at a rotor speed of 11500 rpm, for 15 minutes, in a Teflon beaker of diameter 3.5 cm. The suspension went through the selective centrifugation process. The last supernatant was collected, washed with the same solvent and re-dispersed in 20 mL of the same solvent.

IV.4 Comparison with sonication

Exfoliation of $C_{12}O$-HST: 20 mg (0.03 mmol) of $C_{12}O$-HST was dispersed in 40 mL of acetonitrile. The mixture was sonicated for 1 hour (*i.e.* 3 hours by considering the alternate between sonication and rest, described above) at 40% of the nominal power in a Teflon beaker of diameter 3.5 cm. The suspension went through the selective centrifugation process. The last supernatant was collected, washed with acetonitrile by centrifugation (14000 rpm, 10 minutes) and re-dispersed in acetonitrile.

Chapter V

V.2 Shear force exfoliation of layered phosphonic acid-based hybrid

Exfoliation of $C_{10}PO_3$-HST (shear-force): 20 mg (0.025 mmol) of $C_{10}PO_3$-HST were dispersed in 40 mL of isopropanol. The mixture was sheared using the high-shear disperser at a speed of 11500 rpm for 1 hour of exfoliation, in a Teflon beaker of diameter 3.5 cm. The suspension went through the selective centrifugation process. The last supernatant and the bottoms of each centrifugation step were collected, washed with isopropanol by centrifugation (14000 rpm, 10 minutes) and re-dispersed in 20 mL of isopropanol. Note: for the last supernatant, the isopropanol for re-dispersion was filtered using a 0.22 μm-filter.

C_3PO_3-HST, **C_6PO_3-HST** and **$C_{10}PO_3$-HLN** were exfoliated using the same procedure as for $C_{10}PO_3$-HST.

Exfoliation of $C_{10}PO_3$-HST (Y. Oaki's method): 20 mg (0.025 mmol) of $C_{10}PO_3$-HST were dispersed in 50 mL of toluene in a 100 mL-flask, at 60°C for 5 days. The suspension was then centrifuged at 1600 rpm for 20 minutes. The resulting supernatant and bottom were collected, washed with toluene by centrifugation (14000 rpm, 10 minutes) and re-dispersed in toluene

V.3 Near-field characterization of functionalized nanosheets

V.3.4 Atomic-force microscopy

Substrate cleaning and activation: a Si/SiO_2 wafer (50 mm, Si thickness 500.μm, passivation layer SiO_2 thickness 100 nm, provider CODEX) was cleaved into small 1 cm×1cm substrates. These substrates were cleaned by two sonication steps in ethanol then isopropanol for 5 minutes, rinsed with isopropanol and dried in air. The substrates were then poured into a HCl:MeOH solution 1:1 in volume for 20 minutes and rinsed abundantly with water. The substrates were then poured in a H_2SO_4 concentrated solution for 20 minutes and rinsed abundantly with water then with IPA and finally air-dried.

Coating of PEI onto Si/SiO_2: the cleaned Si/SiO_2 substrate was poured into an aqueous solution of PEI (M = 60000 $g.mol^{-1}$, 50% weight in water) at a concentration of 2.5 $mg.mL^{-1}$ for 1 hour at pH = 9. The substrate was then rinsed with water, IPA and finally dried under N_2 flux.

Dip-coating of NS-$C_{10}PO_3$-HST onto PEI@Si/SiO_2: the PEI-coated substrate was poured into a suspension of $C_{10}PO_3$-HST nanosheets with a gentle stirring for 1 hour. The substrate was then rinsed with water and dried under N_2 flux. Finally, the substrate was put on a hot plate, heating at 120°C for 4 minutes to remove traces of solvent.

Drop-casting of NS-$C_{10}PO_3$-HST onto PEI@Si/SiO_2: the PEI-coated was put either on a hot plate, heated at 120°C or at room temperature. A suspension of $C_{10}PO_3$-HST nanosheets was drop-casted onto the substrate. After the total evaporation of the solvent, the substrate was heated at 120°C on a hot plate to remove traces of solvent.

Spray-deposition NS-$C_{10}PO_3$-HST onto PEI@Si/SiO_2: the PEI-coated substrate was maintained vertically on a plate, heated at 120°C. The sprayed $C_{10}PO_3$-HST nanosheets suspension was a 30 mL solution obtained by dilution of the bare suspension with 20 mL of IPA. The suspension was sprayed onto the substrate for 30 s. The substrate was then rinsed with IPA, air-dried and heated at 120°C for 4 minutes to remove traces of solvents.

Chapter VI

VI.2.1 Guided assembly using π-π interactions

Exfoliation of PyrC_xO-HST(x=0, 1, 4): 20 mg (0.032, 0.031 and 0.028 mmol respectively) of PyrC_xO-HST were dispersed in 40 mL of IPA in a Teflon beaker with a diameter of 3.5 cm. The suspension was sheared at 11500 rpm for 1 hour. The suspension went through the selective centrifugation process. The resulting supernatant and four bottoms were collected, washed with IPA by centrifugation (14000 rpm, 10 minutes) and re-dispersed in 20 mL of IPA.

Exfoliation of graphite: 10 mg of expensed graphite were dispersed in 40 mL of IPA in a beaker with a diameter of 3.5 cm. The mixture was sonicated for 1 hour at 40% of the nominal power while maintaining the beaker in an ice bath. The suspension was then centrifuged at 1600 rpm for 20 minutes. The resulting supernatant was collected under the form of a dark and turbid solution. Note: sedimentation occurred quite rapidly after the synthesis of the nanosheets.

Assembly NS-PyrC_4O-HST@graphene (method1): 10 mL of the PyrC_4O-HST nanosheets suspension was mixed with 2 mL of the graphene suspension. The mixture was stirred at room temperature for 1 hour. Then the solution was directly analyzed without any centrifugation or washing step.

Assembly of NS-PyrC_4O-HST@ graphene (method 2): 15 mg (0.021 mmol) of PyrC_4O-HST and 3 mg of expensed graphite were dispersed in 40 mL of IPA in a Teflon beaker with a diameter of 3.5 cm. The mixture was sonicated for 1 hour at 40% of the nominal power while maintaining the beaker in an ice bath. The suspension was then centrifuged at 1600 rpm for 20 minutes. The resulting supernatant was collected under the form of a dark and turbid solution.

VI.3 Guided assembly using hydrogen bond

VI.3.1 Complementary nucleoside-based hybrid

Exfoliation of Adenosine-HST: 20 mg (0.027 mmol) of Adenosine-HST was dispersed in 40 mL of IPA. The mixture was sheared using the high-shear disperser at a speed of 11500 rpm for 1 hour of exfoliation, in a Teflon beaker of diameter 3.5 cm. The suspension was then centrifuged at 1600 rpm for 20 minutes. The resulting supernatant and bottom were collected, washed with IPA by centrifugation (14000 rpm, 10 minutes) and re-dispersed in 20 mL of IPA.

Exfoliation Thymidine-HST was performed using the same procedure as for Adenosine-HST.

Assembly of Adenosine-HST+Thymidine: 20 mg (0.027 mmol) of Adenosine-HST and 48 mg (0.2 mmol) of Thymidine were dispersed in 25 mL of IPA or water. The mixture was gently stirred at room temperature or at 40°C for 2days. The suspension was then centrifuged at 1600 rpm for 20 minutes. The resulting supernatant and bottom were collected, washed two times with IPA or water by centrifugation (14000 rpm, 10 minutes), re-dispersed in the same solvent and dried at 40 °C in an oven.

Assembly of Thymidine-HST+Adenosine was performed using the same procedure as the assembly of Adenosine-HST+Thymidine.

VI.3.2 Assembly using non-charged polymer coated nanosheets

Exfoliation of $C_{10}PO_3$-HLN with PEG600 was performed using the same procedure developed in **Chapter III**.

Exfoliation of $C_{10}PO_3$-HST with PEI was performed using the same procedure developed in **Chapter III.**

Assembly (PEI-$C_{10}PO_3$-HST@PEG-$C_{10}PO_3$-HLN)$_4$: a PEI-coated Si/SiO_2 substrate was first poured into the PEG-coated $C_{10}PO_3$-HLN nanosheets suspension for 1 hour under gentle stirring. Then the substrate was dried with a flux of dry air and poured into the PEI-coated $C_{10}PO_3$-HST (pH = 9.5). The substrate was then dried with a flux of dry air. This procedure was repeated 4 times on the substrate. Finally, the substrate was heated on a hot plate at 120 °C for 4 minutes to remove traces of solvent.

VI.4 Assembly using covalent bond

Exfoliation of MPTS-HST was performed using the same procedure as for $C_{10}PO_3$-HST in **Chapter V**.

Assembly of MPTS-HST@Au: the gold substrate was cleaned with two sonication steps (5 minutes in ethanol and IPA) then dried with a dried air flux. The substrate was then cleaned and activated using an O_2 plasma for 2 minutes. The MPTS-HST suspension was drop-casted onto the gold substrate and this latter was dried in air at room temperature. The as-deposited nanomaterials were then heated at 80°C for 30 minutes to remove traces of solvents and to allow the Au-S bond to be formed.

III. Bibliography

(1) Paton, K. R.; Varrla, E.; Backes, C.; Smith, R. J.; Khan, U.; O'Neill, A.; Boland, C.; Lotya, M.; Istrate, O. M.; King, P.; Higgins, T.; Barwich, S.; May, P.; Puczkarski, P.; Ahmed, I.; Moebius, M.; Pettersson, H.; Long, E.; Coelho, J.; O'Brien, S. E.; McGuire, E. K.; Sanchez, B. M.; Duesberg, G. S.; McEvoy, N.; Pennycook, T. J.; Downing, C.; Crossley, A.; Nicolosi, V.; Coleman, J. N. Scalable Production of Large Quantities of Defect-Free Few-Layer Graphene by Shear Exfoliation in Liquids. *Nature Materials* **2014**, *13* (6), 624–630.

(2) Juhás, P.; Davis, T.; Farrow, C. L.; Billinge, S. J. L. PDFgetX3: A Rapid and Highly Automatable Program for Processing Powder Diffraction Data into Total Scattering Pair Distribution Functions. *J Appl Cryst* **2013**, *46* (2), 560–566.

(3) Farrow, C. L.; Juhas, P.; Liu, J. W.; Bryndin, D.; Božin, E. S.; Bloch, J.; Proffen, T.; Billinge, S. J. L. PDFfit2 and PDFgui: Computer Programs for Studying Nanostructure in Crystals. *J. Phys.: Condens. Matter* **2007**, *19* (33), 335219..

(4) Finsy, R. Particle Sizing by Quasi-Elastic Light Scattering. *Advances in Colloid and Interface Science* **1994**, *52*, 79–143.

(5) Provencher, S. W. CONTIN: A General Purpose Constrained Regularization Program for Inverting Noisy Linear Algebraic and Integral Equations. *Computer Physics Communications* **1982**, *27* (3), 229–242.

(6) Provencher, S. W. A Constrained Regularization Method for Inverting Data Represented by Linear Algebraic or Integral Equations. *Computer Physics Communications* **1982**, *27* (3), 213–227.

(7) Schosseler, F.; Leibler, L. An Experimental Study of Gelation of Chains. *J. Phyique Lett.* **1984**, *45* (10), 501–507.

(8) Ida, S.; Ogata, C.; Unal, U.; Izawa, K.; Inoue, T.; Altuntasoglu, O.; Matsumoto, Y. Preparation of a Blue Luminescent Nanosheet Derived from Layered Perovskite $Bi_2SrTa_2O_9$. *J. Am. Chem. Soc.* **2007**, *129* (29), 8956–8957.

(9) Wang, Y.; Delahaye, E.; Leuvrey, C.; Leroux, F.; Rabu, P.; Rogez, G. Post-Synthesis Modification of the Aurivillius Phase $Bi_2SrTa_2O_9$ via In Situ Microwave-Assisted "Click Reaction." *Inorg. Chem.* **2016**, *55* (19), 9790–9797.

(10) Gopalakrishnan, J.; Bhat, V.; Raveau, B. $AILaNb_2O_7$: A New Series of Layered Perovskites Exhibiting Ion Exchange and Intercalation Behaviour. *Materials Research Bulletin* **1987**, *22* (3), 413–417.

(11) Takahashi, S.; Nakato, T.; Hayashi, S.; Sugahara, Y.; Kuroda, K. Formation of Methoxy-Modified Interlayer Surface via the Reaction between Methanol and Layered Perovskite $HLaNb_2O_7$.Cntdot.$_XH_2O$. *Inorg. Chem.* **1995**, *34* (20), 5065–5069.

(12) Sasaki, T.; Kooli, F.; Iida, M.; Michiue, Y.; Takenouchi, S.; Yajima, Y.; Izumi, F.; Chakoumakos, B. C.; Watanabe, M. A Mixed Alkali Metal Titanate with the Lepidocrocite-like Layered Structure. Preparation, Crystal Structure, Protonic Form, and Acid−Base Intercalation Properties. *Chem. Mater.* **1998**, *10* (12), 4123–4128.

Appendix II. Complementary Data to Pair-Distribution Function Analysis

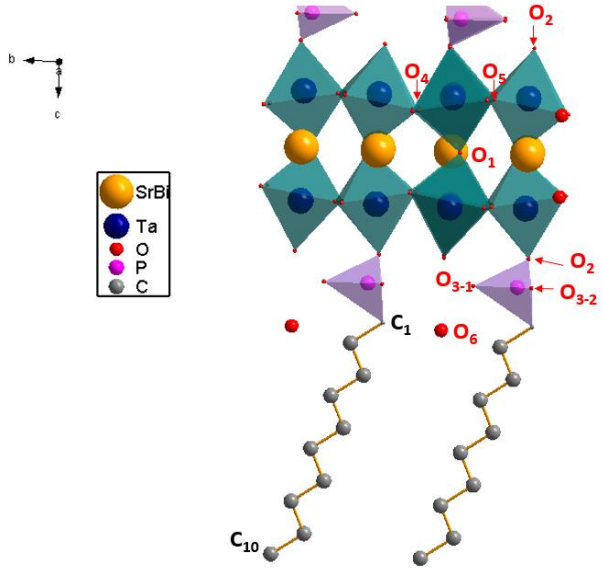

Figure 1: Model structure of $C_{10}PO_3$-HST. The atoms of the perovskite block are named by reference to the model structure reported by Whittle et al.

λ(Å) Silver $K_{\alpha1/\alpha2}$	$\lambda_{\alpha1}$ = 0.559421 Å ; $\lambda_{\alpha2}$ = 0.563812 Å
$Q_{max\ ins}$ ($Å^{-1}$)	21.5
Q_{max} ($Å^{-1}$)	21
Q_{damp} ($Å^{-1}$)	0.01
Unit cell (Å) orthorhombic $A2_1am$	a = 5.52715 (9) b = 5.55459 (12) c = 65.2
r_{cut} (Å)	5.2
S_{rat}	0.0218(6)
R_w	0.086

Table 1: Experimental details and instrumental parameters for the refinement of the PDF of $C_{10}PO_3$-HST in the 1.2–3.2 Å r range.

Table 2: Results of the refinement of the PDF of $C_{10}PO_3$-HST in the 1.2–3.2 Å r range. Errors are not reported for the refined parameters as the standard deviations are not properly calculated by PDFgui (standard data reduction obtained by PDFgetX3 does not include the standard deviations of the experimental PDF, which is needed to properly calculate the errors).[2]

Atomic positions in the orthorhombic cell (SG $A2_1am$)						
	Wyckoff	*x*	*y*	*z*	ADP ($Å^2$)[a]	SOF[b]
Sr	4a	0.06019	0.24357	0	0.0040	0.85
Bi	4a	0.56019	0.25640	0.5	0.0040	0.1
Ta	8b	0.53501	0.74631	0.46755	0.0002	1.0
O_1	4a	0.06530	0.69359	0	0.0100	1.0
O_2	8b	0.50866	0.71750	0.43824	0.0040	1.0
O_4	8b	0.78308	0.97928	0.02393	0.0040	1.0
O_5	8b	0.79971	0.97584	0.53186	0.0002	1.0
P	8b [c]	0.15708 0.65708 0.15708 0.65708	0.21339 0.78660 0.71339 0.28660	0.42102 0.57897 0.92102 0.07897	0.0030 0.0030 0.0030 0.0030	0.9 0.9 0.9 0.9
$O_{3\text{-}1}$	8b [c]	0.15655 0.65655 0.15655 0.65655	0.91868 0.08132 0.41868 0.58132	0.42111 0.57888 0.92111 0.07888	0.0003 0.0003 0.0003 0.0003	0.9 0.9 0.9 0.9
$O_{3\text{-}2}$	8b [c]	0.43761 0.93761 0.43761 0.93761	0.30855 0.69144 0.80855 0.19144	0.42127 0.57872 0.92127 0.07872	0.0110 0.0110 0.0110 0.0110	0.9 0.9 0.9 0.9
$O_6(H_2O)$	8b [c]	0.50720 0.00720 0.50720 0.00720	0.71177 0.28822 0.21177 0.78822	0.39351 0.60648 0.89351 0.10648	0.0006 0.0006 0.0006 0.0006	1.0 1.0 1.0 1.0
C_1	8b [c]	0.99618 0.49618 0.99618 0.49618	0.32121 0.67879 0.82121 0.17879	0.39773 0.60226 0.89773 0.10226	0.0001 0.0001 0.0001 0.0001	0.9 0.9 0.9 0.9
C_2	8b [c]	0.91004 0.41004 0.91004 0.41004	0.10944 0.89055 0.60944 0.39055	0.38512 0.61487 0.88512 0.11487	0.0001 0.0001 0.0001 0.0001	0.9 0.9 0.9 0.9
C_3	8b [c]	0.77848 0.27848 0.77848 0.27848	0.20281 0.79718 0.70281 0.29718	0.36622 0.63377 0.86622 0.13377	0.0001 0.0001 0.0001 0.0001	0.9 0.9 0.9 0.9
C_4	8b [c]	0.69276 0.19276 0.69276 0.19276	0.98680 0.01319 0.48680 0.51319	0.35336 0.64663 0.85336 0.14663	0.0001 0.0001 0.0001 0.0001	0.9 0.9 0.9 0.9
C_5	8b [c]	0.56318 0.06318 0.56318 0.06318	0.07783 0.92216 0.57783 0.42216	0.33428 0.66571 0.83428 0.16571	0.0001 0.0001 0.0001 0.0001	0.9 0.9 0.9 0.9

C_6	8b [c]	0.47538 0.97538 0.47538 0.97538	0.86254 0.13745 0.36254 0.63745	0.32270 0.67730 0.82270 0.17730	0.0001 0.0001 0.0001 0.0001	0.9 0.9 0.9 0.9
C_7	8b [c]	0.34558 0.84558 0.34558 0.84558	0.95565 0.04434 0.45565 0.54434	0.30720 0.69279 0.80720 0.19279	0.0001 0.0001 0.0001 0.0001	0.9 0.9 0.9 0.9
C_8	8b [c]	0.25837 0.75837 0.25837 0.75837	0.74010 0.25989 0.24010 0.75989	0.28977 0.71022 0.78977 0.21022	0.0001 0.0001 0.0001 0.0001	0.9 0.9 0.9 0.9
C_9	8b [c]	0.12798 0.62798 0.12798 0.62798	0.83215 0.16784 0.33215 0.66784	0.27067 0.72932 0.77067 0.22932	0.0001 0.0001 0.0001 0.0001	0.9 0.9 0.9 0.9
C_{10}	8b [c]	0.04002 0.54002 0.04002 0.54002	0.61469 0.38530 0.11469 0.88530	0.25800 0.74199 0.75800 0.24199	0.0001 0.0001 0.0001 0.0001	0.9 0.9 0.9 0.9

Main interatomic distances (Å)					
Sr/Bi-O	2.3422*2 2.5011 2.6335*2 2.7572 2.8135 2.8384*2 2.9155*2 3.0539	Ta-O	1.9245 1.9410 1.9543 2.0186 2.0941 2.1478	P-O P-C	1.4423 1.6371 1.6373 1.8594

[a]ADP Isotropic atomic displacement parameter

[b]SOF site occupancy factor

[c]Half of the positions are occupied to avoid unrealistically close interatomic-intermolecular distances between $C_{10}PO_3$ chains and water molecules.

Résumé de la thèse de doctorat

I. Introduction

Les développements technologiques actuels et la tendance à la miniaturisation sont révélateurs de l'importance des nanomatériaux et particulièrement des matériaux bidimensionnels dits matériaux 2D. Leur champ d'application est très étendu, allant de l'optoélectronique à la catalyse en passant par l'énergie.[1,2] Ces avancées n'ont été possibles que par la mise au point d'un large panel de méthode de synthèse, chacune adaptée à un type de matériaux.[3]

Les voies dites « bottom-up » utilisent des précurseurs atomiques ou moléculaires réactifs pour former la structure 2D. Ces méthodes aboutissent à des nanomatériaux sans défaut, avec un contrôle très précis de l'épaisseur et une taille latérale de l'ordre du micromètre. Néanmoins ces techniques, comme l'ablation laser pulsée,[4] nécessitent l'utilisation d'un substrat et donc impliquent une relation épitaxiale entre le substrat et le matériau formé. De plus, leur coût et les difficultés de mise en œuvre à l'échelle industrielle sont des freins à l'utilisation de ces voies de synthèse.

Les méthodes alternatives, dites « top-down », consistent à séparer les feuillets d'un matériau lamellaire tridimensionnel en feuillets uniques par un processus d'exfoliation. La versatilité de cette approche réside dans la diversité des matériaux lamellaires existant en termes de composition et de structure. On en distingue deux grandes catégories, selon les forces cohésives entre les feuillets : les matériaux dits de « Van der Waals », qui comme leur nom l'indique, possèdent uniquement des interactions faibles entre leurs feuillets et les matériaux chargés, où des interactions électrostatiques fortes participent à la cohésion du matériau.[3,5] Parmi tous ces matériaux, les oxydes lamellaires chargés et plus spécifiquement ceux à structure pérovskite sont au cœur de ces travaux de thèse (***Figure 1 (a)***).[6,7]

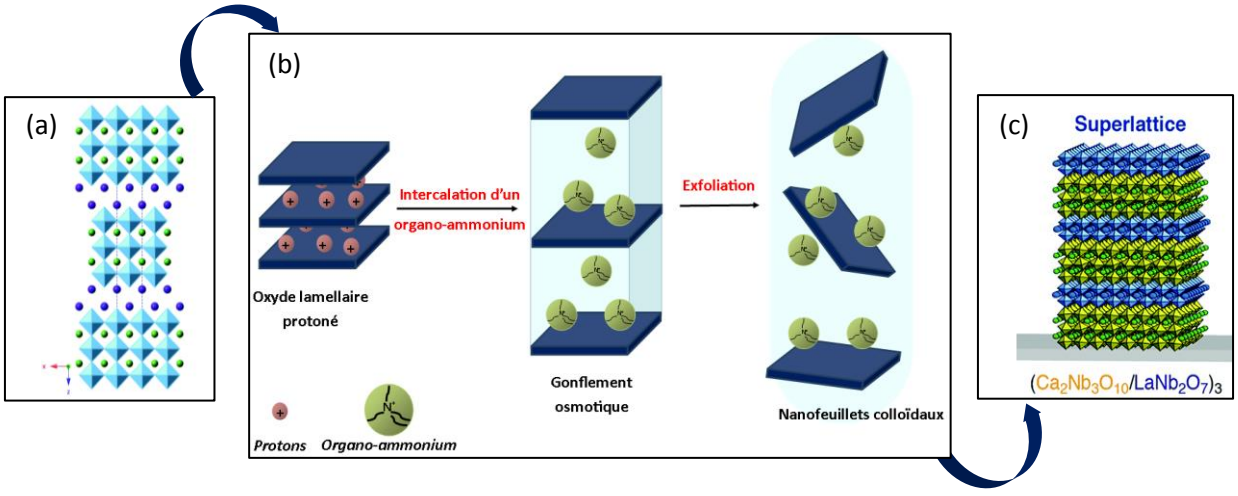

Figure 1: (a) Oxyde lamellaire de type Ruddlesden-Popper. (b) Le processus d'exfoliation utilisant l'ion tetrabutylammonium comme agent d'exfoliation. (c) Les nanofeuillets correspondants peuvent être intégrés dans (c) des hétérostructures alternées obtenues par dépôt couche-par couche.[8]

L'exfoliation, s'est fortement popularisée avec l'obtention du graphène par la méthode de clivage micromécanique. De nombreuses techniques se basant sur l'application de forces mécaniques sur les feuillets se sont développées par la suite.[9–11] Néanmoins, pour les oxydes chargés, une seule option est envisageable, reposant sur l'échange du cation initialement présent dans l'espace interlamellaire par un ion organo-ammonium volumineux. Cette insertion entraine l'apport de solvant dans la structure lamellaire et la séparation progressive des feuillets (***Figure 1 (b)***). Cette méthode d'échange d'ion, essentiellement développée par T. Sasaki *et al*.,[12–14] permet d'obtenir des nanofeuillets d'oxydes en solution, ayant des tailles latérale de l'ordre du micromètre et conservant la cristallinité initiale du matériau. Les principaux inconvénients de l'exfoliation par échange d'ions est le temps de réaction (de plusieurs jours à semaines) et l'utilisation de l'organo-ammonium, qui ne possède pas de propriétés spécifiques et peu parfois gêner dans l'utilisation ultérieure des nanofeuillets.

Les nanofeuillets d'oxydes, obtenus par échange d'ion, peuvent être intégrés dans des architectures multifonctionnelles basées sur l'empilement alternés de nanofeuillets. La plupart de ces assemblages se font par déposition couche-par-couche ou par Langmuir-Blodgett, en alternant couche positives et couches négatives (***Figure 1 (c)***).[8,15,16]

Cependant, la réactivité, à l'échelle bulk, des oxydes considérés pourrait permettre l'hybridation des nanofeuillets correspondants avec des molécules. D'une part, le couplage avec des entités organiques ouvrirait la voie à d'autres possibilités d'assemblages d'hétérostructures, basés sur des liaisons moléculaires de type liaison hydrogène, interactions π-π, etc…[17–19] D'autre part, lorsque l'hybridation est antérieure à l'exfoliation, *i.e.* elle se fait à partir du matériau lamellaire, les molécules organiques éloignent les feuillets entre eux.[20–22] Ainsi, de nouvelles voies d'exfoliation sont envisageables pour les oxydes chargés. Par exemple, Y. Oaki *et al*. tirent parti du possible gonflement de la structure avec du solvant pour exfolier[23,24] tandis que J.-H. Choy *et al*. utilisent des interactions électrostatiques répulsives entre molécules pour séparer les feuillets.[25] Dans ces travaux de thèse, nous avons opté pour l'utilisation de force de cisaillement, comme développée par J. Coleman et al. pour le graphène,[10] évitant ainsi l'utilisation supplémentaire de surfactant ou agent d'exfoliation.

Les objectifs de ces travaux sont donc triples :

- Dans un premier temps, il s'agit de fonctionnaliser un oxyde lamellaire de type pérovskite par des molécules d'intérêt
- Ensuite, il est nécessaire d'optimiser le processus d'exfoliation assistée par force de cisaillement. Un effort particulier est dédié à la caractérisation tant en solution qu'après dépôt des nanofeuillets fonctionnalisés
- Enfin, les nanofeuillets d'oxydes hybrides doivent être intégrés dans des hétérostructures *via* les interactions moléculaires des molécules en surface.

II. Principaux résultats

II.1 Synthèse d'oxydes lamellaires hybrides

Le point de départ d'une voie top-down est la synthèse du matériau lamellaire inorganique. Bien que plusieurs oxydes aient été utilisés, la majorité des travaux présentés sont focalisés sur l'oxyde de type Aurivillius $Bi_2SrTa_2O_9$ (BST). Ce dernier est synthétisé par voie de chimie du solide à haute température et la phase protonée $H_2Bi_{0.1}Sr_{0.85}Ta_2O_7$ (HST) correspondante est obtenue par dissolution de l'oxyde de bismuth, initialement présent dans l'espace interfoliaire, par un traitement acide assisté par micro-onde.[20]

La fonctionnalisation des pérovskites lamellaires par des amines ou des alcools aliphatiques et aromatiques avait déjà été explorée dans notre équipe par Y. Wang. Celui-ci a notamment utilisé le chauffage par micro-onde pour réduire grandement les temps de réaction, tout en obtenant des composés de bonne cristallinité. Dans une première partie, cette expertise est succinctement revue pour rappeler les mécanismes d'insertion et discuter de la réactivité des oxydes lamellaires. Des phases hybrides obtenues dans cette partie comme C_4N-HST ou C_{12}O-HST constituent les principaux précurseurs pour les fonctionnalisations suivantes.

Dans un second temps, il a été fait le choix de modifier la fonction d'ancrage des molécules par souci de préservation lors de l'exfoliation : les amines sont facilement échangeables tandis que les alcools, greffés sous forme d'éther, sont hydrolysables quand soumis à une élévation de température et en présence d'eau. C'est pourquoi le choix des acides phosphoniques est pertinent, la liaison P-OM a été démontrée plus résistance que celle C-OM.[26] Ainsi, une série d'acides phosphoniques aliphatiques a été greffée au sein de HST. Ces composés, dénommés C_xPO_3-HST (x= 3, 6, 10), ont été caractérisés par diffraction des rayons X (DRX) (***Figure 2, Gauche***). Les pics correspondants aux plans (*100*), (*110*) et (*200*) confirment que la structure pérovskite des feuillets d'oxyde est maintenue lors de l'étape de fonctionnalisation tandis que la série de pics (*00l*) atteste de l'insertion de molécules par rapport au précurseur (C_4N-HST). En effet, des modifications de l'espacement entre les feuillets par des molécules se traduisent par une diminution ou augmentation de la distance d_{001} associé au plan (*001*).

La spectroscopie infrarouge à transformée de Fourrier vient corroborer l'insertion des acides phosphoniques (***Figure 2***, ***Droite***). L'intensité des bandes d'élongation des (CH_2) vers 2900 cm^{-1} croît lorsque la longueur de la chaine alkyle augmente, comme observé pour $C_{10}PO_3$-HST. De plus, la bande d'élongation P-C à 1465 cm^{-1} présente sur le spectre des hybrides et des molécules libres est une preuve de l'intégrité des molécules. Néanmoins, les bandes entre 1300 et 1000 cm^{-1} correspondantes au groupement phosphonate diffèrent par rapport aux molécules libres, prouvant notamment le greffage comme indiqué par H. Mutin *et al.*[26]

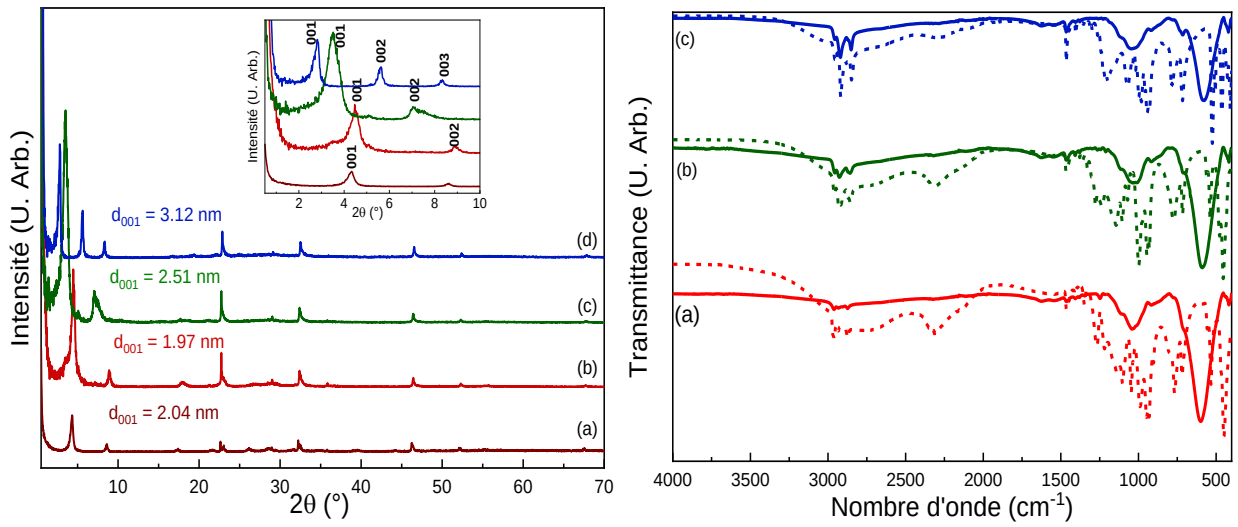

Figure 2: Gauche) Diffractogrammes (a) du précurseur C_4N-HST, (b) C_3PO_3-HST (c) C_6PO_3-HST et (d) $C_{10}PO_3$-HST Droite) Spectres FTIR de (a) C_3PO_3-HST (b) C_6PO_3-HST et (d) $C_{10}PO_3$-HST en ligne pleine et les dérivés d'acide phosphonique correspondants en pointillés.

Une étude plus approfondie de la structure du composé hybride $C_{10}PO_3$-HST est alors menée par analyse de la fonction de distribution de paires (PDF) *via* la diffraction des rayons X. Malgré les difficultés inhérentes à l'étude de composé hybrides, notamment pour de faibles distances, une bonne corrélation entre la fonction de distribution expérimentale et celle simulée à partir du modèle est déterminée (***Figure 3***). Ainsi la PDF permet d'élucider le greffage de l'acide phosphonique sur le feuillet inorganique, notamment en montrant qu'une seule liaison P-OH est hydrolysée et est liée à la structure inorganique. En outre, la simulation confirme que la phase hybride ne présente pas d'interdigitation des chaines alkyles des molécules, qui sont inclinées par rapport au feuillet d'un angle de 57°.

Au-delà de la simple chaine alkyle, des molécules plus complexes comportant des cycles aromatiques et présentant aussi une fonction acide phosphonique, dénotées $HOArPO_3H_2$ et $NCArPO_3H_2$, ont pu être greffées aux feuillets inorganiques par le même procédé (fonctionnalisation par assistance de micro-onde). Les phases hybrides ainsi obtenues sont caractérisées par DRX, FTIR et RMN du solide (^{13}C et ^{31}P). Les composés hybrides ainsi synthétisés sont des composés lamellaires cristallins dans lesquels les molécules insérées n'ont pas été dégradées. Le greffage par l'acide phosphonique est confirmé par les techniques spectroscopiques FTIR et RMN et est similaire à celui de $C_{10}PO_3$-HST.

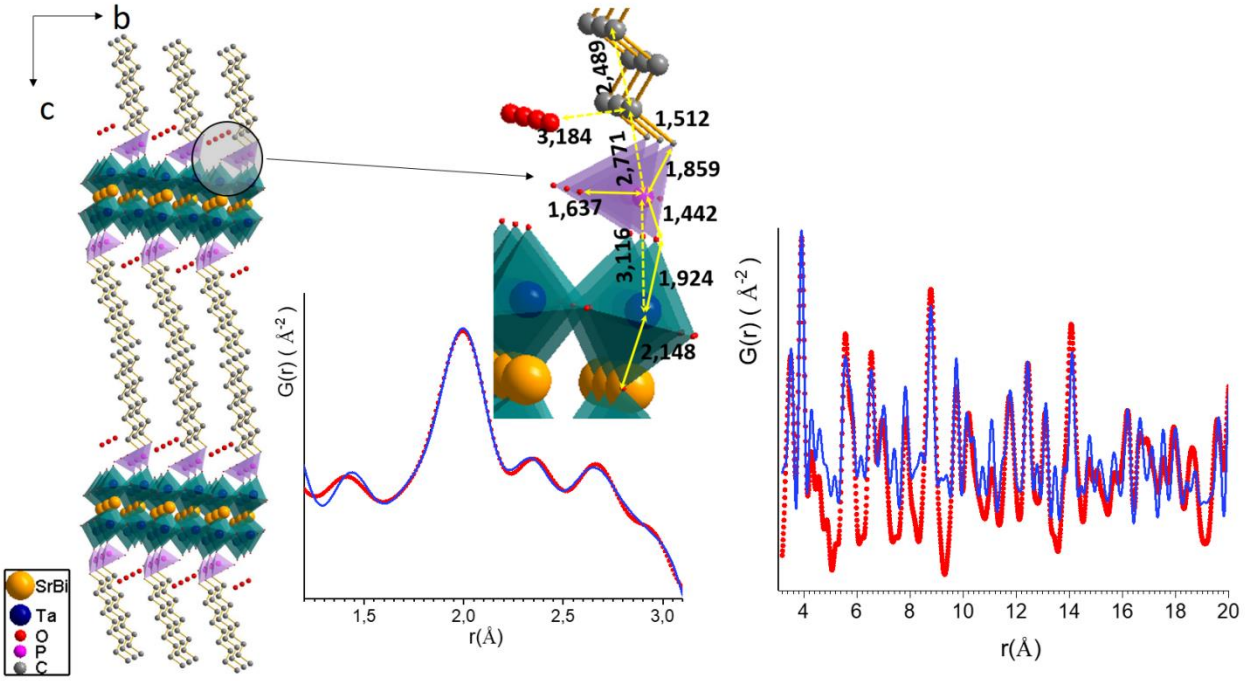

(a) (b) (c)

Figure 3: (a) Proposition d'arrangement des molécules d'acide 1-décylphosphonique entre les feuillets de $Sr_{0.85}Bi_{0.1}Ta_2O_7$ pour le composé $C_{10}PO_3$-HST. (b) Ajustement du moèlel structural (courbe bleue) par rapport à la PDF expérimentale (courbe rouge) aux petites distances i.e.au dessous de 3.2 Å (facteur d'accord R_w= 8.6%) (c) Affinement du modèle structural pour les distances comprises entre 3 et 20 Å (R_w = 59.0%).

Outre les acides phosphoniques une autre stratégie de greffage covalent a été utilisée, tirant parti de la réactivité des organosilanes. Déjà appliquée à la fonctionnalisation d'argile et de titanates lamellaires,[27] cette voie d'approche permet notamment d'obtenir des fonctions réactives de surface sans que ces dernières interagissent avec le feuillet inorganique. Par exemple, en utilisant cette voie d'hybridation, A. Clearfield *et al*. ont pu obtenir un oxyde lamellaire avec des amines en surface,[27] malgré l'interaction généralement préférentielle des amines avec le feuillets chargés pour des molécules multifonctionnelles.[21]

Ainsi, trois organosilanes ont été greffés à partir de la phase intermédiaire HST : le (3-aminopropyl)trimethoxysilane (APTS), le (3-mercapto)propyltriethoxysilane (MPTS) et le octyltriethoxysilane (C8TS), par voie conventionnelle mais aussi par synthèse assistée par micro-onde. Les deux premiers organosilanes comportent une fonction réactive (amine et thiol respectivement) qui peut être utilisée par la suite dans des stratégies de réassemblage non-électrostatiques. Les phases hybrides obtenues sont caractérisées par DRX, FTIR, MEB, ATG-ATD ainsi que par TEM.

La ***Figure 4 (a)*** montre les diffractogrammes des composés hybrides obtenus à partir des organosilanes considérés. Les pics correspondants aux plans (100) (110) et (200) attestent du maintien de la structure inorganique du feuillet tandis que la série de pics (00l) est significative du caractère lamellaire des composés synthétisés. L'augmentation de la distance interlamellaire pour APTS-HST et C8TS-HST

par rapport à C_4N-HST est en faveur de l'insertion d'APTS et C8TS dans la structure. Ces phases hybrides lamellaires se traduisent par une morphologie plaquettaire comme montrée par l'image MEB de la ***Figure 4 (b).*** L'étude MET d'APTS-HST (***Figure 4 (c)***) illustre l'empilement régulier des feuillets inorganiques mais aussi le caractère flexible des matériaux hybrides.

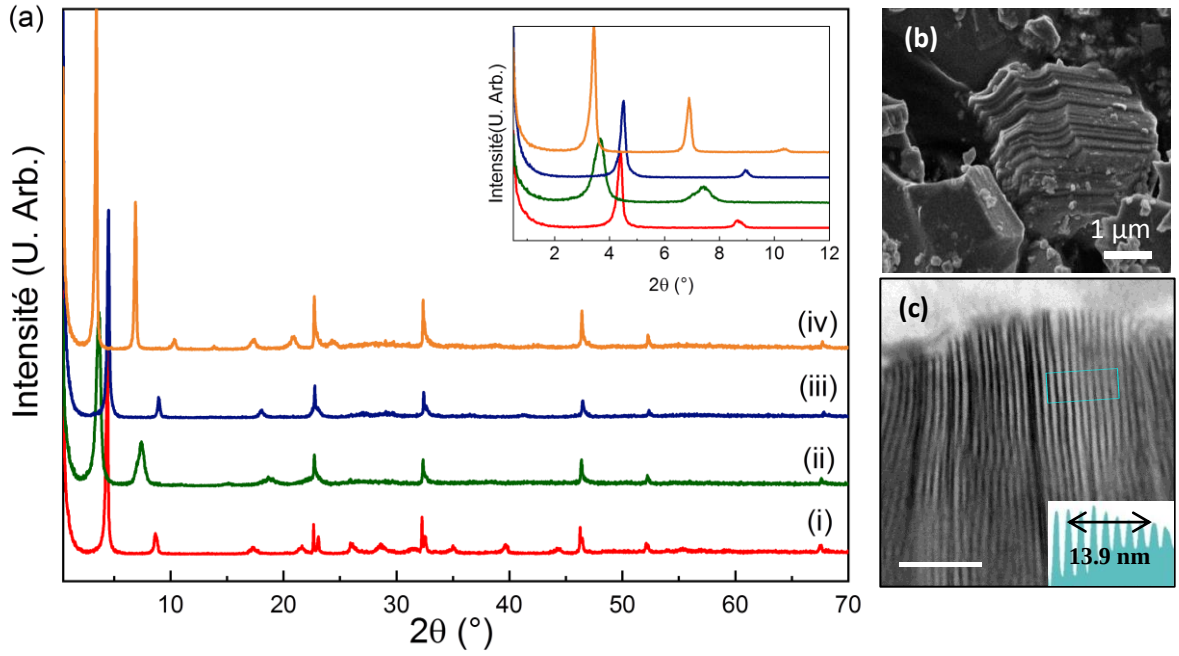

Figure 4: (a) Diffractogrammes (i) de C_4N-HST, le précurseur pour le greffage des organosilanes (ii) de APTS-HST, (iii) de MPTS-HST et (iv) de C8TS-HST. (b) Image MEB de C8TS-HST. (c) Image MET (vue transversale) de APTS-HST.

Dans un troisième temps, il a été fait le choix d'utiliser des alcools pour effectuer le greffage de molécules qui se distinguent par leur structure, leur complexité et leurs propriétés. Ainsi, le choix s'est porté sur des dérivés de pyrènes, molécules comportant quatre cycles aromatiques conjugués et qui possèdent des propriétés de luminescence. L'insertion de telles molécules a pour but d'ajouter cette luminescence aux nanofeuillets hybrides. De même, les pyrènes sont connus pour avoir une luminescence dépendante de leur état d'agrégation (*i.e.* leur concentration et/ou confinement). Ainsi, ces molécules pourraient potentiellement jouer le rôle de sonde pour l'exfoliation top-down de la phase hybride associée. Ces derniers points sont évoqués ci-dessous.

Dans ces travaux, trois dérivés de pyrènes ont été considérés, le 1-hydroxypyrene, le 1-pyrenemethanol et le 1-pyrenebutanol dont les structures sont représentées dans la ***Figure 5 (a)***. Leur insertion s'est faite à partir de la phase intermédiaire C_{12}O-HST, en utilisant l'assistance de micro-onde. Les composés résultants sont colorés, comme montré dans les ***Figure 5 (b)*** à ***(d)***, indiquant la présence de pyrène à entre ou en surface des feuillets inorganiques (non-colorés). Les matériaux hybrides obtenus sont dénommées PyrO-HST, PyrC_1O-HST et PyrC_4o-HST et sont caractérisés par DRX, FTIR, ATG-ATD. La

diffraction confirme le caractère lamellaire et cristallin des composés hybrides. De plus, la diminution de l'espace interlamellaire par rapport au précurseur C_{12}O-HST est en faveur de l'insertion réussie des dérivés de pyrènes. Les spectres infrarouges des composés hybrides et des molécules libres sont présentés dans la ***Figure 5 (e)***. Il est à noter l'absence des bandes fortes des CH aux alentours de 2900 cm^{-1}, très intenses dans le cas de C_{12}O-HST. Ensuite, les bandes caractéristiques des pyrènes comme celle des =C-H à 840 cm^{-1} sont présentes que ce soit dans la molécule libre ou dans le composé hybride correspondant. Enfin, la bande caractéristique de la vibration C-OTa est décalée pour les trois composés hybrides par rapport aux molécules libres, confirmant le greffage covalent des molécules sur le feuillet.

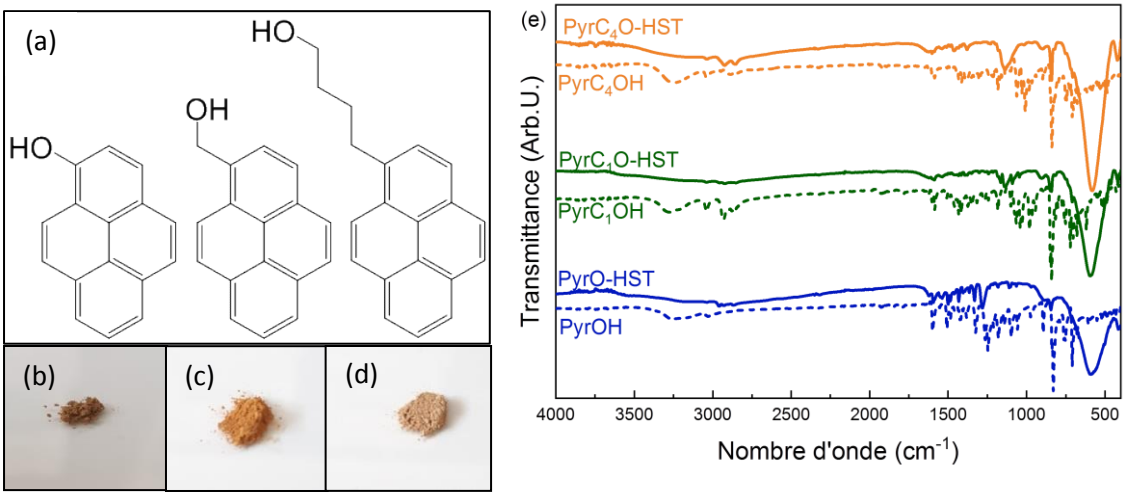

Figure 5: (a) Structure du 1-hydroxypyrene, du 1-pyrenemethanol et du 1-pyrenebutanoll (b) à (d) Photos des composés hybrides obtenus à partir de C_{12}O-HST et des trois pyrènes considérés, respectivement PyrO-HST, PyrC$_1$O-HSt et PyrC$_4$O-HST. (e) Spectres infrarouge de PyrO-HST, PyrC$_1$O-HST et PyrC$_4$O-HST (ligne pleine) et spectres des molécules correspondantes (pointillés).

Enfin, avec pour objectif de réassembler des feuillets par des interactions moléculaires, des molécules pouvant effectuer des liaisons hydrogènes spécifiques doivent être greffées en surface des nanofeuillets. C'est pourquoi, le choix de paires de nucléosides, connus pour s'assembler de manière spécifiques entre elles, sembrle pertinent. L'adénosine et la thymidine possèdent en outre des fonctions alcools qui sont des points d'ancrage possible sur les feuillets inorganiques tandis que le pKa de l'amine est trop faible pour observer la protonation de l'amine et son interaction préférentielle avec le feuillet chargé.

L'adénosine et la thymidine ont été insérées entre les feuillets de $Bi_{0.1}Sr_{0.85}Ta_2O_7^{2-}$ via assistance de rayonnement micro-onde et en utilisant C_{12}O-HST comme précurseur. Les deux phases hybrides obtenues, Adénosine-HST et Thymidine-HST, sont caractérisées par DRX, FTIR, ATG-ATD et RMN. Les composés sont cristallins et lamellaires selon la DRX et la spectroscopie FTIR indique la présence des molécules dans le composé. Les spectres RMN présentés en ***Figure 6*** confirment le greffage des nucléosides et leur intégrité (à la fois la base nucléotidiques et le ribose/désoxyribose). De plus, la RMN indique aussi que plusieurs fonctions alcools sont impliquées dans l'ancrage de la molécule sur le feuillet.

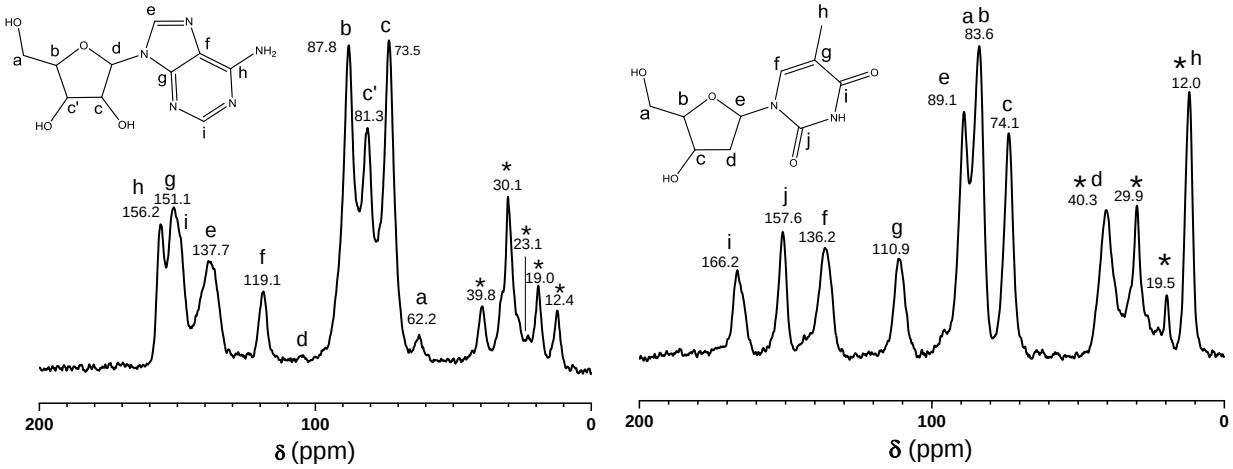

Figure 6: Spectres RMN 13C CP/MAS de (gauche) Adenosine-HST et (droite) Thymidine-HST.

Des nouveaux matériaux hybrides ont été préparés par assistance micro-onde avec soit une fonction d'ancrage plus résistante soit possédant des propriétés comme la luminescence ou des fonctions réactives.

II.2 Exfoliation par mécanisme d'échange

La seconde étape de la voie top-down appliquée dans cette étude est l'exfoliation de l'hybride lamellaire synthétisé précédemment. Parmi les voies d'approche possibles et compte tenu de la charge résiduelle à la surface des feuillets fonctionnalisés, il est *a priori* envisageable d'exfolier ces matériaux en utilisant la voie dite « classique » pour les oxydes chargés *i.e*. l'échange d'ion. Cette méthode se base sur l'utilisation d'un organoammonium, l'ion tetrabutylammonium (TBA^+) dans le cas de ces travaux. D'ailleurs, comme décrit par J. Wiley *et al.*,[28] ce procédé peut être réalisé par assistance de rayonnement micro-onde pour accélérer le processus d'insertion et de gonflement. C'est pourquoi, les phases hybrides ont été exfoliées avec TBA^+ sous chauffage par micro-onde à 80°C. De plus, pour cette étude, le choix a été fait d'étudier les matériaux après exfoliation par diffraction des rayons X et par spectroscopie infrarouge. En effet, tout changement en termes de distance interlamellaire ou en spectroscopie, observé sur le matériau non-exfolié ou ré-empilé s'est indubitablement aussi produit sur les nanofeuillets. L'analyse des nanofeuillets et de l'exfoliation est donc indirecte.

Après avoir vérifié que l'exfoliation de HST par utilisation de TBA^+ est similaire aux travaux de T. Sasaki *et al.*,[13,14] le composé hybride, C_2N-HST, a été exfolié par échange d'ion assistée par micro-onde. La suspension résultante est centrifugée : le culot et le surnageant sont récoltés et séchés pour être analysés par DRX et FTIR. Les caractérisations montrent le remplacement de l'ammonium initial (l'éthylammonium) par le TBA^+ quelle que soit la quantité de TBA^+ introduite au départ. De plus, le matériau récolté dans le culot est un composé cristallisé lamellaire dont la cohérence entre les feuillets a été maintenue lors du processus d'exfoliation. Ces résultats confortent le choix de fonction de greffage plus résistante aux procédés d'exfoliation.

Dans un second temps, l'exfoliation par échange d'ion fut testée sur l'hybride lamellaire C_{12}O-HST, dont les molécules de 1-dodecanol sont attachées de manière covalente aux feuillets inorganiques. Plusieurs expériences d'exfoliation avec une quantité croissante de TBA^+ ont été menées. Dans chaque cas, la suspension obtenue post-exfoliation est centrifugée et les culots sont analysés par DRX et FTIR (***Figure 7***). Les diffractogrammes des matériaux présentent à la fois les pics associés aux feuillets inorganiques et ceux à bas angles correspondant à la distance interfoliaire. Des changements dans la distance (*00l*) sont observés lorsque le ratio $\frac{TBA^+}{H^+}$ augmente : celle-ci-diminue pour aboutir à une distance interlamellaire de 2.1 nm, correspondant à l'insertion de TBA^+. Ce remplacement progressif est aussi souligné par les spectres FTIR et la disparition progressive de la bande C-OTa à 1140 cm^{-1} avec l'augmentation de la quantité de TBA^+.

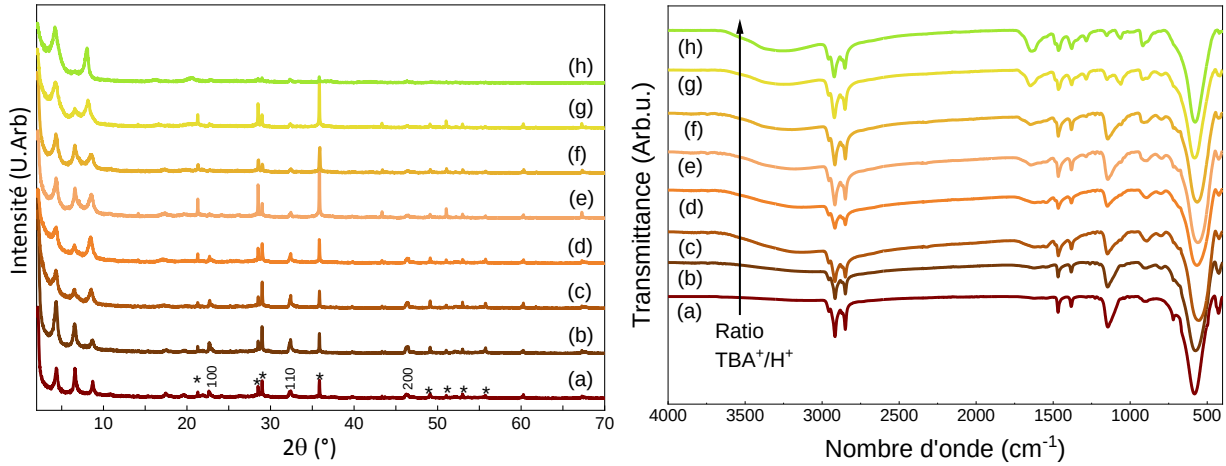

Figure 7: (Gauche) Diffractogrammes et (Droite) spectres FTIR de (a) C_{12}O-HST (b) à (h) des culots résultants de l'exfoliation de C_{12}O-HST par TBA^+ à différents ratios TBA^+/H^+ = 0, 0.5, 1, 3, 5, 10 et 20. Les pics avec l'étoile correspondent à une impureté de BST observée sur cette série d'expériences.

L'échange d'ion n'est donc pas adapté pour exfolier des oxydes lamellaires hybrides tout en maintenant la fonctionnalisation intacte.

Cependant, il est aussi envisageable possible d'exfolier par assistance d'autres espèces chimiques notamment en utilisant des polymères. Cette voie d'approche a été largement étudiée dans le domaine des composites et permet d'obtenir des nanofeuillets dispersés dans une matrice de polymère.[29] C'est pourquoi, il a été envisagé d'utiliser des polymères non-chargés pour exfolier les phases hybrides. Tout d'abord, le choix s'est porté sur des polyéthylène glycols (M = molaire 600 $g.mol^{-1}$, 2000 $g.mol^{-1}$ et 6000 $g.mol^{-1}$), dénoté respectivement PEG600, PEG2000 et PEG6000 ainsi que sur le methoxypoly(ethylene glycol)amine (M = 5000 $g.mol^{-1}$), dénoté PEGN5000. Dans un second temps, l'acide polyacrylique (M =240000 $g.mol^{-1}$) dénoté PAA et le polyéthylène imine (M = 60 000 $g.mol^{-1}$), dénoté PEI ont aussi été utilisé pour l'exfoliation. Tous les essais ont été menés en solution, à température ambiante et sous agitation pendant plusieurs jours.

Concernant l'exfoliation par les PEGs, des essais ont été effectués sur l'oxyde lamellaire « nu » pour comparaison *a posteriori* avec les phases hybrides. Les suspensions résultantes de l'exfoliation ont été centrifugées et les culots ont été analysés par DRX et FTIR. Aucun changement significatif des diffractogrammes n'est observé par rapport à celui de HST. De même, la présence des polymères sur les spectres infrarouge est uniquement visible pour l'expérience avec le PEG2000. L'analyse MEB en mode STEM des surnageants montre des objets partiellement exfoliés dans le cas du PEG600 ainsi que pour le PEG2000 dans une moindre mesure. L'exfoliation assistée par polymères est donc peu efficace pour HST dans les conditions expérimentales choisies.

Par la suite, quatre oxydes lamellaires hybrides, C_4N-HST, BenzSC_2O-HST, $C_{12}O$-HST et $C_{10}PO_3$-HST, ont été exfoliés en utilisant le PEG600 qui semblait le plus prometteur avec HST. Les suspensions ont été centrifugées et les culots ont été analysés par DRX et FTIR. Malgré une légère diminution de la distance interlamellaire, les diffractogrammes de BenzSC_2O-HST et de $C_{10}PO_3$-HST sont cohérents avec la présence des molécules initiales. Cependant, dans le cas de $C_{12}O$-HST et C_4N-HST, la distance interlamellaire correspond à celle de HST. De même les spectres infrarouges montrent une préservation du greffage dans le cas de BenzSC_2O-HST et $C_{10}PO_3$-HST tandis qu'une complète disparition des bandes associées au 1-dodecanol et de la 1-butylamine est observée pour $C_{12}O$-HST et C_4N-HST.

L'analyse MEB des surnageants avec BenzSC_2O-HST et $C_{10}PO_3$-HST (***Figure 8 (a)*** et ***(b)*** respectivement) montre clairement des nanofeuillets en quantité importante malgré une certaine polydispersité en épaisseur et en taille latérale (aucun procédé de sélection n'a été effectué sur les suspensions). Ainsi, le PEG600 convient bien pour l'exfoliation de phase hybride, conduisant à de meilleurs résultats qu'avec HST. Cependant un greffage covalent fort est à privilégier car le polymère tend à partiellement voire totalement dégrader la fonctionnalisation initiale.

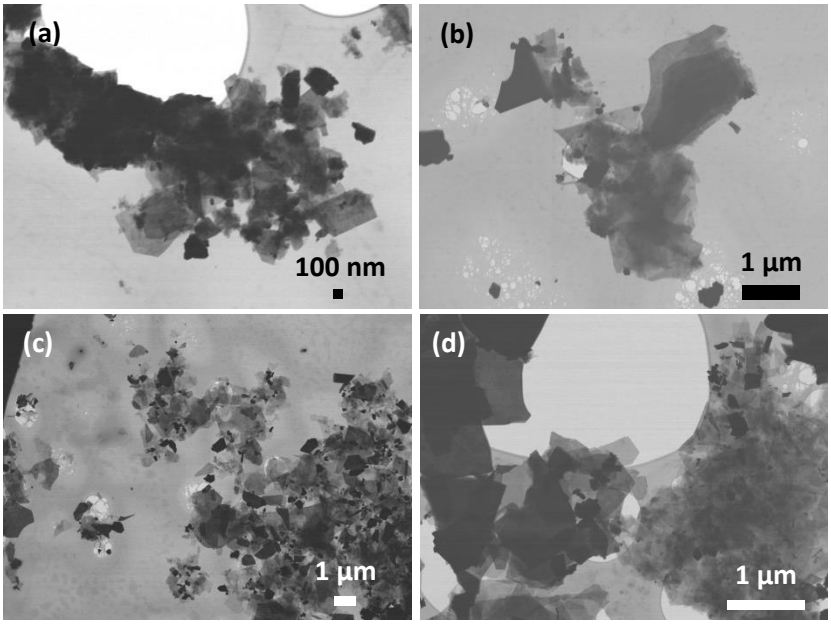

Figure 8: Images MEB des surnageants de (a) BenzSC_2O-HST et (b) $C_{10}PO_3$-HST après exfoliation avec le PEG600 et de (c) de BenzSC_2O-HST et(d) $C_{10}PO_3$-HST après exfoliation avec PEGN5000.

De même, des expériences ont aussi été effectuées sur les quatre hybrides considérés précédemment en utilisant le PEGN5000. La phase $C_{10}PO_3$-HST est là encore exfoliée par assistance du polymère tout en préservant sa fonctionnalisation (***Figure 8 (d)***). Les composés $BenzSC_2O$-HST et $C_{12}O$-HST ont leur couche organique partiellement dégradée (hydrolyse de la liaison C-OTa) mais des nanofeuillets sont obtenus (***Figure 8 (c)***). Dans le cas de C_4N-HST, les amines sont totalement retirées de la surface des feuillets.

Ainsi l'exfoliation par des PEGs permet d'obtenir des nanofeuillets. Néanmoins un ancrage fort des molécules initialement présentes est nécessaire pour assurer leur maintien au cours du processus d'exfoliation.

Par la suite, des expériences utilisant le PAA et PEI ont été menées. Néanmoins ces polymères semblent moins effiaces pour exfolier des hybrides lamellaires dans les conditions expérimentales choisies. Une optimisation des conditions expérimentales doit être menée pour être complètement conclusif quant à l'efficacité de ces deux polymères.

II.3 Exfoliation assistée par force de cisaillement

Les oxydes lamellaires hybrides ont une distance interfoliaire plus importante que la phase « nue » correspondante. Ainsi, les interactions électrostatiques qui participent à la cohésion des feuillets entre eux sont fortement réduites. Il serait donc possible d'utiliser des méthodes d'exfoliation jusqu'alors réservées aux matériaux dits de Van der Waals comme l'exfoliation assistée par force de cisaillement.

Cependant, avant d'étudier expérimentalement l'exfoliation par cette dernière méthode, il est essentiel de déterminer le taux de cisaillement minimal $\dot{\gamma_{min}}$ à appliquer aux feuillets pour les exfolier, à la fois dans le cas de l'oxyde lamellaire HST et dans le cas des hybrides lamellaires obtenus à partir de HST. Pour ce faire, la démarche mise en œuvre dans cette étude se base sur le modèle développé par Coleman *et al* dans leurs travaux sur l'exfoliation du graphène par force de cisaillements.[10] Moyennant certaines hypothèses, le modèle fournit une expression analytique faisant intervenir des caractéristiques du solvant (comme sa viscosité dynamique η ou son énergie de surface E_{LL}), la dimension L des feuillets assimilé à des carrés et l'énergie de surface des feuillets E_{PP} :

$$\dot{\gamma_{min}} = \frac{(\sqrt{E_{PP}} - \sqrt{E_{LL}})^2}{\eta L} \qquad \textbf{\textit{Equation 1}}$$

La grande densité de charge et la petite distance entre deux feuillets chargés (environ 1Å) conduisent à utiliser le modèle de Régime de Couplage Fort au lieu du modèle de Poisson-Boltzmann. Ainsi, dans le cas de HST, nous avons déterminé un taux de cisaillement minimum de $\dot{\gamma_{min}} = 5.6 \times 10^7 s^{-1}$ en considérant l'isopropanol comme solvant d'exfoliation. Cette valeur est au-delà de ce qui peut être fournit par le disperseur à haute vitesse à notre disposition. Ainsi, l'exfoliation par force de

cisaillement ne peut se faire avec HST, ce qui est vérifié expérimentalement par la suite. Dans le cas d'un composé hybride, comme $C_{12}O$-HST avec une distance entre feuillets adjacents de 31 Å, le système n'appartient plus au Régime de Fort Couplage et les interactions électrostatiques sont fortement diminuées, permettant l'utilisation des forces de cisaillements. La méthode a donc été appliquée pour obtenir des nanofeuillets fonctionnalisés en solution.

Dans le but d'obtenir des suspensions contenant le plus de nanofeuillets de grande taille latérale, il est nécessaire d'optimiser les paramètres d'exfoliation, qui sont le solvant, le taux de cisaillement (relié à la vitesse du rotor du disperseur), le temps d'exfoliation ainsi que l'influence du greffage organique à la surface du feuillet.

Selon les travaux de J. Coleman *et al.* sur l'exfoliation par assistance de force mécaniques,[10,30] le paramètre essentiel, inhérent au solvant, est son paramètre de solubilité de Hildebrand. Celui-ci donne une indication des interactions potentielles (non-polaires, polaires, liaison hydrogène, etc) entre le solvant et le nanofeuillet. Dans le cas des oxydes lamellaires fonctionnalisés, l'hypothèse est faite que le paramètre de solubilité doit s'accorder avec celui des molécules en surface. Pour tester cette hypothèse, quatre solvants ont été utilisés pour exfolier $C_{12}O$-HST à vitesse et temps d'exfoliation constant : le toluène, l'isopropanol, l'eau et l'acétonitrile. Après centrifugation, les suspensions sont caractérisées par MEB et par diffusion de lumière (DLS) en utilisant un appareil commercial. Il est à noter que la distribution en taille fournie par l'appareil n'est pas fiable, car se basant sur un modèle de sphères dures et monodisperses. En revanche, les fonctions d'autocorrélation en intensité peuvent être analysés pour déterminer la qualité des suspensions formées. Les résultats de DLS sont présentés dans la ***Figure 9.*** Les fonctions d'autocorrélation des suspensions dans l'eau, l'isopropanol et l'acétonitrile ont les caractéristiques usuelles des fonctions d'autocorrélation de nano-objet en solution (limites en 1 et en 0 pour des temps très courts et très longs respectivement, et semblent suivre une loi exponentielle). Cependant, celle de la suspension dans le toluène est quasiment nulle, signifiant l'absence de particules diffusantes dans la solution. Cette observation est appuyée par les images de MEB.Ainsi, bien que le paramètre de solubilité du toluène soit le plus proche de celui de la chaine alkyl de $C_{12}O$-HST, ce solvant est inefficace pour exfolier la phase hybride en utilisant la méthode des forces de cisaillement. Un solvant polaire apparait donc nécessaire, notamment à cause de la charge résiduelle portée par le feuillet inorganique. L'acétonitrile et l'isopropanol sont les solvants qui ont donné les meilleurs résultats. Etonnamment, l'eau a permis d'obtenir des nano-objets en solution même si la dispersion n'est pas idéale : la dispersion de $C_{12}O$-HST n'est pas simple et les nano-objets formés sédimentent rapidement comparés à ceux stabilisés dans l'acétonitrile.

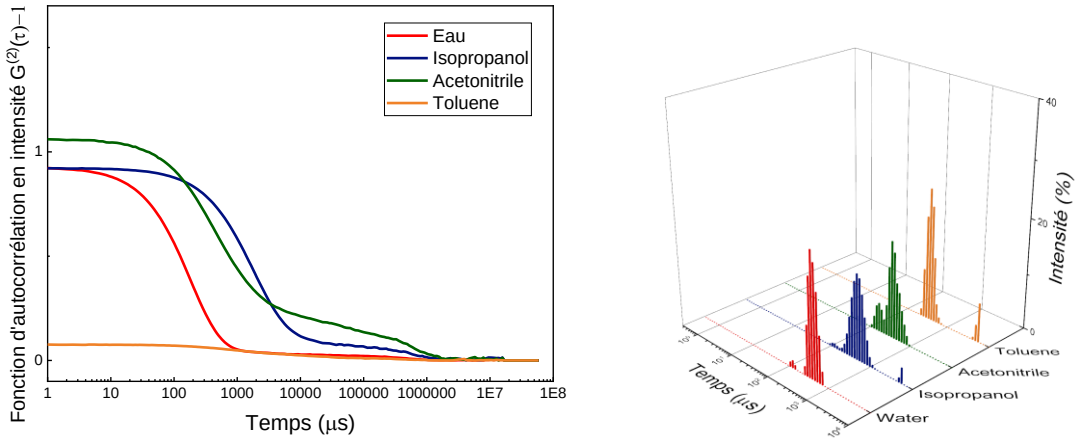

Figure 9: Fonctions d'autocorrélation en intensité de suspension de C_{12}O-HST après exfoliation dans différents solvants et les distributions en taille correspondantes.

Dans un second temps, le taux de cisaillement a été modifié par le biais de la vitesse du rotor, allant de 8000 tours/min à 30000 tours/min. Cette série d'expériences a été conduite sur C_{12}O-HST, à temps d'exfoliation constant et dans l'acétonitrile. Il est apparu qu'augmenter le taux de cisaillement favorise l'exfoliation mais les nanofeuillets obtenus sont plus petits en taille latérale. A l'inverse, un faible taux de cisaillement conduit à des nanomatériaux peu exfolié. C'est pourquoi un taux de cisaillement intermédiaire de 11500 tours/min est privilégié.

Le temps d'exfoliation a aussi été modifié pour l'exfoliation de C_{12}O-HST dans l'acétonitrile à 11500 tours/min. Un temps d'exfoliation trop court (*e.g.* 5 minutes) ne permet pas d'obtenir suffisamment de nanofeuillets en suspension. Le taux d'exfoliation augmente en prolongent la durée d'exfoliation. Ainsi, un temps d'exfoliation de 1 heure a été déterminé comme suffisant.

Enfin, l'influence de la fonctionnalisation fut étudiée en exfoliant un autre hybride lamellaire, BenzO-HST (HST fonctionnalisé avec l'alcool benzylique), dans différent solvants : le toluène, l'eau et l'acétonitrile. A l'instar des expériences menées sur C_{12}O-HST, le toluène ne permet pas d'exfolier BenzO-HST même si plus de matière en solution a été détectée tandis que l'acétonitrile est encore un bon solvant d'exfoliation. Ces expériences confirment la nécessité de la polarité du solvant ainsi que d'adapter le solvant en fonction de la molécule greffée.

Les conditions d'exfoliation optimales sont donc l'utilisation d'un solvant polaire comme l'acétonitrile ou l'isopropanol (à adapter selon le matériau hybride), un taux de cisaillement de 11 500 rpm et un temps d'exfoliation de 1 heure. Ces conditions expérimentales seront utilisées dans les parties suivantes.

II.4 Caractérisation avancée des nanofeuillets hybrides

Les nanofeuillets obtenus dans les conditions optimales d'exfoliation par assistance de force de cisaillement doivent ensuite être caractérisés. Pour des questions évidentes de greffage covalent résistant à l'exfoliation, de signature spectroscopique définie et par simplicité, les caractérisations avancées ont été faites sur l'hydrides lamellaires $C_{10}PO_3$-HST. La suspension obtenue après exfoliation subit un processus de centrifugation sélective pour éliminer les nanomatériaux trop épais ou non-exfoliés. Ainsi la suspension analysée contient majoritairement des objets exfoliés et/ ou de plus petites tailles. La caractérisation des nanofeuillets s'est faite en deux volets. Tout d'abord, les nanomatériaux sont caractérisés par microscopie MEB, MET ou AFM après dépôt sur un substrat adapté. Dans un second temps, les nanofeuillets sont caractérisés en solution par diffusion de lumière, statique ou dynamique (SLS ou DLS) et par diffusion des rayons X à petits et grands angles (SAXS et WAXS).

Dans un premier temps, les nanofeuillets sont analysés en MEB en mode STEM (***Figure 10 (a)***). Les nanomatériaux observés sont de taille latérale de l'ordre du micromètre, même si des nanomatériaux plus petits non-exfoliés sont visibles. L'analyse EDX associé au MEB permet de déterminer la composition élémentaire des nanomatériaux. Les éléments constitutifs du feuillet inorganique comme le tantale et le strontium sont détectés mais aussi le phosphore qui est relatif aux molécules d'acide 1-décylphosphonique greffées Cependant, l'imagerie MEB ne permet pas de donner des informations structurales ou encore déterminer l'épaisseur des feuillets. C'est pourquoi, la microscopie MET est plus adaptée pour une étude approfondie des feuillets. Dans les images ***Figure 10 (b)*** et ***(c)***, des nanofeuillets.de quelques monocouches sont observés, l'épaisseur étant suggérée par les tranches des feuillets perpendiculaires à la membrane.

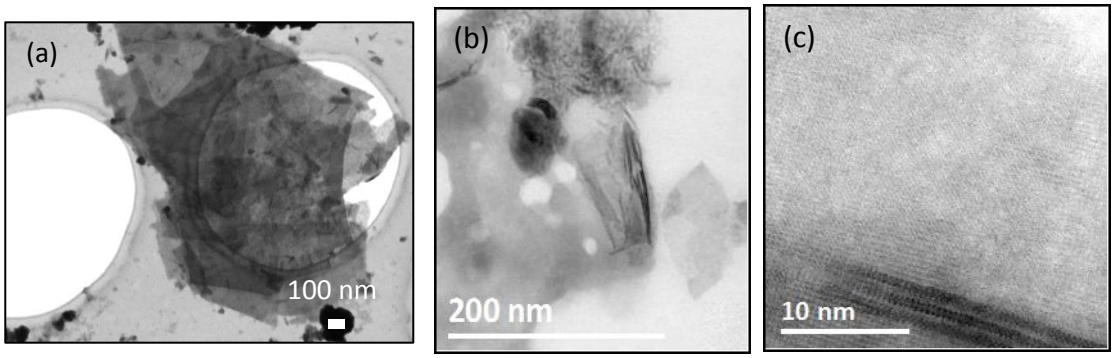

Figure 10 : Image MEB d'un amas de nanofeuillets de grande taille latérale. (b) Images MET montrant à la fois un amas de nanofeuillets désordonnés, des nanofeuillets positionnés à plat et des feuillets positionnés horizontalement par rapport à la membrane.

Néanmoins, une méthode plus précise pour estimer l'épaisseur des nanomatériaux est de tracer leur profile en intensité comme montré dans la ***Figure 11***. En effet, en utilisant le mode STEM HAADF, il est possible de relier l'intensité à l'épaisseur du des nanomatériaux de par la dépendance de cette intensité avec le numéro atomique. Ainsi, il a été possible de déterminer l'intensité associée à une monocouche ainsi que celle d'agrégat de 3 à 6 feuillets.

De plus, l'imagerie MET permet par la diffraction électronique d'évaluer la cristallinité du matériau. A partir d'une monocouche, les paramètres de maille de la structure ont été estimés. Leurs valeurs concordent avec celles déterminées par diffraction des rayons X sur le composé hybride de départ. Ainsi, l'exfoliation n'a pas modifié la structure inorganique.

De même, la spectroscopie EELS associée au MET indique la présence des éléments constitutifs de la couche inorganique mais révèle aussi la présence de phosphore. Cette analyse confirme aussi le maintien de la fonctionnalisation au cours du processus d'exfoliation et de séparation.

Néanmoins, bien que la structure soit majoritairement intacte des défauts apparaissent dus à la fragmentation au cours de l'exfoliation, qui est d'autant plus importante avec une exfoliation mécanique. Par imagerie MET, il a été possible de mettre en évidence deux types de fragmentations comme prévu par A. Liscio *et al.*[31] Le premier produit des fragments de forme parallélépipédique tandis que le second type, qui se produit par la suite conduit à des fragments plus petits de forme variable. Outre ces fragmentations, des dommages sont induits lors de l'exfoliation formant des « trous » à la surface des nanofeuillets.

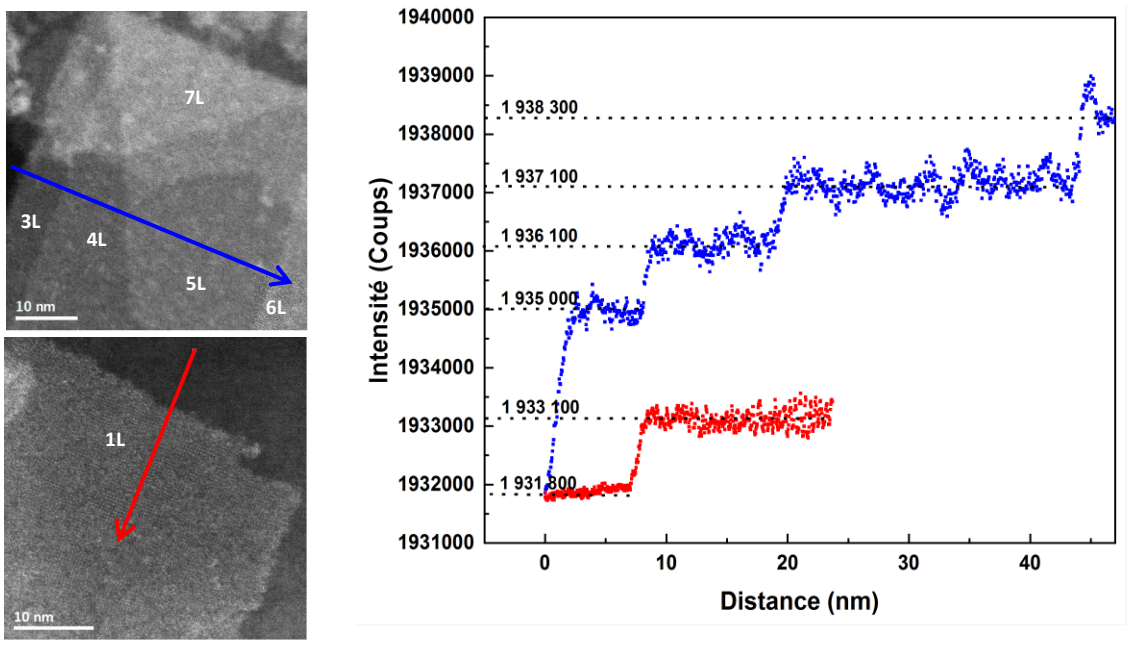

Figure 11: Images MET en mode STEM d'un amas de nanofeuillets et d'un monofeuillet de $C_{10}PO_3$-HST ainsi que le profil d'intensité correspondant.

Enfin, de manière complémentaire, la microscopie à force atomique (AFM) permet un estimation de l'épaisseur des nanofeuillets ainsi que d'estimer leur taille latérale. Cette technique nécessite le dépôt des nanomatériaux sur un substrat non-rugueux. Parmi les diverses méthodes de dépôt envisageables, nous avons opté pour de *drop-casting* de la suspension de nanofeuillets, à température ambiante, sur un substrat de silicium préalablement modifié par le PEI chargé.

Une image type d'AFM est montrée dans la ***Figure 12*** ainsi que les profils topographiques des nanofeuillets. Tout d'abord, il est à noter que la couverture en nanofeuillet n'est pas importante mais que des objets de quelques centaines de nanomètres en taille latérale sont observables. Les profils de hauteur

sont consistants avec des monocouches : l'épaisseur moyenne mesurée est d'environ 4 nm, proche de la valeur théorique de 3.3 nm pour des nanofeuillets de $C_{10}PO_3$-HST, prouvant une fois de plus la présence de la couche organique à la surface des feuillets.

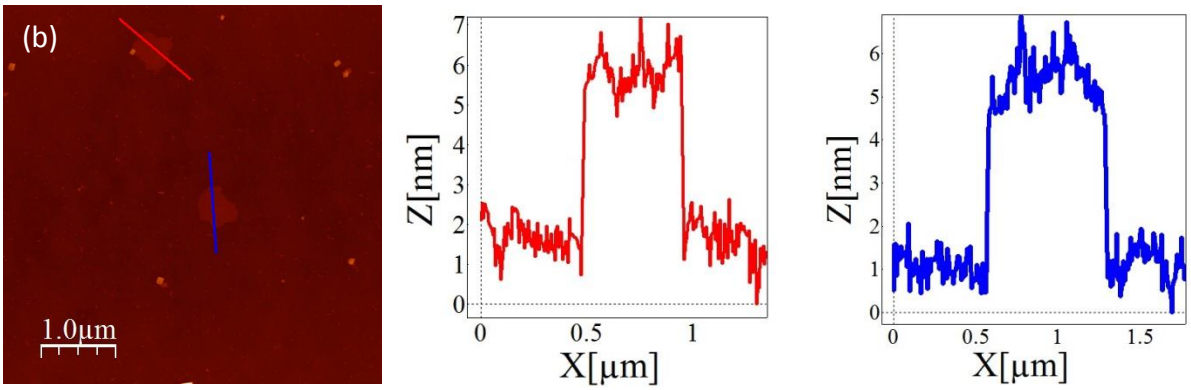

Figure 12: Image AFM de nanofeuillets de $C_{10}PO_3$-HST àprès leur dépôt sur un substrat fonctionnalisé par du PEI en drop-casting ainsi que le profil topographique correspondant.

Bien que les techniques de microscopie soient essentielles pour accéder à des informations structurales et compositionnelles des feuillets, l'estimation de la taille latérale par ces méthodes doit être fait sur un nombre important d'objets pour être pertinents et la phase de dépôt sur un substrat peut venir altérer/occulter une partie des objets. C'est pourquoi, une estimation de la taille moyenne globale des nanomatériaux en solution est nécessaire.

La diffusion de lumière, généralement appliqué à des nanoparticules sphériques monodisperses peut être appliquée à des objets plus anisotropes comme des feuillets. Les travaux de van der Kooij *et al*. ont montré que la diffusion statique et dynamique de la lumière permet d'accéder à la taille latérale moyenne, au coefficient de diffusion et de sédimentation des nanoplaquettes monodisperses de l'ordre d'une centaine de nanomètre. L'analyse des résultats de DLS et SLS fait un intervenir un modèle plus complexe que pour celui des sphères mais repose sur l'utilisation du facteur de structure des nanofeuillets assimilés à des cylindres.

Malheureusement, une application directe de ces travaux n'est pas envisageable dans notre cas : les nanofeuillets synthétisés sont de taille plus importante (hors du régime de Guinier) et présentent une certaine polydispersité. Il a été fait le choix d'utiliser le rayon de giration des objets pour par la suite accéder à leur taille latérale. En effet, le rayon de giration est indépendant du modèle choisi.

Tout d'abord, les profils d'intensité diffusée au cours du temps ont été mesurés à différents angles de diffusion, présentés dans la ***Figure 13 (Gauche)***. Une évolution temporelle de ces profils indique une légère sédimentation. Ainsi, une interpolation exponentielle a été utilisée à la fois pour extrapoler l'intensité diffusée à angle nul et pour déterminer le rayon de giration. Le profil d'intensité extrapolé à angle nul suit aussi une loi exponentielle et donc la même évolution temporelle que les autres profils d'intensité. Cela prouve la cohérence de la méthode.

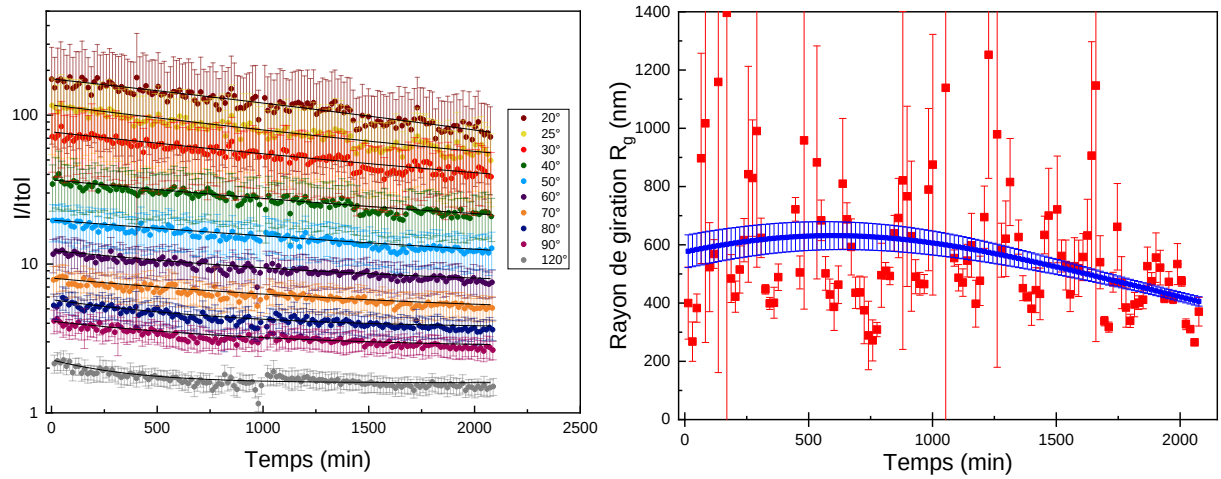

Figure 13: (Gauche) Evolution temporelle de l'intensité diffusée à plusieurs angles de diffusion. Les lignes noires correspondent à l'interpolation en utilisant un fit exponentiel. (Droite) Evolution temporelle rayon de giration apparent. La line continue bleue correspond aux valeurs obtenues avec un fit exponentiel tandis que les carrés rouges sont obtenus à partir d'un fit parabolique.

Ensuite, la détermination du rayon de giration se base sur les coefficients de la courbe extrapolée. Les résultats sont donnés dans la ***Figure 13 (Droite)*** par la courbe bleue. L'évolution du rayon de giration au cours du temps est due à la fois à la sédimentation progressive des nanomatériaux mais aussi de la méthode utilisée (barre d'erreur). Il est à noter qu'en utilisant une interpolation parabolique pour les profils d'intensité, le rayon de giration calculé est grandement modifié : son évolution temporelle est présentée dans ***Figure 13 (Droite)*** par les carrés rouges. Force est de constater que la non-monotonie de son évolution temporelle et la grande dispersité de ces valeurs. Ainsi, notre approche est très dépendante des choix d'interpolation et extrapolation.

En assimilant, les nanofeuillets à des disques, le rayon de giration conduit à une taille latérale moyenne de 1000 nm en fin d'expérience.

La même approche est effectuée pour les fonctions d'autocorrélation. Le coefficient de diffusion moyen déterminée conduit à une taille latérale moyenne de 800 nm en fin d'expérience. Ces deux valeurs de tailles latérales sont cohérentes entre elles mais aussi avec les données fournies par les différentes microscopies.

Une étude préliminaire de SAXS et WAXS a aussi été conduite pour déterminer l'épaisseur moyenne des nanomatériaux. Une suspension de nanofeuillets de $C_{10}PO_3$-HST a été mise à décanter. Après une semaine un échantillonnage vertical de cette solution fut fait et ces échantillons furent analysés en SAXS. Il a été montré que les objets les plus stables sont de petits nanomatériaux de taille latérale et d'épaisseur proche de 30 nm (assimilable à des nanoparticules). Ensuite, des nanofeuillets avec une épaisseur moyenne estimée de 9 couches ont été détectées. Le dernier échantillon contenant contient des matériaux plus épais et non-exfoliés.

Une étude plus approfondie et une meilleure préparation des échantillons sont nécessaires pour être conclusif avec les données de SAXS et WAXS

II.5 Stratégies de réassemblage des nanofeuillets hybrides

Après avoir synthétisé des nanofeuillets fonctionnalisés et les avoir caractérisés, des stratégies d'assemblage de nanofeuillets, basées sur les fonctionnalités de leur partie organique, ont été étudiées.

La première fait intervenir des nanofeuillets obtenus à partir de $PyrC_4O$-HST : la structure polycyclique des pyrènes permet en effet leur couplage par interaction π-π avec du graphène. La ***Figure 14*** montre des images MEB de l'hétérostructure produite par l'assemblage de nanofeuillets d'oxyde fonctionnalisés avec des pyrènes et du graphène. L'absence de nanofeuillets isolés est la preuve d'un assemblage spécifique et dirigé par des interactions moléculaires.

Par ailleurs les propriétés de luminescence des composés hybrides contenant des pyrènes ont été étudiées, tant sous forme de matériau lamellaires que sous forme exfoliée.

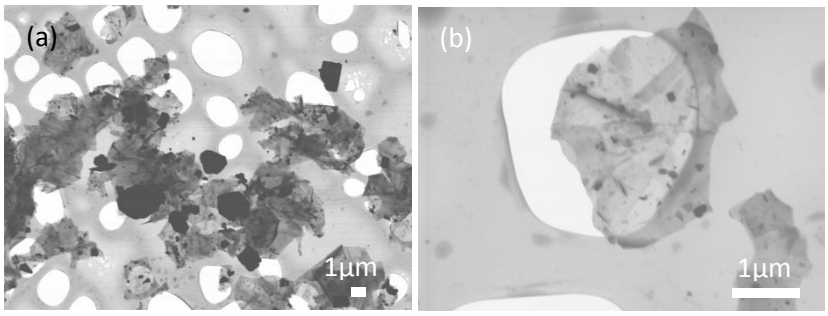

Figure 14: (a) et (b) Images MEB de l'assemblage de nanofeuillets de $PyrC_4O$-HST et de nanofeuillets de graphène.

La seconde stratégie de réassemblage de nanofeuillets est dirigée par des interactions hydrogènes. Précédemment, le composé hybride Thymidine –HST a été obtenu. De manière analogue, le composé Adenosine-HLN a été synthétisé et tous deux ont été exfoliés par assistance de force de cisaillement en suivant selon les optimisations développées dans ces travaux. Les nanofeuillets correspondants ont été alternativement déposés sur un substrat par drop-casting. Bien que prometteuse, cette approche nécessite des améliorations pour maximiser la couverture du substrat par les nanofeuillets et pour optimiser l'assemblage.

Enfin, la troisième voie de réassemblage fait intervenir une liaison covalente : celle Au-S qui est connu pour être facilement produite avec des composés thiolés sur des surfaces d'or (substrat ou nanoparticules). Le composé hybride MPTS-HST présente un thiol terminal, et après exfoliation, les nanofeuillets résultants ont été déposés sur un substrat d'or. L'analyse et l'optimisation de cette stratégie est en cours.

III. Conclusion

La stratégie de synthèse de nanofeuillets d'oxyde fonctionnalisés développées dans cette étude se décompose en deux étapes : synthèse de composés lamellaires hybrides à partir d'un oxyde chargé et exfoliation en phase liquide.

Dans ces travaux, de nombreux hybrides lamellaires ont été synthétisés à partir de l'oxyde HST par assistance de rayonnement micro-onde. Il a été prouvé que la fonction d'ancrage de type acide phosphonique permettait un greffage covalent fort tandis qu'un greffage à partir d'organosilane autorisait l'ajout de fonctionnalités. En outre plusieurs molécules à structure variable ont été greffées avec succès dans l'espace interlamellaire.

L'exfoliation par échange d'ion en utilisant l'ion TBA^+ comme agent d'exfoliation n'est pas adaptée aux composés fonctionnalisés, à cause de la dégradation du greffage initial dans le cas d'alcool ou d'amines. A l'opposé, l'exfoliation par assistance de polymères comme les PEGs permet d'exfolier efficacement les composés hybrides. Cependant, il reste à vérifier que la fonctionnalisation est maintenue.

L'exfoliation par assistance de force de cisaillement est inefficace sur HST : les forces électrostatiques en jeu assurent une trop forte cohésion entre les feuillets. L'hybridation permet de réduire ces forces et permet d'utiliser cette méthode. L'étude des paramètres d'exfoliation comme le solvant, le temps d'exfoliation ou le taux de cisaillement a permis de déterminer les conditions expérimentales optimales.

Ensuite, les nanofeuillets ont été caractérisés de manière plus approfondies par microscopie. Il a été prouvé que la fonctionnalisation par un acide phosphonique est conservée tout au long du processus d'exfoliation mécanique et que la structure inorganique est elle aussi maintenue. La taille latérale et l'épaisseur des nanofeuillets peuvent aussi être évaluées. Une caractérisation inhabituelle et inédite par diffusion de lumière fournit la taille latérale moyenne des nanomatériaux, de l'ordre de 1000 nm, cohérente avec toutes les autres techniques.

Enfin, des stratégies de réassemblages se basant sur les interactions moléculaires des nanofeuillets fonctionnalisés ont été mises en place. Bien que ces résultats soient préliminaires, ils sont prometteurs pour synthétiser de nouvelles hétérostructures aux propriétés inédites.

Bibliographie

(1) Ganter, P.; Lotsch, B. V. Photonic Nanoarchitectonics with Stimuli-Responsive 2D Materials. *Mol. Syst. Des. Eng.* **2019**, *4* (3), 566–579.

(2) Heard, C. J.; Čejka, J.; Opanasenko, M.; Nachtigall, P.; Centi, G.; Perathoner, S. 2D Oxide Nanomaterials to Address the Energy Transition and Catalysis. *Advanced Materials* **2019**, *31* (3), 1801712.

(3) Tan, C.; Cao, X.; Wu, X.-J.; He, Q.; Yang, J.; Zhang, X.; Chen, J.; Zhao, W.; Han, S.; Nam, G.-H.; Sindoro, M.; Zhang, H. Recent Advances in Ultrathin Two-Dimensional Nanomaterials. *Chem. Rev.* **2017**, *117* (9), 6225–6331.

(4) Boyd, I. W. Thin Film Growth by Pulsed Laser Deposition. *Ceramics International* **1996**, *22* (5), 429–434.

(5) Gupta, A.; Sakthivel, T.; Seal, S. Recent Development in 2D Materials beyond Graphene. *Progress in Materials Science* **2015**, *73*, 44–126.

(6) Schaak, R. E.; Mallouk, T. E. Perovskites by Design: A Toolbox of Solid-State Reactions. *Chem. Mater.* **2002**, *14* (4), 1455–1471.

(7) Uppuluri, R.; Gupta, A. S.; Rosas, A. S.; Mallouk, T. E. Soft Chemistry of Ion-Exchangeable Layered Metal Oxides. *Chem. Soc. Rev.* **2018**, *47* (7), 2401–2430.

(8) Osada, M.; Sasaki, T. Nanosheet Architectonics: A Hierarchically Structured Assembly for Tailored Fusion Materials. *Polymer Journal* **2015**, *47* (2), 89.

(9) Coleman, J. N.; Lotya, M.; O'Neill, A.; Bergin, S. D.; King, P. J.; Khan, U.; Young, K.; Gaucher, A.; De, S.; Smith, R. J.; Shvets, I. V.; Arora, S. K.; Stanton, G.; Kim, H.-Y.; Lee, K.; Kim, G. T.; Duesberg, G. S.; Hallam, T.; Boland, J. J.; Wang, J. J.; Donegan, J. F.; Grunlan, J. C.; Moriarty, G.; Shmeliov, A.; Nicholls, R. J.; Perkins, J. M.; Grieveson, E. M.; Theuwissen, K.; McComb, D. W.; Nellist, P. D.; Nicolosi, V. Two-Dimensional Nanosheets Produced by Liquid Exfoliation of Layered Materials. *Science* **2011**, *331* (6017), 568–571.

(10) Paton, K. R.; Varrla, E.; Backes, C.; Smith, R. J.; Khan, U.; O'Neill, A.; Boland, C.; Lotya, M.; Istrate, O. M.; King, P.; Higgins, T.; Barwich, S.; May, P.; Puczkarski, P.; Ahmed, I.; Moebius, M.; Pettersson, H.; Long, E.; Coelho, J.; O'Brien, S. E.; McGuire, E. K.; Sanchez, B. M.; Duesberg, G. S.; McEvoy, N.; Pennycook, T. J.; Downing, C.; Crossley, A.; Nicolosi, V.; Coleman, J. N. Scalable Production of Large Quantities of Defect-Free Few-Layer Graphene by Shear Exfoliation in Liquids. *Nature Materials* **2014**, *13* (6), 624–630.

(11) Biccai, S.; Barwich, S.; Boland, D.; Harvey, A.; Hanlon, D.; McEvoy, N.; Coleman, J. N. Exfoliation of 2D Materials by High Shear Mixing. *2D Mater.* **2019**, *6* (1), 015008.

(12) Sasaki, T.; Watanabe, M.; Hashizume, H.; Yamada, H.; Nakazawa, H. Macromolecule-like Aspects for a Colloidal Suspension of an Exfoliated Titanate. Pairwise Association of Nanosheets and Dynamic Reassembling Process Initiated from It. *J. Am. Chem. Soc.* **1996**, *118* (35), 8329–8335.

(13) Sasaki, T.; Watanabe, M. Osmotic Swelling to Exfoliation. Exceptionally High Degrees of Hydration of a Layered Titanate. *J. Am. Chem. Soc.* **1998**, *120* (19), 4682–4689.

(14) Ebina, Y.; Sasaki, T.; Watanabe, M. Study on Exfoliation of Layered Perovskite-Type Niobates. *Solid State Ionics* **2002**, *151* (1), 177–182.

(15) Ma, W.; Ma, R.; Wang, C.; Liang, J.; Liu, X.; Zhou, K.; Sasaki, T. A Superlattice of Alternately Stacked Ni–Fe Hydroxide Nanosheets and Graphene for Efficient Splitting of Water. *ACS Nano* **2015**, *9* (2), 1977–1984.

(16) Osada, M.; Sasaki, T. Nanoarchitectonics in Dielectric/Ferroelectric Layered Perovskites: From Bulk 3D Systems to 2D Nanosheets. *Dalton Trans.* **2018**, *47* (9), 2841–2851.

(17) Ariga, K.; Komatsu, H.; Hill, J. P. Nanophotonics and Supramolecular Chemistry. *Nanophotonics* **2013**, *2* (4), 265–277.

(18) Sangian, D.; Ide, Y.; Bando, Y.; Rowan, A. E.; Yamauchi, Y. Materials Nanoarchitectonics Using 2D Layered Materials: Recent Developments in the Intercalation Process. *Small* **2018**, *14* (33), 1800551.

(19) Quinn, J. F.; Johnston, A. P. R.; Such, G. K.; Zelikin, A. N.; Caruso, F. Next Generation, Sequentially Assembled Ultrathin Films: Beyond Electrostatics. *Chem. Soc. Rev.* **2007**, *36* (5), 707–718.

(20) Wang, Y.; Delahaye, E.; Leuvrey, C.; Leroux, F.; Rabu, P.; Rogez, G. Efficient Microwave-Assisted Functionalization of the Aurivillius-Phase $Bi_2SrTa_2O_9$. *Inorg. Chem.* **2016**, *55* (8), 4039–4046.

(21) Wang, Y.; Nikolopoulou, M.; Delahaye, E.; Leuvrey, C.; Leroux, F.; Rabu, P.; Rogez, G. Microwave-Assisted Functionalization of the Aurivillius Phase $Bi_2SrTa_2O_9$: Diol Grafting and Amine Insertion vs. Alcohol Grafting. *Chem. Sci.* **2018**, *9* (35), 7104–7114.

(22) Akbarian-Tefaghi, S.; Teixeira Veiga, E.; Amand, G.; Wiley, J. B. Rapid Topochemical Modification of Layered Perovskites via Microwave Reactions. *Inorg. Chem.* **2016**, *55* (4), 1604–1612.
(23) Honda, M.; Oaki, Y.; Imai, H. Hydrophobic Inorganic–Organic Composite Nanosheets Based on Monolayers of Transition Metal Oxides. *Chem. Mater.* **2014**, *26* (11), 3579–3585.
(24) Nakada, G.; Imai, H.; Oaki, Y. Few-Layered Titanate Nanosheets with Large Lateral Size and Surface Functionalization: Potential for the Controlled Exfoliation of Inorganic–Organic Layered Composites. *Chem. Commun.* **2018**, *54* (3), 244–247.
(25) Han, Y.-S.; Park, I.; Choy, J.-H. Exfoliation of Layered Perovskite, $KCa_2Nb_3O_{10}$,into Colloidal Nanosheets by a Novel Chemical Process. *J. Mater. Chem.* **2001**, *11* (4), 1277–1282.
(26) Shimada, A.; Yoneyama, Y.; Tahara, S.; Mutin, P. H.; Sugahara, Y. Interlayer Surface Modification of the Protonated Ion-Exchangeable Layered Perovskite $HLaNb_2O_7$.xH2O with Organophosphonic Acids. *Chem. Mater.* **2009**, *21* (18), 4155–4162.
(27) Sylvester, P.; Cahill, R.; Clearfield, A. Pillaring of Layered Tetravalent Metal Phosphates and Oxides Using (3-Aminopropyl)Trimethoxysilane. *Chem. Mater.* **1994**, *6* (10), 1890–1898.
(28) Akbarian-Tefaghi, S.; Rostamzadeh, T.; Brown, T. T.; Davis-Wheeler, C.; Wiley, J. B. Rapid Exfoliation and Surface Tailoring of Perovskite Nanosheets via Microwave-Assisted Reactions. *ChemNanoMat* **2017**, *3* (8), 538–550
(29) Alexandre, M.; Dubois, P. Polymer-Layered Silicate Nanocomposites: Preparation, Properties and Uses of a New Class of Materials. *Materials Science and Engineering: R: Reports* **2000**, *28* (1), 1–63.
(30) Cunningham, G.; Lotya, M.; Cucinotta, C. S.; Sanvito, S.; Bergin, S. D.; Menzel, R.; Shaffer, M. S. P.; Coleman, J. N. Solvent Exfoliation of Transition Metal Dichalcogenides: Dispersibility of Exfoliated Nanosheets Varies Only Weakly between Compounds. *ACS Nano* **2012**, *6* (4), 3468–3480.
(31) Liscio, A.; Kouroupis-Agalou, K.; Betriu, X. D.; Kovtun, A.; Treossi, E.; Pugno, N. M.; De Luca, G.; Giorgini, L.; Palermo, V. Evolution of the Size and Shape of 2D Nanosheets during Ultrasonic Fragmentation. *2D Mater.* **2017**, *4* (2), 025017.

Frédéric PAYET

Exfoliation d'oxydes lamellaires fonctionnalisés : approches de synthèse et caractérisations avancées. Vers un réassemblage non-électrostatique

Résumé

L'objectif de cette thèse est d'étudier la formation de nanofeuillets d'oxydes fonctionnalisés en solution en vue de les intégrer ensuite sous forme des architectures bidimensionnelles multimatériaux. La voie de synthèse de ces nanomatériaux débute par la conception d'un composé lamellaire hybride. L'oxyde à structure pérovskite considéré voit ainsi son espace interlamellaire modifié par des molécules organiques, choisies pour leur propriétés physiques ou leur potentielles interactions moléculaires pour un réassemblage non-électrostatique. Le composé hybride résultant est ensuite exfolié pour obtenir les nanofeuillets fonctionnalisés. Parmi les diverses méthodes possibles, l'exfoliation par assistance de force de cisaillement, innovante pour les oxydes lamellaires, a été mise en œuvre. Après optimisation des paramètres d'exfoliation, des suspensions colloïdales de nanofeuillets sont obtenues. Ces derniers sont caractérisés tout d'abord par différentes techniques de microscopies, permettant d'évaluer leur distribution en taille, en épaisseur et de confirmer le maintien de la fonctionnalisation au cours du procédé d'exfoliation. Ensuite, les suspensions sont étudiées par des techniques de diffusion, caractérisations non-triviales pour des objets bidimensionnels, pour estimer une épaisseur et une taille latérale moyenne. Enfin, des stratégies de réassemblage de ces nanomatériaux ont été définies et préliminairement testée comme preuve de concept et les premiers résultats préliminaires sont rapportés.

Mots clés: oxydes lamellaires hybrides, exfoliation par force de cisaillement, nanofeuillets fonctionnalisés, réassemblage non-électrostatique

Résumé en anglais

The goal of this PhD work is the study of the formation of functionalized oxide nanosheets in solution for their subsequent assembly into two dimensional heterostructures. The synthetic approach starts with the design of hybrid layered materials. The chosen oxide, with perovskite-like structure, is grafted with organic moieties, designed for their physical properties or their potentiality in terms of non-electrostatic re-assembly. The resulting layered hybrid is then exfoliated to lead to the corresponding functionalized nanosheets. Among all exfoliation method, the shear-force assisted liquid exfoliation is notably studied. After an optimization of the experimental settings, colloidal suspensions of nanosheets are obtained. The nanomaterials are first characterized by microscopic techniques to assess their size and thickness distribution while also probing the preservation of the functionalization during the process. Then, the suspensions are studied scattering techniques, non-trivial techniques for 2D materials, to estimate the mean thickness and lateral size of the nanosheets in solution. Finally, strategies of re-assembly of the functionalized nanosheets are presented, based on the functionality brought by the organic moieties and preliminary results are described

Keywords: hybrid layered oxides, shear-force exfoliation, functionalized nanosheets, non-electrostatic reassembly.